THE UNIVERSITY *of* EDINBURGH

Subduction zone processes and continental crust formation in the southern Central Andes: Insights from geochemistry and geochronology

Rosemary Ellen Jones

THE UNIVERSITY *of* EDINBURGH

A thesis submitted for the degree of Doctor of Philosophy

2014

Declaration

I declare that this thesis has been composed solely by myself and that it has not been submitted, either in whole or in part, in any previous application for a degree. Except where otherwise acknowledged, the work presented is entirely my own.

Rosemary Ellen Jones

Lay summary of Thesis

Subduction zones are convergent plate boundaries where one tectonic plate moves under another. Tectonic plates act as conveyor belts and transport material, including water, from the surface into the mantle. Along the western edge of South America, oceanic plates have been subducting beneath the continental part of the South American plate since the Jurassic (~ 200 Ma). As the oceanic plate (including sediments) is subducted, it dehydrates and causes melting in the mantle, which results in volcanism and intrusive igneous activity in the overlying Andean Cordillera. This igneous activity generates new continental crust and transports certain elemental components from the subducting slab back to the crust. Advancing our understanding of the processes that result in element cycling in subduction zones is core to this thesis. A suite of Late Cretaceous (~ 70 Ma) to Late Miocene (~6 Ma) volcanic and intrusive igneous rocks were sampled in the southern Central Andes and are used to track changes in the subduction zone over time.

As melts from the mantle travel through the crust towards the surface, because of their higher temperatures, they can melt and incorporate the surrounding crust. This process is called assimilation and it affects the composition of the magma. New geochemical evidence presented here suggests that before significant compression and uplift of the Andes (before ~25 Ma), when the continental crust was thinner, mantle-derived melts assimilated very little of the existing continental crust. These magmas cooled at depths of ~5 km below the surface and formed large igneous intrusions running parallel with the western edge of South America. However, the younger volcanic and intrusive rocks, which formed during the uplift of the Andes, display evidence for the assimilation of significantly older crust (up to 1300 million years old) en route to the surface.

Certain elements, such as boron which is mobile in fluids, can be analysed in igneous rocks in order to assess the contributions from different sources (e.g. oceanic crust and sediments) to the melts generated. Here boron isotopes were used to track the importance of fluids released from the subducting plate on the composition of melts produced. New data suggest that between 24 and 16 Ma these fluids dominate the isotopic signal. This can be correlated with a change in angle of the subducting plate, which went from subducting relatively steeply into the mantle (~45°) at ~24Ma, to subducting more shallowly (<30°). It is important to look at the processes affecting the geochemistry of igneous rocks in relatively modern subduction zones as this allows the plate tectonic settings for igneous rocks of unknown origin to be identified.

'It always seems impossible until it's done' – Nelson Mandela (1918 – 2013)

Acknowledgements

First and foremost I would like to acknowledge and thank my primary supervisors. I am exceedingly grateful to Linda Kirstein, my 'onsite' supervisor, for providing me with a great deal of help, encouragement and support over the past four years. Thank you for always providing me with guidance and advice, or if you were unable to, for finding me the person who could. I am also grateful for your continued enthusiasm, even after reading manuscripts numerous times. I would also like to express my gratitude to Simone Kasemann, my 'remote' supervisor, for many interesting discussions and for always making time for meetings, both virtual and face to face, often accompanied by a glass of champagne.

In addition to my primary supervisors I have benefitted from help and guidance from numerous others. Tim Elliott is thanked for numerous engaging discussions and for improving various Chapters of this thesis. Bruno Dhuime not only provided technical assistance in conducting hafnium isotopes analysis but was also forthcoming with helpful suggestions and constructive comments on various manuscripts. I am exceedingly grateful to Vanesa Litvak who has been a constant source of knowledge relating to my field area, both geologically and logistically. Vanesa also kindly provided additional samples for this study, from which this project has greatly benefitted.

I would also like to take this opportunity to sincerely thank Richard Hinton, John Craven (sorry!) and Cee-Jan de Hoog for their continued help, support and encouragement, as well as for all that they have taught me over the past four years. Thank you for the endless advice, discussions of error propagation, provision of excellent tweezers, and for sharing my pain through tricky sample preparation. Thanks also for the many cups of tea and coffee, countless biscuits, and numerous beers which helped to keep me going through it all. It is no over statement to say that I could not have achieved this without you.

Funding for this project was provided by a NERC. This project also benefitted from support from the NERC ion probe steering committee. Additional financial support for the fieldwork involved in this project was provided by a scholarship funded by Derek and Maureen Moss and awarded by the University of Edinburgh. I would like to express my gratitude to Derek and Maureen for their financial support of this project, without which it would not have been possible.

I was fortunate enough during my PhD to partake in fieldwork to the Chilean and Argentinean Andes. Firstly, I would like to thank Linda and Simone for supporting me in this. Dante Scatolon is thanked for being an excellent guide and driver, as well as for teaching me about the Andes and life in Argentina. Eduardo Campos is

thanked for pre-fieldtrip logistical advice and for providing assistance in dealing with the Chilean postal service. Ben Heit is thanked for his assistance in driving and logistics, but mainly for introducing me to fernet-coke and the Argentinean barbeque. I would also like to extend my thanks to Ben's friends and family for being so hospitable during my stay in Salta.

I have been fortunate enough during this project to have used some of the most sophisticated analytical equipment available. Once again, thank you to John (apologies again), Richard and Cees-Jan for help and assistance in all things ion-probe related and for giving up numerous evenings and weekends in order to help me. I would like to thank Nic Oldling for assistance in XRF analysis and Katarzyna Sokol for aiding in sample preparation. I am grateful to Nicola Cayzer for guidance and advice in SEM imaging and for entrusting me to look after 'Sammy the SEM' for a short time – I really enjoyed it. Mike Hall is thanked for preparing the numerous thin sections required by this study and for advice regarding sample preparation. I am grateful to Robert MacDonald for advice relating to mineral separation procedures and for training in the use of the Gemini table and heavy liquids. I appreciated the assistance of guidance of Valerie Olive in conducting ICP-MS analysis. Chris Hayward is thanked for assistance in use of the electron microprobe and Bruno Dhuime for help and guidance in laser ablation ICP-MS. Igor Nikoghosyan is thanked for providing advice on melt inclusion re-homogenisation and for taking the time to show me the setup in Amsterdam. I would also like to extend my thanks to a number of the lecturing and research staff at the University of Edinburgh, including Mikael Attal, Hugh Sinclair, Godfrey Fitton, Alan Hastie, Barry Dawson, Thor Thordarson, Geoffrey Bromiley, Rachel Wood, Andrew Curtis, John Stevenson, and Simon Harley, who have provided me with useful discussions and helpful advice over the years.

I have been very fortunate during my time in Edinburgh to have been surrounded by a fun and supportive group of postgraduate students. In particular I would like to thank the following people for providing endless support, understanding and many welcome distractions (usually involving bikes, mountains and beer) over the last four years; Niklas Hienmann, Simon Haunch, Jamie Stewart, Jen Roberts, Matt Booth, Robyn Tuerena, Matt Clarkson, Maddy-Maddy-Berg, Simon King, Mark Beaumont, Matt Hiscock, Andrew Miles, Lizzie Entwistle, Racheal Kilgallon, Luke Ridley, Sophie Harland, Sigrun Stanton, Laura Comeau, Martin Hurst, Gillian McCay and Tom Russon. A special thank you goes to Alex 'eyeless trilobite' de Joux for the many great times whilst living together, working together, exercising together… Alex, thank you also for your understanding of my perfectionist ways and for dragging me away when I needed it.

I would like to thank Tom Rumsey continuing support and for being a most excellent field assistant/rock smasher/off-road driver and 'orderer' of breakfast eggs. Thank you also for being a calming influence as I worried if my samples would ever make it out of Santiago Airport. And for the record – that 'Oligocene' sample really was useful!

Finally I would like to thank my family. Thank you to my little sisters Ally and Clare for your understanding of my 'fossil' ways and for always helping me to see the funny side of things. Ally your efforts on the table formatting are greatly appreciated and I hope this stands you in good stead as a new managing editor! Mum and Dad, I am sincerely grateful for your unwavering support, particularly during the 'write up' phase of my PhD. Thank you for always providing and listening ear and for trying to help me in any way you could (in my mums case this usually involved baking a cake). And lastly I would like to thank my Grandad, Ralph Jones, for inspiring me about rocks and fossils as a child on Charmouth beach and for setting me off on this geological journey. I wish you had been able to see this.

Abstract

Subduction zones, such as the Andean convergent margin, are the sites at which new continental crust is generated, and where subducting material is either recycled to the crust via arc magmatism or transferred to the deep mantle. The composition of arc magmas and associated new continental crust reflects variable contributions from mantle, crustal and subducted reservoirs. Insights into crustal growth and recycling processes in the southern Central Andes, specifically in the Pampean flat-slab segment, have been gained by utilising a range of petrological, geochronological and geochemical techniques. These techniques have been applied to a suite of Late Cretaceous (~73 Ma) to Late Miocene (~6 Ma) intrusive (granitoids) and extrusive (basalts to rhyolites) arc rocks collected from an east - west transect across the Andean Cordillera. The oxygen and hafnium isotopic composition of the accessory mineral zircon allows mantle-derived melts contaminated with older, upper continental crustal to be identified. Boron isotopic compositions of melt inclusions, combined with concentrations of certain incompatible trace elements, can be used to assess the source and influence of fluids derived from subducting material on the melt source region. The southern Central Andes provides a particularly interesting area to study these processes as the thickness of the continental crust has increased significantly over the course of the Cenozoic (from ~35 km to >50 km) and the angle of the subducting Nazca plate has shallowed since ~18 Ma, causing the position of the volcanic arc to migrate to the east.

In order to unravel the complexities involved with constraining the contributions to arc magmas at an active continental margin, a range of geochronological, geochemical, and geothermobarometric techniques, including high resolution, micro-analysis of mineral phases and melt inclusions, have been applied. High resolution, U-Pb dating of magmatic zircon has improved regional stratigraphy in the Pampean flat-slab segment (between ~29 and 32 °S) and provided an accurate temporal constraint for geochemical and geothermobarometric data. The results of *in-situ* O and Lu-Hf isotope analysis of zircon show both distinct temporal and spatial variations across the Andean arc. The observed isotopic variability is attributed to variable contamination of mantle-derived melts with distinct Andean basement terranes, which vary east – west in composition and age.

'Mantle-like' $\delta^{18}O_{(zircon)}$ values, juvenile initial $\varepsilon Hf_{(zircon)}$ values and a lack of inherited, xenocrystic zircon cores, suggests the Late Cretaceous (~73 Ma) to Eocene (~39 Ma) plutons located in the Principal Cordillera of Chile, experienced very little interaction with the upper continental crust. Amphibole – plagioclase geothermobarometry indicates these calc-alkaline granitoids, which form extensive

north – south trending belts, were emplaced at shallow depths in the crust (~4 – 5 km). Therefore the Late Cretaceous to Late Eocene is interpreted as a period of significant upper crustal growth. The isotopic variability in the Late Oligocene (~26 Ma) to Late Miocene (~6 Ma) arc magmatic rocks demonstrates that during thickening of the continental crust and migration of the Andean arc to the east, arc magmas assimilated Late Paleozoic to Early Mesozoic basement. In addition, arc magmas erupted/emplaced in the Argentinean Precordillera (i.e. farthest east from the trench) assimilated a Grenville-aged (~ 1330 – 1030 Ma) basement. The youngest arc magmas (~6 Ma) erupted in the Frontal Cordillera also show evidence for the assimilation of this ancient basement terrane, potentially signalling under-thrusting beneath the Frontal Cordillera. Overall, the later part of the Cenozoic represents a period of crustal reworking.

Boron concentrations and isotope ratios measured in pyroxene hosted melt inclusions and for the first time in zircon hosted melt inclusions, are higher than the values expected for the mantle wedge and show significant variations with time. The source of the Paleocene (~61 Ma) arc magmas were influenced by fluids primarily derived from altered oceanic crust. Lower $\delta^{11}B$ values and boron concentrations obtained for Oligocene (25 – 23 Ma) arc magmatic rocks reflects a diminished influence of slab-derived fluids reflecting a greater depth to the top of the slab. Fluids derived from serpentinite influenced the source of the arc magmas after ~19.5 Ma. This has been linked with the intersection of the Juan Fernández Ridge, a volcanic seamount chain associated with hydrated and serpentinised oceanic lithosphere.

Table of Contents

Acknowledgements……..ii

Abstract……...v

Table of Contents...……vii

Chapter 1 – Introduction……..1

1.1 Introduction……..1

1.2 Aims and objectives…….3

1.3 A geological overview of the Andean margin……4

1.3.1 The Andean tectonic cycle……..6

1.3.2 Cenozoic arc magmatism in the Pampean flat-slab segment…….10

1.3.3 Justification of the region of study……..12

1.4 The generation of arc magmas and recycling processes at subduction zones……..13

1.4.1 Geochemical characteristics of arc magmas……...13

1.4.2 Recycling processes……14

1.4.2.1 The role of fluids……...16

1.4.2.2. The role of melts……18

1.5 Potential contributions to southern Central Andean arc magmas……..19

1.5.1 The slab component……...19

1.5.2 The crustal component……..20

1.6 Current evidence for the contamination of Cenozoic arc magmas in the Pampean flat-slab segment……...24

1.7 Thesis layout……...26

1.8 Research contributions……..28

1.8.1 Fieldwork and sample collection…….29

1.8.2 Sample preparation and analytical methods…….29

1.9 References……30

Chapter 2 – Petrogenetic constrainsts on the Late Cretaceous – Miocene arc magmas from the southern Central Andes from geochemistry, geochronology and geothermobarometry……..43

2.1 Author Contributions……44

2.2 Abstract……45

2.3 Introduction……47

2.4 Geological setting……...49

2.5 Arc magmatism and stratigraphy……51

2.6 Sample collection……57

2.7 Petrological descriptions……...57

2.8 Sample preparation and analytical methods……..66

2.8.1 Geochronology……...66

2.8.1.1 U-Pb dating……66

2.8.1.2 Ar-Ar dating……..68

2.8.2 Whole-rock major, trace and rare earth element analysis……..68

2.8.3 Mineral composition analysis……..70

2.8.3.1 Geothermobarometry……...70

2.9 Geochronological and geochemical results……71

2.9.1 U-Pb and Ar-Ar dating……..71

2.9.2 Major elements……....77

2.9.3 Trace elements (TE) and rare earth elements (REE)……..84

2.9.4 Mineral compositions ……88

2.9.5 Geothermobarometry……93

2.9.5.1 Mineral compositions……...93

2.9.5.2 Thermobarometric calculations……..93

2.9.5.3 Crystallisation temperatures, pressures and depths……....96

2.10 Discussion……..99

2.10.1 Crystallisation / equilibration depths of arc magmas over time…….99

2.10.2 Trace element systematics……...102

2.10.3 The origins of adakitic signatures……..106

2.10.4 Temporal variations in source and crustal contamination…….112

2.10.4.1 The Late Cretaceous – Eocene……..113

2.10.4.2 Plate reconfiguration and Late Oligocene to Early Miocene arc magmatism…….....116

2.10.4.3 The Mid to Late Miocene and the shallowing of the subducting slab…….123

2.10.4.4 Overall geochemical trends - increased enrichment with time…….125

2.11 Conclusions…….127

2.12 References……131

Chapter 3 – Continental crust formation in the southern Central Andes: new insights from O and Hf isotopes in zircon……...142

3.1 Author Contributions……..143

3.2 Abstract……..145

3.3 Introduction……...147

3.4 Subduction in the Central Andes……..148

3.5 Insights from the isotopic composition of zircon……....151

3.6 Results demonstrating across-arc variations……154

3.6.1 Oxygen isotopes……...158

3.6.2 Hafnium isotopes…….159

3.6.3 Inherited, xenocrystic zircon cores……161

3.7 Discussion …….162

3.7.1 Temporal and spatial variations in isotopic compositions……....162

3.7.1.1 Late Cretaceous – Eocene mantle derived melts…….162

3.7.1.2 Controls on Late Eocene – Late Miocene isotopic variability……163

3.8 Conclusions……...168

3.9 References……..171

Chapter 4 – Temporal variations in the influence of the subducting slab on Cenozoic, Andean arc magmas: Evidence from boron isotope systematics……...177

4.1 Author Contributions……..178

4.2 Abstract……..180

4.3 Introduction……...182

4.4 Geological Setting…….186

4.5 Sample selection and preparation……..190

4.6 Analytical Methods……..194

4.7 Results……195

4.7.1 The effect of differentiation on boron concentrations and isotope ratios……203

4.7.2 Intra-sample variations and the potential effects of melt inclusion re-homogenisation on boron concentrations and isotopic composition……205

4.7.3 Inter-sample variations……207

4.8 Discussion …….209

4.8.1 Potential sources of boron in southern Central Andean arc magmas……...209

4.8.2 Source variations with time……212

4.8.2.1 Paleocene; homogeneous slab-derived fluids…….215

4.8.2.2 Oligocene: a broad magmatic arc……..216

4.8.2.3 Miocene: subduction of a seamount chain……..219

4.9 Conclusions……...222

4.10 References……224

Chapter 5 – A discussion of the geodynamic evolution of the Pampean flat-slab segment, southern Central Andes, between the Late Cretaceous and the Late Miocene……233

5.1 Introduction……...233

5.2 The Late Cretaceous – Early Eocene (~75 – 51 Ma)……..234

5.3 The Early Eocene to Early Oligocene (~50 – 27 Ma)……237

5.4 The Late Oligocene – Early Miocene (~26 – 20 Ma)……242

5.5 Early – Mid Miocene (~19 – 14 Ma)……246

5.6 Mid – Late Miocene (~13 – 6 Ma)……...249

5.7 References……255

Chapter 6 – Conclusions, limitations and recommendations for further work…259

6.1 Conclusions……...259

6.1.1 Timing and duration of arc magmatism in the southern Central Andes……...259

6.1.2 Variable contamination of mantle-derived melts……260

6.1.3 The source and influence of slab-derived fluids……..262

6.2 Limitations of the study……...264

6.3 Recommendations for future work……267

6.4 References……..271

Appendix 1……..274

1.1 U-Pb dating of zircon……...274

1.1.1 Background information……274

1.1.2 Sample preparation……..274

1.1.3 Mineral separation of zircon……...275

1.1.3.1 Density separation using a Gemini table……275

1.1.3.2 Magnetic separation……275

1.1.3.3 Heavy liquid separation……276

1.1.4 Zircon mounting and imaging……...276

1.1.5 Analytical conditions……...277

1.1.6 Data collection……..278

1.1.7 Data correction and reduction……278

1.1.7.1 Calibration of Pb/U ratios……..279

1.1.7.2 Correction for common Pb…….279

1.1.7.3 Correction for 230Th disequilibrium……280

1.1.8 Calculation of Th/U and elemental abundances……..281

1.1.9 Data processing……281

Appendix 1.2 Whole rock major, trace and rare-earth element analysis……...283

1.2.1 Sample preparation……..283

1.2.2 Sample preparation for XRF analysis ……...283

1.2.3 XRF analysis……..284

1.2.4 Sample preparation for ICP-MS analysis……..288

1.2.5 ICP-MS analysis……289

1.2.6 Comparison and evaluation of trace element and rare-earth element concentrations obtained by XRF and ICP-MS……...291

Appendix 1.3 Mineral analysis…….293

Appendix 1.4 Photomicrographs showing the mineralogy and texture of the intrusive and extrusive samples analysed for geothermobarometry with EMPA analysis locations highlighted……..296

Appendix 1.5 Representative petrographic descriptions…….297

1.5.1 Cogotí Supergroup……...297

1.5.1.1 Granite - AM0806……297

1.5.1.2 Granodiorite – AM0816……..297

1.5.1.3 Syeno-diorite – AM0824…….298

1.5.2 Río Frío Basalts…….299

1.5.2.1 Basaltic – Tachy-andesite – RF17……..299

1.5.3 Los Elquinos Formation……..299

1.5.3.1 Basalitic andesite – RJ1111…….299

1.5.4 Tierras Blancas Caldera……...300

1.5.4.1 Amphibole diorite – RJ1106……...300

1.5.5 Bocatoma Unit……..300

1.5.5.1 Andesite - AM0867/68……300

1.5.6 Tilito Formation (Lower Doña Ana Group)……301

1.5.6.1 Rhyolitic ignimbrite – AM0846……301

1.5.7 Las Maquinas Basalts……...301

1.5.7.1 Basalt – MQ8……301

1.5.8 Miocene Intrusives……...302

1.5.8.1 Granodiorite – RJ11A14……..302

1.5.9 Escabroso Formation (Upper Doña Ana Group)……302

1.5.9.1 Basaltic andesite – MQ158……302

1.5.9.2 Andesite – trachy-andesite – 1026……303

1.5.10 Cerro de las Tórtolas Formation……304

1.5.10.1 Trachy-andesite – RF62……304

1.5.11 Upper Cerro de las Tórtolas Formation……304

1.5.11.1 Trachy-andesite – MQ28……..304

1.5.12 Tertiary Intrusives……305

1.5.12.1 Trachy-dacite - RJ11A15……...305

1.5.13 Vacas Heladas Ignimbrites……306

1.5.13.1 Rhyolitic crystal tuff - MQ33……...306

Appendix 1.6 Thin section photomicrographs……307

1.6.1 Photomicrographs showing the mineralogy and texture of the Cogotí Supergroup……307

1.6.2 Photomicrographs showing the mineralogy and texture of the Río Frío Basalts, Los Elquinos Formation, samples of the Tierras Blancas Caldera and Botacoma Unit……308

1.6.3 Photomicrographs showing the mineralogy and texture of the Tilito Formation (Lower Doña Ana Group)……309

1.6.4 Photomicrographs showing the mineralogy and texture of the Las Maquinas Basalts and the Miocene Intrusives……..310

1.6.5 Photomicrographs showing the mineralogy and texture of the Escabroso Formation (Upper Doña Ana Group) and the Cerro de las Tórtolas Formation……311

1.6.6 Photomicrographs showing the mineralogy and texture of the Upper Cerro de las Tórtolas Formation, Tertiary Intrusives and Vacas Heladas Ignimbrites……..312

Appendix 1.7 Mineral composition data – plagioclase feldspar…….313

Appendix 1.8 Mineral composition data – pyroxene……321

Appendix 1.9 Raw mineral composition data – amphibole…….324

Appendix 1.10 Zircon U-Pb data……..331

Appendix 1.11 Concordia diagrams and Terra-Wasserburg plots…….342

Appendix 1.12 Major element data for the Late Cretaceous to Miocene magmatic rocks and samples of the Permian and Triassic basement……...349

Appendix 1.13 Trace and rare earth element data for the Late Cretaceous to Miocene magmatic rocks and samples of the Permian and Triassic basement determined by XRF and ICP-MS…….351

Appendix 1.14 Geothermobarometry……..354

1.14.1 The results of electron microprobe analysis of selected amphibole grains and amphibole-plagioclase geothermobarometry for intrusive sample RJ1103……..354

1.14.2 The results of electron microprobe analysis of selected plagioclase feldspar grains from sample RJ1103……...358

1.14.3 The results of electron microprobe analysis of selected amphibole grains and amphibole geothermobarometry for sample RJ1106……359

1.14.4 The results of electron microprobe analysis of selected amphibole grains and amphibole geothermobarometry for sample AM0867/68……362

1.14.5 The results of electron microprobe analysis of selected amphibole grains and amphibole geothermobarometry for sample AM0870…….365

1.14.6 The results of electron microprobe analysis of selected amphibole grains and amphibole geothermobarometry for sample ZN122……368

1.14.7 The results of electron microprobe analysis of selected amphibole grains and amphibole geothermobarometry for sample MQ28…….371

1.14.8 The results of electron microprobe analysis of selected amphibole grains and amphibole geothermobarometry for sample RJ11A7……...375

1.14.9 The results of electron microprobe analysis of selected amphibole grains and amphibole geothermobarometry for sample RJ11A15…….376

Appendix 1.15 Ar-Ar dating…….380

1.15.1 Sample Preparation……..380

1.15.2 Irradiation……..380

1.15.3 Analysis…….381

1.15.4 Data Reduction…….381

1.15.5 Results……381

1.15.5.1Sample RJ1111……..383

1.15.5.2Sample AM0887……...384

Appendix 1.16 References…….385

Appendix 2……..387

Appendix 2.1 Zircon Imaging……...387

Appendix 2.2 Zircon morphologies and characteristics……...389

Appendix 2.3 Oxygen isotope analysis……...390

2.3.1 Analytical conditions……...390

2.3.2 Data collection……..390

2.3.3 Drift correction…….391

2.3.4 Data correction…….391

2.3.5 Correction for HfO_2 concentrations……..392

Appendix 2.4 Lu-Hf isotope analysis ……..393

2.4.1 Analytical conditions……...393

2.4.2 Data corrections……....394

2.4.3 Data reduction……..395

2.4.4 Calculation of initial εHf values…….395

Appendix 2.5 Zircon oxygen isotope data determined by SIMS…….396

Appendix 2.6 Zircon Lu-Hf isotope data determined by LA-MC-ICP-MS……...416

Appendix 2.7 Lu-Hf isotope data for zircon standards determined by LA-MC-ICP-MS…….428

Appendix 2.8 Major and trace element compositions of zircons determined by EPMA……...436

Appendix 2.9 Major and trace element composition of zircon standard 'Laura' determined by EPMA……446

Appendix 2.10 Compiled zircon isotope data for all analysed zircon grains and cores……..447

Appendix 2.11 References……462

Appendix 3……..463

Appendix 3.1 Sample preparation……...463

3.1.1 Mineral separation……...463

3.1.1.1 Density separation using a Gemini table……463

3.1.1.2 Magnetic separation……464

3.1.1.3 Heavy liquid separation……464

3.1.2 Mounting, grinding and polishing……465

3.1.3 Melt inclusion re-homogenisation……465

Appendix 3.2 Boron isotope analysis ……..468

3.2.1 Analytical conditions……...468

3.2.2 Data correction……469

3.2.3 Data processing……469

Appendix 3.3 Trace and rare earth element analysis ……...472

3.3.1 Analytical conditions……...472

Appendix 3.4 Major element analysis……478

Appendix 3.5 Boron isotopic compositions of pyroxene- and zircon- hosted melt inclusions and host mineral phases, determined by SIMS analysis, and presented in analytical order with associated standard (GSD-1G) analyses……481

Appendix 3.6 Trace and rare earth element concentrations of pyroxene- and zircon hosted melt inclusions determined by SIMS analysis……...490

Appendix 3.7 Trace and rare earth element concentrations of host mineral phases determined by SIMS analysis ……...493

Appendix 3.8 Major element concentrations for pyroxene- and zircon- hosted melt inclusions determined by EPMA……494

Appendix 3.9 An evaluation of the effects of melt inclusion re-homogenisation……..497

3.9.1 The requirement for melt inclusion re-homogenisation……497

3.9.2 Potential effects of the heating process……498

3.9.3 The reliability of trace element concentrations obtained for re-homogenised melt inclusions ……..500

Appendix 3.10 References…….502

Chapter 1 - Introduction

1.1 Introduction

At convergent plate boundaries, such as the Andean margin, volatiles and crustal material are transported into the mantle by the subducting plate. The introduction of volatiles, most notably water, into the mantle lowers the solidus temperature and promotes melting, ultimately generating new crust in the overlying arc. Some components of the subducting material, which includes pelagic and terrigenous sediments, altered oceanic crust (AOC) and serpentinised oceanic lithosphere, are recycled to the crust via arc magmatism and some re-equilibrate with the mantle. As the mantle cannot be directly accessed, studying the products of arc magmatism is important in order to constrain these recycling processes and the contributions to new continental crust from subducted and mantle reservoirs. In addition to this, melts derived from the mantle wedge may also melt and assimilate crustal material en-route to the surface. Determining contributions to arc magmas from mantle, subducting slab and crustal components is important in order to:

- Constrain rates of continental growth and investigate the evolution of the continental crust.
- Determine the processes and mechanisms involved in redistributing subducted material between crustal and mantle reservoirs and to establish which elements, and to what degree these elements are recycled to the crust and subducted into the deeper mantle.
- Improve our understanding of the origin and formation of economic ore deposits, which are often associated with convergent plate margins.

The Andean margin is an active site of modern continental growth and represents a type example of an ocean – continent convergent plate boundary. It provides an ideal location at which to study and assess mass transfer between crustal and mantle reservoirs. The contamination of the melt source region with subducted sediments (e.g., Sigmarsson et al., 1990; Kilian and Behrmann, 2003; Lucassen et al., 2010), crustal material from subduction erosion (e.g., Stern, 1991; Kay et al., 2005; Goss et al., 2013), melts derived from the subducting oceanic plate (e.g., Stern and Kilian, 1996; Reich et al., 2003), as well as the contamination of arc magmas during ascent through the continental crust (e.g., James, 1982; Hildreth and Moorbath, 1988; Davidson et al., 1991), have all previously been suggested to explain the geochemical characteristics of arc magmatic rocks from along the Andean margin. However, the relative contributions from these different components to the genesis of Andean arc magmas and how these contributions may have changed over time remains elusive. The southern Central Andes (Pampean flat-slab segment) provides a particularly interesting area to study these processes in relation to a changing geodynamic setting; specifically the shallowing angle of the subducting plate and thickening of the continental crust which occurred over the later part of the Cenozoic.

Studying the geochemistry of arc magmatic rocks can be used to determine relative contributions to arc magmas from mantle, crustal and subducting reservoirs. However, the identification of geochemical signatures, particularly those which infer the involvement of crustal material in the petrogenesis of arc magmas, from whole rock geochemistry alone does not allow accurate determination of where these signatures were derived from, i.e. in the melt source region or in the continental crust. Andean arc lavas are also porphyritic, i.e. are a mix of melt and crystals and therefore analysing whole rock geochemistry as a stand-alone technique may give misleading information on how these melts evolved. On this basis, this study combines petrology and whole rock geochemistry with high

resolution, *in-situ* elemental and isotopic analysis of mineral phases and melt inclusions in order to more accurately constrain contributions to southern Central Andean arc magmas over time. Specifically, the oxygen and hafnium isotopic composition of the accessory mineral zircon has been used to identify contamination of mantle-derived melts with older continental crust. Select trace element concentrations and the boron isotopic compositions of silicate melt inclusions have been used to assess the recycling of subducting material and the influence of fluids on arc magmas. Although, these methods have successfully be applied at other convergent margins (e.g., Palmer, 1991; Sano et al., 2001; Tonarini et al., 2001; Bolhar et al., 2008) this study represents the first to apply these techniques to arc magmatic rocks from the Pampean flat-slab segment of the Central Andes.

1.2 Aims and objectives

The overall research aims of this project are:

- To better constrain the timing and duration of arc magmatism in the southern Central Andes.

- To assess the contributions from mantle, crustal and subducted reservoirs to Cenozoic arc magmas, by using a range of geochemical and *in-situ*, micro-analytical techniques.

- To relate changes in contributions from mantle, crustal and subducted reservoirs to Cenozoic arc magmas to the changing geodynamic setting of the southern Central Andean margin.

1.3 A geological overview of the Andean margin

The Andean margin extends for over 7500 km along the western edge of South America and is the location of the world's second highest mountain range, the Andes, with peak elevations in excess of 6 km. At this modern convergent plate boundary the oceanic Nazca plate subducts in an eastward direction under the continental part of the South American plate, the exception being in the far south where the Antarctic plate converges with the South American plate (Fig. 1.1). Subduction of oceanic crust beneath the South American continent has been active in this region since the Jurassic and has produced a series of volcanic arcs (e.g., Ramos et al., 2002; Stern, 2004; Charrier et al., 2007).

The Andean margin is divided into a number of segments based on changes in geological, morphological and climatic features (Fig. 1.1). One of the most noticeable features of this along arc segmentation is the presence and absence of active volcanism. There are currently four volcanically active segments; the Northern Volcanic Zone (NVZ, 6°N - 3°S) which lies to the east of the Cocos Ridge, the Central Volcanic Zone (CVZ, 14 - 28°S), the Southern Volcanic Zone (SVZ, 33 - 46°S) and the Austral Volcanic Zone (AVZ, 49 - 55°S) which extends to the Tierra del Fuego archipelago. These volcanic zones are separated by regions of no active volcanism. Changes in subduction zone geometry, specifically in the angle of the subducting plate, are thought to account for the presence and absence of arc magmatism (e.g., Cahill and Isacks, 1992; Stern, 2004). Where the angle of the subducting plate is shallow (<10° at ~100 km depth), and therefore the asthenospheric mantle wedge is restricted, there is currently no active volcanism. These volcanically inactive segments include the Peruvian flat-slab segment (3 - 14°S), the Pampean (Chilean) flat-slab segment (27 - 33°S) and the Patagonian volcanic gap (46 - 49°S). A number of explanations have been proposed to explain the development of flat-slab subduction along the Andean margin including, in the

case of both the Peruvian and Pampean flat-slab segments, the subduction of buoyant oceanic ridges and plateaus (e.g., Gutscher et al., 1999; Yañez et al., 2001). Evidence from the geological record also implies that the Central Andean margin has undergone numerous transitions between normal (~30°) and flat (<10° at ~100 km) subduction over time (e.g., Ramos and Folguera, 2009).

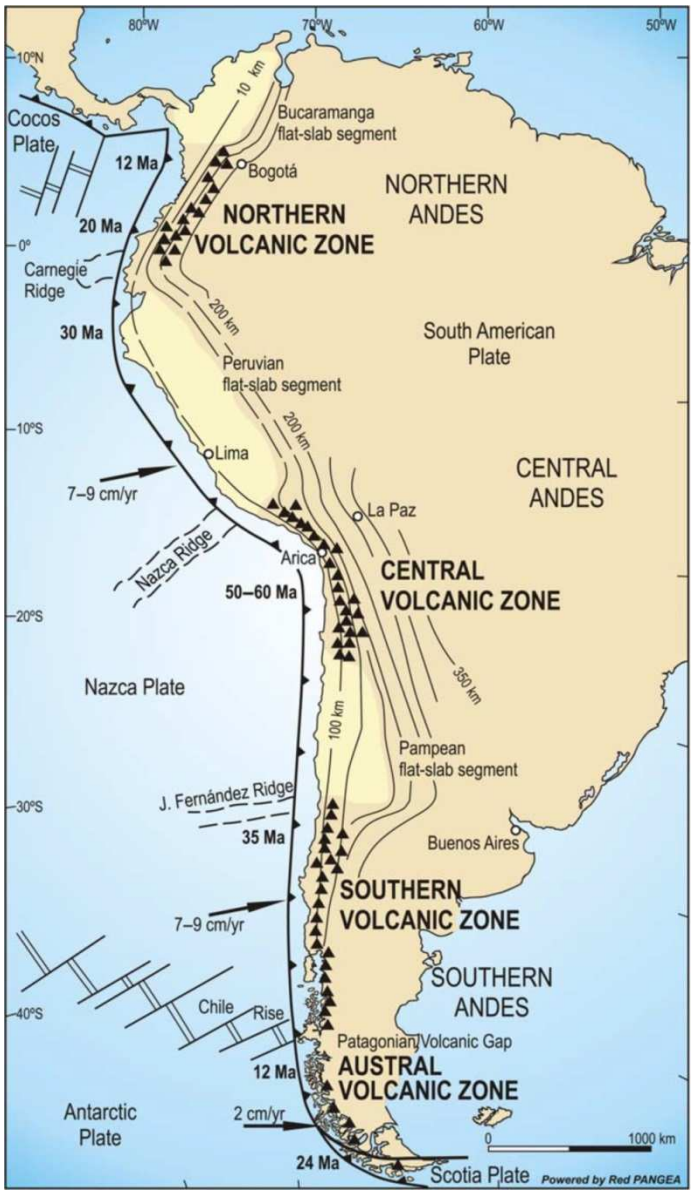

Figure 1.1. Schematic map of the present day Andean margin showing the volcanically active/inactive (triangles/no triangles) segments and the depth to the Wadati-Benioff Zone (WBZ) (from Cahill and Isacks (1992)). The ages relate to the

age of the Nazca plate currently being subducted along the margin. Image modified from Ramos and Folguera (2009).

1.3.1 The Andean tectonic cycle

The Andean tectonic cycle (Jurassic to recent) represents only the latest in a series of orogenic cycles to affect the western edge of the South American continent. Prior to the Andean tectonic cycle, two earlier cycles (Cambrian to Devonian and Carboniferous to Triassic) also affected the continental margin and formed the basement on which the modern Andes are built (Ramos, 1989). The Andean tectonic cycle started in the earliest Jurassic and is associated with the opening of the South Atlantic Ocean (Stern, 2004). Subduction along the western margin of South America was initiated during this time period and subduction-related magmatism in the Central Andes had begun by 185 Ma (Pichowiak et al., 1990). This Jurassic magmatic arc is now positioned in the Coastal Cordillera, located between 50 and 150 km away from the current trench axis (Trumbull et al., 2006).

Throughout the Andean tectonic cycle periods of extension have alternated with periods of contraction and these are thought to have fluctuated on a fairly local scale, so that different tectonic regimes were occurring simultaneously along different parts of the Andean margin (Charrier et al., 2002). These alternations are primarily related to changes in convergence rates and the relative plate motions between the oceanic (Farallon and Nazca) and South American plates. Plate reconstruction models demonstrate periods of fast and slow convergence, and changes in the obliquity of convergence over the course of the Andean tectonic cycle (Somoza and Ghidella, 2012 and references therein). On this basis, the Andean tectonic cycle has been divided into several sub-stages by several workers (e.g., Coira et al., 1982; Charrier et al., 2007). The reader is referred to these works for a

more detailed discussion of the tectonic evolution of the Andes. A brief summary of the Late Cretaceous to present day evolution of the margin is presented here in order to give context for the discussions presented later in this thesis.

In response to a change in plate interactions between the oceanic Farallon and continental South American plates in the Late Cretaceous the margin became more compressional. Prior to the Late Cretaceous the subduction zone boundary was retreating due to slab roll-back and/or slab steepening. During the Late Cretaceous the continental margin was uplifted and the back-arc basins, which were situated to the east of the volcanic arc, were inverted and the basin fill subject to subaerial erosion. The magmatic arc also migrated to the east and a wide fore-arc region developed to the west of the arc (Charrier et al., 2007 and references therein). The Late Cretaceous to Paleocene period is characterised by the emplacement of major plutons and widespread volcanic activity associated with extension (Parada et al., 1988). The dominance of an extensional tectonic setting is thought to be related to the highly oblique angle of convergence between the Farallon and South American plates, in addition to low rates of convergence (Pardo Casas and Molnar, 1987). A period of compression and deformation, which is thought to have resulted in the inversion of the Paleocene extensional basins, has been identified in the Mid to Late Eocene (e.g., Hammerschmidt et al., 1992; Maksaev and Zentilli, 1999). This period of deformation is widely referred to as the Incaic phase and has been associated with a reduction in the obliquity of convergence and an increase in convergence rates to >10 cm/yr (Pilger, 1984; Pardo Casas and Molnar, 1987; Somoza, 1998). Between the Late Eocene and Late Oligocene convergence rates between the Farallon and South American plates are thought to have remained fairly constant (~8 cm/yr) (Somoza and Ghidella, 2012), with the Farallon plate being subducted in a north-easterly direction (Pilger, 1984; Pardo Casas and Molnar, 1987; Somoza, 1998; Somoza and Ghidella, 2012).

A significant change in the tectonic configuration of the Andean margin occurred during the late Oligocene (~25 Ma) due to the break-up of the Farallon plate into the Nazca and Cocos plates (Lonsdale, 2005). This resulted in both an increase in convergence rates (average of ~15 cm/yr) and a change from oblique (NE - SW) to orthogonal (ENE - WSW) convergence (Pardo Casas and Molnar, 1987; Somoza, 1998). The westward migration of the South American plate is also thought to have been initiated after ~30 Ma (Silver et al., 1998). These increased convergence rates are thought to have been partially absorbed through thickening of the continental crust in the northern Central Andes (Isacks, 1988; Jaillard et al., 2000; Oncken et al., 2006) but are believed to have led to an extensional regime in the southern Central Andes (Jordon et al., 2001). However, an increase in magmatic activity and a broadening of the magmatic arc is ubiquitous along the Andean chain during this time interval (Pilger, 1984).

In the southern Central Andes between 27 and 33°S the Juan Fernández Ridge (JFR), a volcanic seamount, began intersecting the Andean margin shortly after the tectonic reconfiguration at ~25 Ma (Yañez et al., 2001; Yañez et al., 2002). This is thought to have resulted in the absence of the central depression in the southern Central Andes and an eastward shift of both the magmatic arc and the deformation front into the Andean foreland (Sierras Pampeanas) (Fig. 1.2) (Ramos et al., 2002; Yañez et al., 2002).

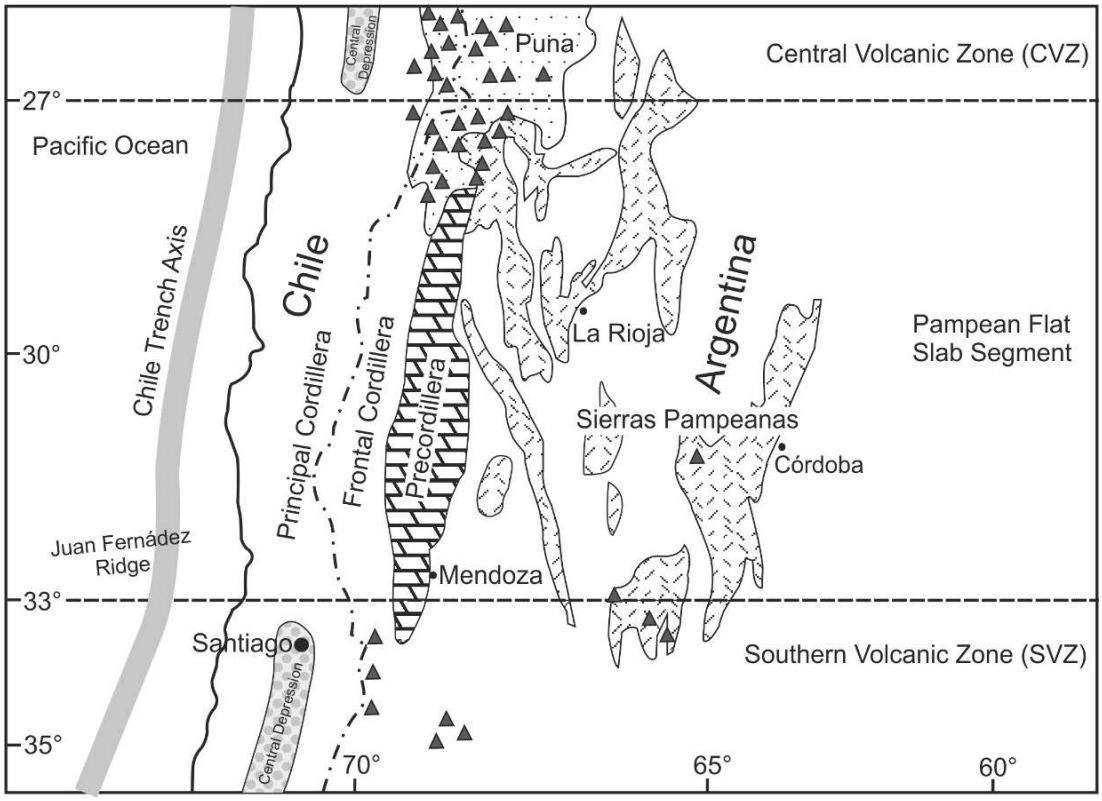

Figure 1.2. A schematic map showing the main features of the Pampean flat-slab segment of the southern Central Andes, specifically highlighting; the locations of active volcanoes (triangles), the absence of the central depression, the presence of the Sierras Pampeanas and the locations of the Principal Cordillera, Frontal Cordillera and Precordillera. Figure developed from Ramos et al. (2002).

High convergence rates (~15 cm/yr) between the Nazca and South American plates were sustained up until ~20 Ma, followed by a gradual decline to present day values (~7 cm/yr) (Pilger, 1984; Somoza and Ghidella, 2012). The main uplift of the Central Andean mountain range is thought to have occurred over the last 10 million years, with evidence from palaeo-botanical studies suggesting that the Altiplano-Puna plateau (CVZ) had attained no more than half its modern elevation by 10.7 Ma (Gregory-Wodzicki, 2000). Thermochronological studies on Miocene plutons present in the Principal Cordillera between 33 and 35 °S also support rapid uplift of the Andean range after late Miocene times (~10 Ma) (Kurtz et al., 1997; Maksaev et al., 2003; Spikings et al., 2008).

1.3.2 Cenozoic arc magmatism in the Pampean flat-slab segment

The region of interest for this study is the Pampean flat-slab segment which is located between 28 and 33°S in the southern Central Andes of Chile and Argentina (Fig. 1.1). The Andean margin in this region is divided from west to east into the Coastal Cordillera, the Principal Cordillera, the Frontal Cordillera, the Precordillera and the Sierras Pampeanas (Fig. 1.2). Cenozoic arc magmatic rocks occur as north - south trending belts which lie to the east of the Coastal Cordillera (primarily Late Paleozoic to Early Cretaceous in age). The older, more continuous western belt was intruded in the Palaeocene - Eocene and the younger more eastern belt is Oligocene - Miocene in age, demonstrating an eastward migration of magmatism with time (Parada et al., 2007). The Palaeocene – Eocene belt is located in the Chilean Principal Cordillera and is primarily composed of epizonal plutons which are thought to be emplaced in a more extensional setting compared to the compressive regime which currently exists along the Andean margin (Charrier et al., 2007 and references therein). The Oligocene – Miocene belt is primarily composed of arc volcanic rocks and is located in the Frontal Cordillera, spanning either side of the Chilean – Argentine boarder. The geographical gap that exists between the two belts corresponds to an apparent reduction in magmatic activity between ~39 – 26 Ma (Parada et al., 1988; Parada et al., 2007). It has been suggested that this reduction in arc magmatism may be related to an earlier flat-slab episode in the Central Andes between the late Eocene and the late Oligocene (O'Driscoll et al., 2012). Some Oligocene to Miocene intrusive and extrusive magmatism is also evident in the Argentinean Precordillera.

As mentioned previously, there is currently no active volcanism in the Pampean flat-slab segment. This is considered to be due to the low angle (<10°) at which the oceanic Nazca plate currently subducts beneath the South American continent in this region (Cahill and Isacks, 1992; Stern, 2004). The shallowing of the Nazca plate

is thought to have been initiated at ~18 Ma on the basis of the initiation of high angle thrust faulting in the main Andean Cordillera (Maksaev et al., 1984), the broadening of the magmatic arc to the east (Kay et al., 1987; Kay et al., 1991; Kay and Abbruzzi, 1996), the termination of back-arc volcanism (Kay and Mpodozis, 2002) and the initiation of deformation in the Precordillera close to 18 Ma (Jordan et al., 1993). The shallowing is proposed to have caused the expansion and migration of the volcanic arc to the east, followed by a reduction and the eventual termination of arc volcanism in the Andean Cordillera in the Late Miocene (~6 Ma) (Kay et al., 1987; Trumbull et al., 2006). Late Miocene (~7 – 5 Ma) volcanic activity in the Pocho volcanic field in central Argentina, ~700 km away from the Chile trench, is thought to represent the arrival of the subducting slab under this part of the South American continent (Kay and Gordillo, 1994). As well as exerting a control on the location of arc magmatism, the shallowing of the slab has also been identified as exerting a primary control on regional crustal shortening (e.g., O'Driscoll et al., 2012).

The exact cause of the recent slab shallowing in the southern Central Andes (28 – 33 °S) remains unclear. Proposed causes include the subduction of the Juan Fernández Ridge (JFR), a buoyant volcanic seamount, which began intersecting the Andean continental margin during the early Miocene (Pilger, 1981; Gutscher et al., 2000b; Yañez et al., 2001; Yañez et al., 2002), the subduction of a less dense, hydrated and serpentinised upper mantle associated with the JFR (Kopp et al., 2004; Marot et al., 2013), the curvature of the subducting slab and Andean margin (Cahill and Isacks, 1992), and the trench-ward motion of thickened lithosphere (Manea et al., 2012). However, there seems to be a strong relationship between the track of the subducting JFR and the occurrence of flat-slab subduction in the southern Central Andes (Anderson et al., 2007) and this is currently the most favoured explanation in the literature.

The JFR originates from a narrow deep seated mantle plume (the Juan Fernández hotspot) focussed at 97.5°W and 34 °S. The JFR currently intersects the Chilean trench at a near normal angle at 32.5 °S. The ridge began intersecting the Andean margin to the north of its current position and is thought to have migrated southward along the Andean margin at a speed of ~200 km/Ma to its current position over the past ~20 Myr (Yañez et al., 2001; Yañez et al., 2002). The oceanic lithosphere associated with the seamount chain is also thought to have been hydrated and serpentinised leading to increased buoyancy, enhancing its link with slab shallowing (Kopp et al., 2004).

1.3.3 Justification of the region of study

The Pampean flat-slab segment was selected to investigate the influence of subducting components and continental crust on the composition of arc magmas, and ultimately new continental crust, for the following reasons:

- The distribution, petrology and whole rock geochemistry of the Cenozoic arc magmatic rocks in the southern Central Andes has been well documented and described by previous studies (e.g., Kay et al., 1987; Parada et al., 1988; Kay et al., 1991; Martin et al., 1997; Bissig et al., 2001; Bissig et al., 2003; Litvak et al., 2007). Detailed in Chapter 2.

- There are sufficient accessible outcrops of Cenozoic arc magmatic rocks which have previously been mapped and described (e.g., Cardó and Díaz, 1999; Emparan and Pineda, 1999; Pineda and Emparan, 2006; Cardó et al., 2007; Pineda and Calderón, 2008).

- The changing subduction zone geometry, which occurred during the Cenozoic, is reasonably well constrained allowing the effects of the changing geodynamic setting on the petrogenesis of arc magmas to be assessed.

- Studies investigating similar processes have been carried out to the north and south of the study area where the Nazca plate is currently subducting at a normal angle, providing an excellent opportunity with which to compare the results of this study. For example, the cycling of boron through the Andean subduction zone has been investigated to the north of the study region in the currently volcanically active Central Volcanic Zone (e.g., Kasemann et al., 2000; Schmitt et al., 2002; Rosner et al., 2003).

1.4 The generation of arc magmas and recycling processes at subduction zones

1.4.1 Geochemical characteristics of arc magmas

Although compositions of arc magmas vary between individual arcs, magmas produced in subduction zone settings generally have a geochemical signature which is distinct from those produced in other tectonic settings, such as intra-plate, mid-ocean ridge and ocean island (Gill, 1981). Magmas produced in subduction zone settings are typically enriched in large ion lithophile elements (LILE, e.g., Rb, K, Ba, Sr), light rare earth elements (LREE, e.g., La, Ce) and fluid-mobile elements (e.g., B, Cs, Pb) in comparison to mid-ocean ridge basalt (MORB) and ocean island basalt (OIB). This enrichment is accompanied by lower abundances of high field strength elements (HFSE, e.g., Nb, Zr, Ta), heavy rare earth elements (HREE, e.g., Yb, Lu), Ti and the transition elements (e.g., Kay, 1980; Gill, 1981; Tatsumi et al., 1986; Hawkesworth et al., 1991; Woodhead et al., 1993). As might be expected, the elements which are enriched in arc magmas are also those which generally have a high abundance in the continental crust (e.g., Plank, 2005). In part these elemental enrichments/depletions in arc magmas reflect distinctive processes occurring in the melt source region and specifically the addition of subduction components

(Hawkesworth et al., 1993). Alternatively, these geochemical characteristics may also reflect crustal contamination processes as the melt ascends through the crust.

A number of studies have demonstrated that the chemical composition of arc magmas reflect the composition of the subducted sediments (e.g., Plank and Langmuir, 1993; Plank and Langmuir, 1998; Plank, 2005). One of the most convincing pieces of evidence for the recycling of subducted sediment through subduction zones is provided by the presence of ^{10}Be in some arc lavas (e.g., Tera et al., 1986; Morris and Tera, 1989; Morris et al., 1990). Beryllium-10 is a cosmogenic radionuclide that can only be produced in the upper atmosphere and is strongly enriched in ocean sediments. Therefore its presence in arc magmas infers the involvement of subducted sediment in the melt source region. Unfortunately for this study, it only has a half-life of 1.5 Myr, so can only be used to ascertain the recycling of sediments in relatively young arc rocks (<~9 Myr).

1.4.2 Recycling processes

The concept that some components, which are subducted into the mantle at convergent plate margins, contribute to arc magmas and are recycled to the crust, either due to melting or via aqueous fluids, is a longstanding one. With the acceptance of the theory of plate tectonics it was suggested that sediments being subducted at continental margins could be the source of arc magmas (e.g., Armstrong, 1968). However, subsequent evidence suggested that dehydration of the subducting slab, due to increasing pressure and temperature, produces hydrous fluids which lower the solidus temperature and cause melting in the mantle wedge. It therefore became generally accepted that the metasomatised mantle wedge is the main source of arc magmas at convergent plate margins and that devolatisation of the subducting slab is the main mechanism of transferring components from the slab and recycling them to arc magmas (e.g., Gill, 1981; Hawkesworth et al., 1993;

Davidson, 1996). Subsequently it was suggested, that to fully account for the geochemical characteristics displayed by the majority of arc magmas, a two component model was required; melting of the subducting sediment and dehydration of the altered oceanic crust (Elliott, 2003).

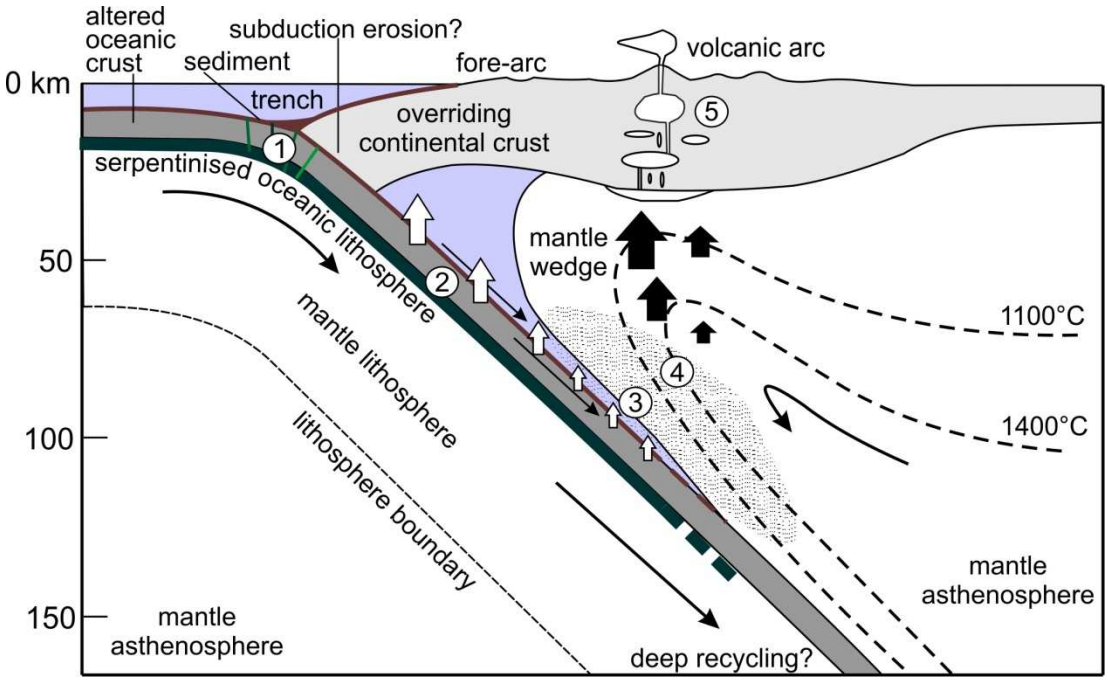

Figure 1.3. A schematic cross section of a subduction zone at an ocean-continent convergent margin. The subducting slab, which includes sediments, altered oceanic crust (AOC), mantle lithosphere and serpentinised mantle lithosphere are shown descending into the mantle at a normal angle of subduction (~30°). Open arrows depict fluid release from components of the subducting slab and oceanic lithosphere due to compaction and the breakdown of hydrous minerals and serpentinite. Filled black arrows represent melt migration through the mantle wedge to the base of the continental crust. The numbers refer to processes occurring during subduction; 1) Potential fracturing of the subducting oceanic crust leading to an influx of seawater and serpentinisation of olivine-rich gabbros in the oceanic crust and peridotite in the mantle lithosphere. 2) Slab dehydration due to progressive metamorphism. 3) Metasomatism of the mantle wedge due to fluids and/or melts released from the subducting slab. 4) Partial melting of the mantle wedge and upward migration of buoyant melts. 5) Ascent of mantle-derived melts through the continental crust; the potential location of fractional crystallisation (FC) and melting, assimilation, storage, and homogenisation (MASH) processes.

As aforementioned, components of the subducting slab, which includes continentally-derived and pelagic sediments, altered and fresh oceanic crust, and serpentinised oceanic lithospheric, can be transferred to the overlying mantle wedge and therefore contribute to the source of arc magmas. This can either be via a fluid derived from the dehydration of the subducting slab (e.g., Elliott et al., 1997) or a melt if the temperature of the slab exceeds the solidus of the subducting sediment (e.g., van Keken et al., 2011) and/or the altered oceanic crust (e.g., Tollstrup et al., 2010). Whether the subducting components melt or are transferred by the release of aqueous fluids governs the recycling of elements through the arc region and determines what is transported to the deep mantle.

1.4.2.1. The role of fluids

Aqueous fluids are released from the subducting slab (sediments, altered oceanic crust and oceanic lithosphere) by a number of different mechanisms and at a range of depths. Experimental studies have shown that the release of aqueous fluids from the subducting slab is a near continuous process, primarily due to continuous metamorphic reactions taking place during progressive subduction (Schmidt and Poli, 1998). However, the greatest volume of fluid is thought to be released beneath the fore-arc with a gradual decrease in volume towards the back-arc.

At shallow depths (<40 kilometres depth) free water present in the pore spaces of subducting sediments and AOC is expelled due to compaction. At greater depths aqueous fluids are produced by the progressive metamorphic devolatilisation of the slab as it descends into the mantle (e.g., Peacock, 1990; Schmidt and Poli, 1998). With increasing temperatures and pressures, hydrous minerals such as phengite and chlorite present in the subducted sediment and hornblende, epidote and chlorite present in the AOC, breakdown and release fluids (Tatsumi, 1989; Kogiso et al., 1997; Aizawa et al., 1999). At temperatures of ~650 °C mineral phases present in

serpentinite, which can be present in the oceanic lithosphere, breakdown into forsterite and enstatite potentially releasing large quantities of water into the mantle wedge. Serpentinite can contain >13 wt.% water in its mineral structures, and the breakdown of antigorite in particular is thought to release an order of magnitude more water than the dehydration of AOC (Ulmer and Trommsdorff, 1995; Wunder et al., 2001). In most subduction zones the conditions necessary for the breakdown of serpentinite correspond to depths of between 90 and 110 km, i.e. sub-arc depths. On this basis, it has been proposed that the breakdown of serpentinite and the associated release of water accounts for the position of volcanic arcs relative to the trench (e.g., Hattori and Guillot, 2003). In addition to the serpentinite present in the subducting oceanic lithosphere, the fore-arc mantle wedge is also likely to contain serpentinised peridotite due to hydration of the mantle wedge at shallow levels (Hyndman and Peacock, 2003; Savov et al., 2007). This serpentinised fore-arc mantle wedge may be down-dragged into a sub-arc position by the subducting plate (Straub and Layne, 2002; Tonarini et al., 2011), and in a similar manner to the serpentinised oceanic lithosphere, may break down and release fluids when it reaches temperatures exceeding ~650 °C.

The aqueous fluids produced from the subducting slab by the various methods of dehydration can mobilise certain elements (e.g., B, Cl, As, Sb) from the subducting component and transfer them into the overlying mantle wedge (e.g., Elliott et al., 1997). The melting of the metasomatised mantle wedge then incorporates these fluid-mobile elements into arc magmas and transports them to the crust. This is thought to account for the distinctive enrichment in fluid-mobile elements observed in arc magmas. A number of studies have shown across arc variations in both the abundance of incompatible, fluid-mobile elements and isotopic compositions (e.g., $\delta^{11}B$, $\delta^{7}Li$) in arc magmas (e.g., Ryan et al., 1995; Moriguti and Nakamura, 1998; Morris and Ryan, 2003). These variations can be related to the progressive metamorphic devolatilisation of the subducting slab and the decrease in the fluid

flux coming off the slab from the arc front to the back arc region (e.g., Moran et al., 1992), as well as due to variations in partial melting of sediments, oceanic crust and the mantle wedge.

1.4.2.2. The role of melts

In most modern subduction zones, thermal models predict that the subducting oceanic crust is too cold to melt beneath the volcanic arc (e.g., Peacock et al., 1994; Peacock, 1996). It is generally thought that the oceanic crust has to be young and relatively hot in order to melt (<~25 Ma) (Defant and Drummond, 1990). However, under certain subduction zone geometries and conditions it is proposed that basaltic crust older than 25 Ma can undergo melting. This is an important consideration in the Pampean flat-slab segment of the southern Central Andes as the age of the slab being subducted during the Cenozoic is considered to have been too old to melt, but decreasing slab angles have been implicated with the melting of the subducting oceanic crust (Gutscher et al., 2000a).

When the subducting oceanic crust does melt it is thought to result in specific, identifiable geochemical characteristics in arc magmas. Partial melting of the subducting oceanic crust should leave a garnet-bearing residue (Sen and Dunn, 1994; Rapp and Watson, 1995) and produce magmas with intermediate SiO_2, elevated Al_2O_3, Sr/Y and La/Y, and low Y (i.e. with adakitic signatures). Slab melting has previously been inferred to account for adakitic signatures at various locations along the Andean margin (e.g., Stern and Kilian, 1996; Reich et al., 2003). Alternatively it has been suggested that adakitic signatures in arc magmas can be generated by a number of other mechanisms, including the partial melting of a mafic lower crust (e.g., Kay et al., 1991; Chung et al., 2003; Garrison and Davidson, 2003; Kay et al., 2005), and high-pressure fractional crystallisation of hydrous mafic arc magmas (e.g., Castillo et al., 1999; Macpherson et al., 2006; Rodríguez et al., 2007;

Rooney et al., 2011). Therefore, the occurrence of arc magmatic rocks with adakitic signatures does not solely imply the melting of subducting basaltic crust.

The melting of sediments being subducted with the oceanic crust and lithosphere is also thought to contribute to the composition of arc magmas (e.g., Ben Othman et al., 1989; Elliott et al., 1997; Plank and Langmuir, 1998). Pelagic sediments have a relatively low temperature wet solidus making them more likely to melt than subducting basaltic oceanic crust (Nichols et al., 1996). This has led to the widely accepted view that in subduction zones sediments melt and oceanic crust dehydrates, and this appears to account for the trace elements and isotopic characteristics displayed in arc magmas (Elliott, 2003).

1.5 Potential contributions to southern Central Andean arc magmas

1.5.1 The slab component

The subducting slab component includes continentally-derived and pelagic sediments, altered and fresh oceanic crust, and serpentinised oceanic lithosphere. The relative proportions of these components entering the Andean subduction zone is likely to have varied over time and what is currently entering the subduction zone trench is unlikely to accurately reflect what was subducted in the past, in particular the quantities of clastic sediment in the trench is likely to have changed. Determining how the contributions from these subducting components to arc magmas have changed over the course of the Cenozoic is a core aim of this thesis.

The oceanic crust currently being subducted along the Andean margin between ~28 and 33°S is composed of a sequence of gabbros and basalts which range in thickness

from 4 to 6 km (Tassara et al., 2006), slightly below the average global thickness for oceanic crust of 7 ±1 km thick (Bown and White, 1994). Geophysical evidence suggests the full thickness of the oceanic lithosphere being subducted is ~50 km (Sodoudi et al., 2011). Oceanic crust is altered due to interaction with hydrothermal fluids and seawater at high and low temperatures. This alteration, which principally occurs in the upper 500 m of the crust, increases the content of volatiles (H_2O, Cl, S, and CO_2), and certain trace elements (K, Rb, Cs, U, Pb, Sr, As and B) (e.g., Jarrard, 2003; Kelley et al., 2003; Staudigel, 2003). Where off-axis deformation is limited alteration primarily takes place near the spreading centre and continues more slowly as the seafloor ages. Fluids derived from AOC on the subducting Nazca plate have previously been invoked in the genesis of arc magmas erupted at Quaternary volcanic centres in the CVZ, to the north of the study area (Rosner et al., 2003).

The influx of seawater and hydrothermal fluids at fracture zones and ridges can also result in the serpentinisation of olivine rich gabbros present in the lower oceanic crust and peridotite present in the lithospheric mantle (e.g., Ranero et al., 2003; Kopp et al., 2004; Ranero and Sallarès, 2004). Serpentinite present in the oceanic lithosphere is an important reservoir of highly fluid-mobile elements such as B, Li, As and Sb (Deschamps et al., 2013). Geophysical evidence suggests the oceanic lithosphere associated with the JFR is hydrated and serpentinised (Kopp et al., 2004). Therefore, this may have led to an increase in the flux of these elements to the source of Andean arc magmas after the intersection of the JFR with the southern Central Andean margin (~30 °S) at ~18 Ma (Yañez et al., 2001; Yañez et al., 2002).

The quantity and composition of the sediment entering the sub-arc region in the southern Central Andes is difficult to estimate and is likely to have changed over the course of the Cenozoic due to a wide range of factors including, climate, productivity, drainage, and levels of sediment accretion. A moderate volume of

sediment (~0.5 km thickness) is currently present in the Chile trench axis between 28 - 33°S (Thornburg and Kulm, 1987a). Compositional data for this sediment is limited, primarily due to the lack of drill cores, and there have been few sedimentological studies. Lamy et al. (1998) found the surface sediments collected at ~30°S to be predominantly clayey silts composed of ~40% plagioclase, ~25% quartz, ~12% pyroxene, ~11% amphibole, ~5% K feldspar, ~6% mica and ~3% chlorite. It is also proposed that the majority of sediment in the Chile trench is continentally derived (Thornburg and Kulm, 1987a; Thornburg and Kulm, 1987b; Lamy et al., 1998), therefore it is likely to reflect the composition of the upper continental crust.

In certain settings the sediments lying on top of the subducting oceanic lithosphere can be scrapped off and accumulated on the leading edge of the overriding plate, forming accretionary prisms (e.g., Cloos and Shreve, 1988). The Central Andean margin is currently non-accretionary and there is an almost complete lack of Mesozoic – Cenozoic accretionary complexes along the entire Andean margin. Even at accretionary margins it is suggested that ~80% of the sediments in the trench are subducted (Von Huene and Scholl, 1991). This implies that sediments present in the Central Andean trench are likely to have been subducted and therefore have the potential to influence the composition of arc magmas.

The involvement of subducted sediments in the genesis of Andean arc magmas has previously been inferred in the SVZ. Sigmarsson et al. (1990) reported ^{10}Be and U enrichment in in volcanic rocks from between 33 - 42°S which they attributed to the preferential partitioning of Be and U into a fluid phase during the dehydration of sediments recently subducted along the Chilean margin. They also suggested the timescales of <~20,000 years for dehydration, melting and eruption of these basaltic arc magmas on the basis of strong ^{238}U - ^{230}Th disequilibria. Kilian and Behrmann

(2003) suggest that the magma source region between 41 and 47°S is contaminated with a 3 – 5 vol.% terrigenous sediment melt.

The down-going plate can also erode crustal material from the leading edge of the continental plate, which can also lead to continental crustal material being subducted to sub-arc depths. High levels of subduction erosion along the Andean margin have been proposed for the Cenozoic (e.g., Rutland, 1971; Stern, 1991; Kay et al., 2005; Goss et al., 2013). Subduction of continental crust due to subduction erosion has been proposed as a mechanism for generating certain geochemical characteristics in Andean arc magmatic rocks. For example, elevated $^{87}Sr/^{86}Sr$ ratios in mafic arc magmas from the northern SVZ have been linked to the effects of subduction erosion (Stern, 1991).

1.5.2 The crustal component

As arc magmas migrate through the overlying crust they have the potential to melt and assimilate the surrounding continental crust, therefore modifying the composition of the magma derived from the mantle wedge. The continental crust in the southern Central Andes currently reaches thicknesses of ~70 km in the Principal Cordillera and thins to 55 km below the Sierras Pampeanas on the Argentinean side of the margin (Gilbert et al., 2006; Heit et al., 2008). Therefore, contamination of arc magmas with continental crust seems likely, at least during the recent (Miocene), more compressional evolution of the Andean margin. The crustal contamination of Andean arc magmas has previously been invoked to account for the geochemical characteristics of Andean arc rocks (e.g., James, 1982; Hildreth and Moorbath, 1988; Davidson and de Silva, 1992). Specifically, the radiogenic isotopic compositions ($^{87}Sr/^{86}Sr$ and $^{208}Pb/^{204}Pb$) of recent arc magmatic rocks in the CVZ are thought to

primarily reflect the contamination of melts derived from the mantle wedge with continental crust (e.g., Davidson et al., 1991).

The pre-Andean basement in the Central Andes varies from Proterozoic to Mesozoic in age and the evolution of the Central Andean crust, prior to the Cenozoic, has been a subject of much debate. It has been proposed that the development of the western margin of South America has involved the subduction and accretion of various allochthonous or par-autochthonous terranes (e.g., Ramos et al., 1986; Thomas and Astini, 2003; Ramos, 2004; Finney, 2007; Ramos, 2010), however this model remains highly controversial (e.g., Lucassen et al., 2000; Lucassen and Franz, 2005). A detailed investigation and discussion of the development of the margin prior to the Cenozoic is beyond the scope of this study and the reader is referred to the references cited above. However, an important consideration for this work is that the age and origin of the basement varies across the Andean Cordillera.

The basement in the Principal and Frontal Cordillera of the southern Central Andes is primarily composed of Paleozoic marine sediments and meta-sediments which have been intruded, and unconformably overlain, by Late Paleozoic – Mesozoic plutonic complexes and volcanic deposits (Kay et al., 1989; Martin et al., 1999). In the southern Central Andes, on the Chilean side of the margin, the Late Paleozoic – Mesozoic plutonic complexes range in composition from gabbros to granites and are grouped into two 'Superunits'; the Late Carboniferous – Early Permian, Elqui Complex and the Permian – Early Jurassic, Ingaguás Superunit (Mpodozis and Cornejo, 1988; Mpodozis and Kay, 1990; Nasi et al., 1990; Mpodozis and Kay, 1992). The Colangüil Batholith has been identified as the age equivalent unit to these 'Superunits' in the Argentinean Frontal Cordillera (e.g., Llambias and Sato, 1990; Llambías and Sato, 1995). The highly silicic volcanic and volcaniclastic sequences of the Early Permian – Early Jurassic Choiyoi Group, and the age equivalent Pastos

Blancos Group, form extensive deposits in the Frontal Cordillera on the Chilean side of the margin and close to the Argentine boarder (Nasi et al., 1985; Martin et al., 1999). These Late Paleozoic to Early Jurassic plutonic and volcanic rocks are thought to have formed during the late stages of Carboniferous – Early Permian subduction along the western margin of Gondwana and in an extensional tectonic setting after the cessation of subduction in the Early Permian (Mpodozis and Kay, 1992; Martin et al., 1999).

There are no outcrops of basement in the Precordillera of Argentina, but evidence from crustal xenoliths present in the Miocene volcanic rocks indicate the presence of a Grenville-aged (~1.3 – 1.0 Ga) basement (Kay et al., 1996). These xenoliths have unradiogenic whole-rock Pb isotopic compositions ($^{206}Pb/^{204}Pb$ = 17.1 – 17.8, $^{207}Pb/^{204}Pb$ = 15.42 – 15.49 and $^{208}Pb/^{204}Pb$ = 36.6 – 37.4) and distinct trace element signatures, which are similar to those found in the North American Grenville Province, leading to the suggestion of a Laurentian origin of this basement terrane (Abbruzzi et al., 1993; Kay and Orrell, 1996). However, this is somewhat disputed and a Gondwanan origin has also been suggested (e.g., Finney, 2007). This Grenville-aged basement is overlain by Cambrian – Ordovician strata and Tertiary sequences (Kay et al., 1996).

1.6 Current evidence for the contamination of Cenozoic arc magmas in the Pampean flat-slab segment

The Cenozoic plutonic belts present in the Principal Cordillera of Chile are relatively understudied, with more focus being applied to the volcanic arc rocks present in the Frontal Cordillera. The few isotopic studies to be conducted have obtained initial $^{87}Sr/^{86}Sr$ values of between 0.7035 and 0.7045 for the Middle Jurassic to Tertiary plutons present in the Pampean flat-slab segment (Parada, 1990 and references

therein). These values are generally lower than those reported for the Late Paleozoic and Early Mesozoic volcanic and plutonic rocks in central Chile (0.704 to 0.707 (Parada, 1990 and references therein) and 0.7032 to 0.721 (Mpodozis and Kay, 1992), which form a significant part of the basement in the Principal and Frontal Cordillera. The relatively low initial $^{87}Sr/^{86}Sr$ values of the Middle Jurassic to Tertiary plutons have been attributed to these plutonic belts being derived from partial melting of the mantle or of a mantle-derived basaltic source, with very little interaction with the continental crust (Parada et al., 1988; Parada, 1990).

A gradual increase in initial $^{87}Sr/^{86}Sr$ values and decrease in εNd values between the Oligocene and the Late Miocene has been reported for arc magmatic rocks from the Pampean flat-slab segment, suggesting an increasing influence of a radiogenic crustal component with time (e.g., Kay et al., 1991; Kay and Abbruzzi, 1996; Litvak et al., 2007). Similar trends have also been reported outside of the Pampean flat-slab segment, at the northern end of the SVZ (Stern and Skewes, 1995; Kurtz et al., 1997; Kay et al., 2005) and at the southern end of the CVZ (27 – 28.5 °S) (Goss et al., 2013). However, the processes involved (i.e. contamination of the melt source region with subducted components and/or crustal material from subduction erosion, versus crustal contamination of arc magmas) in the increased importance of crustally derived components in the petrogenesis of the Oligocene to Late Miocene arc magmas remains unresolved. The generally evolved nature of the arc magmatic rocks in the Pampean flat-slab segment also makes it particularly difficult to identify contamination of the melt source region. On this basis this study applies geochemical techniques not previously applied to arc magmatic rocks from the Pampean flat-slab segment, specifically *in-situ* isotopic analysis of mineral phases and melt inclusions, with the aim of differentiating these processes.

1.7 Thesis layout

The aim and objectives of this study are addressed in the following five chapters, which includes a compilation of three research papers (one in revision and two in preparation).

In Chapter 2 the Cenozoic arc stratigraphy is outlined and the results of high resolution, *in-situ* U-Pb dating of zircon and Ar-Ar dating are presented. This provides a temporal constraint for the whole rock geochemical data and petrological information presented in this chapter, as well as in subsequent chapters. Whole-rock major, trace and rare earth element geochemistry, in particular trace element systematics, are discussed in order to constrain contributions to Cenozoic arc magmas from the asthenospheric mantle, subducting components and the overlying Andean continental crust. The whole rock geochemical data is combined with insights gained from zircon inheritance in order to infer contamination of the Cenozoic arc magmas with the Andean basement. A combination of amphibole and amphibole-plagioclase geothermobarometers have also been applied to a subset of the plutonic and volcanic arc rock samples in order to ascertain temperatures and pressures of crystallisation/equilibration, and hence the crustal depths at which arc magmas may have been assimilating the surrounding continental crust. The data and findings presented in this chapter will be combined with the overall geodynamic discussion presented in Chapter 5 and submitted either to the *Journal of Petrology* or *Contributions to Mineralogy and Petrology*.

Chapter 3 presents the findings of high resolution oxygen and hafnium isotopic analysis of magmatic zircon and combines it with the results of U-Pb dating detailed in Chapter 2. In recent years the isotopic composition of the accessory mineral zircon has been used to develop models of continental crust formation, particularly

in relation to the early evolution of the continental crust (e.g., Hawkesworth and Kemp, 2006; Dhuime et al., 2011; Dhuime et al., 2012). The results presented show striking temporal and spatial variations which can be correlated with the changing subduction zone geodynamics and the consequent interaction of mantle-derived melts with distinct portions of the Andean basement. A key finding is that the pre-existing continental crust, which is spatially variable over the Andean Cordillera, plays a dominant role in modifying the composition of mantle-derived melts and can result in distinct isotopic compositions of magmatic zircon. This has implications for the development of models of continental growth, especially in settings where the geodynamics and plate tectonics are poorly understood, for example in the early Earth. This chapter is an extended version of a paper which is currently in revision for *Geology*.

In Chapter 4 the results of boron isotope and selected major and trace element analysis of pyroxene and zircon hosted melt inclusions, from a subset of samples, are presented. Primary melt inclusions are small quantities (~1 - 300μm) of silicate melt which are trapped within the host mineral phase as it crystallises. Once trapped the melt inclusions are protected from the late-stage processes occurring in the surrounding melt, such as degassing and alteration, and therefore provide a means of determining the composition of the melt at the time of crystallisation (e.g., Sobolev, 1996; Lowenstern, 2003; Schiano, 2003). Boron has been identified as an ideal tracer for mass transfer in subduction zones, especially of recycled slab components, and for assessing the role of fluids in magmas genesis. The results presented are temporally constrained by the results of U-Pb and Ar-Ar dating and significant variations in $\delta^{11}B$ values and trace element compositions are observed with time. These variations are linked with the changing geodynamic setting of the southern Central Andean margin and specifically with the shallowing of the subducting Nazca plate from ~18 Ma. The Central Andean arc magmas received a greater influence from fluids derived from serpentinised oceanic lithosphere after

the intersection of the Juan Fernández Ridge. This chapter is intended for submission to *Earth and Planetary Science Letters.*

In Chapter 5 the results and finding of the previous three data chapters are brought together in order to refine current understanding of the geodynamic evolution of the Pampean flat-slab segment over the course of the Cenozoic. The evolution of the Pampean flat-slab segment is divided into five time frames and a new geodynamic model presented and discussed for each. A particular focus is given to the petrogenesis of the arc magmatic rocks during these time intervals. As aforementioned, the content of this chapter will be combined with Chapter 2 and submitted to either the *Journal of Petrology* or *Contributions to Mineralogy and Petrology*.

Finally, in Chapter 6, the results are summarised and the overall findings of this research study are presented alongside a discussion of the limitations and some recommendations for future work.

1.8 Research contributions

At the beginning of each of the data chapters (Chapters 2, 3 and 4) a detailed account of the research contributions of the co-authors and collaborators is presented. Additional information relevant to this thesis, related to fieldwork and sample analysis, is presented below.

1.8.1 Fieldwork and sample collection

Fieldwork and sample collection in the southern Central Andes was conducted over two field seasons. The first field season was conducted by Andrew Miles and Simone Kasemann in October 2008 and involved the collection of Late Cretaceous to Miocene arc magmatic rocks from the Chilean side of the margin. Further sample collection in the Chilean Andes was conducted by the author in February 2011 in order to complete the Late Cretaceous to Miocene sample suite. The sampling of Cenozoic arc magmatic rocks from the Argentinean side of the margin was carried out by the author, Linda Kirstein and Simone Kasemann in February and March 2011. Due to access problems to the Valle del Cura (a result of mining operations) further samples from this region were provided by Vanesa Litvak at the University of Buenos Aires. The author worked with Vanesa Litvak at the University of Buenos Aires over the course of a week in order to determine a catalogue of suitable samples.

1.8.2 Sample preparation and analytical methods

A wide range of sample preparation techniques and analytical methods have been conducted as part of this study. Full details of all sample preparation, analytical methods and data processing can be found in the Appendix accompanying each chapter. Where appropriate summarised details are given in the thesis chapters, alongside information on the accuracy and precision of the measurements. Over the course of this PhD project three applications were made to the NERC Ion Microprobe Facility Steering Committee for supported analytical time. The applications were written by the author, with assistance from Linda Kirstein, Simone Kasemann and Richard Hinton, and received support from the committee.

1.9 References

Abbruzzi, J., Kay, S.M., and Bickford, M.E., 1993, Implications for the nature of the Precordilleran basement from the geochemistry and age of Precambrian xenoliths in Miocene volcanic rocks, San Juan province: Actas, v. 3, p. 331-339.

Aizawa, Y., Tatsumi, Y., and Yamada, H., 1999, Element transport by dehydration of subducted sediments: Implication for arc and ocean island magmatism: Island Arc, v. 8, p. 38-46.

Anderson, M., Alvarado, P., Zandt, G., and Beck, S., 2007, Geometry and brittle deformation of the subducting Nazca Plate, Central Chile and Argentina: Geophysical Journal International, v. 171, p. 419-434.

Armstrong, R.L., 1968, A model for the evolution of strontium and lead isotopes in a dynamic Earth: Reviews of Geophysics, v. 6, p. 175-199.

Ben Othman, D., White, W.M., and Patchett, J., 1989, The geochemistry of marine sediments, island arc magma genesis, and crust-mantle recycling: Earth and Planetary Science Letters, v. 94, p. 1-21.

Bissig, T., Clark, A.H., Lee, J.K., and von Quadt, A., 2003, Petrogenetic and metallogenetic responses to Miocene slab flattening: new constraints from the El Indio-Pascua Au–Ag–Cu belt, Chile/Argentina: Mineralium Deposita, v. 38, p. 844-862.

Bissig, T., Lee, J.K.W., Clark, A.H., and Heather, K.B., 2001, The Cenozoic History of Volcanism and Hydrothermal Alteration in the Central Andean Flat-Slab Region: New 40Ar-39Ar Constraints from the El Indio–Pascua Au (-Ag, Cu) Belt, 29°20′–30°30′ S: International Geology Review, v. 43, p. 312-340.

Bolhar, R., Weaver, S.D., Whitehouse, M.J., Palin, J.M., Woodhead, J.D., and Cole, J.W., 2008, Sources and evolution of arc magmas inferred from coupled O and Hf isotope systematics of plutonic zircons from the Cretaceous Separation Point Suite (New Zealand): Earth and Planetary Science Letters, v. 268, p. 312-324.

Bown, J.W., and White, R.S., 1994, Variation with spreading rate of oceanic crustal thickness and geochemistry: Earth and Planetary Science Letters, v. 121, p. 435-449.

Cahill, T., and Isacks, B.L., 1992, Seismicty and Shape of the Subducted Nazca Plate: Journal of Geophysical Research, v. 97, p. 17,503 - 17,529.

Cardó, R., and Díaz, I.N., 1999, Hoja Geológica 3169-I, Rodeo, provincias de San Juan: Buenos Aires, Instituto de Geología y Recursos Minerales, Servicio Geológico Minero Argentino.

Cardó, R., Díaz, I.N., Limarino, C.O., Litvak, V.D., Poma, S., and Santamaria, G., 2007, Hoja Geológica 2969-III, Malimán, provincias de San Juan y La Rioja: Buenos Aires, Instituto de Geología y Recursos Minerales, Servicio Geológico Minero Argentino.

Castillo, P.R., Janney, P.E., and Solidum, R.U., 1999, Petrology and geochemistry of Camiguin Island, southern Philippines: insights to the source of adakites and other lavas in a complex arc setting: Contributions to Mineralogy and Petrology, v. 134, p. 33-51.

Charrier, R., Baeza, O., Elgueta, S., Flynn, J.J., Gans, P., Kay, S.M., Muñoz, N., Wyss, A.R., and Zurita, E., 2002, Evidence for Cenozoic extensional basin development and tectonic inversion south of the flat-slab segment, southern Central Andes, Chile (33º - 36ºS.L.: Journal of South American Earth Sciences, v. 15, p. 117 - 139.

Charrier, R., Pinto, L., and Rodríguez, M.P., 2007, Tectonostratigraphic evolution of the Andean Orogen in Chile, *in* Moreno, T., and Gibbons, W., eds., The Geology of Chile: London, The Geological Society, p. 21 - 114.

Chung, S.-L., Liu, D., Ji, J., Chu, M.-F., Lee, H.-Y., Wen, D.-J., Lo, C.-H., Lee, T.-Y., Qian, Q., and Zhang, Q., 2003, Adakites from continental collision zones: Melting of thickened lower crust beneath southern Tibet: Geology, v. 31, p. 1021-1024.

Cloos, M., and Shreve, R.L., 1988, Subduction-Channel Model of Prism Accretion, Melange Formation, Sediment Subduction, and Subduction Erosion at Convergent Plate Margins: 1. Background and Description: Pure and Applied Geophysics, v. 128, p. 455 - 500.

Coira, B., Davidson, C., Mpodozis, C., and Ramos, V.A., 1982, Tectonic and magmatic evolution of the Andes of northern Argentina and Chile Earth Science Reviews, v. 18, p. 303 - 332.

Davidson, J.P., 1996, Deciphering mantle and crustal signatures in subduction zone magmatism: Subduction top to bottom, p. 251-262.

Davidson, J.P., and de Silva, S.L., 1992, Volcanic rocks from the Bolivian Altiplano: Insights into crustal structure, contamination, and magma genesis in the central Andes: Geology, v. 20, p. 1127-1130.

Davidson, J.P., Harmon, R.S., and Wörner, G., 1991, The source of central Andean magmas; Some considerations: Geological Society of America Special Papers, v. 265, p. 233-244.

Defant, M.J., and Drummond, M.S., 1990, Derivation of some modern arc magmas by melting of young subducted lithosphere: Nature, v. 347, p. 662-665.

Deschamps, F., Godard, M., Guillot, S., and Hattori, K., 2013, Geochemistry of subduction zone serpentinites: A review: Lithos, v. 178, p. 96-127.

Dhuime, B., Hawkesworth, C., and Cawood, P., 2011, When Continents Formed: Science, v. 331, p. 154-155.

Dhuime, B., Hawkesworth, C.J., Cawood, P.A., and Storey, C.D., 2012, A Change in the Geodynamics of Continental Growth 3 Billion Years Ago: Science, v. 335, p. 1334-1336.

Elliott, T., 2003, Tracers of the Slab, *in* Eiler, J.M., ed., Inside the Subduction Factory: Washington DC, American Geophysical Union, p. 23-45.

Elliott, T., Plank, T., Zindler, A., White, W., and Bourdon, B., 1997, Element transport from slab to volcanic front at the Mariana arc: Journal of Geophysical Research, v. 102, p. 14991 - 15019.

Emparan, C., and Pineda, G., 1999, Area Condoriaco-Rivadavia, Región de Coquimbo, Volume 12: Santiago, Servicio Nacional de Geologia y Mineria, Mapas Geológicos.

Finney, S.C., 2007, The parautochthonous Gondwanan origin of the Cuyania (greater Precordillera) terrane of Argentina: A re-evaluation of evidence used to support an allochthonous Laurentian origin: Geologica Acta, v. 5, p. 127-158.

Garrison, J.M., and Davidson, J.P., 2003, Dubious case for slab melting in the Northern volcanic zone of the Andes: Geology, v. 31, p. 565-568.

Gilbert, H., Beck, S., and Zandt, G., 2006, Lithospheric and upper mantle structure of the central Chile and Argentina: Geophysical Journal International, v. 165, p. 383 - 398.

Gill, J.B., 1981, Orogenic Andesites and Plate Tectonics: New York, Springer-Verlag.

Goss, A.R., Kay, S.M., and Mpodozis, C., 2013, Andean Adakite-like high-Mg Andesites on the Northern Margin of the Chilean–Pampean Flat-slab (27–28· 5° S) Associated with Frontal Arc Migration and Fore-arc Subduction Erosion: Journal of Petrology, v. 54, p. 2193-2234.

Gregory-Wodzicki, K.M., 2000, Uplift history of the Central and Northern Andes: A review: Geological Society of America Bulletin, v. 112, p. 1091-1105.

Gutscher, M.-A., Maury, R., Eissen, J.-P., and Bourdon, E., 2000a, Can slab melting be caused by flat subduction?: Geology, v. 28, p. 535-538.

Gutscher, M.A., Olivet, J.L., Aslanian, D., Eissen, J.P., and Maury, R., 1999, The "lost inca plateau": cause of flat subduction beneath peru?: Earth and Planetary Science Letters, v. 171, p. 335-341.

Gutscher, M.A., Spakman, W., Bijwaard, H., and Engdahl, E.R., 2000b, Geodynamics of flat subduction: Seismicity and tomographic constraints from the Andean margin: Tectonics, v. 19, p. 814-833.

Hammerschmidt, K., Döbel, R., and Friedrichsen, H., 1992, Implication of 40Ar39Ar dating of Early Tertiary volcanic rocks from the north-Chilean Precordillera: Tectonophysics, v. 202, p. 55-81.

Hattori, K.H., and Guillot, S., 2003, Volcanic fronts form as a consequence of serpentinite dehydration in the forearc mantle wedge: Geology, v. 31, p. 525-528.

Hawkesworth, C.J., Gallagher, K., Hergt, J.M., and McDermott, F., 1993, Mantle and slab contributions in arc magmas: Annual Review of Earth and Planetary Sciences, v. 21, p. 175 - 204.

Hawkesworth, C.J., Hergt, J.M., Ellam, R.M., and Dermott, F.M., 1991, Element Fluxes Associated with Subduction Related Magmatism: Philosophical Transactions of the Royal Society of London. Series A: Physical and Engineering Sciences, v. 335, p. 393-405.

Hawkesworth, C.J., and Kemp, A.I.S., 2006, Using hafnium and oxygen isotopes in zircons to unravel the record of crustal evolution: Chemical Geology, v. 226, p. 144 - 162.

Heit, B., Yuan, X., Bianchi, M., Sodoudi, F., and Kind, R., 2008, Crustal thickness estimation beneath the southern central Andes at 30ºS and 36ºS from S wave receiver function analysis: Geophysical Journal International.

Hildreth, W., and Moorbath, S., 1988, Crustal contributions to arc magmatism in the Andes of Central Chile: Contributions to Mineralogy and Petrology, v. 98, p. 455 - 489.

Hyndman, R.D., and Peacock, S.M., 2003, Serpentinization of the forearc mantle: Earth and Planetary Science Letters, v. 212, p. 417-432.

Isacks, B.L., 1988, Uplift of the Central Andean Plateau and bending of the Bolivian Orocline: Journal of Geophysical Research: Solid Earth, v. 93, p. 3211-3231.

Jaillard, E., Hérail, G., Monfret, T., Díaz-Martínez, E., Baby, P., Lavenu, A., and Dumont, J., 2000, Tectonic evolution of the Andes of Ecuador, Peru, Bolivia and northernmost Chile: Tectonic Evolution of South America (Cordani, UG; Milani, EJ; Thomaz Filho, A, p. 481-559.

James, D.E., 1982, A combined O, Sr, Nd, and Pb isotopic and trace element study of crustal contamination in central Andean lavas, I. Local geochemical variations: Earth and Planetary Science Letters, v. 57, p. 47-62.

Jarrard, R.D., 2003, Subduction fluxes of water, carbon dioxide, chlorine, and potassium: Geochemistry, Geophysics, Geosystems, v. 4.

Jordan, T., Allmendinger, R., Damanti, J., and Drake, R., 1993, Chronology of motion in a complete thrust belt: The Precordillera, 30-31 S, Andes Mountains: The Journal of Geology, p. 135-156.

Jordon, T.E., Burns, W.M., Veiga, R., Pángaro, F., Copeland, P., Kelley, S., and Mpodozis, C., 2001, Extension and basin formation in the southern Andes caused by increased convergence rate: A mid-Cenozoic trigger for the Andes: Tectonics, v. 20, p. 308 - 324.

Kasemann, S., Erzinger, J., and Franz, G., 2000, Boron recycling in the continental crust of the central Andes from the Palaeozoic to Mesozoic, NW Argentina: Contributions to Mineralogy and Petrology, v. 140, p. 328 - 343.

Kay, R.W., 1980, Volcanic arc magmas: Implications of a melting-mixing model for element recycling in the crust-upper mantle system: The Journal of Geology, v. 88, p. 497 - 522.

Kay, S., and Gordillo, C., 1994, Pocho volcanic rocks and the melting of depleted continental lithosphere above a shallowly dipping subduction zone in the central Andes: Contributions to Mineralogy and Petrology, v. 117, p. 25-44.

Kay, S.M., and Abbruzzi, J.M., 1996, Magmatic evidence for Neogene lithospheric evolution of the central Andean "flat slab" between 30ºS and 32ºS: Tectonophysics, v. 259, p. 15 - 28.

Kay, S.M., Godoy, E., and Kurtz, A., 2005, Episodic arc migration, crustal thickening, subduction erosion, and magmatism in the south-central Andes: Geological Society of America Bulletin, v. 117, p. 67-88.

Kay, S.M., Maksaev, V., Moscoso, R., Mpodozis, C., and Nasi, C., 1987, Probing the evolving Andean lithosphere; Mid - Late Tertiary magmatism in Chile (29º - 30º30'S) over the modern zone of subhorizontal subduction: Journal of Geophysical Research, v. 92, p. 6173 - 6189.

Kay, S.M., and Mpodozis, C., 2002, Magmatism as a probe to the Neogene shallowing of the Nazca plate beneath the modern Chilean flat slab: Journal of South American Earth Sciences, v. 15, p. 39 - 57.

Kay, S.M., Mpodozis, C., Ramos, V.A., and Munizaga, F., 1991, Magma source variations for mid-late Tertiary magmatic rocks associated with a shallowing subduction zone and the thickening crust in the central Andes (28-33ºS): Spec. Pap. Geological Society of America Bulletin, v. 265, p. 113 - 137.

Kay, S.M., and Orrell, S., 1996, Zircon and whole rock Nd-Pb isotopic evidence for a Grenville age and a Laurentian origin for the Basement of the Precordillera in Argentina: Journal of Geology, v. 104, p. 637.

Kay, S.M., Orrell, S., and Abbruzzi, J., 1996, Zircon and whole rock Nd-Pb isotopic evidence for a Grenville age and a Laurentian origin for the basement of the Precordillera in Argentina: The Journal of Geology, p. 637-648.

Kay, S.M., Ramos, V.A., Mpodozis, C., and Sruoga, P., 1989, Late Paleozoic to Jurassic silicic magmatism at the Gondwana margin: Analogy to the Middle Proterozoic in North America?: Geology, v. 17, p. 324-328.

Kelley, K.A., Plank, T., Ludden, J., and Staudigel, H., 2003, Composition of altered oceanic crust at ODP Sites 801 and 1149: Geochemistry, Geophysics, Geosystems, v. 4, p. 8910.

Kilian, R., and Behrmann, J.H., 2003, Geochemical constraints on the sources of Southern Chile Trench sediments and their recycling in arc magmas of the Southern Andes: Journal of the Geological Society, v. 160, p. 57-70.

Kogiso, T., Tatsumi, Y., and Nakano, S., 1997, Trace element transport during dehydration processes in the subducted oceanic crust: 1. Experiments and implications for the origin of ocean island basalts: Earth and Planetary Science Letters, v. 148, p. 193 - 205.

Kopp, H., Flueh, E.R., Papenberg, C., and Klaeschen, D., 2004, Seismic investigations of the O'Higgins Seamount Group and Juan Fernández Ridge: Aseismic ridge emplacement and lithosphere hydration: Tectonics, v. 23.

Kurtz, A.C., Kay, S.M., Charrier, R., and Farrar, E., 1997, Geochronology of Miocene plutons and exhumation history of the El Teniente region, Central Chile (34-35° 8): Andean Geology, v. 24, p. 75-90.

Lamy, F., Hebbeln, D., and Wefer, G., 1998, Terrigenous sediment supply along the Chilean continental margin: modern regional patterns of texture and composition: Geol Rundsch, v. 87, p. 447 - 494.

Litvak, V.D., Poma, S., and Kay, S.M., 2007, Paleogene and Neogene magmatism in the Valle del Cura region: New perspective on the evolution of the Pampean flat slab, San Juan province, Argentina: Journal of South American Earth Sciences, v. 24, p. 117 - 137.

Llambias, E.J., and Sato, A.M., 1990, El Batolito de Colangüil (29-31° S) cordillera frontal de Argentina: estructura y marco tectonico: Andean Geology, v. 17, p. 89-108.

Llambías, E.J., and Sato, A.M., 1995, El batolito de Colangüil: transición entre orogénesis y anorogénesis: Revista de la Asociación Geológica Argentina, v. 50, p. 111-131.

Lonsdale, P., 2005, Creation of the Cocos and Nazca plates by fission of the Farallon plate: Tectonophysics, v. 404, p. 237-264.

Lowenstern, J.B., 2003, Melt inclusions come of age: volatiles, volcanoes, and Sorby's legacy, *in* De Vivo, B., and Bodnar, R.J., eds., Melt Inclusions in Volcanic Systems: Methods, Applications and Problems, Volume 5: Amsterdam, Elsevier, p. 1 - 22.

Lucassen, F., Becchio, R., Wilke, H.G., Franz, G., Thirlwall, M.F., Viramonte, J., and Wemmer, K., 2000, Proterozoic–Paleozoic development of the basement of the Central Andes (18–26°S) — a mobile belt of the South American craton: Journal of South American Earth Sciences, v. 13, p. 697-715.

Lucassen, F., and Franz, G., 2005, The early Palaeozoic Orogen in the Central Andes: a non-collisional orogen comparable to the Cenozoic high plateau?: Geological Society, London, Special Publications, v. 246, p. 257-273.

Lucassen, F., Wiedicke, M., and Franz, G., 2010, Complete recycling of a magmatic arc: evidence from chemical and isotopic composition of Quaternary trench sediments in Chile (36°–40°S): International Journal of Earth Sciences, v. 99, p. 687-701.

Macpherson, C.G., Dreher, S.T., and Thirlwall, M.F., 2006, Adakites without slab melting: high pressure differentiation of island arc magma, Mindanao, the Philippines: Earth and Planetary Science Letters, v. 243, p. 581-593.

Maksaev, V., Moscoso, R., Mpodozis, C., and Nasi, C., 1984, Las unidades volcánicas y plutónicas del Cenozoico superior en la Alta Cordilera del Norte Chico (29°–31° S): Geología, Alteración hidrotermal y Mineralización: Revista Geológica de Chile, v. 11, p. 12 - 51.

Maksaev, V., and Zentilli, M., 1999, Fission track thermochronology of the Domeyko Cordillera, northern Chile; implications for Andean tectonics and porphyry copper metallogenesis: Exploration and Mining Geology, v. 8, p. 65 - 89.

Maksaev, V., Zentilli, M., Munizaga, F., and Charrier, R., 2003, Denudación/alzamiento del Mioceno Superior–Plioceno Inferior de la Cordillera de Chile Central (33º–35ºS) inferida por dataciones por trazas de fisión en apatito de plutones miocenos, Congreso Geológico Chileno.

Manea, V.C., Pérez-Gussinyé, M., and Manea, M., 2012, Chilean flat slab subduction controlled by overriding plate thickness and trench rollback: Geology, v. 40, p. 35-38.

Marot, M., Monfret, T., Pardo, M., Ranalli, G., and Nolet, G., 2013, A double seismic zone in the subducting Juan Fernandez Ridge of the Nazca Plate (32°S), central Chile: Journal of Geophysical Research: Solid Earth, v. 118, p. 3462-3475.

Martin, M.W., Clavero R, J., and Mpodozis M, C., 1997, Eocene to Late Miocene magmatic development of El Indio Belt, 30° S, North-central Chile, Congreso Congreso Geológico Chileno, 8 Actas 1: Antofagasta, p. 149–153

Martin, M.W., Clavero R, J., and Mpodozis M, C., 1999, Late Paleozoic to Early Jurassic tectonic development of the high Andean Principal Cordillera, El Indio Region, Chile (29–30°S): Journal of South American Earth Sciences, v. 12, p. 33-49.

Moran, A.E., Sisson, V.B., and Leeman, W.P., 1992, Boron depletion during progressive metamorphism: implications for subduction processes: Earth and Planetary Science Letters, v. 111, p. 331-349.

Moriguti, T., and Nakamura, E., 1998, Across-arc variation of Li isotopes in lavas and implications for crust/mantle recycling at subduction zones: Earth and Planetary Science Letters, v. 163, p. 167-174.

Morris, J., and Ryan, J.G., 2003, Subduction zone processes and implications for changing composition of the upper and lower mantle: Treatise on geochemistry, v. 2, p. 451-470.

Morris, J., and Tera, F., 1989, 10Be and 9Be in mineral separates and whole rocks from volcanic arcs: Implications for sediment subduction: Geochimica et Cosmochimica Acta, v. 53, p. 3197-3206.

Morris, J.D., Leeman, W.P., and Tera, F., 1990, The subducted component in island arc lavas: constraints from Be isotopes and B-Be systematics: Nature, v. 344, p. 31 - 36.

Mpodozis, C., and Cornejo, P.P., 1988, Hoja Pisco Elqui, Region de Coquimbo, *in* Mpodozis, C., Davidson, J., and Rivano, S., eds., Carta Geologica de Chile: Santiago, Servicio Nacional de Geología y Minería (SERNAGEOMIN).

Mpodozis, C., and Kay, S.M., 1990, Provincias magmáticas ácidas y evolución tectónica de Gondwana: Andes chilenos (28-31 S): Andean Geology, v. 17, p. 153-180.

Mpodozis, C., and Kay, S.M., 1992, Late Paleozoic to Triassic evolution of the Gondwana margin: Evidence from Chilean Frontal Cordilleran batholiths (28 S to 31 S): Geological Society of America Bulletin, v. 104, p. 999-1014.

Nasi, C., Moscoso, R., and Maksaev, V., 1990, Hoja Guanta, Regiones de Atacama y Coquimbo, *in* Mpodozis, C., Davidson, J., and Rivano, S., eds., Carta Geologica de Chile: Santiago, Servicio Nacional de Geología y Minería (SERNAGEOMIN).

Nasi, C., Mpodozis M, C., Cornejo, P., Moscoso, R., and Maksaev, V., 1985, El Batolito Elqui-Limarí (Paleozoico Superior Triásico): características petrográficas, geoquímicas y significado tectónico: Revista Geológica de Chile, v. 25, p. 26.

Nichols, G.T., Wyllie, P.J., and Stern, C.R., 1996, Experimental melting of pelagic sediment, constraints relevant to subduction, Subduction top to bottom, Volume 96: Geophys. Monogr. Ser.: Washington, DC, AGU, p. 293-298.

O'Driscoll, L.J., Richards, M.A., and Humphreys, E.D., 2012, Nazca–South America interactions and the late Eocene–late Oligocene flat-slab episode in the central Andes: Tectonics, v. 31.

Oncken, O., Hindle, D., Kley, J., Elger, K., Victor, P., and Schemmann, K., 2006, Deformation of the central Andean upper plate system—Facts, fiction, and constraints for plateau models, The Andes, Springer, p. 3-27.

Palmer, M., 1991, Boron-isotope systematics of Halmahera arc (Indonesia) lavas: Evidence for involvement of the subducted slab: Geology, v. 19, p. 215-217.

Parada, M.A., 1990, Granitoid plutonism in central Chile and its geodynamic implications; A review, *in* Kay, S.M., and Rapela, C.W., eds., Plutonism from Antarctica to Alaska, Volume Special Paper 241: Boulder, Colorado, The Geological Society of America.

Parada, M.A., López-Escobar, L., Oliveros, V., Fuentes, F., Morata, D., Calderón, M., Aguirre, L., Féraud, G., Espinoza, F., Moreno, H., Figueroa, O., Bravo, J.M., Vásquez, R.T., and Stern, C.R., 2007, Andean Magmatism, *in* Moreno, T., and Gibbons, W., eds., The Geology of Chile: London, The Geological Society, p. 115 - 146.

Parada, M.A., Rivano, S., Sepulveda, P., Herve, M., Herve, F., Puig, A., Munizaga, F., Brook, M., Pankhurst, R., and Snelling, N., 1988, Mesozoic and Cenozoic plutonic development in the Andes of central Chile (30º30' - 32º30'S) Journal of South American Earth Sciences, v. 1, p. 249 - 260.

Pardo Casas, F., and Molnar, P., 1987, Relative motion of the Nazca (Farallón) and South America plates since Late Cretaceous time Tectonics, v. 6, p. 233 - 248.

Peacock, S.A., 1990, Fluid processes in subduction zones: Science, v. 248, p. 329-337.

Peacock, S.M., 1996, Thermal and petrologic structure of subduction zones, Subduction top to bottom, Volume 96: Geophys. Monogr. Ser.: Washington, DC, AGU, p. 119-133.

Peacock, S.M., Rushmer, T., and Thompson, A.B., 1994, Partial melting of subducting oceanic crust: Earth and Planetary Science Letters, v. 121, p. 227-244.

Pichowiak, S., Buchelt, M., and Damm, K., 1990, Magmatic activity and tectonic setting of the early stages of the Andean cycle in northern Chile: Plutonism from Antarctica to Alaska (Kay, SM; Rapela, CW, editors) Geological Society of America, Special Paper, v. 241, p. 127-144.

Pilger, R.H., 1981, Plate reconstructions, aseismic ridges, and low angle subduction beneath the Andes: Geological Society of America Bulletin, v. 92, p. 448 - 456.

Pilger, R.H., 1984, Cenozoic plate kinematics, subduction and magmatism: South American Andes: Journal of Geological Society London, v. 141, p. 793 - 802.

Pineda, G., and Calderón, M., 2008, Geología del área Monte Patria-El Maqui, Región de Coquimbo, Carta Geológica de Chile, Serie Geología Básica: Santiago, Servicio Nacional de Geología y Minería.

Pineda, G., and Emparan, C., 2006, Geología del área Vicuña-Pichasca, Región de Coquimbo, Carta Geológica de Chile, Serie Geología Básica Volume 97: Santiago, Servicio Nacional de Geología y Minería.

Plank, T., 2005, Constraints from Thorium/Lanthanum on Sediment Recycling at Subduction Zones and the Evolution of the Continents: Journal of Petrology, v. 46, p. 921 - 944.

Plank, T., and Langmuir, C.H., 1993, Tracing trace elements from sediment input to volcanic output at subduction zones: Nature, v. 362, p. 739 - 743.

Plank, T., and Langmuir, C.H., 1998, The chemical composition of subducting sediment and its consequences for the crust and mantle: Chemical Geology, v. 145, p. 325 - 394.

Ramos, V.A., 1989, The Birth of Southern South America: American Scientist, v. 77, p. 444-450.

Ramos, V.A., 2004, Cuyania, an Exotic Block to Gondwana: Review of a Historical Success and the Present Problems: Gondwana Research, v. 7, p. 1009-1026.

Ramos, V.A., 2010, The Grenville-age basement of the Andes: Journal of South American Earth Sciences, v. 29, p. 77-91.

Ramos, V.A., Cristallini, E.O., and Pérez, D.J., 2002, The Pampean flat-slab of the Central Andes: Journal of South American Earth Sciences, v. 15, p. 59-78.

Ramos, V.A., and Folguera, A., 2009, Andean flat-slab subduction through time: Geological Society, London, Special Publications, v. 327, p. 31-54.

Ramos, V.A., Jordan, T.E., Allmendinger, R.W., Mpodozis, C., Kay, S.M., Cortés, J.M., and Palma, M., 1986, Paleozoic terranes of the central Argentine-Chilean Andes: Tectonics, v. 5, p. 855-880.

Ranero, C.R., Phipps Morgan, J., McIntosh, K., and Reichert, C., 2003, Bending-related faulting and mantle serpentinization at the Middle America trench: Nature, v. 425, p. 367-373.

Ranero, C.R., and Sallarès, V., 2004, Geophysical evidence for hydration of the crust and mantle of the Nazca plate during bending at the north Chile trench: Geology, v. 32, p. 549-552.

Rapp, R.P., and Watson, E.B., 1995, Dehydration melting of metabasalt at 8–32 kbar: implications for continental growth and crust-mantle recycling: Journal of Petrology, v. 36, p. 891-931.

Reich, M., Parada, M.A., Palacios, C., Dietrich, A., Schultz, F., and Lehmann, B., 2003, Adakite-like signature of Late Miocene intrusions at the Los Pelambres giant porphyry copper deposit in the Andes of central Chile: metallogenic implications: Mineralium Deposita, v. 38, p. 876-885.

Rodríguez, C., Sellés, D., Dungan, M., Langmuir, C., and Leeman, W., 2007, Adakitic Dacites Formed by Intracrustal Crystal Fractionation of Water-rich Parent Magmas at Nevado de Longaví Volcano (36·2°S; Andean Southern Volcanic Zone, Central Chile): Journal of Petrology, v. 48, p. 2033-2061.

Rooney, T., Franceschi, P., and Hall, C., 2011, Water-saturated magmas in the Panama Canal region: a precursor to adakite-like magma generation?: Contributions to Mineralogy and Petrology, v. 161, p. 373-388.

Rosner, M., Erzinger, J., Franz, G., and Trumbull, R.B., 2003, Slab-derived boron isotope signatures in arc volcanic rocks from the Central Andes and evidence from boron isotope fractination during progressive slab dehydration: Geochemistry Geophysics Geosystems, v. 4.

Rutland, R.W.R., 1971, Andean Orogeny and Ocean Floor Spreading: Nature, v. 233, p. 252 - 255.

Ryan, J.G., Morris, J.D., Tera, F., Leeman, W.P., and Tsuetkov, A., 1995, Cross-arc geochemical variations in the Kurile arc as a function of slab depth: Science, v. 270, p. 625 - 627.

Sano, T., Hasenaka, T., Shimaoka, A., Yonezawa, C., and Fukuoka, T., 2001, Boron contents of Japan Trench sediments and Iwate basaltic lavas, Northeast Japan arc: estimation of sediment-derived fluid contribution in mantle wedge: Earth and Planetary Science Letters, v. 186, p. 187-198.

Savov, I.P., Ryan, J.G., D'Antonio, M., and Fryer, P., 2007, Shallow slab fluid release across and along the Mariana arc-basin system: Insights from geochemistry of serpentinized peridotites from the Mariana fore arc: Journal of Geophysical Research: Solid Earth (1978–2012), v. 112.

Schiano, P., 2003, Primitive mantle magmas recorded as silicate melt inclusions in igneous minerals: Earth-Science Reviews, v. 63, p. 121-144.

Schmidt, M.W., and Poli, S., 1998, Experimentally based water budgets for dehydrating slabs and consequences for arc magma generation: Earth and Planetary Science Letters, v. 163, p. 361-379.

Schmitt, A.K., Kasemann, S., Meixner, A., and Rhede, D., 2002, Boron in central Andean ignimbrites: implications for crustal boron cycles in active continental margin: Chemical Geology, v. 183, p. 333 - 347.

Sen, C., and Dunn, T., 1994, Dehydration melting of a basaltic composition amphibolite at 1.5 and 2.0 GPa: implications for the origin of adakites: Contributions to Mineralogy and Petrology, v. 117, p. 394-409.

Sigmarsson, O., Condomines, M., Morris, J.D., and Harmon, R.S., 1990, Uranium and 10Be enrichments by fluids in Andean arc magmas: Nature, v. 346, p. 163-165.

Silver, P.G., M. Russo, R., and Lithgow-Bertelloni, C., 1998, Coupling of South American and African Plate Motion and Plate Deformation: Science, v. 279, p. 60-63.

Sobolev, A.V., 1996, Melt Inclusions in Minerals as a Source of Principle Petrological Information: Petrology, v. 4, p. 209 - 220.

Sodoudi, F., Yuan, X., Asch, G., and Kind, R., 2011, High-resolution image of the geometry and thickness of the subducting Nazca lithosphere beneath northern Chile: Journal of Geophysical Research: Solid Earth (1978–2012), v. 116.

Somoza, R., 1998, Updated azca (Farallon)—South America relative motions during the last 40 My: implications for mountain building in the central Andean region: Journal of South American Earth Sciences, v. 11, p. 211-215.

Somoza, R., and Ghidella, M.E., 2012, Late Cretaceous to recent plate motions in western South America revisited: Earth and Planetary Science Letters, v. 331–332, p. 152-163.

Spikings, R., Dungan, M., Foeken, J., Carter, A., Page, L., and Stuart, F., 2008, Tectonic response of the central Chilean margin (35–38 S) to the collision and subduction of heterogeneous oceanic crust: a thermochronological study: Journal of the Geological Society, v. 165, p. 941-953.

Staudigel, H., 2003, Hydrothermal alteration processes in the oceanic crust: Treatise on geochemistry, v. 3, p. 511-535.

Stern, C.R., 1991, Role of subduction erosion in the generation of Andean magmas: Geology, v. 19, p. 78 - 81.

Stern, C.R., 2004, Active Andean volcanism: its geologic and tectonic setting Revista Geológica de Chile, v. 31, p. 161 - 206.

Stern, C.R., and Kilian, R., 1996, Role of the subducted slab, mantle wedge and continental crust in the generation of adakites from the Andean Austral Volcanic Zone: Contributions to Mineralogy and Petrology, v. 123, p. 263-281.

Stern, C.R., and Skewes, M.A., 1995, Miocene to present magmatic evolution at the northern end of the Andean Southern Volcanic Zone, Central Chile: Revista Geológica de Chile, v. 22, p. 261 - 272.

Straub, S.M., and Layne, G.D., 2002, The systematics of boron isotopes in Izu arc front volcanic rocks: Earth and Planetary Science Letters, v. 198, p. 25-39.

Tassara, A., Götze, H.-J., Schmidt, S., and Hackney, R., 2006, Three-dimensional density model of the Nazca plate and the Andean continental margin: Journal of Geophysical Research: Solid Earth, v. 111, p. B09404.

Tatsumi, Y., 1989, Migration of fluid phases and genesis of basalt magmas in subduction zones: Journal of Geophysical Research, v. 94, p. 4697-4707.

Tatsumi, Y., Hamilton, D.L., and Nesbitt, R.W., 1986, Chemical characteristics of fluid phase released from a subducted lithosphere and origin of arc magmas: Evidence from high-pressure experiments and natural rocks: Journal of Volcanology and Geothermal Research, v. 29, p. 293-309.

Tera, F., Brown, L., Morris, J., Sacks, I.S., Klein, J., and Middleton, R., 1986, Sediment incorporation in island-arc magmas: Inferences from 10Be: Geochimica et Cosmochimica Acta, v. 50, p. 535-550.

Thomas, W.A., and Astini, R.A., 2003, Ordovician accretion of the Argentine Precordillera terrane to Gondwana: a review: Journal of South American Earth Sciences, v. 16, p. 67-79.

Thornburg, T.M., and Kulm, L.D., 1987a, Sedimentation in the Chile Trench: Depositional morphologies, lithofacies, and stratigraphy: Geological Society of America Bulletin, v. 98, p. 33 - 52.

Thornburg, T.M., and Kulm, L.D., 1987b, Sedimentation in the Chile Trench; petrofacies and provenance: Journal of Sedimentary Research, v. 57, p. 55-74.

Tollstrup, D., Gill, J., Kent, A., Prinkey, D., Williams, R., Tamura, Y., and Ishizuka, O., 2010, Across-arc geochemical trends in the Izu-Bonin arc: Contributions from the subducting slab, revisited: Geochemistry, Geophysics, Geosystems, v. 11, p. Q01X10.

Tonarini, S., Armienti, P., D'Orazio, M., and Innocenti, F., 2001, Subduction-like fluids in the genesis of Mt. Etna magmas: evidence from boron isotopes and fluid mobile elements: Earth and Planetary Science Letters, v. 192, p. 471-483.

Tonarini, S., Leeman, W.P., and Leat, P.T., 2011, Subduction erosion of forearc mantle wedge implicated in the genesis of the South Sandwich Island (SSI) arc: Evidence from boron isotope systematics: Earth and Planetary Science Letters, v. 301, p. 275-284.

Trumbull, R.B., Riller, U., Oncken, O., Scheuber, E., Munier, K., and Hongn, F., 2006, The time-space distribution of Cenozoic Volcanism in the South-Central Andes: a new data compliation and some tectonic implications, *in* Oncken, O., Chong, G., Franz, G., Giese, P., Götze, H.-J., Ramos, V.A., Strecker, M.R., and Wigger, P., eds., The Andes - active subduction orogeny, Volume 1: Frontiers in Earth Sciences, Springer Verlag, p. 29-43.

Ulmer, P., and Trommsdorff, V., 1995, Serpentine stability to mantle depths and subduction-related magmatism: Science, v. 268, p. 858-861.

van Keken, P.E., Hacker, B.R., Syracuse, E.M., and Abers, G.A., 2011, Subduction factory: 4. Depth-dependent flux of H2O from subducting slabs worldwide: Journal of Geophysical Research: Solid Earth, v. 116, p. B01401.

Von Huene, R., and Scholl, D.W., 1991, Observations at convergent margins concerning sediment subduction, subduction erosion, and the growth of continental crust: Reviews of Geophysics, v. 29.

Woodhead, J., Eggins, S., and Gamble, J., 1993, High field strength and transition element systematics in island arc and back-arc basin basalts: Evidence for multi-phase melt extraction and a depleted mantle wedge: Earth and Planetary Science Letters, v. 114, p. 491-504.

Wunder, B., Wirth, R., and Gottschalk, M., 2001, Antigorite Pressure and temperature dependence of polysomatism and water content: European Journal of Mineralogy, v. 13, p. 485-496.

Yañez, G.A., Cembrano, J., Pardo, M., Ranero, C.R., and Selles, D., 2002, The Challenger - Juan Fernández - Maipo major tectonic transition of the Nazca -

Andean subduction system at 33-34ºS: geodynamic evidence and implications: Journal of South American Earth Sciences, v. 15, p. 28 - 38.

Yañez, G.A., Ranero, C.R., von Huene, R., and Díaz, J., 2001, Magnetic anomaly interpretation across the southern central Andes (32º-34ºS): The role of the Juan Fernández Ridge in the late Tertiary evolution of the margin: Journal of Geophysical Research, v. 106, p. 6325 - 6345.

Chapter 2. Petrogenetic constraints on the Late Cretaceous – Miocene arc magmas from the southern Central Andes from geochemistry, geochronology and geothermobarometry

Rosie E. Jones[1]*, Linda A. Kirstein[1], Simone A. Kasemann[2] Vanesa D. Litvak[4], Richard Hinton[1], and EIMF[5]

[1] School of GeoSciences, University of Edinburgh, West Mains Road, Edinburgh, EH9 3JW, UK

[2] Department of Geosciences & MARUM, Centre for Marine Environmental Sciences, University of Bremen, 28334 Bremen, Germany

[3] School of Earth Sciences, University of Bristol, Wills Memorial Building, Queens Road, Bristol, BS8 1RJ, UK

[4] Instituto de Estudios Andinos Don Pablo Groeber, Departamento de Ciencias Geológicas, Universidad de Buenos Aires – CONICET, Argentina

[5] Edinburgh Ion Microprobe Facility, School of GeoSciences, University of Edinburgh, West Mains Road, Edinburgh, EH9 3JW, UK

The data and findings presented in this chapter will be combined with the overall geodynamic discussion presented in Chapter 5 and submitted either to the *Journal of Petrology* or *Contributions to Mineralogy and Petrology*.

2.1 Author Contributions

All the petrological work required for this study was conducted by the author. I carried out all of the sample preparation and analytical work for the U-Pb dating of zircon. Assistance and guidance in the U-Th-Pb analysis of zircons by secondary ion mass spectrometry (SIMS), and in the various methods of data reduction and correction, was provided by Richard Hinton. Ar-Ar dating of plagioclase separates (separated and picked from two samples by myself) was conducted at the Open University by James Malley and Sarah Sherlock, due to the lack of similar analytical facilities at the University of Edinburgh. The preparation of samples for whole rock major, minor and trace element analysis was on the whole carried out by myself. Due to the large quantity of samples (~60) help with sample preparation for whole rock geochemical analysis was provided by Katarzyna Sokol (undergraduate chemistry student). XRF analysis was conducted by Nic Odling at the University of Edinburgh, with some assistance from myself. I conducted the analysis of rare earth elements (REE) via inductively-coupled plasma mass spectrometry (ICP-MS) at the Scottish Universities Environmental Research Centre (SUERC), East Kilbride, under the direction and supervision of Valerie Olive. The analysis of plagioclase, pyroxene and amphibole by electron microprobe (EPMA) was carried out by myself, with technical support from Chris Hayward. Processing of all the petrological information and geochemical data was conducted by myself. The interpretations and conclusions drawn from the data are my own, but benefitted from discussions with Vanesa Litvak, Linda Kirstein, Richard Hinton, Godfrey Fitton and Alan Hastie.

2.2 Abstract

As magmatic arcs are currently the principal sites for the production of new continental crust, investigation of the petrogenesis of volcanic and plutonic arc rocks is important in order to constrain the relative contributions to crustal growth. This study uses the petrographic and geochemical characteristics of arc magmatic rocks from the southern Central Andes in order to investigate the relative contributions from the asthenospheric mantle, subducting components, and the existing continental crust. Specifically, in relation to the changing geodynamic setting of the Central Andean margin during the Cenozoic and the development from a more extensional convergent margin in the Late Cretaceous (~75 Ma) to a highly compressional margin in the Late Miocene (~ 6 Ma). This has been related to changes in convergence rates and angles, and the angle of the subducting oceanic plate.

Whole rock geochemical data for a suite of Late Cretaceous to Late Miocene arc rocks from the Pampean flat-slab segment (between 29 – 31 ^{0}S) of the southern Central Andes is presented alongside petrographic observations, high resolution U-Pb and Ar-Ar dating, and amphibole-plagioclase geothermobarometry. The high resolution, *in-situ* U-Pb dating of magmatic zircon, combined with Ar-Ar dating, has led to an improved regional stratigraphy and provides an accurate temporal constraint for the geochemical and geothermobarometric data. Trace and rare earth element compositions obtained for the Late Cretaceous to Late Eocene arc magmatic rocks from the Principal Cordillera of Chile, combined with a lack of zircon inheritance, suggests limited assimilation of the overlying continental crust by arc magmas derived from the asthenospheric mantle. A combined general increase in incompatible, fluid- mobile/immobile (e.g., Ba/Nb and Pb/Nb) and fluid-immobile/immobile (e.g., Nb/Zr and Nb/Yb) trace element ratios observed over this time period is attributed to the influence of the subducting slab on the melt source region. The Late Oligocene (~26 Ma) to Early Miocene (~17 Ma), and Late Miocene

(~6 Ma) arc magmatic rocks present in the Frontal Cordillera show evidence for the bulk assimilation of the Permian – Triassic basement by mantle-derived melts, both on the basis of their trace and rare earth element compositions and the presence of Permian – Triassic inherited zircon cores. The Late Miocene (12 – 9 Ma) arc magmatic rocks present in the Argentinean Precordillera (to the east of the Frontal Cordillera) display distinct trace element signatures (specifically low Th, U and REE concentrations) and contain inherited zircon cores of Proterozoic age, suggesting the interaction of mantle-derived melts with a Grenville-aged basement.

The application of amphibole and amphibole-plagioclase geothermobarometers, suggests the Paleocene – Eocene plutonic belts present in the Principal Cordillera crystallised at temperatures ranging between 677 °C (±15 (1σ)) and 844 °C (±26 (1σ)) and pressures of between 1.1 kbars (±0.2 (1σ)) and 1.4 kbars (±0.3 (1σ)). This evidence, combined with petrographic observations, suggests these plutonic rocks were emplaced at shallow crustal depths of between 4.2 and 5.3 km. The average crystallisation/equilibration temperatures and pressures obtained for the Late Eocene to Late Oligocene volcanic rocks range between 862 °C (±25 (1σ)) and 889 °C (±56 (1σ)), and 1.9 kbars (±0.5 (1σ)) and 2.0 kbars (±0.3 (1σ)), equating to crustal depths of between 7.2 and 7.6 km. An increase in crystallisation/equilibration temperatures and pressures is observed after the Early Miocene with average crystallisation/equilibration temperatures and pressures ranging between 845 °C (±36 (1σ)) and 974 °C (±22 (1σ)), and 1.8 kbars (±0.6 (1σ)) and 3.6 kbars (±0.4 (1σ)). The corresponding increase in estimated crustal depths to between 6.7 and 13.5 km suggests arc magmas were pooling and crystallising at deeper levels in the crust after the initiation of the shallowing of the subducting slab (at ~18 Ma) and the associated increase in compression. The occurrence of adakitic signatures in the Mid to Late Miocene magmatic rocks also implies that these arc magmas equilibrated with a garnet bearing, lower crust.

2.3 Introduction

Presently, new continental crust is primarily produced via arc magmatism at convergent plate margins. At these margins crustal material and volatiles are transported into the mantle due to the subduction of oceanic and continental crust, and associated sediments. Some components of this subducted material, which at ocean-continent convergent margins includes pelagic and terrigenous sediments, altered oceanic crust (AOC), serpentinised oceanic upper mantle, and continental crust from subduction erosion, is recycled to the continental crust via arc magmatism and some is transported into the deep mantle. In addition to mantle-derived melts incorporating subducted material in the melt source region (i.e. source contamination), arc magmas may also melt and assimilate existing crustal material en route to the surface (i.e. crustal contamination). Hence the distinct geochemical signature of the continental crust may be imparted on arc magmas either in the melt source region or in the overlying continental crust. Along the Andean margin crustal assimilation (e.g., James, 1982; Hildreth and Moorbath, 1988; Davidson and de Silva, 1992), the subduction of sediments (e.g., Kilian and Behrmann, 2003; Lucassen et al., 2010) and subduction erosion (e.g., Stern, 1991; Kay et al., 2005; Goss et al., 2013) have all been highlighted as important processes in modifying the composition of mantle-derived melts.

The geochemical characteristics of arc magmatic rocks can be used to constrain the relative contributions to new continental crust from subducted components, the existing continental crust and the mantle. Constraining these contributions is important in order to investigate the evolution of the continental crust, assess rates of continental crustal growth and to determine the processes involved in redistributing subducted material between crustal and mantle reservoirs. Subducting components can be added to the overlying mantle wedge, and hence the source of arc magmas, either by fluids derived from the dehydration of the subducting slab (e.g., Elliott et al., 1997) or by melts if temperatures exceed the

solidus of subducting sediments (van Keken et al., 2011) and/or AOC (Tollstrup et al., 2010). Convergent plate margins are also often associated with economically important ore deposits. For example, the southern Central Andes hosts several significant Au-Ag-Cu mineral deposits. Therefore, the investigation of the processes involved in the cycling of elements at convergent plate margins is important in determining the origin and formation of these deposits.

The Pampean flat-slab segment in the southern Central Andes makes a particularly interesting area to investigate these processes (source and crustal contamination) as the geodynamic setting of the margin has changed over the course of the Cenozoic. Specifically, a shallow angle of subduction developed during the Miocene (Yañez et al., 2001), in conjunction with an increase in crustal thickness along the western edge of South America, due to increased compression (Kay et al., 1991). Establishing how this changing geodynamic setting has influenced the recycling of subducting components, and the contamination of mantle-derived melts with existing Andean crust, is a fundamental aim of this study. In order to investigate this, a comprehensive new major, trace and rare earth element data set is presented for a suite of Late Cretaceous to Late Miocene arc rocks, alongside high resolution U-Pb and Ar-Ar dating. In addition to this, in order to constrain the depths in the crust at which these arc magmas were crystallising, and potentially assimilating the surrounding continental crust, a number of amphibole and amphibole-plagioclase geothermobarometers (Holland and Blundy, 1994; Anderson and Smith, 1995; Ridolfi et al., 2010) have been applied to a subset of samples.

The onset and duration of magmatic activity in the southern Central Andes remains poorly constrained due to the limited number of reliable age determinations (Parada et al., 2007). Much of the age information for the Cenozoic arc rocks is from K-Ar dating (e.g., Pineda and Emparan, 2006; Pineda and Calderón, 2008) which in some cases, due to variable hydrothermal alteration (e.g., Maksaev et al., 1984; Bissig et

al., 2001; Litvak et al., 2007), has been found to be unreliable (e.g., Winocur et al., 2013). High resolution, *in-situ* U-Pb dating of magmatic zircon, combined with Ar-Ar dating, has been conducted in order to improve the regional stratigraphy, investigate periods of reduced arc magmatism and to provide an accurate temporal constraint for the geochemical data. Dating of magmatic zircon has a number of advantages; (1) zircon is a common accessory mineral in igneous rocks; (2) it is both chemically and mechanically robust; (3) it readily incorporates U and Th but not Pb into its crystal structure as it crystallises; and (4) it has a high closure temperature (>900°C) (e.g., Cherniak and Watson (2003), Harley and Kelly (2007) and references therein).

Certain trace elements (TE) and rare earth elements (REE) and ratios of these elements can be used to assess contributions from the subducting slab and the mantle (e.g., Hawkesworth et al., 1991; Hawkesworth et al., 1993; Plank and Langmuir, 1993; Davidson, 1996; Elliott, 2003). Specifically, ratios of fluid-mobile/immobile incompatible elements (e.g., Ba/Nb, Pb/Ce, and U/Th) can be used to assess the influence of slab-derived fluids on arc magmas. Ratios of fluid-immobile incompatible elements (e.g., Nb/Zr, Nb/Yb, Th/Yb) can be used to assess different degrees of melting. As differentiation (i.e., fractional crystallisation, magma mixing etc) primarily takes place in the crust, geochemical characteristics that correlate with the degrees of differentiation are most likely to have been imparted from, or within the continental crust (Davidson et al., 2005). Crustal contamination can also be inferred by the identification of inherited zircon cores and grains as a result of U-Pb dating (e.g., Beard et al., 2005).

2.4 Geological setting

The study area is located within the Pampean (Chilean) flat-slab segment (between 29 - 31^{0}S) of the southern Central Andes (Fig. 2.1), and includes the El Indio (Chile)

and Valle del Cura (Argentina) regions. Subduction of oceanic crust beneath the South American continent has been active in this region since the Jurassic and has produced a series of volcanic arcs (e.g., Ramos et al., 2002; Stern, 2004; Charrier et al., 2007). From the Cretaceous through to the Late Oligocene the region is considered to have been more extensional than the current Andean margin (e.g., Charrier et al., 2007 and references therein). At ~25 Ma the oceanic Farallon plate divided into the Nazca and Cocos plates (Lonsdale, 2005). This is thought to have caused an increase in convergence rates (from ~8 cm/yr to ~15 cm/yr) and a change from oblique (NE-SW) to orthogonal (ENE-WSW) convergence (Pardo Casas and Molnar, 1987; Somoza, 1998; Somoza and Ghidella, 2012). The westward migration of the South American plate is also thought to have been initiated after ~30 Ma (Silver et al., 1998). After this time the Andean margin became more compressional and the reconfiguration of the subducting oceanic plates has been linked to a period of major uplift, increased magmatic activity, and a broadening of the magmatic arc (Pilger, 1984). Increased convergence rates (~15 cm/yr) are thought to have been sustained up until ~20 Ma, followed by a gradual decline to present day values (~7 cm/yr) (Pilger, 1984; Somoza and Ghidella, 2012).

There is currently no active volcanism in the Pampean flat-slab segment due to the low angle at which the oceanic Nazca plate subducts beneath the South American continent. This shallow subduction angle has been related to the subduction of the Juan Fernandez Ridge (JFR), a volcanic seamount which began intersecting the Andean continental margin in this region during the early Miocene (~18 Ma) (Nur and Ben-Avraham, 1981; Pilger, 1981, 1984; Kirby et al., 1996; Gutscher et al., 2000b; Yañez et al., 2001; Yañez et al., 2002). This shallowing led to a broadening and eastward migration of the magmatic arc, a reduction in magma volume, and the eventual cessation of arc magmatism in the late Miocene (~6 Ma) (Kay et al., 1987; Ramos et al., 1989; Bissig et al., 2001).

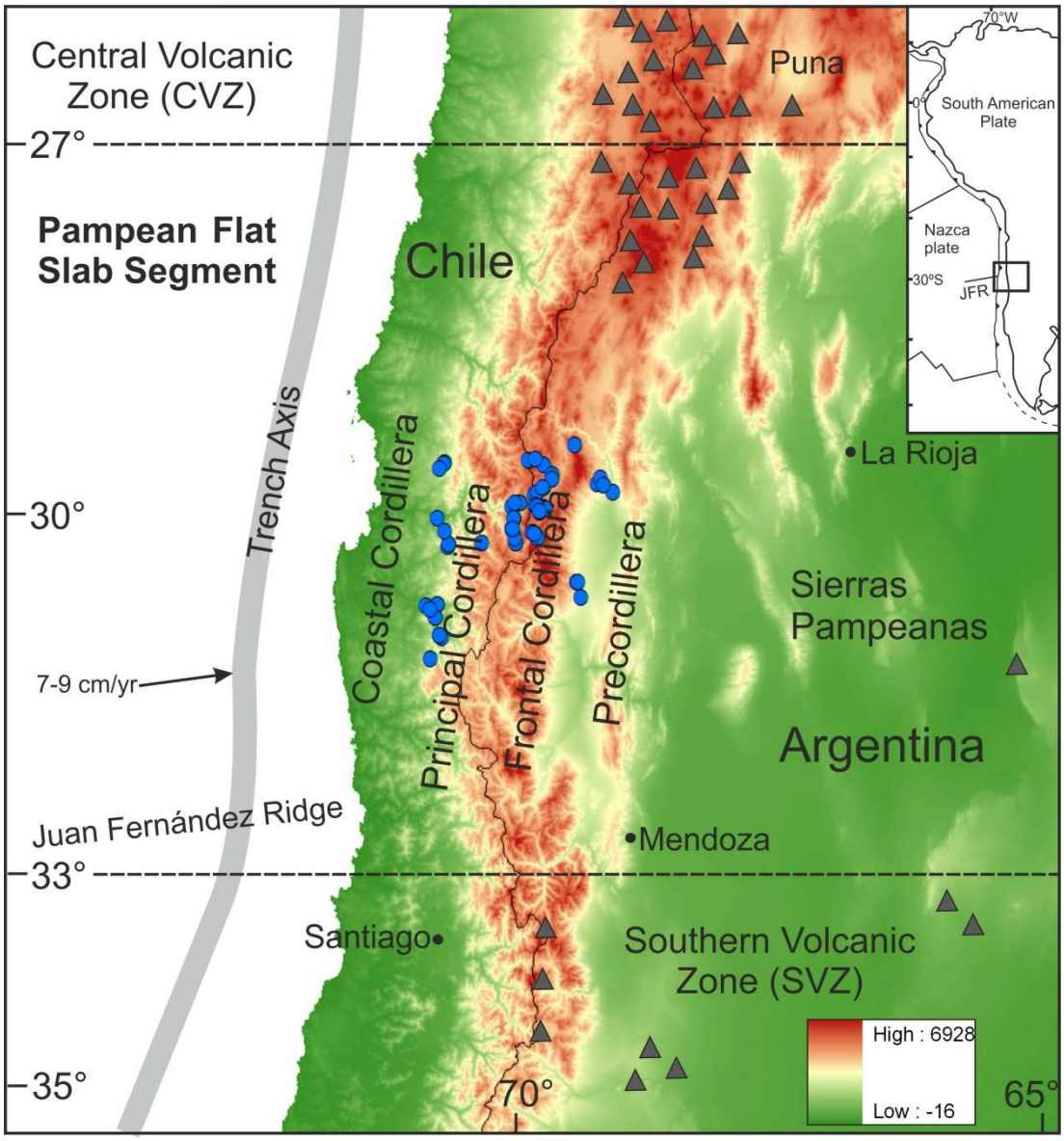

Figure 2.1. Map of the study area showing the main features of the present day southern Central Andean margin. Sample locations are highlighted as blue circles and primary active volcanoes as grey triangles. Digital elevation data from Jarvis et al. (2008).

2.5 Arc magmatism and stratigraphy

Arc magmatism within the southern Central Andes has involved numerous intrusive and volcanic episodes extending from the Late Palaeozoic to Holocene times (Parada et al., 2007). The basement present in the Andean Cordillera, between

28 and 32 °S, is primarily composed of Paleozoic marine sediments and meta-sediments which have been intruded, and unconformably overlain by Late Paleozoic – Mesozoic plutonic complexes and volcanic deposits respectively (Martin et al., 1999). These Late Paleozoic to Early Jurassic plutonic and volcanic rocks are suggested to have formed in the late stages of Carboniferous – Early Permian subduction along the western margin of Gondwana, and in a more extensional tectonic setting after the cessation of subduction in the Early Permian (Mpodozis and Kay, 1992; Martin et al., 1999).

The Cenozoic plutonic and volcanic arc rocks in the southern Central Andes occur as north - south trending belts which lie to the east of the Coastal Batholith (which is primarily late Paleozoic to early Cretaceous in age). The older, more continuous western belt was intruded in the Palaeocene - Eocene and the younger more eastern belt is of Oligocene - Miocene age, demonstrating an eastward migration of magmatism with time (Parada et al., 2007). There is a geographical gap between the two belts which corresponds with a widespread lull in magmatic activity between ~39 – 26 Ma (Parada et al., 1988; Parada et al., 2007). The Cenozoic arc stratigraphy in the southern Central Andes is shown in Figure 2.2 and outlined below.

In the southern Central Andes the Palaeocene - Eocene belt is located in the Chilean Principal Cordillera (Fig. 2.1) and is primarily composed of epizonal plutons which have been assembled into the Cogotí Supergroup (Parada et al., 1988). Granitoids of the Cogotí Supergroup have K-Ar ages between 67 ±2 Ma and 38 ±1 Ma (Parada et al., 1988 and references therein). However, Parada et al. (1988) note there is evidence of partial Ar loss, suggesting the Cogotí Supergroup is Late Cretaceous – Paleocene in age. Coeval to the Cogotí Supergroup is the extrusive Los Elquinos Formation (69.8 ±0.9 Ma to 57.6 ±2.5 Ma (Wunder et al., 2001)) which consists of basaltic to rhyolitic lavas, tuffs and breccias (Charrier et al., 2007). During the Paleocene a

number of calderas, including the Tierras Blancas Caldera, also formed along the margin between 26 and 30 °S (Charrier et al., 2007). Mafic, back-arc volcanism was also concurrent with the emplacement of the Cogotí Supergroup. The Río Frío Basalts were erupted in the Valle del Cura region of the Argentinean Frontal Cordillera and have been dated at 55.9 ±1.9 Ma by K-Ar dating (Litvak and Page, 2002). These high-K basalts have a composition that suggests low degree partial melting of an enriched portion of the lithospheric mantle, in an intra-plate setting, with no contamination from crustally derived components (refer to Litvak and Poma, 2010 for full details).

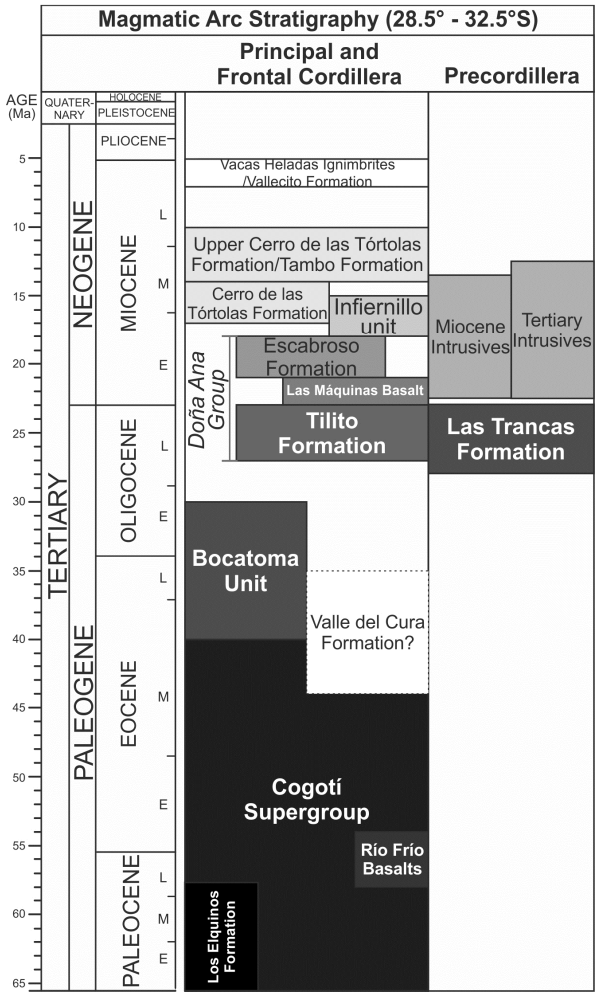

Figure 2.2. The Cenozoic magmatic arc stratigraphy present in the Principal Cordillera, Frontal Cordillera and Precordillera of the southern Central Andes. References are outlined in the text.

A general reduction in magmatic activity has been identified between ~39 and 26 Ma in the southern Central Andes (Parada et al., 1988), however, some arc magmatism continued during this time interval. The Bocatoma Unit has been dated as Eocene to Early Oligocene with reported Ar-Ar and K-Ar ages ranging between 39.5 and 30 ±1.9 Ma (Mpodozis and Cornejo, 1988; Nasi et al., 1990; Martin et al., 1995; Bissig et al., 2001). This primarily intrusive unit consists of fine grained to coarsely porphyritic diorites and granodiorites, and some andesitic porphyries (Maksaev et al., 1984; Bissig et al., 2001).

Following the break-up of the Farallon plate and reconfiguration of the margin, the extensive Doña Ana Group followed the Eocene - Oligocene magmatic lull and was erupted at and near the arc front, spanning either side of the current Chilean - Argentine border. It is composed of two formations; the Tilito Formation (27 – 23 Ma) which is composed of high-K calc-alkaline andesites to rhyolites which have been intruded by basic to intermediate dykes; and the Escabroso Formation (21 – 18 Ma) which is composed of medium-K, pyroxene bearing, calc-alkaline basaltic and andesitic lavas (Kay et al., 1987; Kay et al., 1991; Martin et al., 1997). The Tilito Formation is thought to be derived from a long lived volcanic centre and the volcanic rocks have undergone significant hydrothermal alteration and mineralisation (Bissig et al., 2001; Litvak, 2004; Litvak et al., 2007). The Tilito and Escabroso formations are separated by a major unconformity (Martin et al., 1995) which has been attributed to a period of deformation at ~20 Ma (Kay and Mpodozis, 2002). La/Yb ratios obtained for the Doña Ana Group indicate a crustal thickness of ~35 – 40 km at the time of emplacement (Kay and Mpodozis, 2002; Litvak et al., 2007).

The Valle del Cura Formation, which consists of dacitic and rhyolitic ignimbrites and lava flows, has been identified in the Valle del Cura region (Frontal Cordillera, Argentina). Ages ranging between 44 ±2 and 34 ±1 Ma have been obtained via K-Ar

dating (Limarino et al., 1999; Litvak and Poma, 2005). However, it has been suggested that these Eocene to early Oligocene K-Ar ages are unreliable due to high levels of hydrothermal alteration and that the previously identified Valle del Cura Formation is in fact part of the Doña Ana Group (Winocur et al., 2013).

During the production of the calc-alkaline Doña Ana Group at the arc front, the Las Máquinas back-arc basalts were being erupted in the Valle del Cura region. These alkaline basalts have been K-Ar dated between 22.8 ±1.1 Ma and 22.0 ±0.8 Ma and their trace element geochemistry suggests they were erupted over a greater depth to the top of the subducting slab and in an extensional setting (Kay et al., 1991; Litvak et al., 2005). The volcanic Las Trancas Formation, which outcrops in the Precordillera and consists of proximal block-and-ash pyroclastic flow deposits, ignimbrites, tuffs and dacitic lava flows, has also been dated as coeval with the Tilito Formation (Poma et al., 2005).

The volcanic Cerro de las Tórtolas Formation appears primarily in the region of the Valle del Cura, to the east of the Chilean - Argentinean border. These lavas were erupted during the middle Miocene and are primarily composed of amphibole bearing, medium- to high- K calc-alkaline andesites and dacites. Ramos et al. (1989) and Litvak et al. (2007) identify two separate sequences; an older (17 - 14 Ma) andesitic to basaltic andesitic lower section which appears to have erupted through a normal thickness of crust (30 – 35 km) and a younger (13 – 10 Ma) dacitic upper sequence which displays steeper REE patterns implying they last equilibrated with a higher pressure residual mineral assemblage, and therefore were erupted through a thicker crust (Kay and Mpodozis, 2002; Litvak et al., 2007). La/Yb ratios from the Cerro de Las Tórtolas Formation indicate an increase in crustal thickness to over 45 km (Kay et al., 1991). On the Chilean side of the margin the Upper Cerro de Las Tórtolas sequence has been referred to as the Tambo Formation (e.g., Martin et al., 1997) and the Vacas Heladas Formation (e.g., Martin et al., 1995; Bissig et al., 2001).

In this study we refer to it as the Upper Cerro de las Tórtolas Formation to avoid confusion with the Vacas Heladas Ignimbrites.

The Infiernillo unit (18 – 15 Ma) is thought to be the subvolcanic equivalent of the Cerro de Las Tórtolas Formation and is composed of high-K calc-alkaline, shallow level, intermediate intrusives (Kay et al., 1987). A number of sub-volcanic outcrops identified in the Precordillera of Argentina have been correlated with the Infiernillo Unit are referred to as the Miocene Intrusives and Tertiary Intrusives (Cardó and Díaz, 1999; Cardó et al., 2007). The Miocene Intrusives which primarily consist of granitoids and are located in the Llanos del Molle have been dated between 22.4 ±0.1 and 21.2 ±0.1 Ma (Llambias et al., 1990). Ages as young as 13.5 ±7 Ma have been obtained for other deposits (JICA-MMAJ, 1999) which have also been grouped into the Miocene Intrusives (Cardó et al., 2007). The Tertiary Intrusives consist of sub-volcanic andesites and dacites, and K-Ar dating has given ages of 18.3 ±2.5 Ma and 17.5 ±5 Ma (Leveratto, 1976; Cardó and Díaz, 1999).

The Late Miocene, Vacas Heladas Ignimbrites represent the last significant volcanic activity in the region (Ramos et al., 1989). These high-K rhyolitic and dacitic tuffs lie unconformably over the Oligocene – Miocene sequences and have been correlated with the Vallecito Formation in Chile, which yields the same age (Bissig et al., 2001). They are highly enriched, contain the highest proportion of crustal components and have adakitic signatures (e.g., Litvak et al., 2007). Arc magmatism ceased in the region by the Late Miocene (~5 Ma). Some younger (~2 Ma) isolated and small volume volcanic complexes have been identified, but these are thought to represent crustal melts (Bissig et al., 2001; Bissig et al., 2002) and have not been sampled as part of this study.

2.6 Sample collection

Representative magmatic rock samples were collected from each of the major intrusive/extrusive Cenozoic arc formations present in the Principal Cordillera, Frontal Cordillera and Precordillera between 29 and 31 °S (Fig. 2.1). Due to the eastward migration of the magmatic arc during the Cenozoic, the sample locations form an W – E transect across the Andean Cordillera from Chile into Argentina. The sampled transect includes the El Indio (Chile) and Valle del Cura (Argentina) regions, which contain both epithermal and porphyry Au-Ag-Cu mineral deposits (e.g., Maksaev et al., 1984; Kay et al., 1987; Kay and Mpodozis, 2001; Charchaflié et al., 2007). Additional samples from the Valle del Cura were provided by Vanesa Litvak (collaborator at the University of Buenos Aires). A number of samples of the Late Paleozoic – Early Mesozoic basement were also collected in order to assess their potential role in the contamination of the Cenozoic arc magmas.

2.7 Petrological descriptions

Brief petrographic descriptions of the samples obtained for each of the Cenozoic arc formations/units is presented below, in decreasing age order, and summarised in Table 2.1. Full petrographic descriptions and photomicrographs of representative samples from each of the geological formations/units are presented in Appendices 1.5 and 1.6. The selection of samples for geochronological and geochemical analysis was based on petrographic information.

Geological Group/Formation/Unit	Range in SiO_2 contents (wt.%)	Major mineral phases (incl. modal %)	Minor/accessory mineral phases	Groundmass (modal %)	Notable features
Cogotí Supergroup	55.3 - 68.3	plagioclase(~25-40%) +quartz(~20-30%) +alkali feldspar(~10-30%) +biotite(~3-10%) ±amphibole(~5-20%)	apatite +magnetite +zircon ±muscovite ±sphene ±monazite ±thorite	-	Mafic enclaves, perthitic feldspar textures in some samples
Los Elquinos Formation	53.8 - 54.2	plagioclase(~40-50%) +clinopyroxene(~10-15%) +orthopyroxene(~5%) +opaque oxides(~3-10%)	zircon	~20-40%	
Río Frío Basalts	52.0	plagioclase(~60%) +opaque oxides(~30%)	relict pyroxene (~3%)	aphyric	
Tierras Blancas Caldera	49.7 - 57.2	plagioclase(~45-60%) ±amphibole(~25%) ±quartz(~5%) ±pyroxene(~5%) ±opaque oxides(~5-7%)	apatite ±quartz ±zircon	~50% of the most mafic sample	
Bocatoma Unit	54.9 - 55.9	plagioclase(~30%) +amphibole(~20-25%) +opaque oxides(~10%)	biotite +apatite +zircon	~30-40%	Contains xenoliths and lithic fragments
Tilito Formation	60.7 - 74.7	plagioclase(~25-30%) +alkali feldspar(~5-15%) +quartz(~5-15%)+biotite(~5-10%) +opaque oxides (inc. magnetite and illmenite) (~5-20%)	apatite +zircon	~30-60%	Contains xenoliths and lithic fragments
Las Máquinas Basalts	49.3 - 49.5	plagioclase(~30%) +olivine(~10%) +clinopyroxene(~5%)	opaque oxides	~55%	
Miocene Intrusives	64.6 - 70.6	plagioclase(~25-40%) +quartz(~25-30%) +alkali feldspar(~10-30%) +biotite(~5-10%) ±amphibole(~15%)	opaque oxides (inc. illmenite and magnetite) +apatite +zircon	-	Mafic enclaves
Escabroso Formation	52.3 - 64.2	plagioclase(~35-55%) +clinopyroxene(~10-20%) +orthopyroxene(~5-10%) +opaque oxides(~5-10%)	apatite ±biotite ±zircon	~30-40%	
Cerro de las Tórtolas Formation	58.2 - 59.5	plagioclase(~40%) +clinopyroxene(~15-20%)	orthopyroxene +opaque oxides +apatite + zircon	~30-40%	
Upper Cerro de las Tórtolas Formation	61.2 - 61.7	plagioclase(~40-50%) +amphibole(~10%) +opaque oxides(~5%) ±clinopyroxene(~5%)	apatite	~40-50%	
Tertiary Intrusives	62.0 - 63.0	plagioclase(~25-35%) +alkali feldspar(~5-10%) +amphibole(~20-30%) ±quartz(~3-10%) ±biotite(~5%)	opaque oxides +apatite +zircon ±sphene	~25-40%	
Vacas Heladas Ignimbrites	69.8 - 71.6	plagioclase(~35-40%) +quartz(~35%) +biotite(~5-8%)	opaque oxides +apatite +zircon ±beryl	~20-30%	Contains fiammé and lithic fragments

Table 2.1. A summary of the major, minor and accessory mineral phases present in each of the Cenozoic arc formations/units, listed in decreasing age order. The SiO_2 contents were determined by XRF analysis.

The numerous intrusive samples of the Cogotí Supergroup are medium – coarse grained, inequigranular, and the mineral assemblage is composed of plagioclase (~25 – 40 modal %) + quartz (~20 – 30 modal %) + alkali feldspar (~10 – 30 modal %) + biotite (~3 – 10 modal %) ± amphibole (~5 – 20 modal %) and minor/accessory phases of apatite + magnetite +zircon ± muscovite ± sphene ± monazite ± thorite. In some of these granitoid samples the alkali feldspar is present as microline and microperthite intergrowth textures are apparent (Fig. 2.3a). Alteration of both feldspars to sericite and clays is common, with alkali feldspar generally appearing more altered than plagioclase. In some samples the ferromagnesian minerals appear together in clots and in some instances alteration of the ferromagnesian minerals to chlorite is evident. Enclaves containing the same mineral assemblage but a higher proportion of mafic minerals are also present in some samples.

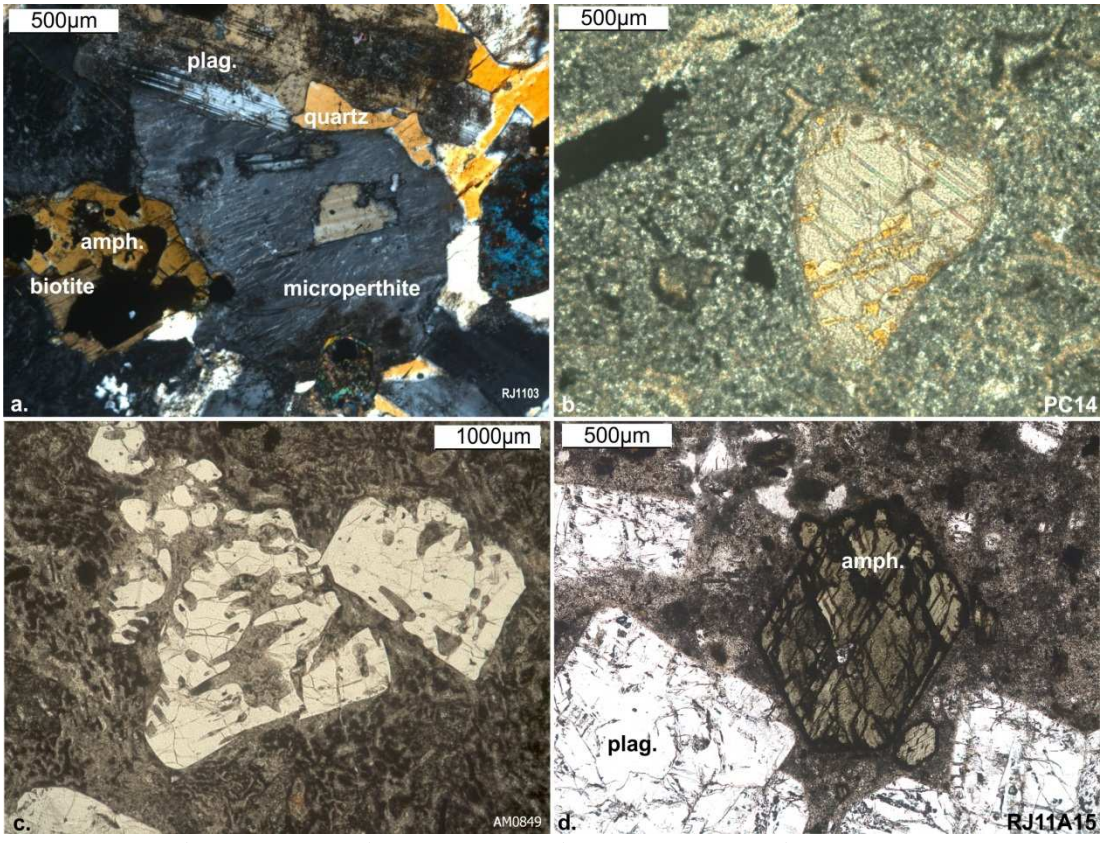

Figure 2.3. Thin section photomicrographs. a) Microperthitic texture present in dioritic sample RJ1103 (Cogotí Supergroup) viewed under cross polarized light. Alteration of the plagioclase feldspar to sericite and clay minerals is also apparent.

The quartz appears yellow due to the thick cut of the polished thin section. b) Photomicrograph of sample PC14 (a rhyolitic tuff from the Tilito Formation) showing replacement of a microphenocryst phase (most likely feldspar) with calcite. c) Embayed quartz surrounded by a devitrified, glassy groundmass in a rhyolitic crystal tuff from the Tilito Formation (sample AM0849). d) Photomicrograph of sample RJ11A15 showing euhedral amphibole displaying a reaction rim composed of opaque oxides, and plagioclase feldspar in a vitreous to fine grained groundmass.

The single sample obtained for the Río Frío Basalts is dark and aphanitic. Under the microscope the sample appears aphyric and is primarily composed of fine grained, acicular plagioclase laths (~60 modal %) and opaque oxides (~30 modal %). Relict pyroxenes are also evident (~3 modal %) and have primarily been altered to iron oxides. Some alteration of the plagioclase to sericite, carbonate and clays is also evident. The plagioclase crystals in this basaltic sample are aligned, with the smaller laths bending around the slightly larger (~0.3mm) plagioclase crystals and opaque oxides. This is indicative of flow and is in keeping with the Río Frío Basalts representing lava flows (Litvak and Page, 2002; Litvak and Poma, 2010).

The samples of the Los Elquinos Formation are porphyritic with a high proportion of microphenocrysts (<3 mm) (~60 – 80 %) in a dark, fine grained matrix. The microphenocryst assemblage is composed of plagioclase (~ 40 - 50 %), clinopyroxene (~10 – 15 %), orthopyroxene (~5 %) and opaque oxides (~3 – 10 %). Alteration of the Los Elquinos Formation is evident with sericite, carbonate and clay minerals partially replacing the plagioclase, and chlorite partially replacing the ferromagnesian minerals. The matrix, which makes up between ~20 and 40 % of these basaltic andesites, is composed of fine grained plagioclase laths, pyroxene and opaque oxides, as well as secondary chlorite, carbonate and clay minerals. The alignment of some microphenocryst phases is indicative of flow, and combined with the fine grained nature of the matrix, supports the extrusive nature of these samples.

The mineral assemblage of the medium grained intrusives of the Tierras Blancas Caldera includes plagioclase (~50 – 60 modal %) + amphibole (~25 modal %) + quartz (~5 modal %) + opaque oxides (~5 – 7 modal %) + apatite ± quartz ± zircon. In these samples the plagioclase shows evidence of alteration to sericite and clay minerals, and the hornblende is being partially replaced by chlorite, particularly in grain cores. A more mafic sample obtained from the Tierras Blancas Caldera is composed of microphenocrysts of plagioclase (~45 %) and pyroxene (~5 %) in a fine grained matrix (~50 %). The matrix is composed of plagioclase, opaque oxides and secondary chlorite, carbonate and clay minerals. This basaltic sample has undergone more significant alteration than the dioritic samples; with plagioclase highly altered to sericite and clays, and chlorite replacing the pyroxene.

Samples assigned to the Bocatoma Unit are porphyritic and composed of between ~50 and 60 % microphenocrysts (<3 mm) and ~30 - 40% groundmass. The mineral assemblage is composed of microphenocrysts of plagioclase (~30 % of the whole rock), amphibole (~20 - 25 %) and opaque oxides (~10 %) and minor/accessory phases of biotite (<~5%), apatite and zircon. The groundmass has a pink colouration and is composed of plagioclase, opaque oxides, and devitrified and altered glass. Both the phenocrysts of plagioclase and the plagioclase present in the groundmass has been partially altered to sericite and clay minerals. Xenoliths and rip up clasts of other volcanic material are present in these andesitic samples.

The numerous samples of the Tilito Formation (Lower Doña Ana Group) are all porphyritic and include microphenocrysts (<3 mm) of plagioclase (~25 - 30 %), alkali feldspar (~ 5 - 15 %), quartz (~5 - 15 %), biotite (~5 - 10 %) and Fe-Ti oxides (~3 - 10 %) and minor/accessory minerals of apatite and zircon, in a fine grained to vitreous groundmass. A number of igneous xenoliths and lithic fragments are also apparent. The groundmass comprises between ~30 and 60 % of the whole rock and is

composed of devitrified glass, sericitised feldspar, opaque oxides and clays. Where present (in sample ZN122) amphibole and clinopyroxene make up < 10 % of the mineral assemblage. The amphiboles present in this andesitic sample often display thick opaque reaction rims composed of Fe-Ti oxides. In the majority of samples the quartz phenocrysts are embayed (Fig. 2.3c) and the groundmass has a pink colouration. In a number of samples flow textures and spherulite textures are observed in the groundmass (refer to Appendix 1.6.3). The Tilito Formation has undergone significant alteration with extensive replacement of the feldspars with sericite and clay minerals. In some samples (e.g., PC14) the feldspars have also been replaced by carbonate (Fig. 2.3b) and the ferromagnesian minerals, chiefly biotite, show evidence for alteration to Fe oxides.

The dark, porphyritic rocks which make up the Las Maquinas Basalts are composed of microphenocrysts of plagioclase (~30 %), olivine (~10 %) and clinopyroxene (~5 %) in a intergranular, fine grained groundmass (~55 %). The same microphenocryst mineral phases exist in the groundmass, along with opaque oxides, and flow textures are apparent. Alteration of the ferromagnesian minerals and the plagioclase microphenocrysts to sericite, clays and carbonate is apparent.

The fine to coarse granitoids grouped into the Miocene Intrusives are composed of plagioclase (~25 - 40 modal %) + alkali feldspar (~10 – 30 modal %) + quartz (~25 – 30 modal %) + biotite (~5 – 10 modal %) ± amphibole (~15 modal %) and minor/accessory phases of opaque oxides (<5 modal %) + apatite + zircon. Some alteration of the feldspars to sericite and clay minerals is evident with the alkali feldspars displaying more alteration than the plagioclase. The ferromagnesian minerals tend to appear together in clots along with opaque oxides, and some alteration of biotite and amphibole to chlorite is apparent. Enclaves, containing the

same mineral assemblage but a higher proportion of mafic minerals, were evident in outcrop and range in size between 2 and 40 cm in diameter.

The samples of Escabroso Formation (Upper Doña Ana Group) have porphyritic textures with visible microphenocrysts (0.3 – 3 mm) in a fine grained to vitreous matrix. The major mineral phases consist of plagioclase (~35 - 55 % of the whole rock) + clinopyroxene (~10 - 20 %) + orthopyroxene (~5 - 10 %) + opaque oxides (~5 - 10 %) and minor/accessory phases of apatite ± biotite ± zircon. In certain samples, relict olivine is also present, these mircophenocrysts have been almost entirely replaced by chlorite and/or carbonate. Some alteration of the plagioclase to sericite and clay minerals is evident. The matrix is composed of very fine grained plagioclase laths, pyroxene, opaque oxides, devitrified glass and secondary minerals (sericite, clay minerals, chlorite and carbonate). An indication of flow is evident from the alignment of micophenocrysts and the preferred orientation of plagioclase laths around the microphenocryst phases. This evidence, combined with the presence of devitrified glass in the matrix, supports the suggestion that these basaltic andesite to andesitic samples represent lava flows (e.g., Kay and Mpodozis, 2002). Similarly to the Tilito Formation, these lavas have undergone a moderate to high degree of alteration and the occurrence of secondary chlorite and carbonate is common.

The dark, porphyritic samples of the Cerro de las Tórtolas Formation consist of 60 – 70 % microphenocrysts (~0.3 – 3 mm) of plagioclase (~40 % overall) and clinopyroxene (15 - 20 %), with minor/accessory mineral phases of orthopyroxene (<5 %), opaque oxides (including magnetite), apatite and zircon, in a vitreous to fine grained groundmass. The plagioclases show varying degrees of alteration to sericite, carbonate and clays. The clinopyroxene appears in clots together with opaque oxides. The groundmass is composed of devitrified glass, plagioclase (with some

alteration to sericite), pyroxene, opaque oxides and clays. Similarly to the Escabroso Formation, the alignment of microphenocrysts phases and the presence of devitrified glass in the matrix suggests these andesitic samples also represent lava flows, as suggested by Kay and Mpodozis (2002).

The samples of the Upper Cerro de las Tórtolas Formation are broadly similar to the Cerro de las Tórtolas Formation and consist of 50 – 60 % microphenocrysts (~0.3 – 3 mm) in a dark, vitreous to fine grained matrix. The mineral assemblage includes plagioclase (~40 to 50 % of the whole rock) + amphibole (~10 %) + opaque oxides (primarily Fe and Ti oxides) ± clinopyroxene (<3 %). The amphibole microphenocrysts are predominantly euhedral and exhibit thick opaque reaction rims. Where present the clinopyroxene appears in clots, associated with Fe-Ti oxides. The microphenocryst phases are present in a matrix composed of plagioclase laths, opaque oxides, devitrified glass and alteration products (sericite and clay minerals). Evidence of flow is also apparent in the matrix (Appendix 1.6.6), in keeping with these andesitic samples representing lava flows.

The mineral assemblage present in the samples of the Tertiary Intrusives is primarily composed of plagioclase + alkali feldspar + amphibole ± quartz ± biotite with minor/accessory phases of Fe-Ti oxides + apatite + zircon ± sphene. The groundmass makes up between 25 and 40 %, is vitreous to fine grained and composed of feldspar, devitrified glass, opaque oxides and alteration products (clays, sericite and carbonate). Microphenocrysts of plagioclase comprise between ~25 and 35 % of the samples, and alkali feldspar between 5 and 10 %. Both feldspars are fractured and partially altered to sericite, carbonate and clays. The amphibole microphenocrysts, which make up between 20 – 30 %, are euhedral – subhedral and exhibit thick opaque reaction rims composed of Fe-Ti oxides (Fig. 2.3d). Where present quartz makes up between 3 and 10 % of the mineral assemblage and biotite

makes up <5 %. In all samples >2 size populations of plagioclase and amphibole crystals are apparent, indicative of a number of stages of crystallisation, and all the major phenocryst phases show some evidence of resorption. Textures indicative of flow are present in both hand specimen and were also evident in outcrop. Despite being grouped as 'Tertiary Intrusives', the outcrops from which these dacitic samples were collected have been identified as shallow, sub-volcanic units which were emplaced into sedimentary sequences (Cardó and Díaz, 1999).

The samples of the Vacas Heladas Ignimbrites are porphyritic and contain microphenocrysts, fiammé and lithic fragments in a glassy, hyalopilitic groundmass. The mineral assemblage constitutes between 70 and 80 % of the whole rock and is composed of microphenocrysts of plagioclase (~35 to 40 % of the whole rock) + quartz (~35 %) + biotite (~5 to 8 %) and with minor/accessory phases of Fe-Ti oxides + apatite + zircon ± beryl. The groundmass is vitreous to fine grained and composed of devitrified glass, quartz, feldspar, opaque oxides and secondary clay minerals. Unlike some of the other samples, very little alteration of plagioclase is apparent in these rhyolitic samples and the microphenocrysts generally appear as subhedral crystal fragments. The quartz crystals are also highly fractured and display undulose extinction, which may be a result of emplacement processes. This evidence is in agreement with these samples representing crystal tuffs, as previously suggested (Ramos et al., 1989; Litvak, 2004).

2.8 Sample preparation and analytical methods

2.8.1 Geochronology

2.8.1.1 U-Pb dating

In order to obtain zircon grains for U-Pb dating ~5 kg of each sample was crushed using a tungsten carbide jaw crusher. The resulting rock chips were then sieved to <2 mm, <1 mm and <0.5 mm size fractions. Any rock chips larger than 2 mm were reintroduced to the jaw crusher. Zircons were then separated from the crushed sample using a combination of density and magnetic separation (see Appendix 1.1). Zircons were successfully separated from 42 samples and individual zircon grains were hand-picked under a binocular microscope and mounted in epoxy resin accompanied by zircon Geostandards 91500 and/or GJ-1. The epoxy mounts were then ground and polished to expose the interior of the zircons at the surface.

Prior to analysis individual zircon grains were imaged and characterised using a Philips XL30CP Scanning Electron Microscope (SEM) at the University of Edinburgh in order to determine the presence or absence of multiple growth phases, xenocrystic cores, inclusions, and cracks. Imaging was carried out in both secondary electron (SE) and backscatter electron (BSE) modes, and suitable, representative zircons and specific locations for analysis were identified. U-Th-Pb analysis of zircons was performed on a Cameca ims 1270 secondary ion mass spectrometer (SIMS) at the NERC Edinburgh Ion Microprobe Facility (EIMF) using analytical procedures similar to those described by Kelly et al. (2008). Full details of analytical methods, applied corrections and data reduction are outlined in Appendix 1.1. Subsequent to analysis all analysed zircons were imaged on a SEM in both cathodoluminescence (CL) and secondary electron (SE) modes to check the exact position of analysis, and to ensure the absence of cracks and inclusions at the bottom of the analysis pits (Fig. 2.4). Data from any problematic analysis locations

(i.e. cracks present) was rejected (Appendix 1.10). A total of 313 successful U-Th-Pb analyses were made on unknown zircons. In most cases at least 8 successful analyses of unknown zircons were made per sample. Multiple analyses (core and rim) were made on selected zircon grains in order to obtain information on growth history and inheritance (Fig. 2.4).

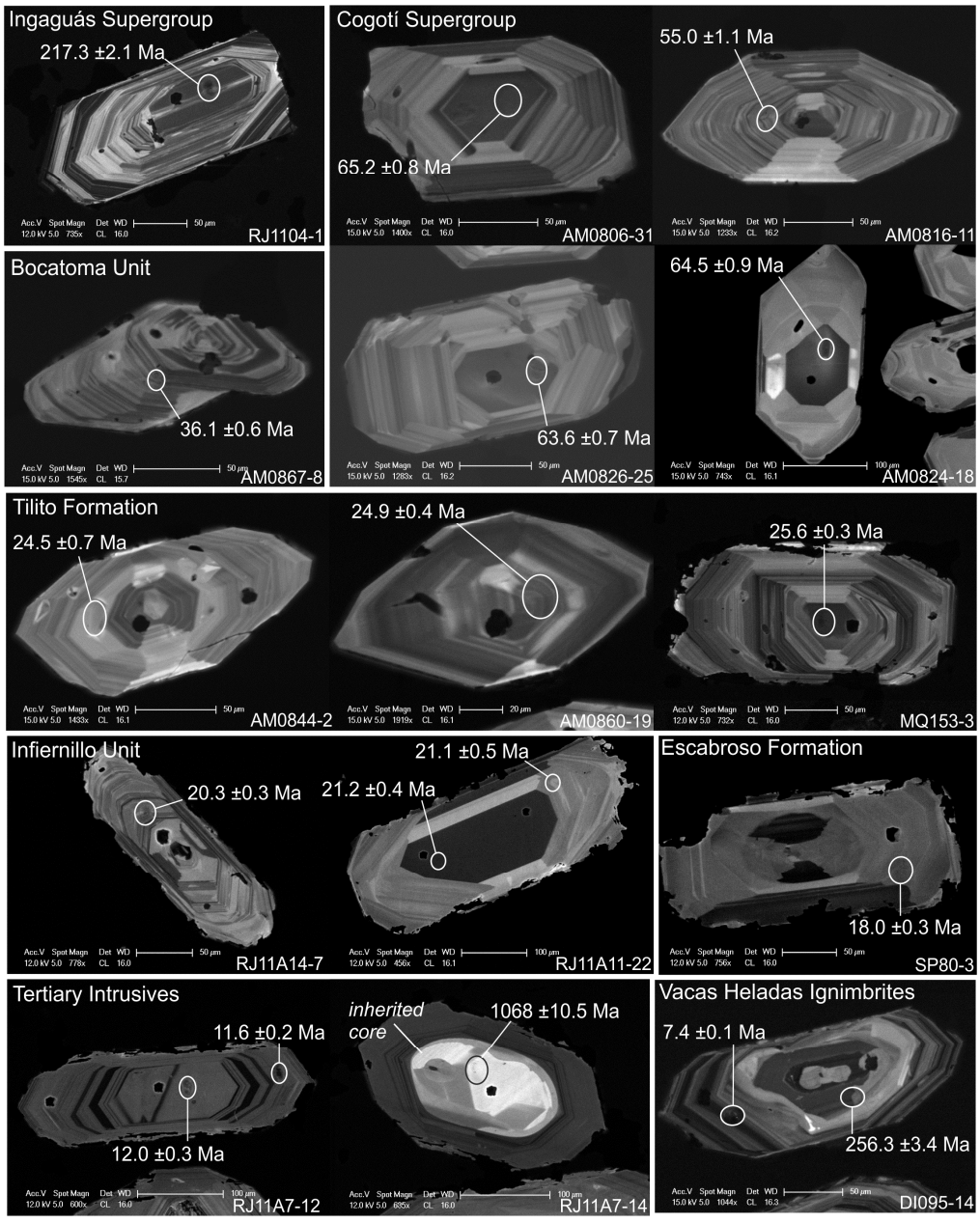

Figure 2.4. Cathdoluminescence (CL) images of representative zircon grains from select samples, highlighting the presence of internal growth zoning, inherited cores

and the location of SIMS analysis. The U-Pb ages are presented as the $^{206}Pb/^{238}U$ ages for the individual zircon grains and the errors are quoted at the 1σ level.

2.8.1.2 Ar-Ar dating

Ar-Ar age dating of plagioclase feldspar was conducted on two samples, a basaltic andesite (RJ1111) and an andesite (AM0887), due to the lack of zircon present in these basic to intermediate magmatic rocks. Plagioclase phenocrysts were separated from the crushed rock samples using similar mineral separation techniques to those used to separate zircon. Plagioclase crystals were hand-picked under a binocular microscope and sent to the Ar-Ar Research Laboratory at the Open University for analysis. Full details of sample preparation procedures and analytical methods are presented in Appendix 1.15.

2.8.2 Whole-rock major, trace and rare earth element analysis

Samples showing the least evidence for alteration and/or weathering (determined by assessing both the hand specimen and thin section) were selected for analysis. For major, TE and REE analysis sample blocks weighing ~50g were cleaned and trimmed of any weathered surfaces, veins and xenoliths. These blocks were then crushed into chips using a tungsten carbide jaw crusher. The chips were also checked to ensure they contained no signs of alteration, veins, xenocrystic and xenolithic material, and then powdered in a tungsten carbide TEMA mill to obtain fine, homogeneous powders for analysis by X-ray florescence spectrometry (XRF) and inductively-coupled plasma mass spectrometry (ICP-MS). Detailed XRF and ICP-MS sample preparation and analytical methods are presented in Appendix 1.2.

XRF analyses were carried out in the School of GeoSciences, University of Edinburgh following the analytical methods outlined in Fitton et al. (1998) and

Fitton and Godard (2004). Major, minor and selected TE compositions of 56 samples were analysed on a Philips PW2404 wavelength-dispersive sequential X-ray spectrometer with a 4 kW Rh-anode end-window X-ray tube. Major element oxide totals were generally within ±0.9% of 100% and have been recalculated to a 100% volatile free basis. Based on the repeated analysis of an individual sample prepared and analysed five times, hence accounting for variability due to sample preparation in addition to analytical uncertainty, the precision for the major elements is always <1.1 % (1σ) (Appendix 1.2, Table A1.3). The accuracy based on repeated analysis of standard BHVO-1 (basalt) compared to the published values is <3.5 % relative (1σ) for all major elements, apart from P_2O_5 where accuracy is 5.5 % relative (1σ) (Appendix 1.2, Table A1.1). Precision for the TE and REE concentrations determined by XRF analysis is <4 % (1σ) apart from for Ni where the precision is much lower (Appendix 1.2, Table A1.3). This may be a result of the low concentrations of Ni in this particular sample. Precision for Ni based of the repeated analysis of BHVO-1 (117.5 ppm Ni) gave a precision of 0.5 % (1σ) (Appendix 2.1, Table A1.2). An evaluation of the accuracy of the TE and REE analysis based on the analysis of a number of international standards is presented in Appendix 2.1, Table A1.2.

A subgroup of 39 samples representing each of the major volcanic and plutonic formations were selected for REE analysis via ICP-MS. Select samples were also analysed for U, Th, Pb and Hf concentrations. Sample powders were dissolved using a tri-acid digestion procedure and analysis was carried out on an Agilent 7500ce ICP-MS at the Scottish Universities Environmental Research Centre (SUERC), East Kilbride. Based on the repeated analysis of international standard BCR-2 the precision is <4 % (1σ) and the accuracy is <7 % relative (1σ) for all elements apart from Pb, where precision and accuracy are much lower (7.3 and 30.9 % relatively) (Appendix 1.2, Table A1.5). On this basis the use of Pb in the interpretations will be limited. A good agreement has been found between the TE and REE concentrations produced by XRF and ICP-MS analysis (Appendix 1.2,

Figures A1.1, A1.2 and A1.3). Therefore, select REE concentrations determined for certain samples by XRF analysis is included alongside the REE concentrations determined by ICP-MS.

2.8.3 Mineral composition analysis

Mineral analyses were conducted using the CAMECA SX100 electron microprobe (EPMA) at the School of GeoSciences, University of Edinburgh. Pyroxene, amphibole and plagioclase were analysed for major and minor elements in polished thin sections and crystal grain mounts. Analyses were made on cores, rims and intermediate points of the mineral phases in order to assess compositional zonation. Full analytical methods are outlined in Appendix 1.3. Based on repeated measurements of internal standards the precision for the major elements of interest (Na, Ca, K, Mg, Fe, Al) is always <2 % (1σ), with the exception of Na where the precision is <5.7 % (1σ). The accuracy based on accepted values for the standards analysed is always <5.1 % for the major elements of interest (Appendix 1.3, Tables A1.6 and A1.7). In order to maintain data quality analysis totals outside the range of 99 and 101 wt.% for plagioclase and pyroxene, and corrected totals outside the range 98.5 and 101.5 wt.% for amphibole, were discarded.

2.8.3.1 Geothermobarometry

Eight representative samples of both intrusive and extrusive rock types containing both amphibole and plagioclase phenocrysts and ranging in age from the Paleocene to the Late Miocene were selected for use in amphibole-plagioclase and amphibole geothermobarometry. The two intrusive samples are medium grained, inequigranular, and range in composition from a syeno-diorite to a diorite. The extrusive samples are porphyritic and range in composition from andesites to

trachy-dacites. Analyses of major and minor elements were carried out on cores, rims and intermediate points of at least 6 representative amphibole and plagioclase grains per sample. Care was taken to select the freshest and most euhedral grains for analysis and where possible, plagioclase grains sharing grain boundaries with amphiboles were analysed (Appendix 1.4). Where this was not possible the closest plagioclase was analysed. Cations were calculated on the basis of 23 oxygens and then recalculated to account for ferric iron (Fe^{2+} and Fe^{3+} were calculated by charge balance).

2.9 Geochronological and geochemical results

2.9.1 U-Pb and Ar-Ar dating

The results of U-Pb dating and Ar-Ar dating for individual samples are presented in Table 2.2 and full results in Appendix 1.10 and 1.15.5. Plots and age calculations have been made using computer program ISOPLOT v3.7 (Ludwig, 2008). To obtain overall U-Pb ages for the Late Cretaceous – Late Miocene samples the data has been plotted on Tera-Wasserburg plots, where the U-Pb data is uncorrected for common Pb and the mixing line is anchored to the $^{207}Pb/^{206}Pb$ ratio for modern day common Pb (0.84) (Appendix 1.11). The overall sample U-Pb ages are given by the intercept on the Tera-Wasserburg plot and uncertainties are quoted at the 2σ or 95% confidence level. The overall U-Pb ages for the samples of the Permian – Triassic basement are Concordia ages or intercept ages with uncertainties quoted at the 2σ or 95% confidence level (Appendix 1.11). The Ar-Ar ages obtained for the two basic to intermediate samples (RJ1111 and AM0887) are plateau ages with uncertainties quoted at the 2σ level (Appendix 1.15.5).

						Previously assigned geological groups/formations/units								This Study
						Geological Maps of Chile						Geological Maps of Argentina		
Sample	**Latitude (S)**	**Longitude (W)**	**Rock type**	**Age (Ma)**	**±2σ or 95% conf.**	**Geological unit from José Frutos et al. (2004)**	**Geological unit from Emparan and Pineda (1999)**	**Geological unit from Pineda and Emparan (2006)**	**Geological unit from Pineda and Calderón (2008)**	**Geological unit from Mpodozis and Cornejo (1988)**	**Geological unit from Nasi et al. (1990)**	**Geological unit from Cardó et al. (2007)**	**Geological unit from Cardó and Díaz (1999)**	**Assigned Geological Unit**
RJ11A18	-30.55025	-69.46478	Granodiorite	**280.2**	3.5								Agua Negra Formation	Pluton Tocota (Colangüil Batholith)
MQ39*	-29.98694	-69.81694	Rhyolite	**269.7**	2.6							Cerro de las Tórtolas Formation		Choiyoi Group
RJ11A20	-30.20286	-69.82981	Rhyolite	**269.6**	7.0	Guanaco Sonso Unit (Pastos Blancos Group)				Tilito Formation (Lower Doña Ana Group)		Doña Ana Group		Choiyoi Group
AM0862	-30.16139	-69.86500	Rhyolite	**269.3**	5.2	Tilito Formation (Lower Doña Ana Group)				Tilito Formation (Lower Doña Ana Group)				Choiyoi Group
AM0853	-30.20482	-70.04247	Rhyolite	**261.0**	6.0	Escabroso Formation (Upper Doña Ana Group)				Escabroso Formation (Upper Doña Ana Group)				Pastos Blancos Group
AM0855	-30.12487	-70.06505	Rhyolite	**248.6**	5.5	Pleistocene-Holocene alluvial deposits				Pastos Blancos Group				Pastos Blancos Group
AM0856	-30.12633	-70.06672	Rhyolite			Pleistocene-Holocene alluvial deposits				Pastos Blancos Group				Pastos Blancos Group
RJ1104	-30.23869	-70.34286	Granite	**221.0**	4.4	Elqui-Limarí Batholith (Ingaguás Supergroup)				Botacoma Unit				El León Unit (Ingaguás Supergroup)
AM0812	-30.74000	-70.86083	Diorite	**72.55**	0.77	Paleocene-Eocene (63-38Ma)			Diorite Pichasca (66-64 Ma)					Cogotí Supergroup
AM0823	-30.98639	-70.74083	Granodiorite	**69.80**	0.73	Eocene (52-33Ma)			Granodiorita Guatulame (48Ma)	Fredes Unit (Cogotí Supergroup)				Cogotí Supergroup
AM0824	-30.98639	-70.74083	Syeno-diorite	**64.59**	0.65	Eocene (52-33Ma)			Granodiorita Guatulame (48Ma)	Fredes Unit (Cogotí Supergroup)				Cogotí Supergroup
AM0806	-30.73500	-70.75861	Granite	**64.39**	0.66	Paleocene-Eocene (63-38Ma)			Diorite Pichasca (66-64 Ma)					Cogotí Supergroup
RJ1103	-31.00108	-70.72181	Syeno-diorite	**64.33**	0.59	Eocene (52-33Ma)								Cogotí Supergroup
AM0826	-30.98639	-70.74083	Granite	**64.21**	0.69	Eocene (52-33Ma)			Granodiorita Guatulame (48Ma)	Fredes Unit (Cogotí Supergroup)				Cogotí Supergroup
AM0890	-29.94444	-70.07111	Basaltic andesite	**61.92**	9.11	Pliocene-Pleistocene								Los Elquinos Formation
RJ1111	-30.14294	-70.69167	Basaltic andesite	***61.20***	*1.0*	Late Cretaceous		Eocene Intrusives (41-34Ma)		Los Elquinos Formation				Los Elquinos Formation
AM0819	-30.26583	-70.65861	Diorite			Paleocene-Eocene (63-38Ma)		Monzogranito El Bosque (56-41Ma)		Fredes Unit (Cogotí Supergroup)				Cogotí Supergroup
AM0822	-30.25250	-70.65028	Granodiorite	**57.30**	1.70	Late Cretaceous		Monzogranito El Bosque (56-41Ma)		Los Elquinos Formation or Fredes Unit (Cogotí Supergroup)				Cogotí Supergroup
AMO814	-30.77167	-70.82694	Diorite			Paleocene-Eocene (63-38Ma)			Diorite Pichasca (66-64 Ma)					Cogotí Supergroup
AM0815	-30.84111	-70.77167	Granodiorite	**55.00**	1.70	Paleocene-Eocene (63-38Ma)			Granodiorita Guatulame (48Ma)					Cogotí Supergroup
AM0816	-30.84111	-70.77167	Granodiorite	**54.06**	0.76	Paleocene-Eocene (63-38Ma)			Granodiorita Guatulame (48Ma)					Cogotí Supergroup
RF17*	-29.82614	-69.82978	Basaltic-Trachyandesite									Doña Ana Group		Río Frío Basalts
RJ1105	-29.59417	-70.69061	Diorite	**40.20**	1.20	Paleocene-Eocene	Tierras Blancas Caldera							Tierras Blancas Caldera
RJ1106	-29.60525	-70.69497	Diorite			Paleocene-Eocene	Eocene (41-34Ma)							Tierras Blancas Caldera
RJ1107	-29.64144	-70.73597	Basalt			Late Cretaceous	Los Elquinos Formation							Tierras Blancas Caldera
RJ1101	-31.16878	-70.81919	Granite	**38.89**	0.99	Pleistocene-Holocene alluvial deposits								Cogotí Supergroup
RJ1109	-30.03569	-70.75431	Diorite			Paleocene-Eocene (63-38Ma)		Eocene Intrusives (41-34Ma)						Cogotí Supergroup
AM0867	-30.15667	-69.87972	Andesite	**35.58**	0.78	Pleistocene-Holocene glacial deposits				sediments, close to Tilito Formation (Lower Doña Ana Group)				Bocatoma Unit
AM0866	-30.15667	-69.87972	Andesite			Pleistocene-Holocene glacial deposits				sediments, close to Tilito Formation (Lower Doña Ana Group)				Bocatoma Unit
AM0870	-30.15667	-69.87972	Trachy-andesite			Pleistocene-Holocene glacial deposits				sediments, close to Tilito Formation (Lower Doña Ana Group)				Bocatoma Unit
AM0846	-30.04278	-70.05417	Rhyolite	**26.10**	1.60	Tilito Formation (Lower Doña Ana Group)				Tilito Formation (Lower Doña Ana Group)				Tilito Formation (Lower Doña Ana Group)
MQ153*	-29.85272	-69.86294	Andesite	**25.20**	0.26							Doña Ana Group		Tilito Formation (Lower Doña Ana Group)
AM0847	-30.04278	-70.05417	Rhyolite			Tilito Formation (Lower Doña Ana Group)				Tilito Formation (Lower Doña Ana Group)				Tilito Formation (Lower Doña Ana Group)
AM0845	-30.04278	-70.05417	Rhyolite	**24.90**	0.32	Tilito Formation (Lower Doña Ana Group)				Tilito Formation (Lower Doña Ana Group)				Tilito Formation (Lower Doña Ana Group)
AM0860	-30.16139	-69.86500	Dacite	**24.86**	0.40	Tilito Formation (Lower Doña Ana Group)				Tilito Formation (Lower Doña Ana Group)				Tilito Formation (Lower Doña Ana Group)
ZN122*	-29.57619	-69.92303	Andesite	**24.78**	0.37							Doña Ana Group		Tilito Formation (Lower Doña Ana Group)
AM0844	-30.04250	-70.05194	Rhyolite	**24.72**	0.28	Tilito Formation (Lower Doña Ana Group)				Tilito Formation (Lower Doña Ana Group)				Tilito Formation (Lower Doña Ana Group)
AM0849	-30.04278	-70.05417	Rhyolite	**24.69**	0.43	Tilito Formation (Lower Doña Ana Group)				Tilito Formation (Lower Doña Ana Group)				Tilito Formation (Lower Doña Ana Group)
RF64*	-29.79425	-69.77597	Rhyolite	**24.26**	0.70							Valle del Cura Formation		Tilito Formation (Lower Doña Ana Group)
PC14*	-29.44883	-69.49070	Rhyolite	**23.61**	0.21							Cerro de las Tórtolas Formation		Tilito Formation (Lower Doña Ana Group)
Z27*	-29.61389	-69.77611	Dacite	**23.18**	0.30							Valle del Cura Formation		Tilito Formation (Lower Doña Ana Group)
MQ8*	-29.95578	-69.77517	Basalt									landslide deposits close to Vacas Heladas Ignimbrites		Las Maquinas Basalts
MQ145*	-29.96111	-69.75711	Basalt									Iglesia Formation (Holocene)		Las Maquinas Basalts

						Previously assigned geological groups/formations/units								This Study
						Geological Maps of Chile						Geological Maps of Argentina		
Sample	Latitude (S)	Longitude (W)	Rock type	Age (Ma)	±2σ or 95% conf.	Geological unit from José Frutos et al. (2004)	Geological unit from Emparan and Pineda (1999)	Geological unit from Pineda and Emparan (2006)	Geological unit from Pineda and Calderón (2008)	Geological unit from Mpodozis and Cornejo (1988)	Geological unit from Nasi et al. (1990)	Geological unit from Cardó et al. (2007)	Geological unit from Cardó and Díaz (1999)	Assigned Geological Unit
RJ11A5	-29.83542	-69.13511	Rhyolite	**22.55**	0.33							Las Trancas Formation		Las Trancas Formation
RJ11A10	-29.76408	-69.28128	Granite	**22.17**	0.23							Miocene Intrusives (Infiernillo Unit)		Miocene Intrusives
RJ11A11	-29.71292	-69.25514	Granite	**21.37**	0.29							Miocene Intrusives (Infiernillo Unit)		Miocene Intrusives
RJ11A14	-29.77164	-69.22322	Granodiorite	**20.43**	0.31							Miocene Intrusives (Infiernillo Unit)		Miocene Intrusives
AM0887	-29.91972	-69.99472	Andesite	***19.34***	*0.3*	Cerro de las Tórtolas Formation					Hydrothermally altered, close to Tilito Formation			Escabroso Formation (Upper Doña Ana Group)
1026*	-29.69056	-69.69500	Andesite - Trachyandesite	**18.21**	0.28							Valle del Cura Formation		Escabroso Formation (Upper Doña Ana Group)
SP80*	-29.72392	-69.69964	Andesite	**18.06**	0.37							Valle del Cura Formation		Escabroso Formation (Upper Doña Ana Group)
AMO886	-29.91667	-69.99444	Andesite			Cerro de las Tórtolas Formation					Hydrothermally altered, close to Tilito Formation			Escabroso Formation (Upper Doña Ana Group)
MQ158*	-29.56583	-69.85639	Basaltic andesite									Doña Ana Group		Escabroso Formation (Upper Doña Ana Group)
AMO871	-30.24194	-70.03000	Basaltic andesite			Miocene (20-12Ma)				Infiernillo Unit				Escabroso Formation (Upper Doña Ana Group)
AMO872	-30.24194	-70.03000	Dacite			Miocene (20-12Ma)				Infiernillo Unit				Escabroso Formation (Upper Doña Ana Group)
RF62*	-29.79403	-69.78217	Trachyandesite	**17.06**	0.63							Valle del Cura Formation		Cerro de las Tórtolas Formation
RF65*	-29.79403	-69.78217	Andesite									Valle del Cura Formation		Cerro de las Tórtolas Formation
MQ28*	-29.94333	-69.85611	Trachyandesite									Cerro de las Tórtolas Formation		Upper Cerro de las Tórtolas Formation
MQ30*	-29.93583	-69.84997	Trachyandesite									Cerro de las Tórtolas Formation		Upper Cerro de las Tórtolas Formation
RJ11A7	-30.68222	-69.43619	Trachyandesite	**11.65**	0.21								Tertiary Intrusives	Tertiary Intrusives
RJ11A17	-30.55664	-69.46964	Dacite	**9.45**	0.18								Tertiary Intrusives	Tertiary Intrusives
RJ11A15	-30.55139	-69.46786	Trachydacite	**9.43**	0.18								Agua Negra Formation	Tertiary Intrusives
MQ33*	-29.95314	-69.83447	Rhyolite	**6.16**	0.19							Vacas Heladas Ignimbrites		Vacas Heladas Ignimbrites
DI095*	-29.98889	-69.81833	Rhyolite	**6.15**	0.30							Doña Ana Group		Vacas Heladas Ignimbrites
MQ32*	-29.94853	-69.83106	Rhyolite									Vacas Heladas Ignimbrites		Vacas Heladas Ignimbrites
AM0889	-29.92000	-70.03806	Rhyolite			Pliocene-Pleistocene landslide deposits close to Vallecito Formation					Vallecito Formation (Vacas Heladas Ignimbrites)			Vacas Heladas Ignimbrites

Table 2.2. The results of U-Pb dating of zircon and Ar-Ar dating of plagioclase. Sample age calculations have been made using computer program ISOPLOT v3.7 (Ludwig, 2008) (Appendix 1.11 and 1.15.5). Uncertainties are quoted at the 2σ or 95% confidence level. The two sample ages which are displayed in italics and underlined are those obtained by Ar-Ar dating (Appendix 1.15.5), due to the lack of zircon in these samples for U-Pb dating. The results of U-Pb and Ar-Ar dating are presented alongside the previously assigned geological units (Mpodozis and Cornejo, 1988; Nasi et al., 1990; Cardó and Díaz, 1999; Emparan and Pineda, 1999; José Frutos et al., 2004; Pineda and Emparan, 2006; Cardó et al., 2007; Pineda and Calderón, 2008) and the units assigned by this study based on the results of the new age determinations and whole rock geochemical analysis. Sample numbers with * have been provided by V. Litvak.

The results of U-Pb and Ar-Ar dating have led to certain samples being assigned to geological formations and units that are different to those identified for the corresponding sample locations on geological maps of the region. A summary of this is presented in Table 2.2 and Figure 2.5. In particular, a number of samples that were previously identified as Cenozoic in age have been U-Pb dated as Permian – Triassic and assigned to the appropriate geological unit of this age.

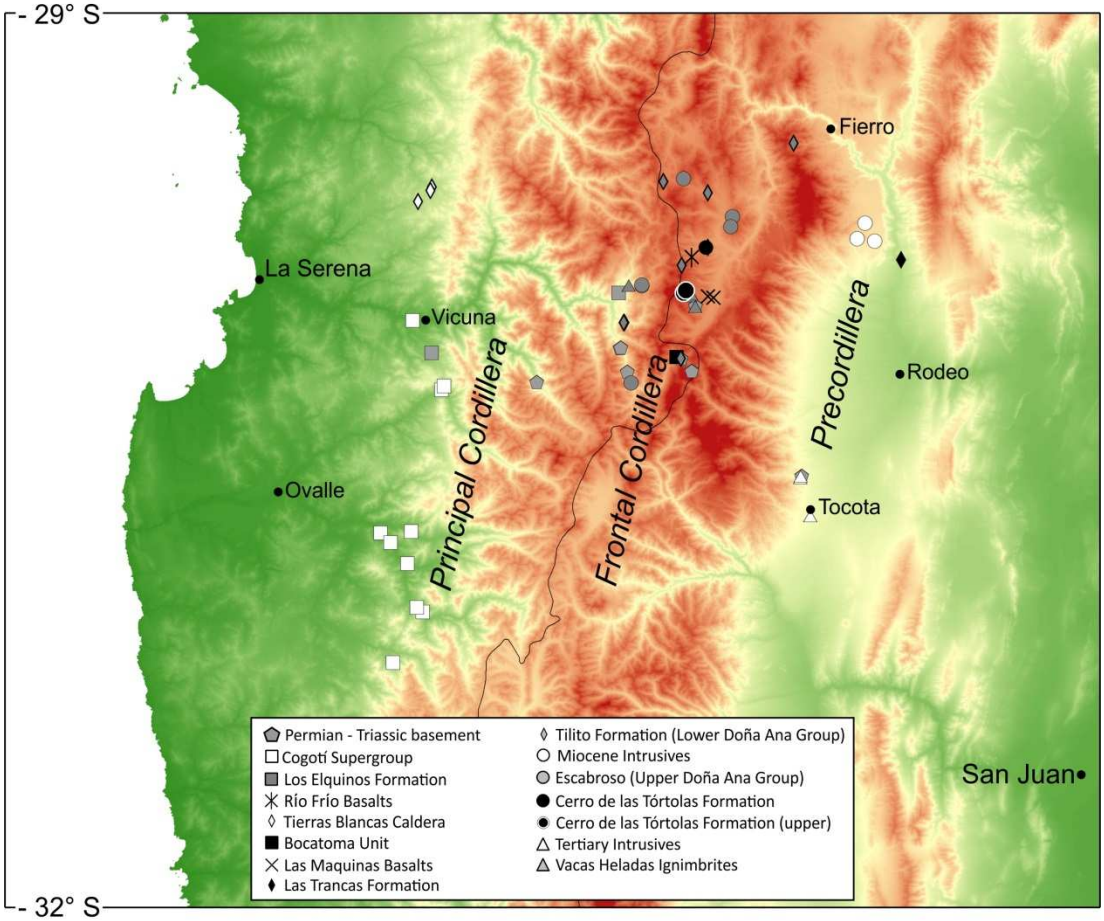

Figure 2.5. Map of the southern Central Andes showing the sample locations and assigned geological units demonstrating a general eastward migration of the magmatic arc over the course of the Cenozoic.

The U-Pb ages obtained for samples of the Cogotí Supergroup range between 72.6 ±0.8 and 38.9 ±1.0 Ma. Some of the ages are slightly older than those previously obtained, but the majority are in keeping with those previously reported (67 ±2 to 38

±1 Ma Parada et al. (1988) and references therein). A U-Pb age of 61.9 ±9.1 Ma was acquired for a sample of the Los Elquinos Formation (AM0890); the large uncertainty reflects the limited number of zircon grains present in this basaltic andesite sample (refer to Appendix 1.10 and 1.11). However, the U-Pb age produced is very similar to the Ar-Ar age produced for basaltic andesite sample RJ1111 (Los Elquinos Formation) of 61.2 ±1.0 Ma (Appendix 1.15.5). A sample of the Terras Blancas Caldera produced a U-Pb age of 40.2 ±1.2 Ma, which is within the range of those previously reported (Emparan and Pineda, 1999). A U-Pb age of 35.6 ±0.8 Ma was obtained for a porphyritic, andesitic sample from the Frontal Cordillera of Chile (previously mapped as Pleistocene-Holocene glacial deposits (José Frutos et al., 2004) and sedimentary deposits (Mpodozis and Cornejo, 1988)) confirming the assignment of this, and similar samples, to the Botacoma Unit which has previously been Ar-Ar and K-Ar dated between 39.5 and 30 ±1.9 Ma (Mpodozis and Cornejo, 1988; Nasi et al., 1990; Martin et al., 1995; Bissig et al., 2001). The U-Pb ages obtained for the Tilito Formation (Lower Doña Ana Group) range between 26.1 ±1.6 and 23.2 ±0.3 Ma and the ages obtained for the Escabroso Formation (Upper Doña Ana Group) range between 19.3 ±0.3 Ma (Ar-Ar age) and 18.1 ±0.4 Ma. The sample of the Las Trancas Formation, obtained from the Argentinean Precordillera, produced a U-Pb age of 22.6 ±0.3 Ma and as previously suggested is coeval with the Doña Ana Group. The Miocene Intrusives present in the Llanos del Molle of the Argentinean Precordillera, which have previously been associated with the Infiernillo Unit on the Chilean side of the margin (Cardó et al., 2007), produced U-Pb ages ranging between 22.2 ±0.2 and 20.4 ± 0.3 Ma. These ages are older than those produced for the Infiernillo Unit on the Chilean side of the margin (18 – 15 Ma) (Kay et al., 1987) and the Cerro de las Tórtolas Formation, with which these intrusive bodies have been associated (Cardó et al., 2007). A U-Pb age of 17.1 ±0.6 was obtained for sample RF62 and this was assigned to the Cerro de las Tórtolas Formation. U-Pb ages ranging between 11.7 ±0.2 and 9.4 ±0.2 Ma were attained for the Tertiary intrusive bodies present in the Argentinean Precordillera near the village of Tocota, much

younger than those previously reported (18.3 ±2.5 Ma and 17.5 ±5 Ma (Leveratto, 1976; Cardó and Díaz, 1999)). Zircons obtained from samples of the Vacas Heladas Ignimbrites produced U-Pb ages of 6.2 ±0.2 and 6.2 ±0.3 Ma and these ages concur with those previously reported (Cardó et al., 2007).

The previously identified Valle del Cura Formation (Limarino et al., 1999; Litvak and Poma, 2005), which consists of dacitic and rhyolitic ignimbrites and lava flows, was originally assigned an Eocene age from the results of K-Ar dating (Limarino et al., 1999). Samples of the Valle del Cura Formation which have been U-Pb dated as part of this study have produced Late Oligocene to Early Miocene ages, ranging between 24.3 and 17.1 Ma (Table 2.2). Winocur et al. (2013) also reported Oligocene to Early Miocene ages for Valle del Cura Formation based on Ar-Ar dating and suggested that the previously obtained K-Ar ages are likely to be unreliable due to high levels of hydrothermal alteration. These authors propose that the Valle del Cura Formation is coeval with the volcanism of the Doña Ana Group and reassign the volcanic deposits as such. The results of U-Pb dating presented here support these findings and we assign four samples previously identified and mapped as the Valle del Cura Formation to the Tilito and Escabroso Formations (Doña Ana Group) and two samples to the Cerro de las Tórtolas Formation (Table 2.2).

A number of intrusive units in the Precordillera of Argentina have been mapped as Miocene and Tertiary Intrusives and correlated with the Infiernillo Unit found on the Chilean side of the border (Cardó and Díaz, 1999; Cardó et al., 2007). However, the U-Pb ages obtained in this study, as well as geochemical evidence, suggest these intrusive bodies are not related. U-Pb ages of between 22.2 ±0.2 and 20.4 ±0.3 Ma were obtained for the Miocene Intrusives present in the Llanos del Molle and mapped by Cardó et al. (2007). These ages are significantly older than the ages reported for the Infiernillo Unit on the Chilean side of the boarder (18 – 15 Ma, (Kay

et al., 1987)). Conversely, much younger U-Pb ages (11.7 ±0.2 to 9.4 ±0.2 Ma) were obtained for the Tertiary Intrusives which outcrop near the village of Tocota (Fig. 2.5). These new U-Pb ages are similar to the K-Ar age of 8.8 ±0.3 Ma reported by Wetten (2005) for the same intrusive bodies, which this author refers to as the Cerro Bola Andesite. Redefining the local stratigraphy is outside the scope of this study and therefore in this instance we retain the nomenclature used by the geological maps (i.e. the Miocene Intrusives and Tertiary Intrusives (Cardó and Díaz, 1999; Cardó et al., 2007)).

2.9.2 Major elements

The results of major oxide analysis are presented in Figures 2.6, 2.7 and 2.8 and Appendix 1.12. The Late Cretaceous to Late Miocene magmatic rocks primarily have medium- to high- K, calc-alkaline compositions (Fig. 2.6a). The intrusive samples range from gabbroic to granitic in composition, with SiO_2 contents ranging between 50.9 and 71.3 wt.% (Fig. 2.7a). The extrusive samples range from basalts to rhyolites with SiO_2 contents ranging between 49.7 and 75.3 wt.% (Fig. 2.7b). All samples plot within the sub-alkaline field on plots of total alkalis versus silica with the exception of the Paleocene Río Frío Basalt, which is alkaline in composition (Fig. 2.7b). All the samples are relatively evolved with an average Mg# of 41 and Ni concentration of 11 ppm (Appendices 1.12 and 1.13). The majority of samples are metaluminous (Fig. 2.6b) with weakly peraluminous compositions displayed by a number of samples of the Tilito Formation, Miocene Intrusives and the Vacas Heladas Ignimbrites. The Permian – Triassic basement rocks have medium- to high-K calc-alkaline to shoshonitic compositions (Fig. 2.6a). The basement samples are peraluminous (Fig. 2.6b) and more felsic than the Late Cretaceous to Late Miocene arc rocks, with SiO_2 contents ranging between 68.7 and 76.7 wt.% (Fig. 2.7a and b).

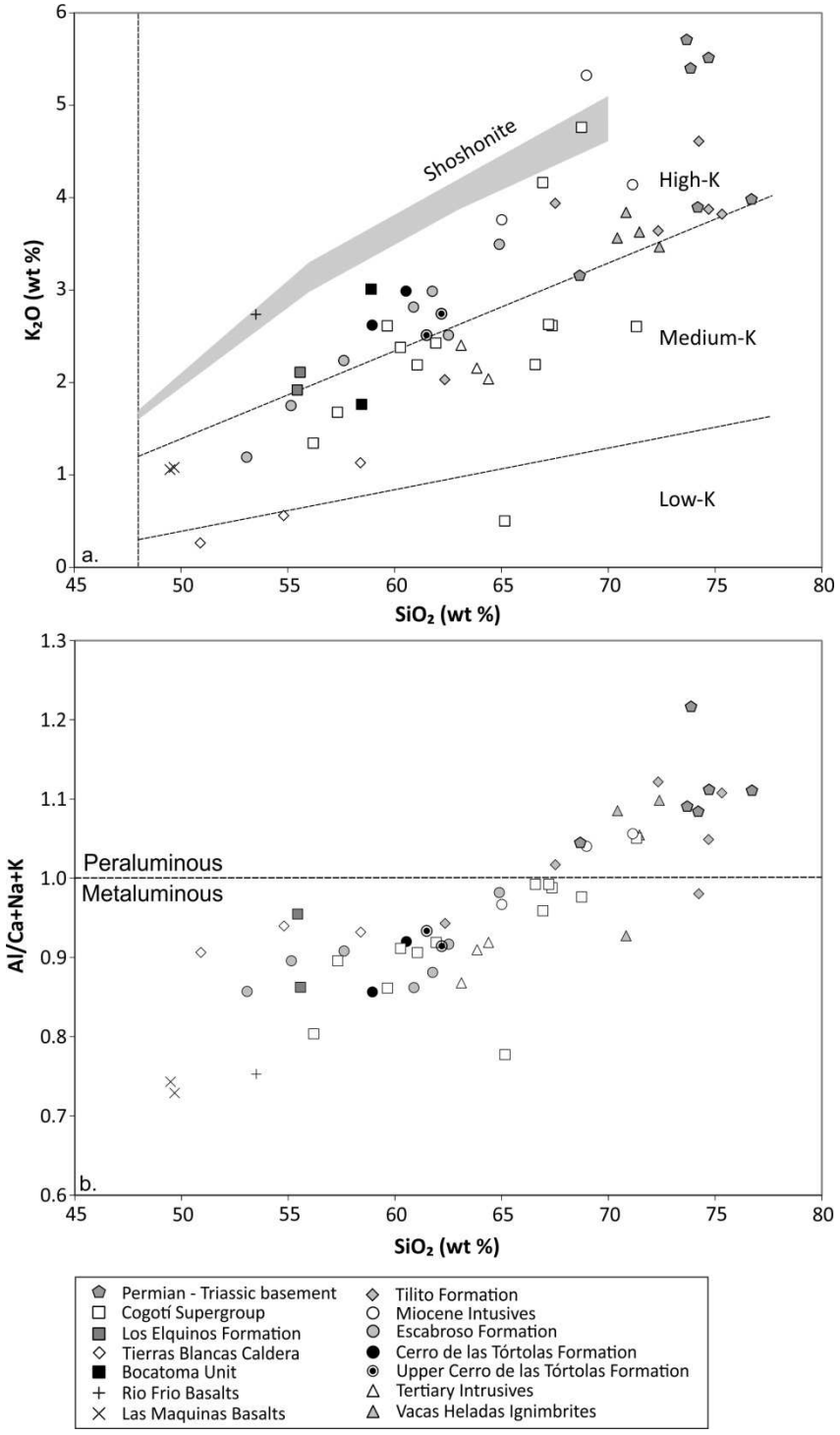

Figure 2.6. Classification diagrams for the Late Cretaceous to Late Miocene magmatic rocks and Permian and Triassic basement; a) K_2O versus SiO_2 content using the discrimination fields of Le Maitre et al. (1989) and the shoshonite boundary of Rickwood (1989); b) aluminum saturation indices (Al/Ca+Na+K) versus silica content.

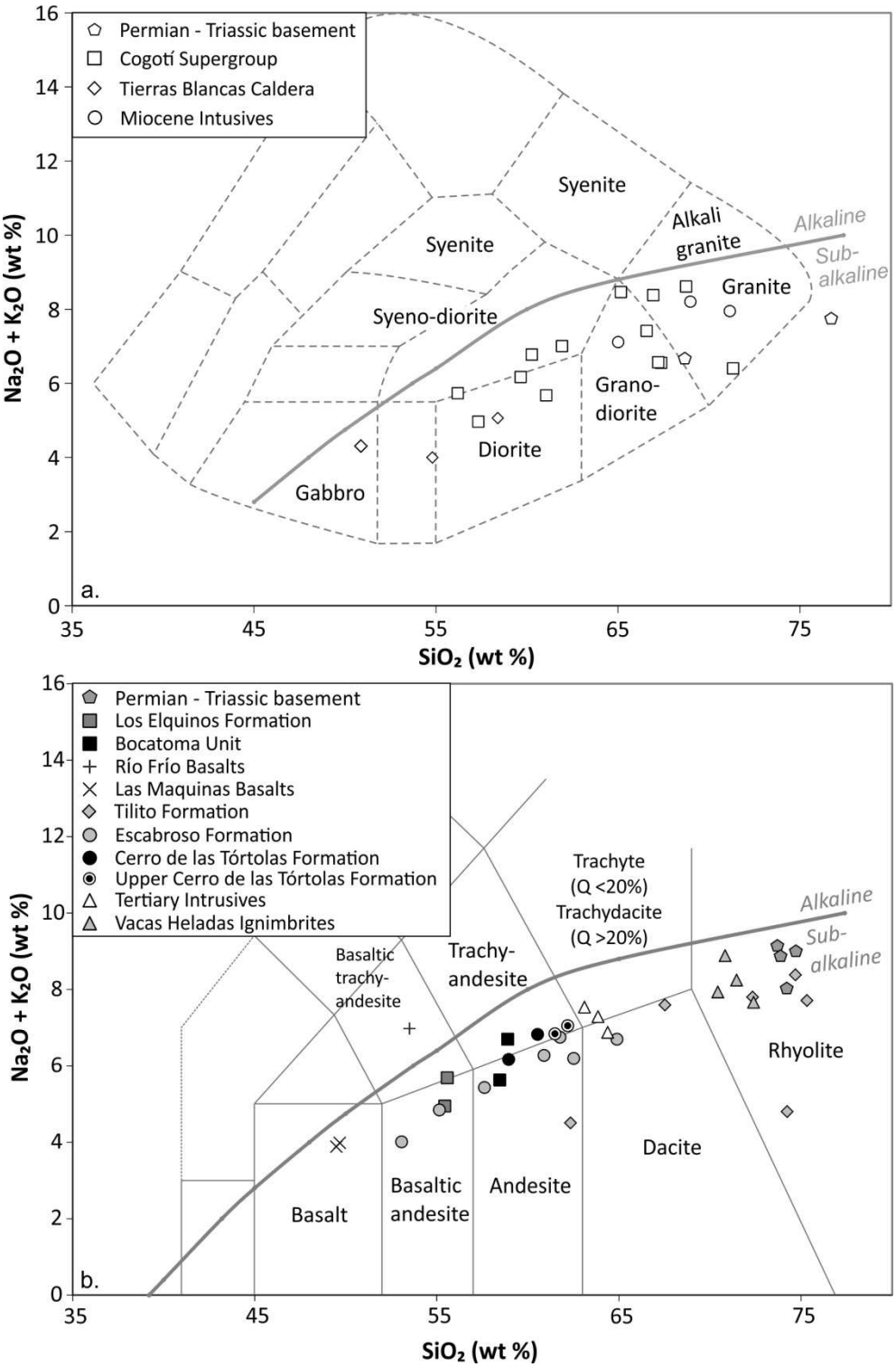

Figure 2.7. Plots of total alkalis versus silica content for a) intrusive samples (fields from Wilson (1989)) and b) extrusive samples (fields from Le Maitre et al. (1989)). The alkaline/subalkaline fields are from Irvine and Baragar (1971).

Major elements, TiO_2, Al_2O_3, Fe_2O_3, MgO, CaO, and to a lesser extent MnO display typical negative correlations with SiO_2 content (Fig. 2.8), whereas K_2O shows a positive correlation (Fig. 2.6). The plot of P_2O_5 versus SiO_2 content shows a convex trend with a general positive correlation between P_2O_5 and SiO_2 content until SiO_2 reaches ~63 wt.%, after which a negative correlation is observed (Fig. 2.8). These trends are likely to reflect fractional crystallisation (FC) processes. The alkali oxides, K_2O and Na_2O show the weakest correlations with SiO_2, suggesting that these elements may have been mobilised during alteration. The highest variation is observed in samples of the Cogotí Supergroup which shows a range of K_2O contents between 0.5 to 4.8% with a limited increase in SiO_2 content (Fig. 2.6a). Values for certain major element oxides, obtained for certain samples, also appear to sit away from the main trends shown by the data. For example, sample PC14 from the Tilito Formation appears to have lost all of its Na_2O and displays higher CaO and MnO contents (Fig. 2.8). This suggests leaching of Na, potentially from plagioclase, and replacement with carbonate minerals. This is confirmed by petrographic analysis of the thin section (Fig. 2.3b). Therefore, some variation in the data away from the main trends displayed on the harker diagrams may be the result of alteration and replacement processes. Overall, the major element compositions of the Late Cretaceous to Late Miocene arc formations overlap with those previously reported for the southern Central Andes (e.g., Kay et al., 1987; Kay et al., 1991; Kay and Abbruzzi, 1996; Bissig et al., 2001; Kay and Mpodozis, 2002; Litvak et al., 2007; Litvak and Poma, 2010).

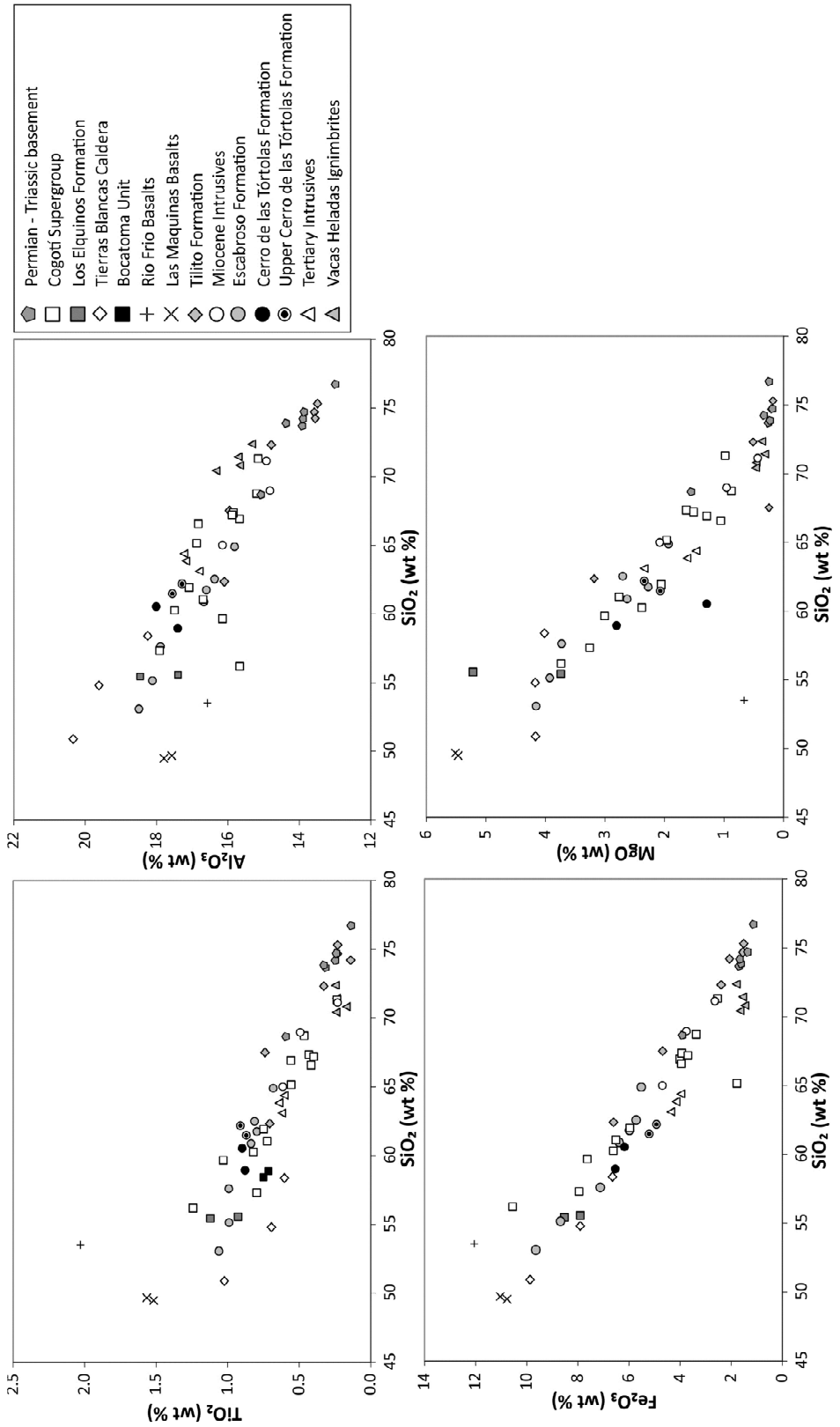

Continued overleaf.

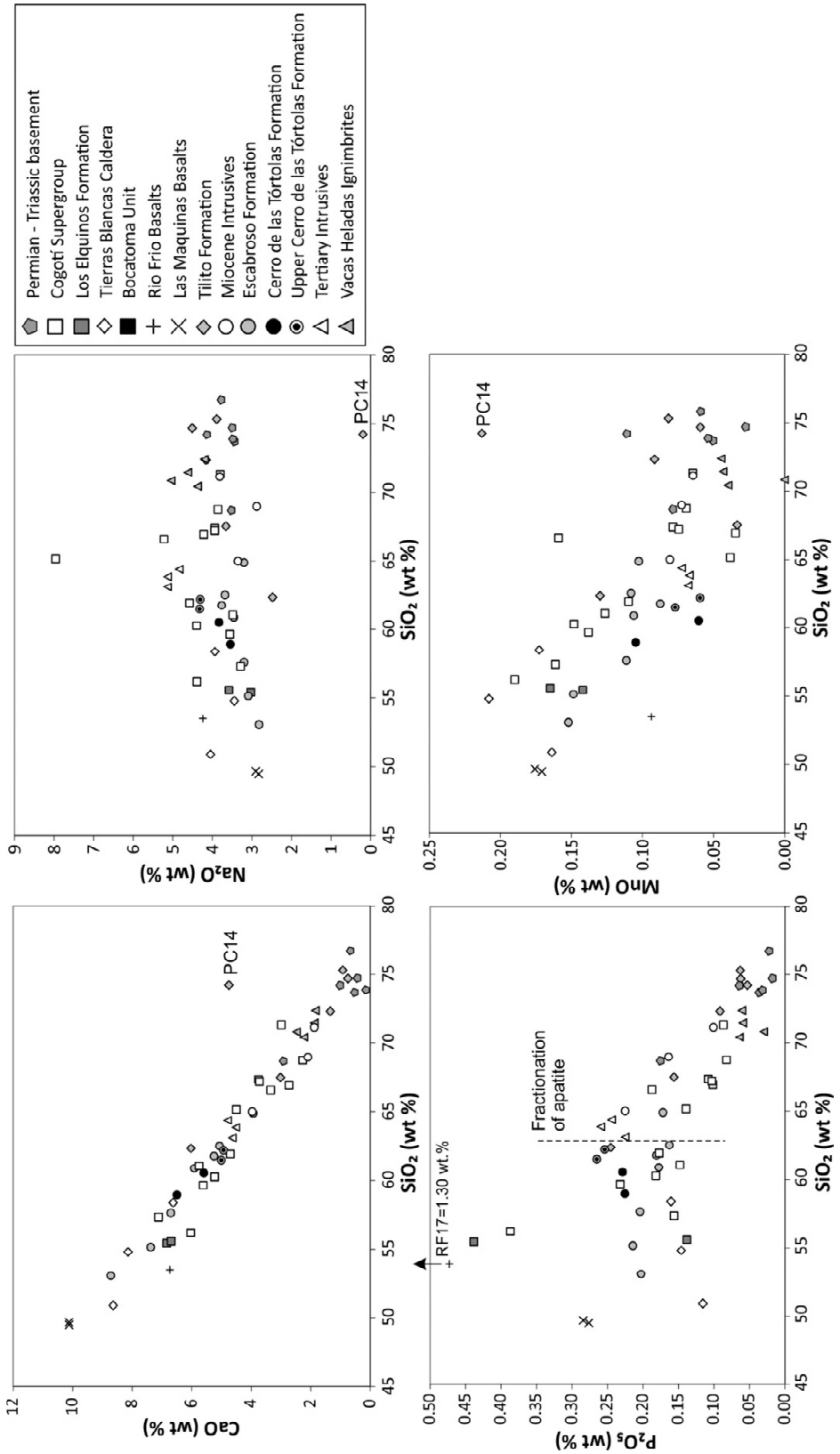

Continued overleaf.

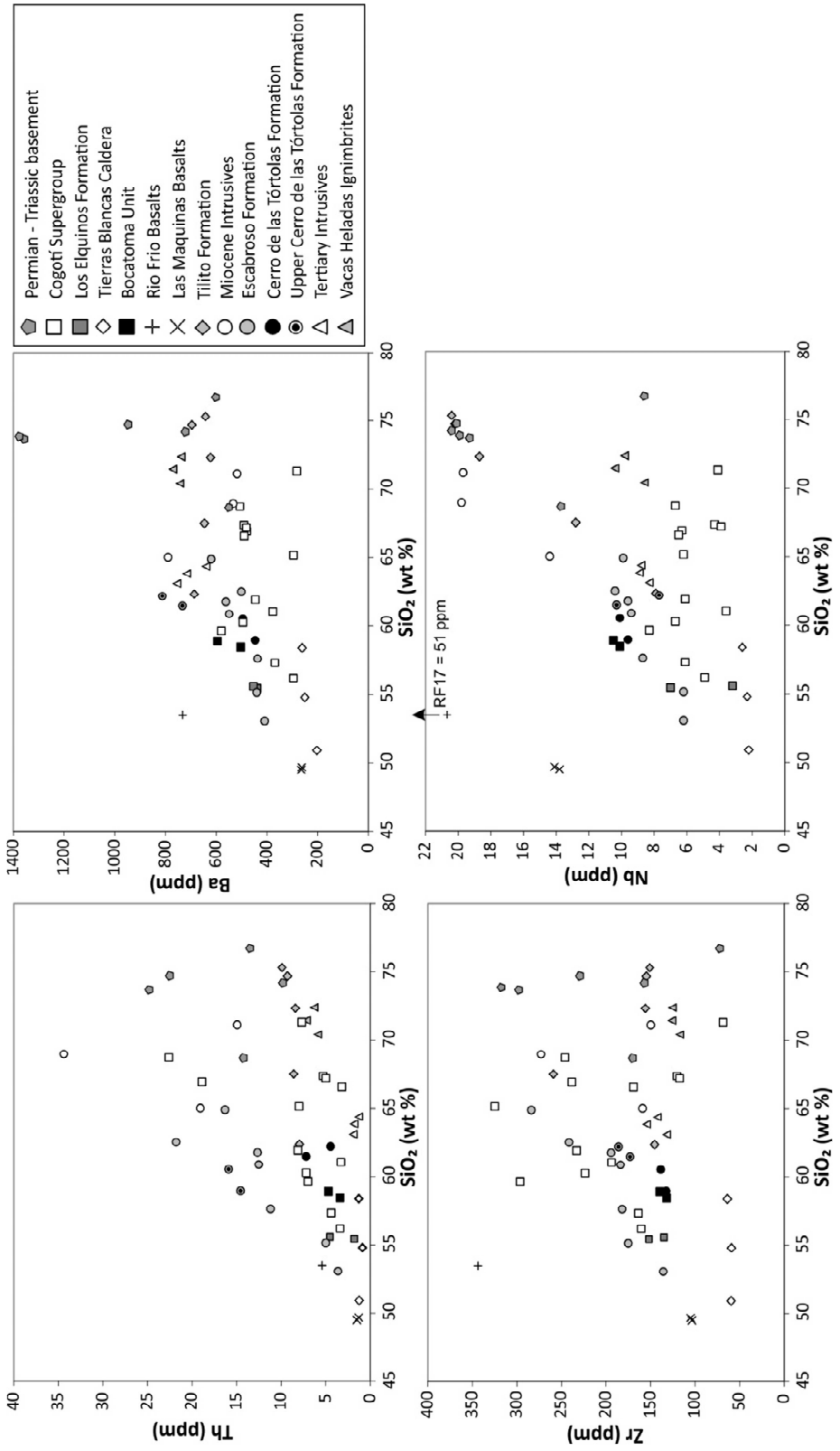

Figure 2.8. Harker-type variation diagrams of major (wt.%) and minor (ppm) elements versus SiO_2 content for the Late Cretaceous to Late Miocene magmatic

rocks and samples of the Permian and Triassic basement. The uncertainty on the data points is less than the size of the symbols (Appendix 1.2). Full results are presented in Appendicies 1.12 and 1.13.

2.9.3 Trace elements (TE) and rare earth elements (REE)

The results of trace and rare earth element analysis are presented in Figure 2.8 and as multi-element and REE diagrams in Figure 2.9. Full results are given in Appendix 1.13. As shown in Figure 2.9 all samples, including the Las Máquinas basalts and those of the Permian – Triassic basement, display typical subduction zone TE and REE signatures with enrichments in the large ion lithophile elements (LILE, e.g., Rb, K, Ba, Sr, Pb) and the light rare earth elements (LREE) relative to the high field strength elements (HFSE, e.g., Nb, Zr, Ti, Y) and heavy rare earth elements (HREE). The multi-element plots for all samples exhibit prominent negative Nb anomalies and positive K and Pb anomalies. With the exception of the most mafic sample of the Las Máquinas basalts, all samples show negative Ti anomalies and depletions relative to N-MORB. All samples with SiO_2 >65 wt.% display negative P anomalies, and a reduction in in P_2O_5 content is observed with SiO_2 after ~63 wt.% SiO_2 (Fig. 2.8). The Late Oligocene, Las Maquinas basalt shows the least enrichment in the LIL elements and the samples of the Terras Blancas Caldera (Eocene) and Bocatoma Unit (Early Oligocene) display limited enrichment in LILE and relatively flat REE patterns, lacking Eu anomalies (Fig. 2.9). The youngest (~13 – 6 Ma) arc formations (Upper Cerro de las Tórtolas Formation, Tertiary Intrusives and Vacas Heladas Ignimbrites) have relatively steeply dipping REE patterns with depletions in the HREE, and lack negative Eu anomalies (Fig. 2.9). Notably, the Paleocene sample (RF17) of the Río Frío Basalts has a distinct TE composition. As well as being alkaline in composition (Fig. 2.7), enrichments in P, Nb and Zr are apparent (Fig. 2.8 and Appendix 1.13). This suggests the Río Frío Basalts are not cogenetic with other Paleocene arc formations (e.g., the Cogotí Supergroup and the Los Elquinos Formation) and that these lavas may have formed in a distinct setting.

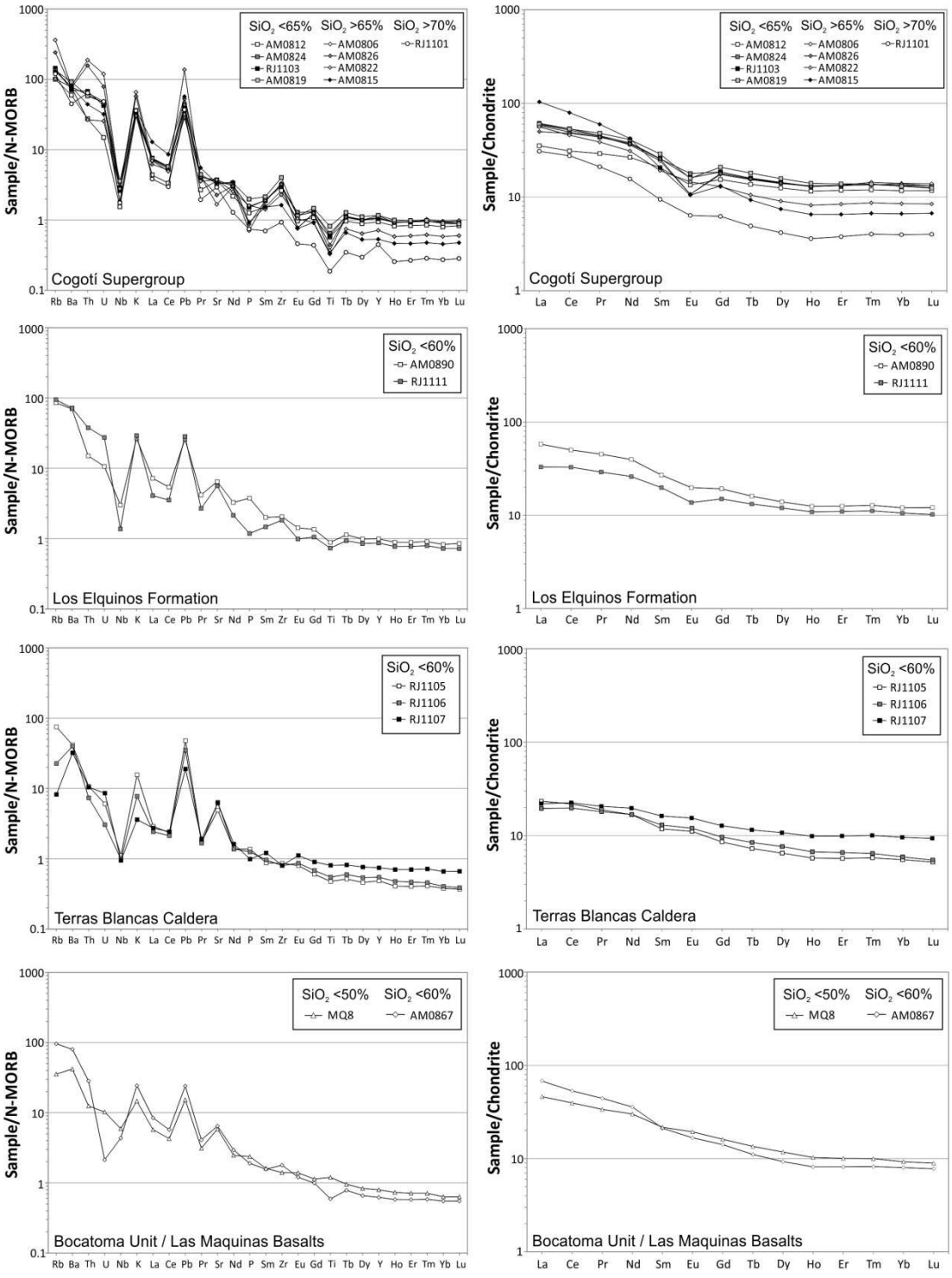

Continued overleaf.

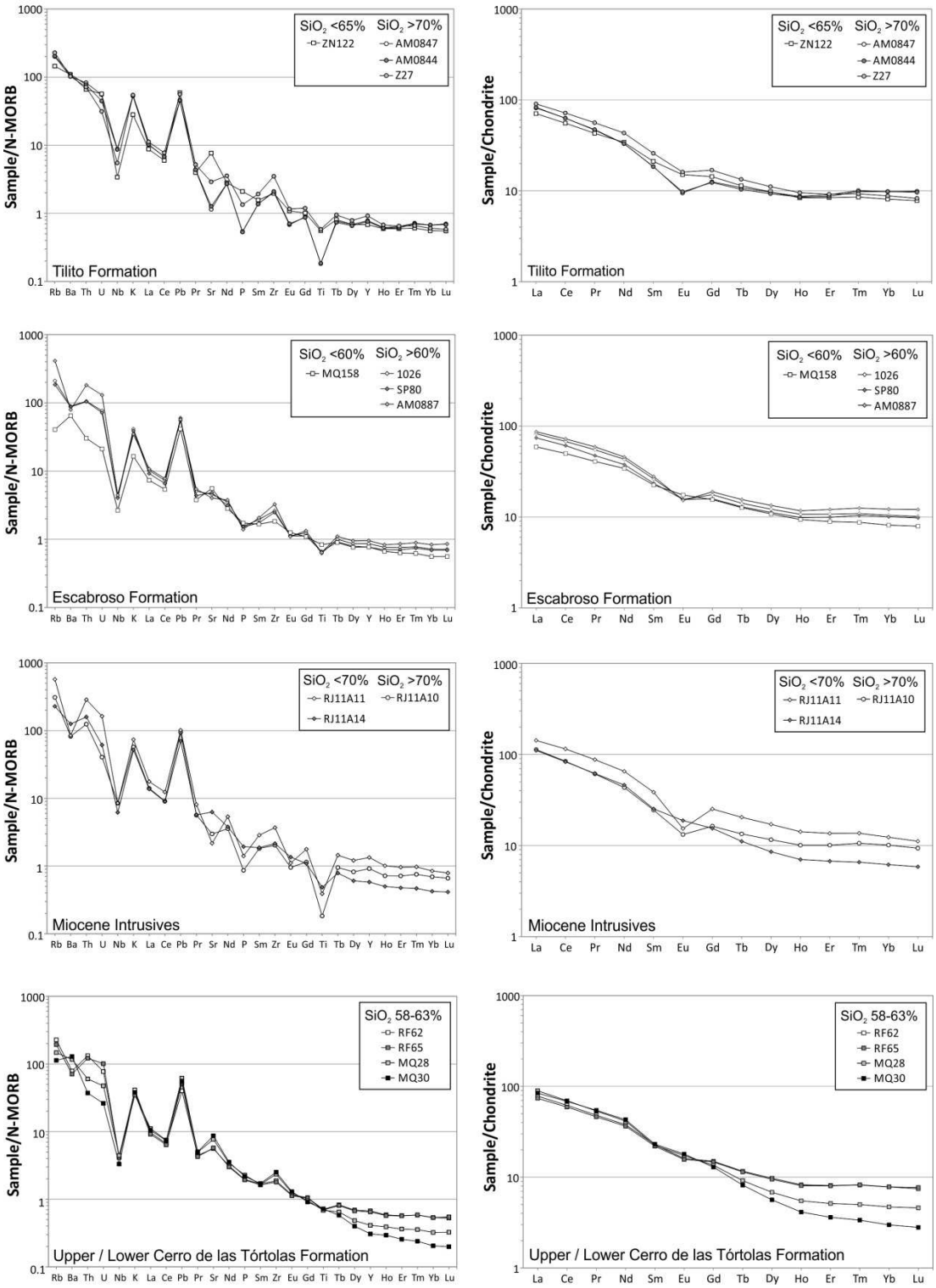

Continued overleaf.

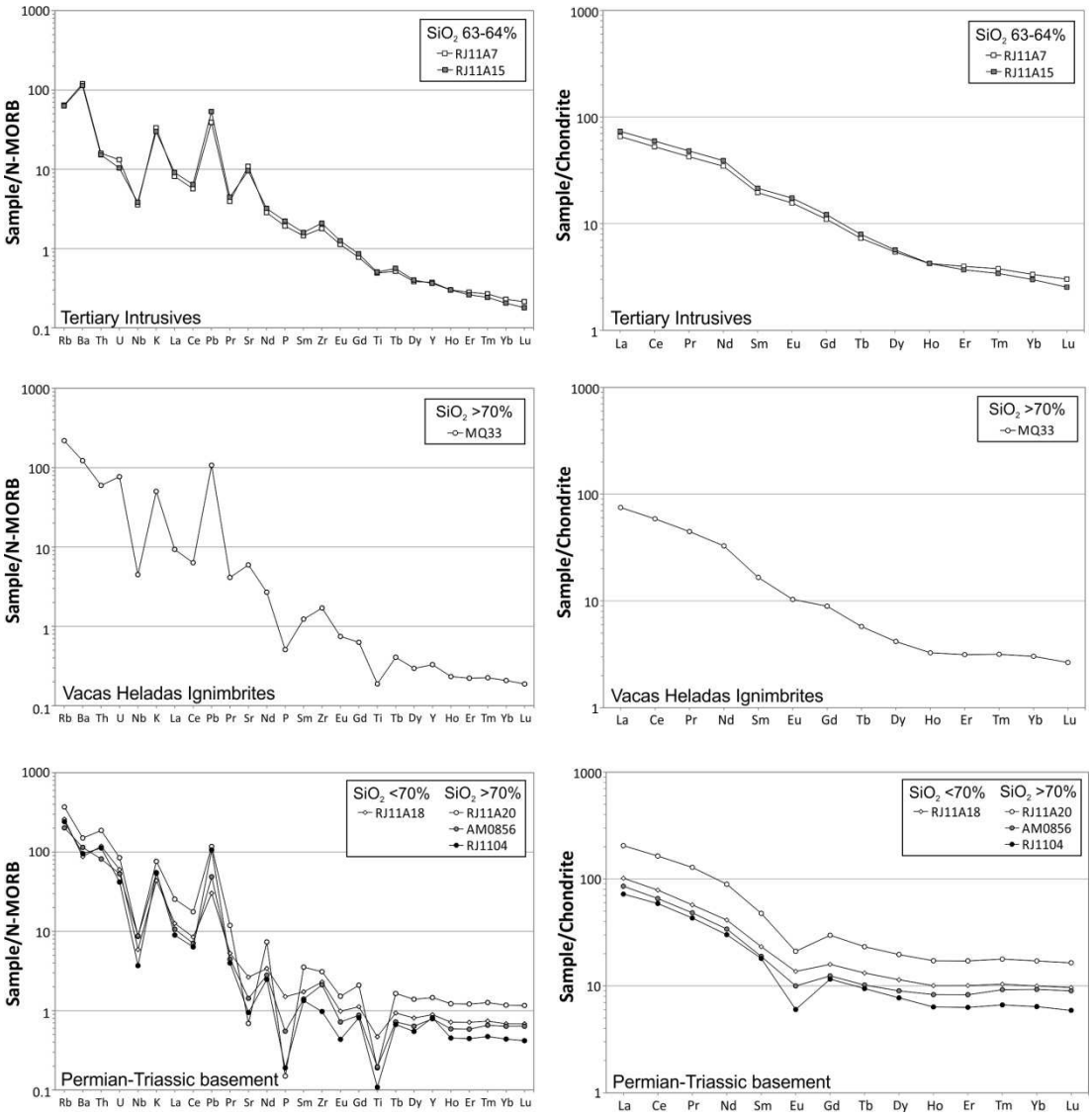

Figure 2.9. Multi-element and REE diagrams for each of the major Cenozoic geological units and the Permian – Triassic basement. Multi-element plots are normalised to the N-MORB values of Sun and McDonough (1989) and REE plots are normalised to the chondrite values of Boynton (1984).

2.9.4 Mineral compositions

The results of major and minor element analysis of plagioclase, pyroxene and amphibole phenocrysts/microphenocrysts, present in select samples, are presented in compositional diagrams in Figures 2.10, 2.11 and 2.12. Full results are presented in Appendices 1.7, 1.8 and 1.9. The plagioclase compositions present in the Late Cretaceous to Late Miocene arc samples range from bytownite to albite (Fig. 2.10). The clinopyroxene compositions range from augite to diopside, and the orthopyroxene present in the Escabroso Formation has been identified as enstatite (Fig. 2.11). The compositions of the amphiboles present in the intrusive samples range from magneso-hornblendes to actinolite (Fig. 2.12). The development of actinolitic-hornblende and actinolite compositions is indicative of alteration and re-equilibration. Although it has been suggested that declining temperatures can favour the production of progressively more siliceous amphiboles (e.g., Helz, 1973), Leake (1971) suggest that amphiboles which have high silica contents (Si > 7.3 in the half unit cell) are unlikely to be truly magmatic and are likely to have crystallised under sub-solidus conditions in the presence of a fluid. On this basis, only the amphiboles present in samples RJ1103 (Cogotí Supergroup) and RJ1106 (Tierras Blancas Caldera), which have magneso-hornblende compositions (Fig. 2.12), are considered suitable for use in amphibole – plagioclase geothermobarometery in order to calculate magmatic crystallisation temperatures and depths (Section 2.9.8). The amphibole compositions in the extrusive and sub-volcanic samples range from magnesio-hornblendes to tschermakitic hornblendes and pargasitic magnesio-hastingites (Fig. 2.12). Notably the two samples of the Tertiary Intrusives have quite different amphibole compositions; phenocrysts in the older sample (RJ11A7) have pargasitic magnesio-hastingite compositions, while the younger sample (RJ11A15) contains primarily magnesio-hornblendes, alongside a few phenocrysts with pargasitic magnesio-hastingite compositions (Fig. 2.12).

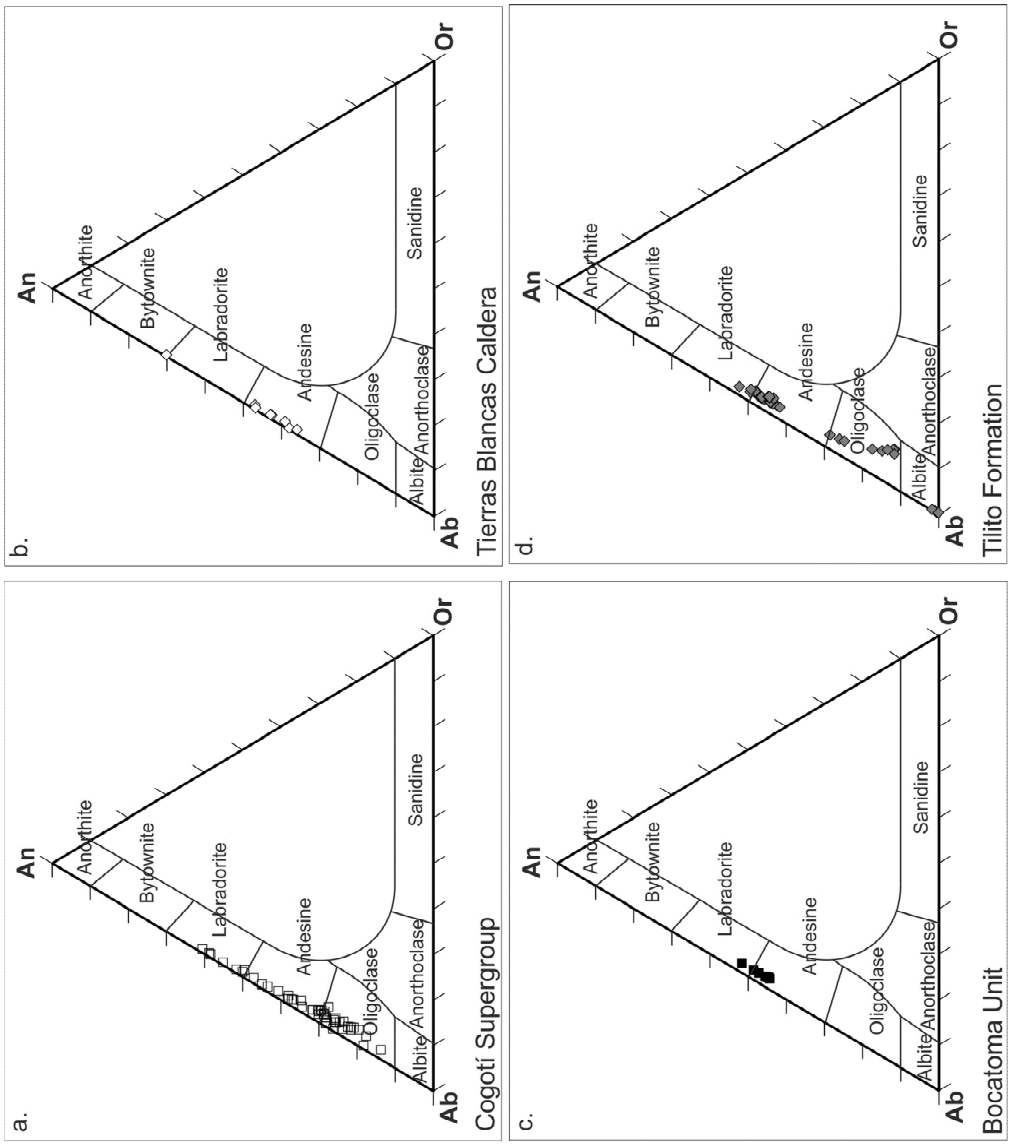

Continued overleaf.

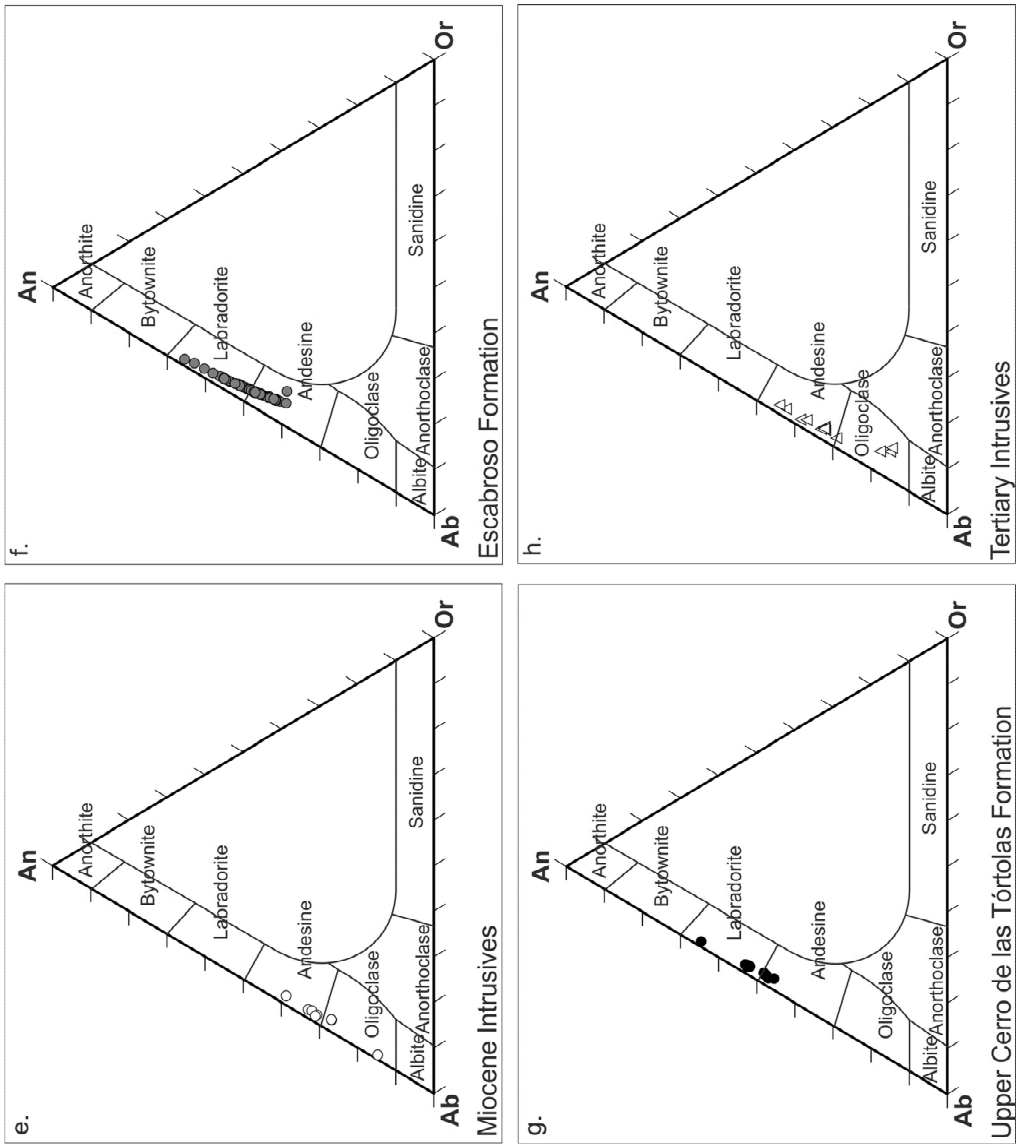

Figure 2.10. Triangular plots of Ab ($NaAlSi_3O_8$), An ($CaAl_2Si_2O_8$) and Or ($KAlSi_3O_8$) compositions for plagioclase microphenocrysts present in the Cenozoic arc magmatic rocks. Compositional data is presented in Appendix 1.7.

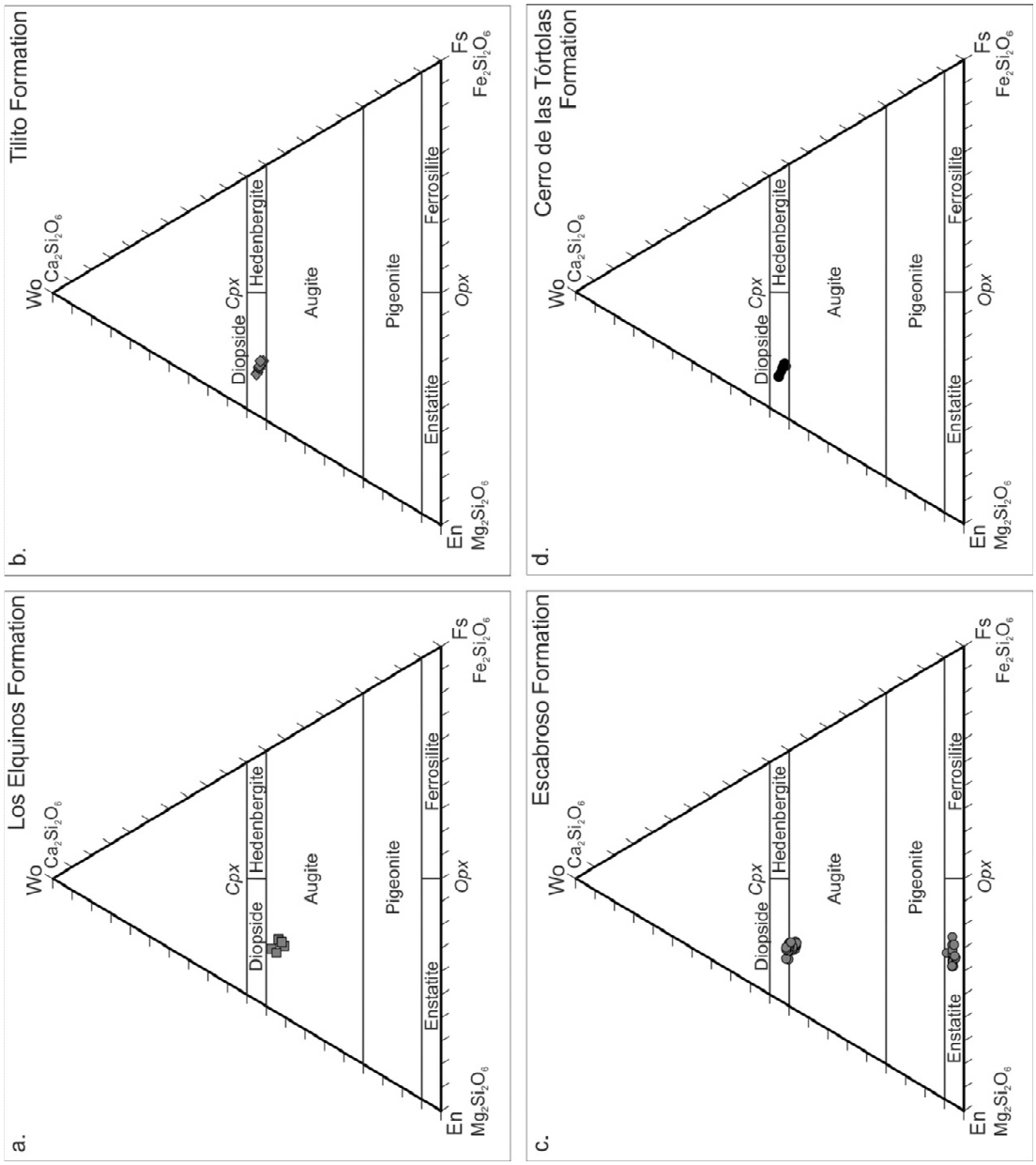

Figure 2.11. Triangular compositional diagrams for pyroxene present in select Cenozoic arc magmatic rocks. Compositional data is presented in Appendix 1.8.

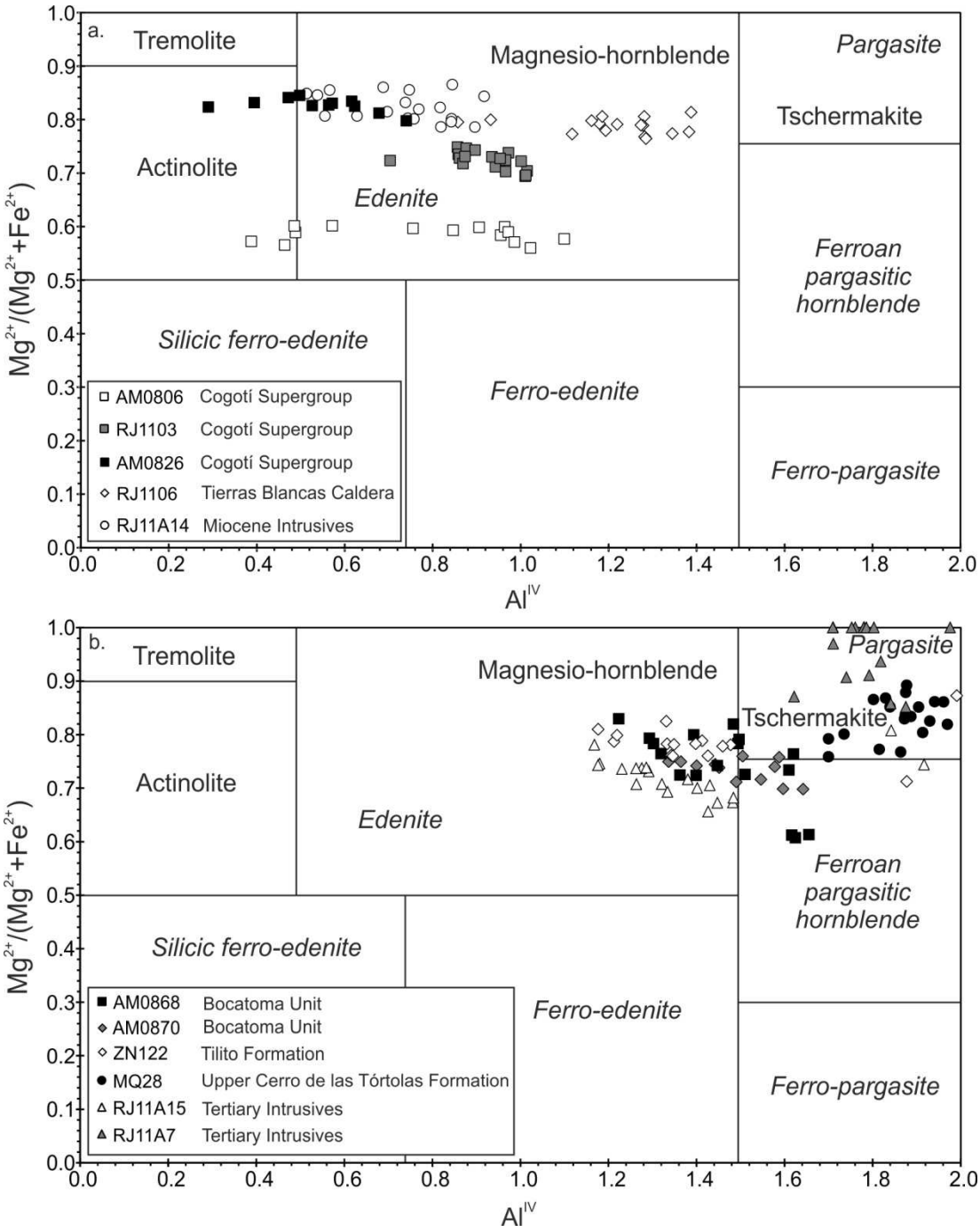

Figure 2.12. Plots of Al^{IV} versus $Mg^{2+}/(Mg^{2+}+Fe^{2+})$, used to classify amphiboles, showing the range of amphibole compositions present in Cenozoic samples. Plot (a) shows intrusive samples and plot (b) shows extrusive/sub-volcanic samples. Compositional data is presented in Appendix 1.9.

2.9.5 Geothermobarometry

The average results of geothermobarometry are presented in Table 2.3 and full, individual analyses are presented in Appendix 1.14.

2.9.5.1 Mineral compositions

All the amphibole analysed were calcic-amphiboles with Ca(B) >1.50 and Na(B) varying between 0.083 and 0.333. The amphiboles present in intrusive samples RJ1103 (Cogotí Supergroup) and RJ1106 (Tierras Blancas Caldera) are all magnesio-hornblendes with some iron and to a lesser extent titanium enrichment. The amphiboles present in the extrusive samples include magnesium-hornblendes, magnesio-hastingsites and tschermakites (Fig. 2.12). An average plagioclase composition of An_{26} and Ab_{71} was obtained for intrusive sample RJ1103 (Appendix 1.14.2) and this value was used in the amphibole-plagioclase thermometer of Holland and Blundy (1994).

2.9.5.2 Thermobarometric calculations

For intrusive sample RJ1103 (Cogotí Supergroup), which contains the mineral assemblage quartz + alkali feldspar + plagioclase + amphibole + biotite + opaques + zircon + apatite, the amphibole-plagioclase thermometer of Holland and Blundy (1994) was intercalated with the Al-in-hornblende geobarometer of Anderson and Smith (1995). The calibration based on the reaction edenite + albite = richterite + anorthite (calibration 2) (Holland and Blundy, 1994) was used to calculate crystallisation temperatures, as Anderson (1996) found the resulting temperatures more precisely matched those produced by other thermometers than those based on the calibration for edenite + 4 quartz = tremolite + albite (calibration 1). Less than a 1 °C difference was found in the crystallisation temperatures obtained for individual

analyses by using the range of pressures produced by a number of additional Al-in-hornblende geobarometers (Hammarstrom and Zen, 1986; Hollister et al., 1987; Johnson and Rutherford, 1989; Schmidt, 1992) in the calibration (2) of Holland and Blundy (1994) (Appendix 1.14.1). The temperatures produced using this calibration also more closely match the temperature estimates produced by the Ti-in-hornblende thermometer in this sample (Otten, 1984) (Appendix 1.14.1).

The Al-in-hornblende geobarometer of Anderson and Smith (1995) has been developed for samples with the specific mineral assemblage quartz + K-feldspar + plagioclase (An_{25-35}) + hornblende + biotite + Fe-Ti oxide + titanite + melt + fluid and is calibrated for crystallisation temperatures ranging between 600 and 800 °C. Using the amphibole-plagioclase thermometer of Holland and Blundy (1994) the calculated crystallisation temperatures for the extrusive samples and intrusive sample RJ1106 (Tierras Blancas Caldera) are all >750 °C. The mineral assemblages in these samples also differ from those required by the Al-in-hornblende geobarometer (Table 2.3). On this basis, the amphibole geothermobarometric formulations of Ridolfi et al. (2010) developed for amphibole-bearing calc-alkaline products of subduction related systems, have been used to calculate the crystallisation temperatures and pressures of these samples.

Sample	Latitude (S)	Longitude (W)	Rock type	Geological Unit	Mineralogy	U-Pb age*[2] (Ma)	±2σ	Average pressure (kbars)	1σ	Average temperature (°C)	1σ	Crustal depth from P=rgh (km)	1σ
RJ1103	-31.00108	-70.72181	Syeno-diorite	Cogotí Supergroup	2 feldspar+quartz+amphibole+biotite+opaques+zircon+apatite	64.3	0.6	1.41	0.27	677	15	5.3	1.0
RJ1106	-29.60525	-70.69497	Diorite	Tierras Blancas Caldera	Plagioclase+amphibole+quartz+opaques+apatite+zircon			1.12	0.21	844	26	4.2	0.8
AM0868	-30.15667	-69.87972	Andesite	Bocatoma Unit	Plagioclase+amphibole+biotite+opaques+apatite+zircon	35.6	0.8	1.90	0.48	862	25	7.2	1.8
AM0870	-30.15667	-69.87972	Trachy-andesite	Bocatoma Unit	Plagioclase+amphibole+biotite+opaques+quartz+apatite			2.02	0.32	869	20	7.6	1.2
ZN122	-29.57619	-69.92303	Andesite	Tilito Formation	Plagioclase+2 pyroxene+amphibole+opaques+zircon	24.8	0.4	2.01	1.29	889	56	7.6	4.9
MQ28	-29.94333	-69.85611	Trachy-andesite	Upper Cerro de las Tórtolas	Plagioclase+amphibole+clinopyroxene+opaques			3.41	0.76	974	22	12.9	2.9
RJ11A7	-30.68222	-69.43619	Trachy-dacite	Tertiary Intrusives	Plagioclase+amphibole+quartz+opaques+sphene+zircon	11.7	0.2	3.57	0.42	964	7	13.5	1.6
RJ11A15	-30.55139	-69.46786	Trachy-dacite	Tertiary Intrusives	Plagioclase+amphibole+biotite+quartz+opaques+zircon	9.4	0.2	1.78	0.63	845	36	6.7	2.4

Table 2.3. Average pressure, temperature and depth calculations based on amphibole-plagioclase and amphibole geothermobarometry. The pressure for sample RJ1103 was calculated using the geobarometer of Anderson and Smith (1995) intercalated with the thermometer of Holland and Blundy (1994). For all other samples the temperatures and pressures were obtained using the amphibole geothermobarometer of Ridolfi et al. (2010). Depth calculations were based on $P=\varrho gh$ where $g = 9.81$ m/s^2, $\varrho=2.7 \times 10^3$ kg/m^3 and h = depth (m). Full results are presented in Appendix 1.14.

2.9.5.3 Crystallisation temperatures, pressures and depths

The temperatures obtained for the intrusive samples range from 643 to 700 °C for sample RJ1103 (Cogotí Supergroup), and 769 and 882 °C for sample RJ1106 (Tierras Blancas Caldera). The pressures obtained for these samples range from 1.0 to 1.8 kbars, and 0.7 to 1.4 kbars respectively. No significant differences in temperatures (T) and pressures (P) were observed between the cores, rims and intermediate points of the phenocrysts (Fig. 2.13 and Appendix 1.14.1 and 1.14.3).

The phenocrysts present in the extrusive samples have formed at a wider range of temperatures and pressures, with generally higher temperature and pressures obtained for the younger arc samples (Mid – Late Miocene). The values obtained for amphiboles from the two samples of the Botacoma Unit (AM0867/68 and AM0870) are in good agreement with each other, with temperatures ranging between 821 and 897 °C and pressures ranging between 1.2 and 2.7 kbars (Fig. 2.13). Amphibole phenocrysts present in the sample of the Tilito Formation (ZN122) appear to have equilibrated and crystallised at two distinct P-T conditions; temperatures and pressures of between 947 and 999 °C, and 2.9 and 4.9 kbars were obtained for two amphibole phenocrysts, while the majority crystallised between 830 and 902 °C, and 1.0 and 1.7 kbars (Fig. 2.13 and Appendix 1.14.6). The amphiboles present in the sample of the Upper Cerro de las Tórtolas Formation have crystallised and equilibrated with the melt over a wide range of P-T conditions, ranging from 928 to 1030 °C, and 2.2 to 5.1 kbars. On average, higher P-T values were obtained for the phenocryst cores in comparison to the rims (Fig. 2.13). Fairly uniform temperatures and pressures were obtained for the older sample of the Tertiary Intrusives (RJ11A7), ranging between 952 and 972 °C, and 3.2 and 4.4 kbars. Lower temperatures and pressures were obtained for the younger sample of the Tertiary Intrusives (RJ11A15) with the majority of values ranging between 805 and 876 °C, and 1.2 and 2.3 kbars. The analysis of the core of one amphibole phenocryst

produced P-T values of 967 °C and 4.0 kbars, which are within the range of values obtained for the older sample (RJ11A7) (Fig. 2.13 and Appendix 1.14.8 and 1.14.9).

Depth estimates have been calculated by assuming a continental crust density of 2.7 $x10^3$ kg/m^3. For the intrusive samples the calculated depth represents the emplacement depth and for the extrusive samples it corresponds to the depth at which the phenocrysts last equilibrated with the melt. An average emplacement depth of 5.3 km was calculated for the Cogotí Supergroup and 4.2 km for the Tierras Blancas Caldera. The average crustal depths at which the amphiboles present in the extrusive samples crystallised and last equilibrated with the melt range from 6.7 km to 13.5 km, with greater depths obtained for the Mid to Late Miocene samples (Table 2.3 and Fig. 2.13).

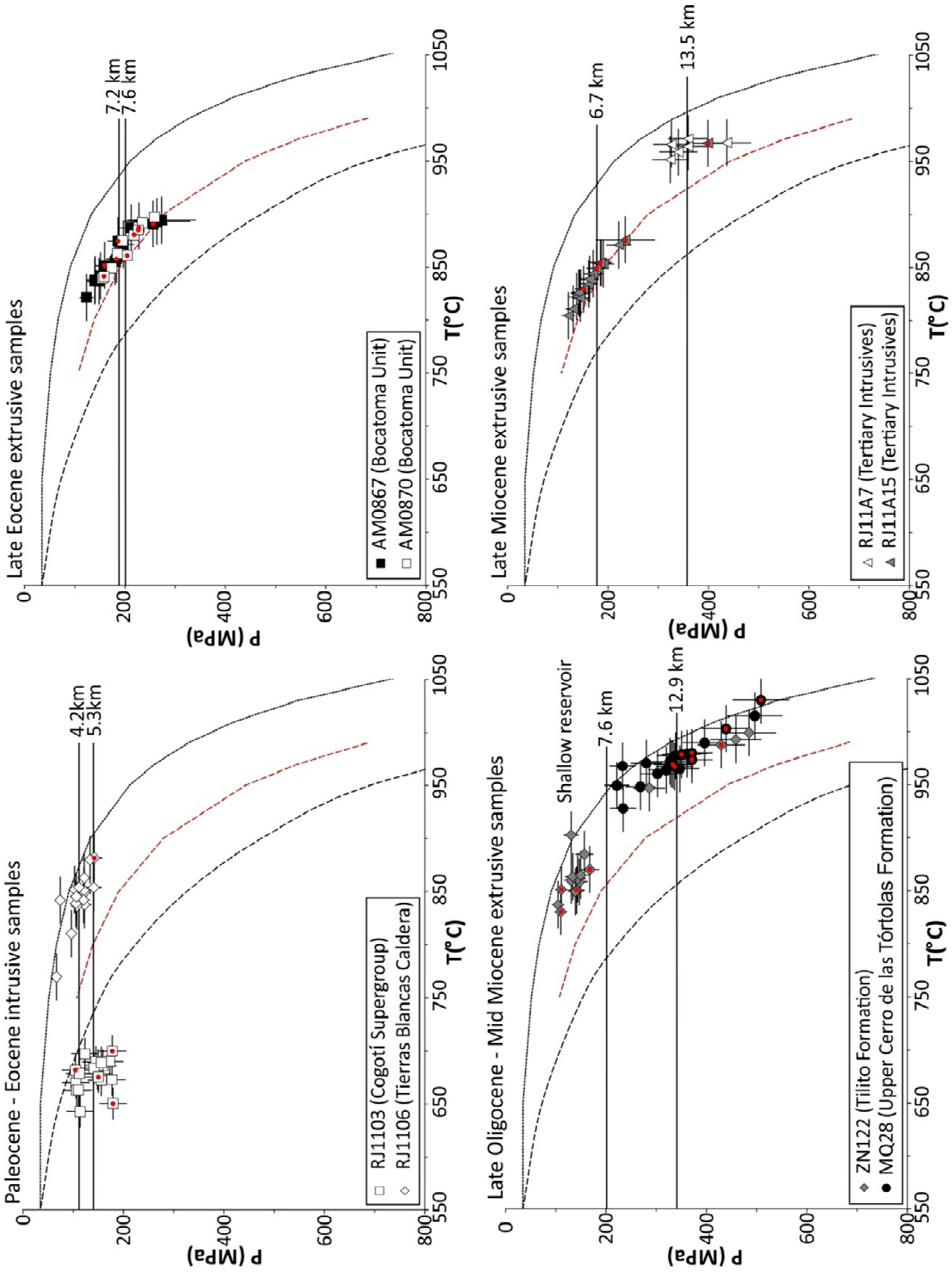
Late Eocene extrusive samples
7.2 km
7.6 km
AM0867 (Bocatoma Unit)
AM0870 (Bocatoma Unit)
Late Miocene extrusive samples
6.7 km
13.5 km
RJ11A7 (Tertiary Intrusives)
RJ11A15 (Tertiary Intrusives)
Paleocene - Eocene intrusive samples
4.2km
5.3km
RJ1103 (Cogotí Supergroup)
RJ1106 (Tierras Blancas Caldera)
Late Oligocene - Mid Miocene extrusive samples
Shallow reservoir
7.6 km
12.9 km
ZN122 (Tilito Formation)
MQ28 (Upper Cerro de las Tórtolas Formation)
P (MPa)
T(°C)

Figure 2.13 (previous page). P-T diagrams calculated using the amphibole geothermobarometry of Ridolfi et al. (2010), with the exception of intrusive sample RJ1103 (Cogotí Supergroup) where the geobarometer of Anderson and Smith (1995) was intercalated with the plagioclase thermometer of Holland and Blundy (1994). The curves on the diagrams are from Ridolfi et al. (2010); the black, dashed lines represent the upper and lower limits of thermal stability of consistent amphiboles and the red, dashed line is derived from experimental products of different crystallinities (i.e. 35–50 wt.% at lower T and 12–35 wt.% at higher T). The average crystallisation depths calculated for individual samples are shown. P-T values obtained for grain cores are highlighted with red dots.

2.10 Discussion

2.10.1 Crystallisation / equilibration depths of arc magmas over time

Variations are apparent in the crystallisation/equilibration depths of arc magmas over time (Table 2.3 and Fig. 2.13). The compositions of the amphibole and plagioclase phases in the intrusive samples (RJ1103, Cogotí Supergroup and RJ1106, Tierras Blancas Caldera) are relatively homogeneous (Fig. 2.12) and the application of amphibole-plagioclase and amphibole geothermobarometers suggest they have formed at relatively uniform temperatures and pressures (Fig. 2.13). The lack of significant difference between the temperatures and pressures obtained for the cores and rims of the phenocrysts provides further evidence that crystallisation occurred at uniform depths within the crust and that the mineral phases do not represent crystals that have been inherited from elsewhere and/or an earlier stage of crystallisation. The depth estimates for the samples of the Cogotí Supergroup (Paleocene) and the Tierras Blancas Caldera (Eocene) are within uncertainty of each other (Table 2.3) and imply a shallow level of emplacement (4.2 – 5.3 km). This supports the earlier suggestion that these Paleocene to Eocene plutonic belts are epizonal (crystallisation depths <6.5 km) (Parada et al., 1988). The presence of microline and microperthite intergrowth textures in some samples of the Cogotí

Supergroup (Fig. 2.3a) is also indicative of slow cooling at shallow levels in the crust. During this time period, the tectonic regime along the southern Central Andean margin was primarily extensional (Charrier et al., 2007) and La/Sm and Sm/Yb ratios (Fig. 2.14c) suggest the magmas were equilibrating with a residual assemblage/fractionating a mineral assemblage which reflects a crust of normal thickness (~30 – 35 km) (e.g., Kay et al., 1991; Kay and Mpodozis, 2001).

A much wider range of mineral compositions (Fig. 2.12), crystallisation temperatures and pressures and hence depth estimates were obtained for the Late Oligocene to Late Miocene extrusive arc rocks (Fig. 2.13). This is likely to reflect the crystallisation and evolution of the magma en route to the surface. The amphibole phenocrysts present in the Late Oligocene sample of the Tilito Formation, which have crystallised at higher temperatures and pressures have magnesio-hastingsite compositions and lower SiO_2 and higher Al_2O_3 and TiO_2 contents (Appendix 1.14.6), which suggests crystallisation from a less evolved melt. In the Tilito Formation no correlation is observed between the size of the phenocrysts and their composition, crystallisation temperatures and pressures. The phenocrysts that have equilibrated at deeper depths in the crust (Fig. 2.13) are likely to represent earlier stages of crystallisation and differentiation of the melt as it migrates through the crust. The majority of amphibole crystallisation in the Tilito Formation appears to have occurred at ~5 km depth, similar to the crystallisation depths of the Paleocene – Eocene plutonics, suggesting magma may have pooled at this level prior to eruption, potentially assimilating continental crust. The amphibole phenocrysts often display thick opaque reaction rims composed of Fe-Ti oxide. This feature is also observed in the Upper Cerro de las Tórtolas Formation and the Tertiary Intrusives, and is likely to be related to decompression during the final stages of magma ascent, as amphibole becomes unstable at low pressure (e.g., Rutherford and Hill, 1993; Browne and Gardner, 2006).

Phenocrysts present in in Mid Miocene sample MQ28 (Upper Cerro de las Tórtolas Formation) also produced a wide range of crystallisation depths and the phenocryst cores generally appear to have formed at deeper crustal levels (Fig. 2.13). Unlike the Tilito Formation there is a relationship between the crystallisation temperatures and pressures and the size of the phenocrysts; the highest depth estimate (19.2 km) was obtained for the core of the largest amphibole phenocryst. This particular phenocryst also has the lowest SiO_2 and highest Al_2O_3 and MgO contents (Appendix 1.14.7), indicative of formation in a less evolved melt. Overall, this combined evidence suggests the slow migration of the Upper Cerro de las Tórtolas Formation magmas through mid-crustal levels, with multiple stages of crystallisation. On this basis, assimilation of the continental crust (i.e., assimilation and fractional crystallisation (AFC) processes) may have also occurred over this wide range of depths. The depths of crystallisation and magma equilibration obtained for the Upper Cerro de las Tórtolas Formation closely match those reported by Litvak and Poma (2013) (which also includes sample MQ28).

The amphibole phenocrysts present in the older sample of the Tertiary Intrusives (RJ11A7) have crystallised and equilibrated with the melt at relatively uniform crustal depths, averaging 13.5 km (Fig. 2.13 and Table 2.3). This depth is similar to the average crystallisation depth obtained for the Upper Cerro de las Tórtolas Formation (12.9 km). The shallower average crystallisation depth of 6.7 km obtained for the younger sample of the Tertiary Intrusives (RJ11A15) may be indicative of the development of magma chambers at shallower levels in the crust of the Precordillera, which prior to the Late Oligocene experienced no Cenozoic arc magmatism (e.g., Cardó and Díaz, 1999; Cardó et al., 2007; Alonso et al., 2011) (Fig. 2.2).

Overall, the wide range of mineral compositions (Fig. 2.12), crystallisation temperatures and pressures, and hence depths obtained for the Late Oligocene to Late Miocene extrusive arc rocks (Fig. 2.13) suggests they represent typical hybrids, with crystal and melt components derived from different times and places in evolving magma systems. The overall general increase in crystallisation depths after the early Miocene, with the eruption of the Upper Cerro de las Tórtolas Formation and the Tertiary Intrusives (Fig. 2.13), suggests arc magmas may have been pooling at deeper levels in the crust after this time. This timing corresponds to the initiation of a more compressive tectonic regime along the Central Andean margin after ~25 Ma and an increase in crustal thickness during the latter part of the Miocene (e.g., Kay et al., 1991). Various crustal discontinuities have been identified in the continental crust of the Pampean flat-slab segment, however all are at a depth of >21 km in the crust (e.g., Gilbert et al., 2006; Alvarado et al., 2007; Ammirati et al., 2013). Amphibole is stable in basaltic melts at pressures of up to 8 kbar (Rapp and Watson, 1995), which equates to a crustal depth of ~30 km. This suggests that magma pooling and crystallisation was not significantly occurring at these crustal discontinuities. Or alternatively the mineral assemblage re-equilibrated with the melt at shallower depths in the crust.

2.10.2 Trace element systematics

Negative Nb, Ti, P, Sr and Eu anomalies and depletions relative to N-MORB are indicative of restite phases present in the magma source region(s) and/or fractional crystallisation processes. Increasingly negative Ti anomalies with increasing magma evolution and a negative correlation between TiO_2 and SiO_2 content (Fig. 2.8) suggests the fractional crystallisation of a Ti bearing phase such as titanite, illmenite or magnetite. Negative P anomalies and the reduction in P_2O_5 content with increasing SiO_2 after ~63 wt.% is indicative of phosphate saturation at ~63 wt.% SiO_2 and the fractionation of apatite. This is supported by petrographic observations

(Table 2.1). Sr contents correlate negatively with SiO_2 content (Fig. 2.14a) and positive Sr anomalies are generally seen in the more mafic samples and negative anomalies in the more felsic samples (Fig. 2.9). Due to their similar atomic radii and charge, Sr^{2+} and Eu^{2+} (dominant form of Eu in reducing conditions) substitute for Ca^{2+} in plagioclase and therefore decreasing Sr and Eu contents can be generated by plagioclase fractionation. Most samples fall on a similar trend on a plot of Sr against SiO_2 content, apart from samples of the Upper Cerro de las Tórtolas Formation, Tertiary Intrusives, Vacas Heladas Ignimbrites and single samples of the Tilito Formation and the Miocene Intrusives, which sit significantly away from the main trend (Fig. 2.14a). The mid to late Miocene samples of the Upper Cerro de las Tórtolas Formation, Tertiary Intrusives and Vacas Heladas Ignimbrites also have positive Sr anomalies, despite SiO_2 contents as high as 72 wt.% (Fig. 2.9), and limited or lack Eu anomalies (Fig. 2.14b). The combination of high Sr contents and limited or lacking Eu anomalies is indicative of a lack of plagioclase fractionation. It could also be interpreted as a sign of feldspar accumulation in these samples, however petrographic evidence suggests this not to be the case as these samples contain similar or lower quantities of feldspar as samples with comparable SiO_2 contents (refer to Section 2.7 and Table 2.1). For example the Upper Cerro de las Tórtolas Formation contains similar quantities of plagioclase as the older, Cerro de las Tórtolas Formation. The samples of the Upper Cerro de las Tórtolas Formation, Tertiary Intrusives and Vacas Heladas Ignimbrites also show steeply dipping REE patterns with depletions in the HREE (Fig. 2.9 and 2.14c) suggesting a residual mineral phase which retains HREE, such as garnet.

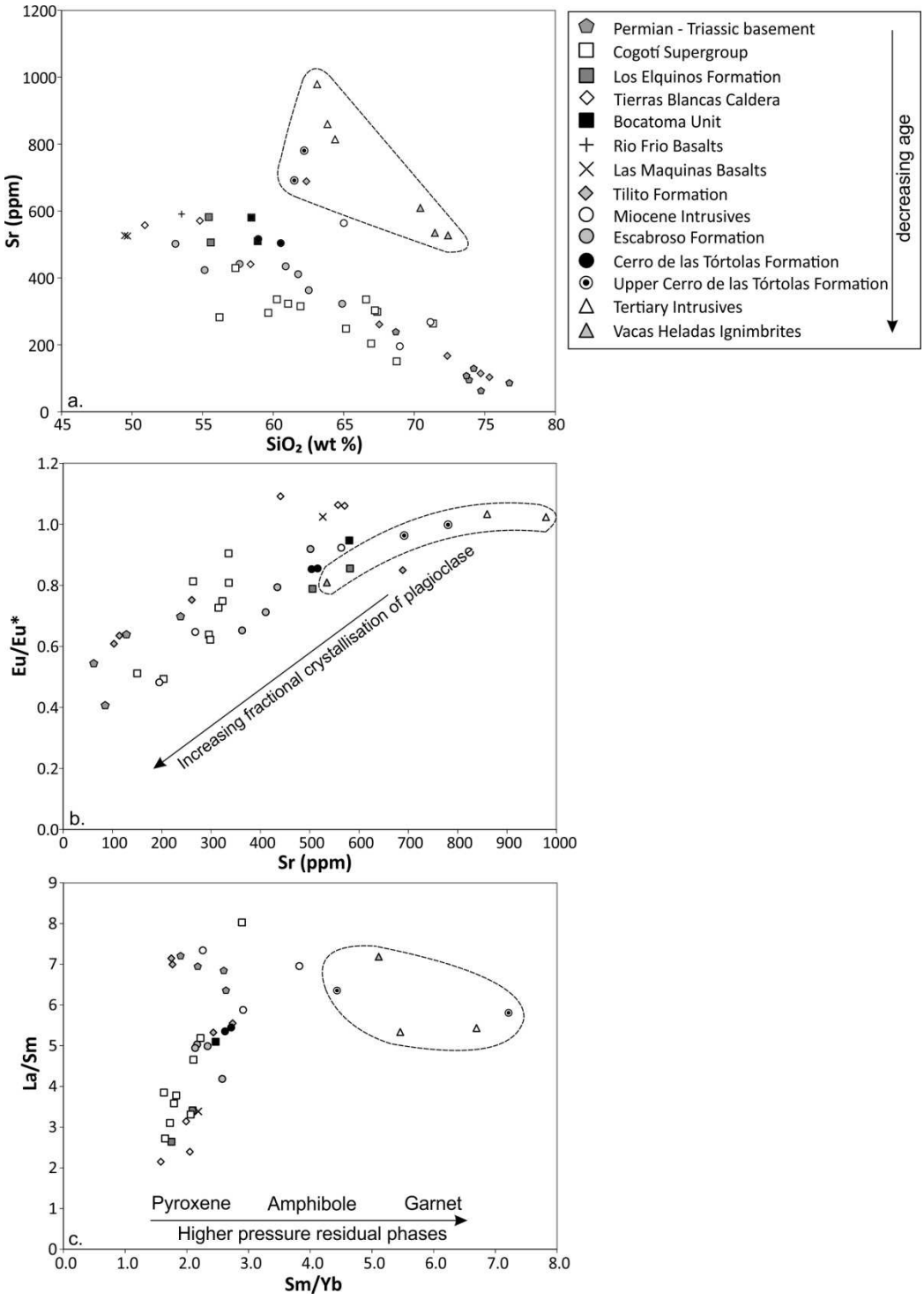

Figure 2.14. a) Sr (ppm) vs. SiO_2 content (wt.%) b) Eu/Eu* vs. Sr (ppm) and c) La/Sm vs. Sm/Yb showing the behaviour of light versus heavy REE in the Cenozoic geological units and how this relates to residual phases. Samples with adakitic signatures, as defined by Defant and Drummond (1990) and Drummond and Defant (1990), are outlined.

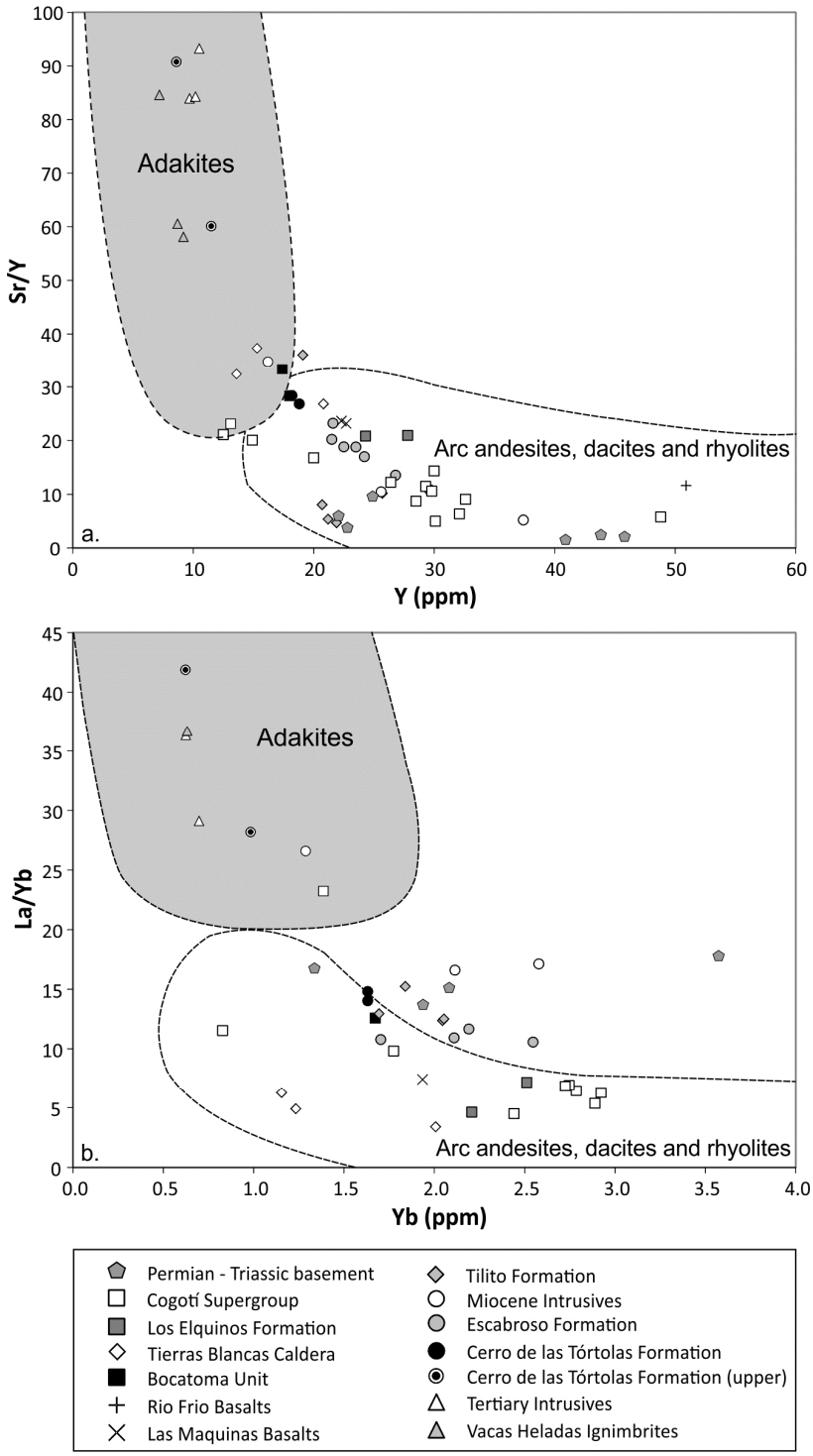

Figure 2.15. a) Sr/Y vs. Y and b) La/Yb vs. Yb diagrams as defined by Defant and Drummond (1990) and Drummond and Defant (1990) that are typically used for distinguishing adakites. The boundaries are from Richards and Kerrich (2007).

2.10.3 The origins of adakitic signatures

The Mid to Late Miocene arc magmatic rocks of the southern Central Andes have adakitic signatures (Fig. 2.15). Adakites are intermediate to high-silica, subduction related rocks with high Sr/Y and La/Yb ratios (Defant and Drummond, 1990). Diagnostic geochemical features of adakites and their mode of formation remain controversial (e.g., Castillo, 2012), but their main compositional traits include; SiO_2 = ≥56 wt.%, Al_2O_3 = ≥15 wt.%, MgO <3 wt.%, NaO_2 = ≥3.5 wt.%, Sr = >400 ppm, Y = ≤18 ppm, Yb = ≤1.9 ppm, Sr/Y = ≥20 and La/Yb = ≥20 (Richards and Kerrich, 2007). Originally it was proposed that adakites formed from the partial melting of young (<25 m.y.), basalt crust being subducted beneath volcanic arcs, where garnet and amphibole are residual phases (Kay, 1978; Defant and Drummond, 1990). Subsequently a number of other mechanisms of producing arc rocks with adakitic signatures have been outlined, including partial melting of a mafic lower crust (which can delaminate) (e.g., Kay et al., 1991; Chung et al., 2003; Kay et al., 2005) and high-pressure fractional crystallisation of hydrous mafic arc magmas (e.g., Castillo et al., 1999; Macpherson et al., 2006; Rodríguez et al., 2007; Rooney et al., 2011).

It is suggested that the Eocene age of the oceanic crust subducting beneath the Central Andean arc during the Mid – Late Miocene was too old and therefore too cold to have melted prior to dehydration (e.g., Kay and Mpodozis, 2002). However, under certain subduction zone geometries subducting basaltic crust older than 25 Ma can undergo melting (Gutscher et al., 2000a). In particular, Gutscher et al. (2000a) suggest that decreasing the angle of the subducting slab can induce slab melting and therefore produce adakites. In the Pampean flat-slab segment, the angle of the subducting oceanic plate is thought to have been shallowing since ~18 Ma, due to the subduction of the Juan Fernandez Ridge (JFR) (Yañez et al., 2001; Yañez et al., 2002). In addition to this, the hotspot-derived crust of the JFR is significantly

younger than the Nazca plate itself (Yañez et al., 2001) and therefore may be at a sufficiently high temperature to reach partial melting before complete dehydration. To the south of the study area (~32 °S), Reich et al. (2003) propose that melting of these young, hotspot-derived rocks has resulted in the adakitic signatures of Late Miocene (~10 Ma) intrusions associated with the Los Pelambres porphyry copper deposit. On the basis of limited crustal thickness (<35 km at 10 Ma) at these latitudes, combined with the non-adakitic signatures of more recent arc rocks, Reich et al. (2003) favour melting of young, basaltic oceanic crust as an explanation for these adakitic signatures.

However, in the Pampean flat-slab segment a number of lines of evidence suggest an alternative explanation for the origin of adakitic signatures. Adakites derived from the melting of the subducting oceanic crust have high Mg# (>50), Cr (≥50 ppm) and Ni (≥20 ppm) contents, which are interpreted as reflecting interaction and equilibration between the ascending adakitic magma and the overlying mantle peridotite (Rapp et al., 1999). The Mid to Late Miocene arc rocks with adakitic signatures from the Pampean flat-slab segment have relatively low Mg# (28.5 – 48.5), and low Cr and Ni concentrations of (≤28 ppm and ≤13 ppm respectively) (Appendix 1.13). Therefore, this precludes a simple model of the interaction of an oceanic slab melt with the overlying mantle wedge. A higher Mg# of 51.5 and higher Cr and Ni contents (97.3 ppm and 22.9 respectively) were obtained for sample RJ11A7 of the Tertiary Intrusives. However, this could be related to the higher contents of amphibole present in this sample (~30 %), as transition metals (Cr, Ni, Co, V) strongly partition into amphibole in melts of intermediate composition (Gill, 1981). The occurrence of this composition in only one sample also suggests a localised process, rather than melting of the subducting oceanic crust, which is likely to be more widespread.

The Mid to Late Miocene magmatic rocks have high Sr contents and lack of Eu anomalies (Fig. 2.14), which is indicative of a lack of plagioclase fractionation. The fractionation of plagioclase can be inhibited at high pressure and high magmatic water content (Moore and Carmichael, 1998; Muntener et al., 2001). These conditions also stabilise amphibole earlier during the crystallisation of a basaltic melt and can generate arc magmas with higher Sr/Y and La/Yb ratios from mafic magmas with initially low Sr/Y and La/Yb ratios (Castillo, 2012 and references therein). If an increase in magmatic water content was responsible for the adakitic signatures, high concentrations of fluid-mobile elements and high fluid mobile/immobile trace element ratios might be expected. This is not observed in the Mid to Late Miocene magmatic rocks relative to the older samples (Fig. 2.16) suggesting that a higher water content derived from the subducting slab is not responsible for the production of adakitic signatures.

There is also evidence to suggest that the Mid to Late Miocene arc rocks were not formed by high-pressure fractional crystallisation of garnet or amphibole from mafic arc magmas (Macpherson et al., 2006; Davidson et al., 2007). The fractionation of garnet, which has $D_{Yb}>D_{Dy}$, would produce an increase in Dy/Yb ratios with increasing SiO_2 (Fig. 2.17). The fractionation of plagioclase and amphibole would produce a concave-upward trend between the MREE and HREE and therefore would result in decreasing Dy/Yb with increasing SiO_2 (Macpherson et al., 2006). These trends are not observed suggesting the Mid to Late Miocene melts underwent gabbroic fractionation (Fig. 2.17), which has a limited effect on the shape of REE patterns (Davidson et al., 2007). Furthermore, geothermobarometry suggests that samples MQ28, RJ11A7 and RJ11A15 equilibrated at pressures of 3.4, 3.6 and 1.8 kbar respectively (Table 2.3). Thus implying that melt differentiation was occurring at relatively shallow levels in the crust (12.9 – 6.7 km) and at pressures significantly lower than those required for garnet stability (Rapp and Watson, 1995).

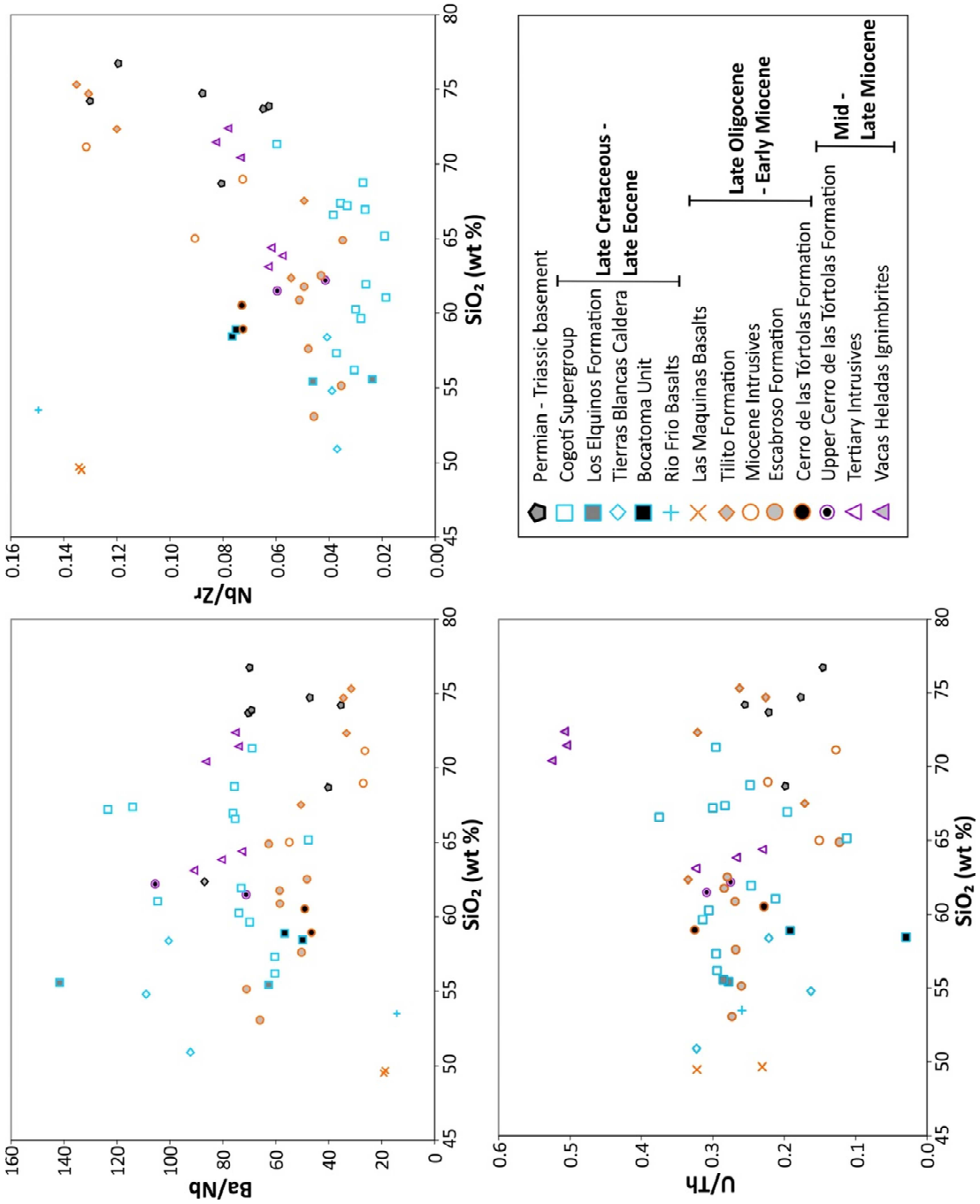

Continued overleaf.

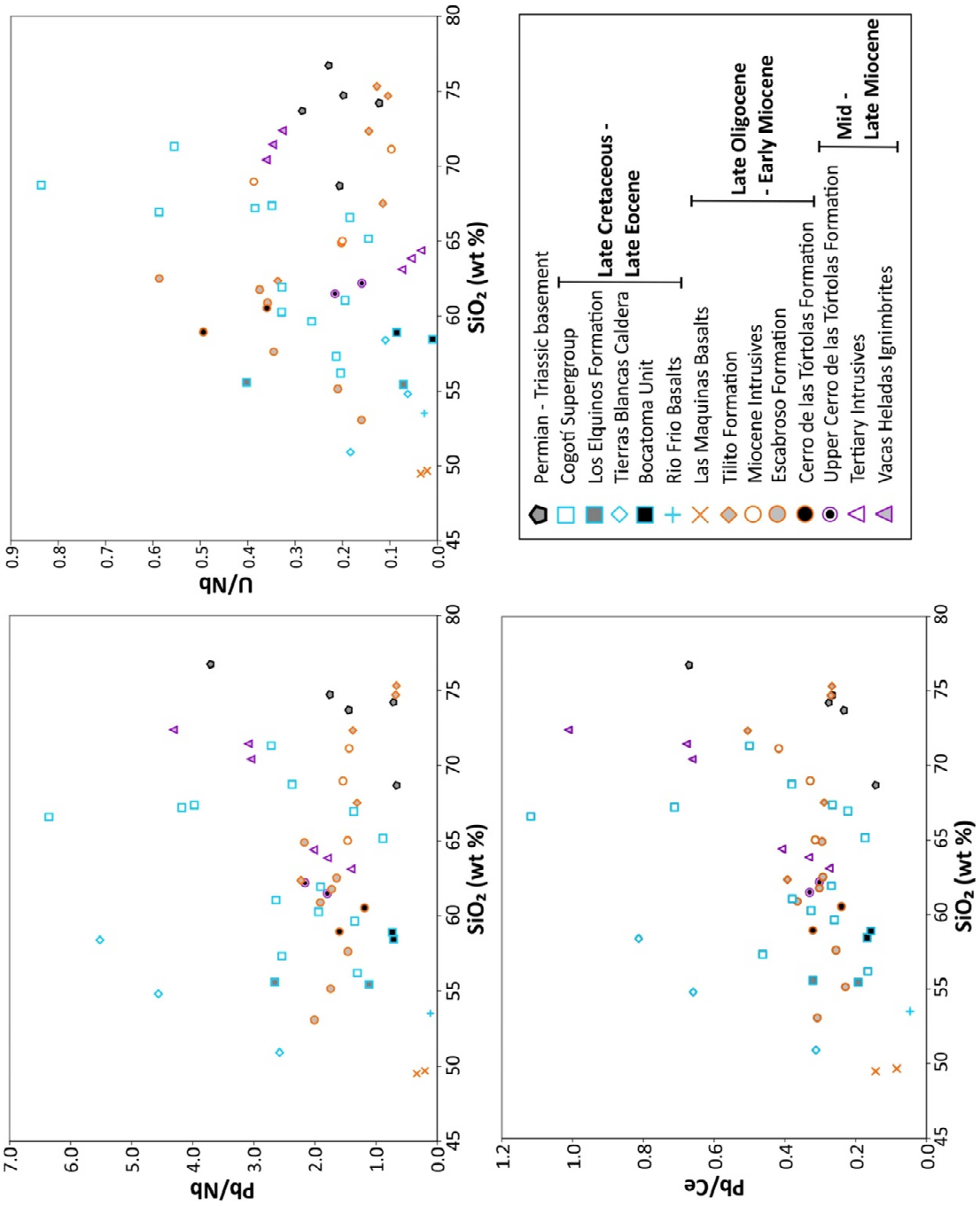

Figure 2.16. Ratios of fluid- mobile/immobile incompatible trace elements (Ba/Nb, U/Th, Pb/Nb, U/Nb and Pb/Ce) and fluid- immobile/immobile incompatible trace elements (Nb/Zr) plotted against SiO_2 content to demonstrate the limited effect of magma differentiation on these ratios.

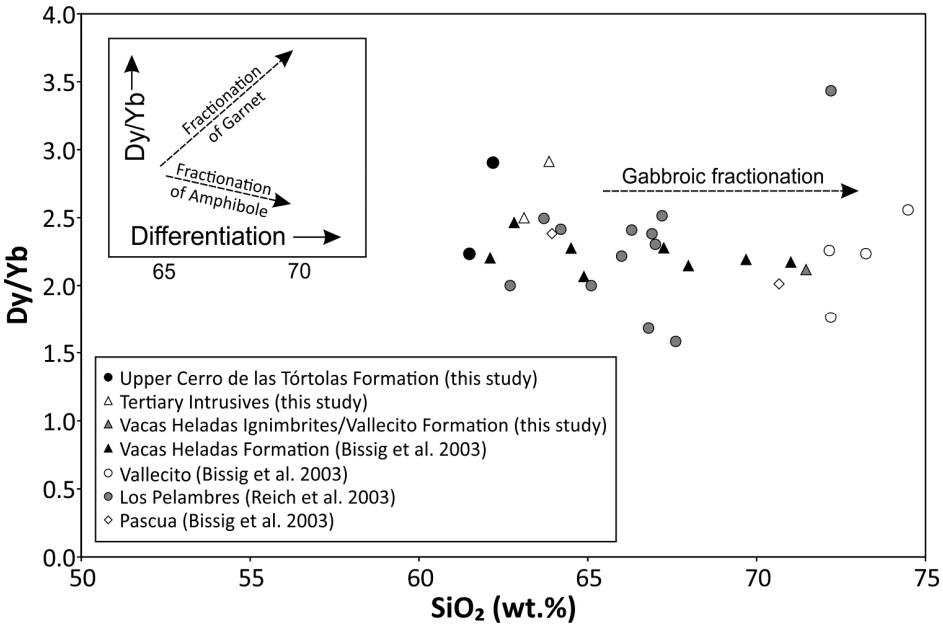

Figure 2.17. Dy/Yb vs. SiO_2 (wt.%) for mid to late Miocene samples with adakitic signatures from the Central Andes demonstrating the fractionation of a gabbroic assemblage (i.e. plagioclase, clinopyroxene, magnetite and olivine (e.g., Woodhead (1988)). Data presented is from this study and from the work of Bissig et al. (2003) and Reich et al. (2003).

By excluding these mechanisms of generating adakites it is likely that the adakitic signatures of the Mid to Late Miocene magmatic rocks in the Pampean flat-slab segment are the result of partial melting of the lower crust where garnet is stable. During this time interval the thickness of the continental crust is suggested to have increased to >45 km as a result of crustal shortening over the later part of the Miocene (e.g., Allmendinger et al., 1990; Kay et al., 1991). This increase in crustal thickness is likely to have resulted in the presence of garnet in the lower crust. This mode of adakite formation has previously been suggested for the Mid to Late Miocene arc magmatic rocks present in the Pampean flat-slab segment (e.g., Bissig et al., 2003; Kay et al., 2005; Litvak et al., 2007; Goss et al., 2011). The geochemical data presented in this study, and discussion in relation to newer models of adakite formation (e.g., Macpherson et al., 2006), finds this previously proposed model to be the most likely explanation for the development of adakitic signatures in the

Pampean flat-slab segment over the later part of the Cenozoic. Overall this suggests that primary arc magmas generated in the asthenospheric mantle wedge were equilibrating with different residual mineral assemblages in the lower crust over the course of the Cenozoic, with the development from lower pressure assemblages (i.e. pyroxene) to higher pressure assemblages (i.e. garnet) (Fig. 2.14c), reflecting the increase in crustal thickness over time.

2.10.4 Temporal variations in source and crustal contamination

It is clear from many of the trace element plots (e.g., Figures 2.8 and 2.9) that there are significant variations in either the composition of the source of the arc magmas or in the level of interaction with the continental crust, over time. Certain elements are fractionated by fluids or hydrous melts and therefore ratios of fluid mobile/immobile and immobile/immobile trace elements can be used to assess the influence of fluids and/or hydrous melts derived from the subducting slab on the source of the arc magma. For example, during dehydration of the subducting slab large ion lithophile elements (e.g., Rb, K, Ba, Sr, Pb) are preferentially partitioned into hydrous fluids, enriching the partial melt generated in the overlying mantle wedge. Other trace elements, such as Nb, Th and Zr are relatively immobile in fluids in comparison to the LILE and therefore can be used to assess contributions from melts. Thorium and the LREE are incompatible and fluid-immobile, unless the solidus is above that for sediments and AOC, in which case they are strongly partitioned into the fluid phase (Johnson and Plank, 1999; Kessel et al., 2005). Therefore enrichments and fractionations in Th and the LREE are often used to infer the melting of subducting components, such as sediments (e.g., Johnson and Plank, 1999; Plank, 2005), or alternatively they could be a product of crustal assimilation.

As the plutonic and volcanic rocks of the southern Central Andes are generally highly differentiated, TE ratios have been plotted against SiO_2 in order to examine the effects of fractional crystallisation (Fig. 2.16). Selected trace element ratios do not correlate or correlate weakly with SiO_2 content, specifically Ba/Nb, Pb/Nb, U/Nb, Nb/Zr, Pb/Ce and U/Th ratios, and therefore are not significantly influenced by differentiation. Therefore these TE ratios can be used to investigate other processes, such as contributions of slab-derived components to the melt source region. How these contributions have changed over the course of the Cenozoic and how arc magmas have been affected by crustal contamination, specifically in relation to the changing tectonic and geodynamic setting are discussed below.

2.10.4.1 The Late Cretaceous – Eocene

Concentrations of incompatible, fluid-mobile (e.g., Ba, Pb, U) and fluid-immobile (e.g., Nb) elements, in the Late Cretaceous – Eocene samples of the Cogotí Supergroup, Los Elquinos Formation, Tierras Blancas Caldera and the Botacoma Unit, remain relatively constant with increasing differentiation (Fig. 2.8, not all elements shown). This suggests that the enrichments in fluid-mobile, incompatible elements (e.g., LILE) and depletions in HFSE and HREE represent a subduction signature developed in the source region rather than as a result of crustal contamination and differentiation processes. The absence of any inherited zircon grains and cores (Appendix 1.10) provides further evidence for limited interaction with the existing continental crust during this time interval. This is also supported by low $^{87}Sr/^{86}Sr$ isotope ratios (Parada et al., 1988) and mantle-like $\delta^{18}O$ values in zircon (discussed in Chapter 3) obtained for the Late Cretaceous – Eocene magmatic belts

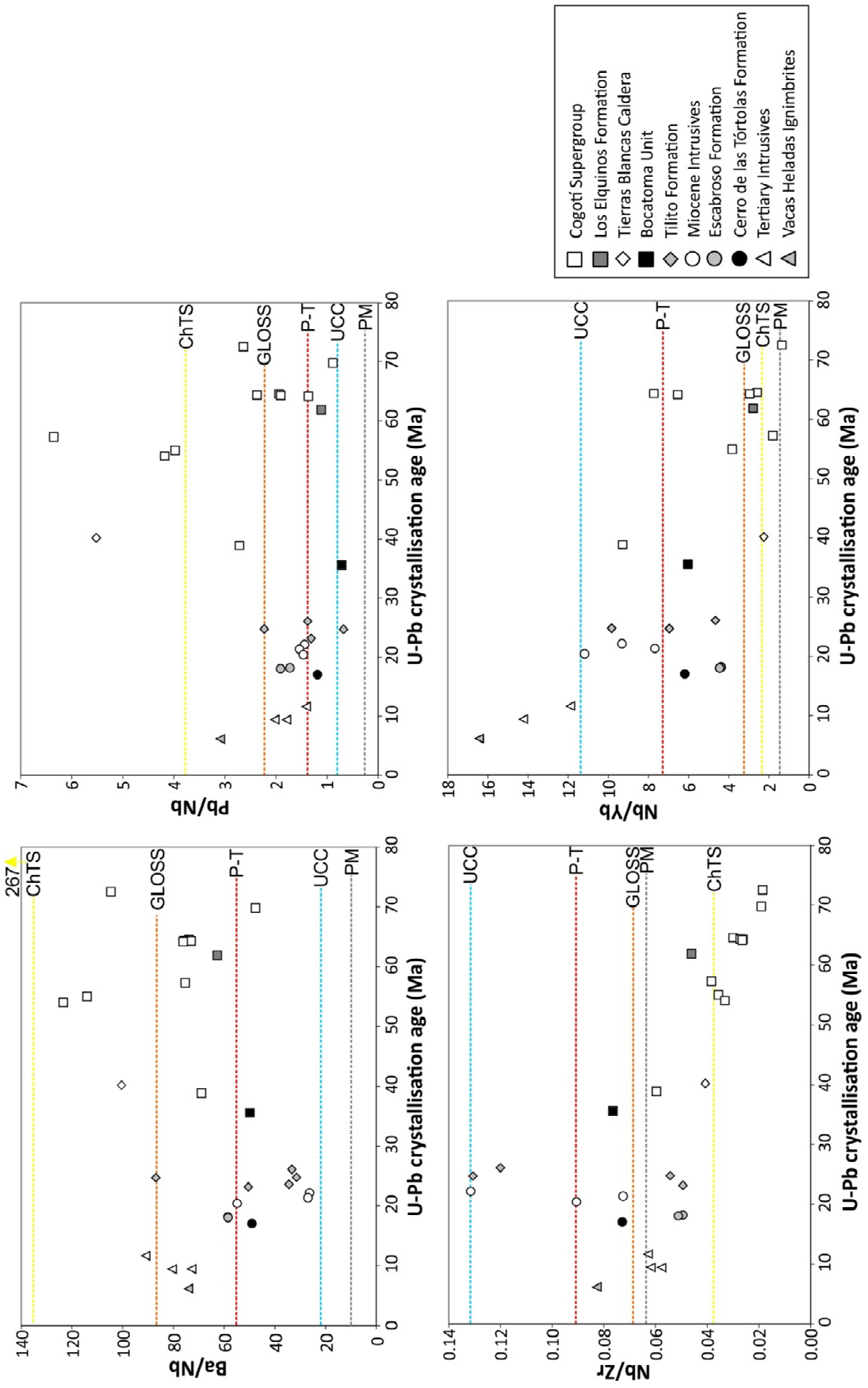
Cogotí Supergroup
Los Elquinos Formation
Tierras Blancas Caldera
Bocatoma Unit
Tilito Formation
Miocene Intrusives
Escabroso Formation
Cerro de las Tórtolas Formation
Tertiary Intrusives
Vacas Heladas Ignimbrites
Pb/Nb
Nb/Yb
Ba/Nb
Nb/Zr
U-Pb crystallisation age (Ma)
ChTS
GLOSS
P-T
UCC
PM
267

Figure 2.18 (previous page). Plots of fluid- mobile/immobile incompatible element ratios (top) and immobile/immobile incompatible element ratios (bottom) against the corresponding U-Pb crystallisation age for the sample. The values for primitive mantle (PM, (Sun and McDonough, 1989)), upper continental crust (UCC (Taylor and McLennan, 1995)), global sediment composition (GLOSS (Plank and Langmuir, 1998)), the composition of sediment currently in the southern Chile trench (ChTS (Jacques et al., 2013)) and the average composition of the Permian-Triassic basement (P-T (this study, refer to Appendix 1.13)).

In the Late Cretaceous – Eocene samples the fractionation of Th from fluid-mobile elements such as Ba and Pb is indicative of a slab-derived fluid influencing the source region rather than a melt. Overall the fluid mobile/immobile element ratios (e.g., Ba/Nb, Pb/Nb, U/Th, Pb/Ce) are highly variable for the Late Cretaceous – Eocene arc rocks (Fig. 2.16) suggesting that the source region has been variably influenced by slab-derived fluids. A general increase in these ratios is observed between the Late Cretaceous (~72 Ma) and the Late Eocene (~35 Ma) suggesting an increased influence of slab-derived fluids on the arc magmas with time (Fig. 2.18).

With an increase in fluid flux from the subducting slab an increase in the amount of partial melting occurring in the mantle wedge might be expected. Due to differences in their bulk distribution coefficients fluid-immobile, incompatible elements (e.g., Nb, Zr, La, Ce, Y) can be fractionated by differing degrees of mantle melting (e.g., Green et al., 2000). An increase in certain element ratios (e.g., Nb/Zr, Nb/Yb, La/Yb (not shown)) between the Late Cretaceous and the Late Eocene (Fig. 2.18) could be interpreted as an indication of a decrease in partial melting of the mantle over time. This is at odds with the evidence for an increase in fluid flux from the slab. Therefore, these element ratios are interpreted as representing an increase in the enrichment of the mantle wedge, with subduction derived components (e.g., sediments). This also suggests that enrichment of the mantle wedge is a more dominant process than the depletion due to partial melting. Subduction along the

Andean margin has been active in this region since the Jurassic (Charrier et al., 2007), so an overall increase in incompatible trace element enrichment might be expected with time due to an increased influence of subducting components on the mantle wedge.

During the emplacement of plutonic belts and arc volcanic deposits in the Principal Cordillera of Chile, back-arc volcanism was occurring farther away from the trench in the Frontal Cordillera with the eruption of the Río Frío Basalts. The high concentrations of fluid immobile trace elements (Fig. 2.8) and fluid immobile/immobile trace element ratios (Fig. 2.16), combined with low fluid mobile trace element ratios (Fig. 2.16), suggests these alkaline basalts formed from small degree partial melts of the mantle without the influence of fluids derived from the subducting slab. This is consistent with their suggested emplacement in a back-arc, extensional setting (e.g., Litvak and Poma, 2010).

2.10.4.2 Plate reconfiguration and Late Oligocene to Early Miocene arc magmatism

After a period of reduced arc magmatism between the Mid Eocene and the Late Oligocene (Parada et al., 1988; Parada et al., 2007) the Doña Ana Group was erupted at the arc front, spanning the current Chile - Argentina border. The samples of the Tilito Formation (Lower Doña Ana Group) on the Chilean side of the border (i.e. closer to the trench), have quite distinct compositions to those collected farther to the east in Argentina, despite their being of the same age (Late Oligocene). The rhyolitic ignimbrites from the Chilean side (AM0844, AM0846 and AM0847) are highly evolved (SiO_2 >72 wt.%), have high concentrations of Nb (>18ppm) accounting for high Nb/Zr and Nb/Yb ratios and relatively low fluid mobile/immobile incompatible element ratios (Fig. 2.18 and 2.19). The samples from

the Argentinean side of the border (ZN122 and Z27) are less siliceous with andesitic – dacitic compositions and have higher fluid mobile/immobile element ratios.

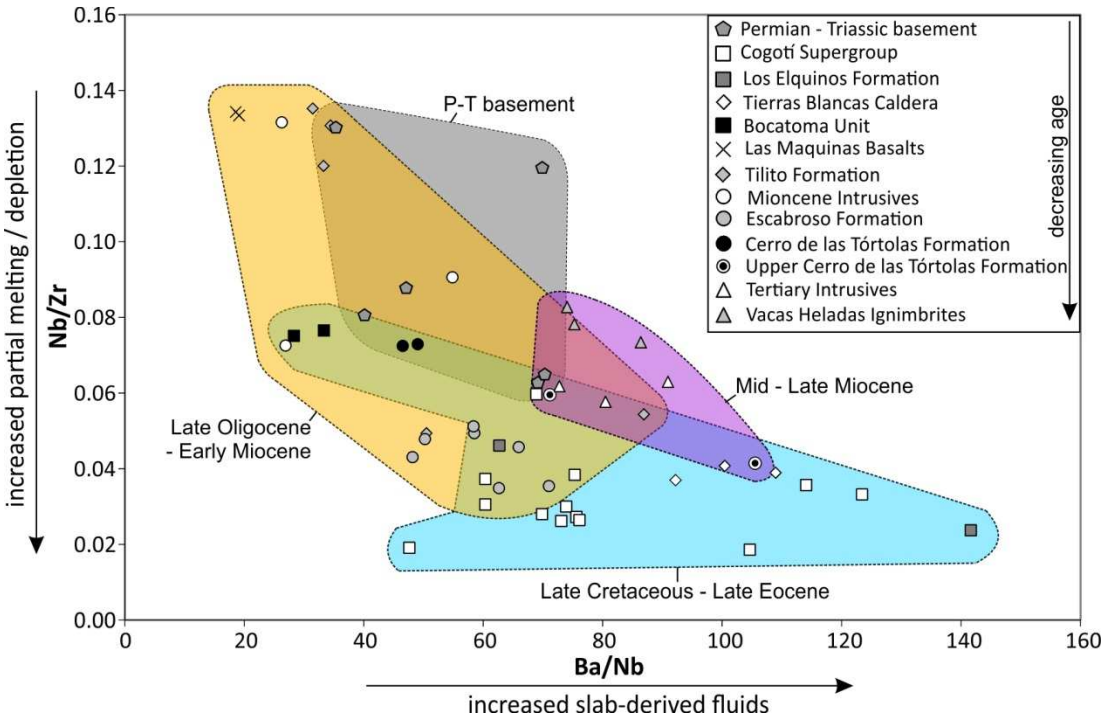

Figure 2.19. A plot of Nb/Zr vs. Ba/Nb for the Late Cretaceous to Late Miocene arc magmatic rocks and samples of the Permian – Triassic basement.

The presence of inherited zircon cores with Permian – Triassic ages (278.5 ±2.9 Ma to 241 ±2.7 Ma) in the samples of the Tilito Formation from the Chilean side of the margin, suggests bulk assimilation of the Permian – Triassic basement (Appendix 1.10) (Beard et al., 2005). The range of inherited zircon ages obtained is within the range of U-Pb ages obtained for the Choiyoi Group and Pastos Blancos Group, which comprise part of the basement stratigraphy (Table 2.2). These basement groups also appear adjacent to the Tilito Formation in outcrop and therefore it seems likely that the magmas of the Tilito Formation have assimilated this crust. The similar geochemical features observed in the Permian - Triassic basement samples and the rhyolitic samples of the Tilito Formation (Figures 2.6, 2.8 and 2.16)

also supports the contamination of the Late Oligocene arc magmas with the Permian – Traissic basement. It has also been noted that the Choiyoi Group and Pastos Blancos Group, which primarily consist of rhyolitic to dacitic welded ignimbrites, are difficult to distinguish from the Tilito Formation in outcrop (e.g., Martin et al., 1995). No inherited zircon cores were found in the more mafic samples from the Argentinean side of the border (Appendix 1.10), providing evidence for a more limited interaction with the basement farther away from the trench.

It has previously been suggested that the contamination of the Late Oligocene – Early Miocene arc magmas with Permian – Triassic aged lower crust accounts for the relatively high $^{87}Sr/^{86}Sr$ ratios ((0.705335) for dacitic sample Z27 (Litvak et al., 2007)) of the Doña Ana Group (e.g., Kay and Abbruzzi, 1996). Geochemical modelling presented here shows that fractional crystallisation combined with assimilation of the Permian – Triassic crust can account for the compositions of the Tilito Formation on the Chilean side of the margin (Fig. 2.20). Andesitic sample ZN122 (Argentinean side), was used as the starting composition in the model. Fractional crystallisation, with or without assimilation of the Permian – Triassic basement, satisfactorily accounts for the majority of trace element compositions (Fig. 2.20 a and b). In this instance it is difficult to separate the effects of fractional crystallisation (FC) from assimilation and fractional crystallisation (AFC) processes, as the fractionating assemblage is virtually the same as the mineral assemblage found in the Permian – Triassic basement. However, high Nb concentrations (average of 17 ppm), and to a lesser extent high K concentrations (not shown), cannot be accounted for by traditional FC and/or AFC processes (e.g., DePaolo, 1981). Cribb and Barton (1996) propose a model of decoupled assimilation and fractional crystallisation (FCA) in which the mass assimilated is decoupled from the mass crystallised. As shown in Figure 2.20, FCA processes can account for the high Nb and K (not shown) concentrations of the rhyolitic samples of the Tilito Formation from the Chilean side of the margin. Alternatively, the high Nb and K

concentrations may reflect AFC processes involving crust which is more enriched in Nb and K than the average Permian – Triassic basement composition obtained by this study.

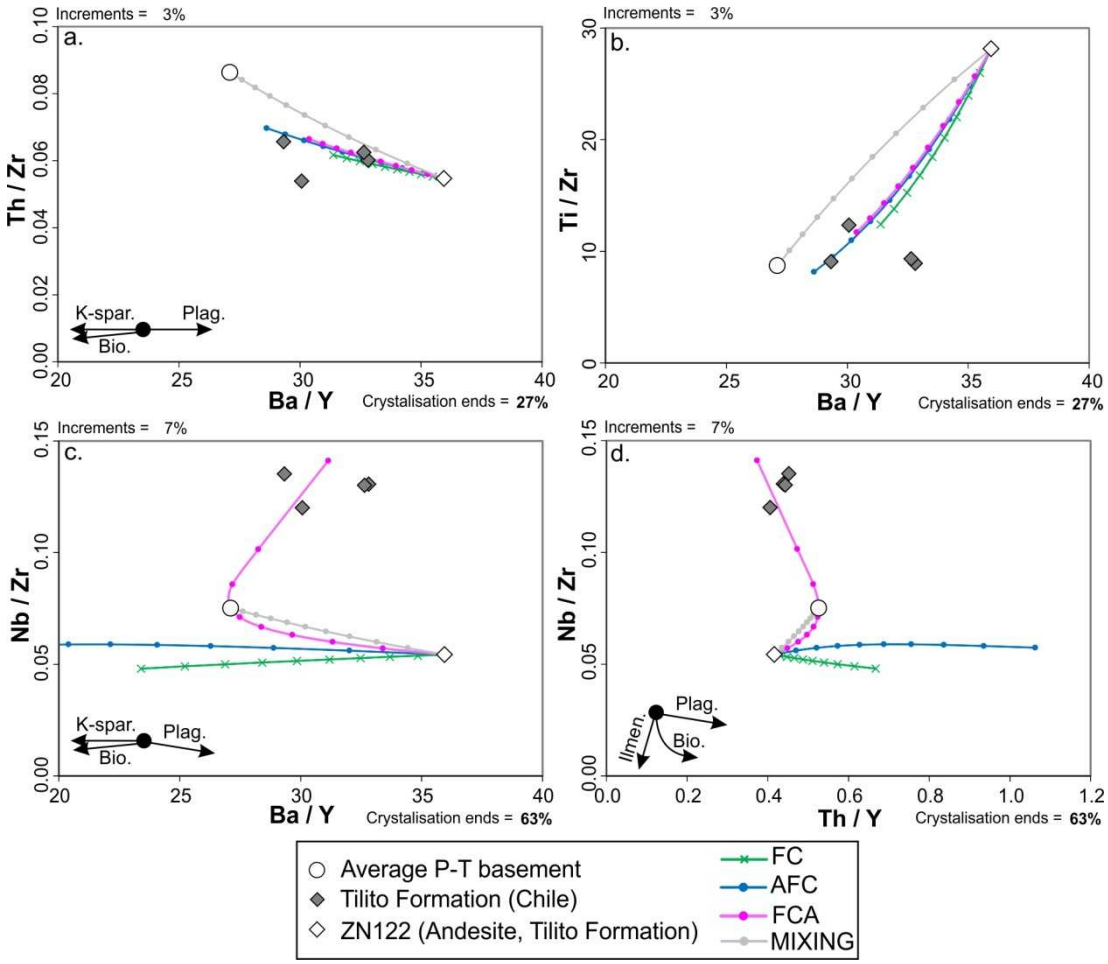

Figure 2.20. FC, AFC and FCA modelling of the Tilito Formation demonstrating that the TE signatures of the samples of the Tilito Formation from the Chilean side of the margin (i.e. closer to the trench) can be accounted for by fractional crystallisation (FC) and assimilation of the Permian - Triassic basement. Modelling was conducted using the FC-AFC-FCA modeler developed by Ersoy and Helvacı (2010). The crystallising assemblage used in the model is composed of plagioclase (78 %), magnetite (10 %), biotite (5 %), alkali feldspar (5 %) and ilmenite (2 %) (all of which are observed in samples of the Tilito Formation) and uses the partition coefficients for an acidic melt composition, as given in the FC-AFC-FCA modeler (Ersoy and Helvacı, 2010). An 'r' value of 0.3 was used in models a and b, and 0.6 in models c and d. The directions the crystallising mineral phases would take the FC trend are

presented on the diagrams for reference. The values used for the average Permian - Triassic basement are those obtained by this study (refer to Appendix 1.13)

Coeval with the eruption of the Tilito Formation, the Las Máquinas Basalts were emplaced on the Argentinean side of the margin. These basalts have high Nb/Zr (Fig. 2.19) and Nb/U ratios and low fluid mobile/immobile incompatible element ratios (e.g., Ba/Nb and Pb/Nb) (Fig. 2.16) suggesting a limited influence of fluids derived from the subducting slab and small degrees of partial melting. This is consistent with these geological units representing back-arc volcanism (Kay and Abbruzzi, 1996; Litvak and Poma, 2010). On a plot of Nb/Yb vs. Th/Yb the Las Máquinas Basalt plots between the fields for E-MORB and OIB (Fig. 2.21) suggesting extraction of small degree melts from a relatively enriched source. These compositions are also similar to those found for Holocene alkali basalts and trachy-basalts erupted in the back-arc region of the Southern Volcanic Zone (Jacques et al., 2013).

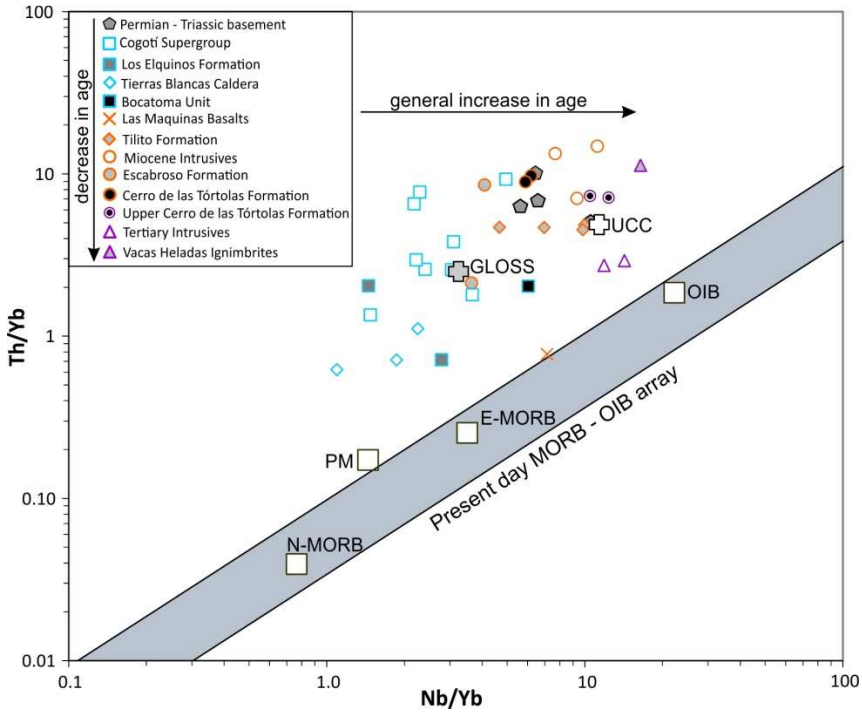

Figure 2.21. Th/Yb vs. Nb/Yb discrimination diagram as defined by Pearce (2008). Values for N-MORB, P-MORB, OIB and primitive mantle (PM) from Sun and

McDonough (1989), for GLOSS from Plank and Langmuir (1998) and upper continental crust (UCC) from Taylor and McLennan (1995).

The Miocene Intrusives, which consist of Early Miocene granitoids that outcrop in the Precordillera of Argentina (Fig. 2.5), are highly enriched in incompatible elements such as Rb, Nb, Th, and Ce. This is likely to reflect their highly evolved nature. Ratios of fluid mobile/immobile incompatible element ratios are generally low suggesting the limited influence of slab-derived fluids on the primary magmas (Fig. 2.16 and 2.19). The high Nb/Zr ratios could be indicative of relatively small degree partial melting of the mantle wedge. This would be consistent with their location relatively far away from the trench and therefore over a potentially more dehydrated slab. The U-Pb zircon ages obtained for the Miocene Intrusives (22.2 ±0.23 to 20.43 ±0.31 Ma) overlap with the ages obtained for the back-arc Las Máquinas Basalts (22.8 ±1.1 Ma to 22.0 ±0.8 Ma (Kay et al., 1991; Litvak et al., 2005)). Geochemical modelling demonstrates that the compositions of the Miocene Intrusives can potentially be generated from the composition of the Las Máquinas Basalts, by a combination of AFC and FCA processes involving the assimilation of the Permian – Triassic crust (Fig. 2.22). Thus the high Nb/Zr ratios may also be derived from AFC and FCA processes. This suggests that these granitoids, which are located farther away from the trench than the Las Máquinas Basalts (Fig. 2.5), have formed in an extensional setting from the interaction of back-arc, alkaline basalts with the Andean basement. This is also consistent with the presence of inherited zircon cores in sample RJ11A14 (Appendix 1.10).

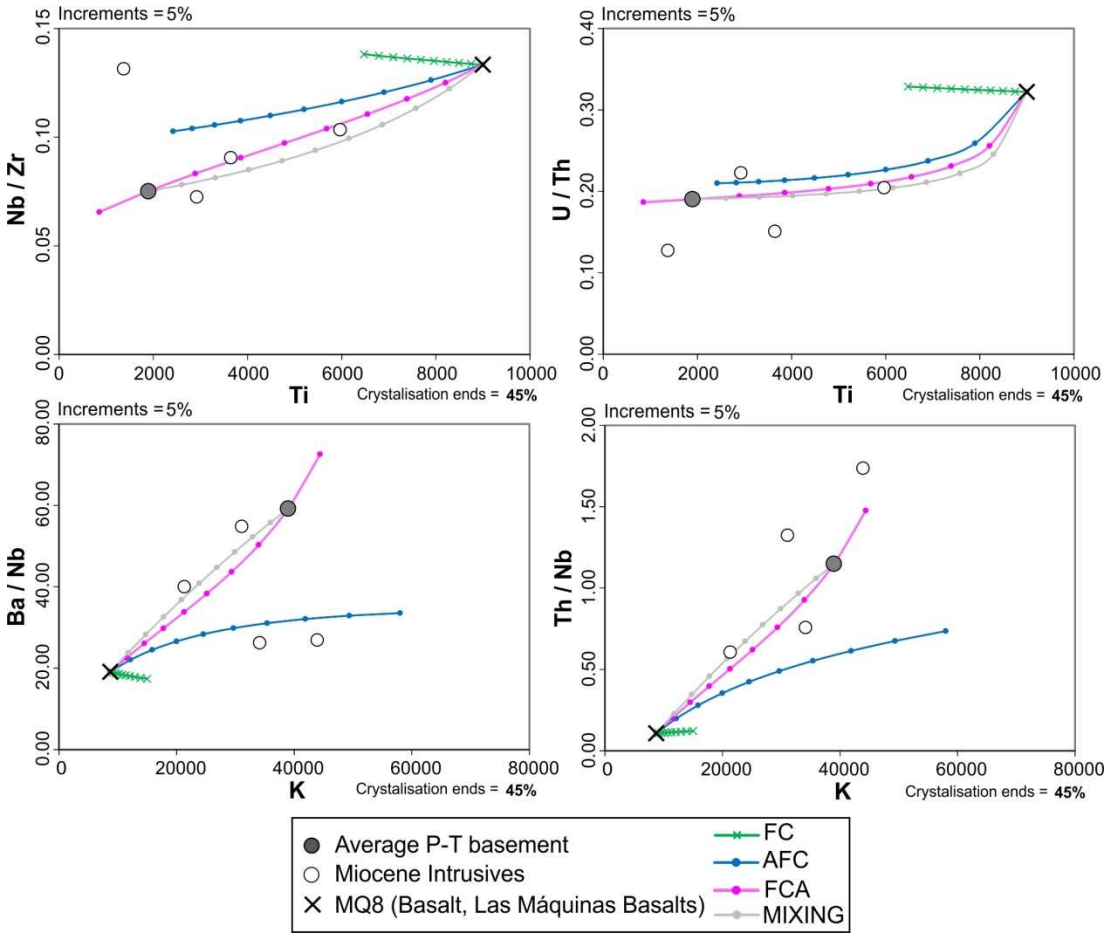

Figure 2.22. FC, AFC and FCA modelling demonstrating that the TE compositions of the Miocene Intrusives can broadly be generated from the composition of the Las Máquinas back-arc basalts by a combination of fractional crystallisation and assimilation processes (AFC and FCA), but not from fractional crystallisation (FC) alone. The average composition of the Permian – Triassic (P-T) basement, as determined by this study (Appendix 1.13), is used as the assimilant in these models. Modelling was carried out using the FC-AFC-FCA modeler developed by Ersoy and Helvacı (2010). The crystallising assemblage used in the model is composed of plagioclase (63 %), amphibole (20 %), magnetite (10 %), clinopyroxene (5 %), apatite (1 %), ilmenite (1 %) and zircon (0.05%) and uses the partition coefficients for intermediate melt compositions, as given in the FC-AFC-FCA modeler (Ersoy and Helvacı, 2010). An 'r' value of 0.6 was used.

The extrusive rocks of the younger Escabroso Formation (Upper Doña Ana Group) and Cerro de Las Tórtolas Formation (Early Miocene) are generally more mafic than the Late Oligocene samples of the Tilito Formation and Miocene Intrusives (Fig. 2.7) and have lower Nb/Zr and Nb/Yb ratios, and higher fluid mobile/immobile incompatible element ratios (e.g., Ba/Nb and U/Nb) (Fig. 2.16, 2.18 and 2.19). This suggests a higher degree of partial melting of the mantle wedge due to an increase in fluids derived from the subducting slab, alongside more limited fractional crystallisation and assimilation of the Andean crust. These Early Miocene arc formations also lack any zircon inheritance (Appendix 1.10) providing further evidence for a reduction in the bulk assimilation of the Andean basement in comparison to the Late Oligocene, Tilito Formation and Miocene Intrusives. However, isotopic data still suggests the involvement of some radiogenic crustal components (Kay et al., 1991; Kay and Abbruzzi, 1996; Bissig et al., 2003). During this time interval (~18 Ma) the Juan Fernández Ridge (JFR) began intersecting the Andean margin in this region leading to the initiation of the shallowing of the subducting slab. Therefore an increase in the influence of fluids derived from the subducting slab on the source of Early Miocene arc magmas might be expected.

2.10.4.3 The Mid to Late Miocene and the shallowing of the subducting slab

The dacitic – trachydacitic, Tertiary Intrusives, which were emplaced in the Argentinean Precordillera, have relatively low Th, U and Rb concentrations, in addition to HREE depletions (Fig. 2.9). Kay and Abbruzzi (1996) have also identified low Th, U and REE concentrations in the Precordilleran, Miocene arc magmatic rocks and also found them to have the least radiogenic Sr and Pb isotopic signatures of all the Cenozoic arc magmatic rocks in the Pampean flat-slab segment. They attribute this to the interaction of the Miocene arc magmas with a distinct Grenvillian aged basement present in the Argentinean Precordillera, which has been inferred from the presence of high-grade metamorphic xenoliths yielding

Grenvillian ages (~1100 Ma) (e.g., Abbruzzi et al., 1993; Kay et al., 1996). These xenoliths have low Th, U and REE concentrations and unradiogenic Pb isotopic ratios (Abbruzzi et al., 1993), thus suggesting the Miocene arc magmas present in the Precordillera have interacted with this Grenvillian basement. This is confirmed by the presence of inherited zircon cores of Grenvillian age (1249.4 ±10.9 to 1039.6 ±14.5 Ma) in all of the samples of the Tertiary Intrusives analysed as part of this study (Fig. 2.4 and Appendix 1.10). Kay and Abbruzzi (1996) go on to suggest that the more radiogenic Pb isotopic composition of the Precordilleran Miocene arc magmas in comparison to the Grenvillian xenoliths, requires the interaction of the magmas with an additional component, which has a Pb isotopic composition similar to that with which the Miocene arc magmas in the Frontal Cordillera have interacted. They propose that this source of radiogenic Pb is subcrustal and derived from the mantle wedge. However, in addition to the Grenvillian aged inherited cores, Permian – Triassic inherited zircon cores (U-Pb age dated between 264.0 ±3.6 and 239.7 ± 3.0 Ma) were also obtained in the Tertiary Intrusives (Appendix 1.10). Thus suggesting that similarly to the Late Oligocene – Early Miocene arc magmas present in the Frontal Cordillera (e.g., the Tilito Formation), these magmas have also interacted with Permian – Triassic aged crust. Therefore, the Permian – Triassic basement may be the source of the radiogenic Pb in the Miocene arc magmatic rocks present in the Precordillera.

As previously described the volcanic front migrated to the east over the course of the Miocene due to the shallowing of the subducting slab. However, the youngest arc rocks in the region, the Vacas Heladas Ignimbrites (Vallecito Formation), occur in the Frontal Cordillera (Fig. 2.5). During the same time interval magmatism was occurring at the Pocho volcanic field in the Sierra de Cordoba, situated directly to the east and 700 km away from the Chile trench. These volcanic rocks are thought to be associated with the arrival of the shallowly dipping subducting slab under this part of the South American continent (e.g., Kay and Gordillo, 1994). From this it can

be inferred that very little of the mantle wedge must have remained under the Frontal Cordillera. Therefore, it is likely that the Vacas Heladas Ignimbrites represent small volume lower crustal melts, generated by the remaining heat and fluids derived from the subducting slab, and which have subsequently been contaminated with the Late Paleozoic – Early Mesozoic basement and the older Cenozoic arc rocks, present in the upper crust. This is consistent with trace element signatures obtained for the Vacas Heladas Ignimbrites; relatively high incompatible trace element ratios (Figures 2.16 and 2.18) could be indicative of either relatively small degree partial melts and/or assimilation of the continental crust. This is also consistent with isotopic evidence; increasing $^{87}Sr/^{86}Sr$ ratios correlate with decreasing εNd values between the Late Oligocene and the Late Miocene, with the highest $^{87}Sr/^{86}Sr$ ratios (0.7055) and lowest εNd values (-2.0) reported for the Vacas Heladas Ignimbrites, suggesting an increase in crustal contamination with time (Kay et al., 1991; Kay and Abbruzzi, 1996; Litvak et al., 2007). In addition to this, the Vacas Heladas Ignimbrites contain inherited zircon cores of Permian – Triassic and Miocene age (Appendix 1.10) and zircon oxygen and hafnium isotopic compositions overlap those of the Permian – Triassic basement (Chapter 3).

2.10.4.4 Overall geochemical trends - increased enrichment with time

There is a general increase in Nb/Zr, Nb/Yb (Fig. 2.18), Nb/Y and La/Sm ratios between the Late Cretaceous and the Late Miocene. These elements are fluid-immobile and due to differences in the bulk distribution coefficients these ratios can be fractionated by differing degrees of melting (e.g., Green et al., 2000). Continued partial melting of the mantle wedge leads to depletion of incompatible trace elements, therefore over time the Nb/Zr and Nb/Yb ratios of the arc magmas produced should decrease reflecting the depletion of the mantle source. However, this relationship is not observed in the arc rocks of the southern Central Andes, despite the sustained presence of a subduction zone and the extraction of mantle-

derived melts. This implies another process is occurring to enrich the arc magmas in incompatible trace elements. Potential processes include, a decrease in the partial melting of the mantle wedge with time, enrichment of the mantle source due to the addition of subducting components or the products of subduction erosion, an increase in crustal contamination, or a combination of all three of these processes.

As the lowering of the solidus due to the dehydration of the subducting slab is considered to be the primary mechanism for melting the mantle wedge and transferring components of the slab to the source of arc magmas (e.g., Gill, 1981; Hawkesworth et al., 1993; Davidson, 1996) a decrease in fluid-mobile, incompatible trace elements might be expected with a decrease in partial melting. This is not apparent in the dataset and concentrations of certain fluid-mobile, incompatible elements (e.g., Rb, Ba, U and Pb) increase over time. The ratios of fluid-mobile/immobile elements are a bit more variable, due in part to some of the high fluid-mobile/immobile ratios obtained for the Late Cretaceous – Eocene samples, however after ~30 Ma an increase in Ba/Nb and Pb/Nb ratios is also observed (Fig. 2.18). On this basis a decrease in the partial melting of the mantle wedge cannot fully account for the enrichment of incompatible trace elements observed over time. Therefore, an increased influence of subducting components on the mantle wedge and the melt source region and/or increased levels of contamination of the arc magmas with Andean crust en route to the surface, must have influenced the southern Central Andean arc magmas, particularly between the Late Oligocene (~26 Ma) and the Late Miocene (~6 Ma). Distinguishing between these two processes is difficult on the basis of whole rock geochemistry alone, as the material contaminating the melt source region is likely to be of a similar composition to that of the overlying crust. On this basis a detailed, multi-isotopic approach is required (outlined in Chapters 3 and 4).

2.11 Conclusions

1) Late Cretaceous (~72 Ma) – Late Miocene (~6 Ma) primary arc magmas, generated in the asthenospheric mantle wedge, have equilibrated with different residual mineral phases in the lower crust. Specifically, the Mid to Late Miocene arc magmas of the Upper Cerro de las Tórtolas Formation, Tertiary Intrusives and Vacas Heladas Ignimbrites, have equilibrated with a higher pressure assemblage containing garnet, leading to the presence of adakitic signatures. The development from lower (i.e. containing pyroxene) to higher pressure assemblages (i.e. containing garnet), over the course of the Cenozoic, can be related to the increase in compression and crustal thickness (from ~30 to >45 km) observed in the southern Central Andes during this time interval, specifically during the Mid to Late Miocene (e.g., Allmendinger et al., 1990; Kay et al., 1991). The attribution of adakitic signatures to the partial melting of a garnet bearing lower crust also suggests the contamination of Mid to Late Miocene mantle-derived melts with a lower crustal component.

2) Evidence from amphibole and amphibole - plagioclase geothermobarometry suggests the Paleocene – Eocene plutonic belts present in the Principal Cordillera of Chile crystallised at temperatures of between 677 °C (±15 (1σ)) and 844 °C (±26 (1σ)) and pressures of between 1.1 kbars (±0.2 (1σ)) and 1.4 kbars (±0.3 (1σ)). These temperatures and pressures equate to shallow depths of emplacement of between 4.2 and 5.3 km in the crust. On this basis it can also be concluded that since the time of emplacement (between ~64 – 40 Ma) ~4 to 5 km of continental crust has either been eroded or tectonically removed from the region in order to expose these plutons at the surface.

3) The average crystallisation/equilibration temperatures and pressures obtained for phenocryst phases from the extrusive Botacoma Unit (~36 Ma)

and Tilito Formation (~25 Ma), are relatively uniform and range between 862 °C (±25 (1σ)) and 889 °C (±56 (1σ)), and 1.9 kbars (±0.5 (1σ)) and 2.0 kbars (±0.3 (1σ)). These temperatures and pressures equate to average crustal depths of between 7.2 and 7.6 km, suggesting the Late Eocene to Late Oligocene arc magmas may have been pooling at these depths prior to eruption.

4) An increase in crystallisation/equilibration temperatures and pressures, and hence crustal depths, is observed after the Early Miocene with the eruption of the Upper Cerro de las Tórtolas Formation and the Tertiary Intrusives. Average crystallisation/equilibration temperatures range between 845 °C (±36 (1σ)) and 974 °C (±22 (1σ)), and pressures between 1.8 kbars (±0.6 (1σ)) and 3.6 kbars (±0.4 (1σ)). The corresponding average crustal depths range between 6.7 and 13.5 km, suggesting that arc magmas were crystallising and equilibrating at deeper levels in the crust after the initiation of flat-slab subduction and the associated increase in compression. This timing is also coeval with the increase in crustal thickness to >45 km and the associated development of adakitic signatures during the Mid to Late Miocene.

5) Overall, the wide range of mineral compositions, crystallisation/equilibration temperatures and pressures, obtained for the Late Oligocene to Late Miocene extrusive arc rocks suggests they represent typical hybrids, with crystal and melt components derived from different times and places in evolving magma systems. Therefore AFC and FCA processes, as suggested to explain the trace element signatures and zircon inheritance present in the Tilito Formation (Late Oligocene), may have also been occurring at these varied depths in the crust.

6) As is evidenced by an increase in incompatible trace element ratios (e.g., Nb/Zr ratios from 0.019 to 0.083 and Nb/Yb from 1.5 to 16.4) a gradual increase in the enrichment of the arc magmas present in the Pampean flat-slab segment is observed between the Late Cretaceous (~72 Ma), when the margin is suggested to have been extensional, and the Miocene when the thickness of the continental crust increased and the angle of the subducting Nazca plate shallowed.

7) On the basis of limited evidence for crustal contamination in the Late Cretaceous to Late Eocene arc magmas, provided by trace and rare earth element compositions and a lack of zircon inheritance, and combined with mantle-like $\delta^{18}O_{zircon}$ values (Chapter 3) and low Sr isotope values (Parada et al., 1988)), it is suggested that the increased enrichment of arc magmas during this time period is related to processes occurring in the melt source region. This may be related to the sustained presence of the subduction zone and gradual enrichment of the asthenospheric mantle wedge due to the increased influence of subducting components.

8) The Late Oligocene (~26 Ma) to Early Miocene (~17 Ma), and Late Miocene (~6 Ma) arc magmatic rocks present in the Frontal Cordillera show evidence for the bulk assimilation of the Permian – Triassic basement by mantle-derived melts, both on the basis of their trace and rare earth element compositions and the presence of Permian – Triassic inherited zircon cores.

9) The Late Miocene, Tertiary Intrusives (11.7 – 9.4 Ma) present in the Argentinean Precordillera (to the east of the Frontal Cordillera) display distinct trace element signatures (specifically low Th, U and REE concentrations), which combined with the presence of inherited zircon cores of Proterozoic age, suggest the interaction of mantle-derived melts with a

Grenville-aged basement. This basement is distinct from that in the Principal and Frontal Cordillera.

10) The progressive enrichment of arc magmas in incompatible trace elements between the Late Oligocene (~26 Ma) and the Late Miocene (~6 Ma) is attributed to a combination of (1) the increased influence of subducting components, including sediments and continental crust removed by subduction erosion, on the mantle wedge and the melt source region, and (2) increased contamination of the arc magmas with existing continental crust en route to the surface.

11) Overall this study clearly demonstrates the link between the changing geodynamic setting in the southern Central Andes, specifically related to changes in the angle of the subducting slab and convergence angles and rates, and the compositions of Late Cretaceous to Late Miocene arc magmas present in the Pampean flat-slab segment.

2.12 References

Abbruzzi, J., Kay, S.M., and Bickford, M.E., 1993, Implications for the nature of the Precordilleran basement from the geochemistry and age of Precambrian xenoliths in Miocene volcanic rocks, San Juan province: Actas, v. 3, p. 331-339.

Allmendinger, R., Figueroa, D., Snyder, D., Beer, J., Mpodozis, C., and Isacks, B., 1990, Foreland shortening and crustal balancing in the Andes at 30 S latitude: Tectonics, v. 9, p. 789-809.

Alonso, M.S., Limarino, C.O., Litvak, V.D., Poma, S.M., Suriano, J., and Remesal, M.B., 2011, Paleogeographic, magmatic and paleoenvironmental scenarios at 30ºS during the Andean orogeny: Cross sections from the volcanic-arc to the orogenic front (San Juan, Argentina): Cenozoic Geology of the Central Andes of Argentina, p. 23.

Alvarado, P., Beck, S., and Zandt, G., 2007, Crustal structure of the south-central Andes Cordillera and backarc region from regional waveform modelling: Geophysical Journal International, v. 170, p. 858-875.

Ammirati, J.-B., Alvarado, P., Perarnau, M., Saez, M., and Monsalvo, G., 2013, Crustal structure of the Central Precordillera of San Juan, Argentina (31° S) using teleseismic receiver functions: Journal of South American Earth Sciences.

Anderson, J.L., 1996, Status of thermobarometry in granitic batholiths: Transactions of the Royal Society of Edinburgh, v. 87, p. 125 - 138.

Anderson, J.L., and Smith, D.R., 1995, The effects of temperature and fo_2 on the Al-in-hornblende barometer: American Mineralogist, v. 80, p. 549 - 559.

Beard, J.S., Ragland, P.C., and Crawford, M.L., 2005, Reactive bulk assimilation: A model for crust-mantle mixing in silicic magmas: Geology, v. 33, p. 681-684.

Bissig, T., Clark, A.H., and Lee, J.K., 2002, Cerro de Vidrio rhyolitic dome: evidence for Late Pliocene volcanism in the central Andean flat-slab region, Lama-Veladero district, 29 20′ S, San Juan Province, Argentina: Journal of South American Earth Sciences, v. 15, p. 571-576.

Bissig, T., Clark, A.H., Lee, J.K., and von Quadt, A., 2003, Petrogenetic and metallogenetic responses to Miocene slab flattening: new constraints from the El Indio-Pascua Au–Ag–Cu belt, Chile/Argentina: Mineralium Deposita, v. 38, p. 844-862.

Bissig, T., Lee, J.K.W., Clark, A.H., and Heather, K.B., 2001, The Cenozoic History of Volcanism and Hydrothermal Alteration in the Central Andean Flat-Slab Region: New 40Ar-39Ar Constraints from the El Indio–Pascua Au (-Ag, Cu) Belt, 29°20′–30°30′ S: International Geology Review, v. 43, p. 312-340.

Boynton, W.V., 1984, Cosmochemistry of the rare earth elements: meteoric studies: Rare earth element geochemistry, p. 63-114.

Browne, B.L., and Gardner, J.E., 2006, The influence of magma ascent path on the texture, mineralogy, and formation of hornblende reaction rims: Earth and Planetary Science Letters, v. 246, p. 161-176.

Cardó, R., and Díaz, I.N., 1999, Hoja Geológica 3169-I, Rodeo, provincias de San Juan: Buenos Aires, Instituto de Geología y Recursos Minerales, Servicio Geológico Minero Argentino.

Cardó, R., Díaz, I.N., Limarino, C.O., Litvak, V.D., Poma, S., and Santamaria, G., 2007, Hoja Geológica 2969-III, Malimán, provincias de San Juan y La Rioja: Buenos Aires, Instituto de Geología y Recursos Minerales, Servicio Geológico Minero Argentino.

Castillo, P.R., 2012, Adakite petrogenesis: Lithos, v. 134, p. 304-316.

Castillo, P.R., Janney, P.E., and Solidum, R.U., 1999, Petrology and geochemistry of Camiguin Island, southern Philippines: insights to the source of adakites and other lavas in a complex arc setting: Contributions to Mineralogy and Petrology, v. 134, p. 33-51.

Charchaflié, D., Tosdal, R.M., and Mortensen, J.K., 2007, Geologic framework of the Veladero high-sulfidation epithermal deposit area, Cordillera Frontal, Argentina: Economic Geology, v. 102, p. 171-192.

Charrier, R., Pinto, L., and Rodríguez, M.P., 2007, Tectonostratigraphic evolution of the Andean Orogen in Chile, *in* Moreno, T., and Gibbons, W., eds., The Geology of Chile: London, The Geological Society, p. 21 - 114.

Cherniak, D.J., and Watson, E.B., 2003, Diffusion in zircon: Reviews in Mineralogy and Geochemistry, v. 53, p. 113-143.

Chung, S.-L., Liu, D., Ji, J., Chu, M.-F., Lee, H.-Y., Wen, D.-J., Lo, C.-H., Lee, T.-Y., Qian, Q., and Zhang, Q., 2003, Adakites from continental collision zones: Melting of thickened lower crust beneath southern Tibet: Geology, v. 31, p. 1021-1024.

Cribb, J.W., and Barton, M., 1996, Geochemical effects of decoupled fractional crystallization and crustal assimilation: Lithos, v. 37, p. 293-307.

Davidson, J., Turner, S., Handley, H., Macpherson, C., and Dosseto, A., 2007, Amphibole "sponge" in arc crust?: Geology, v. 35, p. 787-790.

Davidson, J.P., 1996, Deciphering mantle and crustal signatures in subduction zone magmatism: Subduction top to bottom, p. 251-262.

Davidson, J.P., and de Silva, S.L., 1992, Volcanic rocks from the Bolivian Altiplano: Insights into crustal structure, contamination, and magma genesis in the central Andes: Geology, v. 20, p. 1127-1130.

Davidson, J.P., Hora, J.M., Garrison, J.M., and Dungan, M.A., 2005, Crustal forensics in arc magmas: Journal of Volcanology and Geothermal Research, v. 140, p. 157 -170.

Defant, M.J., and Drummond, M.S., 1990, Derivation of some modern arc magmas by melting of young subducted lithosphere: Nature, v. 347, p. 662-665.

DePaolo, D.J., 1981, A neodymium and strontium isotopic study of the Mesozoic calc-alkaline granitic batholiths of the Sierra Nevada and Peninsular Ranges,

California: Journal of Geophysical Research: Solid Earth, v. 86, p. 10470-10488.

Drummond, M.S., and Defant, M.J., 1990, A model for Trondhjemite-Tonalite-Dacite Genesis and crustal growth via slab melting: Archean to modern comparisons: Journal of Geophysical Research: Solid Earth, v. 95, p. 21503-21521.

Elliott, T., 2003, Tracers of the Slab, *in* Eiler, J.M., ed., Inside the Subduction Factory: Washington DC, American Geophysical Union, p. 23-45.

Elliott, T., Plank, T., Zindler, A., White, W., and Bourdon, B., 1997, Element transport from slab to volcanic front at the Mariana arc: Journal of Geophysical Research, v. 102, p. 14991 - 15019.

Emparan, C., and Pineda, G., 1999, Area Condoriaco-Rivadavia, Región de Coquimbo, Volume 12: Santiago, Servicio Nacional de Geologia y Mineria, Mapas Geológicos.

Ersoy, Y., and Helvacı, C., 2010, FC–AFC–FCA and mixing modeler: A Microsoft® Excel© spreadsheet program for modeling geochemical differentiation of magma by crystal fractionation, crustal assimilation and mixing: Computers & Geosciences, v. 36, p. 383-390.

Fitton, J.G., and Godard, M., 2004, Origin and evolution of magmas on the Ontong Java Plateau: Geological Society, London, Special Publications, v. 229, p. 151-178.

Fitton, J.G., Saunders, A.D., Larsen, L.M., Hardarson, B.S., and Norry, M.J., 1998, Volcanic rocks from the southeast Greenland margin at 63°N : Composition, petrogenesis, and mantle sources: Proceedings of the Ocean Drilling Programme, v. Scientific Results 152, p. 331 - 350.

Gilbert, H., Beck, S., and Zandt, G., 2006, Lithospheric and upper mantle structure of central Chile and Argentina: Geophysical Journal International, v. 165, p. 383-398.

Gill, J.B., 1981, Orogenic Andesites and Plate Tectonics: New York, Springer-Verlag.

Goss, A., Kay, S., and Mpodozis, C., 2011, The geochemistry of a dying continental arc: the Incapillo Caldera and Dome Complex of the southernmost Central Andean Volcanic Zone (~ 28° S): Contributions to Mineralogy and Petrology, v. 161, p. 101-128.

Goss, A.R., Kay, S.M., and Mpodozis, C., 2013, Andean Adakite-like high-Mg Andesites on the Northern Margin of the Chilean–Pampean Flat-slab (27–28· 5° S) Associated with Frontal Arc Migration and Fore-arc Subduction Erosion: Journal of Petrology, v. 54, p. 2193-2234.

Green, T.H., Blundy, J.D., Adam, J., and Yaxley, G.M., 2000, SIMS determination of trace element partition coefficients between garnet, clinopyroxene and hydrous basaltic liquids at 2–7.5 GPa and 1080–1200°C: Lithos, v. 53, p. 165-187.

Gutscher, M.-A., Maury, R., Eissen, J.-P., and Bourdon, E., 2000a, Can slab melting be caused by flat subduction?: Geology, v. 28, p. 535-538.

Gutscher, M.A., Spakman, W., Bijwaard, H., and Engdahl, E.R., 2000b, Geodynamics of flat subduction: Seismicity and tomographic constraints from the Andean margin: Tectonics, v. 19, p. 814-833.

Hammarstrom, J.M., and Zen, E.-a., 1986, Aluminum in hornblende; an empirical igneous geobarometer: American Mineralogist, v. 71, p. 1297-1313.

Harley, S.L., and Kelly, N.M., 2007, Zircon Tiny but Timely: Elements, v. 3, p. 13 - 18.

Hawkesworth, C.J., Gallagher, K., Hergt, J.M., and McDermott, F., 1993, Mantle and slab contributions in arc magmas: Annual Review of Earth and Planetary Sciences, v. 21, p. 175 - 204.

Hawkesworth, C.J., Hergt, J.M., Ellam, R.M., and Dermott, F.M., 1991, Element Fluxes Associated with Subduction Related Magmatism: Philosophical Transactions of the Royal Society of London. Series A: Physical and Engineering Sciences, v. 335, p. 393-405.

Helz, R.T., 1973, Phase Relations of Basalts in their Melting Range at PH2O= 5 kb as a Function of Oxygen Fugacity Part I. Mafic Phases: Journal of Petrology, v. 14, p. 249-302.

Hildreth, W., and Moorbath, S., 1988, Crustal contributions to arc magmatism in the Andes of Central Chile: Contributions to Mineralogy and Petrology, v. 98, p. 455 - 489.

Holland, T., and Blundy, J., 1994, Non-ideal interactions in calcic amphiboles and their bearing on amphibole-plagioclase thermometry: Contributions to Mineralogy and Petrology, v. 116, p. 433-447.

Hollister, L.S., Grissom, G., Peters, E., Stowell, H., and Sisson, V., 1987, Confirmation of the empirical correlation of Al in hornblende with pressure of solidification of calc-alkaline plutons: American Mineralogist, v. 72, p. 231-239.

Irvine, T., and Baragar, W., 1971, A guide to the chemical classification of the common volcanic rocks: Canadian Journal of Earth Sciences, v. 8, p. 523-548.

Jacques, G., Hoernle, K., Gill, J., Hauff, F., Wehrmann, H., Garbe-Schönberg, D., van den Bogaard, P., Bindeman, I., and Lara, L., 2013, Across-arc geochemical variations in the Southern Volcanic Zone, Chile (34.5-38.0° S): Constraints on Mantle Wedge and Slab Input Compositions: Geochimica et Cosmochimica Acta.

James, D.E., 1982, A combined O, Sr, Nd, and Pb isotopic and trace element study of crustal contamination in central Andean lavas, I. Local geochemical variations: Earth and Planetary Science Letters, v. 57, p. 47-62.

Jarvis, A., Reuter, H.I., Nelson, A., and Guevara, E., 2008, Hole-filled SRTM for the globe Version 4, available from the CGIAR-CSI SRTM 90m Database.

JICA-MMAJ, 1999, Informe de la exploración de mineral en la región Cordillera Oriental Andina, República Argentina, *in* SEGEMAR, ed.: Buenos Aires, p. 164.

Johnson, M.C., and Plank, T., 1999, Dehydration and melting experiments constrain the fate of subducted sediments: Geochemistry Geophysics Geosystems, v. 1, p. 1007-26.

Johnson, M.C., and Rutherford, M.J., 1989, Experimental calibration of the aluminum-in-hornblende geobarometer with application to Long Valley caldera (California) volcanic rocks: Geology, v. 17, p. 837-841.

José Frutos, J., Paula Cornejo, P., Tomlinson, A., Arturo Hauser, Y., Carlos Portigliati, N., Aníbal Gajardo, C., Estanislao Godoy, P.-B., Ernesto Pérez, D.A., and Renate Wall, Z., 2004, Mapa Geológico de Chile: versión digital, Carta Geológica de Chile, Serie Geología Básica: Santiago, Servicio Nacional de Geología y Minería (SERNAGEOMIN).

Kay, R.W., 1978, Aleutian magnesian andesites: Melts from subducted Pacific ocean crust: Journal of Volcanology and Geothermal Research, v. 4, p. 117-132.

Kay, S., and Gordillo, C., 1994, Pocho volcanic rocks and the melting of depleted continental lithosphere above a shallowly dipping subduction zone in the central Andes: Contributions to Mineralogy and Petrology, v. 117, p. 25-44.

Kay, S.M., and Abbruzzi, J.M., 1996, Magmatic evidence for Neogene lithospheric evolution of the central Andean "flat slab" between 30ºS and 32ºS: Tectonophysics, v. 259, p. 15 - 28.

Kay, S.M., Godoy, E., and Kurtz, A., 2005, Episodic arc migration, crustal thickening, subduction erosion, and magmatism in the south-central Andes: Geological Society of America Bulletin, v. 117, p. 67-88.

Kay, S.M., Maksaev, V., Moscoso, R., Mpodozis, C., and Nasi, C., 1987, Probing the evolving Andean lithosphere; Mid - Late Tertiary magmatism in Chile (29º - 30º30'S) over the modern zone of subhorizontal subduction: Journal of Geophysical Research, v. 92, p. 6173 - 6189.

Kay, S.M., and Mpodozis, C., 2001, Central Andean ore deposits linked to evolving shallow subduction systems and thickening crust: GSA Today, v. 11, p. 4-9.

Kay, S.M., and Mpodozis, C., 2002, Magmatism as a probe to the Neogene shallowing of the Nazca plate beneath the modern Chilean flat slab: Journal of South American Earth Sciences, v. 15, p. 39 - 57.

Kay, S.M., Mpodozis, C., Ramos, V.A., and Munizaga, F., 1991, Magma source variations for mid-late Tertiary magmatic rocks associated with a shallowing subduction zone and the thickening crust in the central Andes (28-33ºS): Spec. Pap. Geological Society of America Bulletin, v. 265, p. 113 - 137.

Kay, S.M., Orrell, S., and Abbruzzi, J.M., 1996, Zircon and Whole Rock Nd-Pb Isotopic Evidence for a Grenville Age and a Laurentian Origin for the Basement of the Precordillera in Argentina: The Journal of Geology, v. 104, p. 637-648.

Kelly, N., Hinton, R., Harley, S., and Appleby, S., 2008, New SIMS U–Pb zircon ages from the Langavat Belt, South Harris, NW Scotland: implications for the Lewisian terrane model: Journal of the Geological Society, v. 165, p. 967-981.

Kessel, R., Schmidt, M.W., Ulmer, P., and Pettke, T., 2005, Trace element signature of subduction-zone fluids, melts and supercritical liquids at 120-180[thinsp]km depth: Nature, v. 437, p. 724-727.

Kilian, R., and Behrmann, J.H., 2003, Geochemical constraints on the sources of Southern Chile Trench sediments and their recycling in arc magmas of the Southern Andes: Journal of the Geological Society, v. 160, p. 57-70.

Kirby, S., Engdahl, R.E., and Denlinger, R., 1996, Intermediate-depth intraslab earthquakes and arc volcanism as physical expressions of crustal and uppermost mantle metamorphism in subducting slabs: Subduction top to bottom, p. 195-214.

Le Maitre, R.W., Bateman, P., Dudek, A., Keller, J., Lameyre, J., Le Bas, M., Sabine, P., Schmid, R., Sorensen, H., and Streckeisen, A., 1989, A classification of igneous rocks and glossary of terms: Recommendations of the International Union of Geological Sciences Subcommission on the Systematics of Igneous Rocks, Blackwell Oxford.

Leake, B.E., 1971, On aluminous and edenitic hornblendes: Mineral Mag, v. 38, p. 389-407.

Leveratto, M., 1976, Edad de intrusivos cenozoicos en la Precordillera de San Juan y su implicancia estratigráfica: Revista de la Asociación Geológica Argentina, v. 31, p. 53-58.

Limarino, C.O., Gutiérrez, P.R., Malizia, D., Barreda, V., Page, S., Ostera, H., and Linares, E., 1999, Edad de las secuencias paleógenas y neógenas de las cordilleras de La Brea y Zancarrón, Valle del Cura, San Juan: Revista de la Asociación Geológica Argentina, v. 54, p. 177-181.

Litvak, V.D., 2004, Evolución del volcanismo terciario en el Valle del Cura sobre el segmento de subducción horizontal Pampeano, provincia de San Juan: Buenos Aires, Universidad de Buenos Aires.

Litvak, V.D., Kay, S.M., and Mpodozis M, C., 2005, New K/Ar ages on Tertiary Volcanic Rocks in the Valle del Cura, Pampean flat slab segment, Argentina: Actas XVI Congreso Geológico Argentino, v. 2, p. 159 - 164.

Litvak, V.D., and Page, S., 2002, Nueva evidencia cronológica en el Valle del Cura, provincia de San Juan, Argentina: Revista de la Asociación Geológica Argentina, v. 57, p. 483-486.

Litvak, V.D., and Poma, S., 2005, Estratigrafía y facies volcánicas y volcaniclásticas de la Formación Valle del Cura: magmatismo paleógeno en la Cordillera Frontal de San Juan: Revista de la Asociación Geológica Argentina, v. 60, p. 402-416.

Litvak, V.D., and Poma, S., 2010, Geochemistry of mafic Paleocene volcanic rocks in the Valle del Cura region: Implications for the petrogenesis of primary mantle-derived melts over the Pampean flat-slab: Journal of South American Earth Sciences, v. 29, p. 705-716.

Litvak, V.D., and Poma, S., 2013, Petrogenesis of Miocene volcanic arc rocks over the Chilean-Pampean flat-slab segment of the Central Andes constrained by mineral chemistry: Geologica Acta, v. In press.

Litvak, V.D., Poma, S., and Kay, S.M., 2007, Paleogene and Neogene magmatism in the Valle del Cura region: New perspective on the evolution of the Pampean flat slab, San Juan province, Argentina: Journal of South American Earth Sciences, v. 24, p. 117 - 137.

Llambias, E.J., Shaw, S., and Sato, A.M., 1990, Lower Miocene plutons in the Eastern Cordillera frontal of San Juan (29° 75' S, 69° 30' W), 11º Congreso Geológico Argentino, Volume 1: San Juan, p. 83 - 86.

Lonsdale, P., 2005, Creation of the Cocos and Nazca plates by fission of the Farallon plate: Tectonophysics, v. 404, p. 237-264.

Lucassen, F., Wiedicke, M., and Franz, G., 2010, Complete recycling of a magmatic arc: evidence from chemical and isotopic composition of Quaternary trench sediments in Chile (36°–40°S): International Journal of Earth Sciences, v. 99, p. 687-701.

Ludwig, K.R., 2008, User's Manual for Isoplot 3.7 - A Geochronological Toolkit for Microsoft Excel: Berkeley Geochronology Center Special Publication, v. 4.

Macpherson, C.G., Dreher, S.T., and Thirlwall, M.F., 2006, Adakites without slab melting: high pressure differentiation of island arc magma, Mindanao, the Philippines: Earth and Planetary Science Letters, v. 243, p. 581-593.

Maksaev, V., Moscoso, R., Mpodozis, C., and Nasi, C., 1984, Las unidades volcánicas y plutónicas del Cenozoico superior en la Alta Cordilera del Norte Chico (29°–31° S): Geología, Alteración hidrotermal y Mineralización: Revista Geológica de Chile, v. 11, p. 12 - 51.

Martin, M.W., Clavero R, J., and Mpodozis M, C., 1997, Eocene to Late Miocene magmatic development of El Indio Belt, 30° S, North-central Chile, Congreso Congreso Geológico Chileno, 8 Actas 1: Antofagasta, p. 149–153

Martin, M.W., Clavero R, J., and Mpodozis M, C., 1999, Late Paleozoic to Early Jurassic tectonic development of the high Andean Principal Cordillera, El Indio Region, Chile (29–30°S): Journal of South American Earth Sciences, v. 12, p. 33-49.

Martin, M.W., Clavero R, J., Mpodozis M, C., and Cuitiño, L., 1995, Estudio Geológico de la Franja El Indio, Cordillera de Coquimbo: Servicio Nacional de Geología y Minería: Santiago, 1 - 238 p.

Moore, G., and Carmichael, I., 1998, The hydrous phase equilibria (to 3 kbar) of an andesite and basaltic andesite from western Mexico: constraints on water content and conditions of phenocryst growth: Contributions to Mineralogy and Petrology, v. 130, p. 304-319.

Mpodozis, C., and Cornejo, P.P., 1988, Hoja Pisco Elqui, Region de Coquimbo, *in* Mpodozis, C., Davidson, J., and Rivano, S., eds., Carta Geologica de Chile: Santiago, Servicio Nacional de Geología y Minería (SERNAGEOMIN).

Mpodozis, C., and Kay, S.M., 1992, Late Paleozoic to Triassic evolution of the Gondwana margin: Evidence from Chilean Frontal Cordilleran batholiths (28 S to 31 S): Geological Society of America Bulletin, v. 104, p. 999-1014.

Muntener, O., Kelemen, P., and Grove, T., 2001, The role of H2O during crystallization of primitive arc magmas under uppermost mantle conditions and genesis of igneous pyroxenites: an experimental study: Contributions to Mineralogy and Petrology, v. 6.

Nasi, C., Moscoso, R., and Maksaev, V., 1990, Hoja Guanta, Regiones de Atacama y Coquimbo, *in* Mpodozis, C., Davidson, J., and Rivano, S., eds., Carta Geologica de Chile: Santiago, Servicio Nacional de Geología y Minería (SERNAGEOMIN).

Nur, A., and Ben-Avraham, Z., 1981, Volcanic gaps and the consumption of aseismic ridges in South America: Geological Society of America Memoirs, v. 154, p. 729-740.

Otten, M.T., 1984, The origin of brown hornblende in the Artfjället gabbro and dolerites: Contributions to Mineralogy and Petrology, v. 86, p. 189 - 199.

Parada, M.A., López-Escobar, L., Oliveros, V., Fuentes, F., Morata, D., Calderón, M., Aguirre, L., Féraud, G., Espinoza, F., Moreno, H., Figueroa, O., Bravo, J.M., Vásquez, R.T., and Stern, C.R., 2007, Andean Magmatism, *in* Moreno, T., and Gibbons, W., eds., The Geology of Chile: London, The Geological Society, p. 115 - 146.

Parada, M.A., Rivano, S., Sepulveda, P., Herve, M., Herve, F., Puig, A., Munizaga, F., Brook, M., Pankhurst, R., and Snelling, N., 1988, Mesozoic and Cenozoic plutonic development in the Andes of central Chile (30º30' - 32º30'S) Journal of South American Earth Sciences, v. 1, p. 249 - 260.

Pardo Casas, F., and Molnar, P., 1987, Relative motion of the Nazca (Farallón) and South America plates since Late Cretaceous time Tectonics, v. 6, p. 233 - 248.

Pearce, J.A., 2008, Geochemical fingerprinting of oceanic basalts with applications to ophiolite classification and the search for Archean oceanic crust: Lithos, v. 100, p. 14-48.

Pilger, R.H., 1981, Plate reconstructions, aseismic ridges, and low angle subduction beneath the Andes: Geological Society of America Bulletin, v. 92, p. 448 - 456.

Pilger, R.H., 1984, Cenozoic plate kinematics, subduction and magmatism: South American Andes: Journal of Geological Society London, v. 141, p. 793 - 802.

Pineda, G., and Calderón, M., 2008, Geología del área Monte Patria-El Maqui, Región de Coquimbo, Carta Geológica de Chile, Serie Geología Básica: Santiago, Servicio Nacional de Geología y Minería.

Pineda, G., and Emparan, C., 2006, Geología del área Vicuña-Pichasca, Región de Coquimbo, Carta Geológica de Chile, Serie Geología Básica Volume 97: Santiago, Servicio Nacional de Geología y Minería.

Plank, T., 2005, Constraints from Thorium/Lanthanum on Sediment Recycling at Subduction Zones and the Evolution of the Continents: Journal of Petrology, v. 46, p. 921 - 944.

Plank, T., and Langmuir, C.H., 1993, Tracing trace elements from sediment input to volcanic output at subduction zones: Nature, v. 362, p. 739 - 743.

Plank, T., and Langmuir, C.H., 1998, The chemical composition of subducting sediment and its consequences for the crust and mantle: Chemical Geology, v. 145, p. 325 - 394.

Poma, S., Limarino, C., and Litvak, V., 2005, Formación Las Trancas: expresión del arco magmático terciario en el faldeo occidental de la Precordilera de San Juan, Actas, Congreso Geológico Argentino, 16th, La Plata: Buenos Aires, Asociación Geológica Argentina, Volume 1, p. 331-334.

Ramos, V.A., Cristallini, E., and Pérez, D.J., 2002, The Pampean flat-slab of the Central Andes: Journal of South American Earth Sciences, v. 15, p. 59-78.

Ramos, V.A., Kay, S.M., Page, R., and Munizaga, F., 1989, La Ignimbrita Vacas Heladas y el cese del volcanismo en el valle del Cura, provincia de San Juan: Revista de la Asociación Geológica Argentina, v. 44, p. 336-352.

Rapp, R.P., Shimizu, N., Norman, M.D., and Applegate, G.S., 1999, Reaction between slab-derived melts and peridotite in the mantle wedge: experimental constraints at 3.8 GPa: Chemical Geology, v. 160, p. 335-356.

Rapp, R.P., and Watson, E.B., 1995, Dehydration melting of metabasalt at 8–32 kbar: implications for continental growth and crust-mantle recycling: Journal of Petrology, v. 36, p. 891-931.

Reich, M., Parada, M.A., Palacios, C., Dietrich, A., Schultz, F., and Lehmann, B., 2003, Adakite-like signature of Late Miocene intrusions at the Los Pelambres giant porphyry copper deposit in the Andes of central Chile: metallogenic implications: Mineralium Deposita, v. 38, p. 876-885.

Richards, J.P., and Kerrich, R., 2007, Special paper: adakite-like rocks: their diverse origins and questionable role in metallogenesis: Economic Geology, v. 102, p. 537-576.

Rickwood, P.C., 1989, Boundary lines within petrologic diagrams which use oxides of major and minor elements: Lithos, v. 22, p. 247-263.

Ridolfi, F., Renzulli, A., and Puerini, M., 2010, Stability and chemical equilibrium of amphibole in calc-alkaline magmas: an overview, new thermobarometric formulations and application to subduction-related volcanoes: Contributions to Mineralogy and Petrology, v. 160, p. 45-66.

Rodríguez, C., Sellés, D., Dungan, M., Langmuir, C., and Leeman, W., 2007, Adakitic Dacites Formed by Intracrustal Crystal Fractionation of Water-rich Parent Magmas at Nevado de Longaví Volcano (36·2°S; Andean Southern Volcanic Zone, Central Chile): Journal of Petrology, v. 48, p. 2033-2061.

Rooney, T., Franceschi, P., and Hall, C., 2011, Water-saturated magmas in the Panama Canal region: a precursor to adakite-like magma generation?: Contributions to Mineralogy and Petrology, v. 161, p. 373-388.

Rutherford, M.J., and Hill, P.M., 1993, Magma ascent rates from amphibole breakdown: An experimental study applied to the 1980–1986 Mount St.

Helens eruptions: Journal of Geophysical Research: Solid Earth, v. 98, p. 19667-19685.

Schmidt, M.W., 1992, Amphibole composition in tonalite as a function of pressure: an experimental calibration of the Al-in-hornblende barometer: Contributions to Mineralogy and Petrology, v. 110, p. 304-310.

Silver, P.G., Russo, R.M., and Lithgow-Bertelloni, C., 1998, Coupling of South American and African plate motion and plate deformation: Science, v. 279, p. 60 - 63.

Somoza, R., 1998, Updated azca (Farallon)—South America relative motions during the last 40 My: implications for mountain building in the central Andean region: Journal of South American Earth Sciences, v. 11, p. 211-215.

Somoza, R., and Ghidella, M.E., 2012, Late Cretaceous to recent plate motions in western South America revisited: Earth and Planetary Science Letters, v. 331–332, p. 152-163.

Stern, C.R., 1991, Role of subduction erosion in the generation of Andean magmas: Geology, v. 19, p. 78 - 81.

Stern, C.R., 2004, Active Andean volcanism: its geologic and tectonic setting: Revista Geológica de Chile, v. 31, p. 161-206.

Sun, S.S., and McDonough, W.F., 1989, Chemical and isotopic systematics of oceanic basalts: implications for mantle compositions and processes: Geological Society, London, Special Publications, v. 42, p. 313 - 345.

Taylor, S.R., and McLennan, S.M., 1995, The geochemical evolution of the continental crust: Reviews of Geophysics, v. 33, p. 241-265.

Tollstrup, D., Gill, J., Kent, A., Prinkey, D., Williams, R., Tamura, Y., and Ishizuka, O., 2010, Across-arc geochemical trends in the Izu-Bonin arc: Contributions from the subducting slab, revisited: Geochemistry, Geophysics, Geosystems, v. 11, p. Q01X10.

van Keken, P.E., Hacker, B.R., Syracuse, E.M., and Abers, G.A., 2011, Subduction factory: 4. Depth-dependent flux of H2O from subducting slabs worldwide: Journal of Geophysical Research: Solid Earth, v. 116, p. B01401.

Wetten, A.F., 2005, Andesita Cerro Bola: Nueva unidad vinculada al magmatismo mioceno de la Cordillera de Olivares, San Juan, Argentina (30° 35′ S; 69° 30′ O): Revista de la Asociación Geológica Argentina, v. 60, p. 003-008.

Wilson, B.M., 1989, Igneous petrogenesis a global tectonic approach, Springer.

Winocur, D.A., Litvak, V.D., and Ramos, V.A., 2013, Magmatic and tectonic evolution of the Oligocene Valle del Cura basin, Main Andes of Argentina and Chile: Evidence for generalized extension, *in* Sepulveda, P., Giambiagi, L., Pinto, L., Moreiras, S., Tunik, M., Hoke, G., and M., F., eds., Geodynamic processes in the Andes of Central Chile and Argentina, Volume In press, Geological Society of London, Special Publication.

Woodhead, J.D., 1988, The Origin of Geochemical Variations in Mariana Lavas: A General Model for Petrogenesis in Intra-Oceanic Island Arcs?: Journal of Petrology, v. 29, p. 805-830.

Wunder, B., Wirth, R., and Gottschalk, M., 2001, Antigorite Pressure and temperature dependence of polysomatism and water content: European Journal of Mineralogy, v. 13, p. 485-496.

Yañez, G.A., Cembrano, J., Pardo, M., Ranero, C.R., and Selles, D., 2002, The Challenger - Juan Fernández - Maipo major tectonic transition of the Nazca - Andean subduction system at 33-34ºS: geodynamic evidence and implications: Journal of South American Earth Sciences, v. 15, p. 28 - 38.

Yañez, G.A., Ranero, C.R., von Huene, R., and Díaz, J., 2001, Magnetic anomaly interpretation across the southern central Andes (32º-34ºS): The role of the Juan Fernández Ridge in the late Tertiary evolution of the margin: Journal of Geophysical Research, v. 106, p. 6325 - 6345.

Chapter 3. Continental crust formation in the southern Central Andes: new insights from O and Hf isotopes in zircon

Rosie E. Jones[1]*, Linda A. Kirstein[1], Simone A. Kasemann[2], Bruno Dhuime[3], Tim Elliott[3], Vanesa D. Litvak[4], Richard Hinton[1], and Edinburgh Ion Microprobe Facitility (EIMF)[5]

[1] School of GeoSciences, University of Edinburgh, West Mains Road, Edinburgh, EH9 3JW, UK

[2] Department of Geosciences & MARUM, Centre for Marine Environmental Sciences, University of Bremen, 28334 Bremen, Germany

[3] School of Earth Sciences, University of Bristol, Wills Memorial Building, Queens Road, Bristol, BS8 1RJ, UK

[4] Instituto de Estudios Andinos Don Pablo Groeber, Departamento de Ciencias Geológicas, Universidad de Buenos Aires – CONICET, Argentina

[5] Edinburgh Ion Microprobe Facility, School of GeoSciences, University of Edinburgh, West Mains Road, Edinburgh, EH9 3JW, UK

This Chapter forms a longer version of a paper currently in revision for *Geology*.

3.1 Author Contributions

The authors of the manuscript made the following contributions:

Rosie Jones: All of the petrographic work, sample preparation and analytical work was conducted by myself, as was all processing and modelling of the geochemical data. The interpretations and conclusions presented in the manuscript are entirely my own, although the development of the ideas was enhanced by discussions with my co-authors. I wrote and prepared the manuscript and circulated it to my co-authors for feedback.

Linda Kirstein: Provided constructive feedback throughout the preparation of the manuscript and helped me hone my ideas and structure the manuscript more succinctly.

Simone Kasemann: Contributed to the development of the presented ideas and provided useful feedback on the manuscript.

Bruno Dhuime: Provided technical assistance in the Lu-Hf isotopic analysis of zircon on the Finnigan Neptune multi-collector inductively-coupled plasma mass spectrometer combined with a laser ablation system (LA-MC-ICP-MS) at the University of Bristol. My interpretations were aided by early discussions of the dataset with Bruno. He also provided useful suggestions and comments on the manuscript.

Tim Elliott: Facilitated the Lu-Hf isotopic analysis of zircon by LA-MC-ICP-MS at the University of Bristol, as no such instrument is available at the University of Edinburgh. The manuscript benefited from discussions with Tim, who helped me develop and refine my ideas.

Vanesa Litvak: Provided samples for analysis, as well as invaluable knowledge of the regional geology and constructive thoughts and comments on an early version of the manuscript.

Richard Hinton: Gave technical support and assistance in the U-Th-Pb analysis of zircons by secondary ion mass spectrometry (SIMS), and in the various methods of data reduction and correction. He provided useful discussions regarding the data set and provided feedback on an early version of the manuscript.

EIMF: John Craven provided advice in the preparation of zircon grain mounts for SIMS analysis. He also guided and provided technical assistance in the oxygen isotopic analysis of zircons by SIMS and dealt with any analytical problems which arose. He ensured the high quality of the data set and also informed on data correction and reduction methods.

3.2 Abstract

Subduction zones, such as the Andean convergent margin of South America, are sites of active continental growth and crustal recycling. The composition of arc magmas, and therefore new continental crust, reflects variable contributions from mantle, crustal and subducted reservoirs. Assessing the relative contributions from these different components is fundamental in order to comprehensively evaluate net crustal growth and recycling. Temporal (Myr) and spatial (km) variations in these contributions to southern Central Andean arc magmas are investigated by utilising the changing plate geometry and geodynamic setting of the southern Central Andes (28 - 32 °S) during the Cenozoic. The *in-situ* analysis of O and Hf isotopes in zircon, from both intrusive (granitoids) and extrusive (basaltic andesites to rhyolites) Late Cretaceous – Late Miocene arc magmatic rocks, combined with high resolution U-Pb dating, demonstrates distinct across-arc variations. Mantle-like $\delta^{18}O_{(zircon)}$ values (+5.4 ‰ to +5.7 ‰ (±0.4 (2σ))) and juvenile initial $\varepsilon Hf_{(zircon)}$ values (+8.3 (±0.8 (2σ)) to +10.0 (±0.9 (2σ))), combined with a lack of zircon inheritance suggests that the Late Cretaceous (~73 Ma) to Eocene (~39 Ma) granitoids emplaced in the Principal Cordillera of Chile formed from mantle-derived melts with very limited interaction with continental crustal material. Mixing of mantle-derived melts with the Late Paleozoic – Early Mesozoic basement (up to ~20 %) explains the broadly 'mantle-like' $\delta^{18}O_{(zircon)}$ values (+4.8 ‰ (±0.2 (2σ) to +5.8 ‰ (±0.5 (2σ))), but less radiogenic initial $\varepsilon Hf_{(zircon)}$ values (+1.0 (±1.1 (2σ)) to +4.0 (±0.6 (2σ))), obtained for Late Eocene (~36 Ma) to Early Miocene (~17 Ma) volcanic arc rocks present in the Frontal Cordillera. The assimilation of both Late Paleozoic – Early Mesozoic Andean crust and a Grenville-aged basement is required to produce the higher than 'mantle-like' $\delta^{18}O_{(zircon)}$ values (+5.5 ‰ (±0.6 (2σ) to +7.2 ‰ (±0.4 (2σ))) and unradiogenic, initial $\varepsilon Hf_{(zircon)}$ values (-3.9 (±1.0 (2σ)) to +1.6 (±4.4 (2σ))), obtained for the Late Oligocene (~23 Ma) to Late Miocene (~9 Ma) magmatic rocks located in the Argentinean Precordillera, and the Late Miocene (~6 Ma) volcanic rocks present in the Frontal

Cordillera. The observed isotopic variability demonstrates that the assimilation of pre-existing continental crust, which varies in both age and composition over the Andean Cordillera, plays a dominant role in modifying the isotopic composition of mantle-derived magmas. The interaction of arc magmas with distinct basement terranes is controlled by the changing geodynamic setting and the increased compression of the southern Central Andean margin over the latter part of the Cenozoic.

3.3 Introduction

Subduction zones introduce surface materials into the mantle wedge, promoting melting and ultimately generating new crust. Arc magmas, and hence new crust, potentially contain components derived from a number of different reservoirs (e.g., the mantle, subducted sediments, the subducting oceanic lithosphere, continental crust from subduction erosion, and the overlying crust) and the proportions of these various contributions must be investigated and determined in order to quantify net crustal growth. Resolving mantle and subduction components is more straight-forward in oceanic arcs than continental arcs as there is limited interaction with existing continental crust (e.g., Gill, 1981; Elliott et al., 1997). The task is more challenging for arcs built on continental crust as the addition of subducting components is notoriously difficult to resolve from the contamination of magmas with the overlying crust (e.g., Davidson et al., 1991). However, it is in continental settings that the greatest proportion of long-lived crust is generated (e.g., Burchfiel, 1993) and therefore determining contributions from mantle, crustal and subducting reservoirs is important in order to evaluate crustal growth and long-term recycling of crustal material.

The Central Andes is an active site of modern continental growth and represents a type example of an ocean–continent convergent margin. The Andean margin has experienced high levels (50 km^3/km/Myr (Stern, 2011)) of subduction erosion (removal of continental crust from the base of the continental plate by the subducting oceanic lithosphere) (Rutland, 1971; Stern, 1991) and variable sediment flux from the oceans and continents (Von Huene and Scholl, 1991). The geodynamic setting, specifically plate convergence rates and the angle of the subducting oceanic plate, have also changed with time (e.g., Pilger, 1981, 1984; Pardo Casas and Molnar, 1987; Somoza, 1998; Yañez et al., 2001; Yañez et al., 2002; Somoza and Ghidella, 2012). This has resulted in the development of the Central Andean margin from a

generally more extensional regime, operating between the Late Cretaceous and Late Oligocene and associated with a continental crustal thicknesses of between 30 and 35 km, to a more compressional regime in the Late Miocene and an increase in crustal thickness to >45 km (e.g., Kay et al., 1991; Jordon et al., 2001; Haschke et al., 2002; Ramos et al., 2002). This variability makes the southern Central Andes an ideal location at which to investigate the influence of subducting material, and the composition and thickness of the existing Andean continental crust, on mantle-derived arc magmas at an active site of continental crustal growth. Previous studies have identified an increased influence of crustal components on arc magmas from the southern Central Andes over the course of the Cenozoic on the basis of whole rock geochemistry (e.g., Kay et al., 1991; Kay and Abbruzzi, 1996; Litvak et al., 2007; Goss et al., 2013), but discriminating between the processes involved (i.e. contamination of the asthenospheric mantle wedge with subducted components and/or crustal material from subduction erosion, versus arc magmas assimilating existing continental crust en route to the surface) remains unresolved.

3.4 Subduction in the Central Andes

The Andean tectonic cycle (Jurassic to recent) represents only the latest in a series of orogenic cycles to affect the western edge of the South American continent. Earlier tectonic cycles (e.g., the Gondwanan tectonic cycle, Devonian to Triassic) along with episodes of extension, subduction and accretion formed the distinctive basement on which the modern Andes are built (Ramos et al., 1986; Charrier et al., 2007). Subduction has been active along the western margin of South America since the earliest Jurassic, with subduction-related magmatism in the Central Andes initiated at ~185 Ma (Pichowiak et al., 1990; Stern, 2004).

The study area is located within the Pampean (Chilean) flat-slab segment (~28° - 33°S) of the southern Central Andes (Fig. 3.1). This segment of the Andean margin

has been volcanically inactive since the Late Miocene (~6 Ma) due to a decrease in the angle (<10° at 100km depth) at which the oceanic Nazca plate subducts beneath the South American continent (Pilger, 1981, 1984; Yañez et al., 2001). The present day, low angle of subduction has been attributed to the subduction of the Juan Fernandez Ridge (JFR) which began intersecting the Andean margin during the early Miocene (~18 Ma) (Yañez et al., 2001). The shallowing of the Nazca plate caused the position of the volcanic arc to expand and migrate to the east (e.g., Kay et al., 1987; Kay and Mpodozis, 2002). Convergence rates and the relative plate motions between the oceanic (Farallon and Nazca) and South American plates have also changed during the course of the Cenozoic; in particular a major plate reconfiguration occurred in the Late Oligocene (~25 Ma) due to the break-up of the Farallon plate into the Nazca and Cocos plates (Lonsdale, 2005). This resulted in an increase in convergence rates (from ~8 cm/yr to ~15 cm/yr) between the Nazca and South American plates and a change from oblique (NE-SW) to orthogonal (ENE-WSW) convergence (Pardo Casas and Molnar, 1987; Somoza, 1998; Somoza and Ghidella, 2012). This increased convergence, combined with increased compression related to the subduction of the JFR, led to an increase in crustal thickness in the southern Central Andes from ~30 km to >45 km (Kay et al., 1991; Haschke et al., 2002).

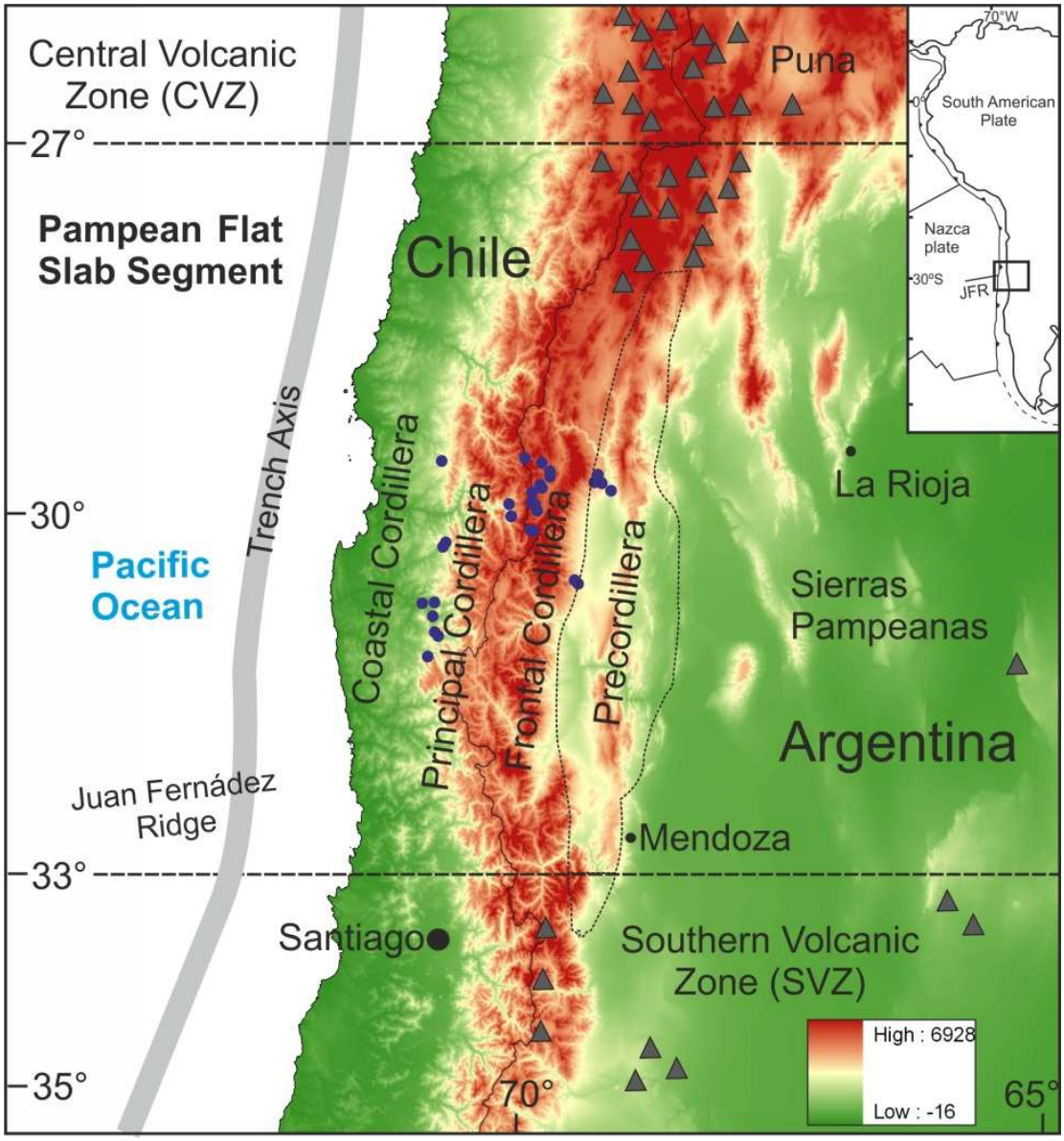

Figure 3.1. Map showing the main features of the southern Central Andean margin. Sample locations are highlighted (blue circles) alongside the locations of the Principal Cordillera, Frontal Cordillera and Precordillera. Digital elevation data from Jarvis et al. (2008). Current active volcanic centres are indicated with grey triangles.

In the Pampean flat-slab segment, the Andean margin is divided from west to east into the Coastal Cordillera, the Principal Cordillera, the Frontal Cordillera, the Precordillera and the Sierras Pampeanas (Fig. 3.1). The age and origin of the basement varies across the Andean Cordillera depending on the extent of these

north-south trending morphostructural units. The basement of the Principal and Frontal Cordillera is composed of highly deformed Paleozoic sediments which have been intruded and covered by extensive Late Palaeozoic – Early Mesozoic plutons and volcanic rocks (Kay et al., 1989). In the Argentinean Precordillera (Fig. 3.1) a Grenville-aged basement is overlain by Cambrian – Ordovician strata (Kay and Abbruzzi, 1996; Kay et al., 1996; Ramos, 2010). As a result of both the regional geology and the changing geodynamics of the margin there is the potential for distinctive spatial contamination of mantle-derived magmas via assimilation and crustal reworking en route to the surface.

3.5 Insights from the isotopic composition of zircon

In continental arcs, the relative contributions to arc magmas, from mantle, crustal and subducted components can be difficult to constrain from whole rock geochemistry alone as it often reflects a complex history of fractional crystallisation and late stage alteration (e.g., McCarthy and Hasty, 1976; Marfil and Maiza, 2012). This is a particular problem in the southern Central Andes where the arc magmatic rocks have been affected by hydrothermal alteration (Bissig et al., 2001; Kay and Mpodozis, 2001; Bissig et al., 2003; Charchaflié et al., 2007; Litvak et al., 2007). A solution is to conduct high resolution, *in-situ* oxygen and hafnium isotopic analysis of the robust accessory mineral zircon and combine it with high resolution U-Pb dating and detailed cathdoluminescence imaging. Zircon grains potentially preserve the development of arc magmatic rocks which are not apparent from whole rock geochemistry (e.g., through the presence of xenocrystic cores and rims). The analysis of individual zircon grains, which unlike whole rocks can be readily dated and reliably analysed for $\delta^{18}O$ (robust to recent alteration), by *in-situ* techniques, enables a much more detailed picture of the relative contributions to arc magmas to be achieved.

Specifically, the combination of oxygen and hafnium isotopic variations in zircon can be used to investigate the interactions between mantle-derived melts and older crustal material (e.g., Hawkesworth and Kemp, 2006; Kemp et al., 2007). Assuming zircon crystallisation is cogenetic, zircon will retain the oxygen isotope composition of the melt from the time of crystallisation (Peck et al., 2003). Zircons crystallising in equilibrium with pristine mantle-derived melts have a narrow range of $\delta^{18}O$ values (5.3 ±0.6‰ (Valley et al., 1998; Valley, 2003)). As oxygen isotopes are sensitive to water-rock interactions and the fractionation of oxygen isotopes increases with decreasing temperature (Clayton et al., 1972), the interaction of magmas with sediments and/or low temperature altered crust leads to elevated $\delta^{18}O_{(zircon)}$ values. Thus, higher than 'mantle like' $\delta^{18}O_{(zircon)}$ values suggests the incorporation of a ^{18}O enriched supracrustal component, such as sediment, into the magma from which the zircon crystallised (e.g., Eiler, 2001).

Hafnium (Hf) is more incompatible than lutetium (Lu) during the melting of spinel and garnet peridotite. Due to the radioactive decay of ^{176}Lu to ^{176}Hf the crust becomes less radiogenic with time, relative to the mantle from which it separated (Patchett et al., 1982; Kinny and Maas, 2003). Therefore, the mixing of new mantle-derived melts with older, and hence less radiogenic crust (e.g., a Grenville-aged basement), will lead to lower epsilon Hf values (relative to CHUR) in the zircon crystallising from the magma. In addition to this, where there is no evidence for mixing with older crustal material (i.e., high initial $\varepsilon Hf_{(zircon)}$ values, 'mantle-like' $\delta^{18}O_{(zircon)}$ values and no zircon inheritance) Hf model ages can be used to identify when a primary melt differentiated from the primitive mantle (Hawkesworth and Kemp, 2006). Combining zircon U-Pb crystallisation ages with Hf model ages therefore has the potential to reveal periods of new crustal growth (e.g., Dhuime et al., 2011).

These techniques are applied to zircons separated from representative samples of both intrusive (diorites to granites) and extrusive (basaltic andesites to rhyolites) Late Cretaceous – Late Miocene arc rocks, collected from an W - E transect across the Andean Cordillera from Chile into Argentina, between 29 and 31 °S (Fig. 3.1). Zircons were also separated from a number of plutonic and volcanic rocks from the Late Palaeozoic – Early Mesozoic basement, in order to characterise a potential contaminant of the Late Cretaceous - Late Miocene arc magmas. Whole rock geochemical compositions and characterisation of all these samples is presented in Chapter 2.

Detailed petrographic analysis and cathdoluminescence imaging (Fig. 3.2) of individual zircon grains was conducted in order to identify the magmatic origin of the zircon grains, and suitable grains and specific locations for isotopic analysis (Appendix 2.1 and 2.2). This included the identification of magmatic zircon grains with simple histories and those with distinct xenocrystic cores which may reveal the nature and age of the contaminating crustal material (Fig. 3.2). Oxygen isotope compositions and U-Pb crystallisation ages were determined from the same zircon growth zones using a Cameca ims 1270 secondary ion mass spectrometer (SIMS). Subsequently, hafnium isotope analysis was conducted on a multi-collector inductively-coupled plasma mass spectrometer combined with a laser ablation system (LA-MC-ICPMS). Full details of analytical methods and data correction are presented in Appendices 1.1 (U-Pb dating), 2.3 ($\delta^{18}O$ analysis) and 2.4 (Lu-Hf isotope analysis).

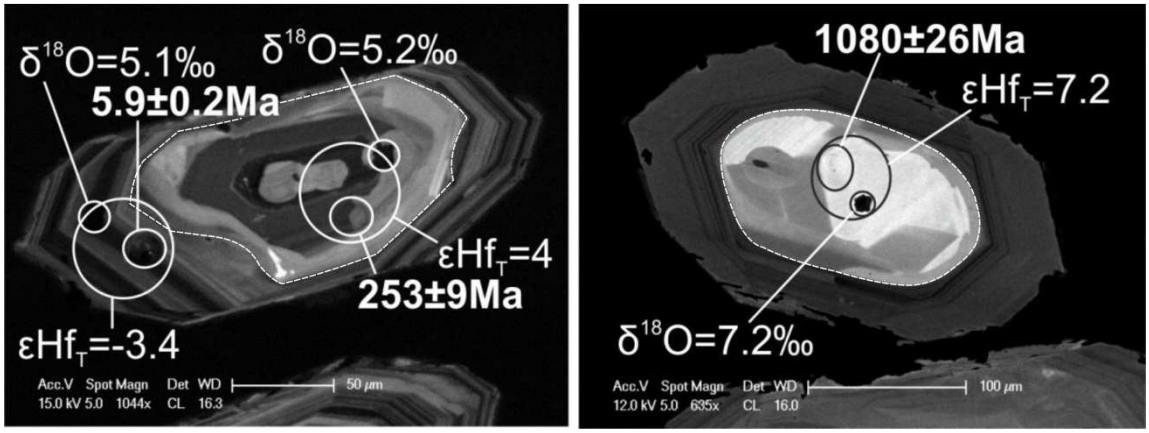

Figure 3.2. Cathodoluminescence (CL) images of select zircon grains. Highlighting the presence of inherited cores (outlined), internal growth zoning, and the locations of *in-situ* isotopic analysis. The left hand image shows a Permian inherited core surrounded by a Late Miocene aged rim present in a sample of the Vacas Heladas Ignimbrites (Frontal Cordillera). The right hand image shows a Mesoproterozoic inherited core present in a sample of the Tertiary Intrusives (Precordillera). The oxygen isotope ratios are expressed in $\delta^{18}O$ notation (‰) relative to VSMOW, the hafnium isotope values are expressed as initial εHf values (calculated using the $^{206}Pb/^{238}U$ age obtained by SIMS) and the ages (in Ma) are presented as $^{206}Pb/^{238}U$ ages. Errors are quoted at the 2σ level. Additional images are presented in Appendix 2.1.

3.6 Results demonstrating across-arc variations

Average results obtained for individual samples are presented in Table 3.1 and full results for individual zircon grains are presented in Appendix 2.10. The results of U-Pb dating were discussed in Chapter 2. The results of O and Hf isotope analysis are discussed below in relation to across-arc position (i.e., location in the Chilean Principal Cordillera (most westerly), Frontal Cordillera or Argentinean Precordillera (most easterly) (Fig. 3.3)), which also varies as a function of age.

Table 3.1

Geological Group/Formation/Unit	Sample	Cordillera	$\delta^{18}O_{(VSMOW)}$ (‰)	±2σ	*n*	$^{176}Hf/^{177}Hf$	±2σ	U-Pb age (Ma)	±2σ	$\varepsilon Hf_{(T)}$	±2σ	*n*	T(NC) (Ma)	±2σ
Pluton Tocota (Colangüil Batholith)	RJ11A18	Prec.	6.11	0.34	16	0.282681	0.000028	280.2	3.5	2.4	0.9	7		
Choiyoi Group	RJ11A20	Fontal.	6.36	0.83	12	0.282613	0.000069	269.6	7.0	-0.3	2.3	6		
	MQ39	Fontal.	5.27	1.37	11	0.282616	0.000091	269.7	2.6	-0.2	3.1	8		
	AM0862	Fontal.	5.79	1.06	10	0.282593	0.000046	269.3	5.2	-1.1	1.6	5		
Formation Plastos Blancos	AM0853	Frontal.	5.12	0.40	10	0.282701	0.000061	261.0	6.0	2.3	2.0	7		
(Ingaguás Supergroup)	AM0855	Frontal.	5.73	0.67	15	0.282622	0.000010	248.6	5.5	-0.5	0.3	3		
El León Unit (Ingaguás Supergroup)	RJ1104	Principal.	6.04	0.36	15	0.282698	0.000032	221.0	4.4	1.7	1.1	8		
Cogotí Supergroup	AM0812	Principal.	5.56	0.50	13	0.283001	0.000018	72.55	0.77	9.2	0.6	9	326	41
	AM0823	Principal.	5.64	0.64	11	0.282989	0.000022	69.80	0.73	8.7	0.8	2	353	54
	AM0815/16*[1]	Principal.	5.40	0.85	5	0.283005	0.000013	66.00	3.10	9.2	0.5	5	320	31
	AM0824	Principal.	5.52	0.54	13	0.282980	0.000023	64.59	0.65	8.3	0.8	8	378	56
	AM0806	Principal.	5.52	0.53	16	0.282997	0.000028	64.39	0.66	8.9	0.9	8	338	62
	RJ1103	Principal.	5.65	0.40	14	0.282998	0.000019	64.33	0.59	8.9	0.7	6	336	44
	AM0826	Principal.	5.40	0.39	14	0.282990	0.000020	64.21	0.69	8.6	0.7	8	354	46
	AM0822	Principal.	5.41	0.27	9	0.283002	0.000056	57.30	1.70	8.8	1.9	6	341	122
	AM0815	Principal.	5.74	0.41	6	0.283016	0.000019	55.00	1.70	9.4	0.7	6	299	44
	AM0816	Principal.	5.73	0.56	8	0.283013	0.000033	54.06	0.76	9.2	1.1	8	307	76
	RJ1101	Principal.	5.52	0.30	14	0.283044	0.000025	38.89	0.99	10.0	0.9	9	243	58
Los Elquinos Formation	AM0890	Frontal.	5.40	1.43	2	0.283002	0.000033	61.92	9.11	9.0	1.0	2	328	72
Tierras Blancas Caldera	RJ1105	Principal.	5.49	0.32	10	0.283022	0.000028	40.20	1.20	9.2	1.0	8	296	66
Botacoma Unit	AM0867	Frontal.	5.80	0.49	4	0.282836	0.000029	35.58	0.78	2.6	1.0	4		
Tilito Formation (Doña Ana Group)	AM0846	Frontal.	5.29	0.26	6	0.282842	0.000081	26.10	1.60	2.6	2.8	6		
	MQ153	Frontal.	5.63	0.85	12	0.282823	0.000047	25.20	0.26	1.9	1.6	6		
	AM0845	Frontal.	5.39	0.37	6	0.282879	0.000046	24.90	0.32	3.8	1.6	6		
	AM0860	Frontal.	4.84	0.22	10	0.282870	0.000045	24.86	0.40	3.5	1.6	5		
	ZN122	Frontal.	5.51	0.39	7	0.282820	0.000031	24.78	0.37	1.8	1.1	5		
	AM0844	Frontal.	5.14	0.46	7	0.282853	0.000025	24.72	0.28	2.9	0.9	7		
	AM0849	Frontal.	5.03	0.72	10	0.282877	0.000034	24.69	0.43	3.7	1.2	6		
	RF64	Frontal.	4.89	0.34	10	0.282886	0.000019	24.26	0.70	4.0	0.6	5		
	PC14	Frontal/Prec.	6.37	0.44	14	0.282716	0.000053	23.61	0.21	-2.0	1.9	7		

Geological Group/Formation/Unit	Sample	Cordillera	$\delta^{18}O_{(VSMOW)}$ (‰)	±2σ	*n*	$^{176}Hf/^{177}Hf$	±2σ	U-Pb age (Ma)	±2σ	$\varepsilon Hf_{(T)}$	±2σ	*n*	T(NC) (Ma)	±2σ
	Z27	Frontal.	5.02	0.53	15	0.282833	0.000061	23.18	0.30	2.2	2.1	8		
Las Trancas Formation	RJ11A5	Prec.	6.68	0.41	4	0.282816	0.000124	22.55	0.33	1.6	4.4	4		
Miocene Intrusives	RJ11A10	Prec.	6.88	0.73	15	0.282697	0.000033	22.17	0.23	-2.6	1.1	7		
	RJ11A11	Prec.	7.14	0.78	14	0.282709	0.000018	21.37	0.29	-2.2	0.6	3		
	RJ11A14	Prec.	7.15	0.42	8	0.282711	0.000058	20.43	0.31	-2.2	2.1	6		
Escabroso (Doña Ana Group)	1026	Fontal.	5.58	0.20	14	0.282802	0.000051	18.21	0.28	1.0	1.8	8		
	SP80	Frontal.	5.54	0.58	9	0.282803	0.000030	18.06	0.37	1.0	1.1	6		
Cerro de las Tórtolas Formation	RF62	Frontal.	5.13	0.35	10	0.282836	0.000020	17.06	0.63	2.2	0.7	6		
Tertiary Intrusives	RJ11A7	Prec.	5.86	0.41	8	0.282808	0.000020	11.65	0.21	1.1	0.7	6		
	RJ11A17	Prec.	6.42	0.58	10	0.282670	0.000028	9.45	0.18	-3.9	1.0	1		
	RJ11A15	Prec.	6.36	0.28	8	0.282680	0.000012	9.43	0.18	-3.5	0.9	6		
Vacas Heladas Ignimbrites	MQ33	Fontal.	5.47	0.55	9	0.282744	0.000008	6.16	0.19	-1.3	0.6	5		
	DI095	Forntal.	5.50	0.35	7	0.282744	0.000040	6.15	0.30	-1.3	2.9	7		

Table 3.1. Average oxygen and hafnium isotope data obtained for zircon populations from samples of the Permian – Triassic basement and the Late Cretaceous to Late Miocene magmatic rock samples from the southern Central Andes. In samples where there is evidence for the inheritance of xenocrystic zircon cores/grains, only oxygen and hafnium isotope analyses from un-inherited cores/grains with corresponding U-Pb ages, have been used to calculate sample averages. The oxygen isotope data is expressed in $\delta^{18}O$ notation, relative to SMOW. The $^{176}Hf/^{177}Hf$ values given are the average measured ratios, uncorrected for crystallisation age. Initial εHf values (εHf_T) were determined using individual zircon $^{206}Pb/^{238}U$ ages obtained by SIMS analysis (Appendix 2.10), and calculated using a ^{176}Lu decay constant of 1.867×10^{-11} (Söderlund et al., 2004) and present day chondritic values of $^{176}Lu/^{177}Hf = 0.0336$ and $^{176}Hf/^{177}Hf = 0.282785$ (Bouvier et al., 2008). Hf model ages (T(NC)) were calculated using the initial $^{176}Hf/^{177}Hf$ ratio (derived from the U-Pb age), a $^{176}Hf/^{177}Hf$ ratio of 0.283158 for present day new crust (NC) (Dhuime et al., 2011), and assuming a $^{176}Lu/^{177}Hf$ ratio of 0.015 (intermediate) for the source magma from which the zircon crystallized (Griffin et al., 2000). The U-Pb ages reported are sample ages given by Concordia diagrams and Tera-Wasserburg plots (Appendix 1.11). *[1] Results obtained for the older population of zircons present in samples AM0815 and AM0816. Full results are presented in Appendix 2.10.

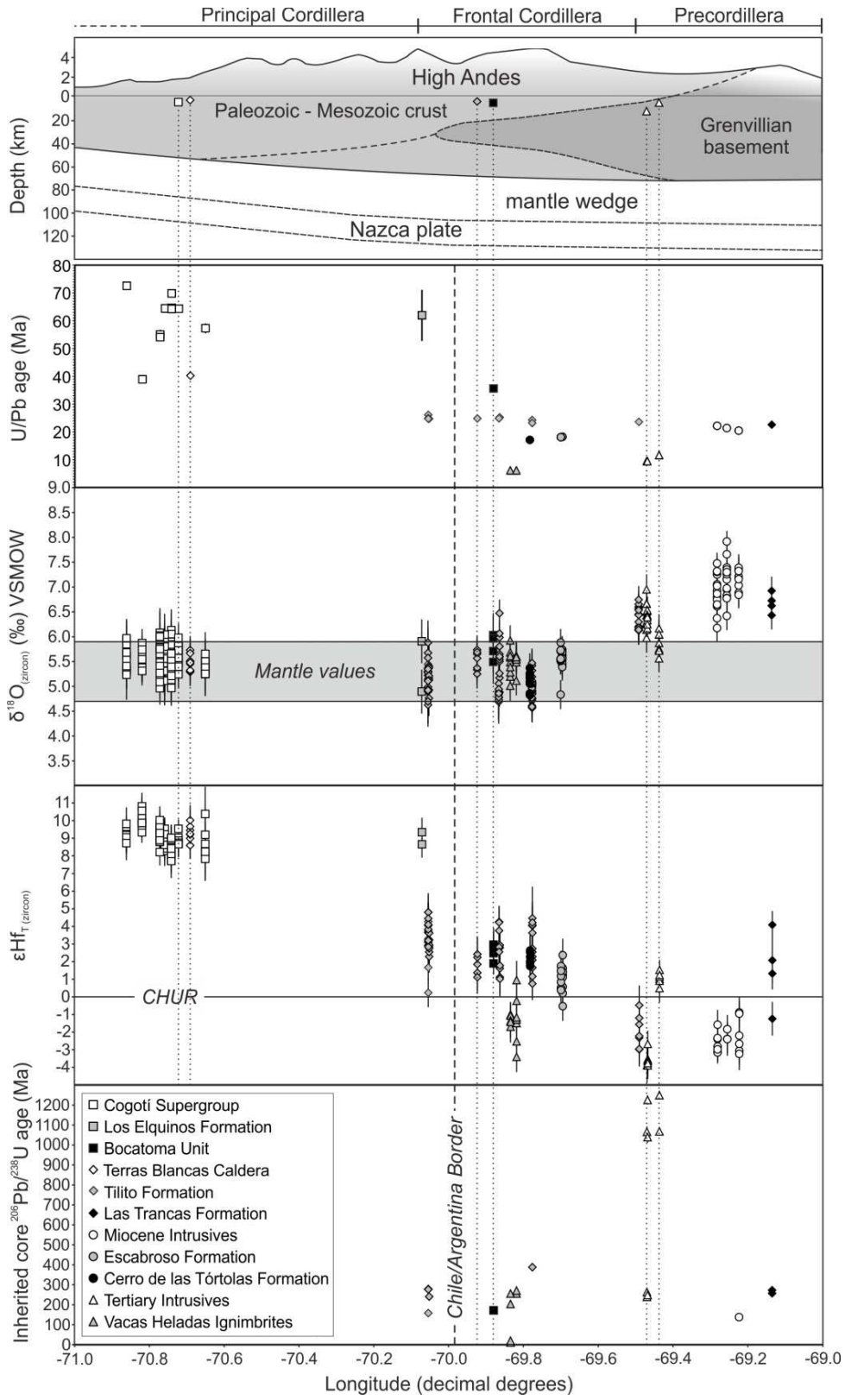

Figure 3.3 (previous page). Across arc variations in U-Pb crystallisation ages, $\delta^{18}O_{(zircon)}$, $\varepsilon Hf_{T(zircon)}$ (of rims or zircons without inherited cores) and inherited core

$^{206}Pb/^{238}U$ ages. Error bars represent 2σ values. The isotopic data is displayed relative to a schematic cross section of the modern day Andean margin at 30°S showing the extent of the different basement terranes (Ramos et al., 2002; Gilbert et al., 2006; Heit et al., 2008). Depths of crystallisation, determined by geothermobarometry (discussed in Chapter 2 and presented in Appendix 1.14), are highlighted on the cross section for a number of across arc samples. The locations of the Principal Cordillera, Frontal Cordillera, Precordillera and the Chile/Argentina border are also shown. Full results are presented in Appendix 2.10.

3.6.1 Oxygen isotopes

The $\delta^{18}O$ values obtained for individual zircon grains from the Late Cretaceous (72.6 Ma) to Eocene (38.9 Ma) plutonic rocks located in the Principal Cordillera of Chile, range between 4.96 ‰ (± 0.33 (2σ)) and 6.13 ‰ (± 0.33 (2σ)) (Fig. 3.3 and Appendix 2.10). These values are all within analytical uncertainty of those expected for zircon crystallising in isotopic equilibrium with mantle-derived melts (5.3 ‰ ± 0.6 (Valley et al., 1998)). With the exception of the most easterly sample of the Tilito Formation (PC14), the majority of $\delta^{18}O_{(zircon)}$ values obtained for the Early Paleocene (61.9 Ma) to Late Miocene (6.2 Ma) arc rocks located in the Frontal Cordillera, also lie within analytical uncertainty of 'mantle-like' values. Oxygen isotope values obtained for individual zircon grains from these primarily extrusive rocks, range between 4.57 ‰ (± 0.27 (2σ)) and 6.47 ‰ (± 0.27 (2σ)), displaying more variation than the plutonic samples from the Principal Cordillera (Fig. 3.3 and Appendix 2.10). The Late Oligocene (22.6 Ma) to Late Miocene (9.4 Ma) intrusive and extrusive arc rocks located in the Precordillera, along with the most easterly sample of the Tilito Formation (PC14, 23.6 Ma), have higher than 'mantle-like' $\delta^{18}O_{(zircon)}$ values, with values ranging from 5.57 ‰ (± 0.29 (2σ)) to 7.92 ‰ (± 0.22 (2σ)) (Fig. 3.3 and Appendix 2.10). Analysis of zircons obtained from plutonic and volcanic rocks comprising the Late Palaeozoic to Early Mesozoic basement produced varied $\delta^{18}O_{(zircon)}$ values ranging between 4.59 ‰ (±0.29 (2σ)) and 7.16 ‰ (±0.29 (2σ)) (Appendix 2.10).

3.6.2 Hafnium isotopes

Initial $\varepsilon Hf_{(zircon)}$ values obtained for individual zircon grains from the Late Cretaceous (72.6 Ma) to Eocene (38.9 Ma) plutonic rocks located in the Principal Cordillera, are distinctly positive and range between +7.7 (±1.0 (2σ)) and +10.8 (±0.8 (2σ)) (Fig. 3.3 and Appendix 2.10). These values lie close to the values projected for mantle-derived melts (i.e., new crust (NC) (Dhuime et al., 2011)), and on the basis that these zircons also have 'mantle-like' $\delta^{18}O_{(zircon)}$ values, hafnium model ages (T(NC)) ranging between 190 and 416 Ma are reported for these individual zircon grains (Fig. 3.4 and Appendix 2.10). With the exception of the Paleocene (61.9 Ma) sample of the Los Elquinos Formation, which has $\varepsilon Hf_{T(zircon)}$ values within the range of values obtained for samples of similar age located in the Principal Cordillera (Fig. 3.3), the initial $\varepsilon Hf_{(zircon)}$ values produced for the Late Eocene (35.6 Ma) – Late Miocene (6.2 Ma) volcanic rocks present in the Frontal Cordillera range between -3.4 (±0.9 (2σ)) and +4.8 (±1.0 (2σ)), with the lowest values obtained for the youngest sample (DI095, Vacas Heladas Ignimbrites) (Fig. 3.3 and Appendix 2.10). These values are significantly lower (i.e., less radiogenic), than those expected for a primary melt derived from the mantle wedge (i.e. new crust (NC)) (Fig. 3.4), suggesting the involvement of an older, less-radiogenic crustal component. The initial $\varepsilon Hf_{(zircon)}$ values produced for individual zircon grains from the Late Oligocene (22.6 Ma) to Late Miocene (9.4 Ma) samples from the Precordillera are generally lower than those obtained for the Principal and Fontal Cordillera and range between -3.9 (±0.6 (2σ)) and +4.1 (±0.8 (2σ)) (Figs. 3.3, 3.4 and Appendix 2.10). The initial $\varepsilon Hf_{(zircon)}$ values obtained from sample PC14, the most easterly sample of the Tilito Formation (23.6 Ma), lie within this range and are lower than the $\varepsilon Hf_{T(zircon)}$ values obtained for other samples of the Tilito Formation located in the Frontal Cordillera (Fig. 3.3). Analysis of zircons obtained from plutonic and volcanic rocks comprising the Late Palaeozoic to Early Mesozoic basement produced initial $\varepsilon Hf_{(zircon)}$ values ranging between -2.2 (±1.0 (2σ)) and +3.0 (±1.0 (2σ)) (Fig. 3.4 and Appendix 2.10).

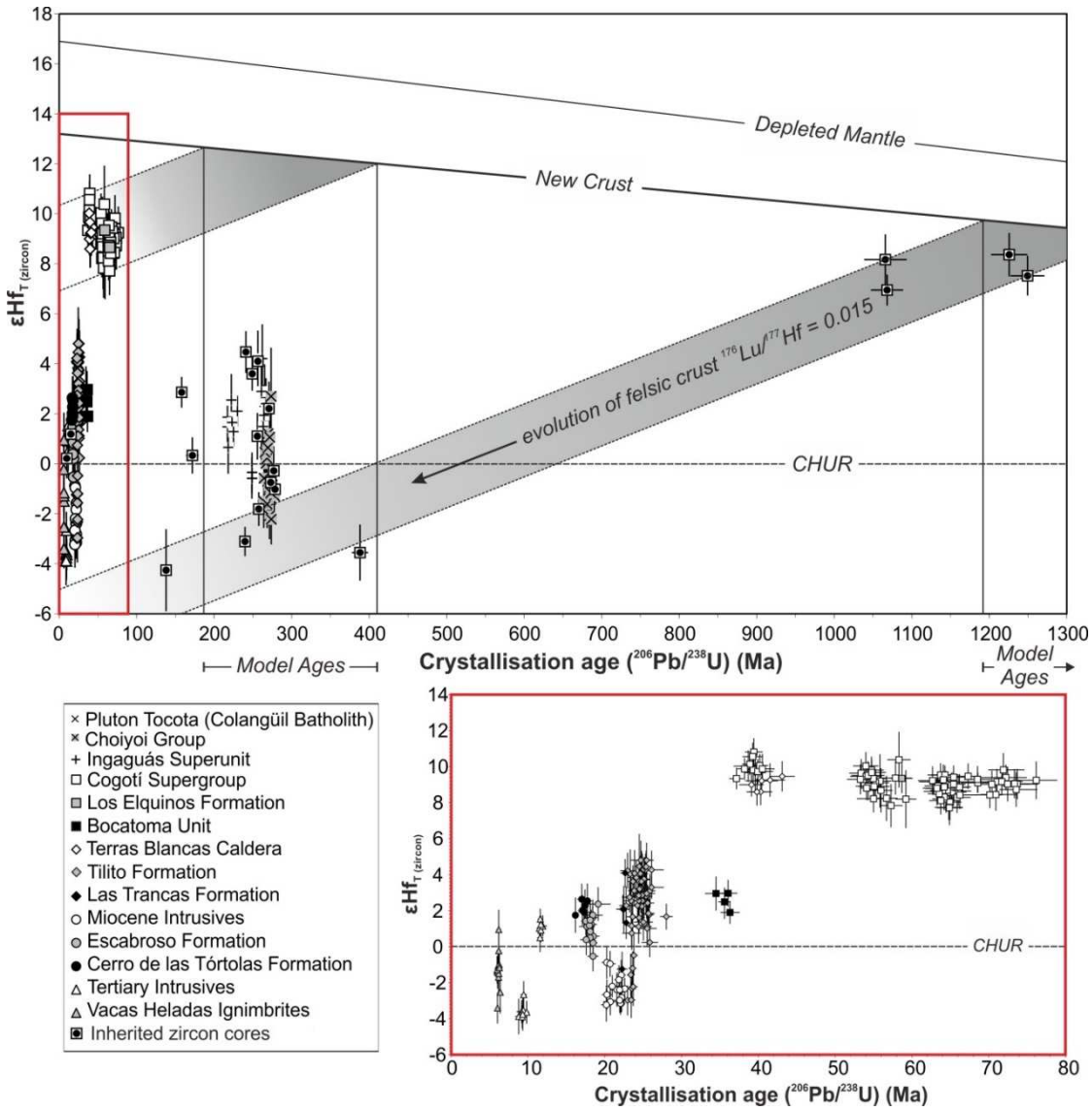

Figure 3.4. Initial $\varepsilon Hf_{(zircon)}$ values plotted against crystallisation ages ($^{206}Pb/^{238}U$) (Ma) for all zircon grains and inherited cores. The data highlighted in the red box is expanded to the bottom right. Depleted mantle (DM) and new crust (NC) evolution lines are shown along with model ages for the Late Cretaceous – Eocene intrusive samples and the Proterozoic inherited cores from the Tertiary Intrusives. Intrusive samples are shown as open symbols and extrusive samples as filled symbols. The initial $\varepsilon Hf_{(zircon)}$ values are presented relative to present day chondritic values (CHUR) (Bouvier et al., 2008). Error bars represent 2σ values. Full results are presented in Appendix 2.10.

3.6.3 Inherited, xenocrystic zircon cores

The occurrence and age of inherited, xenocrystic cores also varies as a function of across-arc position. Devonian to Cretaceous inherited zircon cores, with $^{206}Pb/^{238}U$ ages ranging between 138.1 ±5.2 Ma and 388.1 ±10.5 Ma, were obtained from Late Eocene to Late Miocene plutonic and volcanic rocks from the Frontal Cordillera and Precordillera (Fig. 3.3). These inherited cores produced varied $\delta^{18}O_{(zircon)}$ values ranging between 4.70 ‰ (±0.36 (2σ)) and 9.78 ‰ (±0.29‰ (2σ)) and initial $\varepsilon Hf_{(zircon)}$ values ranging between -4.3 (±1.6 (2σ)) and +4.5 (±0.8 (2σ)) (Fig. 3.4 and Appendix 2.10). These values are more varied than those obtained for zircons from samples of the Late Palaeozoic – Early Mesozoic basement (Fig. 3.4). Mesoproterozoic inherited cores, with $^{206}Pb/^{238}U$ ages ranging between 1249.4 ±21.9 Ma and 1039.6 ±29.0 Ma, were obtained from Late Miocene dacites and trachydacites (the Tertiary Intrusives) present in the Precordillera (Fig. 3.3). Oxygen isotope values ranging between 6.05 ‰ (±0.27 (2σ)) and 7.23 ‰ (±0.22 (2σ)) and initial $\varepsilon Hf_{(zircon)}$ values of between +7.0 (±0.6 (2σ)) and +8.4 (±0.9 (2σ)) were obtained for these inherited cores (Fig. 3.4 and Appendix 2.10). These initial $\varepsilon Hf_{(zircon)}$ values lie close to the projected values for mantle-derived melts (i.e., new crust (NC) (Dhuime et al., 2011)) and the corresponding hafnium model ages (T(NC)) range between 1391 and 1200 Ma (Fig. 3.4 and Appendix 2.10).

3.7 Discussion

3.7.1 Temporal and spatial variations in isotopic compositions

3.7.1.1 Late Cretaceous – Eocene mantle derived melts

The 'mantle-like' $\delta^{18}O_{(zircon)}$ values obtained for the Late Cretaceous to Eocene granitoids located in the Principal Cordillera, combined with the distinctly positive, initial $\varepsilon Hf_{(zircon)}$ values, which lie close to the values projected for mantle-derived melts (Figs. 3.3 and 3.4), suggests the Late Cretaceous to Eocene arc magmas received very little contamination with significantly older, upper continental crust, either in the melt source region or via crustal assimilation. The absence of any significantly older, xenocrystic zircon cores (Fig. 3.3) provides further evidence to indicate limited interaction of these arc magmas with pre-existing continental crust. This evidence supports the findings of Parada et al. (1988) and Parada (1990) who reported initial $^{87}Sr/^{86}Sr$ isotope values of between 0.7035 - 0.7045 for these Late Cretaceous – Eocene plutonic belts and attributed these relatively low values to the parent magmas being derived from the partial melting of the mantle or a mantle-derived basaltic source with virtually no continental crust involvement.

Hafnium model ages suggest the primary melts of the Late Cretaceous – Eocene magmatic belts separated from the depleted mantle during the Devonian – Triassic (Fig. 3.4). During this time interval the western margin of South America was located along the western margin of Gondwana and formed part of the Gondwanan magmatic arc (Kay et al., 1989; Charrier et al., 2007). On the basis of the Hf model ages, combined with the oxygen and hafnium isotope data, and whole rock geochemistry (Chapter 2), it is suggested that the Late Cretaceous (72.6 Ma) to Eocene (38.9 Ma) arc magmas were derived from the asthenospheric mantle wedge with a very minor addition from subducted Paleozoic – Early Mesozoic crust, derived either from the Gondwanan magmatic arc, due to erosion or subduction erosion, and/or a lower crustal reservoir which separated from the mantle during the Gondwanan tectonic cycle. This addition is required to account for initial

$\varepsilon Hf_{(zircon)}$ values which are slightly lower (i.e. less radiogenic) than those expected for melts derived directly from the mantle (Fig. 3.4).

3.7.1.2 Controls on Late Eocene – Late Miocene isotopic variability

As previously mentioned, the contamination of arc magmas with older crustal material can occur either during magma ascent through the crust via crustal assimilation or via the subduction of upper crustal material (including that derived from subduction erosion) to depth (e.g., Davidson, 1987; Hildreth and Moorbath, 1988; Sigmarsson et al., 1990; Stern, 1991; Kilian and Behrmann, 2003). If the melt source was being contaminated little intra- and inter- grain variation in isotopic values for samples of similar ages/from the same formations might be expected, reflecting the crystallisation of zircon from magmas of similar, source derived compositions. A temporal correlation with $\delta^{18}O_{(zircon)}$ and $\varepsilon Hf_{(zircon)}$ values might also be anticipated, reflecting the subduction of different amounts of sediment and/or continental crust from subduction erosion, over time. For example, subduction erosion has been identified an episodic process along the Central Andean margin (Kay et al., 2005; Stern, 2011), and the JFR is thought to have acted as a barrier to the transport of sediments into the trench from farther south (e.g., Bangs and Cande, 1997), after its intersection with the margin at ~20 Ma (Yañez et al., 2001; Yañez et al., 2002). However, the variability in $\delta^{18}O_{(zircon)}$ and $\varepsilon Hf_{(zircon)}$ values obtained for Late Eocene to Late Miocene arc magmatic rocks appears to be spatially, not temporally correlated (Fig. 3.3). For example, sample PC14 (23.6 Ma) is the most easterly sample of the Tilito Formation (Late Oligocene) and is located close to the boundary with the Precordillera, it displays distinctly different $\delta^{18}O_{(zircon)}$ and $\varepsilon Hf_{T(zircon)}$ values compared to other samples from the same formation and of the same age located in the Frontal Cordillera (Fig. 3.3). Furthermore, the youngest samples (Vacas Heladas Ignimbrites), are located in the High Andes of the Frontal Cordillera and have $\delta^{18}O_{(zircon)}$ values which lie within the range of values obtained for other, older samples present in the Frontal Cordillera (Fig. 3.3). Significant intra- and inter-grain

variability, particularly in $\varepsilon Hf_{(zircon)}$ values (Fig. 3.3), is also displayed in a number of Late Eocene – Late Miocene samples, which suggests the isotopic composition of the magma was evolving during zircon crystallisation and was not solely determined in the melt source region.

The basement underlying the Frontal Cordillera is composed of highly deformed Paleozoic sediments which have been intruded and covered by extensive Late Palaeozoic – Early Mesozoic plutons and volcanic rocks (Kay et al., 1989). The assimilation of Paleozoic sediments by Late Eocene to Late Miocene arc magmas would result in elevated $\delta^{18}O_{(zircon)}$ values relative to the mantle. However, the majority of $\delta^{18}O_{(zircon)}$ values obtained for the Late Eocene to Late Miocene samples from the Frontal Cordillera are 'mantle-like', suggesting the contaminant must have close to 'mantle-like' $\delta^{18}O$ values. Analysis of zircons from Permian – Triassic plutonic and volcanic rocks present in the Frontal Cordillera, sampled as part of this study, produced average $\delta^{18}O$ values ranging between 5.1‰ (±0.4‰, *n*=10) and 6.4‰ (±0.9‰, *n*=12) (Table 3.1). Bulk mixing models using the average $\delta^{18}O_{(zircon)}$ values obtained for the Permian - Triassic samples and the projected Permian - Triassic $\varepsilon Hf_{(zircon)}$ values (Fig. 3.4), suggests mixing of typically <20 % of this crust with new mantle-derived melts (NC) (Dhuime et al., 2011) can produce the modest $\delta^{18}O$ but more marked Hf isotopic variability observed in the Late Eocene to Late Miocene samples from the Frontal Cordillera (Fig. 3.5). The presence of primarily Permian – Triassic inherited zircon cores in these samples (Fig. 3.3) supports the assimilation of continental crust of this age.

The Late Oligocene – Late Miocene granitoids, andesites and rhyolites, located in the Precordillera of Argentina have higher than 'mantle-like' $\delta^{18}O_{(zircon)}$ values and un-radiogenic values of $\varepsilon Hf_{T(zircon)}$ (Figs. 3.3, 3.4 and Table 3.1), which are quite distinct from the values obtained in the Principal and Frontal Cordillera. This suggests the interaction of these arc magmas with an ancient, and hence un-

radiogenic (with respect to Hf), crustal reservoir which has experienced low temperature interaction with the near surface, accounting for the elevated $\delta^{18}O$ values. Although no crystalline basement is exposed in the Precordillera, evidence from high-grade metamorphic, xenoliths present in the Miocene volcanic rocks indicates a Grenville-aged basement (Abbruzzi et al., 1993; Kay and Orrell, 1996). It has been suggested that this basement forms part of a rifted fragment of Laurentian continental crust and passive margin cover which was accreted onto the margin of Gondwana during the Ordovician (Sato et al., 2000; Thomas and Astini, 2003). Convincing evidence for the contamination of the Late Oligocene – Late Miocene magmas with this Grenville-aged crust is provided by the presence of inherited Proterozoic cores in a number of the samples present in the Precordillera (Fig. 3.3). This Grenville-aged basement is likely to have unradiogenic, negative εHf values, as shown by projecting the $\varepsilon Hf_{(zircon)}$ values obtained for the Proterozoic cores to the Cenozoic (Fig. 3.4). In addition to this, passive margin cover is likely to have high $\delta^{18}O$ values reflecting low temperature, near surface processes. Bulk mixing suggests that contamination of mantle-derived melts (NC) with up to 15% Proterozoic aged, sedimentary crust can account for the observed isotopic array displayed in zircons from the Late Oligocene – Late Miocene arc rocks of the Argentinian Precordillera (Fig. 3.5). This corroborates the work of Kay and Abbruzzi (1996), who suggest that that mixing between melts derived from the mantle wedge and a Grenville-aged basement accounts for the distinct geochemistry of the Miocene arc magmatic rocks present in the Argentinean Precordillera. However, the presence of inherited cores of Permian to Cretaceous age (Fig. 3.3) suggests that the mantle-derived melts also assimilated Late Paleozoic – Mesozoic crust en route to the surface, and hence the O and Hf isotopic values are more likely to reflect three way mixing processes between mantle-derived melts, a Grenville-aged basement and Late Paleozoic – Mesozoic Andean crust.

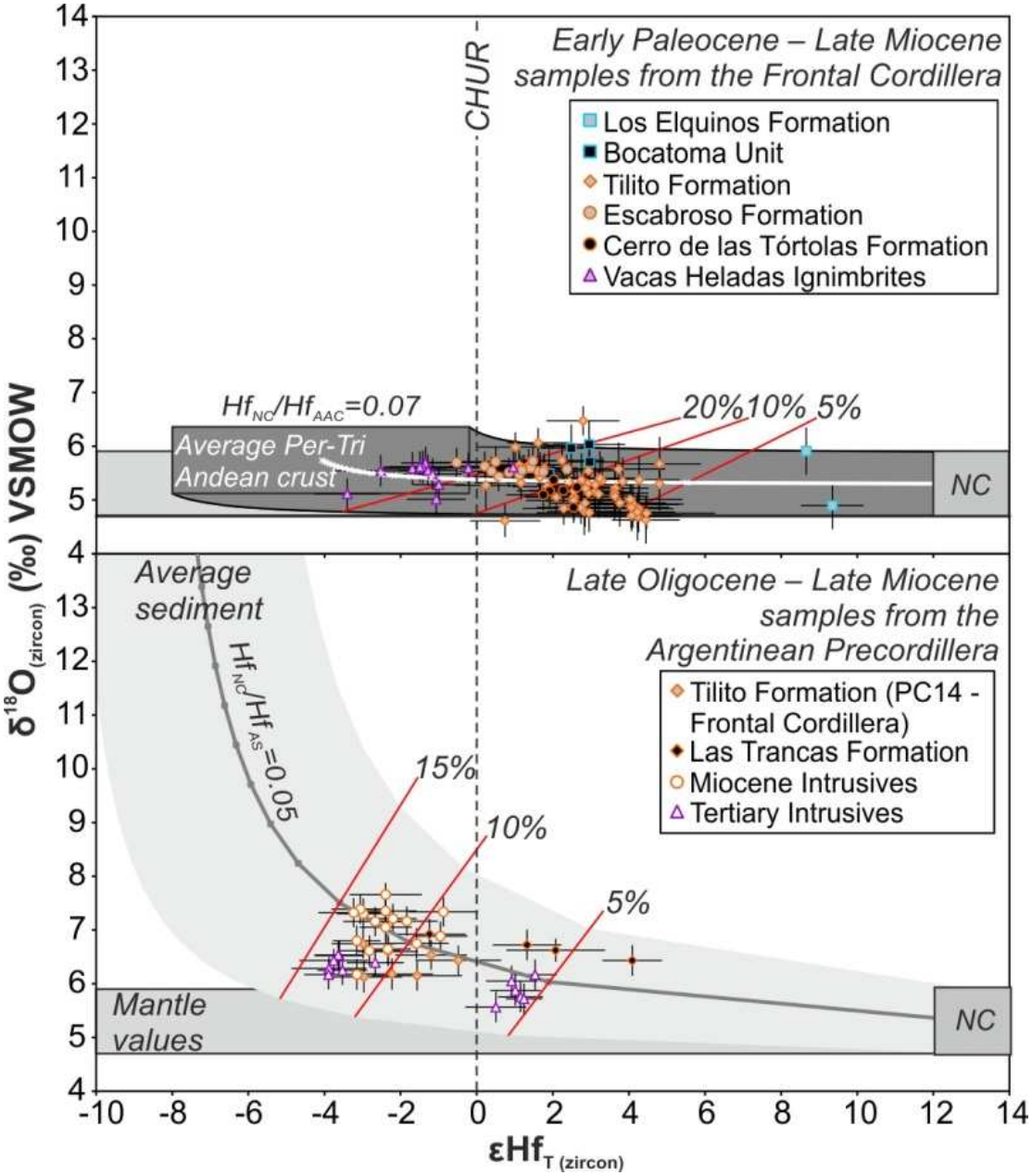

Figure 3.5. Initial $\varepsilon Hf_{(zircon)}$ plotted against the corresponding $\delta^{18}O_{(zircon)}$ for Early Paleocene – Late Miocene samples from the Frontal Cordillera (top) and Late Oligocene – Late Miocene samples from the Argentinean Precordillera (bottom). Bulk mixing between mantle-derived melts (NC) and the Permian – Triassic basement (using a Hf_{NC}/Hf_{ACC} of 0.07) is generates the observed variability in the Early Paleocene – Late Miocene samples from the Frontal Cordillera. Up to 15% bulk mixing between mantle-derived melts (NC) and average sediment (AS) (Savin and Epstein, 1970; Plank and Langmuir, 1998) (using a Hf_{NC}/Hf_{AS} of 0.05) explains the isotopic variability observed in the Late Oligocene – Late Miocene samples from the Argentinean Precordillera. Average sediment values are used to represent the

basement present in the Precordillera which is suggested to be passive margin cover of Grenville-age. The shaded areas represent mixing between mantle-derived melts and the upper and lower values.

The lower $\varepsilon Hf_{T(zircon)}$ values obtained for the youngest volcanic arc samples in the study area, the Vacas Heladas Ignimbrites (~6 Ma) located in the Frontal Cordillera, suggests that these arc magmas may also have interacted with ancient, and hence un-radiogenic, portion of Andean continental crust. Structural models suggest that the Grenville-aged basement currently underthrusts the Frontal Cordillera (e.g., Ramos et al., 2004; Gilbert et al., 2006; Gans et al., 2011). Consequently the $\varepsilon Hf_{T(zircon)}$ values obtained for the Vacas Heladas Ignimbrites, which overlap those obtained for magmatic rocks present in the Precordillera, may reflect the arrival of the Grenville-aged basement under this region of the Frontal Cordillera due to increased crustal shortening (Kley and Monaldi, 1998; Ramos et al., 2002 and references therein). A conclusion reached by Muñoz et al. (2013) to explain the development of enriched εNd_i values (ranging between +2 and -2) for arc magmas erupted after 4.8 Ma, to the south of the study region in the northern, southern volcanic zone (SVZ). A similar whole rock εNd value of -2.0 has been reported for the Vacas Heladas Ignimbrites, and this εNd value is more enriched than those obtained for older arc magmatic rocks present in the Frontal Cordillera (e.g., the Tilito Formation, εNd = +1.2 to -0.1) (Kay et al., 1991), thus supporting the contamination of the Late Miocene arc magmas with older, un-radiogenic continental crust.

3.8 Conclusions

During the early stages of Andean-type subduction (Late Cretaceous – Eocene) extensive magmatic belts were formed from mantle-derived melts with a very minor addition of subducted Paleozoic to Early Mesozoic continental crust, and/or a lower crust which differentiated from the mantle during the Gondwanan tectonic cycle. This time interval therefore represents a sustained period (~35 Ma) of upper crustal growth with magmas which had little interaction with upper crustal material, either in the melt source region due to subduction, or during ascent through the crust via crustal assimilation. As the Nazca plate shallowed, the continental crust thickened, and arc magmatism migrated to the east, the Late Eocene to Late Miocene mantle-derived magmas became contaminated (via assimilation) with distinct basement domains. The Late Eocene (~36 Ma) to Early Miocene (~17 Ma) arc magmas present in the Frontal Cordillera assimilated up to ~20 % Late Paleozoic – Early Mesozoic basement, as is evidenced by the O and Hf isotopic composition of zircon combined with the ages of inherited, xenocrystic zircon cores. Isotopic evidence and the range of U-Pb ages obtained for inherited zircon cores (Mesoproterozoic, Permian-Triassic and Cretaceous) suggests the Late Oligocene (23 Ma) to Late Miocene (9 Ma) arc magmas erupted and emplaced in the Argentinean Precodillera, as well as the most easterly sample of the Tilito Formation (24 Ma), assimilated both a Grenville-aged basement and Late Paleozoic – Mesozoic crust. The Late Miocene (~6 Ma) arc magmas erupted in the Frontal Cordillera also display isotopic evidence for contamination with both Grenville-aged and Late Paleozoic – Early Mesozoic crust. This potentially signals the arrival of the Grenville-aged basement terrane beneath the Frontal Cordillera, as a result of increased compression and crustal shortening over the later part of the Miocene.

During the Late Eocene to Late Miocene the products of subduction erosion and sediments present in the Chile trench may well have entered and influenced the

melt source region in the asthenospheric mantle wedge, as is suggested by high rates of subduction erosion (e.g., Stern, 2011) and exhumation (e.g., Kurtz et al., 1997; Maksaev et al., 2003; Spikings et al., 2008) along the increasingly compressional Central Andean margin. However, any effect which this subducted continental material had on the isotopic composition of the arc magmas in the melt source region appears to have been overprinted by the assimilation of the overlying crust en route to the surface, as is evidenced by the across-arc O and Hf isotopic variations, which reflect distinct basement terranes. Subduction erosion could potentially move continental crust laterally, however, this is still unlikely to generate the observed across-arc isotopic array that correlates so well with the composition of the Andean basement. Overall this demonstrates that the pre-existing continental crust, which is spatially variable over the Andean Cordillera, played a dominant role over the contamination of mantle wedge with subducting components in modifying the isotopic composition of the Late Eocene to Late Miocene mantle-derived melts and suggests that the later part of the Cenozoic represents a sustained period of crustal reworking.

This study successfully demonstrates how combining the *in-situ* analysis of the oxygen and hafnium isotopic composition of magmatic zircon, with high resolution U-Pb dating, can be used to identify the spatial contamination of arc magmas with specific portions of crust during one tectonic cycle. The applied geochemical techniques highlight significant variations both temporally and spatially in magma composition which can be correlated with changing subduction zone geodynamics. Specifically, with the shallowing of the subducting Nazca plate and the consequent expansion and migration of arc magmatism, as well as with the tectonic shortening and thickening of the overriding Andean crust during the Miocene. This has significant implications for models of continental growth, in particular in settings where the geodynamics and plate tectonics are poorly understood, demonstrating that wide variations in $\delta^{18}O_{(zircon)}$ and $\varepsilon Hf_{(zircon)}$ values can be generated over

relatively short distances (10s kms), depending on the age and composition of the overlying continental crust.

3.9 References

Abbruzzi, J., Kay, S.M., and Bickford, M.E., 1993, Implications for the nature of the Precordilleran basement from the geochemistry and age of Precambrian xenoliths in Miocene volcanic rocks, San Juan province: Actas, v. 3, p. 331-339.

Bangs, N.L., and Cande, S.C., 1997, Episodic development of a convergent margin inferred from structures and processes along the southern Chile margin: Tectonics, v. 16, p. 489 - 503.

Bissig, T., Clark, A.H., Lee, J.K., and von Quadt, A., 2003, Petrogenetic and metallogenetic responses to Miocene slab flattening: new constraints from the El Indio-Pascua Au–Ag–Cu belt, Chile/Argentina: Mineralium Deposita, v. 38, p. 844-862.

Bissig, T., Lee, J.K.W., Clark, A.H., and Heather, K.B., 2001, The Cenozoic History of Volcanism and Hydrothermal Alteration in the Central Andean Flat-Slab Region: New 40Ar-39Ar Constraints from the El Indio–Pascua Au (-Ag, Cu) Belt, 29°20′–30°30′ S: International Geology Review, v. 43, p. 312-340.

Bouvier, A., Vervoort, J.D., and Patchett, P.J., 2008, The Lu-Hf and Sm-Nd isotopic composition of CHUR: Constraints from unequilibrated chondrites and implications for the bulk composition of terrestrial planets: Earth and Planetary Science Letters, v. 273, p. 48-57.

Burchfiel, B.C., 1993, Evolution of Continental and Oceanic Crust: Proceedings of the American Philosophical Society, v. 137, p. 1-29.

Charchaflié, D., Tosdal, R.M., and Mortensen, J.K., 2007, Geologic framework of the Veladero high-sulfidation epithermal deposit area, Cordillera Frontal, Argentina: Economic Geology, v. 102, p. 171-192.

Charrier, R., Pinto, L., and Rodríguez, M.P., 2007, Tectonostratigraphic evolution of the Andean Orogen in Chile, *in* Moreno, T., and Gibbons, W., eds., The Geology of Chile: London, The Geological Society, p. 21 - 114.

Clayton, R.N., O'Neil, J.R., and Mayeda, T.K., 1972, Oxygen isotope exchange between quartz and water: Journal of Geophysical Research, v. 77, p. 3057-3067.

Davidson, J.P., 1987, Crustal contamination versus subduction zone enrichment: Examples from the Lesser Antilles and implications for mantle source compositions of island arc volcanic rocks: Geochimica et Cosmochimica Acta, v. 51, p. 2185-2198.

Davidson, J.P., Harmon, R.S., and Wörner, G., 1991, The source of central Andean magmas; Some considerations: Geological Society of America Special Papers, v. 265, p. 233-244.

Dhuime, B., Hawkesworth, C., and Cawood, P., 2011, When Continents Formed: Science, v. 331, p. 154-155.

Eiler, J.M., 2001, Oxygen isotope variations of basaltic lavas and upper mantle rocks: Reviews in Mineralogy and Geochemistry, v. 43, p. 319-364.

Elliott, T., Plank, T., Zindler, A., White, W., and Bourdon, B., 1997, Element transport from slab to volcanic front at the Mariana arc: Journal of Geophysical Research, v. 102, p. 14991 - 15019.

Gans, C.R., Beck, S.L., Zandt, G., Gilbert, H., Alvarado, P., Anderson, M., and Linkimer, L., 2011, Continental and oceanic crustal structure of the Pampean flat slab region, western Argentina, using receiver function analysis: new high-resolution results: Geophysical Journal International, v. 186, p. 45-58.

Gilbert, H., Beck, S., and Zandt, G., 2006, Lithospheric and upper mantle structure of central Chile and Argentina: Geophysical Journal International, v. 165, p. 383-398.

Gill, J.B., 1981, Orogenic Andesites and Plate Tectonics: New York, Springer-Verlag.

Goss, A.R., Kay, S.M., and Mpodozis, C., 2013, Andean Adakite-like high-Mg Andesites on the Northern Margin of the Chilean–Pampean Flat-slab (27–28· 5° S) Associated with Frontal Arc Migration and Fore-arc Subduction Erosion: Journal of Petrology, v. 54, p. 2193-2234.

Griffin, W.L., Pearson, N.J., Belousova, E., Jackson, S.E., van Achterbergh, E., Oâ€™Reilly, S.Y., and Shee, S.R., 2000, The Hf isotope composition of cratonic mantle: LAM-MC-ICPMS analysis of zircon megacrysts in kimberlites: Geochimica et Cosmochimica Acta, v. 64, p. 133-147.

Haschke, M., Siebel, W., Günther, A., and Scheuber, E., 2002, Repeated crustal thickening and recycling during the Andean orogeny in north Chile (21°–26°S): Journal of Geophysical Research: Solid Earth, v. 107, p. ECV 6-1-ECV 6-18.

Hawkesworth, C.J., and Kemp, A.I.S., 2006, Using hafnium and oxygen isotopes in zircons to unravel the record of crustal evolution: Chemical Geology, v. 226, p. 144 - 162.

Heit, B., Yuan, X., Bianchi, M., Sodoudi, F., and Kind, R., 2008, Crustal thickness estimation beneath the southern central Andes at 30ºS and 36ºS from S wave receiver function analysis: Geophysical Journal International.

Hildreth, W., and Moorbath, S., 1988, Crustal contributions to arc magmatism in the Andes of Central Chile: Contributions to Mineralogy and Petrology, v. 98, p. 455 - 489.

Jarvis, A., Reuter, H.I., Nelson, A., and Guevara, E., 2008, Hole-filled SRTM for the globe Version 4, available from the CGIAR-CSI SRTM 90m Database.

Jordon, T.E., Burns, W.M., Veiga, R., Pángaro, F., Copeland, P., Kelley, S., and Mpodozis, C., 2001, Extension and basin formation in the southern Andes caused by increased convergence rate: A mid-Cenozoic trigger for the Andes: Tectonics, v. 20, p. 308 - 324.

Kay, S.M., and Abbruzzi, J.M., 1996, Magmatic evidence for Neogene lithospheric evolution of the central Andean "flat slab" between 30ºS and 32ºS: Tectonophysics, v. 259, p. 15 - 28.

Kay, S.M., Godoy, E., and Kurtz, A., 2005, Episodic arc migration, crustal thickening, subduction erosion, and magmatism in the south-central Andes: Geological Society of America Bulletin, v. 117, p. 67-88.

Kay, S.M., Maksaev, V., Moscoso, R., Mpodozis, C., and Nasi, C., 1987, Probing the evolving Andean lithosphere; Mid - Late Tertiary magmatism in Chile (29º - 30º30'S) over the modern zone of subhorizontal subduction: Journal of Geophysical Research, v. 92, p. 6173 - 6189.

Kay, S.M., and Mpodozis, C., 2001, Central Andean ore deposits linked to evolving shallow subduction systems and thickening crust: GSA Today, v. 11, p. 4-9.

Kay, S.M., and Mpodozis, C., 2002, Magmatism as a probe to the Neogene shallowing of the Nazca plate beneath the modern Chilean flat slab: Journal of South American Earth Sciences, v. 15, p. 39 - 57.

Kay, S.M., Mpodozis, C., Ramos, V.A., and Munizaga, F., 1991, Magma source variations for mid-late Tertiary magmatic rocks associated with a shallowing subduction zone and the thickening crust in the central Andes (28-33ºS): Spec. Pap. Geological Society of America Bulletin, v. 265, p. 113 - 137.

Kay, S.M., and Orrell, S., 1996, Zircon and whole rock Nd-Pb isotopic evidence for a Grenville age and a Laurentian origin for the Basement of the Precordillera in Argentina: Journal of Geology, v. 104, p. 637.

Kay, S.M., Orrell, S., and Abbruzzi, J., 1996, Zircon and whole rock Nd-Pb isotopic evidence for a Grenville age and a Laurentian origin for the basement of the Precordillera in Argentina: The Journal of Geology, p. 637-648.

Kay, S.M., Ramos, V.A., Mpodozis, C., and Sruoga, P., 1989, Late Paleozoic to Jurassic silicic magmatism at the Gondwana margin: Analogy to the Middle Proterozoic in North America?: Geology, v. 17, p. 324-328.

Kemp, A.I.S., Hawkesworth, C.J., Foster, G.L., Paterson, B.A., Woodhead, J.D., Hergt, J.M., Gray, C.M., and Whitehouse, M.J., 2007, Magmatic and crustal differentiation history of granitic rocks from Hf-O isotopes in zircon: Science, v. 315, p. 980 - 983.

Kilian, R., and Behrmann, J.H., 2003, Geochemical constraints on the sources of Southern Chile Trench sediments and their recycling in arc magmas of the Southern Andes: Journal of the Geological Society, v. 160, p. 57-70.

Kinny, P.D., and Maas, R., 2003, Lu–Hf and Sm–Nd isotope systems in zircon, *in* Hanchar, J.M., and Hoskin, P.W.O., eds., Zircon: Reviews in Mineralogy and Geochemistry: Washington DC, Mineralogical Society of America/Geochemical Society, p. 327 – 339.

Kley, J., and Monaldi, C.R., 1998, Tectonic shortening and crustal thickness in the Central Andes: How good is the correlation?: Geology, v. 26, p. 723-726.

Kurtz, A.C., Kay, S.M., Charrier, R., and Farrar, E., 1997, Geochronology of Miocene plutons and exhumation history of the El Teniente region, Central Chile (34-35° 8): Andean Geology, v. 24, p. 75-90.

Litvak, V.D., Poma, S., and Kay, S.M., 2007, Paleogene and Neogene magmatism in the Valle del Cura region: New perspective on the evolution of the Pampean flat slab, San Juan province, Argentina: Journal of South American Earth Sciences, v. 24, p. 117 - 137.

Lonsdale, P., 2005, Creation of the Cocos and Nazca plates by fission of the Farallon plate: Tectonophysics, v. 404, p. 237-264.

Maksaev, V., Zentilli, M., Munizaga, F., and Charrier, R., 2003, Denudación/alzamiento del Mioceno Superior–Plioceno Inferior de la Cordillera de Chile Central (33º–35ºS) inferida por dataciones por trazas de fisión en apatito de plutones miocenos, Congreso Geológico Chileno.

Marfil, S., and Maiza, P., 2012, Geochemistry of Hydrothermal Alteration in Volcanic Rocks, *in* Panagiotaras, D., ed., Geochemistry - Earth's System Processes.

McCarthy, T.S., and Hasty, R.A., 1976, Trace element distribution patterns and their relationship to the crystallization of granitic melts: Geochimica et Cosmochimica Acta, v. 40, p. 1351-1358.

Muñoz, M., Farías, M., Charrier, R., Fanning, C.M., Polvé, M., and Deckart, K., 2013, Isotopic shifts in the Cenozoic Andean arc of central Chile: Records of an evolving basement throughout cordilleran arc mountain building: Geology, v. 41, p. 931-934.

Parada, M.A., 1990, Granitoid plutonism in central Chile and its geodynamic implications; A review, *in* Kay, S.M., and Rapela, C.W., eds., Plutonism from Antarctica to Alaska, Volume Special Paper 241: Boulder, Colorado, The Geological Society of America.

Parada, M.A., Rivano, S., Sepulveda, P., Herve, M., Herve, F., Puig, A., Munizaga, F., Brook, M., Pankhurst, R., and Snelling, N., 1988, Mesozoic and Cenozoic plutonic development in the Andes of central Chile (30º30' - 32º30'S) Journal of South American Earth Sciences, v. 1, p. 249 - 260.

Pardo Casas, F., and Molnar, P., 1987, Relative motion of the Nazca (Farallón) and South America plates since Late Cretaceous time Tectonics, v. 6, p. 233 - 248.

Patchett, J.P., Kouvo, O., Hedge, C., and Tatsumoto, M., 1982, Evolution of continental crust and mantle heterogeneity: Evidence from Hf isotopes: Contributions to Mineralogy and Petrology, v. 78, p. 279-297.

Peck, W.H., Valley, J.W., and Graham, C.M., 2003, Slow oxygen diffusion rates in igneous zircons from metamorphic rocks: American Mineralogist, v. 88, p. 1003-1014.

Pichowiak, S., Buchelt, M., and Damm, K., 1990, Magmatic activity and tectonic setting of the early stages of the Andean cycle in northern Chile: Plutonism from Antarctica to Alaska (Kay, SM; Rapela, CW, editors) Geological Society of America, Special Paper, v. 241, p. 127-144.

Pilger, R.H., 1981, Plate reconstructions, aseismic ridges, and low angle subduction beneath the Andes: Geological Society of America Bulletin, v. 92, p. 448 - 456.

Pilger, R.H., 1984, Cenozoic plate kinematics, subduction and magmatism: South American Andes: Journal of Geological Society London, v. 141, p. 793 - 802.

Plank, T., and Langmuir, C.H., 1998, The chemical composition of subducting sediment and its consequences for the crust and mantle: Chemical Geology, v. 145, p. 325 - 394.

Ramos, V.A., 2010, The Grenville-age basement of the Andes: Journal of South American Earth Sciences, v. 29, p. 77-91.

Ramos, V.A., Cristallini, E., and Pérez, D.J., 2002, The Pampean flat-slab of the Central Andes: Journal of South American Earth Sciences, v. 15, p. 59-78.

Ramos, V.A., Jordan, T.E., Allmendinger, R.W., Mpodozis, C., Kay, S.M., Cortés, J.M., and Palma, M., 1986, Paleozoic terranes of the central Argentine-Chilean Andes: Tectonics, v. 5, p. 855-880.

Ramos, V.A., Zapata, T., Cristallini, E., and Introcaso, A., 2004, The Andean thrust system—Latitudinal variations in structural styles and orogenic shortening: Thrust tectonics and hydrocarbon systems, v. 82, p. 30-50.

Rutland, R.W.R., 1971, Andean Orogeny and Ocean Floor Spreading: Nature, v. 233, p. 252 - 255.

Sato, A., Tickyj, H., Llambıas, E., and Sato, K., 2000, The Las Matras tonalitic–trondhjemitic pluton, central Argentina: Grenvillian-age constraints, geochemical characteristics, and regional implications: Journal of South American Earth Sciences, v. 13, p. 587-610.

Savin, S.M., and Epstein, S., 1970, The oxygen and hydrogen isotope geochemistry of clay minerals: Geochimica et Cosmochimica Acta, v. 34, p. 25-42.

Sigmarsson, O., Condomines, M., Morris, J.D., and Harmon, R.S., 1990, Uranium and 10Be enrichments by fluids in Andean arc magmas: Nature, v. 346, p. 163-165.

Söderlund, U., Patchett, P.J., Vervoort, J.D., and Isachsen, C.E., 2004, The 176Lu decay constant determined by Lu-Hf and U-Pb isotope systematics of Precambrian mafic intrusions: Earth and Planetary Science Letters, v. 219, p. 311-324.

Somoza, R., 1998, Updated Nazca (Farallon) - South America relative motions during the last 40My: implications for mountain building in the central Andean region: Journal of South American Earth Sciences, v. 11, p. 211 - 215.

Somoza, R., and Ghidella, M.E., 2012, Late Cretaceous to recent plate motions in western South America revisited: Earth and Planetary Science Letters, v. 331–332, p. 152-163.

Spikings, R., Dungan, M., Foeken, J., Carter, A., Page, L., and Stuart, F., 2008, Tectonic response of the central Chilean margin (35–38 S) to the collision and subduction of heterogeneous oceanic crust: a thermochronological study: Journal of the Geological Society, v. 165, p. 941-953.

Stern, C.R., 1991, Role of subduction erosion in the generation of Andean magmas: Geology, v. 19, p. 78 - 81.

Stern, C.R., 2004, Active Andean volcanism: its geologic and tectonic setting Revista Geológica de Chile, v. 31, p. 161 - 206.

Stern, C.R., 2011, Subduction erosion: rates, mechanisms, and its role in arc magmatism and the evolution of the continental crust and mantle: Gondwana Research, v. 20, p. 284-308.

Thomas, W.A., and Astini, R.A., 2003, Ordovician accretion of the Argentine Precordillera terrane to Gondwana: a review: Journal of South American Earth Sciences, v. 16, p. 67-79.

Valley, J.W., 2003, Oxygen isotopes in zircon, *in* Hanchar, J.M., and Hoskin, P.W.O., eds., Zircons, Volume 53: Chantilly, Virginia, Reviews in Mineralogy and Geochemistry, Mineralogical Society of America, p. 343 - 386.

Valley, J.W., Kinny, P.D., Schulze, D.J., and Spicuzza, M.J., 1998, Zircon megacrysts from kimberlite: oxygen isotope variability among mantle melts: Contributions to Mineralogy and Petrology, v. 133, p. 1-11.

Von Huene, R., and Scholl, D.W., 1991, Observations at convergent margins concerning sediment subduction, subduction erosion, and the growth of continental crust: Reviews of Geophysics, v. 29.

Yañez, G.A., Cembrano, J., Pardo, M., Ranero, C.R., and Selles, D., 2002, The Challenger - Juan Fernández - Maipo major tectonic transition of the Nazca - Andean subduction system at 33-34ºS: geodynamic evidence and implications: Journal of South American Earth Sciences, v. 15, p. 28 - 38.

Yañez, G.A., Ranero, C.R., von Huene, R., and Díaz, J., 2001, Magnetic anomaly interpretation across the southern central Andes (32º-34ºS): The role of the Juan Fernández Ridge in the late Tertiary evolution of the margin: Journal of Geophysical Research, v. 106, p. 6325 - 6345.

Chapter 4. Temporal variations in the influence of the subducting slab on Cenozoic, Central Andean arc magmas: Evidence from boron isotope systematics

Rosie E. Jones[1]*, Linda A. Kirstein[1], Simone A. Kasemann[2], Richard Hinton[1], Jan C. M. De Hoog[1], Tim Elliott[3], Vanesa D. Litvak[4], and EIMF[5]

[1] School of GeoSciences, University of Edinburgh, West Mains Road, Edinburgh, EH9 3JW, UK

[2] Department of Geosciences & MARUM, Centre for Marine Environmental Sciences, University of Bremen, 28334 Bremen, Germany

[3] School of Earth Sciences, University of Bristol, Wills Memorial Building, Queens Road, Bristol, BS8 1RJ, UK

[4] Instituto de Estudios Andinos Don Pablo Groeber, Departamento de Ciencias Geológicas, Universidad de Buenos Aires – CONICET, Argentina

[5] Edinburgh Ion Microprobe Facility, School of GeoSciences, University of Edinburgh, West Mains Road, Edinburgh, EH9 3JW, UK

This Chapter forms the basis of a paper intended for submission to *Earth and Planetary Science Letters*.

4.1 Author Contributions

The authors of the manuscript made the following contributions:

Rosie Jones: I conducted all of the petrographic work, sample preparation and analytical work, as well as all the data processing and reduction. I also developed the geochemical models, although this benefitted from discussion and suggestions from Cees-Jan de Hoog. The interpretations and conclusions presented in the manuscript are entirely my own, although the interpretations were aided by useful discussions with my supervisors and collaborators. I wrote and prepared the manuscript and circulated it to my co-authors for feedback. Following the submission of this thesis the manuscript will be prepared for submission to *Earth and Planetary Science Letters*.

Linda Kirstein: Provided constructive comments and feedback on the manuscript, leading to an improved flow and structure. Linda also took the lead in the procurement a heating stage for the re-homogenisation of melt inclusions.

Simone Kasemann: Helped me to refine my ideas through useful discussions and provided constructive feedback throughout the preparation of the manuscript. This enabled me to present my interpretations and conclusions in a more clear and coherent manner.

Tim Elliott: The manuscript benefitted from early discussions of the data set with Tim.

Vanesa Litvak: Provided samples from the Valle del Cura (Argentina) for analysis, as well as helpful comments on the manuscript.

EIMF: The staff of the Edinburgh Ion Microprobe Facility contributed to this work in a number of ways. **John Craven** provided assistance in the procurement and setting up of the melt inclusion re-homogenisation stage, and advised on various aspects of the sample preparation. **Richard Hinton** provided technical assistance and guidance in the analysis of boron isotopes on the Cameca ims 1270 ion microprobe, and trace and rare earth element analysis on the Cameca ims 4f ion microprobe. He also dealt with any analytical problems which were encountered during the analytical sessions and was available for discussion of the data quality and analytical setup throughout the study. **Cees-Jan de Hoog** provided technical assistance in some preliminary analysis of boron concentrations in pyroxene hosted melt inclusions. He also helped in the development of the geochemical modelling and provided constructive comments on the manuscript. All three EIMF staff provided advice on data processing and correction methods.

4.2 Abstract

The southern Central Andean margin represents an ideal setting at which to investigate how changing the tectonic configuration of a subduction zone (convergence angles and rates, seamount subduction and shallowing slab angle) affects the recycling of subducted components. To constrain sources of slab-derived fluids and their contribution to arc magmatism, boron isotope and select major and trace element compositions were determined for pyroxene and zircon hosted melt inclusions. Melt inclusions were obtained from a suite of Paleocene to Miocene arc magmatic rocks, ranging in composition from basaltic andesites to dacites, from the southern Central Andes. Considerable variations in $\delta^{11}B$ values and boron concentrations are observed with time. Significantly lower $\delta^{11}B$ values (average = -1.9 ±2.2 ‰ (1σ)) and B/Nb ratios (average = 3.3 ±1.3 (1σ)) were obtained for melt inclusions from Oligocene arc magmatic rocks (25.2 – 23.2 Ma), compared to those obtained for the Paleocene (61.2 Ma) (averages = +1.6 ±0.8 ‰ and 17.8 ±1.4 (1σ)) and the Miocene (19.3 –17.1 Ma) (averages = +4.7 ±1.9 ‰ and 11.9 ±5.5 (1σ)). The highest $\delta^{11}B$ values were obtained for melt inclusions from Miocene lavas.

A slab-derived fluid with a $\delta^{11}B$ composition of +1.6 ‰, primarily derived from altered oceanic crust on the down-going slab, affected the source of the Paleocene arc magmas. The source of the Oligocene arc magmas received less fluid derived from the subducting slab (< ~0.5 % fluid addition), with lower $\delta^{11}B$ values, than the Paleocene and Miocene arc magmas (0.2 - 2 % fluid addition), indicating a greater depth to the slab-mantle interface. This can be related to the widening of the volcanic arc during this time period and more distal position of these samples relative to the trench. The higher $\delta^{11}B$ values (up to +8.6 ±1.2 ‰) obtained for the Miocene melt inclusions record the influence of serpentinite-derived fluids on the source of arc magmas after ~19.5 Ma. This is approximately coeval with the

subduction of the Juan Fernandez Ridge, a volcanic seamount chain, which is associated with hydrated and serpentinised oceanic lithosphere.

4.3 Introduction

The Andean margin represents a type example of an ocean – continent convergent margin. At convergent margins volatiles and crustal material are transported into the mantle by the subducting plate. The recycling of subducted material to mantle and crustal reservoirs, as well as the location and mode (slab-derived fluids versus silicate melts) of mass transfer from the subducting plate to arc magmas, remain outstanding issues in our understanding of subduction zones. The southern Central Andes provide a particularly interesting area to investigate these processes as the plate tectonic configuration of the Andean convergent margin has changed over the course of the Cenozoic. Specifically, the angle of the subducting Nazca plate has shallowed since the early Miocene (e.g., Yañez et al., 2001; Kay and Mpodozis, 2002). This makes the southern Central Andes an ideal location for investigating how changing geodynamic settings may influence the chemistry of arc magmas, and in particular how the contribution and recycling of subducting components (altered oceanic crust (AOC), serpentinised oceanic mantle lithosphere, oceanic and continentally derived sediments) to arc magmas, may change with the angle of the subducting slab.

In most subduction zone settings primary arc magmas are thought to be generated by the partial melting of the asthenospheric mantle wedge caused by the release of hydrous fluids from the subducting slab and the lowering of the solidus temperature (e.g., Gill, 1981; Hawkesworth et al., 1993; Davidson, 1996). As the slab descends into the mantle, hydrous fluids are produced from the breakdown of hydrous minerals, such as phengite and chlorite in subducted sediments, and hornblende, epidote and chlorite in AOC (Tatsumi, 1989; Kogiso et al., 1997; Aizawa et al., 1999). At temperatures of ~650 °C serpentinite mineral phases, present in the subducting oceanic lithosphere, break down into forsterite and enstatite (Ulmer and Trommsdorff, 1995; Wunder et al., 2001). Serpentinite can contain >13 wt.% H_2O in

mineral structures and therefore has the potential to release large quantities of water into the mantle wedge. In the majority of subduction zones this corresponds to depths of between 90 and 110 km and is suggested to account for the position of the volcanic arc away from the trench (e.g., Hattori and Guillot, 2003). In addition to the serpentinite present in the subducting oceanic lithosphere, the fore-arc mantle wedge is also likely to contain serpentinised peridotite as a result of hydration of the mantle wedge at shallow levels (Hyndman and Peacock, 2003; Savov et al., 2007). This serpentinised fore-arc mantle may be down-dragged into a sub-arc position by the subducting plate (Straub and Layne, 2002; Tonarini et al., 2011) where it also breaks down and releases fluids, when temperatures exceed ~650 °C. In the majority of subduction zones temperatures are thought insufficient to cause melting of the subducting slab and therefore mass transfer from the subducting slab to the mantle wedge is thought to be dominated by aqueous fluids rather than silicate melts (e.g., Peacock et al., 1994; Peacock, 1996). Slab-derived fluids transport fluid mobile elements, such as boron, into the mantle wedge. Therefore components of the subducting slab, which includes sediments, AOC, and serpentinised oceanic lithosphere, may be recycled to the crust and influence the chemistry of arc magmas (e.g., Hawkesworth et al., 1993; Elliott et al., 1997).

Boron (B) concentrations and isotope ratios have been identified as sensitive indicators of subducting slab components in arc magmas, in both oceanic and continental settings (e.g., Palmer, 1991; Rosner et al., 2003). This is because (1) B is highly fluid mobile during slab dehydration (Leeman and Sisson, 1996; Noll Jr et al., 1996); (2) B behaves incompatibly in magmatic processes (Brenan et al., 1998); (3) B is relatively enriched in components of the subducting slab compared to the mantle (Fig. 4.1) (e.g., Spivack and Edmond, 1987; Ishikawa and Nakamura, 1993; Chaussidon and Marty, 1995; Smith et al., 1995); and (4) these different components/reservoirs have distinct B isotope compositions (Fig. 4.1). The higher B concentrations found in arc magmatic rocks compared to those found in intra-plate

settings, together with the correlation between B and ^{10}Be (a cosmogenic radionuclide which can only be produced in the upper atmosphere and is strongly enriched in sediments) enrichment, has been used to support boron addition to arc magmas from subducting components (e.g., Morris et al., 1990; Ryan et al., 1995; Leeman and Sisson, 1996).

In arc magmatic rocks, strong across arc variations have been observed in both B concentrations and $\delta^{11}B$ isotope values; with high $\delta^{11}B$ values and the greatest B enrichment at the arc front and decreasing values towards the back arc (e.g., Ryan et al., 1995; Ishikawa and Tera, 1997; Rosner et al., 2003). This is related to progressive metamorphic devolatisation and the reduction of fluids coming off the slab as it descends into the mantle, alongside the preferential release of ^{11}B into the slab-derived fluids (Peacock and Hervig, 1999; King et al., 2007). It is also suggested that boron is readily released from subducting material and is quickly 'flushed' through the mantle. Therefore, the sub-arc mantle wedge should contain limited B-enrichment from earlier subduction processes (Morris et al., 1990).

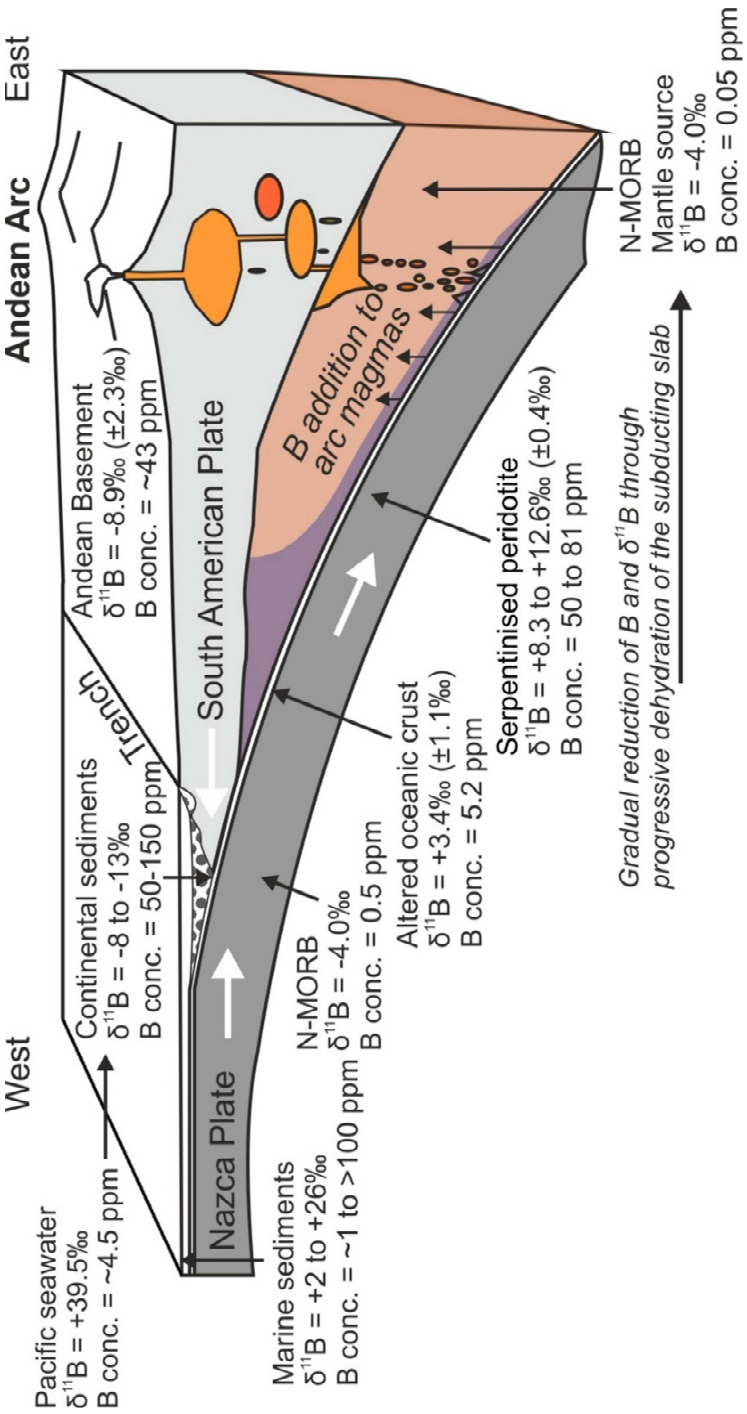

Figure 4.1. Boron concentrations and isotope ratios of different boron reservoirs present along the Andean convergent margin. Values taken from Chaussidon and Jambon (1994), Chaussidon and Marty (1995), Ishikawa and Nakamura (1993), Kasemann et al. (2000), Smith et al. (1995) and Spivack and Edmond (1987).

Here we present boron isotope and select major and trace element compositions of pyroxene and zircon hosted melt inclusions, determined by secondary ion mass spectrometry (SIMS) and electron microprobe (EPMA), for Cenozoic arc magmatic rocks from the southern Central Andes. In this region arc magmatic rocks have been affected by hydrothermal alteration (e.g., Bissig et al., 2001; Bissig et al., 2003; Charchaflié et al., 2007), which has the potential to mobilise fluid-mobile elements such as boron (e.g., Kasemann et al., 2004 and references therein). On this basis melt inclusions were analysed as they are protected by the surrounding host phenocryst phase from the effects of post depositional alteration, as well as from late stage processes occurring in the melt, such as degassing (e.g., Sobolev, 1996; Schmitt et al., 2002; Straub and Layne, 2002; Schiano, 2003). In addition, as boron is a highly incompatible element (Brenan et al., 1998), higher concentrations of boron should be present in the melt inclusion glass compared to the mineral phases. The melt inclusion data is combined with U-Pb and Ar-Ar age data (Chapter 2 and Appendices 1.10 and 1.15) to constrain changes in the influence of the subducting slab on the source of southern Central Andean arc magmas with time.

4.4 Geological Setting

The study area is located between 29.5 and 31 °S in the Pampean (Chilean) flat-slab segment of the southern Central Andes and spans the Principal and Frontal Cordillera of Chile and Argentina (Fig. 4.2). Subduction of oceanic crust beneath the South American continent has been active in this region since the Jurassic and has produced a series of volcanic arcs (e.g., Ramos et al., 2002; Stern, 2004; Charrier et al., 2007). Convergence rates and the relative plate motions between the oceanic (Farallon and Nazca) and South American plates have changed over time (Somoza and Ghidella, 2012). The angle of subduction has also changed over time due to the age of the oceanic crust being subducted and the presence or absence of buoyant

oceanic ridges and plateaus (e.g., Nur and Ben-Avraham, 1981; Pilger, 1981; Yañez et al., 2001; Ramos and Folguera, 2009).

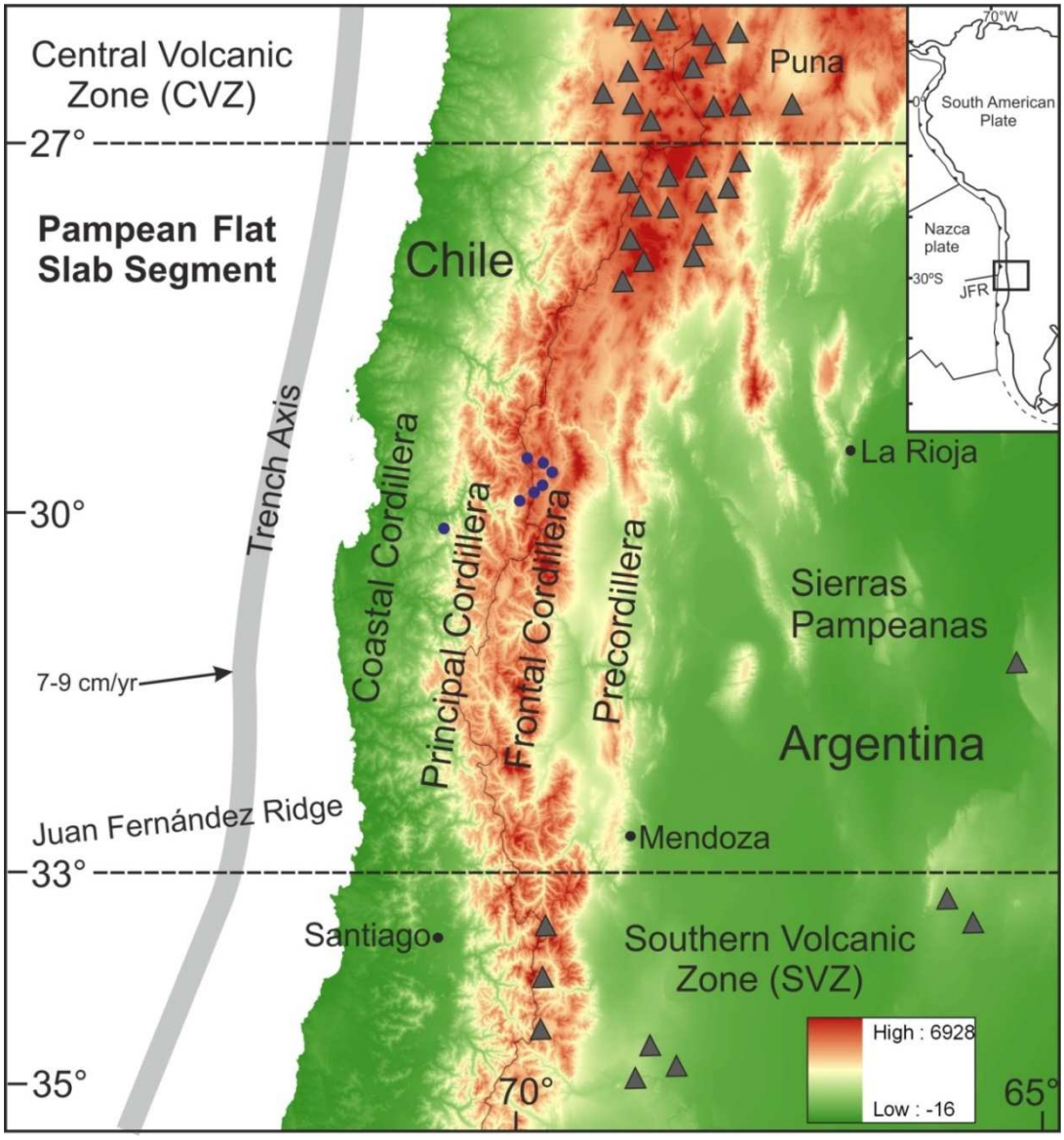

Figure 4.2. Map of the study area showing the main features of the present day southern Central Andean margin. Sample locations are shown as blue circles and primary active volcanoes as grey triangles. Digital elevation data from Jarvis et al. (2008).

Convergence rates between the oceanic Farallon and continental part of the South American plate are thought to have been relatively slow during the Paleocene (~5

cm/yr), with an increase in the Mid Eocene to rates of ~8 cm/yr (Somoza and Ghidella, 2012). This convergence rate is suggested to have remained fairly constant between the Mid Eocene and Late Oligocene, with the Farallon plate being subducted in a north-easterly (NE) direction (Pilger, 1984; Pardo Casas and Molnar, 1987; Somoza, 1998; Somoza and Ghidella, 2012). The oceanic lithosphere being subducted during this time interval is thought to have been Late Cretaceous in age (Somoza and Ghidella, 2012) and subducting at a normal angle (>30°) (Ramos and Folguera, 2009).

A significant change in the tectonic configuration of the Andean margin occurred during the Late Oligocene (~25 Ma) due to the break-up of the Farallon plate into the Nazca and Cocos plates (Lonsdale, 2005). This resulted in both an increase in convergence rates (up to ~15 cm/yr) and a change in convergence direction from oblique (NE-SW) to orthogonal (ENE-WSW) (Pardo Casas and Molnar, 1987; Somoza, 1998). The westward migration of the South American plate is also thought to have been initiated after ~30 Ma (Silver et al., 1998). This reconfiguration has been linked to a period of major uplift, increased magmatic activity, and a broadening of the magmatic arc (Pilger, 1984). The high convergence rates were sustained up until ~20 Ma, and followed by a gradual decline to present day values (~7 cm/yr) (Pilger, 1984; Somoza and Ghidella, 2012). It is suggested that progressively older, Late Cretaceous oceanic lithosphere, originating from the Farallon-Phoenix spreading ridge, was subducted along the South American margin between ~24 and ~16 Ma. This was followed by the subduction of progressively younger oceanic lithosphere, originating from the Farallon-Pacific spreading ridge, after 16 Ma (Somoza and Ghidella, 2012).

There is currently no active volcanism in the Pampean (Chilean) flat-slab segment due to the low angle (<10° at ~100 km depth) at which the oceanic Nazca plate subducts beneath the South American continent in this region and the consequent

restriction of the mantle wedge (Cahill and Isacks, 1992). On the basis of the initiation of high angle thrust faulting in the main Andean Cordillera (Maksaev et al., 1984), the broadening of the magmatic arc to the east (Kay et al., 1987; Kay et al., 1991; Kay and Abbruzzi, 1996), the termination of back-arc volcanism (Kay and Mpodozis, 2002), and the initiation of deformation in the Precordillera (Jordan et al., 1993), shallowing of the subducting Nazca plate is thought to have been initiated ~18 Ma. This slab shallowing is proposed to have caused the expansion and migration of the volcanic arc to the east and the eventual cessation of arc volcanism in the late Miocene (~6 Ma) (Kay et al., 1987; Trumbull et al., 2006).

There are a number of proposed causes of flat-slab subduction in the southern Central Andes. These include; (1) the intersection of the Juan Fernandez Ridge (JFR), a volcanic seamount chain, which began intersecting the Andean continental margin during the Early Miocene (Pilger, 1981; Gutscher et al., 2000; Yañez et al., 2001; Yañez et al., 2002); (2) the curvature of the subducting slab and Andean margin (Cahill and Isacks, 1992); and (3) the trench-ward motion of thickened lithosphere (Manea et al., 2012). There is a strong relationship between the track of the JFR and the location of the flat-slab segment in the southern Central Andes (Anderson et al., 2007), leading to a convincing link between the subduction of the JFR and the shallowing of the subducting plate. The JFR originates from a mantle plume and is suggested to have begun intersecting the Andean margin at ~20 Ma, migrating south along the margin at a rate of ~200 km/Ma to its current position at 32.5 °S (Yañez et al., 2002). The oceanic lithosphere associated with this seamount is also thought to have been hydrated and serpentinised leading to increased buoyancy (Kopp et al., 2004; Marot et al., 2013), hence enhancing the link between the JFR and shallow subduction.

4.5 Sample selection and preparation

Samples of Cenozoic arc magmatic rocks were collected from the Principal and Frontal Cordillera of Chile and Argentina between 29.5 and 31 °S (Fig. 4.2). A subset of eight samples was selected for the analysis of melt inclusions from a larger suite of samples previously characterised and age dated (Chapter 2). The Cenozoic volcanic rocks present in the southern Central Andes are highly differentiated, so in order to assess the contributions from slab-derived fluids to the source of the arc magmas and limit the effects of crustal contamination, the least evolved samples available were selected for the time frame of interest (Palaeocene to Miocene). The selected samples are extrusive, range in composition from basaltic andesites to dacites (SiO_2 contents ranging between 54 and 67 %) and have medium- to high-K, calk-alkaline compositions (Table 4.1). The samples with basaltic-andesite, andesite and trachy-andesite compositions contain major phenocryst phases of plagioclase + augite ± enstatite and accessory opaques ± zircon ± apatite. The dacitic sample contains major phenocryst phases of plagioclase + biotite + amphibole and accessory zircon, apatite and opaque phases. The samples range in age from Paleocene (61.2 Ma) to Early Miocene (17.1 Ma) and represent four major Cenozoic arc formations present in the southern Central Andes; the Los Elquinos Formation (Paleocene), the Tilito Formation (Lower Doña Ana Group, Late Oligocene), the Escabroso Formation (Upper Doña Ana Group, Miocene) and the Cerro de las Tórtolas Formation (Miocene).

Sample	Latitude (S)	Longitude (W)	Formation	Age (Ma)	±(2σ)	Geological Epoch	Rock type	SiO_2 (wt%)	TiO_2 (wt%)	Al_2O_3 (wt%)	Fe_2O_3 (wt%)	MnO (wt%)	MgO (wt%)	CaO (wt%)	Na_2O (wt%)	K_2O (wt%)	P_2O_5 (wt%)	LOI	Total
RJ1111	-30.14294	-70.69167	Los Elquinos Formation	61.2*	1.0	Paleocene	Basaltic-andesite	54.2	0.9	17.0	7.7	0.2	5.1	6.5	3.5	2.1	0.1	2.5	99.7
MQ153	-29.85272	-69.86294	Tilito Formation (Lower Doña Ana Group)	25.2	0.3	Oligocene	Andesite	-	-	-	-	-	-	-	-	-	-	-	-
ZN122	-29.57619	-69.92303	Tilito Formation (Lower Doña Ana Group)	24.8	0.4	Oligocene	Andesite	60.7	0.7	15.7	6.4	0.1	3.1	5.9	2.4	2.0	0.2	2.7	99.8
Z27	-29.61389	-69.77611	Tilito Formation (Lower Doña Ana Group)	23.2	0.3	Oligocene	Dacite	66.9	0.7	15.8	4.6	0.0	0.2	3.0	3.6	3.9	0.2	0.9	99.9
AM0887	-29.91972	-69.99472	Escabroso Formation (Upper Doña Ana Group)	19.3*	0.3	Miocene	Andesite	61.7	0.8	16.2	5.6	0.1	2.7	5.0	3.6	2.5	0.2	1.4	99.7
1026	-29.69056	-69.69500	Escabroso Formation (Upper Doña Ana Group)	18.2	0.3	Miocene	Andesite	61.4	0.8	16.5	5.9	0.1	2.3	5.2	3.7	3.0	0.2	0.6	99.7
RF62	-29.79403	-69.78217	Cerro de las Tórtolas Formation	17.1	0.6	Miocene	Trachy-andesite	59.5	0.9	17.7	6.1	0.1	1.3	5.5	3.8	2.9	0.2	1.8	99.6
RF65	-29.79403	-69.78217	Cerro de las Tórtolas Formation	-	-	Miocene	Andesite	58.2	0.9	17.2	6.5	0.1	2.8	6.4	3.5	2.6	0.2	1.3	99.6

Table 4.1. Sample information, ages and whole rock compositions. Ages have been determined by U-Pb dating of zircon and Ar/Ar dating of plagioclase feldspar (highlighted by *) (Chapter 2 and Appendices 1.10, 1.11 and 1.15). Sample RF65 is assumed to have the same age as RF62 as they are from the same sample location. Whole rock compositions were determined by XRF analysis (Chapter 2).

The selected samples were crushed and melt inclusion hosting phases (pyroxene and zircon) were separated using traditional mineral separation techniques (Appendix 3.1). Pyroxene (augite and enstatite) and zircon grains were screened under a binocular microscope for the presence of both glassy and devitrified melt inclusions. From each sample, representative melt inclusions ranging in size between ~25 and ~100 μm, were selected for analysis (Figures 4.3 and 4.4). The selected melt inclusions were either entirely glassy containing only a minor vapour or shrinkage bubble (VB) (Fig. 4.4a), glassy containing a VB and a minor daughter mineral (DM) phase (primarily Fe-Ti oxides) (Fig. 4.4c), or devitrified containing a VB and daughter minerals (Fig. 4.4b). To obtain a homogeneous glass for analysis devitrified melt inclusions (including those containing vapour bubbles and mineral phases) hosted in pyroxene phenocrysts were re-homogenised using a Linkam TS1400XY heating stage at an average temperature of 1219 °C (Appendix 3.1.3). The pyroxene and zircon grains were then mounted in epoxy resin, ground and polished to expose the interior of the melt inclusions at the surface (Appendix 3.1.2).

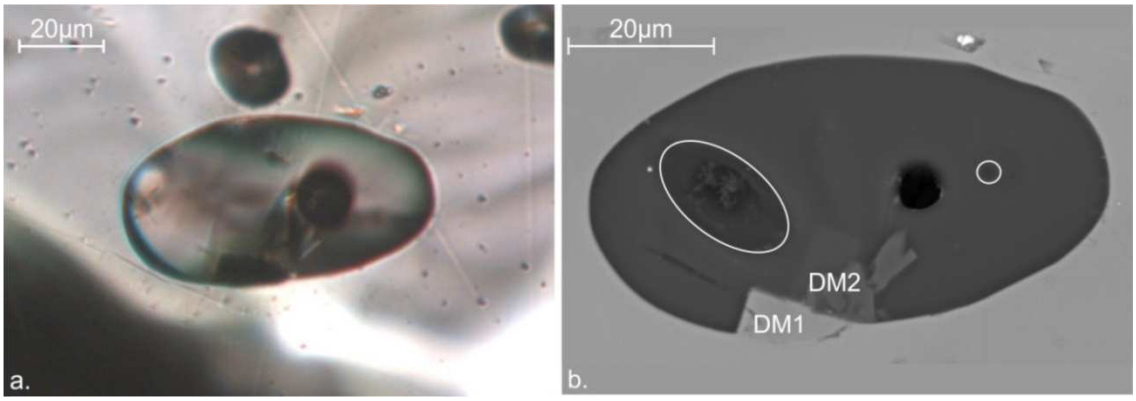

Figure 4.3. Photomicrographs of a zircon-hosted, melt inclusion present in sample 1026 (Escabroso Formation). a) Viewed under plane polarised light prior to analysis. The majority of the inclusion appears glassy with the presence of a vapour or shrinkage bubble and minor daughter minerals. b) A backscattered electron (BSE) image with the locations of SIMS (larger circle) and EPMA (smaller circle) analysis highlighted. Daughter mineral 1 (DM1) was identified as Fe-Ti oxide and daughter mineral 2 (DM2) as amphibole. The vapour bubble appears as a hole near the centre of the inclusion.

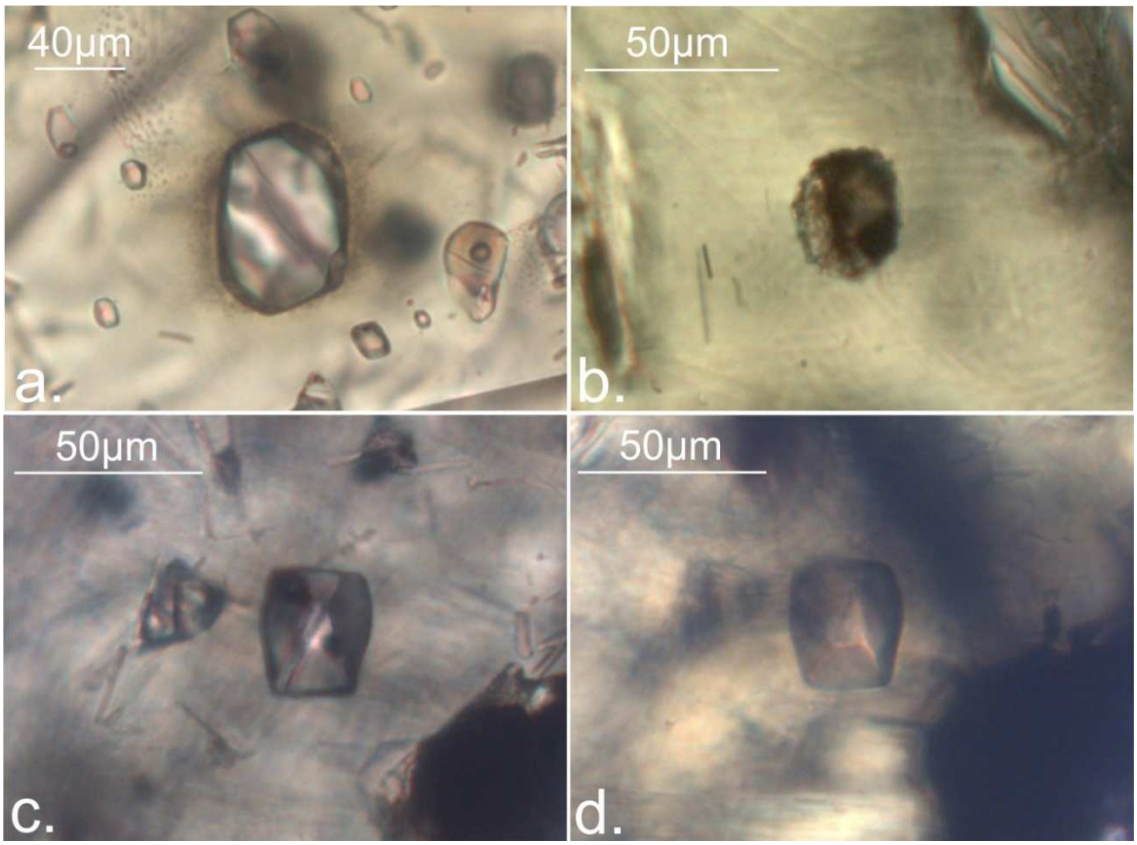

Figure 4.4. Photomicrographs of pyroxene-hosted melt inclusions. a) Re-homogenised melt inclusion from sample 1026 (Escabroso Formation), b) devitrified melt inclusion (prior to re-homogenisation) from sample ZN122 (Tilito Formation), c) glassy melt inclusion containing a vapour or shrinkage bubble and a daughter mineral phase from sample 1026 (Escabroso Formation) prior to re-homogenisation, d) the melt inclusion shown in 3c after re-homogenisation.

4.6 Analytical Methods

Boron isotope analyses were performed on a Cameca ims 1270 secondary ion mass spectrometer (SIMS) and selected trace elements were analysed on the Cameca ims 4f SIMS, both at the NERC Edinburgh Ion Microprobe Facility (EIMF). Subsequent to SIMS analysis the major element compositions of the melt inclusions and host mineral phases were determined using the Cameca SX100 electron microprobe (EPMA) at the School of GeoSciences, University of Edinburgh. Glassy and re-homogenised melt inclusions, as well as the host phenocryst phases (pyroxene and zircon), were analysed. Full details of analytical methods and data processing are presented in Appendices 3.2, 3.3 and 3.4.

A total of 70 successful boron isotope analyses were made on melt inclusions (55 hosted in pyroxene and 15 hosted in zircon) from 8 samples. The boron isotope ratios of the melt inclusions and host phenocrysts were measured relative to the reference material GSD-1G (10.1 $‰_{NIST951}$ ±1.0 (2σ) (Jochum et al., 2011b)), which was analysed throughout the analytical session (Appendix 3.5). Boron isotope ratios are expressed in the conventional $\delta^{11}B$ (‰) notation relative to the reference material NIST SRM 951 (Catanzaro, 1970). The $\delta^{11}B$ of each melt inclusion was calculated using the following equation:

$$\delta^{11}B_{(sample)} = ((\delta^{11}B_{(GSD\text{-}1G\ accepted\ value)} + 1000) \times (^{11}B/^{10}B_{(sample\ measured)} / {}^{11}B/^{10}B_{(GSD\text{-}1G\ measured)})) - 1000$$

The internal precision obtained for the analysis of GSD-1G ranged from 0.55 – 0.68 ‰ (1σ). The internal precision of the unknowns is dependent on boron content and ranged from 0.29 – 1.33 ‰ (1σ) for melt inclusion analyses (Appendix 3.5). The external precision, based on the reproducibility of GSD-1G, is typically 0.23‰ (n=13) (quoted as the standard error of the mean (SEM) at the 1σ level). It is well documented that the ion yields obtained during SIMS analysis can be affected by

the chemical and structural matrices of the sample (e.g., Deline et al., 1978; Shimizu and Hart, 1982; Eiler et al., 1997). However, it has been shown that boron isotope determinations of basaltic to rhyolitic glasses by SIMS are not significantly affected by these matrix effects (e.g., Chaussidon et al., 1997; Rosner et al., 2008).

A total of 72 melt inclusions were analysed for selected trace elements (58 hosted in pyroxene and 14 hosted in zircon). Where possible the same melt inclusions which had previously been analysed for boron isotopic composition were analysed. If the size of the melt inclusions was not sufficient, analyses were made of melt inclusions from the same phenocryst as those analysed for boron isotopes. For the primary elements of interest (B, Nb and Zr), repeated measurement of the standard GSD-1G gave a precision of <2.6 % relative (1σ) (Table A3.3, Appendix 3.3). Analysis of a secondary standard, reference material NIST SRM 610 (Jochum et al., 2011a), indicates that accuracy is <7.3 % (1σ) for B, Nb and Zr concentrations (Table A3.4, Appendix 3.3).

4.7 Results

Full results are presented in Table 4.2 and Appendices 3.5 to 3.8. Boron concentrations obtained from pyroxene and zircon hosted melt inclusions range from 9 to 218 ppm and $\delta^{11}B$ values ranged from -5.4 ±1.6 ‰ to +8.6 ±1.2 ‰. The uncertainties given on individual $\delta^{11}B$ values are propagated analytical uncertainties quoted at the 2σ level (Appendix 3.2.3). Melt inclusions with <50 ppm B generally have lower $\delta^{11}B$ values, but otherwise there is no apparent relationship between boron concentrations and $\delta^{11}B$ values (Fig. 4.5). A number of analyses were also made on the host phenocryst phases, close to the analysed melt inclusions. Boron concentrations obtained for the pyroxene and zircon phenocrysts range between 0.4 and 2.9 ppm (Table 4.2 and Table A3.2, Appendix 3.2).

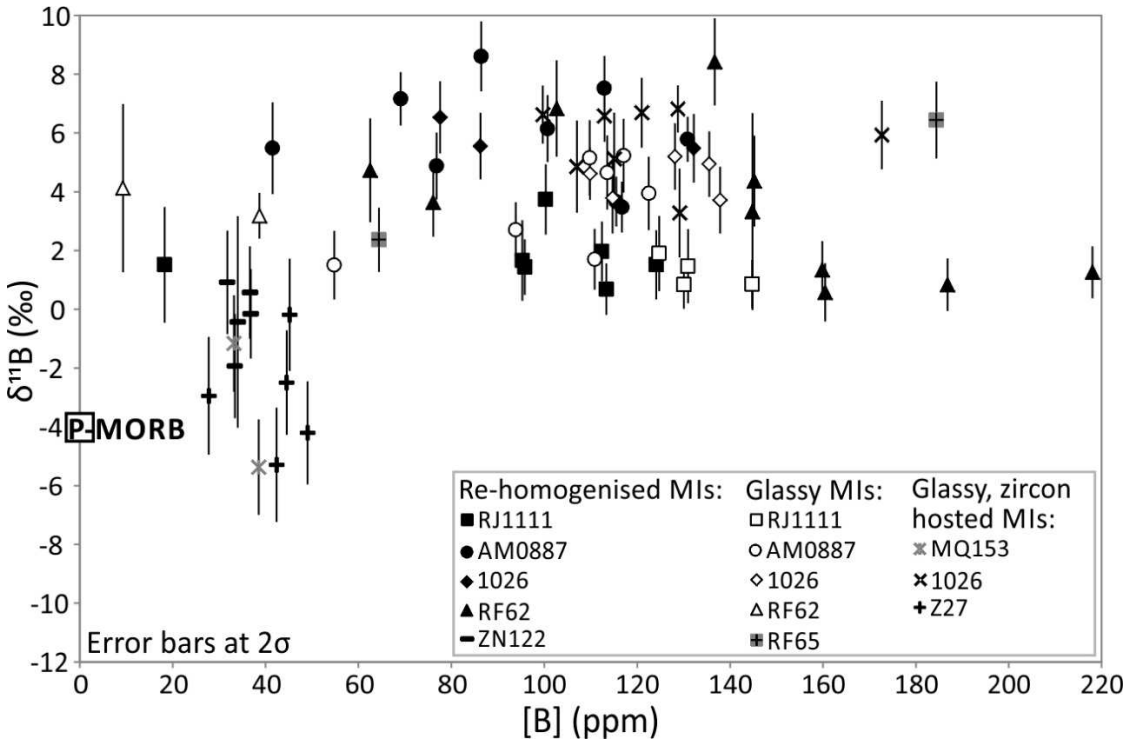

Figure 4.5. Boron concentrations (ppm) plotted against $\delta^{11}B$ (‰) for re-homogenised and glassy (± vapour/shrinkage bubble, ± minor daughter mineral phase e.g., Fe-Ti oxide) melt inclusions (MI). Pyroxene hosted melt inclusions are shown by open and filled symbols and zircon hosted melt inclusions are shown by crossed symbols. Error bars on the $\delta^{11}B$ values represent propagated uncertainties at the 2σ level. Errors bars on the boron concentrations are smaller than the symbol size.

Table 4.2

Sample	Sample-phenocryst-melt inclusion	Host mineral phase	Melt Inclusion condition	Re-homogenisation temperature (^{0}C)	SiO_2 (wt%)	MgO (wt%)	B (ppm)	Zr (ppm)	Nb (ppm)	B/Zr	B/Nb	Nb/B	$\delta^{11}B$	Analytical uncertainty (±)
RJ1111	RJ1111-1-MI1	augite	re-homogenised	1225	-	-	81	161	5.2	0.50	15.6	0.06	-	-
	RJ1111-2-MI1	augite	re-homogenised	1227	-	-	*18*	-	-	-	-	-	1.5	2.0
	RJ1111-4-MI1	augite	re-homogenised	1221	61.3	4.8	113	211	7.1	0.54	15.9	0.06	0.7	0.9
	RJ1111-4-MI2	augite	re-homogenised	1221	67.6	2.7	112	132	6.2	0.85	18.2	0.06	2.0	1.0
	RJ1111-4-MI3	augite	re-homogenised	1221	-	-	96	228	5.5	0.42	17.3	0.06	1.4	0.9
	RJ1111-6-MI1	augite	re-homogenised	1225	62.8	3.7	124	263	6.0	0.47	20.7	0.05	1.5	1.2
	RJ1111-12-MI1	augite	re-homogenised	1217	-	-	100	231	5.7	0.43	17.7	0.06	3.7	1.2
	RJ1111-12-MI2	augite	re-homogenised	1217	62.2	3.7	77	164	4.2	0.47	18.4	0.05	-	-
	RJ1111-15-MI1	augite	re-homogenised	1223	-	-	95	234	5.0	0.41	18.9	0.05	1.7	1.4
	RJ1111-MB1-MI1	augite	glassy (±VB ± minor DM)	-	73.8	0.1	145	283	7.9	0.51	18.4	0.05	0.9	0.8
	RJ1111-MB2-MI1	augite	glassy (±VB ± minor DM)	-	73.6	0.1	130	291	8.2	0.45	15.9	0.06	0.8	0.8
	RJ1111-MB3-MI1	augite	glassy (±VB ± minor DM)	-	-	-	137	270	8.0	0.51	17.2	0.06	-	-
	RJ1111-MB4-MI1	augite	glassy (±VB ± minor DM)	-	-	-	125	230	6.6	0.54	18.8	0.05	1.9	1.3
	RJ1111-MB5-MI1	augite	glassy (±VB ± minor DM)	-	-	-	131	263	7.1	0.50	18.4	0.05	1.5	1.2
Sample average							**106**	**228**	**6.4**	**0.51**	**17.8**	**0.06**	**1.5**	
2σ							65	99	2.5	0.22	2.8	0.01	1.7	
SEM							9	14	0.3	0.03	0.4	0.00	0.2	
Host augite composition							*1.3*	*33.1*	*0.1*				*-10.4*	
MQ153	MQ153-A1-MI1	zircon	glassy (±VB ± minor DM)	-	74.6	0.01	33	-	21.1	-	1.6	0.64	-1.2	1.6
	MQ153-UA2-MI1	zircon	glassy (±VB ± minor DM)	-	75.7	0.02	*39*	-	-	-	-	-	-5.4	1.6
Sample average							**36**						**-3.3**	
2σ							8						6.0	
SEM							3						2.1	

Sample	Sample-phenocryst-melt inclusion	Host mineral phase	Melt Inclusion condition	Re-homogenisation temperature (^{0}C)	SiO_2 (wt%)	MgO (wt%)	B (ppm)	Zr (ppm)	Nb (ppm)	B/Zr	B/Nb	Nb/B	$\delta^{11}B$	Analytical uncertainty (±)
ZN122	ZN122-1-MI1	augite	re-homogenised	1208	-	-	37	197	11.4	0.19	3.2	0.31	0.6	1.6
	ZN122-5-MI1	augite	re-homogenised	1221	-	-	37	99	7.1	0.37	5.2	0.19	-0.2	1.5
	ZN122-6-MI1	augite	re-homogenised	1208	-	-	34	109	9.9	0.31	3.4	0.29	-0.4	3.6
	ZN122-8-MI1	augite	re-homogenised	1207	69.5	2.7	32	165	10.8	0.19	2.9	0.34	0.9	1.7
	ZN122-10-MI1	augite	re-homogenised	1224	-	-	33	121	8.4	0.28	4.0	0.25	-1.9	1.8
Sample average							**35**	**138**	**9.5**	**0.27**	**3.7**	**0.28**	**-0.2**	
2σ							4	83	3.5	0.16	1.7	0.11	2.2	
SEM							1	19	0.8	0.04	0.4	0.03	0.5	
Host augite composition							*1.8*	*25.6*	*0.1*				*-13.1*	
Z27	Z27-UA2-MI1	zircon	glassy (±VB ± minor DM)	-	-	-	45	-	7.9	-	5.7	0.17	-0.2	1.9
	Z27-A6-MI1	zircon	glassy (±VB ± minor DM)	-	-	-	*28*	-	-	-	-	-	-2.9	2.0
	Z27-A6-MI2	zircon	glassy (±VB ± minor DM)	-	74.8	0.28	48	-	15.9	-	3.0	0.33	-	-
	Z27-A9-MI1	zircon	glassy (±VB ± minor DM)	-	-	-	49	-	33.6	-	1.5	0.69	-4.2	1.7
	Z27-A12-MI1	zircon	glassy (±VB ± minor DM)	-	74.7	0.00	42	-	14.3	-	3.0	0.34	-5.3	1.9
	Z27-A13-MI1	zircon	glassy (±VB ± minor DM)	-	75.9	0.09	45	-	16.6	-	2.7	0.37	-2.5	1.8
Sample average							**43**		**17.7**		**3.2**	**0.38**	**-3.0**	
2σ							15		19.1		3.1	0.37	3.9	
SEM							3		4.3		0.7	0.08	0.9	
AM0887	AM0887-6-MI1	augite	re-homogenised	1200	-	-	115	309	12.6	0.37	9.1	0.11	3.7	0.8
	AM0887-6-MI2	augite	re-homogenised	1200	-	-	117	304	13.2	0.38	8.8	0.11	3.5	0.9
	AM0887-10-MI1	augite	re-homogenised	1180	75.6	0.1	131	242	13.4	0.54	9.8	0.10	5.8	0.8
	AM0887-10-MI2	augite	re-homogenised	1180	71.3	1.3	116	301	14.2	0.39	8.2	0.12	-	-
	AM0887-15-MI1	augite	re-homogenised	1202	-	-	113	*334*	12.0	0.34	9.4	0.11	7.5	1.1
	AM0887-15-MI2	augite	re-homogenised	1202	-	-	101	306	13.2	0.33	7.6	0.13	6.1	1.1

Sample	Sample-phenocryst-melt inclusion	Host mineral phase	Melt Inclusion condition	Re-homogenisation temperature (^{0}C)	SiO_2 (wt%)	MgO (wt%)	B (ppm)	Zr (ppm)	Nb (ppm)	B/Zr	B/Nb	Nb/B	$\delta^{11}B$	Analytical uncertainty (±)
	AM0887-17-MI1	augite	re-homogenised	1225	64.3	4.4	42	*153*	10.7	0.27	3.9	0.26	5.5	1.5
	AM0887-MB5-MI1	augite	glassy (±VB ± minor DM)	-	72.9	0.0	117	354	14.1	0.33	8.3	0.12	5.2	1.2
	AM0887-MB6-MI1	augite	glassy (±VB ± minor DM)	-	73.7	0.0	111	328	16.0	0.34	6.9	0.14	1.7	1.0
	AM0887-MB11-MI1	augite	glassy (±VB ± minor DM)	-	-	-	*55*	-	-	-	-	-	1.5	1.2
	AM0887-MB12-MI1	augite	glassy (±VB ± minor DM)	-	-	-	123	329	11.7	0.37	10.5	0.10	3.9	1.2
	AM0887-MB13-MI1	augite	glassy (±VB ± minor DM)	-	-	-	110	333	14.3	0.33	7.7	0.13	5.2	1.3
	AM0887-MB17-MI1	augite	glassy (±VB ± minor DM)	-	-	-	114	163	9.4	0.70	12.1	0.08	4.7	1.2
Sample average for augite-hosted melt inclusions							**105**	**288**	**12.9**	**0.39**	**8.5**	**0.13**	**4.5**	
2σ							52	133	3.5	0.23	4.1	0.09	3.5	
SEM							7	19	0.5	0.03	0.6	0.01	0.5	
Host augite composition							*1.7*	*66.1*	*0.1*				*-7.2*	
	AM0887-8-MI1	enstatite	re-homogenised	1205	-	-	77	239	11.2	0.32	6.9	0.15	4.9	1.1
	AM0887-12-MI1	enstatite	re-homogenised	1226	-	-	69	255	10.4	0.27	6.6	0.15	7.2	0.9
	AM0887-16-MI1	enstatite	re-homogenised	1208	54.6	3.2	86	325	14.4	0.27	6.0	0.17	8.6	1.2
	AM0887-MB2-MI1	enstatite	glassy (±VB ± minor DM)	-	75.2	0.0	*94*	-	-	-	-	-	2.7	0.9
Sample average for enstatite-hosted melt inclusions							**82**	**273**	**12.0**	**0.29**	**6.5**	**0.15**	**5.7**	
2σ							22	92	4.2	0.06	0.9	0.02	5.2	
SEM							5	26	1.2	0.02	0.3	0.01	1.3	
Host enstatite composition							*0.5*	*5.9*	*0.0*				-	
Sample average for AM0887 (augite and enstatite)							**99**	**285**	**12.7**	**0.37**	**8.1**	**0.13**	**4.8**	
2σ							51	124	3.6	0.22	4.0	0.08	4.0	
SEM							6	16	0.5	0.03	0.5	0.01	0.5	

Sample	Sample-phenocryst-melt inclusion	Host mineral phase	Melt Inclusion condition	Re-homogenisation temperature (^{0}C)	SiO_2 (wt%)	MgO (wt%)	B (ppm)	Zr (ppm)	Nb (ppm)	B/Zr	B/Nb	Nb/B	$\delta^{11}B$	Analytical uncertainty (±)
1026	1026-UA-4-MI1	zircon	glassy (±VB ± minor DM)	-	-	-	107	-	14.7	-	7.3	0.14	4.9	1.6
	1026-A2-MI1	zircon	glassy (±VB ± minor DM)	-	74.9	0.0	129	-	29.4	-	4.4	0.23	3.3	1.5
	1026-A3-MI1	zircon	glassy (±VB ± minor DM)	-	70.5	0.1	128	-	-	-	-	-	-	-
	1026-A5-MI1	zircon	glassy (±VB ± minor DM)	-	-	-	113	-	10.7	-	10.6	0.09	6.6	0.9
	1026-A6-MI1	zircon	glassy (±VB ± minor DM)	-	-	-	115	-	11.8	-	9.8	0.10	5.1	1.6
	1026-A7-MI1	zircon	glassy (±VB ± minor DM)	-	75.6	0.0	173	-	9.2	-	18.7	0.05	5.9	1.2
	1026-A7-MI2	zircon	glassy (±VB ± minor DM)	-	-	-	121	-	6.7	-	18.0	0.06	6.7	1.2
	1026-A9-MI1	zircon	glassy (±VB ± minor DM)	-	-	-	129	-	8.4	-	15.4	0.07	6.8	0.8
	1026-A10-MI1	zircon	glassy (±VB ± minor DM)	-	-	-	*100*	-	-	-	-	-	6.6	1.0
Sample average for zircon-hosted melt inclusions							**124**		**13.0**		**12.0**	**0.11**	**6.0**	
2σ							42		15.4		10.9	0.12	2.5	
SEM							7		2.9		2.1	0.02	0.4	
	1026-1-MI1	augite	re-homogenised	1243	68.0	4.3	108	128	8.4	0.84	12.8	0.08	-	-
	1026-2-MI1	augite	re-homogenised	1230	-	-	111	279	11.3	0.40	9.9	0.10	-	-
	1026-3-MI1	augite	re-homogenised	1234	72.9	1.5	111	222	10.0	0.50	11.2	0.09	-	-
	1026-3-MI2	augite	re-homogenised	1234	-	-	83	186	7.6	0.44	10.8	0.09	-	-
	1026-4-MI1	augite	re-homogenised	1239	74.4	1.0	135	161	10.3	0.84	13.2	0.08	-	-
	1026-6-MI1	augite	re-homogenised	1235	-	-	78	245	10.5	0.32	7.4	0.14	6.5	1.2
	1026-8-MI1	augite	re-homogenised	1230	66.0	3.8	86	170	8.3	0.51	10.3	0.10	5.6	1.1
	1026-8-MI2	augite	re-homogenised	1230	-	-	132	232	12.8	0.57	10.3	0.10	5.5	1.2
	1026-B2-MI1	augite	glassy (±VB ± minor DM)	-	-	-	115	223	8.3	0.51	13.8	0.07	3.8	1.2
	1026-B8-MI1	augite	glassy (±VB ± minor DM)	-	-	-	122	216	11.2	0.56	10.8	0.09	-	-
	1026-B11-MI1	augite	glassy (±VB ± minor DM)	-	76.7	0.0	138	219	9.2	0.63	14.9	0.07	3.7	1.1

Sample	Sample-phenocryst-melt inclusion	Host mineral phase	Melt Inclusion condition	Re-homogenisation temperature (^{0}C)	SiO_2 (wt%)	MgO (wt%)	B (ppm)	Zr (ppm)	Nb (ppm)	B/Zr	B/Nb	Nb/B	$\delta^{11}B$	Analytical uncertainty (±)
	1026-B17-MI1	augite	glassy (±VB ± minor DM)	-	74.7	0.0	128	223	10.7	0.57	11.9	0.08	5.2	1.1
	1026-MB2-MI1	augite	glassy (±VB ± minor DM)	-	-	-	*110*	-	-	-	-	-	4.6	0.9
	1026-MB2-MI2	augite	glassy (±VB ± minor DM)	-	76.8	0.0	158	180	13.1	0.88	12.1	0.08	-	-
Sample average for augite-hosted melt inclusions							**115**	**206**	**10.1**	**0.58**	**11.5**	**0.09**	**5.0**	
2σ							45	80	3.4	0.35	3.9	0.03	2.0	
SEM							6	11	0.5	0.05	0.5	0.00	0.4	
Host augite composition							*1.6*	*25.3*	*0.1*				*-9.3*	
	1026-B14-MI1	enstatite	glassy (±VB ± minor DM)	-	74.5	1.3	135	166	9.9	0.82	13.6	0.07	4.9	1.1
	1026-MB11-MI1	enstatite	glassy (±VB ± minor DM)	-	-	-	157	192	13.0	0.82	12.1	0.08	5.2	1.2
Sample average for enstatite-hosted melt inclusions							**146**	**179**	**11.5**	**0.82**	**12.9**	**0.08**	**5.1**	
2σ							31	36	4.3	0.01	2.1	0.01	0.4	
SEM							11	13	1.5	0.00	0.7	0.00	0.2	
Sample average for 1026 (augite, enstatite and zircon)							**121**	**203**	**11.2**	**0.61**	**11.8**	**0.09**	**5.4**	
2σ							45	77	9.1	0.36	6.6	0.07	2.2	
SEM							5	10	1.0	0.05	0.7	0.01	0.3	
RF62	RF62-2-MI1	augite	re-homogenised	1228	-	-	137	220	10.6	0.62	12.9	0.08	8.4	1.5
	RF62-3-MI1	augite	re-homogenised	1225	-	-	103	193	9.4	0.53	10.9	0.09	6.8	1.6
	RF62-4-MI1	augite	re-homogenised	1228	-	-	145	109	10.1	1.33	14.3	0.07	4.4	1.5
	RF62-5-MI1	augite	re-homogenised	1231	-	-	*76*	-	-	-	-	-	3.6	1.2
	RF62-7-MI1	augite	re-homogenised	1221	-	-	187	81	5.2	2.31	36.3	0.03	0.8	0.9
	RF62-7-MI2	augite	re-homogenised	1221	-	-	218	104	10.3	2.10	21.1	0.05	1.3	0.9
	RF62-8-MI1	augite	re-homogenised	1220	-	-	160	119	10.5	1.34	15.4	0.07	0.6	1.0

Sample	Sample-phenocryst-melt inclusion	Host mineral phase	Melt Inclusion condition	Re-homogenisation temperature (^{0}C)	SiO_2 (wt%)	MgO (wt%)	B (ppm)	Zr (ppm)	Nb (ppm)	B/Zr	B/Nb	Nb/B	$\delta^{11}B$	Analytical uncertainty (±)
	RF62-8-MI2	augite	re-homogenised	1220	68.7	3.0	160	112	9.3	1.43	17.1	0.06	1.3	1.0
	RF62-9-MI1	augite	re-homogenised	1220	64.1	4.3	63	144	8.4	0.43	7.5	0.13	4.7	1.8
	RF62-10-MI1	augite	re-homogenised	1221	-	-	*145*	-	-	-	-	-	3.3	3.3
	RF62-MB2-MI1	augite	glassy (±VB ± minor DM)	-	74.9	0.0	39	49	1.9	0.79	20.4	0.05	3.2	0.8
	RF62-MB3-MI1	augite	glassy (±VB ± minor DM)	-	-	-	*9*	-	-	-	-	-	4.1	2.8
Sample average							**120**	**126**	**8.4**	**1.21**	**17.3**	**0.07**	**3.1**	
2σ							125	106	5.9	1.35	16.6	0.06	4.8	
SEM							18	18	1.0	0.23	2.8	0.01	0.7	
Host augite composition							*2.4*	*18.4*	*0.0*				-	
RF65	RF65-1-MI1	augite	glassy (±VB ± minor DM)	-	-	-	184	131.96	8.5	1.40	21.8	0.05	6.4	1.3
	RF65-MB3-MI1	augite	glassy (±VB ± minor DM)	-	71.3	2.2	*64*	-	-	-	-	-	2.4	1.1
Sample average							**124**						**4.2**	
2σ							170						5.8	
SEM							60						2.0	
Host augite composition							*1.9*	*33.9*	*0.0*				*-14.2*	

Table 4.2. Selected major and trace element contents and boron isotope values obtained for pyroxene and zircon hosted melt inclusions from southern Central Andean arc volcanic rocks. The boron concentrations calculated from the average counts from the boron isotope analysis are displayed in italics and underlined. Zirconium concentrations are not given for melt inclusions hosted in zircon due to the high concentrations present in the host. The analytical uncertainties on the individual $\delta^{11}B$ values are propagated uncertainties quoted at the 2σ level (Appendix 3.2.3). The average $\delta^{11}B$ for individual samples are displayed as weighted averages in order to account for the higher analytical uncertainties obtained for some analyses. Average compositions for the host mineral phases are also presented for comparison.

4.7.1 The effect of differentiation on boron concentrations and isotope ratios

There is no observable correlation between boron concentrations and isotope ratios and the degree of differentiation (Figure 4.6). Boron concentrations and isotope ratios obtained for pyroxene and zircon hosted melt inclusions from the same sample (1026) also lie within analytical uncertainty of each other (Fig. 4.6 and Table 4.2), as do values obtained from melt inclusions trapped in augite and enstatite phenocrysts, from the same samples (AM0887 and 1026) (Table 4.2). This suggests that the phenocryst phases are trapping melts with the same boron concentrations and isotopic compositions, despite the fact that they may have crystallised at different times during the differentiation of the magma.

This combined evidence suggests that magma differentiation has a negligible effect on the boron concentrations and $^{11}B/^{10}B$ ratios trapped in silicate melt inclusions. This finding is in line with other studies which found the effect of magmatic processes on boron isotope fractionation to be limited (e.g., Ishikawa and Tera, 1997; Ishikawa et al., 2001). On this basis the boron concentrations and isotope ratios obtained for samples Z27 (dacite) and MQ153 (andesite), which only contain zircon hosted melt inclusions, are included in the dataset alongside data obtained from pyroxene hosted inclusions.

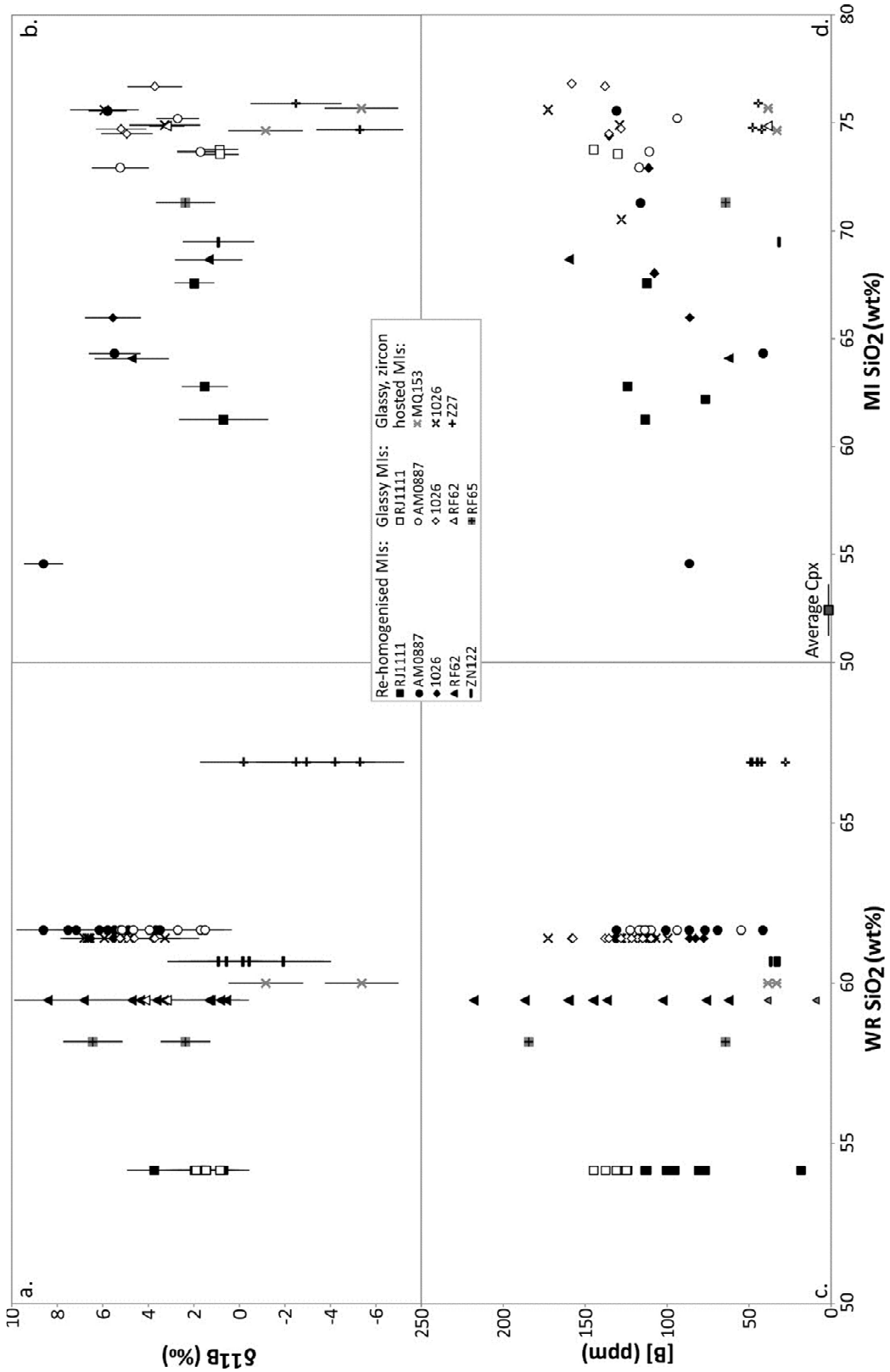

Figure 4.6. Boron concentrations and boron isotope values plotted against the corresponding whole rock (WR) and melt inclusion (MI)

SiO_2 (wt.%) contents for pyroxene and zircon hosted melt inclusions. Whole rock SiO_2 (wt.%) values for individual samples were determined by XRF analysis (Chapter 2 and Appendix 1.12) and melt inclusion SiO_2 (wt.%) contents by EPMA (Appendix 3.8). Error bars on the $\delta^{11}B$ values represent propagated uncertainties at the 2σ level. Errors bars on the boron concentrations are smaller than the symbol size.

4.7.2 Intra-sample variations and the potential effects of melt inclusion re-homogenisation on boron concentrations and isotopic compositions

Boron isotope values, and boron concentrations in certain samples, are highly variable and exceed analytical uncertainties (Fig. 4.5 and 4.6, and Table 4.2). Relative differences of up to 7.9 ‰ and 209 ppm are observed in melt inclusions from a single rock sample. However, melt inclusions from the same phenocryst have $\delta^{11}B$ values within analytical uncertainty of each other (Table 4.2).

Where possible, both re-homogenised and glassy melt inclusions were analysed from the same sample. Where significant numbers of analyses for an individual sample are available (e.g., RJ1111, 1026 and AM0887) the re-homogenised melt inclusions generally have lower boron concentrations than the glassy inclusions (Table 4.2 and Fig. 4.6c). During re-homogenisation any daughter minerals present in the melt inclusion are re-melted and re-equilibrated with the melt inclusion glass. In addition to this, there is evidence to suggest some melting of the host mineral may have occurred during re-homogenisation (refer to Appendix 3.9). This may include host mineral crystallised onto the melt inclusion walls (e.g., Danyushevsky et al., 2002 and references therein). As boron is highly incompatible in mineral phases in basaltic to andesitic melt compositions (Brenan et al., 1998), it is likely to be present in the melt inclusion glass rather than the host phase or any daughter minerals which crystallised post entrapment (daughter minerals present in the pyroxene hosted melt inclusions are primarily Fe and Ti oxides). However, a potential effect of the re-homogenisation processes is to dilute the boron

concentration of the melt inclusion glass with the addition of non-boron containing phases (daughter minerals and/or host mineral).

No systematic variations in $\delta^{11}B$ values are observed between re-homogenised and glassy melt inclusions (where there are a significant number of analyses for an individual sample, e.g., RJ1111, 1026 and AM0887) (Table 4.2 and Fig. 4.6a). Due to the low concentrations of boron in the pyroxene and zircon phenocrysts (range = 0.4 - 2.9 ppm, average = 1.4 ppm) compared to the concentrations obtained for the melt inclusion glasses (range = 9 – 218 ppm, average = 101 ppm), the effect of boron addition from the host mineral phases, either due to melting of the host mineral phase during re-homogenisation, or the overlap of the SIMS analysis onto the host mineral, will have a negligible effect on the $\delta^{11}B$ value of the analysed melt inclusion. Bulk mixing equations show that >80 % of the boron present in the analysed volume would have to be derived from the host phenocryst phase in order to cause a shift of 1‰ in $\delta^{11}B$ values, when using the average values. Even in the worst case scenario, >15 % of the boron in the analysed volume would be required to cause a shift in $\delta^{11}B$ values of 1‰, and the values obtained for this particular inclusion (RF62-MB3-MI1) are within analytical uncertainty of the average $\delta^{11}B$ obtained for the sample.

However, it is possible that re-homogenisation and sample preparation procedures may account for some intra-sample variation in $\delta^{11}B$ values. Virtually all melt inclusions originally contained a visible vapour or shrinkage bubble. During re-homogenisation the vapour phase was re-incorporated and re-equilibrated with the melt. Boron is a minor constituent of volcanic gases (Fogg and Duce, 1985) and $\delta^{11}B$ values of between +2.3 and +21.4 ‰ have been reported for volcanic emissions (Kanzaki et al., 1979; Nomura et al., 1982). Therefore, the addition of any boron present in the vapour phase due to melt inclusion re-homogenisation, or alternatively the loss of any boron present in the vapour phase either due to the re-

homogenisation process or during exposure of melt inclusions at the surface, may result in variations in both boron concentrations and $\delta^{11}B$ values.

In summary, some of the apparent intra-sample variations in both boron concentrations and isotope values (Fig. 4.5 and 4.6 and Table 4.2) are attributed to the effects of sample preparation and re-homogenisation. However, the observed intra-sample heterogeneity in boron concentrations and $\delta^{11}B$ values may also reflect real variations due to the trapping of different melt compositions by phenocrysts phases which crystallised at different times. Variations in the trapped melt compositions may be a result of the assimilation of crustal materials during magma ascent and/or the mixing of magmas with different compositions during progressive crystallisation. Further discussion is presented in Section 4.8.2.

4.7.3 Inter-sample variations

In addition to the observed intra-sample heterogeneity there are also significant differences in boron concentrations and $\delta^{11}B$ values between samples. Due to these significant inter-sample variations all the data obtained from both glassy and re-homogenised melt inclusions are considered for the overall interpretation.

Most strikingly the boron concentrations and $\delta^{11}B$ values vary as a function of age (Fig. 4.7). Boron isotope values obtained for augite hosted melt inclusions from the Paleocene sample (RJ1111 – 61.2 ±1.0 Ma) are positive and range between +0.7 ±0.9 ‰ and +3.7 ±1.2 ‰. These are accompanied by relatively high B/Nb ratios of between 15.6 and 20.7. B has been normalised to Nb as they display different chemical behaviours in fluid related processes but are both incompatible elements and therefore the B/Nb of a magma is not significantly affected by partial melting or fractional crystallisation. Zircon and augite hosted melt inclusions from the late Oligocene samples of the Tilito Formation (MQ153 - 25.2 ±0.3 Ma, ZN122 - 24.8 ±0.4

Ma, and Z27 - 23.2 ±0.3 Ma) produced generally negative $\delta^{11}B$ values between -5.4 ±1.6 ‰ and +0.9 ±1.7 ‰ and low, tightly grouped B/Nb ratios of between 1.5 and 5.7. Boron isotope values obtained for melt inclusions present in zircon, augite and enstatite phenocrysts from the Miocene samples of the Escabroso Formation (AM0887 – 19.3 ±0.3 Ma and 1026 - 18.2 ±0.3 Ma) are positive and range between +1.5 ±1.2 ‰ and +8.6 ±1.2 ‰, with B/Nb ratios ranging between 4.4 and 18.7. Augite hosted melt inclusions from the youngest Miocene samples analysed (Cerro de las Tórtolas Formation, RF65 and RF62 – 17.1 ±0.6 Ma) produced positive $\delta^{11}B$ values of between +0.6 ±1.0 ‰ and +8.4 ±1.5 ‰ and high B/Nb ratios of between 7.5 and 36.3 (Fig. 4.7).

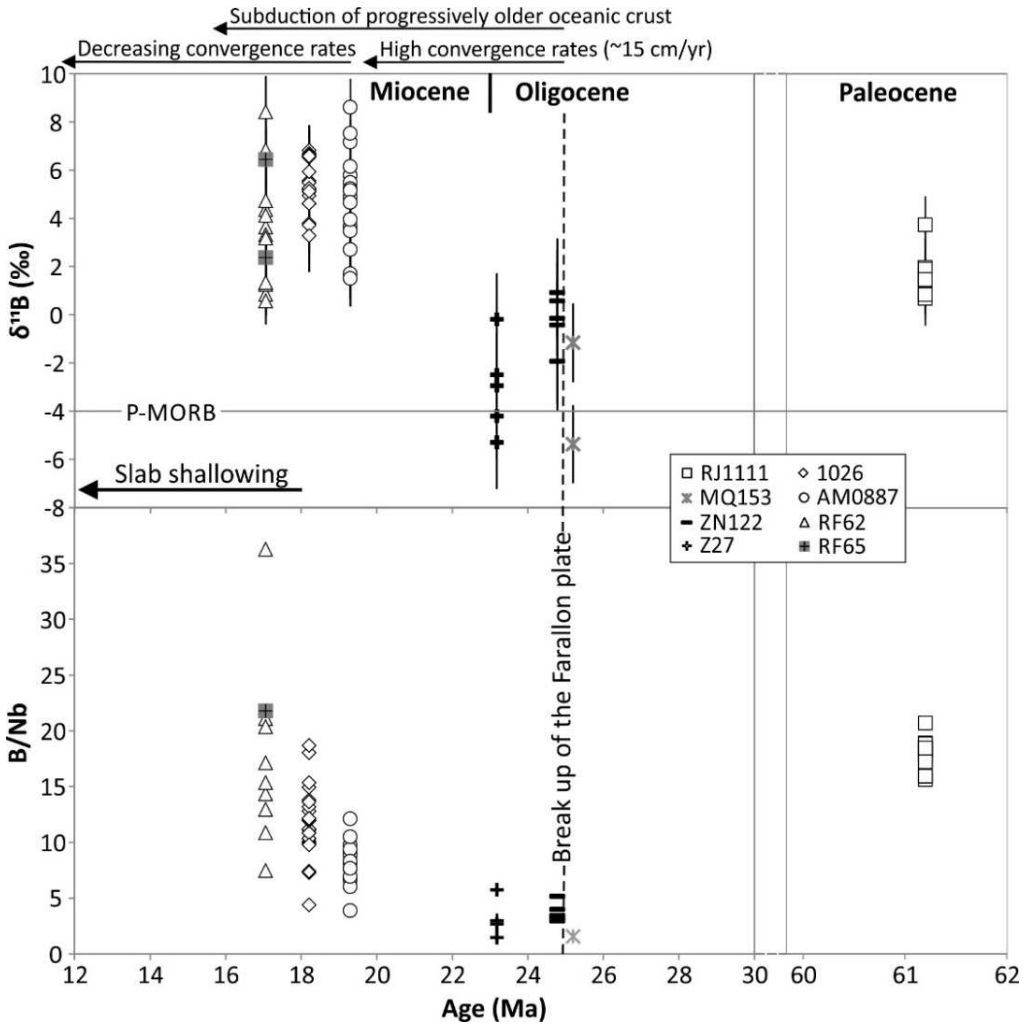

Figure 4.7. Boron isotope values and B/Nb ratios plotted against sample age. Key tectonic events, changes in convergence rates and the $\delta^{11}B$ value for MORB are highlighted (refer to text for references). MORB has a B/Nb ratio of 0.3 (Chaussidon and Marty, 1995; Workman and Hart, 2005). Error bars on the $\delta^{11}B$ values represent propagated uncertainties at the 2σ level.

4.8 Discussion

4.8.1 Potential sources of boron in southern Central Andean arc magmas

The large compositional difference between the samples and variability with time suggests complex sourcing of boron in southern Central Andean arc magmas. Here

we quantify the contribution of different sources using multi-component mixing models in order to investigate the temporal variations in the source of boron in these magmas. Potential sources which may contribute boron to arc magmas include the depleted mantle wedge, serpentinised peridotite from oceanic lithosphere or mantle wedge, altered oceanic crust (AOC), subducted sediments and the continental basement, all of which have varied boron contents and boron isotope compositions (Fig. 4.1). The Andean mantle wedge is considered to have a similar composition to that of MORB-source mantle (Lucassen et al., 2002) which has boron concentrations of ~0.05 ppm with a $\delta^{11}B$ value of -4.0 ‰ (Chaussidon and Jambon, 1994; Chaussidon and Marty, 1995). Therefore melting of the mantle wedge is likely to contribute negligible boron to primary arc magmas and have little impact upon the $\delta^{11}B$ composition. In all samples, boron concentrations are higher than MORB (0.5 ppm (Chaussidon and Marty, 1995)) and the $\delta^{11}B$ values obtained for all but three melt inclusions are more positive than those of MORB (Fig. 4.5).

Crustal contamination and assimilation processes have previously been invoked in the petrogenesis of Central Andean arc magmas (e.g., James, 1982; Hildreth and Moorbath, 1988; Davidson and de Silva, 1992). Oxygen and hafnium isotopic signatures obtained for zircons present in Late Oligocene – Miocene arc samples from the Pampean flat-slab segment, along with the presence of inherited zircon cores, suggests that the arc magmas have been contaminated via assimilation of the Late Palaeozoic – Early Mesozoic basement (Chapter 3). An average boron concentration of 43 ppm and a $\delta^{11}B$ value of -8.9 ±2.3 ‰ has been reported for the Palaeozoic and Mesozoic Central Andean basement (Kasemann et al., 2000). This reported $\delta^{11}B$ value overlaps with the estimated average range of global continental crust (-8 to -13 ‰) (Chaussidon and Albaréde, 1992), however the boron concentrations are distinctly higher than those reported for average upper crust (15 ppm (Taylor and McLennan, 1995)). Consequently, contamination of arc magmas derived from the mantle wedge with Palaeozoic – Early Mesozoic Andean crust

would lead to more negative boron isotope compositions in the melt, relative to the mantle wedge. The higher $\delta^{11}B$ values (-5.4 to +8.6 ‰) and boron concentrations (up to 218 ppm) obtained for the arc volcanic rocks suggests that the majority of boron present is not derived from the continental crust, and therefore must be derived from subducting components.

There are two potential sources of boron-rich, high $\delta^{11}B$ fluids present in the subducting oceanic lithosphere; AOC and serpentinised peridotite. Due to the low-temperature uptake of boron from seawater ([B] = ~4.5 ppm, $\delta^{11}B$ = +39.5 ‰ (Spivack and Edmond, 1987)), altered oceanic crust has higher boron concentrations and $\delta^{11}B$ values than unaltered MORB. Spivack and Edmond (1987) reported $\delta^{11}B$ values ranging between +0.1 and +9.2 (±0.4) ‰ and boron concentrations of between 8.9 and 69 ppm for low temperature altered oceanic crust (potentially including a serpentinite component). Smith et al. (1995) produced a slightly lower average boron content of 5.2 ±1.7 ppm and a $\delta^{11}B$ value of +3.4 ±1.1 ‰ for AOC. During serpentinization, boron and preferentially ^{11}B is added to peridotite, resulting in positive $\delta^{11}B$ values ($\delta^{11}B$ = +8.3 to +12.6 ‰) and boron concentrations (50 – 81 ppm) (Spivack and Edmond, 1987). Heavier $\delta^{11}B$ values ranging between +29.6 and +40.5 ‰ were reported by Vils et al. (2009) for highly serpentinised, spinel harzburgites from the Mid-Atlantic ridge.

Subducting sediments may also influence the composition of the sub arc mantle. Sediments have highly variable boron concentrations and isotope ratios, often reflecting a mixing of different proportions of continental detritus with negative $\delta^{11}B$ values ([B] = 30 - >100 ppm and $\delta^{11}B$ = -8 to -13 ‰), and pelagic sediments with positive $\delta^{11}B$ values composed of marine smectite ([B] = 110 - 150 ppm and $\delta^{11}B$ = +2.3 to +9.2 ‰), biogenic silica ([B] = 60 - 70 ppm and $\delta^{11}B$ = +2.1 to +4.5 ‰), and biogenic carbonate ([B] = 1 - 26 ppm and $\delta^{11}B$ = +8.0 to +26.2 ‰) (Ishikawa and Nakamura, 1993). The composition and quantity of the sediment entering the sub

arc region in the southern Central Andes is difficult to estimate and is likely to have changed over the course of the Cenozoic due to a wide range of factors including climate, productivity, drainage, and levels of sediment accretion. The Central Andean margin is currently non-accretionary (Von Huene and Scholl, 1991) and high levels of subduction erosion have been proposed for the Cenozoic (e.g., Rutland, 1971; Stern, 1991; Kay et al., 2005; Goss et al., 2013). The majority of sediment currently present in the Chile trench appears to be continentally derived from the South American continent (Scholl et al., 1970; Thornburg and Kulm, 1987a; Thornburg and Kulm, 1987b; Kilian and Behrmann, 2003), the basement of which has a $\delta^{11}B$ value of -8.9 ±2.3 ‰ (Kasemann et al., 2000).

4.8.2 Source variations with time

As previously mentioned, one of the most significant features of the melt inclusion data is the variation in boron concentrations and boron isotope ratios with age (Fig. 4.7). Both $\delta^{11}B$ and B/Nb values are significantly lower in pyroxene and zircon hosted melt inclusions from the late Oligocene samples of the Tilito Formation (25.2 – 23.2 Ma) than the values obtained for the Paleocene (61.2 Ma) and Miocene (19.3 – 17.1 Ma) arc samples. In addition to this, significantly higher $\delta^{11}B$ values were obtained for the Miocene samples (average = 4.7 ±1.9 ‰). This variability suggests that (1) the melt source regions were affected by fluids derived from different sources; (2) the melt source region received less fluids derived from the subducting slab due to the slab being at greater depth beneath the arc and therefore more dehydrated; and/or (3) the ascending arc magmas assimilated different volumes of Andean continental crust.

In order to quantify the contribution of different sources multi-component mixing models have been generated using the method of Tonarini et al. (2011). Two major reservoirs are considered; the uppermost slab, which is represented by a mix of 90 %

AOC and 10 % sediments; and the ultramafic portion of the subducting oceanic lithosphere, which includes serpentinite. The values used by Tonarini et al. (2011) are considered appropriate as they include the composition of Boschi et al. (2008) for abyssal serpentinites, and the widely used AOC compositions reported by Smith et al. (1995) and Leeman et al. (2004). There is no boron data available for sediments currently present in the Chile trench, however it is suggested that the majority of sediment is continentally derived (Scholl et al., 1970; Thornburg and Kulm, 1987a; Thornburg and Kulm, 1987b; Kilian and Behrmann, 2003). On this basis a negative boron isotopic composition, similar to that of the Andean basement (-8.9 ±2.3 ‰ (Kasemann et al., 2000)), can be inferred for subducting sediments along the Andean margin. Therefore the sediment composition of 115 ppm B and $\delta^{11}B$ value of -4.1‰, used by Tonarini et al. (2011), is considered a reasonable approximation. In order to account for the reduction in both $\delta^{11}B$ values and the quantities of boron in slab-derived fluids with progressive dehydration of the slab, two different depths to the top of slab beneath the arc have been modelled (90 and 120 km) (Fig. 4.8).

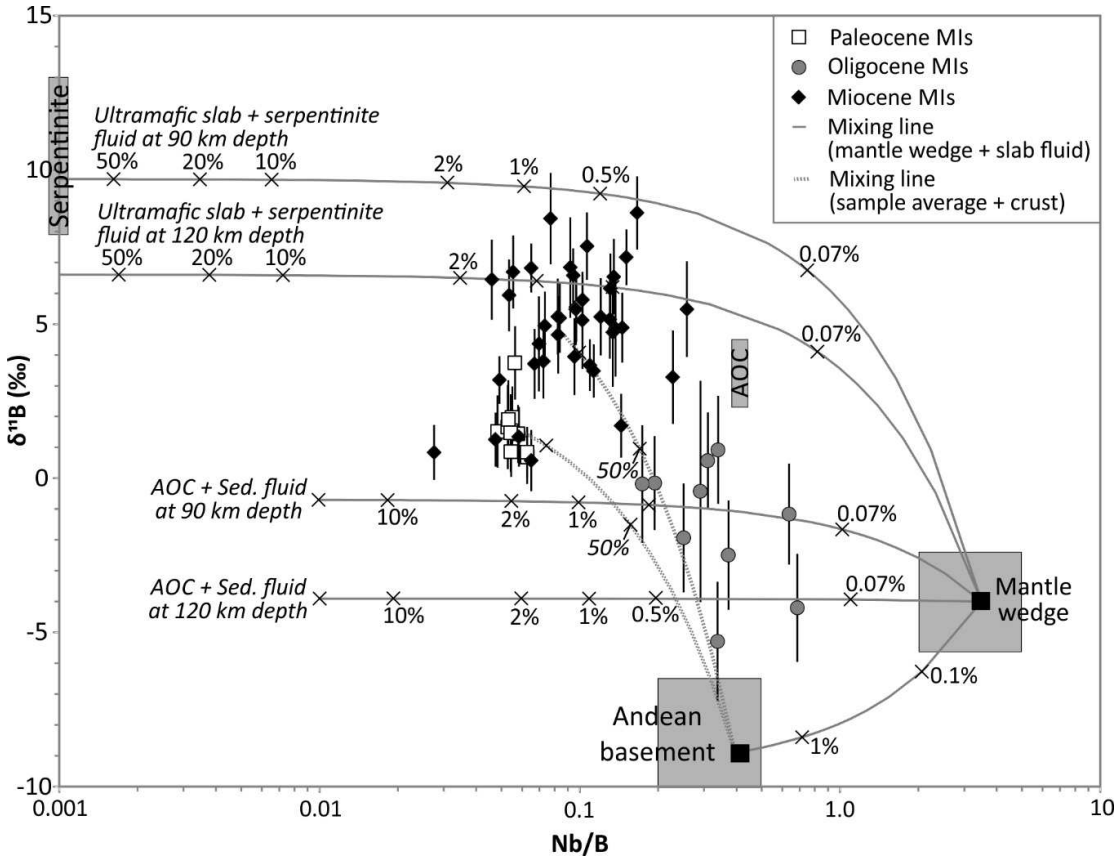

Figure 4.8. Plot of Nb/B ratios versus $\delta^{11}B$ values for melt inclusions from Paleocene, Oligocene and Miocene arc samples. Mixing lines between the mantle wedge (N-MORB source) and fluids derived from AOC + sediment, and the mantle wedge (N-MORB source) and fluids derived from ultramafic slab + serpentinite are shown for different depths (solid lines). The fluids derived from AOC + sediments assumes a ratio of 90:10 following the methods of Tonarini et al. (2011). Bulk mixing lines between the average melt inclusion compositions for the Paleocene and Miocene samples and the average Andean crust are also shown (dashed lines). The numbers indicate the amount of fluid added to the mantle source as a percentage. End member compositions (grey boxes) are also shown for the mantle wedge (Sun and McDonough, 1989; Chaussidon and Marty, 1995), the Andean basement (Kasemann et al., 2000, Appendix 1.13 for Nb concentrations), AOC (Spivack and Edmond, 1987; Sun and McDonough, 1989) and serpentinite (Spivack and Edmond, 1987; Deschamps et al., 2013).

4.8.2.1 Paleocene; homogeneous slab-derived fluids

The $\delta^{11}B$ values obtained from the Paleocene sample (RJ1111) display little variation compared to the Oligocene and Miocene samples (Fig. 4.7 and 4.8), suggesting a more homogeneous boron source. There is also evidence to suggest that the Paleocene arc magmatic rocks, present in the Principal Cordillera of Chile, have received very little contamination with existing continental crust due to crustal assimilation (e.g., Chapters 2 and 3 and Parada et al., 1988). Therefore, virtually all of the boron present in the Paleocene arc magmas is likely to be derived from the subducting slab.

As B is highly fluid-mobile and Nb is highly fluid-immobile, fluids derived from the subducting slab are likely to have very low Nb/B ratios compared to the mantle wedge, which has high Nb/B ratios of ~3.5 (Sun and McDonough, 1989; Chaussidon and Marty, 1995). Simple mixing between MORB and a slab-derived fluid would produce a linear array on an Nb/B vs. $\delta^{11}B$ plot. A number of studies have used this relationship to estimate a $\delta^{11}B$ value for slab-derived fluids by extrapolating the mixing line between MORB and the arc samples, to a Nb/B = 0 (e.g., Ishikawa and Nakamura, 1994; Ishikawa et al., 2001; Rosner et al., 2003).

By mixing a MORB composition with the average $\delta^{11}B$ and Nb/B composition obtained for the Paleocene sample, a $\delta^{11}B$ value of +1.6 ‰ is obtained (Fig. 4.9). The $\delta^{11}B$ values for all but one melt inclusion are within analytical uncertainty of the sample average (+1.5 ‰), suggesting that the mixing of slab-derived fluids with a $\delta^{11}B$ composition of approximately +1.6 ‰ with the mantle wedge explains the boron isotope compositions of sample RJ1111 well. No individual source in our model has a $\delta^{11}B$ value of +1.6 ‰, but as shown in Figure 4.8 the addition of ~2 % fluid derived from AOC (± sediments) with some addition of high $\delta^{11}B$ fluids derived from serpentinite, could account for the boron compositions obtained for the Paleocene sample. The relative amounts of AOC (± sediments) and serpentine-

derived fluids are difficult to quantify due to lack of constraints on the depth of the slab, but AOC will be the largest contributor of fluids at slab depths between 90 and 120 km (Fig. 4.8).

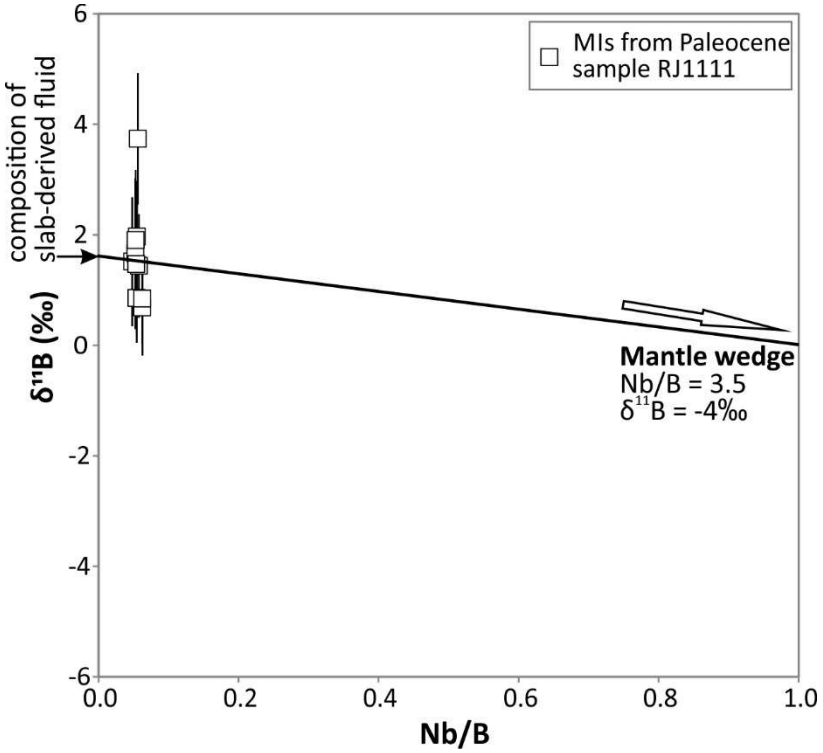

Figure 4.9. Nb/B ratios plotted against $\delta^{11}B$ values for all analysed melt inclusions from Paleocene (61 Ma) sample RJ1111. Error bars on the $\delta^{11}B$ values represent propagated uncertainties at the 2σ level. Extrapolation of the regression line to Nb/B = 0 gives a $\delta^{11}B$ value for the slab-derived fluid of +1.6 ‰ (see text for discussion). Mantle wedge (N-MORB / N-MORB source values for B) from Chaussidon and Marty (1995) and Sun and McDonough (1989). A similar relationship is also displayed between Zr/B and $\delta^{11}B$ values (not shown) suggesting the Nb/B ratios are not controlled by any processes which preferentially reduce Nb from the arc magmas, such as the involvement of residual TiO_2 phase (Green, 1981).

4.8.2.2 Oligocene: a broad magmatic arc

Boron isotopic compositions of Oligocene samples (-5.4 to +0.9 ‰) just overlap with the Paleocene compositions (+0.7 to +3.7 ‰) but extend to lower values (Fig. 4.7 and 4.8). Mixing lines indicate the addition of fluids primarily derived from dehydrating

AOC + sediments to the magma source region may explain the compositions of the Oligocene samples (Fig. 4.8). This fluid source is therefore potentially similar to that in the Paleocene, however the addition of other components (for example, continental crust) is required to account for the intra-sample variability and higher Nb/B values.

The assimilation of continental crust during magma ascent may have modified B isotope compositions. Oxygen and hafnium isotopic compositions obtained for magmatic zircon from these samples, suggests between ~5 to 15 % bulk assimilation of the Palaeozoic – Mesozoic basement by Oligocene mantle-derived melts (Chapter 3). The concentrations of boron in the Oligocene samples of the Tilito Formation (average [B] = 39 ppm ±13 (2σ)) are very similar to those obtained for the Palaeozoic – Mesozoic Central Andean basement (43 ppm). However, the $\delta^{11}B$ values are heavier (-5.4 to +0.9 ‰) than the basement (-8.9 ±2.3 ‰) (Kasemann et al., 2000). As is apparent from mixing relations, the high Nb/B ratios of most of the Oligocene arc volcanic rocks cannot be explained solely by the contamination of arc magmas with a similar composition to those in the Paleocene, with Paleozoic – Mesozoic Andean crust, as large volumes (>50% bulk assimilation) would be needed to explain the majority of $\delta^{11}B$ and Nb/B values (Fig. 4.8). Thermal limits suggest that the assimilation of this quantity of felsic crust by mantle-derived melts is unsupportable (Reiners et al., 1995). Therefore, progressive assimilation of crustal materials could account for some of the intra-sample variation in $\delta^{11}B$ values and Nb/B ratios, but not the overall compositions. This implies that the Oligocene arc magmas received contributions from slab-derived fluids with a different boron composition to those influencing the Paleocene source regions. This could either be a result of a change in the relative proportions, or compositions, of the subducting components and/or changing the depth to the top of the slab beneath the arc.

The change in slab-derived fluid composition may be related to changes in the configuration of the arc during the Oligocene, when convergence rates between the Nazca and the South American plates increased to a rate of ~15 cm/yr and the angle of convergence became more normal with the Andean margin (Pardo Casas and Molnar, 1987; Somoza, 1998; Somoza and Ghidella, 2012). These increased convergence rates resulted in thickening of the continental crust in the northern Central Andes (Isacks, 1988; Oncken et al., 2006) but are believed to have led to a more extensional regime in the southern Central Andes (Jordon et al., 2001). As a result the magmatic arc broadened in the southern Central Andes (Pilger, 1984) and there is coeval back-arc volcanism associated with the emplacement of the Oligocene Tilito Formation (Litvak and Poma, 2010). This implies that arc magmatism during the late Oligocene had a wide across-arc extent and is likely to have been emplaced over a wide range of depths to the slab-mantle interface. This is important because a number of studies have shown that across arc variations in boron abundance and isotopic composition of arc magmas can be related to the depth of the Wadati-Benioff Zone (WBZ) (e.g., Ryan et al., 1995; Ishikawa and Tera, 1997; Ishikawa et al., 2001; Rosner et al., 2003; Leeman et al., 2004). In the Andean Central Volcanic Zone (22 – 27 °S, i.e. north of the Pampean flat-slab region) Rosner et al. (2003) found boron concentrations and $\delta^{11}B$ values, obtained for Late Miocene to Quaternary volcanic rocks, decrease with increasing depth to the WBZ. The range of $\delta^{11}B$ values and low boron concentrations obtained for the Quaternary volcanic rocks ($\delta^{11}B$ values of -2.1 ‰ (±0.1) to -7.2 ‰ (±0.2) and B concentrations of 10 - 20 ppm) (NB. melt inclusions are likely to have higher boron concentrations than whole rock (Schmitt et al., 2002)) located in the back arc, where depths to the WBZ range between 123 and 152 km (Cahill and Isacks, 1992), are very similar to those obtained for the Oligocene samples of the Tilito Formation. On this basis we suggest that the Tilito Formation was emplaced over a greater depth to the WBZ than the Paleocene arc magmatic rocks, and that the lower $\delta^{11}B$ and higher B/Nb ratios reflect

decreasing fluid flux from the slab with progressive dehydration (Fig. 4.10). This is consistent with a low fluid contribution (<0.5%) in the mixing model (Fig. 4.8).

A greater depth to the WBZ is also supported by tectonic evidence and whole rock geochemistry (Chapter 2) which suggests that the most eastern extent of the Oligocene Tilito Formation, which is present in the Frontal Cordillera of Argentina, may have been emplaced in a more extensional setting (Chapter 2 and Winocur et al., 2013). Higher boron concentrations and $\delta^{11}B$ values comparable to the Paleocene rocks are therefore likely to be present in Oligocene arc magmatic rocks closer to the trench, where the depth to the top of the subducting slab was shallower. Unfortunately samples from these frontal arc locations did not contain suitable melt inclusions for boron isotope analysis.

4.8.2.3 Miocene: subduction of a seamount chain

Over the latter part of the Cenozoic the angle at which the oceanic plate subducts beneath the Andean margin, has changed, although the exact timing and cause of the shallowing of the subducting Nazca plate in the Pampean flat-slab segment is somewhat debated (e.g., Cahill and Isacks, 1992; Gutscher et al., 2000; Yañez et al., 2001; Kopp et al., 2004; Manea et al., 2012). The Miocene samples (Escabrosso Formation and Cerro de las Tórtolas Formation) were emplaced at very similar longitudes to the Oligocene samples (Tilito Formation) (Fig. 4.10). However, the lower Nb/B ratios suggest these magmas were emplaced over a less dehydrated slab and therefore a shallower depth to the top of the slab. This is consistent with the shallowing of the subducting plate and the migration of the volcanic arc to the east during the Miocene (e.g., Kay and Abbruzzi, 1996; Kay and Mpodozis, 2002; Kay et al., 2005).

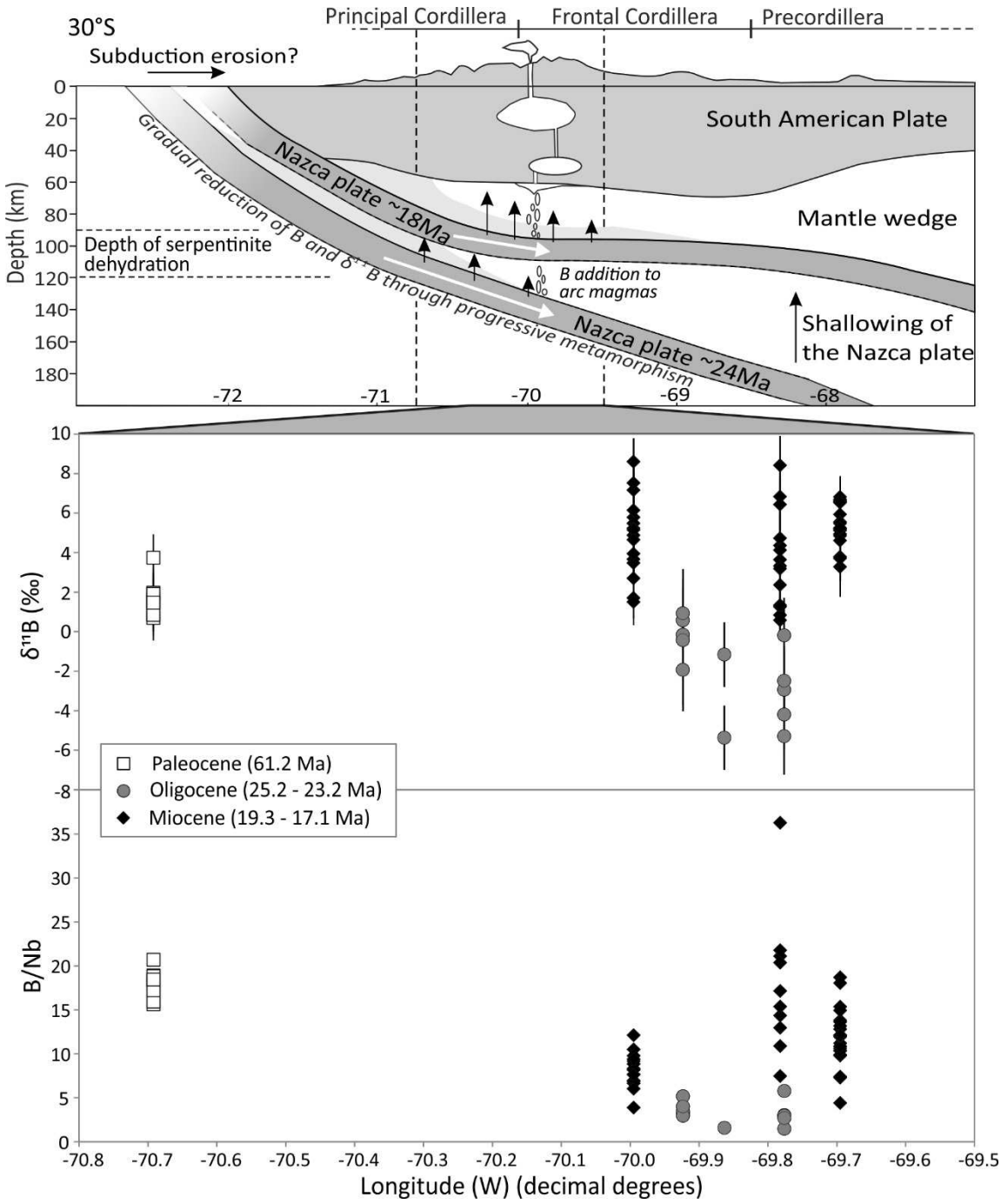

Figure 4.10. Boron isotope values and B/Nb ratios plotted against longitude (^{0}W) and displayed against a schematic cross section of the Andean margin at 30^{0}S showing the approximate depths to the subducting Nazca plate below the volcanic arc during the late Oligocene and the early Miocene. The depths to the top of the subducting slab for the two different time frames (~24 Ma and ~18 Ma) are estimated using the findings of Rosner et al. (2003) (see text for discussion).

The high $\delta^{11}B$ values of the Miocene samples (average = 4.7 ±1.9 ‰) cannot be accounted for by fluids derived from AOC + sediment, which have a maximum value of -0.7 ‰ at a slab depth of 90 km, and are even lower at greater slab depths (Fig. 4.8). The source of heavy boron is considered to be dehydrating serpentinite. The mixing relations in Figure 4.8 suggest the addition of between ~0.2 and 2 % fluid derived largely from dehydrating serpentinite to the mantle source is required to produce the compositions of the Miocene samples. As previously mentioned, serpentinite in subduction zones can either be present in the subducting oceanic lithosphere, or peridotite in the mantle wedge can be serpentinised by slab-derived fluids and dragged down into a sub-arc position (e.g., Straub and Layne, 2002; Hattori and Guillot, 2003; Hyndman and Peacock, 2003; Tonarini et al., 2011). The Juan Fernandez Ridge (JFR), a volcanic seamount chain, began intersecting the Central Andean margin during the Late Miocene (~20 Ma) (Yañez et al., 2001). The oceanic lithosphere associated with the JFR has been affected by hydration and mineral alteration with ~20% serpentinisation (Kopp et al., 2004). Therefore we suggest that fluids affecting the source of the early Miocene arc magmas in the southern Central Andes are derived from serpentinite present in the subducting oceanic lithosphere rather than from a serpentinised mantle wedge dehydrating at sub-arc depths.

However, the Miocene values do not sit on a simple mixing trend and show significant scatter (Fig. 4.8). This implies an additional influence on the boron composition of the arc magmas. A number of separate lines of evidence suggest that the Miocene arc magmas have been affected by crustal contamination during migration through the Andean continental crust (e.g., Chapters 2 and 3, and Kay et al., 2005; Litvak et al., 2007). Evidence from the isotopic variability displayed in zircons from the Miocene samples 1026 and RF62 (Chapter 3) suggests the mantle-derived melts assimilated between 5 and 15 % Palaeozoic – Mesozoic crust en route to the surface, a similar amount to the Oligocene arc magmas. Hence, progressive

assimilation and/or the assimilation of different amounts of Palaeozoic – Mesozoic basement is likely to account for the apparent variability in B/Nb and $\delta^{11}B$ values observed in the Miocene arc magmatic rocks.

4.9 Conclusions

1. Magma differentiation has a negligible effect on boron concentrations and $\delta^{11}B$ values trapped in melt inclusion glasses. It is also demonstrated that melt inclusions trapped in different phenocryst phases (pyroxene and zircon) record the same composition. Therefore the $\delta^{11}B$ and boron concentrations recorded by melt inclusions present in arc magmatic rocks from the southern Central Andes can be used to assess changes in slab-derived fluids to magma source regions over time.

2. The primary source of the boron present in Paleocene arc magmas (Los Elquinos Formation, 61.2 Ma) is fluid derived from the altered oceanic crust of the subducting Farallon plate, with a minor component derived from dehydrating serpentinite. The melt inclusion compositions are consistent with the addition of ~2 % slab-derived fluid with a rather homogeneous boron isotopic composition of +1.6 ‰, to the magma source region.

3. The source of the Oligocene arc magmatic rocks (Tilito Formation, 25.2 – 23.2 Ma) records a diminished influence of slab-derived fluids (<0.5 % fluid addition) with more negative $\delta^{11}B$ values, compared to the Paleocene and Miocene arc magmatic rocks. This is indicative of a greater depth of the slab-mantle interface due to broadening of the southern Central Andean magmatic arc during this time period.

4. Miocene samples (Escabroso Formation and Cerro de las Tórtolas Formation, 19.3 – 17.1 Ma) record the highest $\delta^{11}B$ values (+0.8 to +8.6 ‰) which is indicative of 0.2 – 2 % addition of fluids derived primarily from dehydrating serpentinite to the source of the arc magmas. The timing is approximately coeval with the intersection of the Juan Fernandez Ridge with the Andean margin (~20 Ma, although this is believed to have been north of the study area (Yañez et al., 2001)). This volcanic seamount is thought to include a large component of hydrated and serpentinised oceanic lithosphere (Kopp et al., 2004), thus implying that hydrated, and hence less dense oceanic lithosphere, is likely to be related to the shallowing of the subducting oceanic plate in this region of the southern Central Andes. It also suggests that the hydrated and serpentinised JFR may have begun intersecting the Andean margin at ~30°S slightly earlier (~20 Ma) than previously thought (~18 Ma).

5. Some of the intra-sample variation in the geochemical signatures obtained for melt inclusions from the Oligocene and Miocene arc magmatic rocks is likely to be the result of varying levels (between 5 and 15%) of crustal assimilation en route to the surface, as suggested by O and Hf isotopic compositions of zircon (Chapter 3).

4.10 References

Aizawa, Y., Tatsumi, Y., and Yamada, H., 1999, Element transport by dehydration of subducted sediments: Implication for arc and ocean island magmatism: Island Arc, v. 8, p. 38-46.

Anderson, M., Alvarado, P., Zandt, G., and Beck, S., 2007, Geometry and brittle deformation of the subducting Nazca Plate, Central Chile and Argentina: Geophysical Journal International, v. 171, p. 419-434.

Bissig, T., Clark, A.H., Lee, J.K., and von Quadt, A., 2003, Petrogenetic and metallogenetic responses to Miocene slab flattening: new constraints from the El Indio-Pascua Au–Ag–Cu belt, Chile/Argentina: Mineralium Deposita, v. 38, p. 844-862.

Bissig, T., Lee, J.K.W., Clark, A.H., and Heather, K.B., 2001, The Cenozoic History of Volcanism and Hydrothermal Alteration in the Central Andean Flat-Slab Region: New 40Ar-39Ar Constraints from the El Indio–Pascua Au (-Ag, Cu) Belt, 29°20′–30°30′ S: International Geology Review, v. 43, p. 312-340.

Boschi, C., Dini, A., Früh-Green, G.L., and Kelley, D.S., 2008, Isotopic and element exchange during serpentinization and metasomatism at the Atlantis Massif (MAR 30 N): insights from B and Sr isotope data: Geochimica et Cosmochimica Acta, v. 72, p. 1801-1823.

Brenan, J.M., Neroda, E., Lundstrom, C.C., Shaw, H.F., Ryerson, F.J., and Phinney, D.L., 1998, Behaviour of boron, beryllium, and lithium during melting and crystallization; constrainsts from mineral-melt partitioning experiments.: Geochimica et Cosmochimica Acta, v. 62, p. 2129 - 2141.

Cahill, T., and Isacks, B.L., 1992, Seismicty and Shape of the Subducted Nazca Plate: Journal of Geophysical Research, v. 97, p. 17,503 - 17,529.

Catanzaro, E.J., 1970, Boric acid: isotopic and assay standard reference materials, National Bureau of Standards, Institute for Materials Research.

Charchaflié, D., Tosdal, R.M., and Mortensen, J.K., 2007, Geologic framework of the Veladero high-sulfidation epithermal deposit area, Cordillera Frontal, Argentina: Economic Geology, v. 102, p. 171-192.

Charrier, R., Pinto, L., and Rodríguez, M.P., 2007, Tectonostratigraphic evolution of the Andean Orogen in Chile, *in* Moreno, T., and Gibbons, W., eds., The Geology of Chile: London, The Geological Society, p. 21 - 114.

Chaussidon, M., and Albaréde, F., 1992, Secular boron isotope variations in the continental crust: an ion microprobe study: Earth and Planetary Science Letters, v. 108, p. 229 - 241.

Chaussidon, M., and Jambon, A., 1994, Boron content and isotopic composition of oceanic basalts: geochemical and cosmochemical implications: Earth and Planetary Science Letters, v. 121, p. 277-291.

Chaussidon, M., and Marty, B., 1995, Primitive Boron Isotope Composition of the Mantle: Science, v. 269, p. 383 - 386.

Chaussidon, M., Robert, F., Mangin, D., Hanon, P., and Rose, E.F., 1997, Analytical procedures for the measurement of boron isotope compositions by ion microprobe in meteorites and mantle rocks: Geostandards Newsletter, v. 21, p. 7-17.

Danyushevsky, L.V., McNeill, A.W., and Sobolev, A.V., 2002, Experimental and petrological studies of melt inclusions in phenocrysts from mantle-derived magmas: an overview of techniques, advantages and complications: Chemical Geology, v. 183, p. 5-24.

Davidson, J.P., 1996, Deciphering mantle and crustal signatures in subduction zone magmatism: Subduction top to bottom, p. 251-262.

Davidson, J.P., and de Silva, S.L., 1992, Volcanic rocks from the Bolivian Altiplano: Insights into crustal structure, contamination, and magma genesis in the central Andes: Geology, v. 20, p. 1127-1130.

Deline, V.R., Katz, W., Evans, C.A., and Williams, P., 1978, Mechanism of the SIMS matrix effect: Applied Physics Letters, v. 33, p. 832-835.

Deschamps, F., Godard, M., Guillot, S., and Hattori, K., 2013, Geochemistry of subduction zone serpentinites: A review: Lithos.

Eiler, J.M., Graham, C., and Valley, J.W., 1997, SIMS analysis of oxygen isotopes: matrix effects in complex minerals and glasses: Chemical Geology, v. 138, p. 221-244.

Elliott, T., Plank, T., Zindler, A., White, W., and Bourdon, B., 1997, Element transport from slab to volcanic front at the Mariana arc: Journal of Geophysical Research, v. 102, p. 14991 - 15019.

Fogg, T.R., and Duce, R.A., 1985, Boron in the troposphere: distribution and fluxes: Journal of Geophysical Research: Atmospheres (1984–2012), v. 90, p. 3781-3796.

Gill, J.B., 1981, Orogenic Andesites and Plate Tectonics: New York, Springer-Verlag.

Goss, A.R., Kay, S.M., and Mpodozis, C., 2013, Andean Adakite-like high-Mg Andesites on the Northern Margin of the Chilean–Pampean Flat-slab (27–28· 5° S) Associated with Frontal Arc Migration and Fore-arc Subduction Erosion: Journal of Petrology, v. 54, p. 2193-2234.

Green, T., 1981, Experimental evidence for the role of accessory phases in magma genesis: Journal of Volcanology and Geothermal Research, v. 10, p. 405-422.

Gutscher, M.A., Spakman, W., Bijwaard, H., and Engdahl, E.R., 2000, Geodynamics of flat subduction: Seismicity and tomographic constraints from the Andean margin: Tectonics, v. 19, p. 814-833.

Hattori, K.H., and Guillot, S., 2003, Volcanic fronts form as a consequence of serpentinite dehydration in the forearc mantle wedge: Geology, v. 31, p. 525-528.

Hawkesworth, C.J., Gallagher, K., Hergt, J.M., and McDermott, F., 1993, Mantle and slab contributions in arc magmas: Annual Review of Earth and Planetary Sciences, v. 21, p. 175 - 204.

Hildreth, W., and Moorbath, S., 1988, Crustal contributions to arc magmatism in the Andes of Central Chile: Contributions to Mineralogy and Petrology, v. 98, p. 455 - 489.

Hyndman, R.D., and Peacock, S.M., 2003, Serpentinization of the forearc mantle: Earth and Planetary Science Letters, v. 212, p. 417-432.

Isacks, B.L., 1988, Uplift of the central Andean plateau and bending of the Bolivian orocline: Journal of Geophysical Research: Solid Earth (1978–2012), v. 93, p. 3211-3231.

Ishikawa, T., and Nakamura, E., 1993, Boron isotope systematics of marine sediments: Earth and Planetary Science Letters, v. 117, p. 567 - 580.

Ishikawa, T., and Nakamura, E., 1994, Origin of the slab component in arc lavas from across-arc variation of B and Pb isotopes: Nature, v. 370, p. 205 - 208.

Ishikawa, T., and Tera, F., 1997, Source, composition and distribution of the fluid in the Kurile mantle wedge: Constraints from across-arc variations of B/Nb and B isotopes: Earth and Planetary Science Letters, v. 152, p. 123 - 138.

Ishikawa, T., Tera, F., and Nakazawa, T., 2001, Boron isotope and trace element systematics of the three volcanic zones in the Kamchatka arc: Geochimica et Cosmochimica Acta, v. 65, p. 4523-4537.

James, D.E., 1982, A combined O, Sr, Nd, and Pb isotopic and trace element study of crustal contamination in central Andean lavas, I. Local geochemical variations: Earth and Planetary Science Letters, v. 57, p. 47-62.

Jarvis, A., Reuter, H.I., Nelson, A., and Guevara, E., 2008, Hole-filled SRTM for the globe Version 4, available from the CGIAR-CSI SRTM 90m Database.

Jochum, K.P., Weis, U., Stoll, B., Kuzmin, D., Yang, Q., Raczek, I., Jacob, D.E., Stracke, A., Birbaum, K., Frick, D.A., Günther, D., and Enzweiler, J., 2011a, Determination of Reference Values for NIST SRM 610–617 Glasses Following ISO Guidelines: Geostandards and Geoanalytical Research, v. 35, p. 397-429.

Jochum, K.P., Wilson, S.A., Abouchami, W., Amini, M., Chmeleff, J., Eisenhauer, A., Hegner, E., Iaccheri, L.M., Kieffer, B., and Krause, J., 2011b, GSD-1G

and MPI-DING Reference Glasses for In Situ and Bulk Isotopic Determination: Geostandards and Geoanalytical Research, v. 35, p. 193-226.

Jordan, T., Allmendinger, R., Damanti, J., and Drake, R., 1993, Chronology of motion in a complete thrust belt: The Precordillera, 30-31 S, Andes Mountains: The Journal of Geology, p. 135-156.

Jordon, T.E., Burns, W.M., Veiga, R., Pángaro, F., Copeland, P., Kelley, S., and Mpodozis, C., 2001, Extension and basin formation in the southern Andes caused by increased convergence rate: A mid-Cenozoic trigger for the Andes: Tectonics, v. 20, p. 308 - 324.

Kanzaki, T., Yoshida, M., Nomura, M., Kakihana, H., and Ozawa, T., 1979, Boron isotopic composition of fumarolic condensates and sassolites from Satsuma Iwo-jima, Japan: Geochimica et Cosmochimica Acta, v. 43, p. 1859-1863.

Kasemann, S., Erzinger, J., and Franz, G., 2000, Boron recycling in the continental crust of the central Andes from the Palaeozoic to Mesozoic, NW Argentina: Contributions to Mineralogy and Petrology, v. 140, p. 328 - 343.

Kasemann, S.A., Meixner, A., Erzinger, J., Viramonte, J.G., Alonso, R.N., and Franz, G., 2004, Boron isotope composition of geothermal fluids and borate minerals from salar deposits (central Andes/NW Argentina): Journal of South American Earth Sciences, v. 16, p. 685-697.

Kay, S.M., and Abbruzzi, J.M., 1996, Magmatic evidence for Neogene lithospheric evolution of the central Andean "flat slab" between 30ºS and 32ºS: Tectonophysics, v. 259, p. 15 - 28.

Kay, S.M., Godoy, E., and Kurtz, A., 2005, Episodic arc migration, crustal thickening, subduction erosion, and magmatism in the south-central Andes: Geological Society of America Bulletin, v. 117, p. 67-88.

Kay, S.M., Maksaev, V., Moscoso, R., Mpodozis, C., and Nasi, C., 1987, Probing the evolving Andean lithosphere; Mid - Late Tertiary magmatism in Chile (29º - 30º30'S) over the modern zone of subhorizontal subduction: Journal of Geophysical Research, v. 92, p. 6173 - 6189.

Kay, S.M., and Mpodozis, C., 2002, Magmatism as a probe to the Neogene shallowing of the Nazca plate beneath the modern Chilean flat slab: Journal of South American Earth Sciences, v. 15, p. 39 - 57.

Kay, S.M., Mpodozis, C., Ramos, V.A., and Munizaga, F., 1991, Magma source variations for mid-late Tertiary magmatic rocks associated with a shallowing subduction zone and the thickening crust in the central Andes (28-33ºS): Spec. Pap. Geological Society of America Bulletin, v. 265, p. 113 - 137.

Kilian, R., and Behrmann, J.H., 2003, Geochemical constraints on the sources of Southern Chile Trench sediments and their recycling in arc magmas of the Southern Andes: Journal of the Geological Society, v. 160, p. 57-70.

King, R.L., Bebout, G.E., Grove, M., Moriguti, T., and Nakamura, E., 2007, Boron and lead isotope signatures of subduction-zone mélange formation: Hybridization and fractionation along the slab–mantle interface beneath volcanic arcs: Chemical Geology, v. 239, p. 305-322.

Kogiso, T., Tatsumi, Y., and Nakano, S., 1997, Trace element transport during dehydration processes in the subducted oceanic crust: 1. Experiments and implications for the origin of ocean island basalts: Earth and Planetary Science Letters, v. 148, p. 193 - 205.

Kopp, H., Flueh, E.R., Papenberg, C., and Klaeschen, D., 2004, Seismic investigations of the O'Higgins Seamount Group and Juan Fernández Ridge: Aseismic ridge emplacement and lithosphere hydration: Tectonics, v. 23.

Leeman, W.P., and Sisson, V.B., 1996, Geochemistry of boron and its implications for crustal and mantle processes: Reviews in Mineralogy and Geochemistry, v. 33, p. 645 - 707.

Leeman, W.P., Tonarini, S., Chan, L.H., and Borg, L.E., 2004, Boron and lithium isotopic variations in a hot subduction zone—the southern Washington Cascades: Chemical Geology, v. 212, p. 101-124.

Litvak, V.D., and Poma, S., 2010, Geochemistry of mafic Paleocene volcanic rocks in the Valle del Cura region: Implications for the petrogenesis of primary mantle-derived melts over the Pampean flat-slab: Journal of South American Earth Sciences, v. 29, p. 705-716.

Litvak, V.D., Poma, S., and Kay, S.M., 2007, Paleogene and Neogene magmatism in the Valle del Cura region: New perspective on the evolution of the Pampean flat slab, San Juan province, Argentina: Journal of South American Earth Sciences, v. 24, p. 117 - 137.

Lonsdale, P., 2005, Creation of the Cocos and Nazca plates by fission of the Farallon plate: Tectonophysics, v. 404, p. 237-264.

Lucassen, F., Escayola, M., Romer, R.L., Viramonte, J., Koch, K., and Franz, G., 2002, Isotopic composition of Late Mesozoic basic and ultrabasic rocks from the Andes (23–32 S)–implications for the Andean mantle: Contributions to Mineralogy and Petrology, v. 143, p. 336-349.

Maksaev, V., Moscoso, R., Mpodozis, C., and Nasi, C., 1984, Las unidades volcánicas y plutónicas del Cenozoico superior en la Alta Cordilera del Norte Chico (29°–31° S): Geología, Alteración hidrotermal y Mineralización: Revista Geológica de Chile, v. 11, p. 12 - 51.

Manea, V.C., Pérez-Gussinyé, M., and Manea, M., 2012, Chilean flat slab subduction controlled by overriding plate thickness and trench rollback: Geology, v. 40, p. 35-38.

Marot, M., Monfret, T., Pardo, M., Ranalli, G., and Nolet, G., 2013, A double seismic zone in the subducting Juan Fernandez Ridge of the Nazca Plate (32°S), central Chile: Journal of Geophysical Research: Solid Earth, v. 118, p. 3462-3475.

Morris, J.D., Leeman, W.P., and Tera, F., 1990, The subducted component in island arc lavas: constraints from Be isotopes and B-Be systematics: Nature, v. 344, p. 31 - 36.

Noll Jr, P.D., Newsom, H.E., Leeman, W.P., and Ryan, J.G., 1996, The role of hydrothermal fluids in the production of subduction zone magmas: Evidence from siderophile and chalcophile trace elements and boron: Geochimica et Cosmochimica Acta, v. 60, p. 587-611.

Nomura, M., Kanzaki, T., Ozawa, T., Okamoto, M., and Kakihana, H., 1982, Boron isotopic composition of fumarolic condensates from some volcanoes in Japanese island arcs: Geochimica et Cosmochimica Acta, v. 46, p. 2403-2406.

Nur, A., and Ben-Avraham, Z., 1981, Volcanic gaps and the consumption of aseismic ridges in South America: Geological Society of America Memoirs, v. 154, p. 729-740.

Oncken, O., Hindle, D., Kley, J., Elger, K., Victor, P., and Schemmann, K., 2006, Deformation of the central Andean upper plate system—Facts, fiction, and constraints for plateau models, The Andes, Springer, p. 3-27.

Palmer, M., 1991, Boron-isotope systematics of Halmahera arc (Indonesia) lavas: Evidence for involvement of the subducted slab: Geology, v. 19, p. 215-217.

Parada, M.A., Rivano, S., Sepulveda, P., Herve, M., Herve, F., Puig, A., Munizaga, F., Brook, M., Pankhurst, R., and Snelling, N., 1988, Mesozoic and Cenozoic plutonic development in the Andes of central Chile (30º30' - 32º30'S) Journal of South American Earth Sciences, v. 1, p. 249 - 260.

Pardo Casas, F., and Molnar, P., 1987, Relative motion of the Nazca (Farallón) and South America plates since Late Cretaceous time Tectonics, v. 6, p. 233 - 248.

Peacock, S.M., 1996, Thermal and petrologic structure of subduction zones, Subduction top to bottom, Volume 96: Geophys. Monogr. Ser.: Washington, DC, AGU, p. 119-133.

Peacock, S.M., and Hervig, R.L., 1999, Boron isotopic composition of subduction-zone metamorphic rocks: Chemical Geology, v. 160, p. 281 - 290.

Peacock, S.M., Rushmer, T., and Thompson, A.B., 1994, Partial melting of subducting oceanic crust: Earth and Planetary Science Letters, v. 121, p. 227-244.

Pilger, R.H., 1981, Plate reconstructions, aseismic ridges, and low angle subduction beneath the Andes: Geological Society of America Bulletin, v. 92, p. 448 - 456.

Pilger, R.H., 1984, Cenozoic plate kinematics, subduction and magmatism: South American Andes: Journal of Geological Society London, v. 141, p. 793 - 802.

Ramos, V.A., Cristallini, E.O., and Pérez, D.J., 2002, The Pampean flat-slab of the Central Andes: Journal of South American Earth Sciences, v. 15, p. 59-78.

Ramos, V.A., and Folguera, A., 2009, Andean flat-slab subduction through time: Geological Society, London, Special Publications, v. 327, p. 31-54.

Reiners, P.W., Nelson, B.K., and Ghiorso, M.S., 1995, Assimilation of felsic crust by basaltic magma: Thermal limits and extents of crustal contamination of mantle-derived magmas: Geology, v. 23, p. 563-566.

Rosner, M., Erzinger, J., Franz, G., and Trumbull, R.B., 2003, Slab-derived boron isotope signatures in arc volcanic rocks from the Central Andes and evidence from boron isotope fractination during progressive slab dehydration: Geochemistry Geophysics Geosystems, v. 4.

Rosner, M., Wiedenbeck, M., and Ludwig, T., 2008, Composition-induced variations in SIMS instrumental mass fractionation during boron isotope ratio measurements of silicate glasses: Geostandards and Geoanalytical Research, v. 32, p. 27-38.

Rutland, R.W.R., 1971, Andean Orogeny and Ocean Floor Spreading: Nature, v. 233, p. 252 - 255.

Ryan, J.G., Morris, J.D., Tera, F., Leeman, W.P., and Tsuetkov, A., 1995, Cross-arc geochemical variations in the Kurile arc as a function of slab depth: Science, v. 270, p. 625 - 627.

Savov, I.P., Ryan, J.G., D'Antonio, M., and Fryer, P., 2007, Shallow slab fluid release across and along the Mariana arc-basin system: Insights from geochemistry of serpentinized peridotites from the Mariana fore arc: Journal of Geophysical Research: Solid Earth (1978–2012), v. 112.

Schiano, P., 2003, Primitive mantle magmas recorded as silicate melt inclusions in igneous minerals: Earth-Science Reviews, v. 63, p. 121-144.

Schmitt, A.K., Kasemann, S., Meixner, A., and Rhede, D., 2002, Boron in central Andean ignimbrites: implications for crustal boron cycles in active continental margin: Chemical Geology, v. 183, p. 333 - 347.

Scholl, D.W., Christensen, M.N., Von Huene, R., and Marlow, M.S., 1970, Peru-Chile Trench Sediments and Sea-Floor Spreading: Geological Society of America Bulletin, v. 81, p. 1339 - 1360.

Shimizu, N., and Hart, S., 1982, Isotope fractionation in secondary ion mass spectrometry: Journal of Applied Physics, v. 53, p. 1303-1311.

Silver, P.G., Russo, R.M., and Lithgow-Bertelloni, C., 1998, Coupling of South American and African plate motion and plate deformation: Science, v. 279, p. 60 - 63.

Smith, H.J., Spivack, A.J., Staudigel, H., and Hart, S.R., 1995, The boron isotopic composition of altered oceanic crust: Chemical Geology, v. 126, p. 119 - 135.

Sobolev, A.V., 1996, Melt Inclusions in Minerals as a Source of Principle Petrological Information: Petrology, v. 4, p. 209 - 220.

Somoza, R., 1998, Updated azca (Farallon)—South America relative motions during the last 40 My: implications for mountain building in the central Andean region: Journal of South American Earth Sciences, v. 11, p. 211-215.

Somoza, R., and Ghidella, M.E., 2012, Late Cretaceous to recent plate motions in western South America revisited: Earth and Planetary Science Letters, v. 331–332, p. 152-163.

Spivack, A.J., and Edmond, J.M., 1987, Boron isotope exchenge between seawater and the oceanic crust: Geochimica et Cosmochimica Acta, v. 51, p. 1033 - 1043.

Stern, C.R., 1991, Role of subduction erosion in the generation of Andean magmas: Geology, v. 19, p. 78 - 81.

Stern, C.R., 2004, Active Andean volcanism: its geologic and tectonic setting Revista Geológica de Chile, v. 31, p. 161 - 206.

Straub, S.M., and Layne, G.D., 2002, The systematics of boron isotopes in Izu arc front volcanic rocks: Earth and Planetary Science Letters, v. 198, p. 25-39.

Sun, S.S., and McDonough, W.F., 1989, Chemical and isotopic systematics of oceanic basalts: implications for mantle compositions and processes: Geological Society, London, Special Publications, v. 42, p. 313 - 345.

Tatsumi, Y., 1989, Migration of fluid phases and genesis of basalt magmas in subduction zones: Journal of Geophysical Research, v. 94, p. 4697-4707.

Taylor, S.R., and McLennan, S.M., 1995, The geochemical evolution of the continental crust: Reviews of Geophysics, v. 33, p. 241-265.

Thornburg, T.M., and Kulm, L.D., 1987a, Sedimentation in the Chile Trench: Depositional morphologies, lithofacies, and stratigraphy: Geological Society of America Bulletin, v. 98, p. 33 - 52.

Thornburg, T.M., and Kulm, L.D., 1987b, Sedimentation in the Chile Trench; petrofacies and provenance: Journal of Sedimentary Research, v. 57, p. 55-74.

Tonarini, S., Leeman, W.P., and Leat, P.T., 2011, Subduction erosion of forearc mantle wedge implicated in the genesis of the South Sandwich Island (SSI) arc: Evidence from boron isotope systematics: Earth and Planetary Science Letters, v. 301, p. 275-284.

Trumbull, R.B., Riller, U., Oncken, O., Scheuber, E., Munier, K., and Hongn, F., 2006, The time-space distribution of Cenozoic Volcanism in the South-Central Andes: a new data compliation and some tectonic implications, *in* Oncken, O., Chong, G., Franz, G., Giese, P., Götze, H.-J., Ramos, V.A.,

Strecker, M.R., and Wigger, P., eds., The Andes - active subduction orogeny, Volume 1: Frontiers in Earth Sciences, Springer Verlag, p. 29-43.

Ulmer, P., and Trommsdorff, V., 1995, Serpentine stability to mantle depths and subduction-related magmatism: Science, v. 268, p. 858-861.

Vils, F., Tonarini, S., Kalt, A., and Seitz, H.-M., 2009, Boron, lithium and strontium isotopes as tracers of seawater–serpentinite interaction at Mid-Atlantic ridge, ODP Leg 209: Earth and Planetary Science Letters, v. 286, p. 414-425.

Von Huene, R., and Scholl, D.W., 1991, Observations at convergent margins concerning sediment subduction, subduction erosion, and the growth of continental crust: Reviews of Geophysics, v. 29.

Winocur, D.A., Litvak, V.D., and Ramos, V.A., 2013, Magmatic and tectonic evolution of the Oligocene Valle del Cura basin, Main Andes of Argentina and Chile: Evidence for generalized extension, *in* Sepulveda, P., Giambiagi, L., Pinto, L., Moreiras, S., Tunik, M., Hoke, G., and M., F., eds., Geodynamic processes in the Andes of Central Chile and Argentina, Volume In press, Geological Society of London, Special Publication.

Workman, R.K., and Hart, S.R., 2005, Major and trace element composition of the depleted MORB mantle (DMM): Earth and Planetary Science Letters, v. 231, p. 53-72.

Wunder, B., Wirth, R., and Gottschalk, M., 2001, Antigorite Pressure and temperature dependence of polysomatism and water content: European Journal of Mineralogy, v. 13, p. 485-496.

Yañez, G.A., Cembrano, J., Pardo, M., Ranero, C.R., and Selles, D., 2002, The Challenger - Juan Fernández - Maipo major tectonic transition of the Nazca - Andean subduction system at 33-34ºS: geodynamic evidence and implications: Journal of South American Earth Sciences, v. 15, p. 28 - 38.

Yañez, G.A., Ranero, C.R., von Huene, R., and Díaz, J., 2001, Magnetic anomaly interpretation across the southern central Andes (32º-34ºS): The role of the Juan Fernández Ridge in the late Tertiary evolution of the margin: Journal of Geophysical Research, v. 106, p. 6325 - 6345.

Chapter 5. A discussion of the geodynamic evolution of the Pampean flat-slab segment, southern Central Andes, between the Late Cretaceous and the Late Miocene

5.1 Introduction

Numerous previous studies, employing a wide range of techniques (e.g., geophysical, geochemical, and structural), have demonstrated that the geodynamic setting of the southern Central Andean margin has significantly changed over the course of the Cenozoic (e.g., Kay et al., 1991; Jordon et al., 2001; Yañez et al., 2001; Charrier et al., 2002; Yañez et al., 2002; Ramos et al., 2004; Kay et al., 2005; Ramos and Folguera, 2009). The development of the margin has included changes in convergence angles and rates between the subducting oceanic plate and the South American continent, as well as the angle of subduction (e.g., Pilger, 1981, 1984; Pardo Casas and Molnar, 1987; Somoza, 1998; Yañez et al., 2001; Yañez et al., 2002; Somoza and Ghidella, 2012). The principal aims of this study are to determine contributions to arc magmas from mantle, crustal and subducted reservoirs, and to relate changes in these contributions to the geodynamic evolution of the southern Central Andean margin over the Cenozoic.

Previous investigations into the petrogenesis of Cenozoic arc magmas in the Pampean flat-slab segment have primarily utilised whole rock geochemistry (e.g., Parada, 1990; Kay et al., 1991; Kay and Abbruzzi, 1996; Bissig et al., 2003; Litvak et al., 2007; Litvak and Poma, 2010; Winocur et al., 2013). Although most authors agree that there is an increase in the contributions to arc magmas from crustally derived material over the course of the Cenozoic, the origin (i.e., subducted crustal material or the overlying Andean crust) of these crustal signatures remains unresolved. In order to more accurately determine the contributions to southern Central Andean

arc magmas this study combines petrology and whole rock geochemistry with *in-situ* elemental and isotopic analysis of mineral phases and melt inclusions. These *in-situ* analytical techniques have not previously been applied to Cenozoic arc rocks from this region of the Pampean flat-slab segment. Previous studies have also tended to focus on narrow geological timeframes or geographical areas, with a tendency for studies to focus on either the Chilean or Argentinean side of the margin. This study has applied geochronological, geochemical and geothermobarometric techniques to both plutonic and volcanic arc rocks, which have been emplaced and erupted over a wide time frame (~73 – 6 Ma) and over a wide across-arc extent, from the Principal Cordillera of Chile (-70.8 °W) to the Argentinean Precordillera (-69.1 °W).

As highlighted in the previous three chapters the geochemical and geothermobarometric data display strong temporal variations, which have been accurately constrained by high resolution U-Pb and Ar-Ar dating, conducted as part of this study. This chapter aims to draw together the findings and conclusions presented in the previous three chapters in order to refine current understanding of the geodynamic evolution of the Pampean flat-slab segment over the course of the Cenozoic. On this basis, the evolution of the Pampean flat-slab segment has been divided into five time frames, with a new geodynamic model presented and discussed for each. A particular focus is given to the petrogenesis of the arc magmatic rocks during these time intervals.

5.2 The Late Cretaceous – Early Eocene (~75 – 51 Ma)

During this time interval the magmatic arc along the western margin of South America was somewhat different to the compressional Andean arc which is now in existence. The oblique angle of subduction and the low convergence rates between

the Farallon and South American plates are thought to have caused extension along the Andean margin (Pardo Casas and Molnar, 1987; Somoza, 1998; Charrier et al., 2007). The Late Cretaceous to Early Eocene magmatic rocks, associated with extension, primarily consist of north-south trending plutonic belts which are located in the Principal Cordillera of Chile. In the southern Central Andes, the majority of these plutonic rocks have been grouped into the compositionally varied (gabbros to granites), Cogotí Supergroup (e.g., Parada et al., 1988 and references therein; Parada, 1990; Parada et al., 2007). Volcanic rocks associated with these extensive plutonic belts are scarce. However, evidence from geothermobarometry suggests that at least 5 km of continental crust must have been removed from the Principal Cordillera since the Paleocene (~60 Ma) in order to expose the plutons at the surface. Therefore, the majority of the volcanic deposits associated with, and overlying the Cogotí Supergroup may have been removed by erosion. The basaltic andesites of the Los Elquinos Formation represent the only extrusive rocks from the main Late Cretaceous to Early Eocene magmatic arc to be investigated as part of this study.

Trace element signatures and boron isotopic compositions obtained by this study suggest the Late Cretaceous to Early Eocene arc magmas, emplaced in the Principal and Frontal Cordillera, formed in a subduction zone setting from the partial melting of a metasomatised mantle wedge, which has been variably influenced by slab-derived fluids. Average boron isotope compositions of +1.6 ±0.8 ‰ (1σ) and B/Nb of 17.8 ±1.4 (1σ), obtained for melt inclusions hosted in pyroxene from the Los Elquinos Formation, suggest these fluids were primarily derived from the dehydration of altered oceanic crust (Chapter 4). The release of these aqueous fluids from the subducting Farallon plate is likely to have caused melting in the mantle wedge and subsequent migration of buoyant melts to the base of the continental crust (Fig. 5.1). Trace element signatures, such as low Nb/Zr and Nb/Yb, obtained for both whole rock and melt inclusions, as part of this study, suggests significant partial melting of the mantle wedge took place during this time period. This may be

related to the extensional regime in operation along the convergent margin (Charrier et al., 2007 and references therein) and therefore a combination of melting of the mantle wedge related to the dehydration of the subducting slab and decompression melting due to extension.

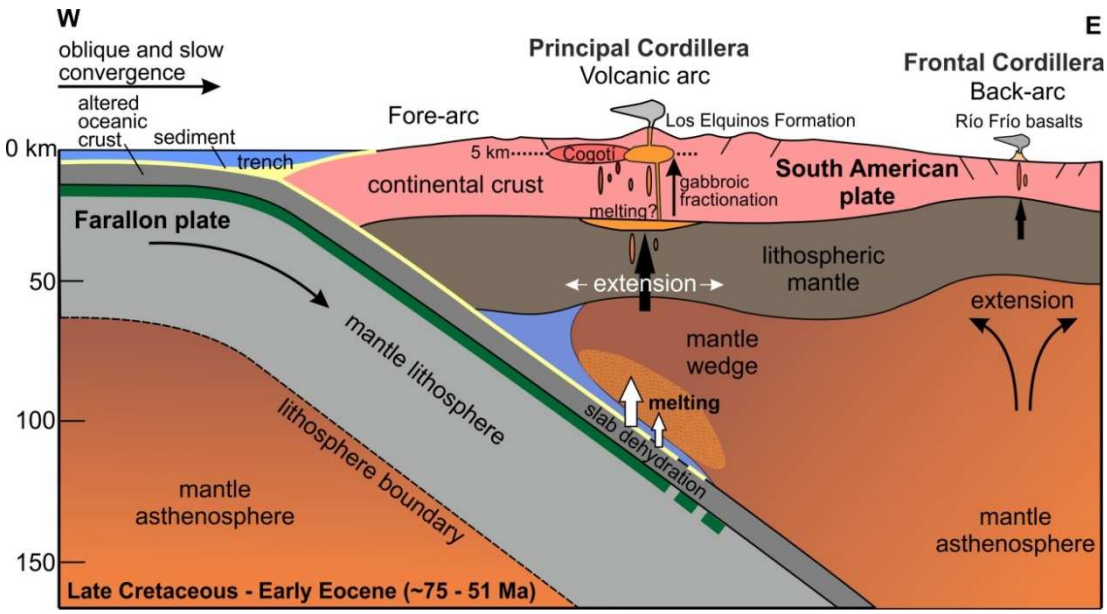

Figure 5.1 A schematic cross section of the southern Central Andean margin, during the Late Cretaceous to Early Eocene (~75 – 51 Ma), at approximately 29 – 31°S.

Extension related magmatism was also occurring in a back-arc setting during this time interval, with the eruption of the Río Frío Basalts (55.9 ±1.9 Ma (Litvak and Page, 2002)) to the east of the main arc, in the Frontal Cordillera (Fig. 5.1). These basalts make up small deposits currently located in the Valle del Cura region of Argentina. High fluid immobile, incompatible trace element ratios (e.g., Nb/Zr) and low fluid mobile, incompatible trace element ratios (e.g., Ba/Nb) obtained for a sample of the Río Frío alkali basalts, implies they represent small degree partial melts which have received little influence from slab-derived fluids. This is consistent with their emplacement in an extensional, back-arc setting (Litvak and Poma, 2010). Isotopic data (low $^{87}Sr/^{86}Sr$ ratios of <0.704 and high εNd values of >4) obtained by Kay et al., (1991) also suggest these basaltic magmas received little

addition of crustal material, either in the melt source region or via crustal assimilation.

The 'mantle-like' oxygen isotope values (+5.4 ‰ to +5.7 ‰ (±0.4)) and juvenile initial εHf values (+8.3 (±0.8) to +9.4 (±0.7)) obtained for magmatic zircon, combined with the lack of zircon inheritance (Chapter 3), suggests very little contamination of the Late Cretaceous to Early Eocene arc magmas with upper continental crust, either in the melt source region or during migration through the continental crust. This supports the previous work of Parada et al. (1988) who obtained low initial $^{87}Sr/^{86}Sr$ ratios for the Cogotí Supergoup and suggested these I-type granitoids were formed from the melting of either the mantle wedge or young, mantle-derived lower crust. On the basis of this combined evidence it is apparent that these plutonic belts represent a sustained period of upper crustal growth in the southern Central Andes, with melts primarily derived from the melting of the metasomatised mantle wedge.

Whole-rock, rare earth element geochemistry (e.g., La/Yb ratios) suggests the Late Cretaceous to Early Eocene mantle-derived melts underwent equilibration with/fractional crystallisation of a gabbroic assemblage (i.e., plagioclase, clinopyroxene, magnetite and olivine), suggesting migration of the arc magmas through a crust of normal thickness (~30 - 35 km). Amphibole - plagioclase geothermobarometry (Chapter 2) suggests magmas of the Cogotí Supergroup crystallised/equilibrated at temperatures of 677 °C (±15 (1σ)) and pressures of 1.4 kbars (±0.3 (1σ)). This evidence combined with petrology, specifically perthitic textures, suggests that the dioritic to granitic melts of the Cogotí Supergroup were emplaced at shallow depths in the continental crust, of ~5 km. This confirms previous suggestions that these extensive plutonic belts emplaced in the Chilean Principal Cordillera are epizonal (Parada et al., 1988).

5.3 The Early Eocene to Early Oligocene (~50 – 27 Ma)

The Early Eocene to Early Oligocene is characterised by a reduction in arc magmatism and a transition from the emplacement of primarily plutonic belts in the Principal Cordillera of Chile, to arc volcanism further away from the subduction zone trench in the Frontal Cordillera (Fig. 5.2). During the Mid to Late Eocene the youngest granitoids of the Cogotí Supergroup (~39 Ma) were emplaced in the Principal Cordillera, along with a number of intrusions related to caldera formation, such as the low- to medium- K amphibole diorites of the Tierras Blancas Caldera (U-Pb age = 40.2 ±1.2 Ma). During the Late Eocene, andesitic porphyries of the Botacoma Unit (U-Pb age = 35.6 ±0.8 Ma) were emplaced in the Frontal Cordillera. It has previously been suggested that the Valle del Cura Formation represented retro-arc magmatism during this time interval (Litvak et al., 2007). However, the new U-Pb dating presented in this study has led to the assignment of these deposits to Late Oligocene - Early Miocene arc formations (Doña Ana Group and the Cerro de las Tórtolas Formation). Hence, there is diminished evidence for magmatism in a retro-arc position during this time interval.

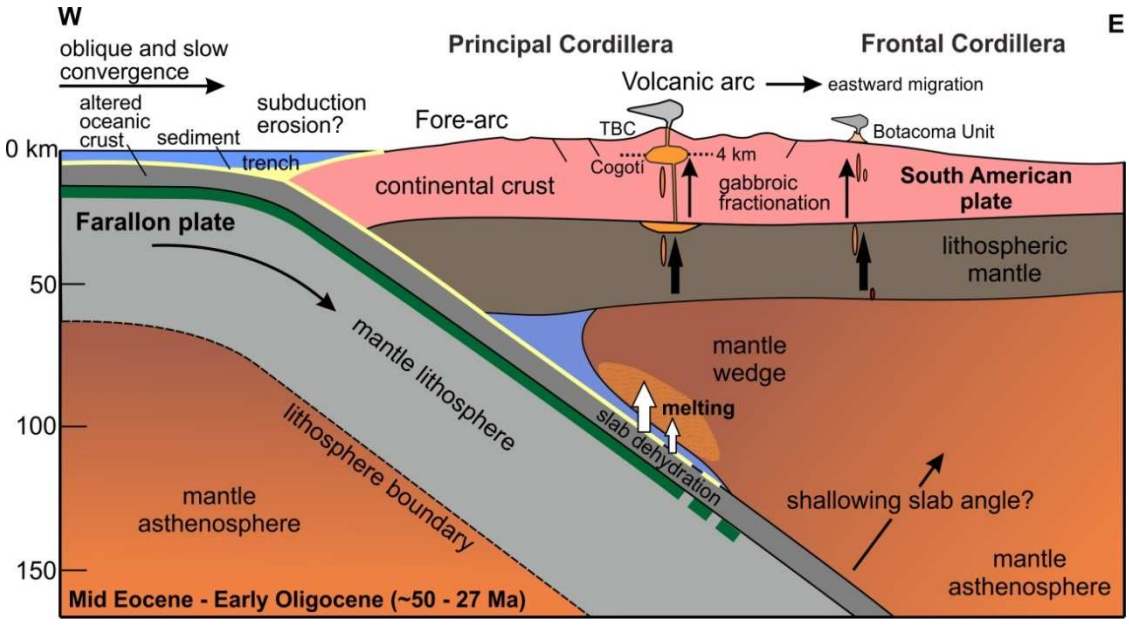

Figure 5.2 A schematic cross section of the southern Central Andean margin,

during the Mid Eocene to Early Oligocene (~50 - 27 Ma), at approximately 29 - 31°S. TBC stands for the Tierras Blancas Caldera.

The poor development of the magmatic arc during this time interval may be related to the low convergence rates (~5 – 8 cm/yr) and oblique angle of subduction (north-easterly direction) operating between the oceanic Farallon and the South American plate (e.g., Pardo Casas and Molnar, 1987; Somoza and Ghidella, 2012). The reduction in arc magmatism has previously been linked with an earlier period of flat-slab subduction along the Central Andean margin (e.g., O'Driscoll et al., 2012). The apparent eastward migration of the arc supports the shallowing angle of subduction, however very little other evidence was found by this study to support flat-slab subduction during this time interval. For example, this study found no evidence for increased compression and thickened continental crust along the margin, or the presence of adakitic signatures, which might be associated with flat-slab subduction (Gutscher et al., 2000). Whole-rock rare earth element geochemistry (e.g., La/Yb ratios) (Chapter 2) suggests that the ascending arc magmas during the Early Eocene to Late Oligocene were equilibrating with/fractionating a mineral assemblage which reflects a continental crust of normal thickness (~30 - 35 km) (i.e., not indicative of a high pressure residual mineral phases such as garnet).

It has also been proposed that the shift in location of the magmatic arc and the location of the Botacoma Unit in the Frontal Cordillera could be related to significant removal of the fore-arc by subduction erosion (e.g., Litvak et al., 2007). This process might be expected to lead to an increase in the contamination of the sub-arc region with continental crust (e.g., Stern, 1991; Stern, 2011; Goss et al., 2013). An increase in subduction erosion is a plausible explanation for the migration of the magmatic arc during this time period. However, due to the similar composition of the continental crust potentially being eroded from fore-arc and the continental crust through which the arc magmas are migrating and potentially assimilating in

the Principal and Frontal Cordillera (Paleozoic sediments and metasediments, and Paleozoic to Mesozoic plutonic complexes and volcanic deposits), this is difficult to positively identify.

An increase in the influence of crustally derived material on the compositions of arc magmas has been identified by this study between the plutonic rocks and caldera related intrusions emplaced in the Principal Cordillera, and the arc magmas of the Botacoma Unit erupted in the Frontal Cordillera. Zircons from the youngest sample to be assigned to the Cogotí Supergroup (U-Pb age = 38.9 ±1.0 Ma) and the sample of the Tierras Blancas Caldera, located in the Principal Cordillera, both have 'mantle-like' $\delta^{18}O_{(zircon)}$ values (+5.5 ‰ (±0.3)) and juvenile initial $\varepsilon Hf_{(zircon)}$ values (+9.2 (±1.0) to +10.0 (±0.9)), which are close to the values expected for new mantle-derived melts (Chapter 3). As suggested for the Late Cretaceous to Early Eocene time frame, this is indicative of melts derived from the mantle which have received little addition from an upper crustal component. The 'mantle-like' $\delta^{18}O_{(zircon)}$ values (+5.8 ‰ (±0.5)), but lower initial $\varepsilon Hf_{(zircon)}$ values (+2.6 (±1.0)), obtained for zircons from the Bocatoma Unit, suggests the addition of an older and hence less radiogenic crustal component. The $\delta^{18}O_{(zircon)}$ and $\varepsilon Hf_{T(zircon)}$ values obtained for the Bocatoma Unit are within the range of values obtained for the Late Oligocene (~26 Ma) to Early Miocene (~17 Ma) arc formations present in the Frontal Cordillera, thus suggesting a similar contaminant. The $^{87}Sr/^{86}Sr$ and $^{143}Nd/^{144}Nd$ values reported by Bissig et al. (2003) for the Botacoma Unit also overlap the values reported for other arc formations present in the Frontal Cordillera (e.g., the Late Oligocene Tilito Formation and the Early Miocene Escabroso Formation) supporting a similar contaminant/degree of contamination. On the basis of the across-arc isotopic trends, as highlighted in Chapter 3, combined with the presence of inherited zircon cores, which can be indicative of bulk crustal assimilation (e.g., Beard et al., 2005), this study proposes that the $\delta^{18}O_{(zircon)}$ and $\varepsilon Hf_{T(zircon)}$ values obtained for the Bocatoma Unit reflect the assimilation of Late Palaeozoic – Early Mesozoic Andean basement rather than the

contamination of the melt source region with the products of subduction erosion. This interpretation is also supported by whole-rock, incompatible trace element ratios (e.g., Ba/Nb, Pb/Nb, Nb/Zr) obtained by this study, which suggests that the Botacoma Unit represents a smaller degree of partial melting of the mantle wedge, with less influence from slab-derived fluids in comparison to the Late Cretaceous to Eocene plutonic belts present in the Principal Cordillera (Chapter 2). The more limited influence of slab-derived fluids on the source region may reflect its position of the Botacoma Unit over a more dehydrated slab, further away from the trench, in comparison to the plutonic belts emplaced in the Principal Cordillera during this time interval (Fig. 5.2).

The application of amphibole geothermobarometry, by this study, to an amphibole diorite of the Tierras Blancas Caldera, produced crystallisation/equilibration temperatures of 844 °C (±26 (1σ)) and pressures of 1.1 kbars (±0.2 (1σ)) (Chapter 2). The compositions of the amphiboles (magnesio-hornblendes with Si < 7.3 in the half unit cell) suggests that they have not crystallised under sub-solidus conditions in the presence of a fluid (Leake, 1971) and therefore are considered likely to be magmatic. On this basis the P-T conditions produced are thought to reflect the conditions of crystallisation, suggesting the Tierras Blancas Caldera was emplaced at a relatively shallow depth in the crust of ~4 km. This depth is very similar to the crustal depths at which the Paleocene plutons of the Cogotí Supergroup crystallised (~5 km), suggesting magma chambers were present at these crustal depths over a sustained period of time (at least ~20 Ma). The phenocryst assemblage present in the Botacoma Unit crystallised over a wider range of temperature and pressures than the intrusive units, reflecting crystallisation and equilibration of the phenocryst assemblage during magma ascent between crustal depths of ~10.0 and 4.7 km. On this basis, this study suggests that the assimilation of the Late Palaeozoic – Early Mesozoic crust may have also occurred at these depths in the crust.

5.4 The Late Oligocene – Early Miocene (~26 – 20 Ma)

After the period of relative magmatic quiescence which spanned the Mid Eocene to Early Oligocene, this time interval is associated with a dramatic increase in magmatic activity and a broadening of the magmatic arc (Pilger, 1984). This has been related to the major change in plate configuration which occurred ~25 Ma due to the break-up of the Farallon plate into the Cocos and Nazca plates (Lonsdale, 2005). This tectonic reconfiguration resulted in subduction becoming more normal (ENE direction) to the margin and convergence rates increasing from ~8 cm/yr to an average of ~15 cm/yr (Pardo Casas and Molnar, 1987; Somoza, 1998; Somoza and Ghidella, 2012).

In the Pampean flat-slab segment, this time period is characterised by the eruption of medium- to high- K, calc-alkaline, andesites to rhyolites of the Tilito Formation (Lower Doña Ana Group) in the main Andean arc, and extensional related magmatism in the back-arc region (Fig. 5.3). The Tilito Formation (26.1 – 23.2 Ma (this study)) was erupted over a wide arc front, which is now situated in the Frontal Cordillera, spanning either side of the present day Chilean - Argentina border. An extensional regime operated to the east of the arc front, both during the late stages, and after the eruption of the Tilito Formation. This back-arc magmatism involved the eruption of the Las Máquinas Basalts (22.8 – 22.0 Ma (Kay et al., 1991; Litvak et al., 2005)) in the Frontal Cordillera, and the emplacement of high-K granitoids (Miocene Intrusives, 22.2 – 20.4 Ma (this study)), and dacitic to rhyolitic ignimbrites and lavas (Las Trancas Formation, 22.6 Ma (this study)), in the Argentinean Precordillera. Between ~23 and 21 Ma there is an apparent reduction in magmatism at the arc-front, with magmatic activity concentrated in the back-arc region. The two members of the Doña Ana Group (the Tilito Formation and the younger, Early Miocene, Escabroso Formation) are also separated by a major unconformity (Martin

et al., 1995) which has been attributed to a period of deformation at ~20 Ma (Kay and Mpodozis, 2002).

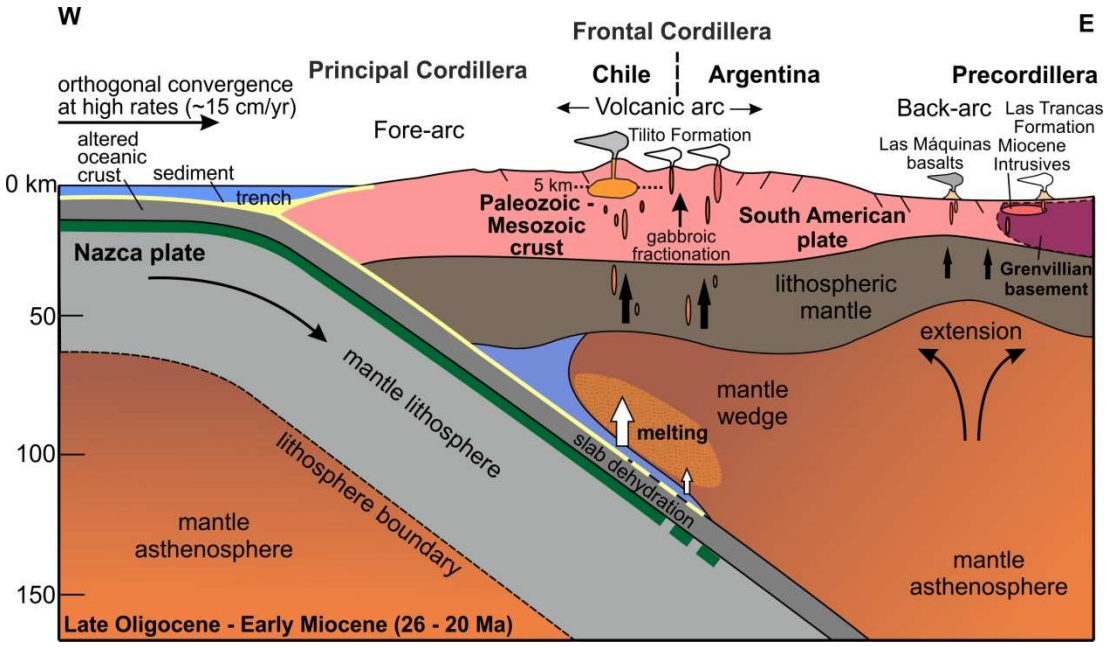

Figure 5.3 A schematic cross section of the southern Central Andean margin, during the Late Oligocene to Early Miocene (~26 - 20 Ma), at approximately 29 - 31°S.

As evidenced by boron isotope and trace element compositions of melt inclusions (average $\delta^{11}B$ values = -1.9 ±2.2 ‰ (1σ) and average B/Nb ratios = 3.3 ±1.3 (1σ)), the melt source region of the Tilito Formation, which represents magmatic activity in the main volcanic arc, was affected by fluids primarily derived from the dehydration of subducting altered oceanic crust. As detailed in Chapter 4, the source of the more mafic (andesitic) units of the Tilito Formation, erupted further away from the trench on the Argentinean side of the margin, received <0.5 % fluid addition from the subducting slab. This is suggested to reflect the wide arc front during this time period and their more distal position from the trench and hence eruption over a more dehydrated slab. The fluids influencing the melt source region appear to be derived from a similar source, i.e. primarily altered oceanic crust, to those influencing the source of the Paleocene (~61 Ma) arc magmas.

Trace element signatures and the presence of inherited zircon grains/cores in the high- K, calc-alkaline rhyolites of the Tilito Formation erupted closest to the trench suggests the magmas bulk assimilated the Late Paleozoic – Early Mesozoic basement en route to the surface (Chapter 2). The generally more mafic (andesitic) units of the Tilito Formation, erupted further away from the trench, show evidence for a more limited interaction with the Andean basement, for example they lack zircon inheritance. However, the oxygen and hafnium isotopic compositions of zircons present in these andesites suggests between 5 and 15 % assimilation of the Late Paleozoic – Early Mesozoic basement by these arc magmas, a similar level to those on the Chilean side of the margin (Chapter 3). Evidence from amphibole geothermobarometry (Chapter 2) suggests that the magmas of the Tilito Formation were crystallising and equilibrating at depths in the crust ranging from between ~18 and 4 km, however the majority of amphibole crystallisation/equilibration appears to have occurred at depths of ~5 km.

As aforementioned, the Las Máquinas Basalts, which are currently located in the Valle del Cura region of Argentina, are thought to represent basaltic lava flows erupted in a back-arc position (e.g., Kay et al., 1991; Litvak and Poma, 2010). The incompatible trace element signatures (e.g., Ba/Nb, Pb/Nb, Nb/Zr) obtained for these basalts, as part of this study, suggests they represent small degree partial melts which have received a limited influence from slab-derived fluids. This is consistent with their eruption in a back-arc position over a dehydrated subducting slab. On this basis, it is therefore likely that these melts were generated due to decompression in an extensional setting. Trace and rare earth element compositions also suggest that these melts were derived from an enriched mantle source region, with a composition between E-MORB and OIB end-members.

New U-Pb ages obtained for the Miocene Intrusives (22.2 – 20.4 Ma) and the Las Trancas Formation (22.6 Ma) suggests that these granitoids, and dacitic to rhyolitic

ignimbrites and lavas, were emplaced/erupted over a similar time interval to the Las Máquinas Basalts (K/Ar dated between 22.8 – 22.0 Ma (Kay et al., 1991; Litvak et al., 2005)). The location of these arc magmatic units further away from the Chilean trench than the Las Máquinas Basalts (Fig. 5.3) implies these arc magmas are likely to have been derived from a similar melt source region, with a limited influence from the subducting slab. However, unlike the composition of the Las Máquinas basalts, which is indicative of very little contamination of the arc magmas with crustal components, the Miocene Intrusives and Las Trancas Formation display geochemical evidence for the assimilation of the basement present in the Argentinean Precordillera. As detailed in Chapter 2, trace element modelling and the presence of inherited, xenocrystic zircon cores suggests decoupled fractional crystallisation and assimilation processes (i.e., FCA (Cribb and Barton, 1996)) and bulk assimilation (e.g., Beard et al., 2005) of the Andean basement as these arc magmas migrated through the continental crust. As modelled in Chapter 3, the higher than 'mantle-like' oxygen isotope values and low initial $\varepsilon Hf_{(zircon)}$ values obtained for both the Miocene Intrusives and the Las Trancas Formation suggest that these arc magmas have interacted with a Grenville-aged basement present, which has been inferred as underlying the Argentinean Precordillera (e.g. Kay and Abbruzzi, 1996; Kay and Orrell, 1996; Ramos, 2010). Assimilation of this basement material accounts for the low initial $\varepsilon Hf_{(zircon)}$ values, which are indicative of ancient, unradiogenic continental crust. The presence of inherited zircon cores, ranging in age from the Permian to the Cretaceous (273.1 ±7.2 to 138.1 ±5.2 Ma) (Chapter 2) also suggests the interaction of these arc magmas with the Late Paleozoic – Mesozoic Andean crust.

Evidence from the higher than 'mantle-like' oxygen isotope values and low initial $\varepsilon Hf_{(zircon)}$ compositions of magmatic zircon present in the rhyolitic sample of the Tilito Formation furthest away from the trench and closest to the boundary with the Precordillera, also suggests these arc magmas interacted with the Grenville-aged

basement (Chapter 3). The observed isotopic differences between this sample and the remainder of the Tilito Formation located in the Frontal Cordillera highlights that the heterogeneous composition of the overlying Andean crust plays a dominant role in imparting crustal signatures on arc magmas, as contamination of the melt source region with continental crust would not be expected to generate the observed across-arc variations, specifically in arc magmas erupted at the same time.

The interaction of ascending mantle-derived melts with the overlying Andean continental crust is generally higher in the Late Oligocene to Early Miocene, than is evident earlier on in the Cenozoic (i.e., Late Cretaceous – Mid Eocene). As determined by this study, the degree of crustal contamination of the Late Oligocene to Early Miocene mantle-derived melts is spatially variable, on a relatively local scale (tens of kilometres), and the melts have been contaminated with distinct portions of Andean basement depending on their E - W across-arc position. The across-arc position at which the magmas have been emplaced / erupted appears to determine the amount, as well as the composition of the crustal contaminant. This is consistent with proposed basement heterogeneity in the region and is reinforced by previously reported whole-rock Sr and Pb isotope data (e.g., Kay and Abbruzzi, 1996). It is evident that the Late Oligocene to Early Miocene represented a period of significant crustal reworking and growth of the upper Andean continental crust due to both arc-related, and extension-related, magmatism.

5.5 Early – Mid Miocene (~19 – 14 Ma)

After the apparent reduction in arc magmatism between ~23 and 21 Ma, arc magmatism at the arc-front was reinitiated with the eruption of the basaltic andesite and andesite lavas of the Escabroso Formation (Upper Doña Ana Group) and the Cerro de las Tórtolas Formation (Fig. 5.4). An eastward migration of the arc-front is

observed with the majority of arc volcanism occurring in the Valle del Cura region, on the Argentinean side of the margin. During this time interval subduction of the Juan Fernández Ridge (JFR) began along the Andean margin. It is evident that the subduction of this volcanic seamount had a dramatic effect on the geodynamic evolution of the margin, as well as on the composition of the arc magmas produced.

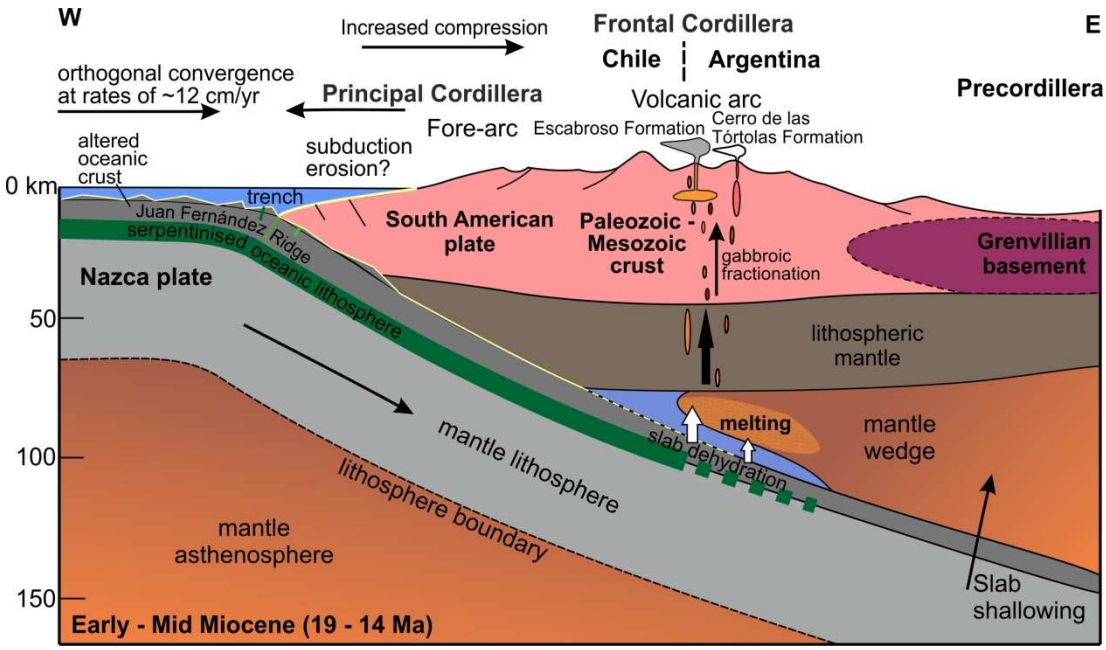

Figure 5.4 A schematic cross section of the southern Central Andean margin, during the Early to Mid Miocene (~19 - 14 Ma), at approximately 29 - 31°S.

The combination of higher fluid-mobile/immobile incompatible trace element ratios and lower fluid-immobile incompatible trace element ratios obtained for the Escabroso and Cerro de las Tórtolas Formations (Chapter 2) are indicative of an increased influence of slab-derived fluids on the melt source region and a higher degree of partial melting, in comparison to the Late Oligocene. This is supported by boron isotopic compositions and concentrations obtained from melt inclusions (average $\delta^{11}B$ values = +4.7 ±1.9 ‰ and average B/Nb ratios = 11.9 ±5.5 (1σ)), which suggest a 0.2 - 2 % fluid addition to the melt source region. Less than 0.5% fluid addition was obtained for samples of the Tilito Formation from a similar across-arc

position (Section 5.4 and Chapter 4). A change in the composition of the slab-derived fluids is also apparent during this time interval. The positive boron isotope values (range = +0.8 to +8.6 ‰) obtained for both the Early - Mid Miocene arc formations suggest these fluids have been derived from the dehydration of serpentinite present in the subducting oceanic lithosphere (Chapter 4). The JFR has been associated with hydrated and serpentinised oceanic lithosphere (Kopp et al., 2004) and therefore seems the likely source of the high $\delta^{11}B$ fluids. This demonstrates the direct influence of the subducting JFR on the composition of arc magmas. It also implies that the JFR may have begun intersecting the margin earlier than previously thought. The JFR is thought to have begun intersecting the Andean margin at these latitudes at ~18 Ma (Yañez et al., 2001), however samples of the Escabroso Formation, which range in age from 19.3 ±0.3 to 18.1 ±0.4 Ma, have boron isotope values indicating the influence of serpentinite-derived fluids. In addition to this, the evidence from boron isotopes also supports the link between the subduction of the JFR and the shallowing angle of the subducting slab, as serpentinisation and hydration of the oceanic lithosphere leads to increased buoyancy.

Although no inherited zircon cores were found in samples of the Escabroso and Cerro de las Tórtolas Formations, 'mantle-like' $\delta^{18}O_{(zircon)}$ values (+5.1 ‰ (±0.4) to +5.6 ‰ (±0.2)) and the range of initial $\varepsilon Hf_{(zircon)}$ values (+1.0 (±1.1) to +2.2 (±0.7)), are indicative of a similar amount of assimilation of the Late Paleozoic to Early Mesozoic basement as modelled for the Tilito Formation (Lower Doña Ana Group) (i.e., between ~5 and 20 %, Chapter 3). The intra-sample heterogeneity observed in $\delta^{11}B$ values and trace element signatures in melt inclusions (Chapter 4) is also indicative of the assimilation of the Andean basement during crystallisation of the arc magmas.

As with the previous time frames, whole-rock rare earth element geochemistry (specifically La/Yb ratios) suggests the Escabroso and Cerro de las Tórtolas Formations were being erupted through continental crust of normal thickness (30 – 35 km) and that high pressure, residual mineral phases (i.e. garnet) were not involved in the petrogenesis of these arc magmas.

5.6 Mid – Late Miocene (~13 – 6 Ma)

During this time interval the angle of the subducting Nazca plate continued to shallow, leading to the migration of arc magmatism to the east and an increase in compression along the southern Central Andean margin, resulting in the main phase of uplift of the Andean range (e.g., Kurtz et al., 1997; Gregory-Wodzicki, 2000). In the Pampean flat-slab segment, Andean arc magmatism during this time interval primarily consists of the eruption of trachyandesitic to dacitic lavas of the Upper Cerro de las Tórtolas Formation (~13 and 10 Ma (Litvak et al., 2007 and references therein)) in the Frontal Cordillera, and the emplacement of shallow level, sub-volcanic andesites, dacites and trachydacites (Tertiary Intrusives, U-Pb ages = 11.7 – 9.4 Ma (this study)) in the Precordillera. Subsequent to this, the last significant magmatic activity in this region is represented by the eruption of small volume, dacitic to rhyolitic ignimbrites (Vacas Heladas Ignimbrites, U-Pb age = 6.2 Ma (this study)) in the Frontal Cordillera (Fig. 5.5).

Towards the end of this time interval (7 – 5 Ma), magmatic activity was initiated in the Pocho volcanic field in the Sierra de Cordoba, Central Argentina. This magmatism, which is ~700 km east of the current Chile trench, has been interpreted as representing the arrival of the subducting Nazca plate under this region of continental crust (Kay and Gordillo, 1994). On this basis it can be assumed that the mantle wedge located under the main Andean arc must have been significantly

reduced in volume. This is reflected in the decrease in magmatic activity and the highly 'enriched' nature of the arc magmas emplaced and erupted during this time interval.

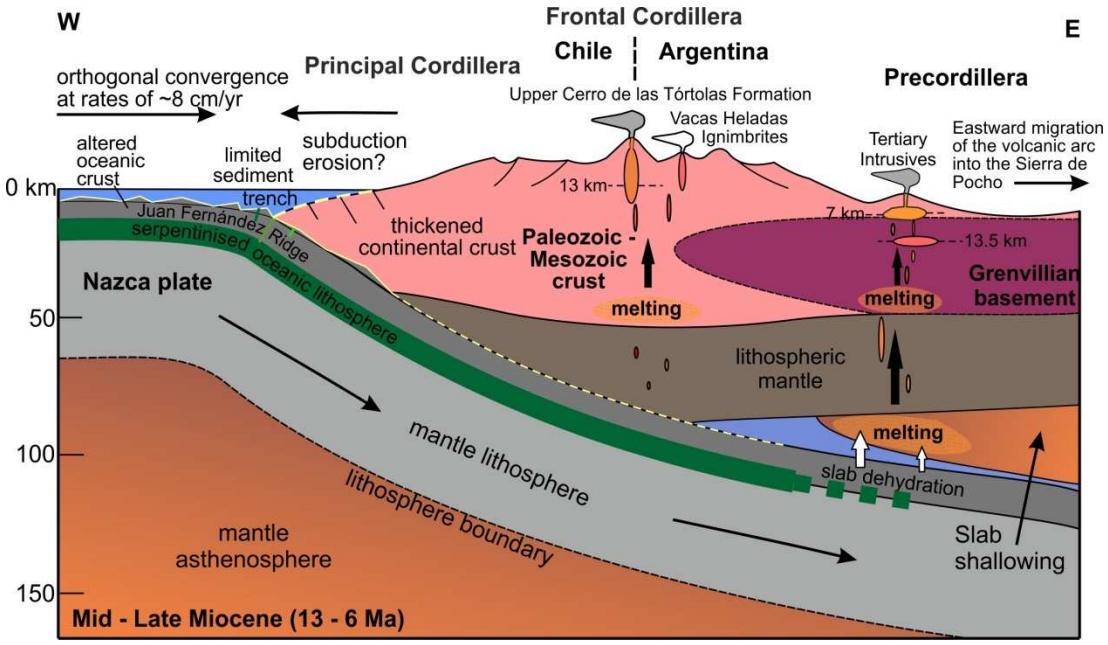

Figure 5.5 A schematic cross section of the southern Central Andean margin, during the Mid to Late Miocene (13 - 6 Ma), at approximately 29 - 31°S.

The broadly similar fluid-mobile/immobile and immobile/immobile incompatible trace element ratios (e.g., Ba/Nb, Pb/Nb, and Nb/Zr) obtained for the Upper Cerro de las Tórtolas Formation and the Tertiary Intrusives (Chapter 2) suggests a similar influence of slab-derived fluids on the mantle wedge and a similar degree of partial melting for both these arc formations. The Vacas Heladas Ignimbrites have the highest fluid-immobile, incompatible trace element ratios (e.g., Nb/Zr and Nb/Yb) of the Mid – Late Miocene arc formations, suggesting they represent small degrees of partial melting. Alternatively this could also reflect increased enrichment, however, the small degree of partial melting is consistent with the small volumes of these melts. Due to the lack of mantle wedge remaining under the Frontal Cordillera during the eruption of the Vacas Heladas Ignimbrites, it is proposed that the Vacas Heladas Ignimbrites are generated in the lower crust due the influence of heat and

fluids derived from the subducting slab. The high ratios of fluid-mobile/immobile incompatible trace elements (e.g., Ba/Nb, Pb/Nb, Pb/Ce) obtained from the Vacas Heladas Ignimbrites compared to the other Mid to Late Miocene arc magmas, is also indicative of a high influence of slab-derived fluids on these magmas.

As is apparent in the Late Oligocene to Early Miocene, the across-arc position of the arc magmatism dictates the crustal contaminant, as a result of the heterogeneity of the Andean basement. As previously highlighted and demonstrated in Chapter 3, this suggests that the assimilation of the Andean crust plays the dominant role in modifying the composition of arc magmas, as opposed to contamination of the melt source region with subducted continental crust, which would not be expected to maintain the observed across-arc isotopic trends. The Tertiary Intrusives, which are situated in the Precordillera, show the most significant evidence for assimilation of the Grenville-aged basement present in the Argentinean Precordillera (e.g., Abbruzzi et al., 1993; Kay et al., 1996) with the presence of inherited zircon cores of Proterozoic age (U-Pb ages ranging between 1249.4 (±21.9) and 1039 (±29.0) Ma). In addition, low $\varepsilon Hf_{T(zircon)}$ values (-3.5 (±0.9) to +1.1 (±0.7)) and higher than 'mantle-like' $\delta^{18}O_{(zircon)}$ values (+5.9 ‰ (±0.4) to +6.4 ‰ (±0.6)) combined with distinct trace element signatures (e.g., low Th and U contents) supports the interaction of melts derived from the mantle with the Grenvillian basement terrane. Some Triassic inherited cores were also identified in the Tertiary Intrusives, suggesting these arc magmas also assimilated crust of this age en route to the surface. This has not been previously identified and previous studies have attributed the Pb isotopic compositions of the Tertiary Intrusives, which are more radiogenic than those obtained for xenoliths of the Grenville-aged basement, to a source in the sub-arc mantle wedge (Kay and Abbruzzi, 1996). This study proposes that interaction of melts derived from the mantle with Permian – Triassic aged crust could account for the radiogenic Pb isotope compositions.

Zircon inheritance (Chapter 2) and O and Hf isotopic compositions of zircons (Chapter 3) obtained from the Vacas Heladas Ignimbrites provides evidence for the involvement of the Grenville-aged basement, Late Paleozoic – Early Mesozoic Andean crust and older, Cenozoic arc rocks on the evolution of the Vacas Heladas magmas. This supports evidence obtained from whole rock Sr and Nd isotopes (Kay et al., 1991), which suggests a significant influence of the Andean crust on the petrogenesis of these arc magmas. The $\varepsilon Hf_{T(zircon)}$ values (-1.3 (±2.9)) obtained for Vacas Heladas Ignimbrites (~6 Ma) are lower (i.e., less radiogenic) than the $\varepsilon Hf_{T(zircon)}$ values obtained for the Late Eocene to Early Miocene arc magmatic rocks located in the Frontal Cordillera. This suggests that these arc magmas have interacted with an ancient, and hence un-radiogenic, portion of crust which did not affect the Late Eocene to Early Miocene arc magmas. This evidence, combined with lower whole-rock εNd values obtained for the Vacas Heladas Ignimbrites compared to older arc magmatic rocks located in the Frontal Cordillera (Kay et al., 1991), and in relation to structural models of the southern Central Andean margin (e.g., Ramos et al., 2004; Gilbert et al., 2006; Gans et al., 2011), suggests the interaction of these arc magmas with a Grenville-aged basement. The interaction of these relatively young (~6 Ma) arc magmas, erupted in the Frontal Cordillera of the Pampean flat-slab segment, with a Grenville-aged basement has not been identified prior to this study. This result supports structural models (e.g., Ramos et al., 2004; Gilbert et al., 2006; Gans et al., 2011), which suggest the Grenville-aged basement, identified in the Argentinean Precordillera (e.g., Abbruzzi et al., 1993; Kay and Orrell, 1996; Rapela et al., 2010), currently under-thrusts the Frontal Cordillera as a result of crustal shortening in the region. In addition, the isotopic results presented in this study suggest this under-thrusting occurred prior to 6 Ma.

A principal feature of the Mid to Late Miocene arc magmatic rocks is their adakitic signatures (e.g., high Sr/Y and La/Yb ratios). These signatures have been interpreted as representing the melting and equilibration of arc magmas with a higher pressure

mineral assemblage, present in the lower crust, where garnet is a residual phase (Chapter 2). The whole-rock trace and rare earth element signatures (e.g., high Sr/Y ratios and limited Eu anomalies) also suggest the suppression of plagioclase fractionation under higher pressure conditions. These higher pressure conditions are consistent with the timing of significant tectonic shortening in the region and the proposed timing of the main uplift of the Andean range (e.g., Kurtz et al., 1997; Gregory-Wodzicki, 2000). In the Pampean flat-slab segment this increase in crustal thickness has been linked to the increase in compression, in part due to the shallowing of the subducting slab (e.g., Jordan et al., 1983; Kay et al., 1991). The presence of adakitic signatures in the Tertiary Intrusives, emplaced in the Argentinean Precordillera, suggests the continental crust must have thickened to >50 km at this across-arc position, as well as beneath the Frontal Cordillera.

In conjunction with the thickening of the continental crust, and the generation of magmas with adakitic signatures, an increase in the crustal depths at which phenocryst assemblages are crystallising and equilibrating with the surrounding melt is also observed in the Mid – Late Miocene magmatic rocks. Amphibole geothermobarometry, conducted as part of this study (Chapter 2), produced an average estimated crystallisation/equilibration depth of 13 km for the Upper Cerro de las Tórtolas Formation and average depths of 14 km and 7 km for the Tertiary Intrusives. This suggests a deepening of magma crystallisation depths (an average depth of 8 km was produced for the Late Oligocene, Tilito Formation) during a time when the thickness of the crust was increasing. In addition, this depth increase may also influence the depths at which the arc magmas were potentially assimilating Andean crust. The crystallisation/equilibration depth obtained for the Upper Cerro de las Tórtolas Formation is in agreement with a crustal depth of ~14 km, recently reported by Litvak and Poma (2013) for the Upper Cerro de las Tórtolas Formation (13 – 10 Ma). This study also obtained crustal crystallisation/equilibration depths of ~14 km for the Cerro de las Tórtolas Formation (17 – 14 Ma). This suggests that the

increase in arc magma crystallisation/equilibration depths in the Pampean flat-slab segment occurred prior to ~13 Ma, potentially at a similar time to the intersection of the JFR with the southern Central Andean margin (~18 Ma) (Yañez et al., 2001).

Overall, the new geochronological, geochemical and geothermobarometric data presented in this study, for Late Cretaceous to Late Miocene arc magmatic rocks, has provided new evidence with which to refine models of the tectonic and geodynamic evolution of the Pampean flat-slab segment during the Cenozoic.

5.7 References

Abbruzzi, J., Kay, S.M., and Bickford, M.E., 1993, Implications for the nature of the Precordilleran basement from the geochemistry and age of Precambrian xenoliths in Miocene volcanic rocks, San Juan province: Actas, v. 3, p. 331-339.

Beard, J.S., Ragland, P.C., and Crawford, M.L., 2005, Reactive bulk assimilation: A model for crust-mantle mixing in silicic magmas: Geology, v. 33, p. 681-684.

Bissig, T., Clark, A.H., Lee, J.K., and von Quadt, A., 2003, Petrogenetic and metallogenetic responses to Miocene slab flattening: new constraints from the El Indio-Pascua Au–Ag–Cu belt, Chile/Argentina: Mineralium Deposita, v. 38, p. 844-862.

Charrier, R., Baeza, O., Elgueta, S., Flynn, J.J., Gans, P., Kay, S.M., Muñoz, N., Wyss, A.R., and Zurita, E., 2002, Evidence for Cenozoic extensional basin development and tectonic inversion south of the flat-slab segment, southern Central Andes, Chile (33º - 36ºS.L.: Journal of South American Earth Sciences, v. 15, p. 117 - 139.

Charrier, R., Pinto, L., and Rodríguez, M.P., 2007, Tectonostratigraphic evolution of the Andean Orogen in Chile, *in* Moreno, T., and Gibbons, W., eds., The Geology of Chile: London, The Geological Society, p. 21 - 114.

Cribb, J.W., and Barton, M., 1996, Geochemical effects of decoupled fractional crystallization and crustal assimilation: Lithos, v. 37, p. 293-307.

Gans, C.R., Beck, S.L., Zandt, G., Gilbert, H., Alvarado, P., Anderson, M., and Linkimer, L., 2011, Continental and oceanic crustal structure of the Pampean flat slab region, western Argentina, using receiver function analysis: new high-resolution results: Geophysical Journal International, v. 186, p. 45-58.

Gilbert, H., Beck, S., and Zandt, G., 2006, Lithospheric and upper mantle structure of central Chile and Argentina: Geophysical Journal International, v. 165, p. 383-398.

Goss, A.R., Kay, S.M., and Mpodozis, C., 2013, Andean Adakite-like high-Mg Andesites on the Northern Margin of the Chilean–Pampean Flat-slab (27–28· 5° S) Associated with Frontal Arc Migration and Fore-arc Subduction Erosion: Journal of Petrology, v. 54, p. 2193-2234.

Gregory-Wodzicki, K.M., 2000, Uplift history of the Central and Northern Andes: A review: Geological Society of America Bulletin, v. 112, p. 1091-1105.

Gutscher, M.-A., Maury, R., Eissen, J.-P., and Bourdon, E., 2000, Can slab melting be caused by flat subduction?: Geology, v. 28, p. 535-538.

Jordan, T.E., Isacks, B.L., Allmendinger, R.W., Brewer, J.A., Ramos, V.A., and Ando, C.J., 1983, Andean tectonics related to geometry of subducted Nazca plate: Geological Society of America Bulletin, v. 94, p. 341-361.

Jordon, T.E., Burns, W.M., Veiga, R., Pángaro, F., Copeland, P., Kelley, S., and Mpodozis, C., 2001, Extension and basin formation in the southern Andes

caused by increased convergence rate: A mid-Cenozoic trigger for the Andes: Tectonics, v. 20, p. 308 - 324.

Kay, S., and Gordillo, C., 1994, Pocho volcanic rocks and the melting of depleted continental lithosphere above a shallowly dipping subduction zone in the central Andes: Contributions to Mineralogy and Petrology, v. 117, p. 25-44.

Kay, S.M., and Abbruzzi, J.M., 1996, Magmatic evidence for Neogene lithospheric evolution of the central Andean "flat slab" between 30ºS and 32ºS: Tectonophysics, v. 259, p. 15 - 28.

Kay, S.M., Godoy, E., and Kurtz, A., 2005, Episodic arc migration, crustal thickening, subduction erosion, and magmatism in the south-central Andes: Geological Society of America Bulletin, v. 117, p. 67-88.

Kay, S.M., and Mpodozis, C., 2002, Magmatism as a probe to the Neogene shallowing of the Nazca plate beneath the modern Chilean flat slab: Journal of South American Earth Sciences, v. 15, p. 39 - 57.

Kay, S.M., Mpodozis, C., Ramos, V.A., and Munizaga, F., 1991, Magma source variations for mid-late Tertiary magmatic rocks associated with a shallowing subduction zone and the thickening crust in the central Andes (28-33ºS): Spec. Pap. Geological Society of America Bulletin, v. 265, p. 113 - 137.

Kay, S.M., and Orrell, S., 1996, Zircon and whole rock Nd-Pb isotopic evidence for a Grenville age and a Laurentian origin for the Basement of the Precordillera in Argentina: Journal of Geology, v. 104, p. 637.

Kay, S.M., Orrell, S., and Abbruzzi, J., 1996, Zircon and whole rock Nd-Pb isotopic evidence for a Grenville age and a Laurentian origin for the basement of the Precordillera in Argentina: The Journal of Geology, p. 637-648.

Kopp, H., Flueh, E.R., Papenberg, C., and Klaeschen, D., 2004, Seismic investigations of the O'Higgins Seamount Group and Juan Fernández Ridge: Aseismic ridge emplacement and lithosphere hydration: Tectonics, v. 23.

Kurtz, A.C., Kay, S.M., Charrier, R., and Farrar, E., 1997, Geochronology of Miocene plutons and exhumation history of the El Teniente region, Central Chile (34-35° 8): Andean Geology, v. 24, p. 75-90.

Leake, B.E., 1971, On aluminous and edenitic hornblendes: Mineral Mag, v. 38, p. 389-407.

Litvak, V.D., Kay, S.M., and Mpodozis M, C., 2005, New K/Ar ages on Tertiary Volcanic Rocks in the Valle del Cura, Pampean flat slab segment, Argentina: Actas XVI Congreso Geológico Argentino, v. 2, p. 159 - 164.

Litvak, V.D., and Page, S., 2002, Nueva evidencia cronológica en el Valle del Cura, provincia de San Juan, Argentina: Revista de la Asociación Geológica Argentina, v. 57, p. 483-486.

Litvak, V.D., and Poma, S., 2010, Geochemistry of mafic Paleocene volcanic rocks in the Valle del Cura region: Implications for the petrogenesis of primary mantle-derived melts over the Pampean flat-slab: Journal of South American Earth Sciences, v. 29, p. 705-716.

Litvak, V.D., and Poma, S., 2013, Petrogenesis of Miocene volcanic arc rocks over the Chilean-Pampean flat-slab segment of the Central Andes constrained by mineral chemistry: Geologica Acta, v. In press.

Litvak, V.D., Poma, S., and Kay, S.M., 2007, Paleogene and Neogene magmatism in the Valle del Cura region: New perspective on the evolution of the Pampean flat slab, San Juan province, Argentina: Journal of South American Earth Sciences, v. 24, p. 117 - 137.

Lonsdale, P., 2005, Creation of the Cocos and Nazca plates by fission of the Farallon plate: Tectonophysics, v. 404, p. 237-264.

Martin, M.W., Clavero R, J., Mpodozis M, C., and Cuitiño, L., 1995, Estudio Geológico de la Franja El Indio, Cordillera de Coquimbo: Servicio Nacional de Geología y Minería: Santiago, 1 - 238 p.

O'Driscoll, L.J., Richards, M.A., and Humphreys, E.D., 2012, Nazca–South America interactions and the late Eocene–late Oligocene flat-slab episode in the central Andes: Tectonics, v. 31.

Parada, M.A., 1990, Granitoid plutonism in central Chile and its geodynamic implications; A review, *in* Kay, S.M., and Rapela, C.W., eds., Plutonism from Antarctica to Alaska, Volume Special Paper 241: Boulder, Colorado, The Geological Society of America.

Parada, M.A., López-Escobar, L., Oliveros, V., Fuentes, F., Morata, D., Calderón, M., Aguirre, L., Féraud, G., Espinoza, F., Moreno, H., Figueroa, O., Bravo, J.M., Vásquez, R.T., and Stern, C.R., 2007, Andean Magmatism, *in* Moreno, T., and Gibbons, W., eds., The Geology of Chile: London, The Geological Society, p. 115 - 146.

Parada, M.A., Rivano, S., Sepulveda, P., Herve, M., Herve, F., Puig, A., Munizaga, F., Brook, M., Pankhurst, R., and Snelling, N., 1988, Mesozoic and Cenozoic plutonic development in the Andes of central Chile (30º30' - 32º30'S) Journal of South American Earth Sciences, v. 1, p. 249 - 260.

Pardo Casas, F., and Molnar, P., 1987, Relative motion of the Nazca (Farallón) and South America plates since Late Cretaceous time Tectonics, v. 6, p. 233 - 248.

Pilger, R.H., 1981, Plate reconstructions, aseismic ridges, and low angle subduction beneath the Andes: Geological Society of America Bulletin, v. 92, p. 448 - 456.

Pilger, R.H., 1984, Cenozoic plate kinematics, subduction and magmatism: South American Andes: Journal of Geological Society London, v. 141, p. 793 - 802.

Ramos, V.A., 2010, The Grenville-age basement of the Andes: Journal of South American Earth Sciences, v. 29, p. 77-91.

Ramos, V.A., and Folguera, A., 2009, Andean flat-slab subduction through time: Geological Society, London, Special Publications, v. 327, p. 31-54.

Ramos, V.A., Zapata, T., Cristallini, E., and Introcaso, A., 2004, The Andean thrust system—Latitudinal variations in structural styles and orogenic shortening: Thrust tectonics and hydrocarbon systems, v. 82, p. 30-50.

Rapela, C.W., Pankhurst, R.J., Casquet, C., Baldo, E., Galindo, C., Fanning, C.M., and Dahlquist, J.M., 2010, The Western Sierras Pampeanas: Protracted Grenville-

age history (1330–1030 Ma) of intra-oceanic arcs, subduction–accretion at continental-edge and AMCG intraplate magmatism: Journal of South American Earth Sciences, v. 29, p. 105-127.

Somoza, R., 1998, Updated Nazca (Farallon) - South America relative motions during the last 40My: implications for mountain building in the central Andean region: Journal of South American Earth Sciences, v. 11, p. 211 - 215.

Somoza, R., and Ghidella, M.E., 2012, Late Cretaceous to recent plate motions in western South America revisited: Earth and Planetary Science Letters, v. 331–332, p. 152-163.

Stern, C.R., 1991, Role of subduction erosion in the generation of Andean magmas: Geology, v. 19, p. 78 - 81.

Stern, C.R., 2011, Subduction erosion: rates, mechanisms, and its role in arc magmatism and the evolution of the continental crust and mantle: Gondwana Research, v. 20, p. 284-308.

Winocur, D.A., Litvak, V.D., and Ramos, V.A., 2013, Magmatic and tectonic evolution of the Oligocene Valle del Cura basin, Main Andes of Argentina and Chile: Evidence for generalized extension, *in* Sepulveda, P., Giambiagi, L., Pinto, L., Moreiras, S., Tunik, M., Hoke, G., and M., F., eds., Geodynamic processes in the Andes of Central Chile and Argentina, Volume In press, Geological Society of London, Special Publication.

Yañez, G.A., Cembrano, J., Pardo, M., Ranero, C.R., and Selles, D., 2002, The Challenger - Juan Fernández - Maipo major tectonic transition of the Nazca - Andean subduction system at 33-34ºS: geodynamic evidence and implications: Journal of South American Earth Sciences, v. 15, p. 28 - 38.

Yañez, G.A., Ranero, C.R., von Huene, R., and Díaz, J., 2001, Magnetic anomaly interpretation across the southern central Andes (32º-34ºS): The role of the Juan Fernández Ridge in the late Tertiary evolution of the margin: Journal of Geophysical Research, v. 106, p. 6325 - 6345.

Chapter 6

Conclusions, limitations and recommendations for further work

6.1 Conclusions

The principal aims of this thesis were to:

- Better constrain the timing and duration of arc magmatism in the southern Central Andes.
- Assess the contributions from mantle, crustal and subducted reservoirs to Cenozoic arc magmas, by using a range of geochemical and *in-situ*, micro-analytical techniques.
- Relate changes in contributions from mantle, crustal and subducted reservoirs to Cenozoic arc magmas to the changing geodynamic setting of the southern Central Andean margin.

The main findings and conclusions are summarised below.

6.1.1 Timing and duration of arc magmatism in the southern Central Andes

The production of 44 new age determinations by high resolution, *in-situ* U-Pb dating of magmatic zircon and Ar-Ar dating of plagioclase has led to an improved regional stratigraphy in the southern Central Andes, between 29 and 31 °S. Prior to this study a high proportion of the ages reported for arc magmatic rocks from this region of the Central Andes were obtained by K-Ar dating, which on the basis of evidence for high levels of hydrothermal alteration observed in some arc formations has been called into question (e.g., Winocur et al., 2013). The U-Pb and Ar-Ar age determinations produced by this study provide an accurate temporal constraint for the geochemical data presented in this study, as well as geochemical data presented in previous studies (e.g., Leveratto, 1976; Litvak et al., 2007).

6.1.2 Variable contamination of mantle-derived melts

The Late Cretaceous (~72 Ma) to Late Eocene (~39 Ma) arc magmatic rocks, which primarily occur as north-south trending plutonic belts in the Principal Cordillera of Chile, were formed in a subduction zone setting from the partial melting of a metasomatised mantle wedge. On the basis of 'mantle-like' $\delta^{18}O_{(zircon)}$ values and juvenile initial $\varepsilon Hf_{(zircon)}$ values, combined with a lack of zircon inheritance, it is concluded that during the early stages of Andean-type subduction, these extensive magmatic belts were formed from mantle-derived melts which experienced very limited interaction with upper continental crustal material, either in the melt source region or due to assimilation of crustal material en route to the surface. Amphibole – plagioclase geothermobarometry indicates these calc-alkaline granitoids were emplaced at shallow depths in the crust (~4 – 5 km). Therefore it is concluded that the Late Cretaceous to Late Eocene represents a period of significant upper crustal growth with melts derived from the mantle.

It is concluded that the Late Eocene (~36 Ma) to Early Miocene (~17 Ma) arc magmas erupted in the Frontal Cordillera assimilated up to ~20 % of the Late Paleozoic to Early Mesozoic basement, in order to account for the broadly 'mantle-like' $\delta^{18}O_{(zircon)}$ values but lower (i.e., less radiogenic) initial $\varepsilon Hf_{(zircon)}$ values than those expected from melts derived from the mantle wedge. This is supported by the U-Pb ages (Devonian to Triassic) obtained for inherited, xenocrystic zircon cores, as well as evidence from whole-rock trace element compositions, which modelling has shown to be indicative of decoupled assimilation and fractional crystallisation processes.

The higher than 'mantle-like' $\delta^{18}O_{(zircon)}$ values and unradiogenic, initial $\varepsilon Hf_{(zircon)}$ values obtained for the Late Oligocene (~23 Ma) to Late Miocene (~9 Ma) magmatic rocks located in the Argentinean Precordillera (i.e., furthest east from the trench), as well as the most easterly sample of the Tilito Formation (24 Ma), are indicative of the assimilation of ancient continental crust (>500 Ma), which has been affected by

low temperature processes (e.g., interaction with the hydrosphere). Additional evidence from whole-rock trace element compositions (e.g., low U and Th concentrations) and the range of U-Pb ages obtained for inherited zircon cores (Mesoproterozoic, Permian-Triassic and Cretaceous) suggests these arc magmas have interacted both a Grenville-aged basement terrane, inferred to be present in the Precordillera (e.g., Abbruzzi et al., 1993; Kay and Orrell, 1996; Rapela et al., 2010), and the Late Paleozoic to Early Mesozoic Andean crust. The isotopic variability displayed in the youngest, Late Miocene (~6 Ma) arc volcanic rocks in the Frontal Cordillera, also suggests the assimilation of the Grenville-aged basement in addition to Late Paleozoic to Early Mesozoic crust. This potentially signals the arrival of the Grenville-aged basement terrane beneath the Frontal Cordillera, as a result of increased compression and crustal shortening over the later part of the Miocene.

It is concluded that the overlying Andean continental crust, which varies E - W across the Andean Cordillera in both age and composition, has played a dominant role in modifying the isotopic composition of the Late Eocene to Late Miocene mantle-derived melts. It is therefore evident that the later part of the Cenozoic (post ~26 Myr) represents a sustained period of crustal reworking, with arc magmas assimilating continental crust as they migrate through a crust of progressively increasing thickness. Subducted sediments and continental crust derived from subduction erosion may be influencing the melt source region during this time interval. However, in light of the correlation between the O and Hf isotopic compositions of zircon and the proposed locations of distinct Andean basement terranes, it is suggested that isotopic signatures derived from the melt source region have been overprinted as a result of assimilation processes occurring in the Andean crust.

6.1.3 The source and influence of slab-derived fluids

The successful analysis of boron isotope ratios and select trace elements in melt inclusions has led to an increased understanding of the source and influence of slab-derived fluids on the sub-arc mantle between the Paleocene (61.2 Ma) and the Miocene (17.1 Ma). The melt inclusions analysed for trace element and boron isotopic compositions were hosted in both pyroxene and zircon phenocrysts. To the authors knowledge this is the first time melt inclusions hosted in zircon have been analysed for boron concentrations and isotopic compositions. This study found no difference in boron concentrations and $\delta^{11}B$ values between melt inclusions hosted in pyroxene and zircon from the same sample. The successful application of this *in-situ* technique reveals a potentially useful geochemical tool, as zircon is a particularly useful accessory mineral, being both chemically and mechanically extremely robust and relatively easily dated by U-Th-Pb analysis (Harley and Kelly, 2007). The ability to analyse elemental and isotopic compositions in melt inclusions hosted in zircon would allow correlations and comparisons to be made between different datasets which allude to different processes (e.g., contributions to arc magmas from the mantle, slab-derived fluids, sediment melts and the assimilation of continental crust). These could all be accurately time constrained by high resolution U-Pb dating.

The boron concentrations obtained for all melt inclusions hosted in pyroxene and zircon, are higher than those expected for a NMORB-source mantle (i.e., B = ~0.05 ppm (Chaussidon and Marty, 1995)), as well as the majority of $\delta^{11}B$ values (NMORB-source $\delta^{11}B$ = -4.0 (±1.6) ‰ (Chaussidon and Marty, 1995)). Both boron concentrations and $\delta^{11}B$ values show considerable variations as a function of age. During the Paleocene, and the emplacement of extensive plutonic belts in the Chilean Principal Cordillera, the sub-arc region was influenced by fluids with a relatively homogeneous $\delta^{11}B$ composition of +1.6 ‰. Mixing modelling suggests this fluid is primarily derived from altered oceanic crust in the subducting Farallon

plate. The rather uniform $\delta^{11}B$ values and B/Nb ratios obtained for melt inclusions confirms the conclusions drawn from zircon O and Hf isotope data (Chapter 3); that the Late Cretaceous – Late Eocene arc magmas assimilated little upper crustal material en route to the surface. This may be related to the more extensional regime in operation along the Andean margin during this time interval (e.g., Charrier et al., 2007 and references therein).

The significantly lower (i.e., more negative) $\delta^{11}B$ values and B/Nb ratios obtained for the Late Oligocene arc rocks of the Tilito Formation, in comparison to those obtained for the Paleocene and Early Miocene reflects a diminished influence of slab-derived fluids (primarily derived from altered oceanic crust) on the melt source region (<0.5 % fluid addition). This suggests the eruption of these arc magmas over a greater depth to the slab-mantle interface, evidence which supports the existence of a wide magmatic arc during the Late Oligocene (e.g., Winocur et al., 2013). The intra-sample heterogeneity in both boron concentrations and isotopic compositions obtained for melt inclusions from both the Late Oligocene and Early Miocene samples is indicative of modifications by the assimilation of the Andean continental crust as the arc magmas migrate to the surface. This supports the evidence provided by the oxygen and hafnium isotopic composition of zircons (Chapter 3) for increased interaction of arc magmas with the overlying Andean crust after the Late Oligocene (~26 Ma).

This study has demonstrated that fluids derived from serpentinite in the subducting oceanic lithosphere affected the melt source region and had a direct influence on the composition of arc magmas after 19.5 Ma (i.e., the Early Miocene). This has led to the proposal that hydrated and serpentinised oceanic lithosphere associated with the Juan Fernandez Ridge may have begun intersecting the Andean margin at these latitudes (i.e., ~30 °S) earlier than previously suggested (~18 Ma (Yañez et al., 2001)). In turn this also increases the strength of the link between the subduction of the JFR

and the shallowing of the subducting Nazca plate, which has been somewhat debated (e.g., Cahill and Isacks, 1992; Yañez et al., 2001; Yañez et al., 2002; Manea et al., 2012), as hydration and serpentinisation of oceanic lithosphere leads to increased buoyancy.

6.2 Limitations of the study

Some of the principal limitations of this study are outlined below.

- One of the primary aims of this study was to determine and assess contributions to arc magmas from mantle, subducting and continental crustal reservoirs. As demonstrated by the distinct spatial variations in O and Hf isotope values obtained for magmatic zircon, which correlate with distinct ages and compositions of Andean basement, this study concludes that assimilation of the continental crust en route to the surface has played a dominant role in determining the isotopic composition of the arc magmas in the Pampean flat-slab segment since the Late Oligocene (~26 Ma). However, both exhumation and erosion (e.g., Maksaev and Zentilli, 1999; Oncken et al., 2006 and references therein), and high levels of subduction erosion have been identified along the Central Andean margin during the Cenozoic (e.g., Stern, 2011 and references therein). Geothermobarometric data presented in this study also suggests the removal of between ~4 and 5 km of continental crust since the Eocene (~40 Ma) and from the lack of accretionary complexes apparent along the southern Central Andean margin (e.g., Von Huene and Scholl, 1991), it is evident that sediments present in the Chile trench must have been subducted during the course of the Cenozoic. On this basis it seems likely that fluids or melts derived from sediments or continental crust from subduction erosion, have influenced the sub-arc region in the southern Central Andes over this time interval and hence the composition of arc

magmas. However, in the younger arc magmatic rocks (post ~26 Ma) it is extremely difficult to identify these sediment signals due to the dominance of crustal assimilation in modifying the composition of the arc magmas, as identified by this study. The analysis of boron isotopes and trace element compositions in melt inclusions was conducted with the aim of potentially detecting fluids derived from subducting continental crustal material (Andean continental crust and continentally derived sediments have been determined to have negative boron isotope ratios of -8.9 (±2.3) ‰ (Kasemann et al., 2000) and -13 to -8 ‰ (Ishikawa and Nakamura, 1993) respectively). However boron isotopic compositions and trace element compositions reflect the dominant influence of fluids derived from altered oceanic crust and serpentinite present in the subducting oceanic lithosphere, which have distinctly positive boron isotope compositions (e.g., Spivack and Edmond, 1987; Smith et al., 1995).

- This work is limited by the restricted compositional information available for sediments present in the Chile trench, particularly offshore of the Pampean flat-slab segment. This is primarily related to the lack of drill cores from this region. Although it is possible that the composition of the sediments may have changed over time, the lack of a sedimentary end member leads to some limitations in the geochemical modelling presented in this study. For example, there is currently no boron concentration or isotope data for sediments currently in the Chile trench. On this basis the values of Tonarini et al. (2011) were used in the modelling of boron isotope data presented in Chapter 4. Although these sediment values are considered a reasonable approximation (detailed in Chapter 4) they do not necessarily reflect the true sediment composition in the region under investigation.

- The restricted number of suitable samples containing suitable melt inclusions for analysis, in the same mineral phase as other samples, presented a further limitation to this study. In particular, due to the intrusive nature of the majority of the Late Cretaceous to Eocene arc magmatic rocks, very few samples with suitable melt inclusions were found for this timeframe. In addition a lack of suitable samples containing melt inclusions were available for the Mid to Late Miocene. Analysis of melt inclusions from this lastest timeframe would have allowed the effect of the increased shallowing of the subducting Nazca plate on fluids influencing the melt source region to be assessed.

- The various methods of *in-situ* elemental and isotopic analysis conducted by this study (SIMS, LA-MC-ICP-MS and EPMA) require different volumes of material. For example, oxygen isotope analysis via SIMS requires a volume of only ~20 μm^3 whereas hafnium isotope analysis via LA-ICP-MS requires a volume of up to ~1500 μm^3 (i.e., 50 μm x 30 μm). Due to the fine scale composition growth zoning observed in zircon grains (Appendix A2.1) this meant exactly the same zircon growth zones could not be targeted by all analyses (i.e., O isotope, U-Pb dating and Lu-Hf isotope analysis). In addition, due to the small size of the majority of zircons obtained for the volcanic samples (i.e., <~200μm in length), only one Lu-Hf via LA-ICP-MS could be conducted per grain.

6.3 Recommendations for future work

Although this thesis contributes to our understanding of the petrogenesis of Cenozoic arc magmas in the southern Central Andes, a number of outstanding questions remain and some additional questions have been raised by this work. Some recommendations of how to address these questions are outlined below. In addition, some potential lines of future research, using the methods and techniques applied by this study, are also suggested.

- *In-situ* analysis of Pb isotope compositions of melt inclusions could provide further constraints on contributions to arc magmas, particularly from continental crustal material. In the Central Andes, to the north of the Pampean flat-slab segment, the Pb isotopic compositions of arc magmatic rocks have revealed the interaction of arc magmas with distinct basement domains (e.g., Wörner et al., 1992; Aitcheson et al., 1995). Similar processes may be revealed in the Pampean flat-slab segment in support of the findings presented in this study on the basis of the O and Hf isotopic composition of zircon (Chapter 3). Melt inclusions could also be analysed from a wider range of mineral phases than utilised as part of this study. For example, melt inclusions hosted in quartz have been identified in samples of the Tilito Formation (Late Oligocene) and the Vacas Heladas Ignimbrites (Late Miocene) during petrographic analysis conducted as part of this study.

- In order to investigate further the influence and source of slab-derived fluids on the melt source region and the effects of changing geodynamic setting (e.g., slab shallowing), other fluid-mobile trace elements could be analysed in melt inclusions (e.g., Cl, F, As, Sb and Li), as well as the isotopic compositions of lithium. Such methods have previously been proposed and implemented by a number of studies of various subduction zones (e.g.,

Moriguti and Nakamura, 1998; Chan and Kastner, 2000; Straub and Layne, 2003). As well as potentially strengthening the argument for the addition of fluids primarily derived from altered oceanic crust (Paleocene - Late Oligocene) and serpentinite (Miocene), it would allow for the behaviour of other elements and isotope systems to be compared to the behaviour of boron and boron isotopes.

- One method of identifying sediment contributions to the Late Miocene arc magmas in the Pampean flat-slab segment would be to analyse ^{10}Be (a cosmogenic radionuclide) in the youngest arc magmas (<6 Ma). As ^{10}Be can only be produced in the upper atmosphere it is strongly enriched in sediments and therefore may allow the positive identification of the influence of subducted sediments on the melt source region. Unfortunately, it has a half-life of 1.5 Myr, making analysis only worthwhile on the very youngest arc rocks present in the region. This method has been successfully applied to identify subducted pelagic sediments in the source of arc magmas along the Andean margin, outside of the Pampean flat-slab segment (e.g., Sigmarsson et al., 1990).

- Detailed *in-situ* analysis of elemental and isotopic compositions of other mineral phases present in arc magmatic rocks could be utilised to reveal further information on contributions to arc magmas, particularly from crustal components. Specifically, the investigation into how isotopic compositions develop from core to rim of individual crystals could shed light on processes ongoing in the arc magma as it crystallises, such as magma mixing, recharge, and importantly for the questions posed by this study, crustal contamination. As detailed above, due to the limited size of the zircon phenocrysts and the beam size required by the analytical techniques implemented by this study (up to 50μm for hafnium isotope

analysis via LA-ICP-MS), limited core to rim analyses could be carried out on individual zircon grains. *In-situ*, core to rim isotopic analysis of other, larger mineral phases (e.g., O, Sr and Pb isotope ratios in plagioclase phenocrysts), has the potential to reveal a detailed picture of the timing of crustal contamination, as well as information regarding the composition of the contaminant (e.g., Davidson et al., 2005; Charlier et al., 2006; Davidson et al., 2007).

- Although some previous investigations have been conducted into crustal xenoliths present in arc magmatic rocks from the Pampean flat-slab segment, these have tended to focus on the Argentinean Precordillera (e.g., Abbruzzi et al., 1993; Kay and Orrell, 1996). Crustal xenoliths were identified in arc magmatic rocks in the Frontal Cordillera, but were not investigated further as part of this study. Separation and analysis of these crustal xenoliths, and the minerals they contain, could provide interesting additional insights into crustal recycling and reveal further information regarding the composition of the Andean basement and potential contaminant of Cenozoic arc magmas. It would be particularly interesting to see whether any xenoliths of the Grenville-aged basement, similar to those identified in the Precordillera (e.g., Abbruzzi et al., 1993; Kay and Orrell, 1996), are present in the Vacas Heladas Ignimbrites (Late Miocene, Frontal Cordillera). This would confirm the interaction of these magmas with the Grenville-aged basement and therefore support the under-thrusting of this basement terrane beneath the Frontal Cordillera.

- This study has demonstrated that boron concentrations and isotopic compositions obtained from melt inclusions present in arc magmatic rocks can be used to identify and infer changes in the geodynamic setting of a convergent plate margin. Specifically, the shallowing of the subducting slab

and in this particular case, the increase in fluids derived from hydrated and serpentinised oceanic lithosphere (a potential cause of slab shallowing). Flat-slab subduction currently occurs in other regions of the Andean margin and earlier periods of flat-slab subduction along the Andean margin have also been proposed (e.g., Ramos and Folguera, 2009 and references therein; O'Driscoll et al., 2012). A potential lead from this work would to be to analyse boron isotopic compositions and trace element concentrations of melt inclusions obtained for arc magmatic rocks from other regions and timeframes linked with development of flat-slab subduction, both along the Andean margin (e.g., the Peruvian flat slab segment) and elsewhere (e.g., Mexico and southern Alaska). Due to the across-arc variations in $\delta^{11}B$ values and boron concentrations as a function of depth to the slab-mantle interface (Ryan et al., 1995; Ishikawa and Tera, 1997; Rosner et al., 2003), and the distinct boron concentrations and compositions of different subducting reservoirs (outlined in Chapter 4), this has the potential to lead to increased understanding of the development and cause of earlier periods of flat-slab subduction.

6.4 References

Abbruzzi, J., Kay, S.M., and Bickford, M.E., 1993, Implications for the nature of the Precordilleran basement from the geochemistry and age of Precambrian xenoliths in Miocene volcanic rocks, San Juan province: Actas, v. 3, p. 331-339.

Aitcheson, S., Harmon, R., Moorbath, S., Schneider, A., Soler, P., Soria-Escalante, E., Steele, G., Swainbank, I., and Wörner, G., 1995, Pb isotopes define basement domains of the Altiplano, central Andes: Geology, v. 23, p. 555-558.

Cahill, T., and Isacks, B.L., 1992, Seismicty and Shape of the Subducted Nazca Plate: Journal of Geophysical Research, v. 97, p. 17,503 - 17,529.

Chan, L.-H., and Kastner, M., 2000, Lithium isotopic compositions of pore fluids and sediments in the Costa Rica subduction zone: implications for fluid processes and sediment contribution to the arc volcanoes: Earth and Planetary Science Letters, v. 183, p. 275-290.

Charlier, B.L.A., Ginibre, C., Morgan, D., Nowell, G.M., Pearson, D.G., Davidson, J.P., and Ottley, C.J., 2006, Methods for the microsampling and high-precision analysis of strontium and rubidium isotopes at single crystal scale for petrological and geochronological applications: Chemical Geology, v. 232, p. 114-133.

Charrier, R., Pinto, L., and Rodríguez, M.P., 2007, Tectonostratigraphic evolution of the Andean Orogen in Chile, *in* Moreno, T., and Gibbons, W., eds., The Geology of Chile: London, The Geological Society, p. 21 - 114.

Chaussidon, M., and Marty, B., 1995, Primitive Boron Isotope Composition of the Mantle: Science, v. 269, p. 383 - 386.

Davidson, J.P., Hora, J.M., Garrison, J.M., and Dungan, M.A., 2005, Crustal forensics in arc magmas: Journal of Volcanology and Geothermal Research, v. 140, p. 157 -170.

Davidson, J.P., Morgan, D.J., Charlier, B.L.A., Harlou, R., and Hora, J.M., 2007, Microsampling and Isotopic Analysis of Igneous Rocks: Implications for the Study of Magmatic Systems: Annual Review of Earth and Planetary Sciences, v. 35, p. 273-311.

Harley, S.L., and Kelly, N.M., 2007, Zircon Tiny but Timely: Elements, v. 3, p. 13-18.

Ishikawa, T., and Nakamura, E., 1993, Boron isotope systematics of marine sediments: Earth and Planetary Science Letters, v. 117, p. 567 - 580.

Ishikawa, T., and Tera, F., 1997, Source, composition and distribution of the fluid in the Kurile mantle wedge: Constraints from across-arc variations of B/Nb and B isotopes: Earth and Planetary Science Letters, v. 152, p. 123 - 138.

Kasemann, S., Erzinger, J., and Franz, G., 2000, Boron recycling in the continental crust of the central Andes from the Palaeozoic to Mesozoic, NW Argentina: Contributions to Mineralogy and Petrology, v. 140, p. 328 - 343.

Kay, S.M., and Orrell, S., 1996, Zircon and whole rock Nd-Pb isotopic evidence for a Grenville age and a Laurentian origin for the Basement of the Precordillera in Argentina: Journal of Geology, v. 104, p. 637.

Leveratto, M., 1976, Edad de intrusivos cenozoicos en la Precordillera de San Juan y su implicancia estratigráfica: Revista de la Asociación Geológica Argentina, v. 31, p. 53-58.

Litvak, V.D., Poma, S., and Kay, S.M., 2007, Paleogene and Neogene magmatism in the Valle del Cura region: New perspective on the evolution of the Pampean flat slab, San Juan province, Argentina: Journal of South American Earth Sciences, v. 24, p. 117 - 137.

Maksaev, V., and Zentilli, M., 1999, Fission track thermochronology of the Domeyko Cordillera, northern Chile; implications for Andean tectonics and porphyry copper metallogenesis: Exploration and Mining Geology, v. 8, p. 65 - 89.

Manea, V.C., Pérez-Gussinyé, M., and Manea, M., 2012, Chilean flat slab subduction controlled by overriding plate thickness and trench rollback: Geology, v. 40, p. 35-38.

Moriguti, T., and Nakamura, E., 1998, Across-arc variation of Li isotopes in lavas and implications for crust/mantle recycling at subduction zones: Earth and Planetary Science Letters, v. 163, p. 167-174.

O'Driscoll, L.J., Richards, M.A., and Humphreys, E.D., 2012, Nazca–South America interactions and the late Eocene–late Oligocene flat-slab episode in the central Andes: Tectonics, v. 31.

Oncken, O., Hindle, D., Kley, J., Elger, K., Victor, P., and Schemmann, K., 2006, Deformation of the central Andean upper plate system—Facts, fiction, and constraints for plateau models, The Andes, Springer, p. 3-27.

Ramos, V.A., and Folguera, A., 2009, Andean flat-slab subduction through time: Geological Society, London, Special Publications, v. 327, p. 31-54.

Rapela, C.W., Pankhurst, R.J., Casquet, C., Baldo, E., Galindo, C., Fanning, C.M., and Dahlquist, J.M., 2010, The Western Sierras Pampeanas: Protracted Grenville-age history (1330–1030 Ma) of intra-oceanic arcs, subduction–accretion at continental-edge and AMCG intraplate magmatism: Journal of South American Earth Sciences, v. 29, p. 105-127.

Rosner, M., Erzinger, J., Franz, G., and Trumbull, R.B., 2003, Slab-derived boron isotope signatures in arc volcanic rocks from the Central Andes and evidence from boron isotope fractination during progressive slab dehydration: Geochemistry Geophysics Geosystems, v. 4.

Ryan, J.G., Morris, J.D., Tera, F., Leeman, W.P., and Tsuetkov, A., 1995, Cross-arc geochemical variations in the Kurile arc as a function of slab depth: Science, v. 270, p. 625 - 627.

Sigmarsson, O., Condomines, M., Morris, J.D., and Harmon, R.S., 1990, Uranium and 10Be enrichments by fluids in Andean arc magmas: Nature, v. 346, p. 163-165.

Smith, H.J., Spivack, A.J., Staudigel, H., and Hart, S.R., 1995, The boron isotopic composition of altered oceanic crust: Chemical Geology, v. 126, p. 119 - 135.

Spivack, A.J., and Edmond, J.M., 1987, Boron isotope exchenge between seawater and the oceanic crust: Geochimica et Cosmochimica Acta, v. 51, p. 1033 - 1043.

Stern, C.R., 2011, Subduction erosion: rates, mechanisms, and its role in arc magmatism and the evolution of the continental crust and mantle: Gondwana Research, v. 20, p. 284-308.

Straub, S.M., and Layne, G.D., 2003, The systematics of chlorine, fluorine, and water in Izu arc front volcanic rocks: Implications for volatile recycling in subduction zones: Geochimica et Cosmochimica Acta, v. 67, p. 4179-4203.

Tonarini, S., Leeman, W.P., and Leat, P.T., 2011, Subduction erosion of forearc mantle wedge implicated in the genesis of the South Sandwich Island (SSI) arc: Evidence from boron isotope systematics: Earth and Planetary Science Letters, v. 301, p. 275-284.

Von Huene, R., and Scholl, D.W., 1991, Observations at convergent margins concerning sediment subduction, subduction erosion, and the growth of continental crust: Reviews of Geophysics, v. 29.

Winocur, D.A., Litvak, V.D., and Ramos, V.A., 2013, Magmatic and tectonic evolution of the Oligocene Valle del Cura basin, Main Andes of Argentina and Chile: Evidence for generalized extension, *in* Sepulveda, P., Giambiagi, L., Pinto, L., Moreiras, S., Tunik, M., Hoke, G., and M., F., eds., Geodynamic processes in the Andes of Central Chile and Argentina, Volume In press, Geological Society of London, Special Publication.

Wörner, G., Moorbath, S., and Harmon, R.S., 1992, Andean Cenozoic volcanic centers reflect basement isotopic domains: Geology, v. 20, p. 1103-1106.

Yañez, G.A., Cembrano, J., Pardo, M., Ranero, C.R., and Selles, D., 2002, The Challenger - Juan Fernández - Maipo major tectonic transition of the Nazca - Andean subduction system at 33-34ºS: geodynamic evidence and implications: Journal of South American Earth Sciences, v. 15, p. 28 - 38.

Yañez, G.A., Ranero, C.R., von Huene, R., and Díaz, J., 2001, Magnetic anomaly interpretation across the southern central Andes (32º-34ºS): The role of the Juan Fernández Ridge in the late Tertiary evolution of the margin: Journal of Geophysical Research, v. 106, p. 6325 - 6345.

Appendix 1

Appendix 1.1 U-Pb dating of zircon

1.1.1 Background information

U-Pb dating of zircons allows the precise measurement of crystallisation ages and is based on the radioactive decay of U and Th to stable isotopes of Pb. U occurs naturally as radiogenic isotopes ^{238}U, ^{235}U, and ^{234}U (^{234}U is the product of ^{238}U decay) and Th occurs primarily as one radioactive isotope, ^{232}Th. Pb occurs as three naturally occurring radiogenic isotopes ^{206}Pb, ^{207}Pb and ^{208}Pb, which form from U and Th decay, and one non-radiogenic isotope, ^{204}Pb. Concentrations of U and Th are very low in common rock forming minerals but high abundances can be present in certain accessory minerals, such as zircon. Once crystallised the U and Th radioactively decay over time into stable isotopes of Pb; ^{238}U decays to ^{206}Pb with a half-life of 4468 Myr, ^{235}U decays to ^{207}Pb with a half-life of 704 Myr, and ^{232}Th decays to ^{208}Pb with a half-life of 14.05 Gyr. Therefore, by measuring the concentrations of U, Th and Pb in zircon and determining the isotopic composition of the Pb, the age of the zircon can be calculated. Zircon is a common accessory mineral in many igneous rocks and is particularly suitable for U-Pb dating as it readily incorporates U and Th, but not Pb, as it crystallises and is both chemically and mechanically robust. The U-Th-Pb closure temperature is high (>900°C) and zircon has been shown to preserve original U and accumulated radiogenic Pb contents even through re-melting events (e.g., Davis et al. (2003), Ireland and Williams (2003)).

1.1.2 Sample preparation

In order to obtain zircon grains for U-Pb dating ~5 kg of each sample was broken down into ~6 cm square blocks and crushed using a tungsten carbide jaw crusher. The exact amount of each sample crushed depended upon the size of the sample and the number of zircons identified in thin section. The rock chips resulting from

crushing were then sieved to < 2mm, < 1mm and < 0.5 mm size fractions. Any rock chips larger than 2mm were reintroduced to the jaw crusher. In order to avoid the possibility of cross contamination all machinery, sieves and glassware were cleaned thoroughly before and after every sample. Zircons were then separated from the crushed and sieved samples using a number of mineral separation techniques.

1.1.3 Mineral separation of zircon

1.1.3.1 Density separation using a Gemini table

A Gemini table at the University of Glasgow was used to separate out minerals of different density from the crushed samples. Each sample was introduced to the Gemini table in turn. As water flowed over the ribbed surface of the table and the table shook, the high density minerals were trapped in the ribs and carried down to the far end of the table, while the low density minerals were washed off early. The minerals were then collected in different containers depending where they were washed off the table. The exact set up of the table varied depending on the quantity of the sample being separated. Once collected the different density separations were dried in a drying cupboard. Zircon appears in the high density (heavy) mineral fraction.

1.1.3.2 Magnetic separation

A strong hand magnet was then passed over each of the heavy mineral fractions in order to remove any magnetic minerals such as magnetite and any iron fillings that may have been picked up off the equipment. A Frantz magnetic separator was then used to further separate minerals according to their magnetic susceptibility. The Frantz was set up with a slope of 20° and a tilt of 20°. Each sample was then run though the Frantz in turn and the voltage was increased in a stepwise fashion to remove minerals with different magnetic susceptibilities. Non-metamict zircon is nonmagnetic at 1.5 amperes so occurs in the nonmagnetic fraction.

1.1.3.3 Heavy liquid separation

Lithium heteropolytungstate (LST), a heavy liquid with a normal operating density of 2.85g/cc, was used to separate out minerals of different densities from the nonmagnetic fraction. The LST was held in a separating funnel and the nonmagnetic fraction of each sample was poured into the LST in turn. The sample was stirred into the LST so that all the grains were 'wetted' and then left until the sink had settled out, with occasional stirring. The sink was then drained off onto a filter paper and the pure LST collected. The sink was then washed with distilled water and the washings containing LST collected separately. The float was then drained through a different filter paper and the pure LST collected. The float was also washed with distilled water and the washings containing LST collected. Both the sink and the float were then dried in a drying cupboard at ~40 °C. The pure LST was reused in further separations, while the diluted LST was filtered under vacuum and heated, in order to remove any water and restore the correct density. As zircon has a specific gravity ranging between 4.6 and 4.7 it appears in the sink. If necessary, the sink was run though the Frantz magnetic separator again in order to remove any magnetic minerals which may have not been separated on the previous occasion.

1.1.4 Zircon mounting and imaging

Zircons were successfully separated from 42 samples and individual zircon grains (approximately 40 zircon grains per sample) were hand-picked under a binocular microscope and mounted in epoxy resin accompanied by zircon Geostandards 91500 or GJ-1. The epoxy mounts were then ground and polished to expose the interior of the zircons at the surface. Prior to analysis individual zircon grains were imaged and characterised, using a Philips XL30CP Scanning Electron Microscope (SEM) at the University of Edinburgh, in order to determine the presence or absence of multiple growth phases, xenocrystic cores, inclusions and cracks. Imaging was carried out in both secondary electron (SE) and backscatter electron (BSE) modes, and suitable, representative zircons and specific locations for analysis were identified. Cathodoluminesence (CL) imaging was not carried out prior to analysis

in order to limit the burning of the epoxy mount surface and the creation of topography on the surface of the grain mounts. Subsequent to analysis all analysed zircons were imaged on a SEM in both CL and SE modes to check the exact position of analysis, and to ensure the absence of cracks and inclusions at the bottom of the analysis pits.

1.1.5 Analytical conditions

U-Th-Pb analysis of zircons was performed on a Cameca ims 1270 secondary ion mass spectrometer (SIMS) at the NERC Edinburgh Ion Microprobe Facility (EIMF), University of Edinburgh between 28th August - 2nd September 2011 and 13th – 17th February 2012.

Prior to SIMS analysis the epoxy grain mounts were ultrasonically cleaned in petroleum spirit and Au-coated to create a uniform surface for analysis and to prevent the sample from charging during analysis. The zircons were analysed using a ~4nA O_2^- primary ion source with a 22.5keV net impact energy. The beam was focused using Köhler illumination to ensure a uniform beam density. The primary beam alignment resulted in ellipsoidal analysis pits with a maximum diameter of ~25 μm. In order to limit peripheral contamination the spatial resolution of the analysed area was limited further by the use of a field aperture, which restricts the secondary ion signal to the centre of the analysis pit. The instrument was operated in 'rectangular mode' in order to maintain optimum conditions for flat topped peaks.

U, Th and Pb were analysed at a mass resolution of >4000R using a peak switching routine. The HfO peak was used for energy centring on each analysis and a 60eV energy window was used throughout. Secondary ion intensities were measured using an electron multiplier in ion counting mode. Pre-rastering was carried out for 120 seconds over an area of ~40 μm in order to remove any surface contamination (e.g., ^{204}Pb). The surface of the sample was also flooded with O_2 to enhance the

yields of Pb (Schuhmacher et al., 1993). Twenty cycles of analysis were then made over the following masses of interest; ^{196}(HfO), ^{204}Pb, $^{204.3}$background, ^{206}Pb, ^{207}Pb, ^{208}Pb, ^{212}(Zr_2O_2), ^{238}U, ^{248}(ThO), ^{254}(UO), and ^{270}(UO_2). Mass 204.3 was measured to check for background counts. Each analysis lasted 27 minutes in total.

1.1.6 Data collection

A total of 313 *in-situ* U-Th-Pb analyses were made on unknown zircons, by SIMS, from 42 samples over 9 analytical sessions (a separate session is counted as a period in which no changes to the instrument have been made). In most cases at least 8 analyses of unknown zircons were made per sample. In a number of samples there were <8 suitable zircons for analysis in which case as many analyses as possible were made. Multiple analyses (core and rim) were made on selected zircon grains in order to obtain information on growth history and inheritance.

The U/Pb ratios were calibrated against measurements of zircon Geostandards 91500 (~1062.5 Ma and assumed ^{206}Pb/^{238}U ratio = 0.17918 (Wiedenbeck et al., 1995)) and GJ-1 (~608.5Ma and assumed ^{206}Pb/^{238}U ratio = 0.09761 (Jackson et al., 2004)). Analyses of these standards were made after every 4 unknown zircons throughout the analytical sessions. When GJ-1 was used as the primary standard, Geostandard 91500 was run on a separate mount to establish approximate U and Hf concentrations. Internal standard 'Laura' was also run as a secondary standard to demonstrate low background of common lead on a young, low U, sample. Phalabora baddelyite was run as a check on the absolute mass fractionation of lead and the dead time corrections.

1.1.7 Data correction and reduction

Data obtained from the Cameca ims 1270 has been corrected and reduced using an in-house spreadsheet developed by R. Hinton. Initially, data from the first 5 cycles through the masses is excluded. Raw counting data from the remaining 15 cycles is

then corrected for instrumental drift, dead time on the electron multiplier (51 nsec) and detector background (0.008 - 0.016 counts per second). The standard deviation of the Pb/U ratios is then calculated and any single cycles with a variation in the measured Pb/U ratio greater than 2σ are also excluded.

1.1.7.1 Calibration of Pb/U ratios

In SIMS analysis the inter-element isotope ratios, such as Pb/U, are determined directly from the measured secondary ion ratios of the different isotopes. Due to different elements having different secondary ionisation efficiencies and different propensities to form multiple oxides, a calibration is used to correct for these effects. The procedure used here is a variant of the procedures employed by other Cameca ims 1270 and SHRIMP laboratories. Numerous studies have based corrections on the observed relationship between Pb/U and ratios of UO/U (e.g., Compston et al., 1984; Williams and Claesson, 1987; Schuhmacher et al., 1993; Claoué-Long et al., 1995; Whitehouse et al., 1997). Conventionally the relationships ln(Pb/U) vs. ln(UO/U) or ln(Pb/U) vs. ln(UO_2/U) have been used. However, on the Cameca ims 1270 ion microprobe at the University of Edinburgh, the relationship ln(Pb/U) vs. ln(UO_2/UO) has been found to give better within-session reproducibility, therefore, the following data correction equation has been applied:

$$(Pb/U)_{corrected} = (Pb/U)_{measured} / [\ln(UO_2/UO\ measured)]^{2.6}$$

For each session the corrected average Pb/U ratio for the main standard (91500 or GJ-1) is calculated and then all other U/Pb ratios are scaled to this value.

1.1.7.2 Correction for common Pb

Although most magmatic zircon incorporates very little Pb at the time of crystallisation common Pb could be incorporated into zircon from a number of sources, including; Pb trapped in micro-fractures, Pb present in mineral inclusions, Pb added to zircon due to alteration, and Pb from laboratory preparation methods

(e.g. polishing). Therefore, in order to obtain an accurate crystallisation age, a correction needs to be applied to account for the presence of common Pb in zircon. This is particularly important when dealing with young zircons, which are likely to have low concentrations of radiogenic Pb.

For very young zircons (<100 Ma) corrections for common Pb based on the measured ^{204}Pb can lead to large counting errors; even single counts measured on ^{204}Pb may give significant changes to the calculated age. Therefore, a correction based on the measured $^{207}Pb/^{206}Pb$ ratios has been applied to young zircons with <0.2 ppm ^{207}Pb to give a corrected $^{206}Pb/^{238}U$ age. For zircons with higher concentrations of radiogenic Pb (>0.2 ppm ^{207}Pb) common Pb corrections have been made on the basis of their measured ^{204}Pb counts, above that of detector background (0.008 - 0.016 cps). All corrections assume a modern day composition of common Pb.

1.1.7.3 Correction for ^{230}Th disequilibrium

Disequilibrium of the U decay series caused by initial ^{230}Th has been found to effect young U-Pb ages (Schärer, 1984). In zircon this is due to a deficit of ^{206}Pb caused by a deficiency of initial ^{230}Th, resulting from the fractionation of U and Th between the crystallising zircon and the melt. Therefore the following correction, proposed by Schärer (1984), has been applied:

$$^{206}Pb = {}^{238}U[(e^{\lambda 238T} - 1) + (\lambda_{238}/\lambda_{230})*(f - 1)]$$

Where; ^{206}Pb is the total amount of measured ^{206}Pb; ^{238}U is the total amount of measured ^{238}U; λ of $^{238}U = 1.55125 \times 10^{-10}$ y^{-1} and λ of $^{230}Th = 0.922 \times 10^{-5}$ y^{-1}; and T is the real crystallisation age of the zircon. The value for f is given by:

$$f = (Th/U)_{zircon} / (Th/U)_{magma}$$

Where $(Th/U)_{magma}$ = 4.42, based on the average whole rock Th/U ratios (from 19 samples) and $(Th/U)_{zircon}$ = 0.62, based on the average Th/U obtained from all unknown zircon analyses. This gives an *f* value of 0.14, which is similar to that obtained by Schärer (1984).

1.1.8 Calculation of Th/U and elemental abundances

Th/U ratios of the unknowns were calculated using measurements of Th/U and $^{208}Pb/^{206}Pb$ on the standards. Elemental concentrations of the unknowns were determined on the basis of the observed oxide ratios of the standards. U concentrations were determined based on the observed UO_2/Zr_2O_2 (assuming a U content of 81 ppm for 91500 and 269 ppm for GJ-1). Pb and Th concentrations were then calculated relative to the U concentration. Hf concentrations were determined based on the HfO/Zr_2O_2 ratio (assuming a Hf content of 5880 ppm for 91500 and 7410 ppm for GJ-1).

1.1.9 Data processing

Subsequent to SIMS analysis all the analysed zircons were imaged on an SEM in both cathodoluminescence (CL) and secondary electron (SE) modes to check the exact position of analysis, and to ensure the absence of cracks and inclusions at the bottom of the analysis pits. Data was rejected from any problematic analysis locations (e.g., cracks identified). Data was also rejected from zircon grains showing high common Pb concentrations and those containing >3000 ppm U, as metamict zircons may give false age information. Any analyses which encountered analytical problems (e.g., primary beam drop) were also rejected. The analysis of old oxygen pits often produced high values of common Pb and generally produced lower $^{206}Pb/^{238}U$ ages. On this basis all analyses conducted on old oxygen pits were rejected (Appendix 1.10).

Plots and age calculations have been made using computer program ISOPLOT v3.7 (Ludwig, 2008). To obtain overall U-Pb ages for the Late Cretaceous – Late Miocene samples the data have been plotted on Tera-Wasserburg plots, where the U-Pb data is uncorrected for common Pb and the mixing line is anchored to the $^{207}Pb/^{206}Pb$ ratio for modern day common Pb (0.84). The overall sample ages are given by the intercept on the Tera-Wasserburg plot and uncertainties are quoted at the 2σ or 95% confidence level (Appendix 1.11). The overall U-Pb ages for the samples of the Permian – Triassic basement are Concordia ages or intercept ages with uncertainties quoted at the 2σ or 95% confidence level (Appendix 1.11). Ages for individual zircon grains are presented as $^{206}Pb/^{238}U$ ages with uncertainties quoted at the 1σ level (Appendix 1.10).

Appendix 1.2 Whole rock major, trace and rare-earth element analysis

Major, trace and rare-earth element analysis was conducted via X-ray Fluorescence Spectrometry (XRF) and inductively-coupled plasma mass spectrometry (ICP-MS).

1.2.1 Sample preparation

The samples were assessed prior to analysis to ensure limited alteration by hydrothermal fluids and/or weathering. For major, trace and rare earth element analysis sample blocks weighing ~50g (the exact size was dependent on grain size) were cleaned and trimmed of any weathered surfaces, veins and xenoliths (which could introduce contamination), using a diamond encrusted clipper saw. These blocks were then crushed into chips using a tungsten carbide jaw crusher. In order to minimise the effects of alteration and contamination chips were checked to ensure they contained no signs of alteration, veins, xenocrystic and xenolithic material. The chips were then powered in a tungsten carbide TEMA mill to obtain fine, homogeneous powders for analysis by XRF and ICP-MS. All areas of the machinery were cleaned with water and acetone before and after each sample to avoid the possibility of cross contamination.

1.2.2 Sample preparation for XRF analysis

For major and minor element analysis the sample powders were dried in an oven at ~110 °C for ~2 hours. Once dried, a nominal amount of between 0.9g and 1.0g (+/- 0.05g) of sample was weighed into a Pt5%Au crucible and ignited in a muffle furnace at 1100 °C for 20 minutes to determine the mass loss on ignition (LOI). A lithium borate/carbonate flux (Johnson Matthey Spectroflux™ 105), containing La_2O_3 as a heavy absorber, was then added at a sample:flux ratio of 1:5 (based on the unignited sample mass) and mixed with the sample. This was then fused at 1100 °C for 20 minutes and allowed to cool. After this initial fusion the crucible was

reweighed and, if necessary, further flux was added to make up for any flux weight loss. The samples were then fused for a second time over a Bunsen burner and swirled several times to ensure homogeneity of the molten material. The molten material was then immediately cast into a graphite mould, annealed at approximately 250 °C for ten minutes, and then allowed to cool before being trimmed and stored in a desiccator prior to analysis.

For trace element analysis, 8g (+/- 0.1g) of sample powder was mixed thoroughly with eight drops of a 2 % aqueous solution of polyvinyl alcohol, which acts as a binding agent. The mixture was then loaded into a 40mm diameter aluminium cup and compressed against a polished tungsten carbide disc, in a hydraulic press, at 0.6 tons/cm^2 for 2 minutes.

1.2.3 XRF analysis

The fused glass discs and pressed powder pellets were analysed for major oxide and trace element concentrations on a Philips PW2404 wavelength-dispersive sequential X-ray spectrometer with a 4 kW Rh-anode end-window X-ray tube in the School of GeoSciences, University of Edinburgh. The analytical conditions used were similar to those outlined in Fitton et al. (1998) and Fitton and Godard (2004). Long count times were used at both peak and background positions. Trace element background positions were placed as close as possible to peaks. For most trace element determinations, background count rates were measured on either side of the peak, with the count time divided evenly between the two positions. Corrections for matrix effects on the intensities of major element lines were made using theoretical alpha coefficients calculated using the Philips software. The coefficients were calculated to allow for the additional flux replacing volatile components in the sample, such that the analytical totals should be 100% less the measured LOI. Matrix corrections were applied to the intensities of the longer wavelength trace element lines (La, Ce, Nd, Zn, Cu, Ni, Co, Cr, V, Ba and Sc) using alpha coefficients based on

major element concentrations measured at the same time on the pressed powder samples. The intensities of the remaining trace elements were corrected for matrix effects by using the count rate from the RhKα Compton scatter line as an internal standard (Reynolds, 1963). Line overlap corrections were applied using synthetic standards.

The spectrometer was calibrated with USGS and CRPG reference standards using the values given by Govindaraju (1994). The analytical precision and accuracy are comparable to the values reported by Fitton, et al. (1998) and Fitton and Godard (2004). A number of USGS geostandards were analysed alongside the Andean samples and used to assess accuracy and precision (Tables A1.1 and A1.2). The LOI values range between 0.34 and 6.02 with an average of 1.54. Major element oxide totals are all within ±0.9% of 100% and have been recalculated to a 100% volatile free basis.

	Edinburgh Average (2004-2011)	1σ	%P	Edinburgh Average (2009 - 2012)	Published values	Accuracy (% difference) (2009 - 2012)
SiO_2 (wt.%)	50.23	0.40	0.8	50.244	49.94	0.6
Al_2O_3	13.69	0.17	1.2	13.752	13.80	0.3
Fe_2O_3	12.37	0.06	0.5	12.343	12.23	0.9
MgO	7.18	0.09	1.3	7.186	7.23	0.6
CaO	11.45	0.11	0.9	11.408	11.40	0.1
Na_2O	2.47	0.27	10.8	2.339	2.26	3.5
K_2O	0.527	0.006	1.2	0.528	0.520	1.5
TiO_2	2.726	0.021	0.8	2.718	2.710	0.3
MnO	0.170	0.003	1.9	0.173	0.168	3.0
P_2O_5	0.292	0.016	5.6	0.288	0.273	5.5
n	*136*			*26*		

Table A1.1. Accuracy and precision estimates for major element concentrations (wt.%) determined by XRF analysis, based on the repeated analysis of standard BHVO-1 (basalt) at the School of Geosciences, University of Edinburgh. The average values obtained between 2004 and 2011, and 2009 and 2012 (i.e. during this study), are given. 1σ represents the standard deviation of the repeat analyses and %P is the percentage precision at the 1σ level. Accuracy is expressed as the percentage difference between the measured and the published values. The published values are those of Govindaraju (1994).

	BCR-1					BEN				
	Average measured	1σ	%P	Published values	Accuracy % difference	Average measured	1σ	%P	Published values	Accuracy % difference
La (ppm)	25.5	1.9	7.5	24.9	2.5	87.8	1.2	1.3	82.0	7.1
Ce	55.6	1.2	2.2	53.7	3.5	155.8	0.7	0.4	152.0	2.5
Rb	48.0	0.3	0.6	47.2	1.7	47.5	0.1	0.1	47.0	1.0
Ba	682.7	2.0	0.3	681	0.2	1021.4	6.6	0.6	1025.0	0.4
U	2.5	0.2	9.4	1.8	37.0	2.9	0.3	10.4	2.4	22.2
Th	6.8	0.5	7.8	5.98	13.7	12.2	0.6	4.6	10.4	17.3
Pb	14.0	0.2	1.1	13.6	2.7	4.3	0.2	4.0	4.0	7.5
Nb	12.9	0.1	0.4	14	8.1	117.5	0.3	0.2	105.0	11.9
Sr	336.0	1.6	0.5	330	1.8	1382.8	7.2	0.5	1370.0	0.9
Zr	193.4	0.3	0.1	190	1.8	271.7	1.2	0.4	260.0	4.5
Y	38.5	0.1	0.2	38	1.2	30.0	0.2	0.5	30.0	0.0
Zn	127.8	0.9	0.7	129.5	1.3	132.8	0.8	0.6	120.0	10.7
Cu	17.9	0.6	3.1	19	5.8	74.4	0.9	1.2	72.0	3.3
Sc	34.1	0.3	0.7	32.6	4.7	23.0	0.2	0.9	-	-
V	400.4	1.6	0.4	407	1.6	242.9	1.9	0.8	235.0	3.3
Cr	18.7	0.3	1.7	16	17.1	369.6	0.8	0.2	360.0	2.7
Ni	14.7	0.8	5.2	13	13.3	276.4	0.2	0.1	267.0	3.5
Nd	30.1	1.2	4.0	28.8	4.6	68.0	0.4	0.5	67.0	1.4
n	*3*					*3*				
	BHVO-1					**RGM-1**				
	Average measured	1σ	%P	Published values	Accuracy % difference	Average measured	1σ	%P	Published values	Accuracy % difference
La (ppm)	11.7	1.3	11.3	15.8	25.9	24.7	0.5	2.1	24.0	2.9
Ce	39.2	1.4	3.5	39	0.6	47.9	1.1	2.2	47.0	1.8
Rb	9.5	0.1	0.6	11	13.9	142.9	0.2	0.1	149.0	4.1
Ba	133.0	0.7	0.5	139	4.3	768.2	4.7	0.6	807.0	4.8
U	0.8	0.1	12.5	0.4	100.0	5.9	0.1	1.7	5.8	1.7
Th	0.1	0.2	173.2	1.08	90.7	14.2	0.1	0.7	15.1	6.0
Pb	2.2	0.2	7.9	2.6	15.4	22.2	0.3	1.4	24.0	7.5
Nb	19.4	0.1	0.3	19.8	1.9	9.4	0.1	0.6	8.9	6.0
Sr	393.7	0.6	0.1	403	2.3	101.2	0.4	0.3	108.0	6.3
Zr	174.6	0.3	0.2	182	4.1	224.5	0.3	0.1	219.0	2.5
Y	27.4	0.3	0.9	27.6	0.6	24.8	0.2	0.7	25.0	0.8
Zn	105.4	0.6	0.6	105	0.3	25.7	0.9	3.6	32.0	19.8
Cu	131.9	0.5	0.3	136	3.0	11.3	0.8	6.9	11.6	3.0
Sc	35.1	0.3	0.9	31.8	10.3	34.3	0.2	0.6	-	-
V	305.8	1.7	0.6	317	3.5	11.7	1.0	8.5	13.0	10.0
Cr	284.6	0.9	0.3	289	1.5	3.4	0.8	23.2	3.7	9.5
Ni	117.5	0.6	0.5	121	2.9	3.4	0.2	6.3	4.4	23.9
Nd	26.5	0.6	2.1	25.2	5.0	19.5	0.4	2.1	19.0	2.6
n	*3*					*3*				

Table A1.2. Accuracy and precision estimates for trace element concentrations (ppm) determined by XRF analysis at the University of Edinburgh, based on the repeated analysis of standards BCR-1 (basalt), BEN (basalt), BHVO-1 (basalt) and RGM-1 (rhyolite powder). 1σ represents the standard deviation and %P is the percentage precision at the 1σ level. Accuracy is expressed as the percentage

difference between the measured and the published values. The published values are those of Govindaraju (1994). Note that the low values of precision and accuracy obtained for certain elements in certain standards (e.g., U and Th in BHVO-1) are related to the low concentrations of these elements in these standards, which are close to the detection limit. Hence a range of standards with different compositions were analysed.

Sample name	CD09	CD09 DUP1	CD09 DUP2	CD09 DUP3	CD09 DUP4	CD09 Mean	1σ	%P
SiO_2 (wt.%)	63.24	63.34	63.18	63.43	63.09	63.26	0.13	0.2
Al_2O_3	16.06	16.09	16.04	16.16	16.02	16.07	0.05	0.3
Fe_2O_3	6.12	6.14	6.14	6.13	6.14	6.13	0.01	0.1
MgO	1.79	1.76	1.77	1.76	1.78	1.77	0.01	0.7
CaO	2.42	2.42	2.41	2.42	2.40	2.41	0.01	0.4
Na_2O	5.69	5.71	5.76	5.74	5.72	5.72	0.03	0.5
K2O	2.03	2.05	2.04	2.04	2.03	2.04	0.01	0.3
TiO_2	0.86	0.86	0.86	0.86	0.86	0.86	0.00	0.1
MnO	0.10	0.10	0.10	0.10	0.10	0.10	0.00	1.1
P_2O_5	0.28	0.28	0.29	0.29	0.29	0.28	0.00	1.1
LOI	0.76	0.54	0.51	0.54	0.65	0.60	0.10	17.0
Total Majors (%)	99.35	99.29	99.10	99.46	99.08	99.25	0.17	0.2
Zn (ppm)	60.0	59.2	59.3	59.7	60.4	59.7	0.5	0.8
Cu (ppm)	9.5	9.8	9.8	10.1	9.8	9.8	0.2	2.2
Ni (ppm)	2.3	1.8	1.8	4.1	3.6	2.7	1.1	39.2
V (ppm)	48.2	49.1	50.9	51.0	50.2	49.9	1.2	2.4
Ba (ppm)	533.6	536.5	533.7	536.0	540.0	536.0	2.6	0.5
Sc (ppm)	12.5	12.5	13.1	13.5	13.4	13.0	0.5	3.7
Nb (ppm)	13.5	13.5	13.5	13.5	13.4	13.5	0.0	0.3
Zr (ppm)	245.3	244.9	244.7	244.7	244.9	244.9	0.2	0.1
Y (ppm)	31.9	31.8	31.7	31.8	32.0	31.8	0.1	0.4
Sr (ppm)	144.9	145.5	145.3	145.5	145.0	145.2	0.3	0.2
Rb (ppm)	79.9	80.0	79.8	79.6	79.4	79.7	0.2	0.3
U(ppm)	5.1	5.1	5.0	5.1	5.0	5.1	0.1	1.1
Th (ppm)	19.8	19.8	19.9	19.8	20.0	19.9	0.1	0.5
Pb (ppm)	13.6	13.4	13.4	13.5	13.3	13.4	0.1	0.8
La (ppm)	61.7	63.2	61.6	60.5	60.4	61.5	1.1	1.8
Ce (ppm)	113.5	115.5	113.8	114.2	114.2	114.2	0.8	0.7
Nd (ppm)	41.4	43.3	41.0	43.9	42.1	42.3	1.2	2.9
Total Traces	1436.7	1444.9	1438.3	1446.5	1447.1	1442.7	4.8	0.3
Total Majors + Traces	99.5	99.4	99.2	99.6	99.2	99.4	0.2	0.2

Table A1.3. Analyses of 5 aliquots of a felsic volcanic rock (CD09) prepared separately in order to constrain the variability induced by sample preparation, in addition to the analytical uncertainty involved with the XRF analysis. 1σ is the

standard deviation of the measurements and %P is the percentage precision at the 1σ level. The LOI (loss on ignition) values are determined during sample preparation and not directly measured during XRF analysis. Data courtesy of Alex de Joux.

1.2.4 Sample preparation for ICP-MS analysis

A subgroup of 39 samples analysed for major oxide and trace element concentrations, representing each of the major volcanic and plutonic formations, were selected for rare earth element (REE) analysis via ICP-MS. Select samples were also analysed for U, Th, Pb and Hf concentrations. Analysis was carried out on an Agilent 7500ce ICP-MS at the Scottish Universities Environmental Research Centre (SUERC), East Kilbride.

Samples were prepared for ICP-MS analysis using a tri-acid digestion procedure similar to that described by Olive et al. (2001). Between 0.095 and 0.105g of each sample powder was weighed out into separate, clean 15ml PFA Teflon screw capped beakers. To this was added 0.5 ml of 50% nitric acid (HNO_3) and 5ml of hydrofluoric acid (HF). The beakers were covered and placed on a hotplate at 100 °C for 24 hours in order to allow the acids to break down the silicate lattice. After 24 hours the lids were removed from the beakers and the samples were left on the hotplate to dry out. Once dry, 2ml of HNO_3 was added to each sample beaker, again the beakers were covered and placed on the hotplate at 100 °C. After 24 hours the lids were removed and the samples were left on the hotplate to dry out. Once dry, 1ml of HCl was added to each sample beaker, the beakers were covered and placed on the hotplate at 100 °C. After 24 hours the lids were removed from the beakers and the samples were left on the hotplate until very nearly dry, then ~3ml of 5% HNO_3 was added to dissolve the sample again. The solutions were checked to ensure all the sample had dissolved and were then transferred to 100 ml volumetric flasks. The beakers were thoroughly rinsed out with 5% HNO_3 and the volumetric flasks were filled with 5% HNO_3, gently shaken and allowed to stand overnight. The solutions were then transferred into pre-rinsed polythene bottles which were sealed

for storage. At this stage the samples were at a 1:1000 dilution. Standard reference solutions (BCR-1, BCR-2 and GSP-1) and procedural blank solutions were also prepared alongside the sample solutions using the same method.

1.2.5 ICP-MS analysis

The solutions were analysed on an Agilent 7500ce ICP-MS at SUERC. The acquisition parameters are presented in Table A1.4.

Sample uptake rate	0.1 ml min^{-1}
Washout time	180s
Uptake time	60 s
Internal standards	^{102}Ru, ^{115}In, ^{185}Re or ^{209}Bi
Data acquisition mode	Peak jumping
Number of replicate	25
Points per peak	3
No. of replicates	3

Table A1.4. ICP-MS acquisition parameters

For REE analysis the instrument was calibrated using an internal standard 'α' solution (a mixture of the fourteen REEs and Ba (Olive et al., 2001)). Prior to each analysis run the 'α' solution at dilutions of 1:1, 1:4 and 1:9 with 5% HNO_3, was used to construct a calibration curve. Calibrations were accepted for correlation coefficients (r) >0.99. Additional elements U, Th, Hf and Pb were analysed for select samples in a separate run using a different internal standard calibration solution.

In, Ru and Re were used as internal standards for the REE analysis and Bi for the analysis of U, Th, Hf and Pb. These internal standards allow any variations in sensitivity to be monitored and corrected throughout the analytical run. The ICP-MS was flushed with dilute HNO_3 between each analysis. A standard solution (BCR-1, BCR-2 or GSP-1) was analysed after every two sample solutions. BCR-1 was

normalised to agree with the published values (Govindaraju, 1994) and the resulting correction factor was applied to all the analyses, including those of standards BCR-2 and GSP-1. Analyses of secondary standards BCR-2 and GSP-1 have been used to evaluate analytical precision and accuracy (Table A1.5).

	BCR-2					GSP-1				
	Average measured	1σ	% P	Published Values	Accuracy % difference	Average measured	1σ	% P	Published Values	Accuracy % difference
La (ppm)	25.00	0.35	1.4	24.9	0.4	162.63	1.20	0.7	184.00	11.6
Ce	53.36	0.99	1.9	52.9	0.9	372.52	2.76	0.7	399.00	6.6
Pr	6.81	0.10	1.5	6.7	1.6	48.23	0.33	0.7	52.00	7.3
Nd	28.71	0.42	1.5	28.7	0.0	179.69	1.55	0.9	196.00	8.3
Sm	6.54	0.12	1.8	6.58	0.6	22.98	0.22	1.0	26.30	12.6
Eu	1.93	0.03	1.6	1.96	1.3	2.09	0.02	0.9	2.33	10.5
Gd	6.54	0.26	3.9	6.75	3.1	13.25	0.14	1.0	12.10	9.5
Tb	1.04	0.03	2.5	1.07	3.2	1.29	0.01	1.1	1.34	4.0
Dy	6.27	0.12	2.0	6.41	2.2	5.16	0.00	0.1	5.50	6.1
Ho	1.25	0.02	1.7	1.28	2.4	0.83	0.02	2.1	1.01	17.7
Er	3.61	0.09	2.6	3.66	1.3	2.04	0.00	0.1	2.70	24.4
Tm	0.55	0.01	1.6	0.54	2.7	0.25	0.00	1.1	0.38	33.4
Yb	3.37	0.06	1.7	3.38	0.4	1.31	0.02	1.7	1.70	23.1
Lu	0.50	0.01	2.6	0.50	0.0	0.16	0.00	0.4	0.21	23.0
n	*9*					*2*				
Hf	5.12	0.06	1.2	4.9	4.4					
Pb	14.40	1.05	7.3	11	30.9					
Th	6.10	0.05	0.8	5.7	7.0					
U	1.78	0.01	0.8	1.69	5.5					
n	*7*									

Table A1.5. Accuracy and precision estimates for trace and rare earth element concentrations (ppm) based on the repeated measurement of USGS international standards, BCR-2 (basalt) and GSP-1 (granite), by ICP-MS at the Scottish Universities Environmental Research Centre (SUERC), East Kilbride. 1σ represents the standard deviation of the standard measurements and % P is the percentage precision at the 1σ level. Accuracy is expressed as the percentage difference between the measured and the published values. The published values are those of Govindaraju (1994) for BCR-2 and Jochum and Nohl (2008) for GSP-1. Note that the apparent low values of accuracy obtained for certain elements (e.g., Lu, Yb, Tm) in GSP-1 is likely to partially reflect the low concentrations of these elements in this standard, as well as the low number of repeat measurements made on GSP-1 (i.e. 2).

1.2.6 Comparison and evaluation of trace element and rare-earth element concentrations obtained by XRF and ICP-MS

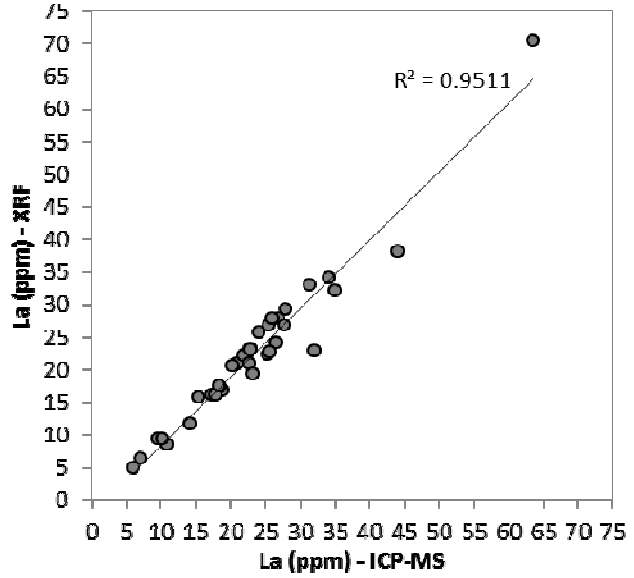

Figure A1.1. La concentration (ppm) determined by XRF analysis plotted against La concentrations (ppm) determined by ICP-MS analysis for the same sample powders. This highlights a good correlation between the two analytical techniques.

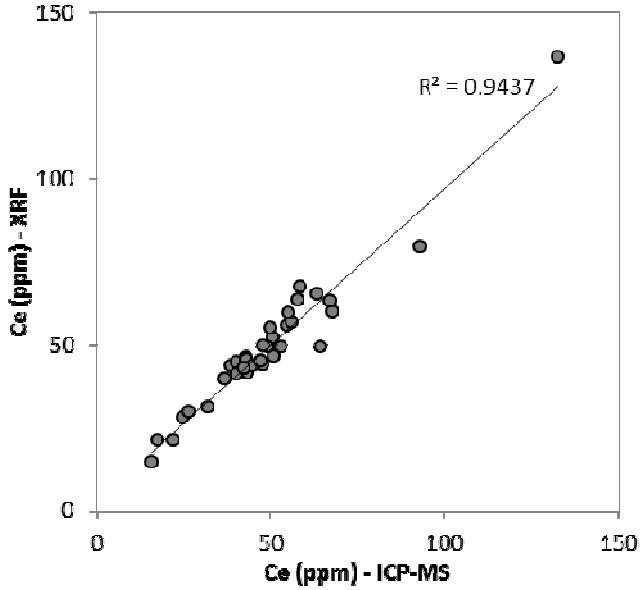

Figure A1.2. Ce concentration (ppm) determined by XRF analysis plotted against Ce concentrations (ppm) determined by ICP-MS analysis for the same sample powders. This highlights a good correlation between the two analytical techniques.

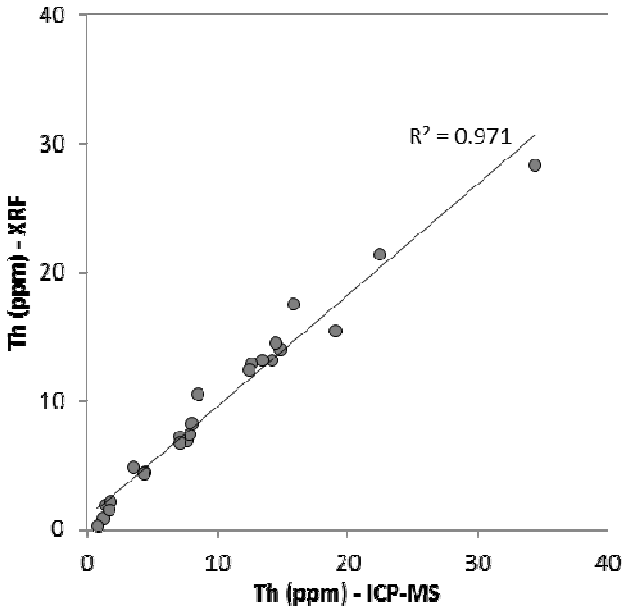

Figure A1.3. Th concentration (ppm) determined by XRF analysis plotted against Th concentrations (ppm) determined by ICP-MS analysis for the same sample powders. This highlights a good correlation between the two analytical techniques.

Appendix 1.3 Mineral analysis

Mineral analyses were conducted using the CAMECA SX100 electron microprobe (EMPA) at the School of GeoSciences, University of Edinburgh. Concentrations of major and minor elements in pyroxene, amphibole and plagioclase phenocrysts were analysed in polished thin sections and mineral grain mounts. These were ultrasonically cleaned in petroleum spirit and DI water, and carbon coated prior to analysis.

Analyses were performed over 3 analytical sessions in February 2010, August 2012 and March 2013 (analytical sessions indicated in Appendices 1.7, 1.8 and 1.9). A range of standards were used to calibrate the spectrometers; jadeite for Na, spinel for Mg and Al, wollastonite for Si and Ca, orthoclase for K, synthetic fayalite for Fe, rutile for Ti, Durango apatite for P, $RbMnF_3$ for F, and pure metals for Mn, Cr and Ni. Repeat analyses were also made on various mineral standards throughout the analytical sessions in order to assess the instrumental accuracy and precision. In all analytical sessions Na and K were always analysed first to minimise the effect of volatisation and for all elements the Kα line was measured. Internal data reduction was carried out on Cameca's PeakSight software. In order to maintain data quality analysis totals outside the range of 99 and 101 wt.% for plagioclase and pyroxene and corrected totals outside the range 98.5 and 101.5 wt.% for amphibole were discarded.

In sessions 1 and 2, analyses of pyroxenes, plagioclase feldspars and amphiboles were made using an accelerating voltage of 15 kV and a defocused beam of 8 μm. For each analysis two different beam currents were used; condition 1 used a beam current of 10 nA and was used to detect the most abundant elements; condition 2 used a beam current of 100 nA and was used to detect elements in lower abundances. Precision estimates based on the repeat analysis of internal standards are given in Table A1.6.

	Block 7 - K-feldspar			Published	Accuracy	Block 8 - cpx			Published	Accuracy
	Average	1σ	%P	values	% difference	Average	1σ	%P	values	% difference
SiO_2	64.87	0.73	1.1	64.99	0.2	50.59	0.53	1.0	50.72	0.2
Al_2O_3	17.98	0.21	1.2	17.97	0.1	0.62	0.01	1.9	0.59	5.1
Na_2O	1.10	0.06	5.7	1.08	1.9	0.71	0.03	3.6	0.73	3.1
K_2O	15.16	0.17	1.1	15.36	1.3	n.d.	-	-	-	-
CaO	0.02	0.002	9.6	-	-	22.98	0.20	0.9	22.80	0.8
SrO	0.05	0.01	21.2	-	-	-	-	-	-	-
TiO_2	n.d.	-	-	-	-	n.d.	-	-	-	-
FeO	0.47	0.01	1.9	0.48	2.5	16.74	0.17	1.0	16.75	0.0
MnO	n.d.	-	-	-	-	0.49	0.01	2.2	0.53	7.6
NiO	n.d.	-	-	-	-	n.d.	-	-	-	-
MgO	n.d.	-	-	-	-	8.01	0.08	1.1	8.02	0.2
BaO	0.11	0.02	15.5	-	-	n.d.	-	-	-	-
F	-	-	-	-	-	0.02	0.01	64.5	-	-
Total	99.8	1.0				100.2	0.8			
n	*26*					*25*				

Table A1.6. Accuracy and precision estimates for major and minor element concentrations (wt.%) measured on internal standards by electron microprobe at the University of Edinburgh during sessions 1 and 2. 1σ is the standard deviation of the repeat analyses and %P is the percentage precision. Accuracy is expressed as a percentage difference between the measured and the accepted values.

In session 3, pyroxenes (mineral separates in grain mounts) were analysed using an accelerating voltage of 15 kV and a 5 μm beam. A beam current of 4 nA was used to detect the most abundant elements (Na, Mg, Al, Si, Ca and Fe), and a beam current of 100 nA was used to detect the elements in lower abundance (K, Ti, Mn, Cr and Ni). Peak counting times were 20s on majors, 30s on traces. Mineral standard, Block 8 - cpx (clinopyroxene), was analysed routinely throughout the analyses. Precision and accuracy estimates based on the analysis of this internal standard are given in Table A1.7.

	Block 8 - cpx			Published	Accuracy %
	Average	1σ	%P	values	difference
SiO_2	50.92	0.28	0.5	50.72	0.4
Na_2O	0.76	0.04	5.6	0.73	3.5
MgO	8.31	0.08	0.9	8.02	3.6
K_2O	n.d.	-	-	-	-
CaO	23.27	0.17	0.7	22.8	2.0
FeO	16.42	0.19	1.1	16.75	2.0
P_2O_5	-	-	-	-	-
TiO_2	n.d.	-	-	-	-
MnO	0.51	0.01	2.5	0.53	3.1
NiO	n.d.	-	-	-	-
Total	100.2	0.4			
n	*34*				

Table A1.7. Accuracy and precision estimates for major and minor element concentrations (wt.%) measured on internal standard, Block 8 – cpx (clinopyroxene), by electron microprobe at the University of Edinburgh during session 3. 1σ is the standard deviation of the repeat analyses and %P is the percentage precision. Accuracy is expressed as a percentage difference between the measured and the accepted values.

Appendix 1.4 Photomicrographs showing the mineralogy and texture of the intrusive and extrusive samples analysed for geothermobarometry with EMPA analysis locations highlighted.

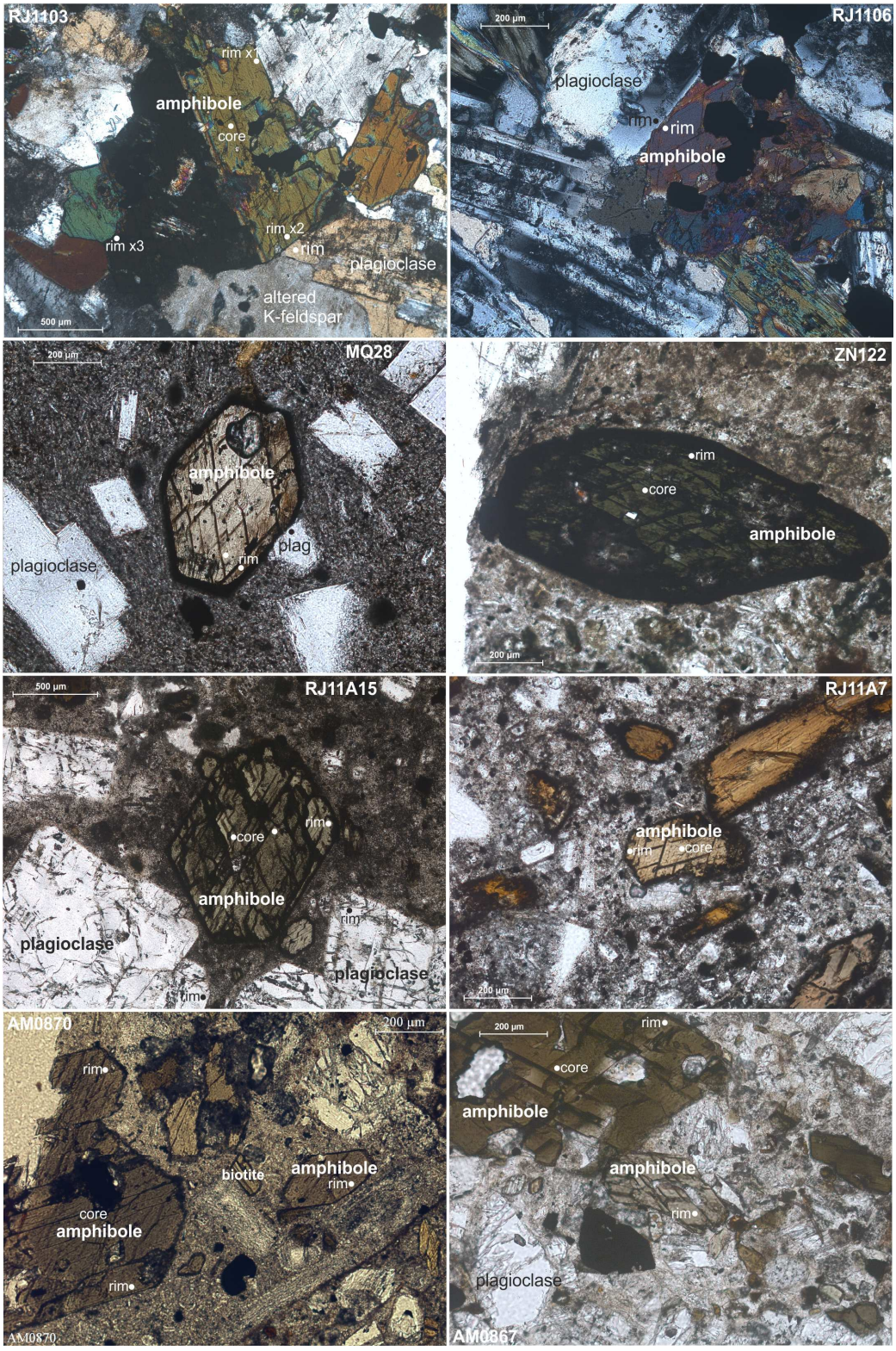

Appendix 1.5 Representative petrographic descriptions

Detailed petrographic descriptions of representative samples from each of the Late Cretaceous – Late Miocene geological units are presented below.

1.5.1 Cogotí Supergroup

1.5.1.1 Granite - AM0806

A medium to coarse grained intrusive with grains of plagioclase feldspar, alkali feldspar, quartz, and biotite visible in hand specimen. The plagioclase and alkali feldspar crystals are euhedral - subhedral and up to 2 cm in size. In thin section the sample consists of quartz (~30 modal %), alkali feldspar (~30 modal %), plagioclase (~25 modal %), biotite (~8 modal %), hornblende (<5 modal %), with minor/accessory phases of magnetite (and other opaque minerals ~3 modal %), apatite and zircon. The quartz and feldspar grains have interlocking grain boundaries and both feldspars are partially altered to sericite and clays, with the alkali feldspar being more altered than the plagioclase. Albite twinning and growth zoning is apparent in the plagioclase feldspars and the composition ranges from andesine to oligoclase. The biotite crystals are tabular in shape, show some alteration to chlorite and are associated with the opaque minerals. The hornblendes are subhedral, occasionally twinned, and range in composition from magnesio-hornblendes to actinolitic-hornblende, which is indicative of alteration. The ferromagnesian minerals and opaque oxides tend to appear together in clusters.

1.5.1.2 Granodiorite – AM0816

A medium grained intrusive with visible grains of plagioclase, quartz, hornblende and biotite visible in hand specimen. Mafic enclaves of up to ~20 cm in diameter are also apparent. The primary mineral phases are plagioclase (~35 modal %), quartz (~30 modal %), alkali feldspar (~10 modal %), hornblende (~8 modal %), biotite (~4 modal %), with minor/accessory phases of sphene, opaque oxides (including magnetite), apatite and zircon. The plagioclase crystals are euhedral - subhedral,

show some alteration to sericite, and display albite twinning and complex growth zonation (Appendix 1.6.1 d). The alkali feldspar is highly altered to sericite. Quartz crystals have intergrown grain boundaries with other mineral phases and in some places form oikocrysts enclosing/partially enclosing feldspar and biotite crystals. The hornblende crystals form subhedral, elongate prisms, some of which show simple twinning (Appendix 1.6.1 e). Alteration of the hornblende to chlorite is evident in some places. The biotite crystals are tabular in shape and highly altered to chlorite.

1.5.1.3 Syeno-diorite – AM0824

Medium grained (average = 1 – 2 mm) crystals of quartz, plagioclase, alkali feldspar, biotite and hornblende are visible in hand specimen. In some areas the ferromagnesian minerals appear in clusters and some mafic enclaves (up to ~ 5cm in diameter) are apparent. In thin section the sample appears inequgranular and is composed of plagioclase (~40 modal %), quartz (~20 modal %), alkali feldspar (~10 modal %), hornblende (~10 modal %) and biotite (~8 modal %), alongside minor/accessory phases of magnetite, opaque oxides, apatite and zircon. The plagioclase crystals are subhedral and display albite twinning and growth zonation. Both of the feldspars are partially altered to sericite, this is particularly prominent in the cores of the plagioclase feldspar grains. The quartz and alkali feldspar crystals sometimes occur as oikocrysts enclosing other mineral phases. Some microperthite intergrowth textures are also present (Appendix 1.6.1 f). The hornblende is subhedral - anhedral, displays simple twinning and has interlocking grain boundaries with feldspar grains. Both ferromagnesian minerals are associated with opaque oxides and have been partially altered to chlorite. Cross cutting calcite veins are also evident in thin section.

1.5.2 Río Frío Basalts

1.5.2.1 Basaltic – Tachy-andesite – RF17

This sample is fine grained, inequigranular, and predominately composed of fine grained, acicular plagioclase feldspar laths (~60 modal %) and opaque oxides (~30 modal %). The plagioclase crystals are aligned, indicative of flow, with the smaller laths bending around the larger subhedral plagioclase microphenocrysts (>0.4 mm) and opaque oxides (Appendix 1.6.2 a). Some alteration of plagioclase to sericite, carbonate and clays is evident and there are a number of carbonate veins cross cutting the sample. Fine grained relic pyroxenes are apparent (~3 modal %) and have been almost completely altered to iron oxide.

1.5.3 Los Elquinos Formation

1.5.3.1 Basalitic andesite – RJ1111

In hand specimen pyroxene and plagioclase feldspar microphenocrysts (<3 mm) are visible in a dark grey matrix. The plagioclase microphenocrysts, which make up ~40 % of the sample, range in size from ~0.5 to 3 mm, are subhedral and display albite and carlsbad twinning. Alteration to sericite and carbonate is apparent in thin section. The clinopyroxene (augite) microphenocrysts which make up ~10 % of the sample, range in size from ~1 – 2.5 mm, are subhedral, display simple twinning and some grains show some alteration to chlorite. Opaque oxides form the primary accessory phase. The augite microphenocrysts and opaque oxides tend appear as clusters. Some alignment of the mineral phases is apparent in thin section, giving an indication of flow. The matrix, which makes up ~40 % of the sample, is composed of fine grained plagioclase laths, pyroxene and opaque oxide minerals, as well as secondary chlorite and carbonate. Some cross cutting carbonate veins are also visible in thin section.

1.5.4 Tierras Blancas Caldera

1.5.4.1 Amphibole diorite – RJ1106

This medium grained instrusive contains plagioclase and hornblende which are visible in hand specimen. Alteration is also evident in hand specimen. The major mineral phases present are plagioclase feldspar (~50 modal %), hornblende (~25 modal %), quartz (~5 modal %), and minor/accessory phases of opaque oxides (~5 modal %), apatite and zircon. The plagioclase is partially altered to sericite and chlorite is replacing hornblende, particularly in the grain cores (Appendix 1.6.2 d). The plagioclase grains range in size from ~0.2 – 2 mm, are subhedral - anhedral, display albite and simple twinning, as well as complex and sector growth zoning. The amphibole grains are subhedral, range in size from ~0.2 – 2 mm and have interlocking grain boundaries with plagioclase feldspars. The quartz grains are smaller (<0.3 mm) and appear to be interstitial, filling the gaps between the plagioclase and the hornblende grains. The opaque oxides are associated with the hornblende.

1.5.5 Bocatoma Unit

1.5.5.1 Andesite - AM0867/68

This sample is composed of ~60% microphenocrysts (<3 mm) and ~40% matrix, which appears slightly pink in hand specimen, suggesting oxidation. Xenoliths and rip up clasts of other volcanic material are visible in hand specimen. In thin section the sample consists of microphenocrysts of plagioclase (~30 %), hornblende (~20 %) and opaque oxides (~10 %) and minor/accessory phases of apatite and zircon (Appendix 1.6.2 f). The plagioclase microphenocrysts are subhedral – anhedral, on average range in size from ~0.3 – 1.5 mm, are highly fractured and display albite twining and zonation. The plagioclase crystals have also been altered to sericite. The hornblende microphenocrysts are euhedral – subhedral, have an average grainsize of ~0.5mm and display simple twinning. Plagioclase and hornblende phenocrysts share grain boundaries in some cases. The matrix is composed of feldspar, which

has primarily been altered, opaque oxides and devitrified and altered glass. No flow texture is apparent.

1.5.6 Tilito Formation (Lower Doña Ana Group)

1.5.6.1 Rhyolitic ignimbrite – AM0846

Microphenocrysts of plagioclase, quartz and biotite are visible within a very fine grained grey matrix with a slight pinkish coloration, indicative of oxidation. A number of igneous xenoliths and lithic fragments are also apparent. The primary mineral phases include plagioclase (~20 %), quartz (~15 %), alkali feldspar (~10 %), biotite (~5 %) and opaque oxides (~3 %) with minor/accessory phases of apatite and zircon. The plagioclase phenocrysts are subhedral and display both albite and carlsbad twinning. The composition of the plagioclase ranges from andesine to oligoclase and the phenocrysts are partially altered to sericite, carbonate and clays. The quartz phenocrysts are embayed and exhibit undulose extinction. Acicular to tabular biotite microphenocrysts show evidence of resorption and alteration to oxide mineral phases. The matrix, which makes up ~50 % of the sample, is vitreous to fine grained and composed of devitrified glass, quartz and feldspar (Appendix 1.6.3 a and b). Spherulite texture is visible in the matrix, as well as some foliation and flow patterns (Appendix 1.6.3 e – sample AM0860). The phenocryst phases are also aligned in places, providing further evidence of deformation and flow.

1.5.7 Las Maquinas Basalts

1.5.7.1 Basalt – MQ8

This lava sample was collected from what has been interpreted as a volcanic neck (Vanesa Litvak, Pers. Comm.). The dark, porphyritic volcanic rock contains microphenocrysts of plagioclase feldspar, olivine (primarily in relic form), and clinopyroxene. The plagioclase microphenocrysts (~0.3 – 1 mm), which make up ~30 % of the sample, are subhedral, display albite twinning and zonation and show evidence of alteration to sericite, clays and carbonate. Olivine microphenocrysts

(~0.5 mm), which make up ~8 % of the sample, are primarily euhedral but have been highly altered and in thin section appear dark red/brown under plane polarized light. Pyroxene is a minor phenocryst phase (~5 %) and appears as small (~0.2 – 0.4 mm) subhedral to anhedral crystals. The matrix, which comprises ~55 % of the sample, is intergranular, fine grained and composed of plagioclase feldspar laths, olivine, pyroxene and opaque oxides, and displays flow textures.

1.5.8 Miocene Intrusives

1.5.8.1 Granodiorite – RJ11A14

A fine to medium grained intrusive with plagioclase, quartz, alkali feldspar, hornblende and biotite visible in hand specimen. In thin section the sample is composed of plagioclase (~40 modal %), quartz (~25 modal %), alkali feldspar (~10 modal %), hornblende (~15 modal %) and biotite (<5 modal %) and minor/accessory phases of opaque oxides (~3 modal %), apatite and zircon (Appendix 1.6.4 e and f). The plagioclase crystals are subhedral, display albite twinning and zonation, are generally ~ 1mm in size and have grain boundaries which interlock with the other mineral phases. The composition of the plagioclase feldspar ranges from andesine to oligoclase and some alteration to sericite is evident. The alkali feldspar displays simple twinning and is generally more altered than the plagioclase. The hornblendes are subhedral, occasionally twinned, and range in composition from magnesio-hornblendes to actinolitic hornblendes. The ferromagnesian minerals tend to appear in clots along with opaque oxides and also show some alteration to chlorite. Mafic enclaves ranging between 2 and 40 cm in diameter were visible in outcrop.

1.5.9 Escabroso Formation (Upper Doña Ana Group)

1.5.9.1 Basaltic andesite – MQ158

Contains microphenocrysts (0.3 – 3 mm) of plagioclase (~55 modal %), clinopyroxene (~10 modal %), orthopyroxene (~5 modal %) and opaque oxides (~5

modal %) in a fine grained groundmass. An indication of flow is evident from the alignment of the plagioclase microphenocrysts. These plagioclase microphenocrysts are generally subhedral, display albite twinning and growth zonation and have been partially altered to sericite, clays and carbonate (Appendix 1.6.5 a). The clinoproxene has been identified as augite and the orthopyroxene as enstatite. Both are subhedral and associated with opaque oxides. The augite displays simple twinning and both pyroxenes show some alteration to clay minerals and carbonate. The matrix, which makes up ~25% of the sample, is composed of plagioclase, pyroxene, and opaque oxides and has undergone some alteration to sericite and clays.

1.5.9.2 Andesite – trachy-andesite – 1026

A porphyritic sample containing phenocrysts of plagioclase feldspar and pyroxene are visible in a fine grained, dark grey – brown matrix. In thin section the sample, contains phenocrysts of plagioclase (~35 modal %), clinopyroxene (~20 %) and orthopyroxene (~10 %) and minor/accessory phases of opaque oxides (~10 %), apatite and zircon. The plagioclase phenocrysts range in size from 0.3 – 3 mm, are euhedral – subhedral, display albite twinning and some growth zonation. Some of the plagioclase has been altered to sericite and clays, particularly the cores of the grains. The clinoproxene has been identified as augite and the orthopyroxene as enstatite. Both pyroxenes are subhedral and appear primarily in mafic clots along with opaque oxides. Simple twinning is frequently apparent in the augite microphenocrysts along with the significant numbers of melt inclusions. The matrix, which makes up ~25% of the sample, is fine grained and composed of plagioclase, opaque oxides and clays. In some places the feldspars appear as laths and show a preferred orientation around the phenocryst phases.

1.5.10 Cerro de las Tórtolas Formation

1.5.10.1 Trachy-andesite – RF62

Microphenocrysts of plagioclase feldspar (~40 %) and clinopyroxene (~15 %), along with opaque oxides (~5 %) are present in a vitreous to fine grained goundmass. Minor/accessory mineral phases of apatite and zircon have also been identified in thin section. The plagioclase feldspars are euhedral - subhedral, show varying degrees of alteration to sericite, carbonate and clays, and display a large range of sizes (0.3 – 2 mm). Alteration is particularly apparent around the rims of the plagioclase crystals. The clinoproxene, which has been identified as diopside, is predominately subhedral, on average ranges in size from ~0.5 – 1 mm and contains inclusions of opaque oxides, apatite and melt. The opaque oxides are primarily associated with the clinoproxene microphenocrysts. The matrix is composed of plagioclase (with some alteration to sericite), opaque oxides and clays, and makes up ~40 % of the sample. In hand specimen the matrix has a pink coloration, indicative of oxidation. Cross cutting veins and alteration is also evident.

1.5.11 Upper Cerro de las Tórtolas Formation

1.5.11.1 Trachy-andesite – MQ28

Microphenocrysts of plagioclase (~40 %), amphibole (~10 %) and opaque oxides (~5 %) are present in a vitreous to fine grained matrix. The matrix, which makes up ~45 % of the sample, has a slight pink coloration in hand specimen and appears to have undergone oxidation. In thin section it is evident that the matrix is composed of plagioclase laths, opaque oxides, devitrified glass and clays. The plagioclase laths bend around the larger mineral phases giving an indication of flow. The microphenocrysts (0.3 – 2 mm) of plagioclase are euhedral – subhedral, with well-developed albite twinning and growth zonation. The composition of the plagioclase feldspar has been determined as ranging from labradorite to andesine. The amphibole phenocrysts are predominantly euhedral, commonly display simple twinning, and thick opaque reaction rims composed of Fe-Ti oxides (Appendix 1.6.6

c). Some of the smaller amphibole crystals (<0.1 mm) appear to have been entirely replaced by Fe-Ti oxides. The composition of the amphiboles has been determined as pargasitic magnesio-hastingite.

1.5.12 Tertiary Intrusives

1.5.12.1 Trachy-dacite - RJ11A15

This trachy-dacitic sample which has been previously been identified as being sub volcanic (Cardó and Díaz, 1999) consists of ~70 % microphenocrysts in a fine grained to vitreous groundmass. The microphenocryst assemblage is primarily composed of plagioclase (~30 modal %), amphibole (~20 modal %) and alkali feldspar (~10 modal %) accompanied by minor/accessory phases of biotite, quartz, Fe-Ti oxides, apatite and zircon. The groundmass is composed of feldspar, opaque oxides and alteration products (clays, sericite and carbonate). All the major phenocryst phases show evidence of resorption (Appendix 1.6.6 d and e). The plagioclase microphenocrysts, which range in composition from andesine to oligoclase, are predominantly subhedral, display albite and calsbad twinning and growth zonation. The alkali feldspars display simple twinning and growth zonation. Both feldspars are fractured and partially altered to sericite, carbonate and clays. The amphibole microphenocrysts are primarily subhedral and exhibit thick opaque reaction rims, composed of Fe-Ti oxides. In the older sample (RJ11A7) the amphibole microphenocrysts show a preferred orientation, indicative of flow. Compositionally they are primarily magnesio-hornblendes but a few have pargasitic magnesio-hastingite compositions. The biotite crystals are tabular and make up <5 % of the mineral assemblage. Quartz makes up <3 % of the mineral assemblage and appears as rounded microphenocrysts, which show strong evidence for resportion (Appendix 1.6.6 e). The quartz grains are also highly fractured and display undulose extinction which may be a result of emplacement processes.

1.5.13 Vacas Heladas Ignimbrites

1.5.13.1 Rhyolitic crystal tuff - MQ33

This porphyritic volcanic rock contains microphenocrysts of plagioclase feldspar (~40 %), quartz (35 %), biotite (~5 %), and minor/accessory phases of opaque oxides, apatite, zircon and beryl, in a vitreous to fine grained groundmass. Fiamme and lithic fragments are also present. The microphenocrysts of plagioclase have an average grainsize of ~1.5 mm, are generally subhedral crystal fragments (Appendix 1.6.6 f) and display albite twinning. Unlike some of the other formations very little alteration of the plagioclase is apparent. The biotite microphenocrysts are generally ~0.5 mm, tabular and bladed in shape, and show a preferred orientation which includes appearing to have been deformed around the other major mineral phases. The quartz crystals range in size between ~ 0.5 and 2 mm and are highly fractured, a possible result of emplacement processes. The groundmass is fine grained to vitreous and composed of devitrified glass, feldspar, quartz, opaque oxides and alteration products (sericite and clay minerals).

Appendix 1.6 Thin section photomicrographs

1.6.1 Photomicrographs showing the mineralogy and texture of the Cogotí Supergroup.

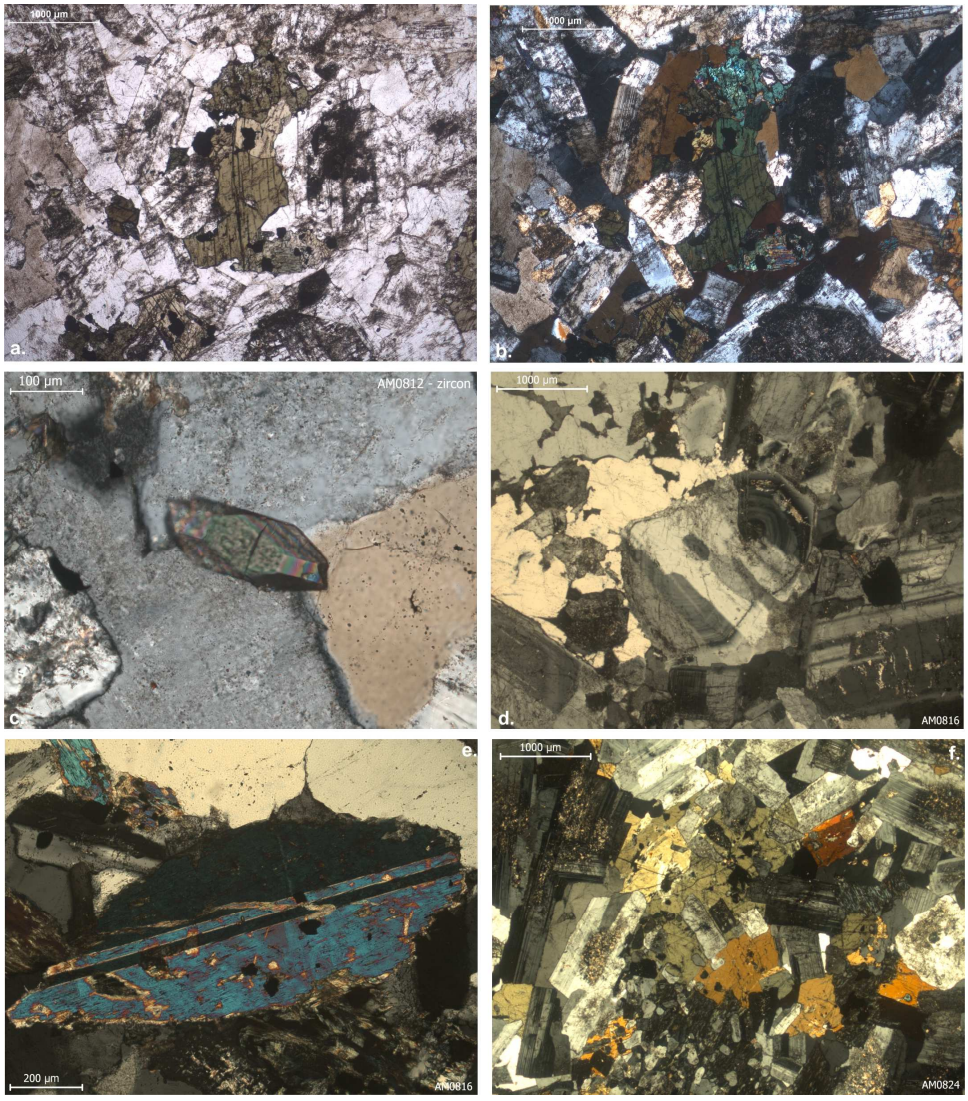

a) A photomicrograph of dioritic sample RJ1103 showing a medium grained, inequigranular texture composed of hornblende, quartz, plagioclase and alkali feldspar. Alteration of the feldspars to sericite and clays is evident. b) The same as previous but under crossed polarised light. The quartz grains appear yellow – brown due to the thick cut of the polished thin section. c) Zircon present in sample AM0812, viewed under crossed polarized light, displaying typical birefringence. The zircon is surrounded by alkali feldspar and quartz (yellow colouration) d) Plagioclase feldspar (central crystal) from granodioritic sample AM0816 showing complex growth zonation and twinning under crossed polarised light. Quartz and alkali feldspar is also present. e) A subhedral amphibole crystal present in sample AM0816 displaying simple twinning under crossed polarised light. f) Photomicrograph of sample AM0824 displaying microperthite texture and oikocrysts of alkali feldspar and quartz. Alteration of plagioclase to sericite and carbonate is evident, particularly in the centre of the certain grains. Viewed under crossed polarised light.

1.6.2 Photomicrographs showing the mineralogy and texture of the Río Frío Basalts, Los Elquinos Formation, samples of the Tierras Blancas Caldera and Botacoma Unit.

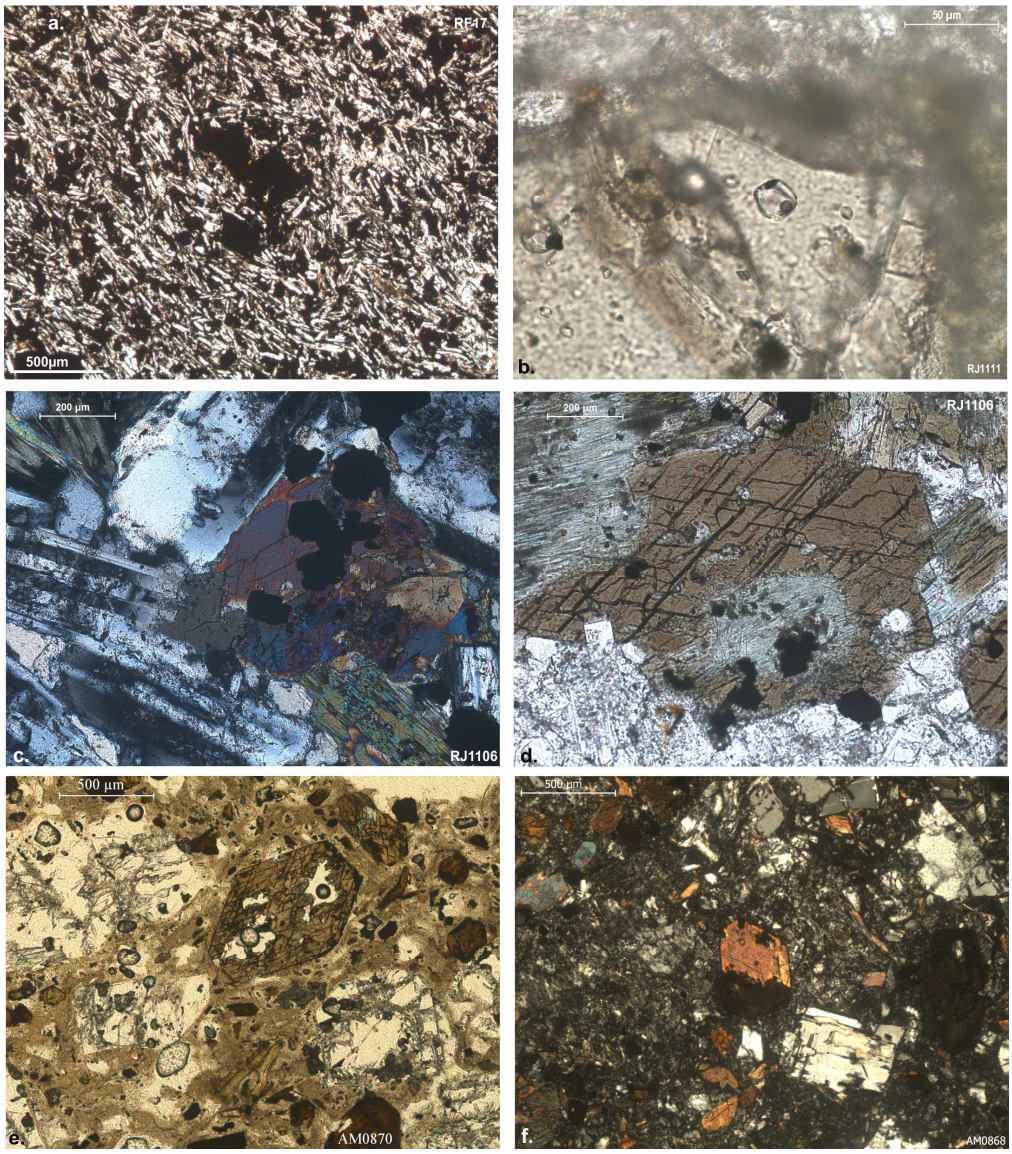

a) A photomicrograph of basaltic sample RF17 from the Río Frío Basalts showing the alignment of plagioclase laths and a high proportion of opaque oxides. b) Melt inclusions present in an augite microphenocryst from sample RJ1111 (Los Elquinos Formation). c) Photomicrograph of dioritic sample RJ1106 (Tierras Blancas Caldera) under crossed polarised light showing subhedral amphibole (central) associated with opaque oxides and surrounded by twinned plagioclase feldspar and minor amounts of quartz. Alteration of the amphibole to chlorite is evident in the top left and bottom right of the image. d) A subhedral amphibole showing evidence of alteration to chlorite, present in sample RJ1106. e) Microphenocrysts of amphibole, plagioclase and biotite in a vitreous groundmass (trachy-andesitic sample AM0870 – Botacoma Unit). f) Photomicrograph of andesitic sample AM0868 (Bocatoma Unit) under crossed polarised light showing a twinned, euhedral amphibole microphenocrysts (central) alongside plagioclase feldspar, quartz and subhedral amphibole phenocrysts in a vitreous to fine grained groundmass.

1.6.3 Photomicrographs showing the mineralogy and texture of the Tilito Formation (Lower Doña Ana Group).

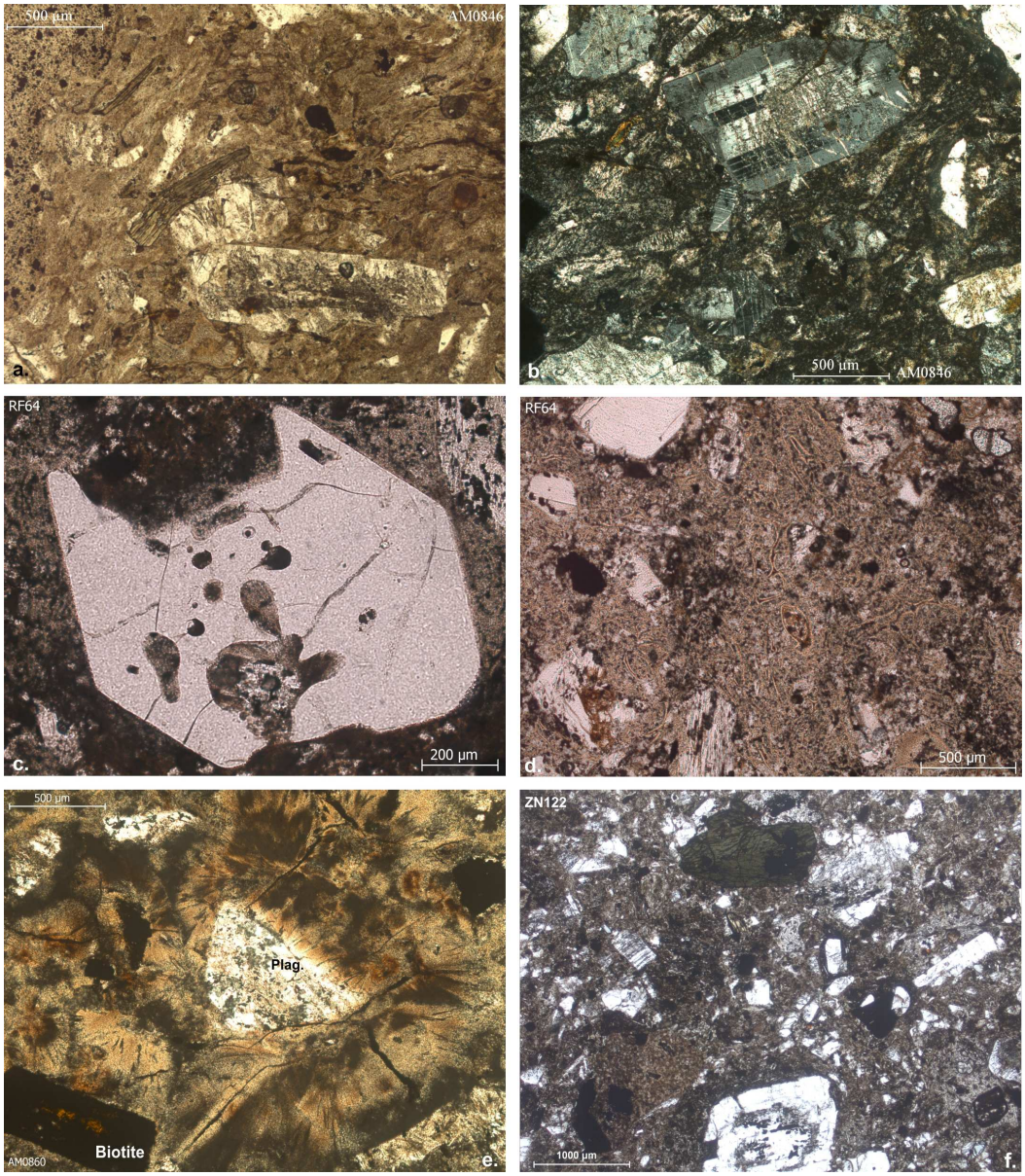

a) A photomicrograph of sample AM0846 showing microphenocrysts of biotite and plagioclase feldspar in a glassy, oxidised groundmass. The biotite crystal is deformed around plagioclase feldspar and alteration of the plagioclase feldspar to sericite and clay minerals is apparent. b) Photomicrograph of sample AM0846 under crossed polarised light showing subhedral microphenocrysts of plagioclase and alkali feldspar in a vitreous groundmass. Fracturing and alteration of the large plagioclase grain, which shows albite twinning, to carbonate is evident. c) An embayed quartz grain present in sample RF64. The quartz grain is fractured and contains melt inclusions, as well as inclusions of the groundmass. d) Deformed, devitrified glass shards present in the groundmass of sample RF64. e) Spherulite texture present in the oxidised groundmass of dacitic sample AM0860. The biotite microphenocryst is primarily composed of Fe-oxide. f) A photomicrograph of andesitic sample ZN122 showing plagioclase feldspar, alkali feldspar, amphibole and opaque oxide minerals in a vitreous to fine grained groundmass.

1.6.4 Photomicrographs showing the mineralogy and texture of the Las Maquinas Basalts and the Miocene Intrusives.

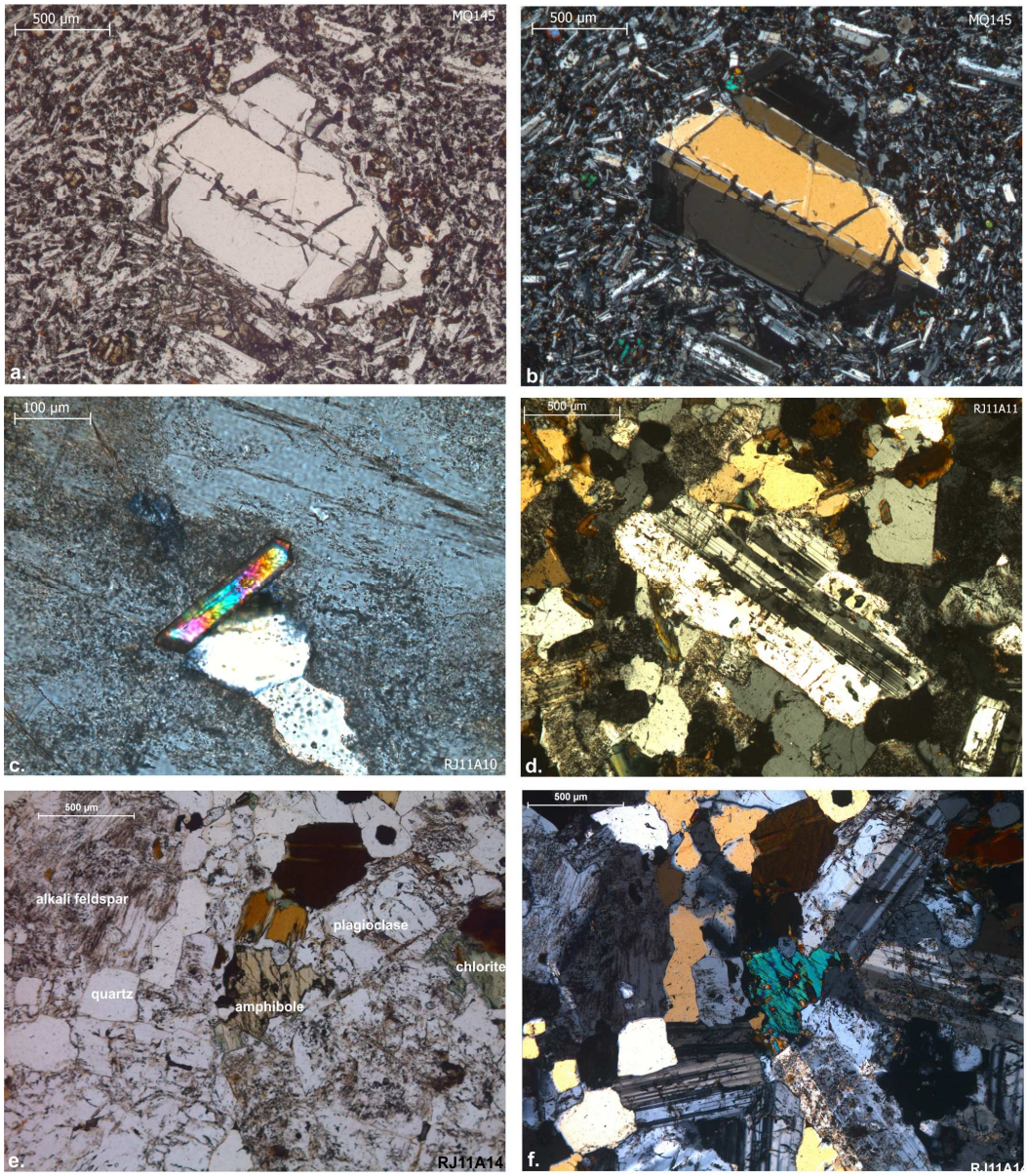

a) A plagioclase microphenocryst (MQ145, Las Maquinas basalts) showing evidence partial resorption, in a fine grained matrix, composed of plagioclase feldspar laths, pyroxene and opaque oxides. b) The same view as previous but under crossed polarised light. c) A zircon present in granitic sample, RJ11A10 (Miocene Intrusives) showing typical birefringence colours. d) Photomicrograph of sample RJ11A11 (Miocene Intrusives) showing a fine to medium grained, inequgranular texture containing plagioclase and alkali feldspar (more altered), quartz (some yellow colouration due to the thick cut of the polished section), biotite and zircon. Viewed under crossed polarised light. e) Photomicrograph of sample RJ11A14 (Miocene Intrusives) showing alteration of the feldspars to sericite and clays and the presence of chlorite. f) The same view as previous but under crossed polarised light and slightly offset.

1.6.5 Photomicrographs showing the mineralogy and texture of the Escabroso Formation (Upper Doña Ana Group) and the Cerro de las Tórtolas Formation.

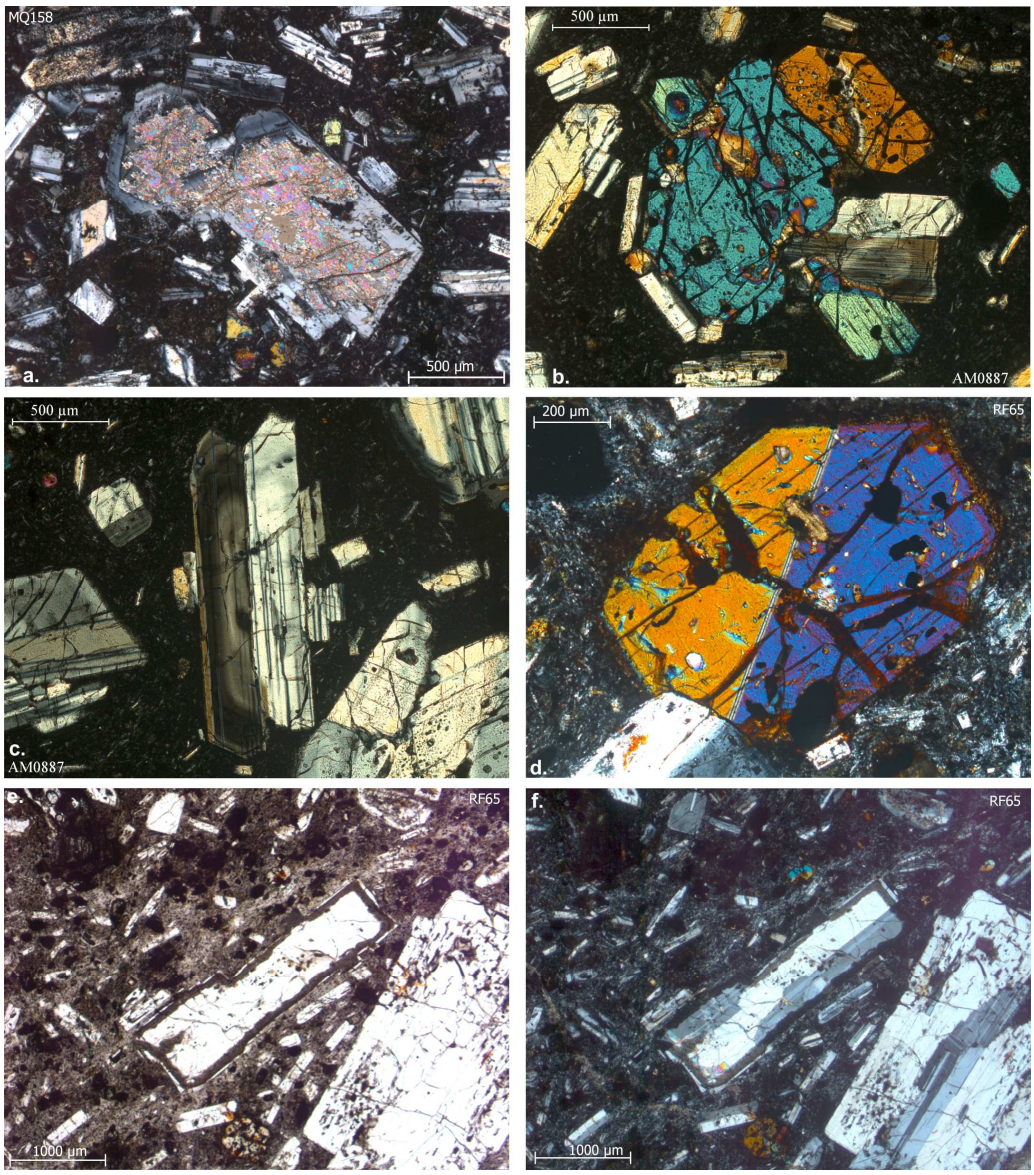

a) A subhedral microphenocryst of plagioclase feldspar (central) showing alteration to sericite and carbonate (MQ158, Escabroso Formation). b) Intergrown microphenocrysts of augite, enstatite and plagioclase (centre) in sample AM0887, Escabroso Formation. The pyroxenes contain inclusions of opaque oxides, apatite and melt inclusions. c) Euhedral and subhedral microphenocrysts of plagioclase feldspar, displaying albite and carlsbad twinning and growth zonation, in a fine grained matrix (AM0887, Escabroso Formation). d) A subhedral microphenocrysts of augite present in sample RF65 (Cerro de las Tórtolas Formation) displaying simple twinning and inclusions of opaque oxides, apatite and melt inclusions. e) Plagioclase phenocrysts present in sample RF65 (Cerro de las Tórtolas Formation) showing evidence of partial resorption (rim displayed in central grain). The larger plagioclase (bottom right) displays a sieve texture. f) The same as previous but under crossed polarised light.

1.6.6 Photomicrographs showing the mineralogy and texture of the Upper Cerro de las Tórtolas Formation, Tertiary Intrusives and Vacas Heladas Ignimbrites.

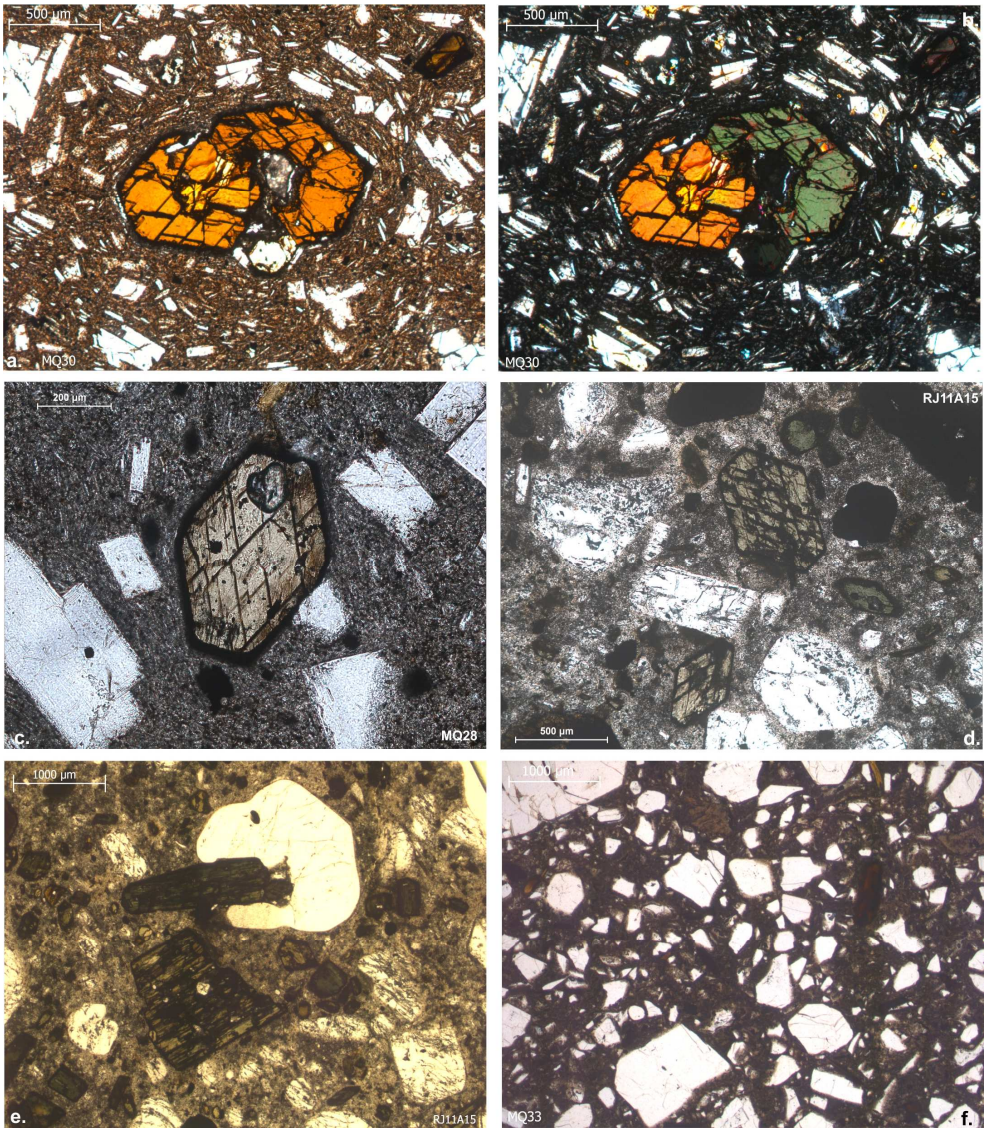

a) An amphibole microphenocryst and plagioclase feldpars in a vitreous to fine grained matrix (MQ30, Upper Cerro de las Tórtolas Formation). Indication of flow is given by the orientation of the smaller plagioclase feldspars around the larger amphibole microphenocrysts. b) The same as previous but under crossed polarised light. c) A euhedral pargasitic magnesio-hastingite microphenocryst with a thick opaque reaction rim composed of Fe oxide in a fine grained matrix (MQ28, Upper Cerro de las Tórtolas Formation). Plagioclase feldspar microphenocrysts and opaque oxides are also visible. d) Amphibole, plagioclase feldspar and opaque oxides present in a vitreous – fine grained groundmass (RJ11A15, Tertiary Intrusives). Some alteration and resportion of the plagioclase is apparent microphenocrysts. e) Fractured quartz microphenocryst (central, top) showing interlocking grain boundaries with and elongate amphibole microphenocryst (RJ11A15, Tertiary Intrusives). f) Crystal fragments of plagioclase feldspar, quartz and microphenocrysts of biotite in a vitreous groundmass (MQ33, Vacas Heladas Ignimbrites).

Appendix 1.7 Mineral composition data – plagioclase feldspar

	Sample	Analytical session	SiO_2	Na_2O	K_2O	CaO	Al_2O_3	MgO	MnO	FeO	SrO	TiO_2	NiO	BaO	Total	An	Or	Ab
Cogoti Supergroup	**AM0822**	1	60.40	7.97	0.45	6.42	24.78	0.00	0.00	0.23	0.08	0.01	-	-	**100.3**	30.0	2.5	67.5
		1	58.73	7.13	0.28	7.83	26.12	0.00	0.00	0.18	0.10	0.02	-	-	**100.4**	37.2	1.6	61.3
		1	62.33	8.52	0.62	4.98	23.88	0.00	0.00	0.17	0.08	0.00	-	-	**100.6**	23.5	3.5	73.0
		1	63.10	9.01	0.66	4.16	22.96	0.00	0.01	0.16	0.06	0.00	-	-	**100.1**	19.6	3.7	76.7
		1	61.15	8.21	0.38	6.02	24.81	0.00	0.01	0.22	0.05	0.01	-	-	**100.9**	28.2	2.1	69.7
		1	58.77	7.33	0.46	7.33	26.08	0.01	0.02	0.26	0.12	0.01	-	-	**100.4**	34.7	2.6	62.7
		1	60.46	8.09	0.43	6.09	24.71	0.00	0.00	0.21	0.11	0.01	-	-	**100.1**	28.7	2.4	68.9
		1	60.30	7.80	0.36	6.72	25.36	0.01	0.00	0.22	0.12	0.01	-	-	**100.9**	31.6	2.0	66.4
		1	58.27	6.95	0.34	7.96	26.43	0.01	0.00	0.21	0.13	0.02	-	-	**100.3**	38.0	2.0	60.1
		1	60.20	7.86	0.48	6.42	24.96	0.01	0.00	0.22	0.12	0.00	-	-	**100.3**	30.3	2.7	67.1
		1	60.68	8.07	0.48	6.13	25.00	0.01	0.00	0.21	0.10	0.00	-	-	**100.7**	28.8	2.7	68.6
		1	61.46	8.32	0.46	5.51	24.50	0.00	0.01	0.24	0.07	0.01	-	-	**100.6**	26.1	2.6	71.3
		1	52.79	4.41	0.16	12.55	30.14	0.05	0.00	0.26	0.16	0.02	-	-	**100.5**	60.6	0.9	38.5
		1	54.40	5.51	0.15	10.85	28.70	0.00	0.01	0.26	0.13	0.02	-	-	**100.0**	51.7	0.8	47.5
		1	56.59	6.50	0.20	9.22	27.35	0.00	0.01	0.24	0.15	0.02	-	-	**100.3**	43.4	1.1	55.4
		1	58.20	7.15	0.31	7.70	25.96	0.00	0.00	0.27	0.11	0.01	-	-	**99.7**	36.7	1.7	61.6
		1	60.85	8.20	0.37	5.96	24.40	0.00	0.01	0.24	0.08	0.00	-	-	**100.1**	28.1	2.1	69.9
		1	63.66	9.67	0.14	3.96	23.05	0.00	0.00	0.19	0.06	0.01	-	-	**100.7**	18.3	0.8	80.9
		1	52.79	4.65	0.14	12.27	29.84	0.00	0.01	0.34	0.15	0.02	-	-	**100.2**	58.8	0.8	40.3
		1	52.76	4.71	0.14	12.22	29.64	0.00	0.02	0.33	0.17	0.02	-	-	**100.0**	58.5	0.8	40.8
		1	54.83	5.64	0.32	10.40	28.33	0.18	0.02	0.59	0.16	0.03	-	-	**100.5**	49.6	1.8	48.6
		1	59.47	7.45	0.23	7.22	25.56	0.00	0.01	0.23	0.12	0.01	-	-	**100.3**	34.4	1.3	64.3
		1	61.51	8.59	0.09	5.60	24.25	0.00	0.00	0.21	0.06	0.00	-	-	**100.3**	26.3	0.5	73.2
		1	59.62	7.74	0.36	6.71	25.19	0.00	0.00	0.22	0.14	0.00	-	-	**100.0**	31.7	2.0	66.3
		1	57.09	6.66	0.29	8.50	26.46	0.01	0.02	0.64	0.15	0.01	-	-	**99.8**	40.7	1.6	57.7

	Sample	Analytical session	SiO_2	Na_2O	K_2O	CaO	Al_2O_3	MgO	MnO	FeO	SrO	TiO_2	NiO	BaO	Total	An	Or	Ab
		1	53.77	5.06	0.12	11.45	29.67	0.00	0.00	0.22	0.15	0.02	-	-	**100.5**	55.2	0.7	44.1
		1	56.28	6.28	0.17	9.46	27.49	0.00	0.00	0.17	0.11	0.02	-	-	**100.0**	45.0	1.0	54.1
		1	60.87	8.40	0.14	6.02	24.53	0.00	0.01	0.18	0.07	0.01	-	-	**100.2**	28.2	0.8	71.1
		1	55.88	6.01	0.23	9.92	27.69	0.01	0.01	0.34	0.14	0.02	-	-	**100.2**	47.1	1.3	51.6
		1	54.73	5.63	0.19	10.42	28.14	0.01	0.01	0.32	0.12	0.01	-	-	**99.6**	50.0	1.1	48.9
		1	62.46	8.92	0.53	4.84	23.62	0.01	0.00	0.18	0.08	0.00	-	-	**100.6**	22.4	2.9	74.7
		1	60.15	7.99	0.32	6.40	24.96	0.00	0.01	0.20	0.10	0.01	-	-	**100.1**	30.1	1.8	68.1
	AM0806	2	61.72	8.56	0.41	5.55	24.22	0.00	0.00	0.24	0.04	0.00	0.00	0.00	**100.7**	25.8	2.2	72.0
		2	60.66	8.02	0.56	6.37	24.51	0.01	0.01	0.24	0.06	0.01	0.00	0.05	**100.5**	29.6	3.1	67.3
		2	60.77	7.92	0.84	5.82	24.35	0.01	0.02	0.31	0.08	0.00	0.00	0.05	**100.2**	27.5	4.7	67.8
		2	63.80	9.39	0.58	3.78	22.42	0.00	0.01	0.16	0.02	0.01	0.02	0.00	**100.2**	17.6	3.2	79.1
	AM0826	2	65.13	10.10	0.39	2.99	22.15	0.00	0.00	0.17	0.04	0.00	0.00	0.01	**101.0**	13.8	2.2	84.1
		2	62.45	8.89	0.31	5.13	23.54	0.00	0.01	0.26	0.04	0.01	0.01	0.04	**100.7**	23.8	1.7	74.5
	RJ1103	2	62.00	8.93	0.47	4.61	23.27	0.00	0.00	0.16	0.06	0.00	0.00	0.00	**99.5**	21.6	2.6	75.8
		2	57.13	7.06	0.20	8.04	26.04	0.02	0.01	0.41	0.12	0.03	0.00	0.03	**99.1**	38.2	1.1	60.7
		2	61.01	8.39	0.15	6.03	24.87	0.01	0.00	0.24	0.10	0.01	0.00	0.03	**100.8**	28.2	0.9	71.0
		2	60.17	8.00	0.55	6.28	24.55	0.00	0.00	0.21	0.07	0.01	0.01	0.06	**99.9**	29.3	3.1	67.6
		2	60.74	8.50	0.51	5.21	23.72	0.00	0.00	0.21	0.07	0.02	0.00	0.02	**99.0**	24.6	2.8	72.6
		2	61.14	8.06	0.58	6.09	24.62	0.01	0.00	0.18	0.09	0.01	0.00	0.05	**100.8**	28.5	3.2	68.3
		2	61.91	8.87	0.57	4.62	23.18	0.01	0.00	0.21	0.06	0.02	0.00	0.00	**99.4**	21.7	3.2	75.2
		2	62.77	9.04	0.63	4.52	23.28	0.01	0.01	0.22	0.06	0.01	0.00	0.01	**100.6**	20.9	3.5	75.6
		2	61.31	8.56	0.42	5.47	23.99	0.01	0.00	0.21	0.05	0.01	0.00	0.01	**100.0**	25.5	2.3	72.2
		2	61.41	8.41	0.56	5.49	23.87	0.00	0.00	0.21	0.06	0.02	0.00	0.02	**100.0**	25.7	3.1	71.2
Tierras Blancas Caldera	**RJ1106**	2	57.81	7.34	0.09	8.18	26.23	0.01	0.00	0.28	0.11	0.02	0.00	0.01	**100.1**	37.9	0.5	61.6
		2	55.72	6.12	0.20	10.00	27.97	0.03	0.00	0.46	0.13	0.03	0.00	0.01	**100.6**	46.9	1.1	52.0
		2	49.70	3.45	0.08	14.87	31.24	0.05	0.01	0.63	0.12	0.03	0.01	0.01	**100.2**	70.1	0.4	29.4

	Sample	Analytical session	SiO_2	Na_2O	K_2O	CaO	Al_2O_3	MgO	MnO	FeO	SrO	TiO_2	NiO	BaO	Total	An	Or	Ab
		2	55.83	6.23	0.10	10.00	27.79	0.03	0.00	0.49	0.14	0.03	0.00	0.03	**100.7**	46.8	0.5	52.7
		2	57.38	6.70	0.19	9.13	27.00	0.03	0.00	0.35	0.11	0.02	0.00	0.04	**100.9**	42.5	1.0	56.5
		2	56.98	6.64	0.17	9.16	27.30	0.03	0.02	0.54	0.13	0.03	0.01	0.00	**101.0**	42.8	1.0	56.2
		2	56.75	7.02	0.24	8.32	26.07	0.02	0.00	0.37	0.11	0.02	0.01	0.03	**99.0**	39.0	1.3	59.6
		2	59.09	7.49	0.21	7.72	25.95	0.02	0.02	0.38	0.11	0.02	0.00	0.01	**101.0**	35.9	1.2	63.0
Bocatoma Unit	**AM0868**	2	55.83	5.90	0.39	9.98	27.65	0.01	0.01	0.32	0.14	0.00	0.00	0.04	**100.3**	47.2	2.2	50.6
		2	56.84	6.12	0.44	9.47	27.43	0.01	0.01	0.23	0.14	0.00	0.01	0.02	**100.7**	45.0	2.5	52.6
		2	56.75	6.12	0.46	9.34	27.23	0.01	0.02	0.24	0.14	0.01	0.00	0.00	**100.3**	44.6	2.6	52.8
		2	55.96	5.75	0.38	10.26	27.87	0.01	0.00	0.23	0.14	0.00	0.01	0.01	**100.6**	48.6	2.2	49.2
		2	57.37	6.19	0.42	9.33	27.30	0.01	0.00	0.22	0.13	0.00	0.00	0.03	**101.0**	44.4	2.4	53.3
		2	56.56	6.11	0.41	9.66	27.61	0.01	0.01	0.23	0.13	0.00	0.01	0.03	**100.8**	45.6	2.3	52.1
		2	55.33	5.36	0.37	10.84	28.58	0.01	0.01	0.31	0.13	0.01	0.00	0.03	**101.0**	51.7	2.1	46.2
	AM0870	1	56.91	6.20	0.48	9.03	27.33	0.01	0.01	0.21	0.13	0.00	-	-	**100.3**	43.4	2.8	53.9
		1	56.32	5.75	0.42	9.76	27.52	0.01	0.00	0.23	0.14	0.00	-	-	**100.1**	47.2	2.4	50.3
		1	57.31	6.28	0.49	8.85	27.06	0.01	0.01	0.22	0.14	0.00	-	-	**100.4**	42.5	2.8	54.6
		1	57.25	6.40	0.48	8.68	26.80	0.01	0.00	0.23	0.14	0.00	-	-	**100.0**	41.7	2.8	55.6
		1	55.81	5.83	0.41	9.69	27.48	0.01	0.02	0.24	0.14	0.00	-	-	**99.6**	46.7	2.4	50.9
		1	57.10	6.19	0.47	9.01	26.99	0.01	0.01	0.24	0.13	0.00	-	-	**100.2**	43.4	2.7	53.9
		1	57.07	6.10	0.47	9.08	27.25	0.01	0.00	0.23	0.16	0.01	-	-	**100.4**	43.9	2.7	53.4
		1	56.46	5.81	0.41	9.52	27.71	0.02	0.01	0.22	0.13	0.00	-	-	**100.3**	46.4	2.4	51.2
		1	56.47	5.90	0.43	9.42	27.36	0.01	0.00	0.22	0.13	0.00	-	-	**100.0**	45.7	2.5	51.8
		1	55.38	5.55	0.38	10.24	27.97	0.01	0.01	0.22	0.15	0.00	-	-	**99.9**	49.4	2.2	48.4
		1	56.12	5.86	0.45	9.64	27.77	0.01	0.01	0.25	0.13	0.01	-	-	**100.3**	46.4	2.6	51.0
		1	54.67	5.22	0.33	10.77	28.77	0.01	0.00	0.26	0.15	0.00	-	-	**100.2**	52.2	1.9	45.8
		1	56.59	6.16	0.45	9.32	27.34	0.01	0.00	0.23	0.15	0.00	-	-	**100.2**	44.4	2.6	53.1
		1	56.92	6.18	0.46	9.24	27.18	0.01	0.01	0.24	0.13	0.00	-	-	**100.4**	44.1	2.6	53.3
Tilito Formation	**AM0844**	1	68.71	11.67	0.07	0.21	20.04	0.00	0.00	0.00	0.04	0.00	-	-	**100.7**	1.0	0.4	98.6

	Sample	Analytical session	SiO_2	Na_2O	K_2O	CaO	Al_2O_3	MgO	MnO	FeO	SrO	TiO_2	NiO	BaO	Total	An	Or	Ab
		1	68.51	11.78	0.05	0.11	19.95	0.00	0.00	0.00	0.04	0.00	-	-	**100.4**	0.5	0.3	99.2
		1	68.44	11.82	0.05	0.38	20.15	0.00	0.00	0.00	0.04	0.00	-	-	**100.9**	1.7	0.3	98.0
		1	68.69	12.00	0.06	0.02	19.72	0.00	0.00	0.02	0.02	0.00	-	-	**100.5**	0.1	0.3	99.6
	AM0846	1	61.43	8.24	0.64	5.50	24.49	0.01	0.01	0.22	0.10	0.00	-	-	**100.6**	26.0	3.6	70.4
		1	63.98	8.93	0.99	3.66	22.62	0.00	0.01	0.17	0.07	0.00	-	-	**100.4**	17.4	5.6	76.9
		1	65.34	9.39	1.37	2.53	21.66	0.00	0.00	0.16	0.04	0.00	-	-	**100.5**	11.9	7.7	80.3
		1	65.37	9.38	1.52	2.45	21.49	0.00	0.00	0.16	0.04	0.00	-	-	**100.4**	11.6	8.5	79.9
		1	65.41	9.23	1.46	2.49	21.47	0.00	0.00	0.16	0.04	0.01	-	-	**100.3**	11.9	8.3	79.8
		1	60.48	7.96	0.57	6.01	24.69	0.00	0.00	0.24	0.11	0.01	-	-	**100.1**	28.5	3.2	68.3
		1	64.65	9.18	1.16	3.13	22.41	0.00	0.01	0.18	0.07	0.00	-	-	**100.8**	14.8	6.5	78.6
		1	64.94	9.23	1.33	2.82	21.88	0.00	0.00	0.17	0.06	0.00	-	-	**100.4**	13.4	7.5	79.1
		1	64.98	9.44	1.32	2.45	21.51	0.00	0.01	0.16	0.04	0.00	-	-	**99.9**	11.6	7.5	80.9
		1	61.68	8.39	0.67	5.25	23.90	0.01	0.01	0.20	0.10	0.01	-	-	**100.2**	24.7	3.7	71.5
	ZN122	2	56.31	5.70	0.55	10.07	27.87	0.02	0.00	0.33	0.12	0.01	0.00	0.04	**101.0**	47.9	3.1	49.0
		2	56.05	5.72	0.53	10.17	27.99	0.02	0.00	0.34	0.13	0.01	0.00	0.04	**101.0**	48.1	3.0	48.9
		2	56.36	6.05	0.68	8.95	26.47	0.02	0.00	0.45	0.15	0.01	0.00	0.07	**99.2**	43.3	3.9	52.9
		2	56.25	5.93	0.62	9.25	26.39	0.02	0.00	0.34	0.14	0.00	0.01	0.05	**99.0**	44.6	3.6	51.8
		2	56.18	6.02	0.62	9.26	26.67	0.02	0.01	0.34	0.14	0.00	0.00	0.05	**99.3**	44.3	3.5	52.1
		2	54.88	5.57	0.51	10.34	27.66	0.02	0.01	0.33	0.15	0.00	0.01	0.03	**99.5**	49.2	2.9	48.0
		2	56.20	5.95	0.64	9.19	26.75	0.02	0.00	0.36	0.14	0.00	0.01	0.07	**99.3**	44.4	3.7	52.0
Miocene Intrusives	**RJ11A14**	2	59.04	7.60	0.35	6.95	24.88	0.01	0.00	0.33	0.12	0.02	0.00	0.01	**99.3**	32.9	2.0	65.1
		2	64.11	10.02	0.20	3.17	22.09	0.00	0.00	0.11	0.11	0.00	0.01	0.00	**99.8**	14.7	1.1	84.2
		2	61.00	8.35	0.50	5.74	24.15	0.01	0.00	0.26	0.11	0.00	0.01	0.00	**100.1**	26.8	2.8	70.5
		2	59.54	7.73	0.39	6.80	24.92	0.01	0.00	0.32	0.12	0.01	0.00	0.02	**99.9**	32.0	2.2	65.8
		2	61.28	8.32	0.51	5.75	24.12	0.01	0.00	0.28	0.12	0.01	0.00	0.02	**100.4**	26.9	2.8	70.3
		2	59.56	7.99	0.35	6.56	24.78	0.01	0.00	0.27	0.13	0.01	0.00	0.03	**99.7**	30.6	2.0	67.4
		2	58.83	7.96	0.27	6.64	24.97	0.00	0.00	0.23	0.12	0.01	0.00	0.02	**99.0**	31.1	1.5	67.4

	Sample	Analytical session	SiO_2	Na_2O	K_2O	CaO	Al_2O_3	MgO	MnO	FeO	SrO	TiO_2	NiO	BaO	Total	An	Or	Ab
		2	57.91	7.00	0.37	8.28	26.37	0.01	0.00	0.26	0.12	0.01	0.01	0.03	**100.4**	38.7	2.1	59.2
Escabroso																		
Formation	**AM0887**	1	53.75	4.81	0.44	11.49	28.67	0.04	0.01	0.46	0.12	0.04	-	-	**99.8**	55.5	2.5	42.0
		1	57.28	6.18	0.81	8.70	26.65	0.03	0.01	0.42	0.11	0.03	-	-	**100.2**	41.7	4.6	53.7
		1	55.70	5.43	0.57	10.23	27.86	0.04	0.01	0.46	0.12	0.04	-	-	**100.4**	49.3	3.3	47.4
		1	55.63	5.50	0.58	10.15	27.76	0.06	0.01	0.54	0.13	0.03	-	-	**100.4**	48.8	3.3	47.9
		1	56.40	5.69	0.63	9.74	27.30	0.05	0.01	0.53	0.12	0.04	-	-	**100.5**	46.9	3.6	49.5
		1	56.74	5.77	0.68	9.38	27.29	0.05	0.01	0.52	0.13	0.03	-	-	**100.6**	45.5	3.9	50.6
		1	55.72	5.43	0.59	10.03	27.64	0.04	0.00	0.49	0.12	0.03	-	-	**100.1**	48.8	3.4	47.8
		1	56.01	5.64	0.63	9.69	27.25	0.04	0.00	0.49	0.12	0.03	-	-	**99.9**	46.9	3.7	49.4
		1	56.77	5.90	0.68	9.32	26.89	0.04	0.00	0.49	0.12	0.03	-	-	**100.2**	44.8	3.9	51.3
		1	54.65	5.12	0.49	10.73	28.21	0.04	0.01	0.48	0.11	0.04	-	-	**99.9**	52.1	2.9	45.0
		1	55.14	5.37	0.54	10.39	27.87	0.04	0.00	0.46	0.12	0.04	-	-	**100.0**	50.1	3.1	46.8
		1	55.95	5.66	0.59	9.92	27.58	0.05	0.00	0.50	0.12	0.02	-	-	**100.4**	47.5	3.4	49.1
		1	55.15	5.31	0.53	10.49	27.72	0.05	0.00	0.53	0.12	0.03	-	-	**99.9**	50.6	3.0	46.4
		1	54.96	5.15	0.54	10.54	28.24	0.04	0.00	0.52	0.12	0.03	-	-	**100.1**	51.4	3.1	45.5
		1	55.50	5.45	0.55	10.02	27.74	0.06	0.00	0.49	0.14	0.02	-	-	**100.0**	48.8	3.2	48.0
		1	56.17	5.70	0.59	9.67	27.21	0.06	0.01	0.51	0.12	0.03	-	-	**100.1**	46.7	3.4	49.9
		1	57.52	5.93	0.77	8.90	26.53	0.04	0.00	0.43	0.11	0.04	-	-	**100.3**	43.3	4.5	52.2
		1	55.55	5.40	0.58	10.21	27.74	0.04	0.00	0.43	0.12	0.04	-	-	**100.1**	49.4	3.3	47.3
		1	57.71	6.16	0.80	8.50	26.22	0.04	0.00	0.50	0.12	0.03	-	-	**100.1**	41.3	4.6	54.1
		1	55.80	5.62	0.61	9.86	27.32	0.04	0.00	0.49	0.12	0.02	-	-	**99.9**	47.5	3.5	49.0
		1	55.24	5.24	0.51	10.56	28.37	0.04	0.00	0.45	0.12	0.04	-	-	**100.6**	51.2	2.9	45.9
		1	56.40	5.84	0.65	9.47	27.23	0.04	0.01	0.45	0.13	0.04	-	-	**100.3**	45.5	3.7	50.8
		1	56.27	5.88	0.68	9.46	27.09	0.04	0.00	0.46	0.13	0.04	-	-	**100.1**	45.2	3.9	50.9
		1	55.59	5.55	0.60	10.02	27.69	0.04	0.00	0.46	0.12	0.04	-	-	**100.1**	48.2	3.4	48.3
		1	54.96	5.32	0.55	10.47	28.08	0.04	0.00	0.46	0.10	0.04	-	-	**100.0**	50.4	3.2	46.4

Sample	Analytical session	SiO_2	Na_2O	K_2O	CaO	Al_2O_3	MgO	MnO	FeO	SrO	TiO_2	NiO	BaO	Total	An	Or	Ab
	1	54.87	5.34	0.55	10.47	28.26	0.04	0.01	0.45	0.11	0.04	-	-	**100.1**	50.4	3.1	46.5
	1	55.85	5.56	0.61	9.84	27.40	0.04	0.00	0.45	0.12	0.04	-	-	**99.9**	47.7	3.5	48.8
	1	55.57	5.51	0.61	10.08	27.86	0.04	0.01	0.49	0.12	0.03	-	-	**100.3**	48.5	3.5	48.0
	1	56.69	5.78	0.65	9.40	27.01	0.04	0.01	0.49	0.12	0.04	-	-	**100.2**	45.6	3.8	50.7
	1	57.24	6.24	0.82	8.51	26.34	0.04	0.00	0.47	0.12	0.03	-	-	**99.8**	40.9	4.7	54.3
	1	58.10	6.32	0.83	8.40	26.07	0.04	0.00	0.45	0.11	0.03	-	-	**100.3**	40.4	4.7	54.9
	1	57.06	6.27	0.77	8.68	26.33	0.04	0.00	0.46	0.13	0.03	-	-	**99.8**	41.5	4.4	54.2
	1	57.32	6.22	0.78	8.70	26.55	0.05	0.00	0.46	0.12	0.03	-	-	**100.2**	41.6	4.5	53.9
	1	58.68	6.00	1.34	7.82	25.17	0.06	0.00	0.59	0.11	0.06	-	-	**99.8**	38.6	7.9	53.5
	1	56.56	6.03	0.72	9.12	27.03	0.04	0.00	0.47	0.12	0.03	-	-	**100.1**	43.6	4.1	52.3
	1	51.74	4.02	0.34	12.99	30.34	0.03	0.01	0.48	0.13	0.03	-	-	**100.1**	62.8	2.0	35.2
	1	52.39	4.32	0.36	12.50	29.88	0.03	0.01	0.49	0.12	0.04	-	-	**100.1**	60.2	2.1	37.7
	1	55.77	5.51	0.57	10.02	27.79	0.04	0.00	0.47	0.13	0.03	-	-	**100.3**	48.5	3.3	48.2
	1	58.06	6.49	0.91	8.14	26.14	0.04	0.00	0.45	0.12	0.02	-	-	**100.4**	38.8	5.2	56.0
	1	53.55	4.73	0.42	11.61	28.95	0.05	0.01	0.49	0.12	0.04	-	-	**100.0**	56.2	2.4	41.4
	1	51.23	3.78	0.27	13.57	30.77	0.05	0.00	0.52	0.10	0.04	-	-	**100.3**	65.4	1.6	33.0
	1	53.27	4.51	0.38	11.91	29.34	0.05	0.00	0.50	0.12	0.05	-	-	**100.1**	58.0	2.2	39.8
	1	54.03	4.85	0.42	11.43	28.97	0.05	0.00	0.48	0.14	0.04	-	-	**100.4**	55.2	2.4	42.4
	1	54.40	5.06	0.46	11.08	28.28	0.05	0.02	0.47	0.13	0.04	-	-	**100.0**	53.3	2.6	44.1
	1	54.24	5.03	0.45	11.11	28.71	0.05	0.01	0.49	0.14	0.04	-	-	**100.3**	53.6	2.6	43.9
	1	54.01	4.93	0.44	11.05	28.69	0.05	0.01	0.49	0.12	0.04	-	-	**99.8**	53.9	2.6	43.5
	1	53.95	4.87	0.43	11.23	28.65	0.05	0.01	0.50	0.11	0.04	-	-	**99.8**	54.6	2.5	42.9
	1	53.66	4.86	0.43	11.40	28.73	0.05	0.00	0.47	0.13	0.03	-	-	**99.8**	55.1	2.4	42.5
	1	55.02	5.29	0.52	10.58	28.05	0.05	0.01	0.51	0.13	0.03	-	-	**100.2**	51.0	3.0	46.1
	1	56.35	5.54	0.58	9.89	27.44	0.05	0.01	0.50	0.13	0.03	-	-	**100.5**	48.0	3.4	48.6
	1	55.96	5.62	0.59	9.75	27.57	0.05	0.00	0.50	0.13	0.03	-	-	**100.2**	47.3	3.4	49.3
	1	56.09	5.67	0.61	9.67	27.20	0.05	0.00	0.52	0.11	0.03	-	-	**99.9**	46.8	3.5	49.7

	Sample	Analytical session	SiO_2	Na_2O	K_2O	CaO	Al_2O_3	MgO	MnO	FeO	SrO	TiO_2	NiO	BaO	Total	An	Or	Ab
		1	56.96	5.98	0.70	8.99	26.75	0.05	0.00	0.50	0.13	0.03	-	-	**100.1**	43.6	4.0	52.4
		1	56.66	5.74	0.64	9.35	26.83	0.05	0.00	0.52	0.14	0.03	-	-	**100.0**	45.6	3.7	50.7
		1	57.34	5.95	0.72	8.80	26.79	0.05	0.01	0.52	0.12	0.02	-	-	**100.3**	43.1	4.2	52.7
		1	57.53	6.09	0.76	8.65	26.44	0.05	0.00	0.51	0.14	0.03	-	-	**100.2**	42.0	4.4	53.5
		1	55.94	5.69	0.60	9.74	27.38	0.05	0.01	0.53	0.13	0.04	-	-	**100.1**	46.9	3.5	49.6
		1	54.81	5.14	0.48	10.78	28.44	0.05	0.00	0.51	0.12	0.04	-	-	**100.4**	52.2	2.8	45.0
Upper Cerro de las	**MQ28**	2	54.86	5.39	0.38	10.94	28.30	0.04	0.01	0.64	0.23	0.04	0.00	0.05	**100.9**	51.7	2.1	46.1
Tórtolas Formation		2	50.47	3.93	0.23	13.44	30.32	0.04	0.00	0.59	0.23	0.03	0.00	0.04	**99.3**	64.6	1.3	34.2
		2	53.85	5.21	0.34	11.07	28.28	0.05	0.00	0.54	0.23	0.03	0.00	0.03	**99.6**	53.0	2.0	45.1
		2	55.30	5.75	0.42	9.87	27.22	0.05	0.00	0.49	0.22	0.03	0.00	0.04	**99.4**	47.5	2.4	50.1
		2	55.00	5.74	0.45	10.12	27.73	0.04	0.01	0.55	0.23	0.04	0.00	0.03	**99.9**	48.1	2.5	49.4
		2	54.72	5.73	0.39	9.90	27.42	0.04	0.00	0.56	0.24	0.04	0.00	0.03	**99.1**	47.8	2.2	50.0
		2	55.45	5.98	0.46	9.46	27.03	0.04	0.00	0.46	0.21	0.02	0.00	0.05	**99.1**	45.4	2.6	52.0
		2	54.95	5.93	0.34	9.84	27.10	0.03	0.01	0.57	0.19	0.04	0.00	0.05	**99.0**	46.9	1.9	51.1
		2	53.90	5.28	0.29	10.93	28.15	0.05	0.00	0.51	0.22	0.03	0.00	0.04	**99.4**	52.5	1.7	45.9
		2	53.74	5.28	0.38	10.96	28.11	0.05	0.00	0.63	0.22	0.05	0.01	0.04	**99.5**	52.3	2.2	45.6
Tertiary Intrusives	**RJ11A15**	2	60.09	7.59	0.48	6.90	25.45	0.00	0.00	0.20	0.28	0.00	0.00	0.04	**101.0**	32.5	2.7	64.8
		2	60.78	8.09	0.40	6.19	24.93	0.00	0.00	0.18	0.24	0.00	0.00	0.07	**100.9**	29.1	2.3	68.7
	RJ11A17	2	58.97	7.59	0.45	6.72	24.90	0.01	0.00	0.31	0.32	0.01	0.00	0.09	**99.4**	32.0	2.6	65.5
		2	57.64	6.89	0.29	8.03	26.35	0.00	0.00	0.08	0.30	0.01	0.00	0.02	**99.6**	38.5	1.7	59.8
		2	60.00	7.52	0.57	6.75	25.33	0.01	0.03	0.25	0.44	0.00	0.00	0.06	**100.9**	32.1	3.2	64.7
		2	58.59	7.05	0.41	7.73	26.28	0.07	0.01	0.41	0.44	0.00	0.01	0.07	**101.0**	36.9	2.3	60.8
		2	64.69	9.25	1.14	3.19	22.19	0.00	0.00	0.12	0.22	0.00	0.01	0.03	**100.8**	15.0	6.4	78.7
		2	64.43	9.25	1.33	3.10	22.19	0.00	0.00	0.12	0.23	0.00	0.00	0.08	**100.7**	14.5	7.4	78.1
		2	59.49	7.59	0.39	7.02	25.48	0.01	0.00	0.30	0.28	0.00	0.00	0.07	**100.6**	33.1	2.2	64.7
		2	63.70	9.02	0.90	3.71	22.83	0.00	0.01	0.09	0.39	0.00	0.01	0.05	**100.7**	17.6	5.1	77.4
		2	59.56	7.64	0.49	6.87	25.59	0.01	0.00	0.18	0.39	0.01	0.01	0.04	**100.8**	32.3	2.7	65.0

	Sample	Analytical session	SiO_2	Na_2O	K_2O	CaO	Al_2O_3	MgO	MnO	FeO	SrO	TiO_2	NiO	BaO	Total	An	Or	Ab
		2	56.31	6.40	0.35	8.79	26.87	0.01	0.00	0.30	0.47	0.02	0.01	0.04	**99.6**	42.3	2.0	55.7
		2	56.57	6.28	0.35	9.26	27.48	0.01	0.01	0.30	0.47	0.02	0.00	0.04	**100.8**	44.0	2.0	54.0

Appendix 1.8 Mineral composition data – pyroxene

Formation	Sample	Analytical session	Sample-Grain	Na_2O	K_2O	MgO	CaO	MnO	FeO	NiO	Al_2O_3	Cr_2O_3	SiO_2	TiO_2	Total	Wo	Fs	En
Los Elquinos Formation	**RJ1111**	3	RJ1111-3cpx	0.30	0.00	15.18	19.21	0.35	11.36	0.01	-	0.01	51.98	0.62	**99.0**	40.36	15.27	44.37
		3	RJ1111-6cpx	0.49	0.65	14.14	19.87	0.34	11.46	0.01	-	0.00	52.01	0.69	**99.7**	43.71	13.01	43.28
		3	RJ1111-11cpx	0.33	0.00	15.14	19.94	0.34	11.13	0.02	-	0.01	51.50	0.61	**99.0**	42.40	12.82	44.79
		3	RJ1111-12cpx	0.31	0.00	14.25	19.76	0.41	12.20	0.00	-	0.01	51.76	0.51	**99.2**	41.84	16.18	41.98
		3	MBRJ1111-1-cpx	0.26	0.00	14.59	20.13	0.36	11.45	0.00	-	0.01	52.44	0.52	**99.8**	41.87	15.90	42.23
		3	MBRJ1111-2-cpx	0.25	0.00	14.80	19.66	0.35	11.31	0.01	-	0.01	52.08	0.65	**99.1**	41.04	15.95	43.01
		3	MBRJ1111-5-cpx	0.30	0.00	14.57	19.26	0.38	12.57	0.01	-	0.00	51.29	0.65	**99.0**	41.03	15.78	43.19
Tilito Formation	**ZN122**	3	ZN122-1cpx	0.39	0.01	14.29	21.73	0.45	10.17	0.01	-	0.03	51.96	0.30	**99.3**	46.33	11.28	42.39
		3	ZN122-5cpx	0.32	0.00	14.44	21.99	0.47	9.43	0.01	-	0.00	53.00	0.19	**99.9**	45.76	12.44	41.80
		3	ZN122-6cpx	0.40	0.00	14.57	21.99	0.50	9.80	0.01	-	0.00	51.76	0.18	**99.2**	47.23	9.24	43.53
		3	ZN122-8cpx	0.46	0.59	14.60	22.04	0.39	8.68	0.01	-	0.00	53.14	0.23	**100.1**	47.51	8.71	43.79
		3	ZN122-10cpx	0.29	0.00	14.74	22.40	0.44	9.48	0.01	-	0.01	52.58	0.22	**100.2**	46.82	10.31	42.88
		3	MBZN122-6-cpx	0.33	0.00	14.52	22.32	0.48	9.23	0.00	-	0.00	52.54	0.16	**99.6**	46.91	10.61	42.48
		3	MBZN122-5-cpx	0.31	0.00	14.63	22.47	0.48	8.98	0.00	-	0.00	52.96	0.18	**100.0**	46.72	10.95	42.33
		3	MBZN122-7-cpx	0.33	0.00	14.23	22.21	0.59	9.89	0.00	-	0.00	52.87	0.16	**100.3**	46.49	12.06	41.45
Escabroso Formation	**AM0887**	1	AM0887-3x1	0.32	0.00	14.60	20.87	0.36	10.23	0.00	1.19	0.00	52.28	0.39	**100.2**	43.80	13.56	42.64
		1	AM0887-3x2	0.02	0.00	22.84	1.51	0.70	21.48	0.01	0.68	0.00	52.86	0.26	**100.4**	3.10	31.90	65.01
		1	AM0887-3x3	0.35	0.00	14.25	20.22	0.37	10.69	0.01	1.72	0.01	51.13	0.57	**99.3**	43.44	13.96	42.60
		1	AM0887-5x1	0.03	0.00	23.58	1.42	0.67	20.16	0.01	0.81	0.00	52.97	0.27	**99.9**	2.89	30.11	67.00
		1	AM0887-5x2	0.03	0.00	23.71	1.46	0.68	20.08	0.01	0.80	0.00	52.85	0.26	**99.9**	2.99	29.48	67.53
		1	AM0887-6x1	0.33	0.00	14.64	20.90	0.38	9.74	0.00	1.35	0.00	51.80	0.41	**99.5**	44.30	12.50	43.19
		1	AM0887-6x2	0.31	0.00	14.64	21.08	0.39	9.85	0.00	1.26	0.00	51.90	0.38	**99.8**	44.60	12.29	43.11
		1	AM0887-7x1	0.02	0.00	23.39	1.45	0.67	20.51	0.00	0.73	0.00	53.11	0.26	**100.2**	2.96	30.79	66.25
		1	AM0887-7x2	0.01	0.00	23.58	1.38	0.68	20.61	0.02	0.75	0.00	53.09	0.28	**100.4**	2.82	30.46	66.73
		1	AM0887-7x3	0.37	0.00	14.52	20.33	0.36	10.35	0.01	1.62	0.02	51.79	0.52	**99.9**	43.19	13.88	42.93
		1	AM0887-7x4	0.34	0.00	14.70	20.44	0.38	10.36	0.01	1.47	0.00	51.66	0.46	**99.8**	43.50	12.97	43.53
		1	AM0887-12x1	0.02	0.00	20.96	1.42	0.84	24.23	0.00	0.82	0.02	51.71	0.29	**100.3**	2.97	35.94	61.09
		1	AM0887-12x2	0.01	0.00	21.80	1.46	0.68	23.15	0.01	0.77	0.00	52.12	0.28	**100.3**	3.02	34.14	62.84

Formation	Sample	Analytical session	Sample-Grain	Na_2O	K_2O	MgO	CaO	MnO	FeO	NiO	Al_2O_3	Cr_2O_3	SiO_2	TiO_2	Total	Wo	Fs	En
		1	AM0887-13x1	0.02	0.00	21.88	2.10	0.78	21.61	0.01	0.70	0.00	51.64	0.28	**99.0**	4.40	31.77	63.84
		1	AM0887-13x2	0.34	0.00	14.58	20.50	0.42	10.54	0.01	1.32	0.00	52.13	0.41	**100.3**	43.28	13.88	42.84
		1	AM0887-13x3	0.34	0.00	14.42	20.42	0.39	10.43	0.01	1.36	0.01	51.99	0.41	**99.8**	43.20	14.36	42.44
		1	AM0887-13x4	0.31	0.00	14.48	21.32	0.36	9.85	0.00	0.92	0.00	52.47	0.28	**100.0**	44.64	13.17	42.18
		1	AM0887-14x1	0.34	0.00	14.58	20.76	0.39	10.24	0.01	1.37	0.01	51.55	0.44	**99.7**	44.27	12.45	43.28
		1	AM0887-14x2	0.30	0.00	14.73	20.88	0.38	9.77	0.02	1.38	0.00	51.86	0.43	**99.8**	44.16	12.49	43.35
		1	AM0887-14x3	0.30	0.00	14.49	20.74	0.37	9.80	0.01	1.39	0.01	51.95	0.43	**99.5**	43.75	13.73	42.53
		1	AM0887-16x1	0.32	0.00	14.60	20.70	0.39	10.32	0.00	1.03	0.01	51.92	0.31	**99.6**	43.86	13.10	43.04
		1	AM0887-16x2	0.37	0.00	14.27	20.59	0.40	10.61	0.00	1.50	0.00	51.75	0.46	**100.0**	43.82	13.92	42.26
		1	AM0887-16x5	0.33	0.00	14.47	20.72	0.41	10.20	0.00	1.10	0.00	52.04	0.34	**99.6**	43.82	13.61	42.56
		1	AM0887-16x6	0.03	0.00	22.65	1.40	0.75	21.78	0.00	0.62	0.01	52.56	0.28	**100.1**	2.87	32.22	64.91
		1	AM0887-16x7	0.01	0.00	22.50	1.42	0.77	21.41	0.01	0.56	0.00	52.96	0.25	**99.9**	2.90	33.11	63.98
		1	AM0887-16x8	0.03	0.00	22.29	1.43	0.76	21.86	0.01	0.66	0.00	52.50	0.28	**99.8**	2.94	33.08	63.98
		3	AM0887-6cpx	0.27	0.00	15.17	21.29	0.38	9.99	0.00	-	0.00	51.48	0.45	**99.0**	45.19	10.02	44.80
		3	AM0887-10cpx	0.30	0.00	14.82	21.54	0.38	9.72	0.00	-	0.00	52.31	0.28	**99.3**	45.22	11.50	43.28
		3	AM0887-12cpx	0.02	0.00	23.41	1.40	0.68	21.03	0.00	-	0.00	52.81	0.26	**99.6**	2.87	30.48	66.65
		3	AM0887-15cpx	0.33	0.00	14.33	20.68	0.37	10.81	0.01	-	0.00	52.36	0.39	**99.3**	43.40	14.75	41.85
		3	AM0887-16cpx	0.03	0.00	23.74	1.34	0.65	21.17	0.00	-	0.00	52.88	0.22	**100.0**	2.74	29.71	67.55
		3	MBAM0887-2cpx	0.03	0.00	22.49	1.25	0.73	22.29	0.00	-	0.01	53.76	0.25	**100.8**	2.52	34.47	63.01
		3	MBAM0887-6cpx(2)	0.26	0.00	15.10	21.66	0.34	9.77	0.00	-	0.00	51.79	0.29	**99.2**	45.76	9.85	44.38
		3	MBAM0887-9-cpx	0.36	0.00	14.47	20.46	0.39	10.67	0.00	-	0.01	52.25	0.51	**99.1**	43.08	14.54	42.38
		3	MBAM0887-10-cpx	0.00	0.00	23.88	1.50	0.67	20.43	0.01	-	0.00	53.22	0.27	**100.0**	3.04	29.64	67.32
		3	MBAM0887-12-cpx	0.35	0.00	14.66	20.85	0.38	10.63	0.00	-	0.00	52.07	0.43	**99.4**	44.03	12.89	43.07
		3	MBAM0887-17-cpx	0.32	0.00	14.58	20.96	0.41	11.21	0.02	-	0.01	52.17	0.46	**100.1**	44.12	13.20	42.69
	1026	3	1026-2cpx	0.36	0.01	14.62	21.36	0.36	10.41	0.01	-	0.00	52.16	0.30	**99.6**	45.19	11.79	43.02
		3	1026-3cpx	0.42	0.00	14.35	21.25	0.35	10.33	0.00	-	0.00	52.35	0.34	**99.4**	44.90	12.92	42.18
		3	1026-4cpx	0.38	0.00	14.74	21.95	0.35	9.48	0.00	-	0.01	53.39	0.22	**100.5**	45.41	12.17	42.42
		3	1026-5cpx	0.40	0.00	14.51	21.46	0.37	10.21	0.00	-	0.00	52.91	0.22	**100.1**	44.89	12.86	42.25
		3	1026-6cpx	0.44	0.00	14.34	21.50	0.40	10.23	0.01	-	0.00	52.24	0.30	**99.5**	45.69	11.90	42.41
		3	1026-7cpx	0.35	0.00	14.32	21.64	0.48	10.31	0.01	-	0.00	52.59	0.27	**100.0**	45.45	12.69	41.86

Formation	Sample	Analytical session	Sample-Grain	Na_2O	K_2O	MgO	CaO	MnO	FeO	NiO	Al_2O_3	Cr_2O_3	SiO_2	TiO_2	Total	Wo	Fs	En
		3	1026-13cpx	0.35	0.00	14.21	21.36	0.39	10.37	0.00	-	0.00	51.99	0.38	**99.0**	45.22	12.92	41.86
		3	1026block-2cpx	0.34	0.00	14.29	21.41	0.36	10.50	0.00	-	0.00	52.28	0.34	**99.5**	45.08	13.08	41.85
		3	1026block-8cpx	0.33	0.00	14.49	21.71	0.37	9.68	0.00	-	0.02	52.28	0.23	**99.1**	45.73	11.80	42.48
		3	1026block-11-cpx	0.31	0.02	14.48	21.89	0.35	9.53	0.00	-	0.01	53.48	0.22	**100.3**	45.01	13.57	41.42
		3	1026block-14cpx	0.02	0.00	23.32	1.04	0.70	21.50	0.00	-	0.00	53.20	0.12	**99.9**	2.12	31.84	66.04
		3	1026block-17cpx	0.37	0.00	14.16	21.35	0.41	10.54	0.01	-	0.00	52.51	0.29	**99.6**	44.91	13.66	41.44
		3	MB1026-2cpx	0.35	0.00	14.23	21.58	0.57	10.09	0.01	-	0.00	52.19	0.21	**99.2**	45.78	12.23	41.99
		3	MB1026-11-cpx	0.00	0.00	23.54	1.18	0.79	21.02	0.00	-	0.00	54.07	0.20	**100.8**	2.37	32.10	65.53
		3	MB1026glassy11-cpx	0.38	0.00	14.30	21.36	0.35	10.59	0.01	-	0.00	52.94	0.28	**100.2**	44.55	13.98	41.47
Cerro de las	**RF62**	3	RF62-3cpx	0.35	0.00	14.91	22.34	0.33	8.98	0.02	-	0.00	51.85	0.21	**99.0**	47.52	8.35	44.13
Tórtolas Formation		3	RF62-4cpx	0.37	0.00	15.18	22.79	0.35	8.57	0.00	-	0.00	52.66	0.20	**100.1**	47.81	7.88	44.31
		3	RF62-5cpx	0.29	0.00	14.96	22.69	0.33	8.83	0.01	-	0.01	53.18	0.23	**100.5**	46.81	10.23	42.96
		3	RF62-8cpx	0.34	0.00	15.27	22.75	0.39	7.86	0.00	-	0.01	52.72	0.17	**99.5**	47.61	7.93	44.46
		3	RF62-9cpx	0.31	0.00	14.93	22.41	0.35	8.71	0.01	-	0.00	52.43	0.17	**99.3**	47.01	9.40	43.59
		3	RF62-10cpx	0.39	0.00	14.85	21.98	0.33	9.19	0.00	-	0.02	53.00	0.23	**100.0**	45.82	11.11	43.07
		3	RF62-12cpx	0.37	0.00	14.78	22.38	0.36	8.92	0.01	-	0.02	53.13	0.20	**100.2**	46.53	10.73	42.74
		3	MBRF62-2cpx	0.37	0.00	14.61	22.24	0.32	9.00	0.00	-	0.01	52.95	0.23	**99.7**	46.36	11.27	42.37
		3	MBRF62-3-cpx	0.34	0.00	14.76	22.43	0.35	8.32	0.01	-	0.00	53.12	0.19	**99.5**	46.53	10.85	42.62
	RF65	3	MBRF65-3-cpx	0.33	0.00	14.72	22.28	0.35	8.45	0.00	-	0.00	53.20	0.18	**99.5**	46.12	11.48	42.40

Appendix 1.9 Raw mineral composition data – amphibole

Formation	Sample	Analytical session	Sample-Grain	Na_2O	MgO	SiO_2	CaO	FeO	Al_2O_3	F	K_2O	TiO_2	Cr_2O_3	MnO	NiO	Total
Cogoti Supergroup	**AM0806**	2	AM0806-2g2c	1.72	10.27	46.71	10.72	20.37	5.84	0.70	0.69	1.39	0.01	0.61	0.00	**99.0**
		2	AM0806-2g2r	1.70	10.65	47.25	10.63	20.17	5.47	0.67	0.61	1.16	0.00	0.59	0.01	**98.9**
		2	AM0806-2r	1.45	11.00	47.61	10.99	20.04	4.84	0.72	0.52	0.97	0.00	0.57	0.00	**98.7**
		2	AM0806-3	1.07	11.63	50.15	11.15	19.64	3.31	0.72	0.34	0.53	0.00	0.50	0.01	**99.0**
		2	AM0806-4r1	1.79	10.59	46.18	10.83	19.95	6.29	0.75	0.74	1.57	0.01	0.49	0.01	**99.2**
		2	AM0806-4r2	0.66	11.55	51.78	12.00	19.37	2.19	0.55	0.20	0.16	0.01	0.42	0.01	**98.9**
		2	AM0806-5	0.92	11.70	50.82	11.39	19.27	2.82	0.70	0.29	0.36	0.01	0.51	0.00	**98.8**
		2	AM0806-6c	0.93	11.76	50.28	11.33	19.42	2.79	0.72	0.29	0.37	0.00	0.50	0.00	**98.4**
		2	AM0806-6r	1.25	11.03	48.05	10.97	20.18	4.32	0.65	0.47	0.79	0.01	0.56	0.01	**98.3**
		2	AM0806-7	1.66	10.77	46.73	10.56	20.02	5.50	0.76	0.61	1.28	0.00	0.57	0.01	**98.5**
		2	AM0806-8c	1.69	10.71	46.62	10.70	20.15	5.55	0.78	0.63	1.38	0.00	0.57	0.01	**98.8**
		2	AM0806-8r	1.69	10.75	46.84	10.50	20.25	5.16	0.75	0.58	1.30	0.00	0.59	0.02	**98.4**
		2	AM0806-9c	0.66	11.35	50.74	11.62	19.18	2.69	0.59	0.25	0.28	0.01	0.48	0.00	**97.9**
		2	AM0806-9r	0.60	11.76	50.89	12.06	19.55	2.22	0.53	0.22	0.14	0.01	0.42	0.00	**98.4**
		2	AM0806-10r	1.71	10.40	46.90	10.57	20.20	5.63	0.74	0.62	1.38	0.00	0.57	0.00	**98.7**
	AM0826	2	AM0826-1-1	0.81	18.32	54.11	12.48	9.65	2.39	0.64	0.23	0.36	0.01	0.22	0.02	**99.2**
		2	AM0826-1-2	1.07	17.92	53.05	11.91	10.09	2.84	0.65	0.35	0.67	0.00	0.20	0.01	**98.8**
		2	AM0826-2c1	0.85	18.41	54.08	12.33	9.48	3.05	0.71	0.33	0.66	0.01	0.18	0.01	**100.1**
		2	AM0826-2r	1.23	16.80	50.72	11.82	10.81	4.00	0.64	0.43	0.87	0.00	0.18	0.00	**97.5**
		2	AM0826-2rx2	1.16	17.70	52.25	12.05	10.13	3.43	0.75	0.40	0.75	0.00	0.18	0.01	**98.8**
		2	AM0826-4c	1.31	16.42	50.28	11.79	11.30	4.36	0.72	0.48	0.93	0.01	0.18	0.01	**97.8**
		2	AM0826-4r	0.88	17.63	52.64	12.16	9.80	3.21	0.61	0.33	0.64	0.00	0.22	0.00	**98.1**
		2	AM0826-4rx2	1.15	17.31	51.46	11.98	10.37	3.70	0.66	0.42	0.78	0.01	0.21	0.00	**98.0**
		2	AM0826-5r	1.24	17.91	52.28	12.16	10.09	3.72	0.81	0.42	0.87	0.01	0.12	0.00	**99.6**
		2	AM0826-5rx2	0.59	18.01	53.87	12.37	9.72	1.72	0.60	0.14	0.18	0.00	0.19	0.00	**97.4**

Formation	Sample	Analytical session	Sample-Grain	Na_2O	MgO	SiO_2	CaO	FeO	Al_2O_3	F	K_2O	TiO_2	Cr_2O_3	MnO	NiO	Total
		2	AM0826-5rx3	0.97	17.33	51.80	11.89	9.95	3.33	0.68	0.36	0.69	0.00	0.19	0.00	**97.2**
	RJ1103	2	RJ1103-1c	1.26	12.58	46.26	11.03	16.72	5.78	0.23	0.60	1.32	0.00	0.57	0.00	**96.3**
		2	RJ1103-1r	1.26	13.17	47.15	11.09	15.63	5.44	0.22	0.54	1.30	0.01	0.58	0.00	**96.4**
		2	RJ1103-1rx2	1.24	13.33	47.26	11.02	15.63	5.60	0.26	0.57	1.27	0.00	0.59	0.01	**96.8**
		2	RJ1103-1rx3	1.18	12.97	47.36	10.99	16.18	5.47	0.23	0.52	1.27	0.00	0.59	0.01	**96.8**
		2	RJ1103-2r	1.15	12.88	47.39	11.01	16.22	5.41	0.22	0.53	1.15	0.00	0.57	0.00	**96.5**
		2	RJ1103-2r	1.88	13.95	46.19	10.82	14.17	6.81	0.20	0.22	1.99	0.01	0.40	0.01	**96.6**
		2	RJ1103-3c	0.99	14.06	48.84	11.34	14.52	4.98	0.21	0.46	1.07	0.00	0.57	0.00	**97.0**
		2	RJ1103-3r	1.23	13.43	47.55	11.34	15.58	5.58	0.24	0.52	1.27	0.00	0.57	0.00	**97.3**
		2	RJ1103-3rx2	0.90	14.26	50.50	11.72	14.99	4.14	0.26	0.37	0.80	0.00	0.55	0.00	**98.5**
		2	RJ1103-4	1.13	13.45	48.56	11.09	16.20	5.01	0.25	0.47	1.08	0.00	0.61	0.00	**97.8**
		2	RJ1103-4rg2	1.13	13.04	47.56	10.88	16.22	4.93	0.22	0.47	1.07	0.00	0.61	0.01	**96.2**
		2	RJ1103-4x2	1.29	12.67	46.62	11.20	16.41	5.77	0.24	0.58	1.29	0.01	0.60	0.00	**96.7**
		2	RJ1103-5g2	1.12	13.43	47.66	10.99	15.90	5.05	0.25	0.46	1.15	0.00	0.57	0.00	**96.6**
		2	RJ1103-5g3r	1.23	13.26	47.16	11.23	15.48	5.76	0.29	0.53	1.33	0.00	0.56	0.00	**96.8**
		2	RJ1103-5r	1.13	13.11	47.96	10.69	16.09	5.17	0.25	0.45	1.08	0.00	0.64	0.00	**96.6**
		2	RJ1103-5rx2	1.08	13.34	47.37	11.15	15.21	5.35	0.22	0.50	1.16	0.01	0.56	0.00	**95.9**
		2	RJ1103-6c	1.40	12.56	47.19	10.96	17.10	5.85	0.21	0.57	1.35	0.01	0.58	0.00	**97.8**
		2	RJ1103-6r	1.24	12.90	47.56	11.16	16.38	5.58	0.22	0.55	1.26	0.00	0.61	0.00	**97.5**
		2	RJ1103-7	1.13	13.39	48.02	11.30	15.73	5.01	0.25	0.45	1.01	0.00	0.52	0.01	**96.8**
		2	RJ1103-8c	1.27	13.49	47.88	11.29	15.74	5.55	0.28	0.55	1.27	0.00	0.60	0.01	**97.9**
		2	RJ1103-8r	1.05	13.69	48.13	11.32	14.72	5.02	0.24	0.47	1.12	0.00	0.58	0.01	**96.4**
Tierras Blances Caldera	**RJ1106**	2	RJ1106-1c	2.29	14.11	44.48	10.69	13.87	8.01	0.31	0.25	2.19	0.00	0.33	0.01	**96.5**
		2	RJ1106-1r	2.17	13.58	44.77	10.60	13.93	7.96	0.17	0.27	2.43	0.01	0.36	0.01	**96.3**
		2	RJ1106-3r	2.19	13.97	46.06	10.90	14.30	7.51	0.22	0.28	2.29	0.00	0.36	0.00	**98.1**
		2	RJ1106-4r	1.80	14.01	47.34	10.78	14.53	6.56	0.16	0.25	2.06	0.00	0.38	0.00	**97.9**
		2	RJ1106-4x2	1.23	14.87	49.55	11.07	14.02	5.09	0.18	0.24	1.60	0.00	0.36	0.00	**98.2**

Formation	Sample	Analytical session	Sample-Grain	Na_2O	MgO	SiO_2	CaO	FeO	Al_2O_3	F	K_2O	TiO_2	Cr_2O_3	MnO	NiO	Total
		2	RJ1106-5r	2.13	13.77	46.02	10.77	14.37	7.50	0.25	0.30	2.26	0.00	0.36	0.01	**97.7**
		2	RJ1106-5rx2	2.22	14.30	45.78	10.73	14.10	7.50	0.26	0.26	2.18	0.00	0.36	0.01	**97.7**
		2	RJ1106-6	2.02	13.95	45.87	10.70	14.05	6.88	0.18	0.26	2.06	0.00	0.35	0.02	**96.3**
		2	RJ1106-6r	1.79	14.74	47.12	10.97	14.17	5.41	0.16	0.23	1.74	0.01	0.36	0.00	**96.7**
		2	RJ1106-7	2.22	13.65	44.45	10.79	14.40	7.73	0.24	0.29	2.38	0.00	0.35	0.02	**96.5**
		2	RJ1106-7r	2.02	14.27	46.17	10.78	13.83	6.84	0.21	0.24	2.00	0.00	0.36	0.00	**96.7**
		2	RJ1106-8	2.12	13.87	45.40	10.61	14.17	7.39	0.18	0.27	2.19	0.00	0.38	0.01	**96.6**
		2	RJ1106-8r	1.62	13.69	45.35	10.79	14.17	7.34	0.14	0.28	2.29	0.00	0.35	0.01	**96.0**
		2	RJ1106-9x2	2.06	14.32	46.51	10.78	14.47	6.82	0.19	0.24	2.13	0.01	0.37	0.01	**97.9**
		2	RJ1106-9	2.17	14.68	46.66	10.80	13.56	6.97	0.27	0.25	2.14	0.01	0.36	0.00	**97.9**
		2	RJ1106-10	2.12	14.29	46.40	10.91	14.48	7.18	0.21	0.27	2.10	0.00	0.36	0.01	**98.3**
Bocatoma Unit	**AM0868**	2	AM0868-1g1c	1.45	13.63	44.64	11.58	14.08	9.20	0.18	0.71	1.59	0.01	0.50	0.00	**97.6**
		2	AM0868-1g1r	1.53	13.35	43.85	11.18	13.81	9.16	0.20	0.67	1.51	0.00	0.50	0.00	**95.8**
		2	AM0868-1g2	1.37	13.54	43.90	11.07	13.85	8.74	0.15	0.64	1.53	0.01	0.55	0.00	**95.3**
		2	AM0868-2r	1.52	12.39	43.43	11.43	15.70	9.92	0.17	0.90	1.55	0.01	0.54	0.00	**97.5**
		2	AM0868-2rx2	1.47	12.71	43.25	11.35	15.45	9.62	0.17	0.88	1.57	0.01	0.57	0.00	**97.0**
		2	AM0868-3c	1.43	10.66	42.90	11.79	17.87	10.27	0.09	1.23	1.33	0.01	0.60	0.00	**98.2**
		2	AM0868-3r	1.37	10.51	42.65	11.73	17.74	10.34	0.11	1.28	1.45	0.00	0.62	0.01	**97.8**
		2	AM0868-3rx2	1.34	10.46	42.62	11.72	18.17	10.52	0.15	1.31	1.30	0.00	0.63	0.00	**98.2**
		2	AM0868-4r	1.33	14.04	46.42	11.54	13.85	8.14	0.21	0.64	1.50	0.01	0.52	0.00	**98.2**
		2	AM0868-5r	1.31	12.70	45.20	11.60	15.58	8.29	0.16	0.65	1.31	0.01	0.70	0.01	**97.5**
		2	AM0868-6r	1.36	12.69	45.11	11.49	15.05	9.03	0.15	0.80	1.44	0.00	0.59	0.00	**97.7**
		2	AM0868-7	1.40	12.53	44.23	11.53	15.63	9.36	0.18	0.91	1.47	0.00	0.57	0.01	**97.8**
		2	AM0868-8c	1.36	13.90	45.73	11.44	14.07	8.65	0.18	0.64	1.50	0.00	0.54	0.00	**98.0**
		2	AM0868-8r	1.27	14.70	47.24	11.36	13.15	7.65	0.18	0.50	1.31	0.01	0.55	0.00	**97.9**
		2	AM0868-9c	1.40	12.78	45.10	11.38	15.46	9.16	0.18	0.79	1.48	0.01	0.58	0.00	**98.3**
		2	AM0868-9r	1.31	13.49	46.23	11.50	14.71	8.35	0.18	0.65	1.31	0.00	0.57	0.00	**98.3**

Formation	Sample	Analytical session	Sample-Grain	Na_2O	MgO	SiO_2	CaO	FeO	Al_2O_3	F	K_2O	TiO_2	Cr_2O_3	MnO	NiO	Total
		2	AM0868-10	1.40	14.14	46.43	11.45	13.64	8.11	0.20	0.58	1.41	0.00	0.53	0.01	**97.9**
	AM0870	1	AM0870-01x2	1.40	12.80	44.67	11.34	14.78	9.18	0.20	0.82	1.47	0.01	0.59	0.00	**97.3**
		1	AM0870-03x2	1.53	12.61	43.83	11.43	15.14	9.96	0.21	0.89	1.65	0.00	0.56	0.00	**97.8**
		1	AM0870-03x3	1.41	13.07	44.18	11.44	14.48	9.31	0.23	0.80	1.65	0.02	0.51	0.00	**97.1**
		1	AM0870-06	1.31	11.95	44.48	11.30	16.39	9.54	0.15	0.90	1.38	0.01	0.64	0.00	**98.0**
		1	AM0870-07	1.28	12.95	45.55	11.32	15.35	8.46	0.17	0.77	1.41	0.00	0.60	0.01	**97.9**
		1	AM0870-11	1.53	11.72	42.77	11.36	15.97	10.33	0.21	1.04	1.61	0.01	0.54	0.01	**97.1**
		1	AM0870-11x2	1.48	12.75	44.52	11.37	15.05	9.09	0.21	0.82	1.39	0.01	0.57	0.00	**97.3**
		1	AM0870-11x3	1.54	12.01	43.14	11.44	15.55	9.96	0.14	0.94	1.82	0.00	0.51	0.00	**97.1**
		1	AM0870-12x1	1.57	12.33	43.93	11.34	15.52	9.77	0.19	0.99	1.65	0.00	0.54	0.00	**97.8**
		1	AM0870-12x2	1.55	12.67	43.82	11.30	15.25	9.95	0.24	0.79	1.57	0.00	0.55	0.00	**97.7**
		1	AM0870-13	1.41	12.74	45.25	11.24	15.25	8.91	0.24	0.76	1.47	0.00	0.64	0.00	**97.9**
		1	AM0870-17x1	1.21	13.16	45.93	11.57	14.87	8.58	0.22	0.72	1.29	0.01	0.63	0.01	**98.2**
Tilito Formation	**ZN122**	2	ZN122-1c	1.59	14.17	45.90	11.47	13.60	8.12	0.48	0.95	1.93	0.00	0.25	0.00	**98.5**
		2	ZN122-1r	1.43	15.18	47.18	11.59	13.21	6.95	0.54	0.70	1.64	0.00	0.25	0.01	**98.7**
		2	ZN122-2c	2.12	14.44	41.04	11.44	11.36	12.52	0.21	0.87	2.45	0.00	0.14	0.01	**96.6**
		2	ZN122-2r	2.27	14.38	41.28	11.47	11.94	12.95	0.22	0.85	2.49	0.01	0.14	0.00	**98.0**
		2	ZN122-2r-repeat	2.20	14.21	40.71	11.47	11.77	13.05	0.22	0.87	2.45	0.01	0.14	0.00	**97.1**
		2	ZN122-3c	1.44	14.66	46.98	11.48	13.74	7.15	0.43	0.76	1.74	0.00	0.29	0.00	**98.7**
		2	ZN122-3r	1.55	14.05	45.70	11.46	13.76	8.01	0.34	0.91	1.93	0.00	0.27	0.02	**98.0**
		2	ZN122-4c	1.41	14.98	46.37	11.69	13.14	7.14	0.51	0.77	1.74	0.00	0.25	0.01	**98.0**
		2	ZN122-4r	1.54	14.57	44.33	11.34	13.86	7.67	0.47	0.86	1.86	0.00	0.24	0.03	**96.8**
		2	ZN122-5	1.54	14.03	44.66	11.18	13.57	8.13	0.48	0.90	1.97	0.00	0.24	0.00	**96.7**
		2	ZN122-5x2	1.61	14.28	45.12	11.41	13.49	8.12	0.48	0.88	1.97	0.00	0.24	0.01	**97.6**
		2	ZN122-6	1.48	14.02	44.86	11.27	13.87	7.66	0.39	0.87	1.85	0.00	0.29	0.01	**96.6**
		2	ZN122-7r	1.51	14.08	44.85	11.34	13.81	7.76	0.44	0.86	1.87	0.00	0.28	0.00	**96.8**
		2	ZN122-8c	1.63	13.96	44.80	11.35	13.91	8.78	0.38	0.90	1.99	0.00	0.23	0.01	**98.0**

Formation	Sample	Analytical session	Sample-Grain	Na_2O	MgO	SiO_2	CaO	FeO	Al_2O_3	F	K_2O	TiO_2	Cr_2O_3	MnO	NiO	Total
		2	ZN122-8r	1.66	13.78	44.26	11.30	14.59	8.45	0.38	0.97	1.95	0.00	0.27	0.01	**97.6**
		2	ZN122-9	1.56	13.73	44.18	11.36	13.74	8.14	0.36	0.95	1.95	0.01	0.26	0.00	**96.2**
		2	ZN122-10	1.97	12.17	41.34	11.42	15.92	10.79	0.44	0.95	3.07	0.00	0.27	0.01	**98.4**
Miocene Intrusives	**RJ11A14**	2	RJ11A14-1c	0.98	16.03	49.60	11.90	12.16	4.52	0.30	0.38	0.87	0.00	0.55	0.00	**97.3**
		2	RJ11A14-1r	0.99	16.06	50.34	11.96	11.88	4.39	0.33	0.36	0.92	0.00	0.54	0.00	**97.8**
		2	RJ11A14-1rx2	0.99	16.09	50.50	11.95	11.61	4.48	0.32	0.37	0.95	0.00	0.53	0.02	**97.8**
		2	RJ11A14-2c	0.89	16.26	50.42	11.96	11.57	4.10	0.31	0.33	0.82	0.00	0.53	0.00	**97.2**
		2	RJ11A14-2r	0.67	17.29	52.50	12.10	10.62	3.22	0.28	0.23	0.49	0.00	0.56	0.00	**98.0**
		2	RJ11A14-4r	1.01	15.80	49.94	11.13	12.29	4.40	0.29	0.36	0.90	0.01	0.83	0.00	**97.0**
		2	RJ11A14-4rx2	1.00	15.47	49.87	11.78	12.32	4.90	0.32	0.43	1.06	0.01	0.55	0.00	**97.7**
		2	RJ11A14-5c	0.67	16.66	51.93	12.24	11.40	3.30	0.27	0.24	0.53	0.01	0.47	0.01	**97.7**
		2	RJ11A14-5r	0.76	16.56	51.35	12.17	11.08	3.71	0.30	0.29	0.66	0.01	0.48	0.01	**97.4**
		2	RJ11A14-5rx2	0.91	16.05	49.97	11.66	11.76	4.33	0.32	0.29	0.68	0.01	0.57	0.00	**96.5**
		2	RJ11A14-6c	1.18	16.22	49.31	11.36	12.29	5.01	0.35	0.48	1.08	0.00	0.54	0.01	**97.8**
		2	RJ11A14-6r	1.18	15.22	47.61	11.07	12.74	5.30	0.30	0.49	1.07	0.01	0.59	0.00	**95.6**
		2	RJ11A14-7rx1	1.03	15.82	49.37	12.03	12.37	4.96	0.32	0.45	0.88	0.00	0.48	0.00	**97.7**
		2	RJ11A14-7rx2	0.57	17.19	52.12	12.06	10.61	3.05	0.31	0.19	0.42	0.00	0.54	0.00	**97.0**
		2	RJ11A14-9r	0.97	16.27	50.23	11.29	11.91	4.06	0.31	0.36	0.90	0.00	0.64	0.00	**96.9**
		2	RJ11A14-9rx2	1.05	16.15	49.60	11.93	11.98	4.83	0.29	0.43	0.93	0.01	0.53	0.00	**97.7**
		2	RJ11A14-10c	1.12	15.59	50.12	11.79	12.96	5.03	0.35	0.47	1.10	0.00	0.62	0.01	**99.2**
		2	RJ11A14-10r	1.17	15.34	49.29	11.79	12.88	5.29	0.32	0.50	1.14	0.01	0.56	0.00	**98.3**
		2	RJ11A14-10x2	0.64	17.45	52.20	12.21	10.60	3.40	0.28	0.27	0.62	0.00	0.53	0.00	**98.2**
Upper Cerro de las	**MQ28**	2	MQ28-1r	2.49	14.09	41.90	11.11	13.04	9.99	1.15	0.73	3.24	0.00	0.23	0.00	**98.0**
Tórtolas Formation		2	MQ28-1x2	2.31	15.21	41.35	12.02	9.86	12.64	0.21	0.81	2.30	0.03	0.10	0.00	**96.8**
		2	MQ28-2r	2.40	13.65	41.62	11.18	12.54	10.47	0.38	0.76	3.28	0.01	0.24	0.00	**96.5**
		2	MQ28-3	2.46	14.18	40.84	11.63	11.54	12.09	0.36	0.63	2.68	0.01	0.15	0.01	**96.6**
		2	MQ28-3r	2.46	14.51	42.58	11.38	11.96	9.81	1.06	0.72	3.27	0.00	0.21	0.01	**98.0**

Formation	Sample	Analytical session	Sample-Grain	Na_2O	MgO	SiO_2	CaO	FeO	Al_2O_3	F	K_2O	TiO_2	Cr_2O_3	MnO	NiO	Total
		2	MQ28-4r	2.42	15.09	42.18	11.49	10.21	11.48	0.35	0.59	2.88	0.01	0.09	0.01	**96.8**
		2	MQ28-5c	2.58	14.33	41.23	11.29	11.35	11.64	0.30	0.67	3.09	0.00	0.20	0.01	**96.7**
		2	MQ28-5r	2.44	13.83	42.95	11.19	12.58	10.05	0.42	0.73	3.32	0.00	0.22	0.01	**97.7**
		2	MQ28-6c	2.41	15.22	42.51	11.40	9.92	11.63	0.17	0.64	2.72	0.24	0.10	0.03	**97.0**
		2	MQ28-6r	2.42	15.41	41.98	11.34	9.90	11.46	0.52	0.62	2.79	0.23	0.10	0.03	**96.8**
		2	MQ28-7g1c	2.43	14.78	41.62	11.47	10.54	11.93	0.20	0.65	2.76	0.07	0.11	0.03	**96.6**
		2	MQ28-7g1r	2.38	14.20	41.67	11.25	11.56	11.61	0.63	0.61	2.78	0.00	0.12	0.03	**96.8**
		2	MQ28-7g2r	2.38	14.37	41.52	11.16	11.65	11.02	0.92	0.65	3.06	0.01	0.15	0.01	**96.9**
		2	MQ28-9c	2.39	14.96	42.06	11.59	10.22	12.00	0.15	0.67	2.65	0.16	0.10	0.02	**97.0**
		2	MQ28-9i	2.49	15.50	42.98	11.51	9.96	11.51	0.19	0.62	2.73	0.04	0.09	0.02	**97.6**
		2	MQ28-9r	2.42	14.83	41.73	11.42	11.07	11.92	0.81	0.67	2.97	0.07	0.10	0.02	**98.0**
		2	MQ28-10c	2.48	15.90	40.85	12.29	8.53	13.28	0.09	0.76	2.18	0.32	0.10	0.01	**96.8**
		2	MQ28-10i	2.60	14.24	40.31	11.80	11.00	13.00	0.31	0.74	2.51	0.01	0.17	0.00	**96.7**
		2	MQ28-10r	2.77	13.96	41.38	11.29	12.06	10.69	0.95	0.70	3.72	0.00	0.21	0.00	**97.7**
		2	MQ28-11c	2.50	14.50	41.76	11.39	11.50	11.50	0.26	0.61	2.80	0.01	0.18	0.00	**97.0**
		2	MQ28-11r	2.57	14.23	41.33	11.48	11.55	11.49	0.36	0.64	3.13	0.00	0.19	0.01	**97.0**
Tertiary Intrusives	**RJ11A15**	2	RJ11A15-1c	1.77	12.97	46.21	11.22	15.51	8.38	0.18	0.49	0.99	0.00	0.49	0.00	**98.2**
		2	RJ11A15-1g2	1.67	13.12	46.52	11.21	15.29	8.26	0.19	0.50	1.24	0.00	0.47	0.00	**98.5**
		2	RJ11A15-1r	1.75	12.59	45.52	11.26	16.05	8.85	0.17	0.66	1.13	0.00	0.46	0.00	**98.5**
		2	RJ11A15-1rx2	1.63	13.46	47.44	11.19	14.83	7.86	0.19	0.49	1.09	0.00	0.49	0.01	**98.7**
		2	RJ11A15-2r	1.65	13.21	46.71	11.32	15.49	8.05	0.21	0.47	1.17	0.00	0.47	0.00	**98.8**
		2	RJ11A15-2rx2	1.59	13.09	46.30	11.30	15.61	8.17	0.16	0.54	1.04	0.01	0.43	0.00	**98.2**
		2	RJ11A15-3c	2.63	14.24	42.76	11.51	11.83	12.43	0.11	0.62	2.20	0.02	0.10	0.00	**98.4**
		2	RJ11A15-3r	2.61	13.33	42.02	11.91	13.51	12.43	0.14	0.56	2.47	0.00	0.13	0.00	**99.1**
		2	RJ11A15-4c	1.93	11.96	44.58	11.43	15.54	10.09	0.20	0.70	1.36	0.30	0.43	0.01	**98.5**
		2	RJ11A15-4m	1.92	12.09	44.83	11.41	16.13	9.92	0.21	0.73	1.37	0.02	0.42	0.01	**99.1**
		2	RJ11A15-4r	1.84	11.87	44.81	11.41	17.10	9.17	0.18	0.67	1.18	0.02	0.46	0.00	**98.7**

Formation	Sample	Analytical session	Sample-Grain	Na_2O	MgO	SiO_2	CaO	FeO	Al_2O_3	F	K_2O	TiO_2	Cr_2O_3	MnO	NiO	Total
		2	RJ11A15-5rx1	1.70	12.61	46.05	11.36	16.06	8.66	0.18	0.56	1.04	0.00	0.43	0.00	**98.7**
		2	RJ11A15-5rx2	1.58	13.35	47.23	11.24	15.45	7.51	0.21	0.39	0.96	0.00	0.41	0.00	**98.3**
		2	RJ11A15-7r	1.81	11.62	44.68	11.42	17.13	9.20	0.19	0.68	1.08	0.01	0.44	0.00	**98.3**
		2	RJ11A15-8c	1.89	12.41	45.37	11.26	16.19	9.01	0.20	0.63	1.30	0.01	0.45	0.00	**98.7**
		2	RJ11A15-8rx1	1.75	12.44	45.69	11.44	16.10	8.65	0.19	0.52	1.13	0.00	0.43	0.01	**98.3**
		2	RJ11A15-8rx2	1.71	12.88	46.43	11.49	15.82	8.13	0.18	0.50	1.04	0.01	0.45	0.00	**98.6**
		2	RJ11A15-9c	1.91	12.42	45.23	11.35	16.31	9.19	0.18	0.55	1.19	0.00	0.46	0.00	**98.8**
		2	RJ11A15-9r	1.70	13.14	46.71	11.15	15.03	8.22	0.18	0.50	1.02	0.00	0.45	0.00	**98.1**
		2	RJ11A15-10	1.54	14.02	47.83	11.19	14.67	7.48	0.18	0.45	1.06	0.02	0.47	0.00	**98.9**
	RJ11A7	2	RJ11A7-1c	2.77	17.83	44.13	11.15	7.31	11.42	0.10	0.77	1.53	0.80	0.09	0.02	**97.9**
		2	RJ11A7-1r	2.98	15.09	42.15	11.19	10.47	11.83	0.56	0.63	2.02	0.01	0.12	0.00	**97.0**
		2	RJ11A7-2r	2.89	14.07	41.86	10.65	11.51	12.59	0.17	0.72	1.87	0.00	0.15	0.01	**96.5**
		2	RJ11A7-2rx2	2.64	15.67	43.45	11.11	8.48	11.12	0.20	0.59	1.95	0.00	0.10	0.01	**95.3**
		2	RJ11A7-3c	3.01	17.47	44.01	10.71	7.71	12.27	0.18	0.84	1.52	0.04	0.09	0.01	**97.8**
		2	RJ11A7-3r	3.07	17.51	43.94	10.78	7.33	12.32	0.21	0.84	1.43	0.18	0.10	0.02	**97.7**
		2	RJ11A7-4r	2.92	16.06	43.24	10.92	9.53	12.09	0.25	0.71	1.90	0.02	0.11	0.01	**97.8**
		2	RJ11A7-5g1r	2.74	17.09	43.65	10.71	7.57	12.01	0.19	0.73	1.53	0.15	0.11	0.02	**96.5**
		2	RJ11A7-5g2r	3.01	17.43	43.42	10.89	7.16	11.98	0.39	0.79	1.52	0.21	0.08	0.03	**96.9**
		2	RJ11A7-6c	3.02	17.00	42.42	10.59	8.11	13.61	0.07	0.83	1.48	0.39	0.10	0.00	**97.6**
		2	RJ11A7-6r	3.00	17.89	44.72	10.78	6.78	11.93	0.29	0.85	1.41	0.51	0.09	0.03	**98.3**
		2	RJ11A7-7r	2.84	17.00	43.92	10.97	7.38	11.84	0.09	0.78	1.57	0.15	0.10	0.01	**96.7**
		2	RJ11A7-8r	2.93	15.99	43.83	11.05	9.69	11.67	0.18	0.68	1.80	0.06	0.12	0.01	**98.0**
		2	RJ11A7-9g2r	2.92	18.24	44.52	11.04	7.02	11.29	0.30	0.72	1.49	0.27	0.09	0.04	**97.9**
		2	RJ11A7-9r	2.75	16.33	43.36	11.55	9.34	11.67	0.18	0.69	1.84	0.07	0.10	0.02	**97.9**
		2	RJ11A7-10	2.86	17.10	43.89	10.94	8.15	12.27	0.17	0.79	1.63	0.13	0.10	0.03	**98.1**

Appendix 1.10 Zircon U-Pb data

Sample	Grain	Analysis location	U (ppm)	Th (ppm)	Pb (ppm)	Th/U (atomic)	^{204}Pb (ppb)	f206 (%)	^{204}Pb/^{206}Pb	Corrected ratios ^{207}Pb/^{206}Pb	1σ	^{208}Pb/^{206}Pb	1σ	^{207}Pb/^{235}U	1σ	^{206}Pb/^{238}U	1σ	ρ	Ages (Ma) ^{206}Pb/^{238}U	1σ	^{207}Pb/^{235}U	1σ	^{207}Pb/^{206}Pb	1σ	% con.	Comment
Pluton Tocota (Colangüil Batholith)																										
RJ11A18	4		89.8	37.0	4.1	0.42	0.7	0.35	0.00019	0.0498	0.0010	0.1301	0.0011	0.3031	0.0069	0.0442	0.0004	0.44	**278.7**	**2.7**	268.8	5.3	183.0	46.0	52.3	
	9	rim	63.7	32.5	3.0	0.52	0.2	0.14	Th cor	0.0508	0.0008	Th cor	Th cor	0.3135	0.0059	0.0447	0.0005	0.59	**282.0**	**3.1**	207/206		207/206			
	11		82.2	73.0	4.1	0.91	0.5	0.33	0.00018	0.0495	0.0009	0.2907	0.0034	0.2928	0.0064	0.0429	0.0005	0.49	**270.8**	**2.9**	260.8	5.0	171.0	44.0	58.3	
	13	rim	56.4	33.5	2.7	0.61	0.2	0.13	Th cor	0.0508	0.0010	Th cor	Th cor	0.3141	0.0069	0.0448	0.0005	0.48	**282.6**	**2.9**	207/206		207/206			
	14		38.3	15.8	1.7	0.42	0.4	0.56	Th cor	0.0508	0.0016	Th cor	Th cor	0.3086	0.0105	0.0441	0.0006	0.40	**278.1**	**3.7**	207/206		207/206			
	19		49.5	31.1	2.4	0.64	0.4	0.35	Th cor	0.0509	0.0013	Th cor	Th cor	0.3153	0.0086	0.0450	0.0005	0.39	**283.5**	**2.9**	207/206		207/206			
	29		62.3	41.4	3.0	0.68	0.5	0.37	Th cor	0.0508	0.0013	Th cor	Th cor	0.3094	0.0084	0.0442	0.0005	0.43	**278.8**	**3.2**	207/206		207/206			
Choiyoi Group/Pastos Blancos Group																										
MQ39	13		100.2	71.9	4.8	0.74	0.4	0.20	0.00011	0.0500	0.0005	0.2378	0.0018	0.2961	0.0052	0.0429	0.0006	0.83	**270.9**	**3.8**	263.3	4.0	196.0	23.0	38.2	
	21		151.3	101.9	7.1	0.69	0.5	0.17	0.00009	0.0506	0.0008	0.2250	0.0013	0.2975	0.0062	0.0427	0.0006	0.67	**269.3**	**3.7**	264.5	4.8	221.0	35.0	21.9	
	22		220.2	129.9	10.2	0.60	0.8	0.17	0.00009	0.0502	0.0004	0.1939	0.0016	0.2978	0.0044	0.0430	0.0005	0.79	**271.6**	**3.1**	264.7	3.4	204.0	20.0	33.1	
	23	core	67.5	62.3	3.4	0.95	0.3	0.19	Th cor	0.0509	0.0012	Th cor	Th cor	0.3041	0.0083	0.0434	0.0005	0.44	**273.6**	**3.2**	207/206		207/206			
	24		296.6	312.8	15.5	1.08	0.7	0.12	0.00007	0.0523	0.0005	0.3547	0.0028	0.3123	0.0047	0.0433	0.0005	0.73	**273.5**	**2.9**	276.0	3.6	296.0	23.0	-7.6	
	28		130.3	81.1	5.9	0.64	0.1	0.06	0.00003	0.0531	0.0008	0.2078	0.0025	0.3067	0.0057	0.0419	0.0005	0.59	**264.3**	**2.8**	271.6	4.4	334.0	34.0	-20.9	
	30		128.6	85.9	6.1	0.69	0.8	0.30	0.00016	0.0491	0.0008	0.2187	0.0015	0.2906	0.0066	0.0430	0.0006	0.64	**271.1**	**3.9**	259.0	5.2	150.0	40.0	80.8	
	31		169.7	121.0	8.1	0.73	0.7	0.20	0.00011	0.0507	0.0005	0.2345	0.0022	0.3025	0.0053	0.0433	0.0006	0.82	**273.1**	**3.8**	268.3	4.1	226.0	23.0	20.9	
RJ11A20	12		227.1	197.6	11.1	0.89	0.2	0.05	0.00003	0.0527	0.0005	0.2910	0.0015	0.3084	0.0043	0.0425	0.0005	0.77	**268.1**	**2.9**	273.0	3.4	314.0	20.0	-14.6	
	14	core	227.7	143.8	10.5	0.65	0.7	0.16	0.00008	0.0509	0.0006	0.2076	0.0011	0.2985	0.0049	0.0425	0.0005	0.70	**268.3**	**3.0**	265.3	3.8	238.0	27.0	12.7	
	15		339.4	256.6	16.8	0.78	1.0	0.14	0.00008	0.0499	0.0006	0.2479	0.0019	0.3028	0.0049	0.0440	0.0005	0.70	**277.5**	**3.0**	268.6	3.8	191.0	27.0	45.3	
	18		285.9	427.6	16.3	1.53	0.5	0.08	0.00004	0.0514	0.0004	0.5023	0.0018	0.3039	0.0041	0.0429	0.0005	0.83	**270.7**	**3.0**	269.5	3.2	258.0	17.0	4.9	
	20		116.2	132.6	6.0	1.17	0.7	0.32	0.00017	0.0493	0.0009	0.3788	0.0023	0.2856	0.0062	0.0421	0.0005	0.54	**265.5**	**3.0**	255.1	4.9	160.0	42.0	66.0	
	35	rim	169.7	179.1	8.6	1.08	0.9	0.26	0.00014	0.0495	0.0007	0.3475	0.0030	0.2879	0.0056	0.0422	0.0005	0.63	**266.2**	**3.2**	256.9	4.4	172.0	35.0	54.8	
AM0862	10		73.9	58.7	3.6	0.81	0.4	0.28	Th cor	0.0507	0.0008	Th cor	Th cor	0.3042	0.0063	0.0435	0.0006	0.67	**274.7**	**3.8**	207/206		207/206			
	13		87.1	93.7	4.4	1.10	1.3	0.79	0.00042	0.0476	0.0013	0.3369	0.0032	0.2742	0.0083	0.0418	0.0006	0.49	**263.9**	**3.8**	246.0	6.6	78.0	62.0	238.3	
	20	core	168.6	116.0	8.0	0.71	0.2	0.07	0.00004	0.0528	0.0007	0.2215	0.0016	0.3128	0.0063	0.0430	0.0007	0.75	**271.4**	**4.0**	276.4	4.9	318.0	30.0	-14.6	
	20	rim	280.8	80.4	11.9	0.29	0.1	0.02	0.00001	0.0528	0.0007	0.0909	0.0007	0.3117	0.0061	0.0428	0.0006	0.71	**270.3**	**3.6**	275.5	4.7	319.0	31.0	-15.3	
	24		138.1	162.3	7.2	1.21	0.2	0.09	0.00005	0.0515	0.0010	0.3765	0.0029	0.3001	0.0073	0.0423	0.0006	0.58	**266.8**	**3.6**	266.5	5.7	263.0	44.0	1.5	
	32		71.5	62.4	3.5	0.89	1.0	0.71	Th cor	0.0506	0.0015	Th cor	Th cor	0.2992	0.0099	0.0429	0.0007	0.48	**270.6**	**4.2**	207/206		207/206			
AM0853	8		392.6	341.2	18.7	0.89	3.2	0.42	0.00023	0.0495	0.0007	0.2782	0.0015	0.2826	0.0049	0.0414	0.0004	0.62	**261.4**	**2.7**	252.7	3.9	172.0	32.0	52.0	rejected, high common-Pb

Sample	Grain	Analysis location	U (ppm)	Th (ppm)	Pb (ppm)	Th/U (atomic)	^{204}Pb (ppb)	f206 (%)	^{204}Pb/^{206}Pb	Corrected ratios ^{207}Pb/^{206}Pb	1σ	^{208}Pb/^{206}Pb	1σ	^{207}Pb/^{235}U	1σ	^{206}Pb/^{238}U	1σ	ρ	Ages (Ma) ^{206}Pb/^{238}U	1σ	^{207}Pb/^{235}U	1σ	^{207}Pb/^{206}Pb	1σ	% con.	Comment
	15		281.3	247.8	13.7	0.90	0.9	0.16	0.00009	0.0501	0.0004	0.2843	0.0031	0.2901	0.0040	0.0420	0.0005	0.80	**265.1**	**2.9**	258.6	3.2	200.0	19.0	32.5	
	15		289.9	264.5	14.1	0.94	1.1	0.19	0.00010	0.0498	0.0004	0.2918	0.0029	0.2862	0.0037	0.0417	0.0004	0.83	**263.4**	**2.8**	255.6	2.9	184.0	17.0	43.2	
	19		273.6	233.4	13.0	0.87	0.8	0.15	0.00008	0.0509	0.0006	0.2750	0.0022	0.2915	0.0047	0.0415	0.0004	0.67	**262.1**	**2.8**	259.7	3.7	238.0	27.0	10.1	
	20	rim	250.6	260.3	12.7	1.07	1.7	0.34	0.00019	0.0488	0.0009	0.3273	0.0017	0.2841	0.0063	0.0423	0.0005	0.49	**266.8**	**2.8**	253.9	5.0	136.0	44.0	96.2	
	22		237.0	176.3	11.1	0.76	0.8	0.17	0.00009	0.0498	0.0005	0.2389	0.0011	0.2869	0.0045	0.0418	0.0005	0.71	**264.0**	**2.9**	256.1	3.5	184.0	26.0	43.5	
	23		264.8	320.7	13.4	1.24	2.0	0.41	0.00022	0.0483	0.0004	0.3973	0.0021	0.2692	0.0040	0.0404	0.0005	0.78	**255.4**	**2.9**	242.0	3.2	114.0	22.0	124.0	rejected, old oxygen analysis pit
	38		269.4	219.9	12.8	0.84	0.7	0.14	0.00008	0.0501	0.0007	0.2657	0.0027	0.2880	0.0052	0.0417	0.0005	0.62	**263.2**	**2.9**	257.0	4.1	200.0	33.0	31.6	
AM0855	2	core	116.6	110.2	5.4	0.97	1.8	0.82	0.00045	0.0460	0.0012	0.2953	0.0048	0.2506	0.0074	0.0395	0.0005	0.40	**250.0**	**2.9**	227.1	6.0	#N/A	#N/A	#N/A	
	3		334.1	283.8	15.4	0.87	3.7	0.59	0.00032	0.0462	0.0005	0.2659	0.0014	0.2540	0.0042	0.0399	0.0005	0.70	**252.0**	**2.9**	229.8	3.4	1.0	36.0	#####	
	9	core	111.0	108.5	5.2	1.00	1.3	0.66	0.00036	0.0467	0.0010	0.3088	0.0035	0.2529	0.0063	0.0393	0.0005	0.49	**248.5**	**3.0**	228.9	5.1	32.0	52.0	676.4	
	11		118.0	80.2	5.1	0.70	1.9	0.89	0.00048	0.0476	0.0022	0.2150	0.0055	0.2579	0.0124	0.0393	0.0005	0.27	**248.7**	**3.2**	232.9	9.9	77.0	106.0	223.0	
	23		111.5	78.9	4.7	0.73	0.3	0.16	0.00009	0.0500	0.0013	0.2314	0.0030	0.2602	0.0075	0.0377	0.0005	0.42	**238.7**	**2.8**	234.8	6.0	196.0	60.0	21.8	rejected, old oxygen analysis pit
	23	rim	267.1	197.5	11.6	0.76	0.5	0.11	0.00006	0.0502	0.0008	0.2362	0.0015	0.2701	0.0055	0.0391	0.0005	0.57	**247.0**	**2.8**	242.8	4.4	202.0	38.0	22.3	rejected, old oxygen analysis pit
	30	core	180.9	212.9	8.8	1.21	0.5	0.15	0.00008	0.0517	0.0007	0.3744	0.0030	0.2795	0.0049	0.0392	0.0005	0.69	**248.0**	**3.0**	250.3	3.9	271.0	29.0	-8.5	rejected, old oxygen analysis pit
	30	rim	132.5	94.9	5.8	0.73	0.5	0.21	0.00011	0.0515	0.0008	0.2325	0.0024	0.2795	0.0057	0.0394	0.0005	0.62	**248.9**	**3.1**	250.3	4.5	262.0	37.0	-5.0	
Ingaguás Supergroup																										
RJ1104	1		111.2	260.2	5.9	2.40	0.1	0.07	0.00004	0.0520	0.0011	0.7851	0.0054	0.2459	0.0056	0.0343	0.0003	0.44	**217.3**	**2.1**	223.2	4.5	286.0	46.0	-24.0	
	3		244.9	240.7	10.2	1.01	0.9	0.22	0.00012	0.0493	0.0007	0.3254	0.0021	0.2390	0.0040	0.0352	0.0003	0.59	**222.8**	**2.2**	217.6	3.3	161.0	32.0	38.4	
	8		70.3	38.9	2.5	0.57	0.1	0.12	Th cor	0.0497	0.0012	Th cor	Th cor	0.2357	0.0068	0.0344	0.0005	0.50	**218.2**	**3.1**	207/206		207/206			
	14		128.7	84.1	4.8	0.67	0.2	0.10	0.00006	0.0506	0.0008	0.2163	0.0025	0.2391	0.0048	0.0343	0.0004	0.57	**217.2**	**2.4**	217.7	3.9	223.0	38.0	-2.6	
	18		97.7	76.1	3.8	0.80	0.2	0.12	Th cor	0.0497	0.0007	Th cor	Th cor	0.2416	0.0044	0.0352	0.0004	0.57	**223.2**	**2.2**	207/206		207/206			
	20	core	343.3	134.5	11.8	0.40	11.6	2.12	0.00116	0.0499	0.0041	0.1339	0.0122	0.2315	0.0193	0.0337	0.0006	0.20	**213.4**	**3.6**	211.4	15.8	189.0	180.0	12.9	rejected, old oxygen analysis pit
	20	rim	654.4	463.1	25.7	0.73	0.6	0.06	0.00003	0.0504	0.0004	0.2369	0.0013	0.2466	0.0032	0.0355	0.0003	0.74	**224.9**	**2.1**	223.8	2.6	212.0	20.0	6.1	
	23		382.7	284.5	15.5	0.76	0.5	0.08	0.00004	0.0497	0.0004	0.2480	0.0082	0.2491	0.0035	0.0363	0.0004	0.79	**230.0**	**2.5**	225.8	2.8	182.0	20.0	26.4	
	36		297.6	324.0	12.7	1.12	0.7	0.14	0.00007	0.0495	0.0003	0.3789	0.0024	0.2393	0.0037	0.0351	0.0005	0.89	**222.1**	**3.0**	217.8	3.1	171.0	16.0	29.9	
Cogotí Supergroup																										
AM0812	10		123.2	91.2	1.5	0.76	0.3	0.49	Th cor	0.0472	0.0022	Th cor	Th cor	0.0733	0.0035	0.0113	0.0001	0.28	**72.2**	**1.0**	207/206		207/206			
	11		81.3	66.9	1.0	0.84	0.2	0.35	Th cor	0.0472	0.0021	Th cor	Th cor	0.0756	0.0037	0.0116	0.0002	0.35	**74.5**	**1.2**	207/206		207/206			
	14		88.4	76.5	1.2	0.89	0.6	1.29	Th cor	0.0472	0.0037	Th cor	Th cor	0.0748	0.0060	0.0115	0.0002	0.23	**73.7**	**1.4**	207/206		207/206			
	16		57.9	33.9	0.7	0.60	0.7	2.38	Th cor	0.0471	0.0048	Th cor	Th cor	0.0732	0.0078	0.0113	0.0003	0.28	**72.2**	**2.1**	207/206		207/206			
	19		90.1	78.7	1.2	0.90	0.8	1.66	Th cor	0.0472	0.0038	Th cor	Th cor	0.0774	0.0065	0.0119	0.0002	0.25	**76.2**	**1.6**	207/206		207/206			
	21	core	113.0	104.7	1.4	0.95	0.4	0.70	Th cor	0.0471	0.0024	Th cor	Th cor	0.0720	0.0063	0.0111	0.0008	0.82	**71.1**	**5.1**	207/206		207/206			rejected, primary beam drop

Sample	Grain	Analysis location	U (ppm)	Th (ppm)	Pb (ppm)	Th/U (atomic)	^{204}Pb (ppb)	f206 (%)	^{204}Pb/^{206}Pb		Corrected ratios ^{207}Pb/^{206}Pb	1σ	^{208}Pb/^{206}Pb	1σ	^{207}Pb/^{235}U	1σ	^{206}Pb/^{238}U	1σ	ρ	Ages (Ma) ^{206}Pb/^{238}U	1σ	^{207}Pb/^{235}U	1σ	^{207}Pb/^{206}Pb	1σ	% con.		Comment
	22		86.2	44.4	1.0	0.53	0.3	0.58		Th cor	0.0471	0.0019	Th cor	Th cor	0.0727	0.0032	0.0112	0.0002	0.31	**71.7**	**1.0**	207/206		207/206				
	23	core	122.1	109.1	1.6	0.92	0.2	0.37		Th cor	0.0472	0.0020	Th cor	Th cor	0.0735	0.0033	0.0113	0.0002	0.30	**72.5**	**1.0**	207/206		207/206				
	26	core	110.6	105.7	1.5	0.98	0.0	0.01		Th cor	0.0472	0.0031	Th cor	Th cor	0.0745	0.0052	0.0114	0.0003	0.32	**73.4**	**1.6**	207/206		207/206				
	38	core	83.9	74.7	1.1	0.91	0.0	0.01		Th cor	0.0472	0.0014	Th cor	Th cor	0.0747	0.0024	0.0115	0.0002	0.46	**73.6**	**1.1**	207/206		207/206				
	40	core	107.4	89.8	1.4	0.86	0.1	0.26		Th cor	0.0472	0.0019	Th cor	Th cor	0.0730	0.0032	0.0112	0.0002	0.32	**71.9**	**1.0**	207/206		207/206				
AM0823	11		171.1	87.7	1.9	0.53	0.0	0.02		Th cor	0.0472	0.0011	Th cor	Th cor	0.0714	0.0018	0.0110	0.0001	0.45	**70.4**	**0.8**	207/206		207/206				
	12	core	343.3	192.9	4.0	0.58	0.3	0.19		Th cor	0.0472	0.0010	Th cor	Th cor	0.0720	0.0019	0.0111	0.0002	0.55	**70.9**	**1.0**	207/206		207/206				
	13	core	239.1	136.9	2.7	0.59	0.0	0.02		Th cor	0.0471	0.0008	Th cor	Th cor	0.0696	0.0015	0.0107	0.0001	0.56	**68.7**	**0.8**	207/206		207/206				rejected, old oxygen analysis pit
	19	core	163.4	69.7	1.8	0.44	0.4	0.55		Th cor	0.0471	0.0008	Th cor	Th cor	0.0692	0.0015	0.0107	0.0001	0.60	**68.3**	**0.9**	207/206		207/206				
	23		114.3	49.8	1.3	0.45	0.1	0.15		Th cor	0.0472	0.0016	Th cor	Th cor	0.0723	0.0028	0.0111	0.0002	0.45	**71.3**	**1.2**	207/206		207/206				
	32		80.6	55.5	1.0	0.71	0.0	0.01		Th cor	0.0472	0.0017	Th cor	Th cor	0.0714	0.0029	0.0110	0.0002	0.48	**70.4**	**1.3**	207/206		207/206				
	35	core	235.9	148.9	2.8	0.65	0.3	0.23		Th cor	0.0472	0.0013	Th cor	Th cor	0.0709	0.0021	0.0109	0.0001	0.42	**69.9**	**0.9**	207/206		207/206				
	38	core	749.0	1050.1	10.6	1.44	0.4	0.11		0.00006	0.0469	0.0007	0.4515	0.0099	0.0704	0.0013	0.0109	0.0001	0.62	**69.8**	**0.8**	69.0	1.2	43.0	33.0	62.3		
AM0824	15		102.1	57.9	1.1	0.58	0.3	0.64		Th cor	0.0470	0.0022	Th cor	Th cor	0.0653	0.0032	0.0101	0.0002	0.32	**64.6**	**1.0**	207/206		207/206				
	16		113.4	98.6	1.3	0.89	0.4	0.68		Th cor	0.0470	0.0021	Th cor	Th cor	0.0645	0.0031	0.0100	0.0002	0.34	**63.8**	**1.0**	207/206		207/206				
	18	core	112.1	78.6	1.2	0.72	0.3	0.56		Th cor	0.0470	0.0016	Th cor	Th cor	0.0652	0.0024	0.0100	0.0001	0.38	**64.5**	**0.9**	207/206		207/206				
	20		147.1	123.7	1.7	0.86	0.0	0.01		Th cor	0.0471	0.0020	Th cor	Th cor	0.0662	0.0030	0.0102	0.0001	0.29	**65.4**	**0.9**	207/206		207/206				
	21	rim	124.4	71.7	1.4	0.59	0.2	0.38		Th cor	0.0471	0.0017	Th cor	Th cor	0.0668	0.0026	0.0103	0.0001	0.33	**66.1**	**0.8**	207/206		207/206				
	22		187.9	155.7	2.2	0.85	0.5	0.56		Th cor	0.0471	0.0013	Th cor	Th cor	0.0657	0.0020	0.0101	0.0001	0.40	**64.9**	**0.8**	207/206		207/206				
	23	core	94.1	55.2	1.0	0.60	0.4	0.83		Th cor	0.0471	0.0024	Th cor	Th cor	0.0655	0.0035	0.0101	0.0001	0.27	**64.8**	**0.9**	207/206		207/206				
	23		128.0	95.6	1.4	0.77	0.1	0.17		Th cor	0.0470	0.0013	Th cor	Th cor	0.0631	0.0020	0.0097	0.0002	0.52	**62.5**	**1.0**	207/206		207/206				rejected, old oxygen analysis pit
	47		156.2	130.7	1.8	0.86	0.2	0.27		Th cor	0.0471	0.0023	Th cor	Th cor	0.0657	0.0033	0.0101	0.0001	0.26	**64.9**	**0.8**	207/206		207/206				
AM0806	8		170.4	93.1	1.8	0.56	0.0	0.03		Th cor	0.0471	0.0011	Th cor	Th cor	0.0665	0.0018	0.0102	0.0001	0.47	**65.7**	**0.8**	207/206		207/206				
	11		114.7	59.3	1.2	0.53	0.0	0.01		Th cor	0.0471	0.0014	Th cor	Th cor	0.0666	0.0022	0.0103	0.0001	0.42	**65.9**	**0.9**	207/206		207/206				
	12	core	370.0	263.3	4.1	0.73	0.2	0.11		Th cor	0.0471	0.0010	Th cor	Th cor	0.0662	0.0016	0.0102	0.0001	0.53	**65.4**	**0.8**	207/206		207/206				
	13	core	155.1	102.5	1.8	0.68	0.2	0.22		Th cor	0.0471	0.0012	Th cor	Th cor	0.0711	0.0019	0.0109	0.0001	0.43	**70.2**	**0.8**	207/206		207/206				inherited core/grain
	18		165.5	93.3	1.7	0.58	0.1	0.13		Th cor	0.0470	0.0013	Th cor	Th cor	0.0644	0.0020	0.0099	0.0001	0.43	**63.7**	**0.9**	207/206		207/206				
	31	core	342.6	259.6	3.9	0.78	0.0	0.01		Th cor	0.0471	0.0009	Th cor	Th cor	0.0660	0.0015	0.0102	0.0001	0.51	**65.2**	**0.8**	207/206		207/206				
	34		190.6	130.5	2.0	0.70	0.2	0.24		Th cor	0.0470	0.0023	Th cor	Th cor	0.0634	0.0033	0.0098	0.0001	0.30	**62.7**	**0.9**	207/206		207/206				
	37		235.7	129.7	2.4	0.56	0.2	0.19		Th cor	0.0470	0.0013	Th cor	Th cor	0.0640	0.0019	0.0099	0.0001	0.46	**63.3**	**0.9**	207/206		207/206				
RJ1103	40	rim	159.6	88.3	1.7	0.57	0.6	0.78		Th cor	0.0471	0.0019	Th cor	Th cor	0.0648	0.0027	0.0100	0.0001	0.30	**64.0**	**0.8**	207/206		207/206				
	14	core	223.8	136.2	2.4	0.62	0.1	0.13		Th cor	0.0471	0.0013	Th cor	Th cor	0.0652	0.0022	0.0100	0.0002	0.50	**64.4**	**1.1**	207/206		207/206				
	16		134.3	56.9	1.4	0.43	0.1	0.19		Th cor	0.0471	0.0018	Th cor	Th cor	0.0647	0.0027	0.0100	0.0001	0.34	**64.0**	**0.9**	207/206		207/206				

Sample	Grain	Analysis location	U (ppm)	Th (ppm)	Pb (ppm)	Th/U (atomic)	^{204}Pb (ppb)	f206 (%)	^{204}Pb/^{206}Pb	Corrected ratios ^{207}Pb/^{206}Pb	1σ	^{208}Pb/^{206}Pb	1σ	^{207}Pb/^{235}U	1σ	^{206}Pb/^{238}U	1σ	ρ	Ages (Ma) ^{206}Pb/^{238}U	1σ	^{207}Pb/^{235}U	1σ	^{207}Pb/^{206}Pb	1σ	% con.	Comment
	17	core	973.9	928.8	12.6	0.98	0.6	0.13	0.00007	0.0452	0.0007	0.3128	0.0035	0.0685	0.0013	0.0110	0.0001	0.52	**70.4**	**0.7**	67.3	1.3	#N/A	#N/A	#N/A	inherited core/grain
	17	rim	97.1	47.5	1.0	0.50	0.3	0.62	Th cor	0.0470	0.0020	Th cor	Th cor	0.0650	0.0029	0.0100	0.0001	0.31	**64.3**	**0.9**	207/206		207/206			
	19	core	280.6	158.4	3.1	0.58	0.0	0.01	Th cor	0.0471	0.0009	Th cor	Th cor	0.0670	0.0015	0.0103	0.0001	0.52	**66.2**	**0.7**	207/206		207/206			
	22		138.9	77.2	1.5	0.57	0.2	0.33	Th cor	0.0471	0.0012	Th cor	Th cor	0.0654	0.0019	0.0101	0.0001	0.39	**64.6**	**0.7**	207/206		207/206			
	26	rim	130.9	72.5	1.4	0.57	0.2	0.31	Th cor	0.0471	0.0015	Th cor	Th cor	0.0647	0.0022	0.0100	0.0001	0.31	**64.0**	**0.7**	207/206		207/206			
	30		111.0	66.4	1.2	0.61	0.1	0.21	Th cor	0.0470	0.0017	Th cor	Th cor	0.0645	0.0025	0.0099	0.0001	0.34	**63.8**	**0.8**	207/206		207/206			
AM0826	1		199.8	131.6	2.2	0.68	0.3	0.28	Th cor	0.0471	0.0016	Th cor	Th cor	0.0659	0.0024	0.0102	0.0001	0.34	**65.1**	**0.8**	207/206		207/206			
	14	core	453.4	284.6	4.7	0.64	0.8	0.41	0.00022	0.0447	0.0005	0.2070	0.0018	0.0587	0.0009	0.0095	0.0001	0.75	**61.1**	**0.7**	58.0	0.9	#N/A	#N/A	#N/A	rejected, old oxygen analysis pit
	14	rim	212.9	85.1	2.1	0.41	0.1	0.11	Th cor	0.0470	0.0014	Th cor	Th cor	0.0624	0.0020	0.0096	0.0001	0.35	**61.7**	**0.7**	207/206		207/206			rejected, old oxygen analysis pit
	19	core	175.4	121.1	1.9	0.71	0.1	0.11	Th cor	0.0470	0.0013	Th cor	Th cor	0.0641	0.0020	0.0099	0.0001	0.45	**63.4**	**0.9**	207/206		207/206			
	25	core	291.0	188.7	3.1	0.67	0.2	0.17	Th cor	0.0471	0.0006	Th cor	Th cor	0.0643	0.0011	0.0099	0.0001	0.68	**63.6**	**0.7**	207/206		207/206			
	27		345.1	186.9	3.6	0.56	0.1	0.07	Th cor	0.0471	0.0007	Th cor	Th cor	0.0645	0.0013	0.0099	0.0001	0.61	**63.8**	**0.8**	207/206		207/206			
	32	core	564.5	401.6	6.5	0.73	1.0	0.37	0.00020	0.0456	0.0009	0.2254	0.0050	0.0649	0.0018	0.0103	0.0002	0.67	**66.2**	**1.2**	63.9	1.7	#N/A	#N/A	#N/A	
	35	core	230.6	141.0	2.5	0.63	0.2	0.19	Th cor	0.0471	0.0013	Th cor	Th cor	0.0662	0.0020	0.0102	0.0001	0.40	**65.4**	**0.8**	207/206		207/206			
AM0822	10	core	257.6	216.5	2.5	0.86	0.2	0.16	Th cor	0.0469	0.0017	Th cor	Th cor	0.0564	0.0022	0.0087	0.0001	0.34	**56.0**	**0.8**	207/206		207/206			
	12	core	189.8	144.9	1.8	0.78	0.0	0.01	Th cor	0.0469	0.0013	Th cor	Th cor	0.0563	0.0017	0.0087	0.0001	0.43	**55.9**	**0.7**	207/206		207/206			
	14		600.7	559.0	6.4	0.95	0.7	0.29	0.00016	0.0446	0.0009	0.3061	0.0042	0.0559	0.0013	0.0091	0.0001	0.56	**58.3**	**0.8**	55.2	1.3	#N/A	#N/A	#N/A	
	15		1527.2	1903.9	17.8	1.28	0.9	0.13	0.00007	0.0467	0.0005	0.4057	0.0020	0.0594	0.0009	0.0092	0.0001	0.73	**59.2**	**0.7**	58.6	0.9	32.0	25.0	85.1	
	15	rim	3351.9	10335.1	56.2	3.16	2.0	0.13	0.00007	0.0468	0.0004	1.0079	0.0020	0.0608	0.0009	0.0094	0.0001	0.80	**60.5**	**0.7**	59.9	0.8	38.0	21.0	59.1	rejected, high U
	16	core	291.3	231.7	2.9	0.82	0.0	0.01	Th cor	0.0469	0.0012	Th cor	Th cor	0.0578	0.0017	0.0089	0.0001	0.45	**57.3**	**0.7**	207/206		207/206			
	19		180.5	115.8	1.7	0.66	0.1	0.18	Th cor	0.0469	0.0015	Th cor	Th cor	0.0572	0.0020	0.0088	0.0001	0.37	**56.7**	**0.7**	207/206		207/206			
AM0815	1	core	182.8	103.1	2.0	0.58	0.1	0.10	Th cor	0.0471	0.0012	Th cor	Th cor	0.0682	0.0019	0.0105	0.0001	0.45	**67.3**	**0.8**	207/206		207/206			inherited core/grain
	9	core	229.7	156.2	2.6	0.70	0.2	0.15	Th cor	0.0471	0.0011	Th cor	Th cor	0.0695	0.0019	0.0107	0.0002	0.58	**68.6**	**1.1**	207/206		207/206			inherited core/grain
	10		171.9	78.4	1.6	0.47	0.4	0.61	Th cor	0.0469	0.0017	Th cor	Th cor	0.0584	0.0024	0.0090	0.0002	0.44	**57.9**	**1.0**	207/206		207/206			
	12	core	208.1	185.7	2.4	0.92	0.0	0.01	Th cor	0.0471	0.0013	Th cor	Th cor	0.0649	0.0019	0.0100	0.0001	0.40	**64.1**	**0.8**	207/206		207/206			inherited core/grain
	14		234.8	186.1	2.6	0.81	0.3	0.26	Th cor	0.0470	0.0011	Th cor	Th cor	0.0640	0.0018	0.0099	0.0001	0.54	**63.3**	**0.9**	207/206		207/206			inherited core/grain
	19	core	98.6	51.3	0.9	0.53	0.1	0.33	Th cor	0.0469	0.0019	Th cor	Th cor	0.0538	0.0024	0.0083	0.0001	0.33	**53.4**	**0.8**	207/206		207/206			
	21		129.4	84.3	1.2	0.67	0.1	0.23	Th cor	0.0469	0.0025	Th cor	Th cor	0.0552	0.0030	0.0085	0.0001	0.27	**54.7**	**0.8**	207/206		207/206			
	24	core	51.1	26.6	0.5	0.54	0.0	0.01	Th cor	0.0469	0.0036	Th cor	Th cor	0.0557	0.0044	0.0086	0.0001	0.20	**55.3**	**0.9**	207/206		207/206			
	24		59.4	23.6	0.5	0.41	0.0	0.01	Th cor	0.0469	0.0031	Th cor	Th cor	0.0575	0.0039	0.0089	0.0002	0.28	**57.1**	**1.1**	207/206		207/206			
	25		102.3	49.8	0.9	0.50	0.0	0.01	Th cor	0.0469	0.0021	Th cor	Th cor	0.0547	0.0026	0.0085	0.0001	0.32	**54.3**	**0.8**	207/206		207/206			
AM0816	1	core	77.7	52.5	0.7	0.69	0.3	0.89	Th cor	0.0469	0.0029	Th cor	Th cor	0.0544	0.0035	0.0084	0.0002	0.30	**54.0**	**1.0**	207/206		207/206			
	1	rim	82.5	61.0	0.8	0.76	0.2	0.64	Th cor	0.0469	0.0018	Th cor	Th cor	0.0558	0.0024	0.0086	0.0002	0.45	**55.4**	**1.1**	207/206		207/206			

Sample	Grain	Analysis location	U (ppm)	Th (ppm)	Pb (ppm)	Th/U (atomic)	^{204}Pb (ppb)	f206 (%)	^{204}Pb/^{206}Pb	Corrected ratios									Ages (Ma)								
										^{207}Pb/^{206}Pb	1σ	^{208}Pb/^{206}Pb	1σ	^{207}Pb/^{235}U	1σ	^{206}Pb/^{238}U	1σ	ρ	^{206}Pb/^{238}U	1σ	^{207}Pb/^{235}U	1σ	^{207}Pb/^{206}Pb	1σ	% con.	Comment
	9		98.6	50.5	0.8	0.53	0.5	1.35	Th cor	0.0469	0.0022	Th cor	Th cor	0.0537	0.0026	0.0083	0.0001	0.34	**53.3**	**0.9**	207/206		207/206			
	10	core	91.2	46.4	0.8	0.52	0.4	1.10	Th cor	0.0469	0.0030	Th cor	Th cor	0.0547	0.0036	0.0085	0.0002	0.30	**54.3**	**1.1**	207/206		207/206			
	11	core	134.1	72.2	1.2	0.55	0.4	0.75	Th cor	0.0469	0.0019	Th cor	Th cor	0.0554	0.0025	0.0086	0.0002	0.43	**55.0**	**1.1**	207/206		207/206			
	17		118.1	88.5	1.1	0.77	1.6	3.47	Th cor	0.0469	0.0074	Th cor	Th cor	0.0555	0.0088	0.0086	0.0002	0.12	**55.1**	**1.0**	207/206		207/206			rejected, high common-Pb
	28		135.5	90.2	1.3	0.68	0.0	0.01	Th cor	0.0469	0.0024	Th cor	Th cor	0.0552	0.0030	0.0085	0.0001	0.31	**54.8**	**0.9**	207/206		207/206			
	32	core	125.3	57.8	1.1	0.47	0.3	0.66	Th cor	0.0469	0.0022	Th cor	Th cor	0.0544	0.0027	0.0084	0.0001	0.31	**54.0**	**0.8**	207/206		207/206			
	38	core	259.6	151.1	2.9	0.60	0.0	0.01	Th cor	0.0471	0.0010	Th cor	Th cor	0.0695	0.0018	0.0107	0.0001	0.51	**68.6**	**0.9**	207/206		207/206			inherited core/grain
RJ1101	4	core	152.3	80.2	0.9	0.54	0.3	0.78	Th cor	0.0466	0.0021	Th cor	Th cor	0.0372	0.0017	0.0058	0.0001	0.27	**37.2**	**0.5**	207/206		207/206			
	10	core	51.6	21.2	0.3	0.42	0.1	0.60	Th cor	0.0466	0.0025	Th cor	Th cor	0.0394	0.0022	0.0061	0.0001	0.32	**39.3**	**0.7**	207/206		207/206			
	11	core	47.4	15.8	0.3	0.34	0.1	0.66	Th cor	0.0466	0.0026	Th cor	Th cor	0.0400	0.0024	0.0062	0.0002	0.42	**39.9**	**1.0**	207/206		207/206			
	15	core	88.2	53.0	0.6	0.62	0.1	0.21	Th cor	0.0467	0.0019	Th cor	Th cor	0.0402	0.0017	0.0063	0.0001	0.32	**40.2**	**0.6**	207/206		207/206			
	18	core	112.1	77.4	0.7	0.71	0.0	0.08	Th cor	0.0467	0.0023	Th cor	Th cor	0.0395	0.0020	0.0061	0.0001	0.29	**39.4**	**0.6**	207/206		207/206			
	18	rim	63.2	28.2	0.4	0.46	0.4	2.63	Th cor	0.0466	0.0045	Th cor	Th cor	0.0369	0.0037	0.0057	0.0001	0.23	**36.9**	**0.8**	207/206		207/206			rejected, high common-Pb
	25		66.2	30.0	0.4	0.47	0.1	0.58	Th cor	0.0467	0.0021	Th cor	Th cor	0.0393	0.0019	0.0061	0.0001	0.36	**39.3**	**0.7**	207/206		207/206			
	26		122.0	47.9	0.7	0.40	0.2	0.56	Th cor	0.0466	0.0023	Th cor	Th cor	0.0382	0.0019	0.0059	0.0001	0.25	**38.2**	**0.5**	207/206		207/206			
	34	rim	110.2	45.0	0.7	0.42	0.1	0.23	Th cor	0.0467	0.0020	Th cor	Th cor	0.0406	0.0019	0.0063	0.0001	0.42	**40.5**	**0.8**	207/206		207/206			
Los Elquinos Formation																											
AM0890	1	core	329.2	236.3	3.7	0.74	0.0	0.00	Th cor	0.0471	0.0012	Th cor	Th cor	0.0659	0.0019	0.0102	0.0001	0.44	**65.1**	**0.8**	207/206		207/206			
	4	core	874.9	130.7	7.6	0.15	0.9	0.24	0.00013	0.0464	0.0006	0.0467	0.0023	0.0585	0.0011	0.0091	0.0001	0.67	**58.7**	**0.7**	57.8	1.0	19.0	32.0	209.0	
Tierras Blancas Caldera																											
RJ1105	1	core	37.2	27.4	0.2	0.76	0.1	1.05	Th cor	0.0466	0.0032	Th cor	Th cor	0.0391	0.0028	0.0061	0.0001	0.29	**39.1**	**0.8**	207/206		207/206			
	2	core	41.8	20.1	0.2	0.49	0.1	1.14	Th cor	0.0466	0.0042	Th cor	Th cor	0.0404	0.0038	0.0063	0.0002	0.28	**40.4**	**1.1**	207/206		207/206			
	3		52.6	38.7	0.4	0.75	0.2	1.28	Th cor	0.0467	0.0046	Th cor	Th cor	0.0404	0.0041	0.0063	0.0001	0.19	**40.3**	**0.8**	207/206		207/206			
	4		29.2	16.1	0.2	0.57	0.1	0.72	Th cor	0.0467	0.0053	Th cor	Th cor	0.0432	0.0050	0.0067	0.0001	0.17	**43.1**	**0.8**	207/206		207/206			
	5		56.1	26.0	0.3	0.47	0.1	0.85	Th cor	0.0467	0.0038	Th cor	Th cor	0.0399	0.0033	0.0062	0.0001	0.21	**39.8**	**0.7**	207/206		207/206			
	6		45.9	19.4	0.3	0.43	0.2	1.32	Th cor	0.0467	0.0045	Th cor	Th cor	0.0416	0.0041	0.0065	0.0002	0.24	**41.5**	**1.0**	207/206		207/206			
	11		79.9	45.9	0.5	0.59	0.0	0.01	Th cor	0.0466	0.0015	Th cor	Th cor	0.0396	0.0015	0.0062	0.0001	0.48	**39.6**	**0.7**	207/206		207/206			
	17	core	57.7	34.4	0.4	0.61	0.2	1.00	Th cor	0.0466	0.0042	Th cor	Th cor	0.0387	0.0036	0.0060	0.0002	0.27	**38.7**	**1.0**	207/206		207/206			
Bocatoma Unit																											
AM0867	5	core	272.2	194.2	1.7	0.73	0.0	0.01	Th cor	0.0466	0.0023	Th cor	Th cor	0.0363	0.0019	0.0056	0.0001	0.33	**36.3**	**0.6**	207/206		207/206			
	8		197.5	158.9	1.2	0.83	0.3	0.59	Th cor	0.0466	0.0025	Th cor	Th cor	0.0361	0.0020	0.0056	0.0001	0.31	**36.1**	**0.6**	207/206		207/206			
	9		216.4	131.5	6.3	0.62	0.1	0.04	0.00002	0.0504	0.0009	0.1769	0.0019	0.1876	0.0055	0.0270	0.0007	0.82	**171.8**	**4.1**	174.5	4.7	212.0	38.0	-19.0	inherited core/grain
	11		148.8	92.3	0.9	0.64	0.2	0.60	Th cor	0.0466	0.0025	Th cor	Th cor	0.0345	0.0020	0.0054	0.0001	0.37	**34.5**	**0.7**	207/206		207/206			

Sample	Grain	Analysis location	U (ppm)	Th (ppm)	Pb (ppm)	Th/U (atomic)	^{204}Pb (ppb)	f206 (%)	^{204}Pb/^{206}Pb	Corrected ratios ^{207}Pb/^{206}Pb	1σ	^{208}Pb/^{206}Pb	1σ	^{207}Pb/^{235}U	1σ	^{206}Pb/^{238}U	1σ	ρ	Ages (Ma) ^{206}Pb/^{238}U	1σ	^{207}Pb/^{235}U	1σ	^{207}Pb/^{206}Pb	1σ	% con.	Comment
	13	core	174.9	79.1	0.9	0.46	0.0	0.03	Th cor	0.0466	0.0013	Th cor	Th cor	0.0339	0.0011	0.0053	0.0001	0.50	**33.9**	**0.5**	207/206		207/206			rejected, old oxygen analysis pit
Tilito Formation (Lower Doña Ana Group)																										
AM0846	8	core	263.8	142.4	1.1	0.55	0.0	0.01	Th cor	0.0464	0.0023	Th cor	Th cor	0.0258	0.0013	0.0040	0.0001	0.26	**25.9**	**0.4**	207/206		207/206			
	14	core	226.3	89.6	5.7	0.41	0.2	0.09	0.00005	0.0516	0.0007	0.1420	0.0018	0.1767	0.0036	0.0248	0.0004	0.77	**158.0**	**2.4**	165.2	3.1	269.0	29.0	-41.3	inherited core/grain
	14	rim	270.4	214.1	1.3	0.81	0.0	0.09	Th cor	0.0465	0.0022	Th cor	Th cor	0.0279	0.0014	0.0044	0.0001	0.29	**28.0**	**0.4**	207/206		207/206			
	17	core	108.6	131.4	0.5	1.24	0.0	0.01	Th cor	0.0464	0.0025	Th cor	Th cor	0.0244	0.0014	0.0038	0.0001	0.39	**24.5**	**0.6**	207/206		207/206			rejected, bad analysis location
	18	core	115.4	44.4	0.4	0.39	0.0	0.01	Th cor	0.0464	0.0022	Th cor	Th cor	0.0238	0.0012	0.0037	0.0001	0.37	**24.0**	**0.5**	207/206		207/206			rejected, old oxygen analysis pit
	18	rim	122.7	50.1	0.5	0.42	0.1	0.46	Th cor	0.0464	0.0031	Th cor	Th cor	0.0255	0.0018	0.0040	0.0001	0.32	**25.6**	**0.6**	207/206		207/206			
	20	core	75.3	31.9	0.3	0.44	0.1	0.67	Th cor	0.0464	0.0035	Th cor	Th cor	0.0257	0.0020	0.0040	0.0001	0.26	**25.9**	**0.5**	207/206		207/206			
	22	core	104.6	90.4	0.5	0.89	0.0	0.11	Th cor	0.0464	0.0027	Th cor	Th cor	0.0244	0.0015	0.0038	0.0001	0.31	**24.6**	**0.5**	207/206		207/206			
MQ153	1	rim	210.1	89.1	0.8	0.44	0.1	0.33	Th cor	0.0464	0.0029	Th cor	Th cor	0.0249	0.0016	0.0039	0.0001	0.21	**25.0**	**0.3**	207/206		207/206			
	3	core	410.9	392.2	1.9	0.98	0.0	0.01	Th cor	0.0464	0.0013	Th cor	Th cor	0.0254	0.0008	0.0040	0.0000	0.35	**25.6**	**0.3**	207/206		207/206			
	4	core	179.8	127.3	0.7	0.73	0.2	0.63	Th cor	0.0464	0.0020	Th cor	Th cor	0.0253	0.0012	0.0039	0.0001	0.35	**25.4**	**0.4**	207/206		207/206			
	4	rim	390.1	192.6	1.6	0.51	0.4	0.60	Th cor	0.0464	0.0017	Th cor	Th cor	0.0249	0.0010	0.0039	0.0001	0.36	**25.0**	**0.4**	207/206		207/206			
	5		74.6	59.6	0.3	0.82	0.2	1.35	Th cor	0.0464	0.0027	Th cor	Th cor	0.0254	0.0016	0.0040	0.0001	0.39	**25.5**	**0.6**	207/206		207/206			
	6	core	245.3	125.4	1.0	0.52	0.2	0.43	Th cor	0.0464	0.0021	Th cor	Th cor	0.0244	0.0012	0.0038	0.0001	0.31	**24.5**	**0.4**	207/206		207/206			
	9		161.1	123.8	0.7	0.79	0.2	0.78	Th cor	0.0464	0.0028	Th cor	Th cor	0.0248	0.0015	0.0039	0.0001	0.23	**24.9**	**0.3**	207/206		207/206			
	12		265.0	150.6	1.1	0.58	0.3	0.57	Th cor	0.0464	0.0015	Th cor	Th cor	0.0257	0.0009	0.0040	0.0000	0.34	**25.8**	**0.3**	207/206		207/206			
AM0845	14	core	156.4	147.3	0.7	0.97	0.0	0.01	Th cor	0.0464	0.0020	Th cor	Th cor	0.0251	0.0012	0.0039	0.0001	0.38	**25.2**	**0.4**	207/206		207/206			
	14		198.2	276.1	0.9	1.43	0.1	0.23	Th cor	0.0464	0.0031	Th cor	Th cor	0.0253	0.0018	0.0040	0.0001	0.27	**25.4**	**0.5**	207/206		207/206			
	16	core	917.7	535.9	43.4	0.60	0.3	0.01	0.00001	0.0521	0.0003	0.1891	0.0013	0.3169	0.0039	0.0441	0.0005	0.89	**278.5**	**2.9**	279.5	3.0	288.0	12.0	-3.3	inherited core/grain
	17	rim	151.9	143.3	0.7	0.97	0.0	0.01	Th cor	0.0464	0.0033	Th cor	Th cor	0.0256	0.0019	0.0040	0.0001	0.27	**25.7**	**0.5**	207/206		207/206			
	17	core	149.4	168.2	0.7	1.16	0.1	0.33	Th cor	0.0464	0.0021	Th cor	Th cor	0.0243	0.0012	0.0038	0.0001	0.39	**24.5**	**0.5**	207/206		207/206			
	21	core	78.9	95.9	0.3	1.25	0.0	0.18	Th cor	0.0464	0.0037	Th cor	Th cor	0.0246	0.0021	0.0038	0.0001	0.32	**24.7**	**0.7**	207/206		207/206			
	23	core	152.4	186.3	0.7	1.25	0.0	0.01	Th cor	0.0464	0.0020	Th cor	Th cor	0.0251	0.0011	0.0039	0.0001	0.31	**25.2**	**0.4**	207/206		207/206			
	25		446.6	906.8	2.5	2.08	0.1	0.13	Th cor	0.0464	0.0015	Th cor	Th cor	0.0250	0.0009	0.0039	0.0001	0.38	**25.1**	**0.3**	207/206		207/206			
	26		454.8	229.0	21.0	0.52	0.4	0.04	0.00002	0.0507	0.0005	0.1629	0.0007	0.3065	0.0044	0.0439	0.0005	0.75	**276.7**	**2.9**	271.5	3.4	226.0	22.0	22.4	inherited core/grain
	34		134.3	186.9	0.6	1.43	0.2	0.64	Th cor	0.0464	0.0041	Th cor	Th cor	0.0237	0.0021	0.0037	0.0001	0.19	**23.8**	**0.4**	207/206		207/206			
AM0860	3	core	192.9	180.1	0.8	0.96	0.0	0.06	Th cor	0.0464	0.0019	Th cor	Th cor	0.0246	0.0011	0.0038	0.0001	0.43	**24.7**	**0.5**	207/206		207/206			
	11		167.9	149.7	0.7	0.91	0.1	0.32	Th cor	0.0464	0.0022	Th cor	Th cor	0.0252	0.0013	0.0039	0.0001	0.36	**25.3**	**0.5**	207/206		207/206			
	13	core	77.6	90.3	0.3	1.19	1.4	9.01	Th cor	0.0464	0.0222	Th cor	Th cor	0.0265	0.0127	0.0041	0.0002	0.09	**26.6**	**1.2**	207/206		207/206			rejected, high common-Pb
	14	core	100.8	114.4	0.5	1.16	0.1	0.56	Th cor	0.0464	0.0035	Th cor	Th cor	0.0248	0.0019	0.0039	0.0001	0.22	**24.9**	**0.4**	207/206		207/206			

Sample	Grain	Analysis location	U (ppm)	Th (ppm)	Pb (ppm)	Th/U (atomic)	^{204}Pb (ppb)	f206 (%)	^{204}Pb/^{206}Pb	Corrected ratios									Ages (Ma)								
										^{207}Pb/^{206}Pb	1σ	^{208}Pb/^{206}Pb	1σ	^{207}Pb/^{235}U	1σ	^{206}Pb/^{238}U	1σ	ρ	^{206}Pb/^{238}U	1σ	^{207}Pb/^{235}U	1σ	^{207}Pb/^{206}Pb	1σ	% con.	Comment
	19		146.0	312.4	0.8	2.20	0.0	0.13	Th cor	0.0464	0.0028	Th cor	Th cor	0.0247	0.0016	0.0039	0.0001	0.29	**24.9**	**0.4**	207/206		207/206			
	22	core	232.1	274.4	1.1	1.21	0.1	0.16	Th cor	0.0464	0.0016	Th cor	Th cor	0.0250	0.0010	0.0039	0.0001	0.37	**25.1**	**0.4**	207/206		207/206			
ZN122	15		70.2	42.1	0.3	0.61	0.0	0.38	Th cor	0.0464	0.0035	Th cor	Th cor	0.0249	0.0020	0.0039	0.0001	0.31	**25.0**	**0.6**	207/206		207/206			
	16		66.0	42.2	0.3	0.66	0.1	1.26	Th cor	0.0464	0.0041	Th cor	Th cor	0.0235	0.0022	0.0037	0.0001	0.27	**23.6**	**0.6**	207/206		207/206			
	17		67.7	41.8	0.3	0.63	0.1	0.64	Th cor	0.0464	0.0039	Th cor	Th cor	0.0243	0.0021	0.0038	0.0001	0.26	**24.4**	**0.6**	207/206		207/206			
	18	core	121.3	105.7	0.5	0.89	0.0	0.20	Th cor	0.0464	0.0015	Th cor	Th cor	0.0247	0.0009	0.0039	0.0001	0.50	**24.8**	**0.5**	207/206		207/206			
	18	rim	77.8	47.9	0.3	0.63	0.0	0.30	Th cor	0.0464	0.0023	Th cor	Th cor	0.0238	0.0013	0.0037	0.0001	0.38	**23.9**	**0.5**	207/206		207/206			
	19		92.6	67.0	0.4	0.74	0.1	0.46	Th cor	0.0464	0.0024	Th cor	Th cor	0.0244	0.0014	0.0038	0.0001	0.37	**24.5**	**0.5**	207/206		207/206			
	19		75.5	40.7	0.3	0.55	0.3	1.94	Th cor	0.0464	0.0037	Th cor	Th cor	0.0255	0.0021	0.0040	0.0001	0.20	**25.6**	**0.4**	207/206		207/206			
	25	core	73.1	52.7	0.3	0.74	0.2	1.38	Th cor	0.0464	0.0040	Th cor	Th cor	0.0256	0.0022	0.0040	0.0001	0.18	**25.7**	**0.4**	207/206		207/206			
AM0844	1		196.9	178.7	0.8	0.93	0.3	0.87	Th cor	0.0464	0.0014	Th cor	Th cor	0.0241	0.0008	0.0038	0.0001	0.42	**24.3**	**0.3**	207/206		207/206			
	2	core	28.7	35.9	0.1	1.29	0.2	4.32	Th cor	0.0464	0.0046	Th cor	Th cor	0.0243	0.0025	0.0038	0.0001	0.28	**24.5**	**0.7**	207/206		207/206			
	3		1655.5	1128.1	69.3	0.70	1.2	0.04	0.00002	0.0504	0.0005	0.2148	0.0012	0.2648	0.0039	0.0381	0.0004	0.77	**241.0**	**2.7**	238.5	3.1	214.0	21.0	12.6	inherited core/grain
	4		122.0	60.9	0.5	0.51	0.1	0.27	Th cor	0.0464	0.0031	Th cor	Th cor	0.0252	0.0017	0.0039	0.0001	0.24	**25.3**	**0.4**	207/206		207/206			
	5		163.7	210.9	0.7	1.32	0.2	0.71	Th cor	0.0464	0.0023	Th cor	Th cor	0.0247	0.0013	0.0039	0.0001	0.29	**24.9**	**0.4**	207/206		207/206			
	6		179.0	212.1	0.8	1.22	0.2	0.51	Th cor	0.0464	0.0031	Th cor	Th cor	0.0245	0.0017	0.0038	0.0001	0.26	**24.6**	**0.4**	207/206		207/206			
	7		56.6	39.5	0.3	0.72	0.9	8.03	Th cor	0.0465	0.0115	Th cor	Th cor	0.0268	0.0067	0.0042	0.0002	0.17	**26.9**	**1.1**	207/206		207/206			rejected, high common-Pb
	7	core	130.1	49.7	0.5	0.39	0.0	0.01	Th cor	0.0464	0.0026	Th cor	Th cor	0.0253	0.0015	0.0040	0.0001	0.36	**25.5**	**0.6**	207/206		207/206			
	7	rim	229.9	98.9	0.9	0.44	0.2	0.40	Th cor	0.0464	0.0018	Th cor	Th cor	0.0255	0.0011	0.0040	0.0001	0.40	**25.6**	**0.4**	207/206		207/206			
	20		236.8	302.1	1.0	1.31	0.0	0.01	Th cor	0.0464	0.0022	Th cor	Th cor	0.0247	0.0012	0.0039	0.0001	0.27	**24.8**	**0.3**	207/206		207/206			
	26		266.6	312.7	1.1	1.20	3.0	6.02	Th cor	0.0464	0.0059	Th cor	Th cor	0.0246	0.0032	0.0039	0.0001	0.14	**24.8**	**0.4**	207/206		207/206			rejected, high common-Pb
	34		147.9	128.8	0.6	0.89	0.2	0.91	Th cor	0.0464	0.0036	Th cor	Th cor	0.0242	0.0019	0.0038	0.0001	0.18	**24.3**	**0.3**	207/206		207/206			
AM0849	10	core	176.8	246.0	0.9	1.43	0.2	0.65	Th cor	0.0464	0.0021	Th cor	Th cor	0.0247	0.0012	0.0039	0.0001	0.35	**24.8**	**0.4**	207/206		207/206			
	16		128.8	152.7	0.6	1.22	0.0	0.01	Th cor	0.0464	0.0020	Th cor	Th cor	0.0243	0.0012	0.0038	0.0001	0.43	**24.4**	**0.5**	207/206		207/206			
	17	core	306.3	267.0	1.3	0.89	0.0	0.01	Th cor	0.0464	0.0020	Th cor	Th cor	0.0253	0.0011	0.0039	0.0001	0.33	**25.4**	**0.4**	207/206		207/206			
	18		103.6	98.9	0.4	0.98	0.0	0.17	Th cor	0.0464	0.0036	Th cor	Th cor	0.0244	0.0020	0.0038	0.0001	0.29	**24.5**	**0.6**	207/206		207/206			
	25	core	106.3	140.0	0.5	1.35	0.2	1.11	Th cor	0.0464	0.0034	Th cor	Th cor	0.0240	0.0018	0.0037	0.0001	0.30	**24.1**	**0.5**	207/206		207/206			
	27		124.5	127.4	0.5	1.05	0.3	1.19	Th cor	0.0464	0.0027	Th cor	Th cor	0.0238	0.0015	0.0037	0.0001	0.30	**24.0**	**0.4**	207/206		207/206			rejected, old oxygen analysis pit
RF64	10		155.4	169.3	0.7	1.12	0.1	0.40	Th cor	0.0464	0.0027	Th cor	Th cor	0.0244	0.0015	0.0038	0.0001	0.30	**24.6**	**0.5**	207/206		207/206			
	13		173.3	210.9	0.8	1.25	0.2	0.50	Th cor	0.0464	0.0024	Th cor	Th cor	0.0245	0.0013	0.0038	0.0001	0.29	**24.6**	**0.4**	207/206		207/206			
	17	core	139.0	191.6	0.6	1.41	0.2	0.64	Th cor	0.0464	0.0025	Th cor	Th cor	0.0232	0.0013	0.0036	0.0001	0.29	**23.3**	**0.4**	207/206		207/206			
	18		88.8	65.6	0.3	0.76	0.1	0.89	Th cor	0.0464	0.0023	Th cor	Th cor	0.0238	0.0013	0.0037	0.0001	0.32	**23.9**	**0.4**	207/206		207/206			
	23	core	1671.3	2781.7	8.9	1.71	3.4	1.14	0.00062	0.0368	0.0007	0.5435	0.0036	0.0193	0.0004	0.0038	0.0000	0.50	**24.5**	**0.3**	19.4	0.4	#N/A	#N/A	#N/A	

Sample	Grain	Analysis location	U (ppm)	Th (ppm)	Pb (ppm)	Th/U (atomic)	^{204}Pb (ppb)	f206 (%)	^{204}Pb/^{206}Pb	Corrected ratios ^{207}Pb/^{206}Pb	1σ	^{208}Pb/^{206}Pb	1σ	^{207}Pb/^{235}U	1σ	^{206}Pb/^{238}U	1σ	ρ	Ages (Ma) ^{206}Pb/^{238}U	1σ	^{207}Pb/^{235}U	1σ	^{207}Pb/^{206}Pb	1σ	% con.	Comment
	24	core	109.9	102.3	0.5	0.95	0.2	1.00	Th cor	0.0464	0.0021	Th cor	Th cor	0.0236	0.0011	0.0037	0.0001	0.33	**23.7**	**0.4**	207/206		207/206			
	26		180.4	7.2	10.2	0.04	0.3	0.05	0.00003	0.0602	0.0006	0.0214	0.0005	0.5149	0.0089	0.0620	0.0009	0.80	**388.1**	**5.3**	421.7	6.0	610.0	22.0	-36.4	inherited core/grain
PC14	3		1799.0	915.8	6.9	0.52	0.3	0.09	0.00005	0.0461	0.0006	0.1708	0.0014	0.0231	0.0004	0.0036	0.0000	0.61	**23.4**	**0.2**	23.2	0.4	1.0	33.0	2239.7	
	4		880.8	366.3	3.2	0.43	0.1	0.09	Th cor	0.0464	0.0011	Th cor	Th cor	0.0234	0.0006	0.0037	0.0000	0.46	**23.5**	**0.3**	207/206		207/206			
	6	rim	2714.4	1105.0	10.3	0.42	1.0	0.20	0.00011	0.0461	0.0007	0.1352	0.0009	0.0235	0.0004	0.0037	0.0000	0.56	**23.8**	**0.2**	23.6	0.4	1.0	38.0	2279.1	
	7		2301.7	948.3	8.7	0.42	1.1	0.28	0.00015	0.0448	0.0009	0.1337	0.0012	0.0227	0.0005	0.0037	0.0000	0.49	**23.6**	**0.3**	22.8	0.5	#N/A	#N/A	#N/A	
	8		320.5	167.2	1.2	0.54	0.1	0.19	Th cor	0.0464	0.0017	Th cor	Th cor	0.0228	0.0009	0.0036	0.0000	0.35	**23.0**	**0.3**	207/206		207/206			
	23	rim	1944.4	968.4	7.4	0.51	0.9	0.27	0.00015	0.0466	0.0007	0.1636	0.0013	0.0234	0.0004	0.0036	0.0000	0.60	**23.4**	**0.3**	23.5	0.4	29.0	35.0	-19.2	
	27		1683.6	918.7	6.6	0.56	0.6	0.20	0.00011	0.0463	0.0007	0.1830	0.0013	0.0235	0.0005	0.0037	0.0000	0.61	**23.7**	**0.3**	23.6	0.5	14.0	37.0	69.4	
Z27	7		179.1	208.1	0.7	1.19	0.0	0.14	Th cor	0.0464	0.0015	Th cor	Th cor	0.0234	0.0008	0.0037	0.0000	0.34	**23.5**	**0.3**	207/206		207/206			
	11		95.1	72.1	0.4	0.78	0.2	1.28	Th cor	0.0464	0.0034	Th cor	Th cor	0.0235	0.0018	0.0037	0.0001	0.25	**23.6**	**0.5**	207/206		207/206			
	13	core	153.4	184.7	0.6	1.24	0.1	0.52	Th cor	0.0464	0.0019	Th cor	Th cor	0.0233	0.0011	0.0036	0.0001	0.42	**23.4**	**0.4**	207/206		207/206			
	13	rim	45.4	29.0	0.2	0.66	0.1	1.25	Th cor	0.0464	0.0052	Th cor	Th cor	0.0231	0.0026	0.0036	0.0001	0.19	**23.2**	**0.5**	207/206		207/206			
	14		69.1	48.0	0.3	0.71	0.1	0.64	Th cor	0.0464	0.0044	Th cor	Th cor	0.0234	0.0023	0.0037	0.0001	0.27	**23.5**	**0.6**	207/206		207/206			
	15	core	88.7	72.8	0.3	0.84	0.2	1.44	Th cor	0.0464	0.0031	Th cor	Th cor	0.0228	0.0016	0.0036	0.0001	0.29	**23.0**	**0.5**	207/206		207/206			
	17	core	104.7	119.7	0.4	1.17	0.1	0.64	Th cor	0.0464	0.0018	Th cor	Th cor	0.0222	0.0010	0.0035	0.0001	0.44	**22.4**	**0.4**	207/206		207/206			
	18	core	120.7	141.5	0.5	1.20	0.3	1.25	Th cor	0.0464	0.0031	Th cor	Th cor	0.0226	0.0016	0.0035	0.0001	0.29	**22.8**	**0.5**	207/206		207/206			
	33	core	147.9	170.1	0.6	1.18	0.3	1.11	Th cor	0.0464	0.0032	Th cor	Th cor	0.0232	0.0017	0.0036	0.0001	0.24	**23.3**	**0.4**	207/206		207/206			
Las Trancas Formation																										
RJ11A5	3		716.5	585.2	2.8	0.84	0.3	0.23	Th cor	0.0464	0.0009	Th cor	Th cor	0.0227	0.0005	0.0035	0.0000	0.49	**22.8**	**0.3**	207/206		207/206			
	6		39.5	50.0	2.0	1.30	0.6	0.81	Th cor	0.0504	0.0012	Th cor	Th cor	0.2831	0.0075	0.0408	0.0005	0.44	**257.5**	**2.9**	207/206		207/206			inherited core/grain
	7		269.8	145.4	1.0	0.55	0.3	0.79	Th cor	0.0464	0.0021	Th cor	Th cor	0.0225	0.0011	0.0035	0.0000	0.28	**22.7**	**0.3**	207/206		207/206			
	8	core	195.6	180.6	0.8	0.95	0.1	0.38	Th cor	0.0464	0.0027	Th cor	Th cor	0.0221	0.0013	0.0035	0.0001	0.27	**22.3**	**0.4**	207/206		207/206			
	18		811.6	17.9	32.1	0.02	0.3	0.02	0.00001	0.0513	0.0004	0.0071	0.0002	0.3059	0.0046	0.0433	0.0006	0.89	**273.1**	**3.6**	271.0	3.6	253.0	16.0	7.9	inherited core/grain
	26	core	635.4	146.9	2.1	0.24	0.5	0.52	Th cor	0.0464	0.0022	Th cor	Th cor	0.0223	0.0011	0.0035	0.0001	0.34	**22.5**	**0.4**	207/206		207/206			
Miocene Intrusives																										
RJ11A10	2		216.2	176.9	0.8	0.84	0.1	0.36	Th cor	0.0464	0.0023	Th cor	Th cor	0.0220	0.0012	0.0034	0.0001	0.34	**22.1**	**0.4**	207/206		207/206			
	9	rim	387.7	130.5	1.3	0.35	0.2	0.26	Th cor	0.0464	0.0012	Th cor	Th cor	0.0221	0.0006	0.0034	0.0000	0.40	**22.2**	**0.3**	207/206		207/206			
	11		742.0	181.4	2.5	0.25	0.3	0.23	Th cor	0.0464	0.0010	Th cor	Th cor	0.0220	0.0005	0.0034	0.0000	0.46	**22.1**	**0.2**	207/206		207/206			
	13	rim	450.3	117.1	1.5	0.27	0.1	0.10	Th cor	0.0464	0.0015	Th cor	Th cor	0.0219	0.0008	0.0034	0.0000	0.38	**22.1**	**0.3**	207/206		207/206			
	14	core	642.6	166.7	2.2	0.27	0.3	0.25	Th cor	0.0464	0.0013	Th cor	Th cor	0.0225	0.0007	0.0035	0.0000	0.36	**22.6**	**0.2**	207/206		207/206			
	17		349.6	69.8	1.1	0.20	0.1	0.23	Th cor	0.0464	0.0013	Th cor	Th cor	0.0220	0.0007	0.0034	0.0000	0.44	**22.1**	**0.3**	207/206		207/206			
	21	core	137.7	52.5	0.5	0.39	0.2	0.72	Th cor	0.0464	0.0027	Th cor	Th cor	0.0218	0.0014	0.0034	0.0001	0.34	**21.9**	**0.5**	207/206		207/206			

Sample	Grain	Analysis location	U (ppm)	Th (ppm)	Pb (ppm)	Th/U (atomic)	^{204}Pb (ppb)	f206 (%)	^{204}Pb/^{206}Pb	Corrected ratios									Ages (Ma)								
										^{207}Pb/^{206}Pb	1σ	^{208}Pb/^{206}Pb	1σ	^{207}Pb/^{235}U	1σ	^{206}Pb/^{238}U	1σ	ρ	^{206}Pb/^{238}U	1σ	^{207}Pb/^{235}U	1σ	^{207}Pb/^{206}Pb	1σ	% con.	Comment
RJ11A11	9		199.7	150.8	0.7	0.77	0.1	0.23	Th cor	0.0464	0.0018	Th cor	Th cor	0.0217	0.0009	0.0034	0.0000	0.33	**21.8**	**0.3**	207/206		207/206			
	11		81.2	41.3	0.2	0.52	0.1	0.57	Th cor	0.0463	0.0040	Th cor	Th cor	0.0199	0.0018	0.0031	0.0001	0.29	**20.1**	**0.5**	207/206		207/206			
	12	core	71.7	43.8	0.2	0.63	0.0	0.29	Th cor	0.0463	0.0034	Th cor	Th cor	0.0205	0.0016	0.0032	0.0001	0.29	**20.6**	**0.5**	207/206		207/206			
	15		70.8	35.1	0.2	0.51	0.0	0.07	Th cor	0.0464	0.0028	Th cor	Th cor	0.0217	0.0014	0.0034	0.0001	0.32	**21.8**	**0.5**	207/206		207/206			
	22	core	131.7	96.3	0.5	0.75	0.0	0.19	Th cor	0.0464	0.0020	Th cor	Th cor	0.0210	0.0010	0.0033	0.0001	0.41	**21.2**	**0.4**	207/206		207/206			
	22	core	77.8	38.8	0.3	0.51	0.1	0.59	Th cor	0.0464	0.0037	Th cor	Th cor	0.0210	0.0017	0.0033	0.0001	0.27	**21.1**	**0.5**	207/206		207/206			
	23		108.9	50.9	0.3	0.48	0.1	0.30	Th cor	0.0464	0.0019	Th cor	Th cor	0.0210	0.0010	0.0033	0.0001	0.51	**21.1**	**0.5**	207/206		207/206			
	35	core	107.1	67.0	0.4	0.64	0.1	0.72	Th cor	0.0464	0.0030	Th cor	Th cor	0.0214	0.0014	0.0034	0.0001	0.29	**21.6**	**0.4**	207/206		207/206			
	36		152.4	111.4	0.6	0.75	0.0	0.01	Th cor	0.0464	0.0019	Th cor	Th cor	0.0218	0.0010	0.0034	0.0001	0.40	**21.9**	**0.4**	207/206		207/206			
RJ11A14	7	core	237.7	136.0	0.8	0.59	0.1	0.28	Th cor	0.0464	0.0028	Th cor	Th cor	0.0201	0.0013	0.0031	0.0001	0.26	**20.3**	**0.3**	207/206		207/206			
	15		213.7	67.9	4.6	0.33	0.8	0.39	0.00021	0.0499	0.0009	0.0196	0.0012	0.1489	0.0040	0.0216	0.0004	0.71	**138.1**	**2.6**	140.9	3.5	189.0	43.0	-26.9	inherited core/grain
	16		67.4	31.9	0.2	0.49	0.1	0.76	Th cor	0.0463	0.0041	Th cor	Th cor	0.0206	0.0019	0.0032	0.0001	0.24	**20.7**	**0.5**	207/206		207/206			
	17	core	617.9	223.8	2.0	0.37	0.4	0.47	Th cor	0.0464	0.0011	Th cor	Th cor	0.0206	0.0006	0.0032	0.0001	0.59	**20.7**	**0.4**	207/206		207/206			
	18	core	134.7	136.2	0.5	1.04	0.2	1.00	Th cor	0.0464	0.0021	Th cor	Th cor	0.0208	0.0010	0.0033	0.0001	0.42	**21.0**	**0.4**	207/206		207/206			
	20		134.8	75.4	0.4	0.57	0.1	0.60	Th cor	0.0464	0.0024	Th cor	Th cor	0.0201	0.0011	0.0032	0.0001	0.31	**20.3**	**0.3**	207/206		207/206			
	23		101.7	65.5	0.3	0.66	0.2	1.30	Th cor	0.0463	0.0029	Th cor	Th cor	0.0201	0.0013	0.0031	0.0001	0.27	**20.2**	**0.4**	207/206		207/206			
Escabroso Formation (Upper Doña Ana Group)																											
1026	4	core	165.1	162.6	0.5	1.01	0.0	0.11	Th cor	0.0463	0.0022	Th cor	Th cor	0.0183	0.0009	0.0029	0.0000	0.30	**18.5**	**0.3**	207/206		207/206			
	9		51.0	29.8	0.2	0.60	0.1	1.30	Th cor	0.0463	0.0058	Th cor	Th cor	0.0184	0.0023	0.0029	0.0001	0.17	**18.5**	**0.4**	207/206		207/206			
	11	core	105.5	90.8	0.3	0.88	0.2	1.16	Th cor	0.0463	0.0031	Th cor	Th cor	0.0181	0.0013	0.0028	0.0001	0.30	**18.2**	**0.4**	207/206		207/206			
	14		140.1	138.3	0.5	1.01	0.3	1.62	Th cor	0.0463	0.0037	Th cor	Th cor	0.0183	0.0015	0.0029	0.0001	0.24	**18.5**	**0.4**	207/206		207/206			
	16		154.7	159.6	0.5	1.06	0.3	1.28	Th cor	0.0463	0.0028	Th cor	Th cor	0.0183	0.0011	0.0029	0.0001	0.29	**18.4**	**0.3**	207/206		207/206			
	18		70.6	51.0	0.2	0.74	0.1	0.54	Th cor	0.0463	0.0038	Th cor	Th cor	0.0175	0.0015	0.0027	0.0001	0.33	**17.7**	**0.5**	207/206		207/206			
	19	core	28.8	24.8	0.1	0.88	0.1	2.05	Th cor	0.0463	0.0066	Th cor	Th cor	0.0190	0.0028	0.0030	0.0001	0.29	**19.1**	**0.8**	207/206		207/206			
	33		87.6	51.5	0.2	0.60	0.0	0.01	Th cor	0.0463	0.0050	Th cor	Th cor	0.0174	0.0019	0.0027	0.0000	0.17	**17.5**	**0.3**	207/206		207/206			
SP80	1		187.8	112.8	0.5	0.62	0.1	0.54	Th cor	0.0463	0.0031	Th cor	Th cor	0.0180	0.0012	0.0028	0.0001	0.28	**18.1**	**0.3**	207/206		207/206			
	2		62.8	41.7	0.2	0.68	0.2	2.53	Th cor	0.0463	0.0078	Th cor	Th cor	0.0183	0.0031	0.0029	0.0001	0.20	**18.4**	**0.6**	207/206		207/206			
	3		82.6	63.8	0.3	0.79	0.3	3.14	Th cor	0.0463	0.0046	Th cor	Th cor	0.0179	0.0018	0.0028	0.0001	0.19	**18.0**	**0.3**	207/206		207/206			
	4		81.9	60.8	0.2	0.76	0.1	1.24	Th cor	0.0463	0.0041	Th cor	Th cor	0.0175	0.0016	0.0027	0.0001	0.25	**17.6**	**0.4**	207/206		207/206			
	5	core	203.9	239.8	0.5	1.21	6.3	17.30	Th cor	0.0463	0.0085	Th cor	Th cor	0.0197	0.0036	0.0031	0.0001	0.11	**19.9**	**0.4**	207/206		207/206			rejected, high common-Pb
	10		87.6	57.5	0.3	0.67	0.2	1.98	Th cor	0.0463	0.0030	Th cor	Th cor	0.0184	0.0013	0.0029	0.0001	0.31	**18.6**	**0.4**	207/206		207/206			
Cerro de las Tórtolas Formation																Th cor											
RF62	8		350.4	196.4	1.0	0.58	0.1	0.30	Th cor	0.0463	0.0019	Th cor	Th cor	0.0173	0.0008	0.0027	0.0000	0.33	**17.4**	**0.3**	207/206		207/206			

Sample	Grain	Analysis location	U (ppm)	Th (ppm)	Pb (ppm)	Th/U (atomic)	^{204}Pb (ppb)	f206 (%)	^{204}Pb/^{206}Pb	Corrected ratios ^{207}Pb/^{206}Pb	1σ	^{208}Pb/^{206}Pb	1σ	^{207}Pb/^{235}U	1σ	^{206}Pb/^{238}U	1σ	ρ	Ages (Ma) ^{206}Pb/^{238}U	1σ	^{207}Pb/^{235}U	1σ	^{207}Pb/^{206}Pb	1σ	% con.	Comment
	9	core	703.4	421.9	2.1	0.62	0.2	0.17	Th cor	0.0463	0.0011	Th cor	Th cor	0.0176	0.0005	0.0028	0.0000	0.57	**17.7**	**0.3**	207/206		207/206			
	10	core	318.3	190.3	0.9	0.61	0.7	1.90	Th cor	0.0463	0.0023	Th cor	Th cor	0.0169	0.0009	0.0026	0.0000	0.33	**17.0**	**0.3**	207/206		207/206			
	11		318.4	178.8	0.8	0.58	0.0	0.01	Th cor	0.0463	0.0019	Th cor	Th cor	0.0164	0.0007	0.0026	0.0000	0.34	**16.6**	**0.2**	207/206		207/206			
	11		270.1	154.8	0.8	0.59	0.1	0.41	Th cor	0.0463	0.0016	Th cor	Th cor	0.0172	0.0007	0.0027	0.0001	0.48	**17.3**	**0.3**	207/206		207/206			
	12	core	305.4	192.4	0.8	0.65	0.3	0.82	Th cor	0.0463	0.0032	Th cor	Th cor	0.0167	0.0012	0.0026	0.0000	0.22	**16.8**	**0.3**	207/206		207/206			rejected, old oxygen analysis pit
	15	core	259.1	160.3	0.7	0.63	1.9	6.28	Th cor	0.0463	0.0089	Th cor	Th cor	0.0163	0.0031	0.0025	0.0000	0.07	**16.4**	**0.2**	207/206		207/206			rejected, high common-Pb
	21		474.1	405.7	1.5	0.88	0.2	0.25	Th cor	0.0463	0.0017	Th cor	Th cor	0.0179	0.0007	0.0028	0.0000	0.41	**18.0**	**0.3**	207/206		207/206			
	22		490.0	282.1	1.3	0.59	0.3	0.60	Th cor	0.0463	0.0016	Th cor	Th cor	0.0160	0.0006	0.0025	0.0000	0.36	**16.2**	**0.2**	207/206		207/206			
Tertiary Intrusives																										
RJ11A7	10	rim	87.2	16.0	0.1	0.19	0.2	3.31	Th cor	0.0462	0.0093	Th cor	Th cor	0.0114	0.0023	0.0018	0.0000	0.08	**11.5**	**0.2**	207/206		207/206			
	12	core	202.0	27.3	0.3	0.14	0.2	1.07	Th cor	0.0462	0.0038	Th cor	Th cor	0.0119	0.0010	0.0019	0.0000	0.29	**12.0**	**0.3**	207/206		207/206			
	12	rim	221.3	19.6	0.3	0.09	0.2	0.89	Th cor	0.0462	0.0048	Th cor	Th cor	0.0115	0.0012	0.0018	0.0000	0.13	**11.6**	**0.2**	207/206		207/206			
	13	core	19.2	4.4	0.0	0.24	0.1	6.13	Th cor	0.0462	0.0175	Th cor	Th cor	0.0115	0.0044	0.0018	0.0001	0.12	**11.6**	**0.5**	207/206		207/206			rejected, high common-Pb
	14		40.5	7.8	7.1	0.20	0.4	0.13	0.00007	0.0739	0.0008	0.0590	0.0009	1.8350	0.0274	0.1802	0.0019	0.71	**1068.1**	**10.5**	1058.1	9.8	1037.0	21.0	3.0	inherited core/grain
	15		133.5	11.2	0.2	0.09	0.2	1.96	Th cor	0.0462	0.0022	Th cor	Th cor	0.0118	0.0006	0.0019	0.0000	0.43	**11.9**	**0.3**	207/206		207/206			
	21	core	159.6	36.6	0.3	0.24	0.1	0.63	Th cor	0.0462	0.0033	Th cor	Th cor	0.0115	0.0008	0.0018	0.0000	0.23	**11.6**	**0.2**	207/206		207/206			
	28	core	1136.5	341.4	244.5	0.31	1.3	0.01	0.00001	0.0813	0.0001	0.0932	0.0009	2.3964	0.0235	0.2139	0.0021	0.98	**1249.4**	**10.9**	1241.5	7.0	1227.0	4.0	1.8	inherited core/grain
RJ11A17	1		102.2	62.6	0.2	0.63	0.1	0.75	Th cor	0.0462	0.0063	Th cor	Th cor	0.0094	0.0013	0.0015	0.0001	0.26	**9.5**	**0.3**	207/206		207/206			
	3		301.6	293.1	0.5	1.00	0.0	0.01	Th cor	0.0462	0.0030	Th cor	Th cor	0.0097	0.0007	0.0015	0.0000	0.32	**9.8**	**0.2**	207/206		207/206			
	6		133.7	55.7	0.2	0.43	0.0	0.14	Th cor	0.0462	0.0047	Th cor	Th cor	0.0093	0.0010	0.0015	0.0000	0.20	**9.5**	**0.2**	207/206		207/206			
	7		514.8	47.7	18.2	0.10	0.4	0.04	0.00002	0.0504	0.0004	0.0318	0.0006	0.2631	0.0038	0.0379	0.0005	0.86	**239.7**	**3.0**	237.2	3.1	212.0	17.0	13.1	inherited core/grain
	8		124.4	55.5	0.2	0.46	0.1	1.36	Th cor	0.0462	0.0055	Th cor	Th cor	0.0092	0.0011	0.0014	0.0000	0.18	**9.3**	**0.2**	207/206		207/206			
	10		45.9	20.3	0.1	0.45	0.1	2.05	Th cor	0.0462	0.0086	Th cor	Th cor	0.0083	0.0016	0.0013	0.0001	0.22	**8.4**	**0.4**	207/206		207/206			rejected
	11	core	74.4	23.5	0.1	0.32	0.0	0.49	Th cor	0.0462	0.0048	Th cor	Th cor	0.0097	0.0010	0.0015	0.0000	0.21	**9.8**	**0.2**	207/206		207/206			
	13	core	464.1	110.4	18.9	0.24	0.4	0.05	0.00003	0.0515	0.0004	0.0853	0.0008	0.2967	0.0048	0.0418	0.0006	0.87	**264.0**	**3.6**	263.8	3.7	262.0	18.0	0.8	inherited core/grain
	13	rim	58.9	19.6	0.1	0.34	0.0	0.71	Th cor	0.0462	0.0057	Th cor	Th cor	0.0094	0.0012	0.0015	0.0001	0.27	**9.5**	**0.3**	207/206		207/206			
	15		90.7	43.2	0.1	0.49	0.1	0.88	Th cor	0.0462	0.0071	Th cor	Th cor	0.0092	0.0015	0.0014	0.0001	0.26	**9.3**	**0.4**	207/206		207/206			
	22		436.0	59.3	74.9	0.14	1.1	0.03	0.00002	0.0757	0.0002	0.0430	0.0010	1.8771	0.0266	0.1798	0.0025	0.99	**1066.0**	**13.7**	1073.0	9.4	1087.0	5.0	-1.9	inherited core/grain
	26		110.7	37.8	0.1	0.35	0.1	1.73	Th cor	0.0462	0.0045	Th cor	Th cor	0.0087	0.0009	0.0014	0.0000	0.27	**8.8**	**0.2**	207/206		207/206			
RJ11A15	7		77.0	35.7	16.9	0.48	0.2	0.03	0.00002	0.0813	0.0008	0.1441	0.0005	2.3468	0.0331	0.2094	0.0022	0.74	**1225.7**	**11.7**	1226.6	10.0	1228.0	18.0	-0.2	inherited core/grain
	11	core	109.8	36.1	0.2	0.34	0.2	2.23	Th cor	0.0462	0.0039	Th cor	Th cor	0.0092	0.0008	0.0014	0.0000	0.28	**9.3**	**0.2**	207/206		207/206			
	14	core	62.9	19.0	0.1	0.31	0.0	0.01	Th cor	0.0462	0.0049	Th cor	Th cor	0.0086	0.0010	0.0014	0.0000	0.30	**8.7**	**0.3**	207/206		207/206			
	14	rim	85.0	34.1	0.1	0.41	0.1	1.89	Th cor	0.0462	0.0058	Th cor	Th cor	0.0091	0.0012	0.0014	0.0001	0.28	**9.2**	**0.3**	207/206		207/206			

Sample	Grain	Analysis location	U (ppm)	Th (ppm)	Pb (ppm)	Th/U (atomic)	^{204}Pb (ppb)	f206 (%)	^{204}Pb/^{206}Pb	Corrected ratios ^{207}Pb/^{206}Pb	1σ	^{208}Pb/^{206}Pb	1σ	^{207}Pb/^{235}U	1σ	^{206}Pb/^{238}U	1σ	ρ	Ages (Ma) ^{206}Pb/^{238}U	1σ	^{207}Pb/^{235}U	1σ	^{207}Pb/^{206}Pb	1σ	% con.	Comment
	15	core	37.7	14.7	0.0	0.40	0.1	4.95	Th cor	0.0462	0.0106	Th cor	Th cor	0.0085	0.0020	0.0013	0.0001	0.20	**8.6**	**0.4**	207/206		207/206			rejected, high common-Pb
	16		114.1	21.7	4.3	0.20	0.1	0.07	0.00004	0.0516	0.0008	0.0640	0.0013	0.2800	0.0054	0.0394	0.0004	0.56	**249.0**	**2.6**	250.6	4.2	265.0	37.0	-6.0	inherited core/grain
	19	core	164.0	66.2	0.2	0.41	0.1	0.91	Th cor	0.0462	0.0043	Th cor	Th cor	0.0097	0.0009	0.0015	0.0000	0.19	**9.8**	**0.2**	207/206		207/206			
	22	core	19.1	2.5	2.8	0.13	0.5	0.34	0.00018	0.0735	0.0014	0.0190	0.0010	1.5811	0.0372	0.1559	0.0022	0.61	**934.0**	**12.4**	962.8	14.5	1029.0	37.0	-9.2	rejected, bad analysis location
	22	core	402.1	157.3	71.9	0.40	0.5	0.02	0.00001	0.0770	0.0003	0.1334	0.0011	1.8582	0.0289	0.1750	0.0026	0.97	**1039.6**	**14.5**	1066.3	10.2	1121.0	7.0	-7.3	inherited core/grain
	22	rim	134.4	55.2	0.2	0.42	0.0	0.04	Th cor	0.0462	0.0033	Th cor	Th cor	0.0095	0.0007	0.0015	0.0000	0.30	**9.6**	**0.2**	207/206		207/206			
	27		185.8	141.6	0.3	0.78	0.0	0.01	Th cor	0.0462	0.0041	Th cor	Th cor	0.0092	0.0008	0.0014	0.0000	0.26	**9.3**	**0.2**	207/206		207/206			
	29		105.4	51.5	0.1	0.50	0.0	0.64	Th cor	0.0462	0.0041	Th cor	Th cor	0.0093	0.0009	0.0015	0.0000	0.24	**9.4**	**0.2**	207/206		207/206			
Vacas Heladas Ignimbrites																										
MQ33	4	core	1414.7	792.1	1.5	0.57	0.1	0.16	Th cor	0.0461	0.0012	Th cor	Th cor	0.0064	0.0002	0.0010	0.0000	0.46	**6.5**	**0.1**	207/206		207/206			
	7		1170.4	498.1	1.1	0.44	0.2	0.45	Th cor	0.0461	0.0017	Th cor	Th cor	0.0062	0.0002	0.0010	0.0000	0.32	**6.3**	**0.1**	207/206		207/206			
	9		811.1	407.8	27.3	0.52	0.3	0.03	0.00001	0.0514	0.0003	0.2112	0.0015	0.2281	0.0028	0.0322	0.0004	0.90	**204.1**	**2.2**	208.6	2.3	260.0	13.0	-21.5	inherited core/grain
	10	rim	1036.0	295.8	0.9	0.29	0.2	0.42	Th cor	0.0461	0.0021	Th cor	Th cor	0.0060	0.0003	0.0009	0.0000	0.29	**6.1**	**0.1**	207/206		207/206			
	11	core	1152.8	294.2	1.0	0.26	0.3	0.53	Th cor	0.0461	0.0022	Th cor	Th cor	0.0061	0.0003	0.0010	0.0000	0.33	**6.2**	**0.1**	207/206		207/206			
	11	rim	1645.3	472.5	1.5	0.29	0.3	0.45	Th cor	0.0461	0.0012	Th cor	Th cor	0.0059	0.0002	0.0009	0.0000	0.42	**6.0**	**0.1**	207/206		207/206			
	12	core	444.1	198.4	0.7	0.46	0.1	0.45	Th cor	0.0462	0.0023	Th cor	Th cor	0.0097	0.0005	0.0015	0.0000	0.33	**9.8**	**0.2**	207/206		207/206			inherited core/grain
	14		773.4	576.6	2.0	0.76	0.3	0.39	Th cor	0.0463	0.0012	Th cor	Th cor	0.0150	0.0004	0.0023	0.0000	0.42	**15.1**	**0.2**	207/206		207/206			inherited core/grain
	15		1571.8	536.3	1.4	0.35	0.1	0.12	Th cor	0.0461	0.0014	Th cor	Th cor	0.0060	0.0002	0.0009	0.0000	0.39	**6.0**	**0.1**	207/206		207/206			
	17		1229.0	209.4	47.6	0.17	0.5	0.02	0.00001	0.0511	0.0003	0.0570	0.0006	0.2852	0.0034	0.0405	0.0004	0.91	**255.7**	**2.7**	254.8	2.7	246.0	12.0	3.9	inherited core/grain
DI095	12		668.8	279.9	0.7	0.43	0.3	0.81	Th cor	0.0462	0.0025	Th cor	Th cor	0.0074	0.0004	0.0012	0.0000	0.33	**7.4**	**0.1**	207/206		207/206			rejected, bad analysis location
	14	core	630.4	254.2	26.1	0.41	2.3	0.19	0.00010	0.0500	0.0004	0.1346	0.0015	0.2794	0.0043	0.0406	0.0005	0.87	**256.3**	**3.4**	250.2	3.4	193.0	17.0	32.8	inherited core/grain
	14	rim	1600.6	396.7	1.2	0.25	0.1	0.15	Th cor	0.0461	0.0014	Th cor	Th cor	0.0060	0.0002	0.0009	0.0000	0.47	**6.0**	**0.1**	207/206		207/206			
	15	core	37.8	24.9	0.0	0.68	1.2	21.84	Th cor	0.0461	0.0230	Th cor	Th cor	0.0067	0.0034	0.0010	0.0001	0.13	**6.8**	**0.4**	207/206		207/206			rejected, high common-Pb
	15	rim	1026.6	265.0	0.8	0.26	0.6	1.21	Th cor	0.0461	0.0030	Th cor	Th cor	0.0059	0.0004	0.0009	0.0000	0.24	**6.0**	**0.1**	207/206		207/206			
	16		205.2	174.3	10.1	0.87	2.7	0.65	0.00035	0.0487	0.0009	0.2679	0.0013	0.2880	0.0061	0.0429	0.0005	0.53	**270.7**	**3.0**	257.0	4.8	133.0	42.0	103.5	inherited core/grain
	17	rim	1829.9	614.7	1.7	0.34	0.5	0.57	Th cor	0.0461	0.0012	Th cor	Th cor	0.0062	0.0002	0.0010	0.0000	0.50	**6.3**	**0.1**	207/206		207/206			
	20	core	727.4	198.1	0.7	0.28	0.1	0.21	Th cor	0.0461	0.0016	Th cor	Th cor	0.0063	0.0002	0.0010	0.0000	0.47	**6.4**	**0.1**	207/206		207/206			
	21		49.4	38.6	0.1	0.80	0.1	6.28	Th cor	0.0461	0.0133	Th cor	Th cor	0.0058	0.0017	0.0009	0.0000	0.18	**5.9**	**0.3**	207/206		207/206			rejected, high common-Pb

Appendix 1.11 Concordia diagrams and Tera-Wasserburg plots

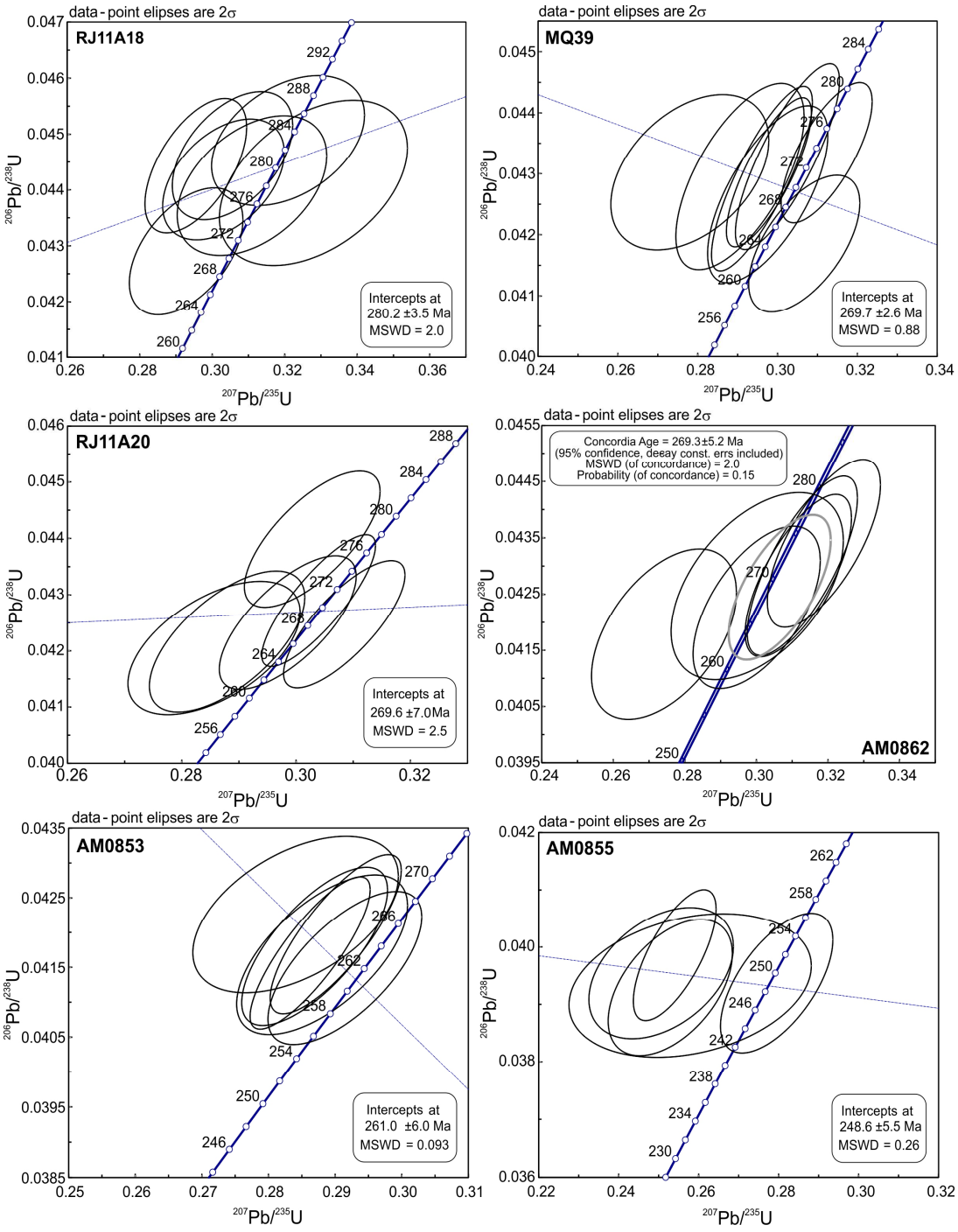

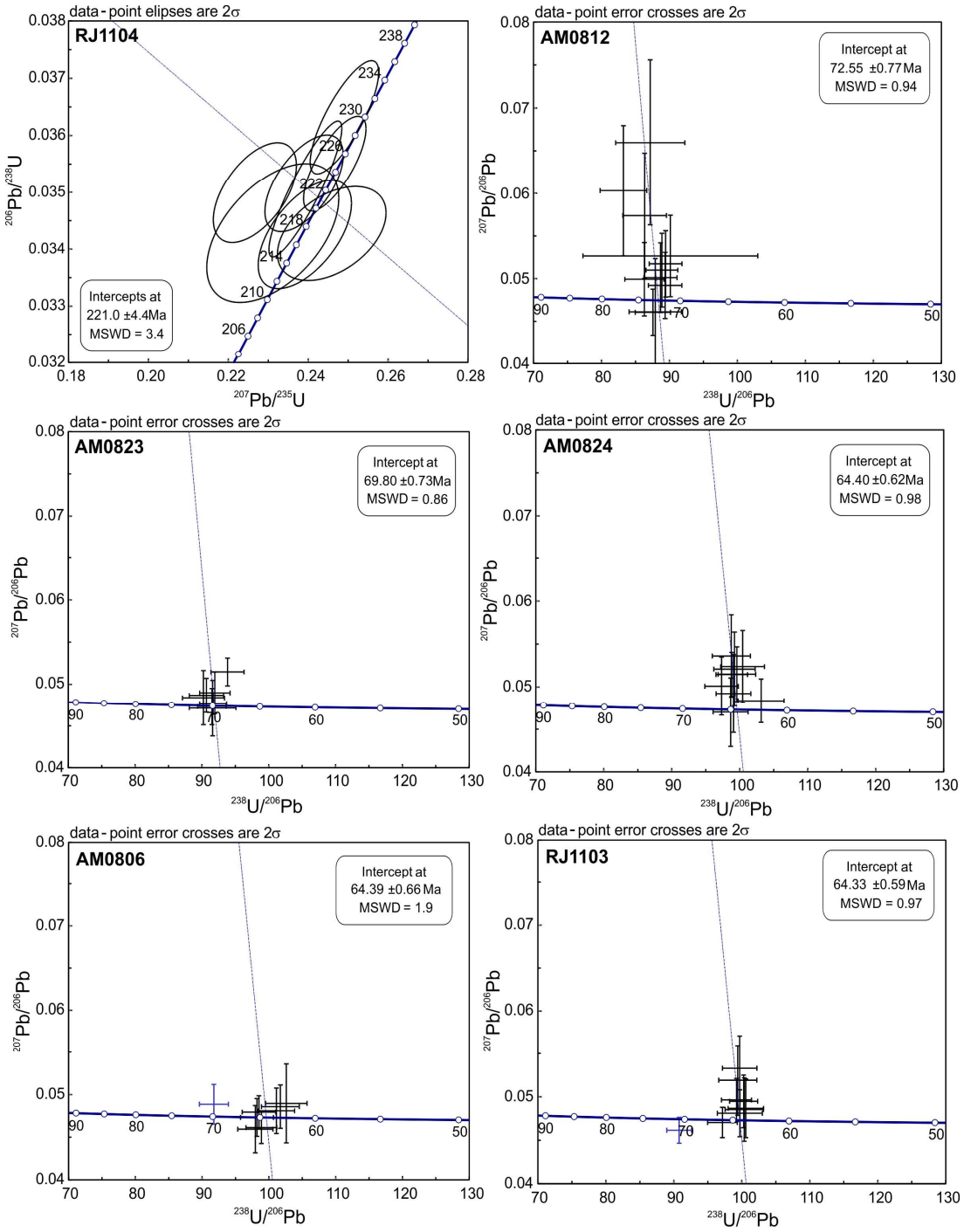
data-point elipses are 2σ
RJ1104
Intercepts at
221.0 ±4.4Ma
MSWD = 3.4
$^{206}Pb/^{238}U$
$^{207}Pb/^{235}U$
data-point error crosses are 2σ
AM0812
Intercept at
72.55 ±0.77Ma
MSWD = 0.94
$^{207}Pb/^{206}Pb$
$^{238}U/^{206}Pb$
data-point error crosses are 2σ
AM0823
Intercept at
69.80 ±0.73Ma
MSWD = 0.86
$^{207}Pb/^{206}Pb$
$^{238}U/^{206}Pb$
data-point error crosses are 2σ
AM0824
Intercept at
64.40 ±0.62Ma
MSWD = 0.98
$^{207}Pb/^{206}Pb$
$^{238}U/^{206}Pb$
data-point error crosses are 2σ
AM0806
Intercept at
64.39 ±0.66Ma
MSWD = 1.9
$^{207}Pb/^{206}Pb$
$^{238}U/^{206}Pb$
data-point error crosses are 2σ
RJ1103
Intercept at
64.33 ±0.59Ma
MSWD = 0.97
$^{207}Pb/^{206}Pb$
$^{238}U/^{206}Pb$

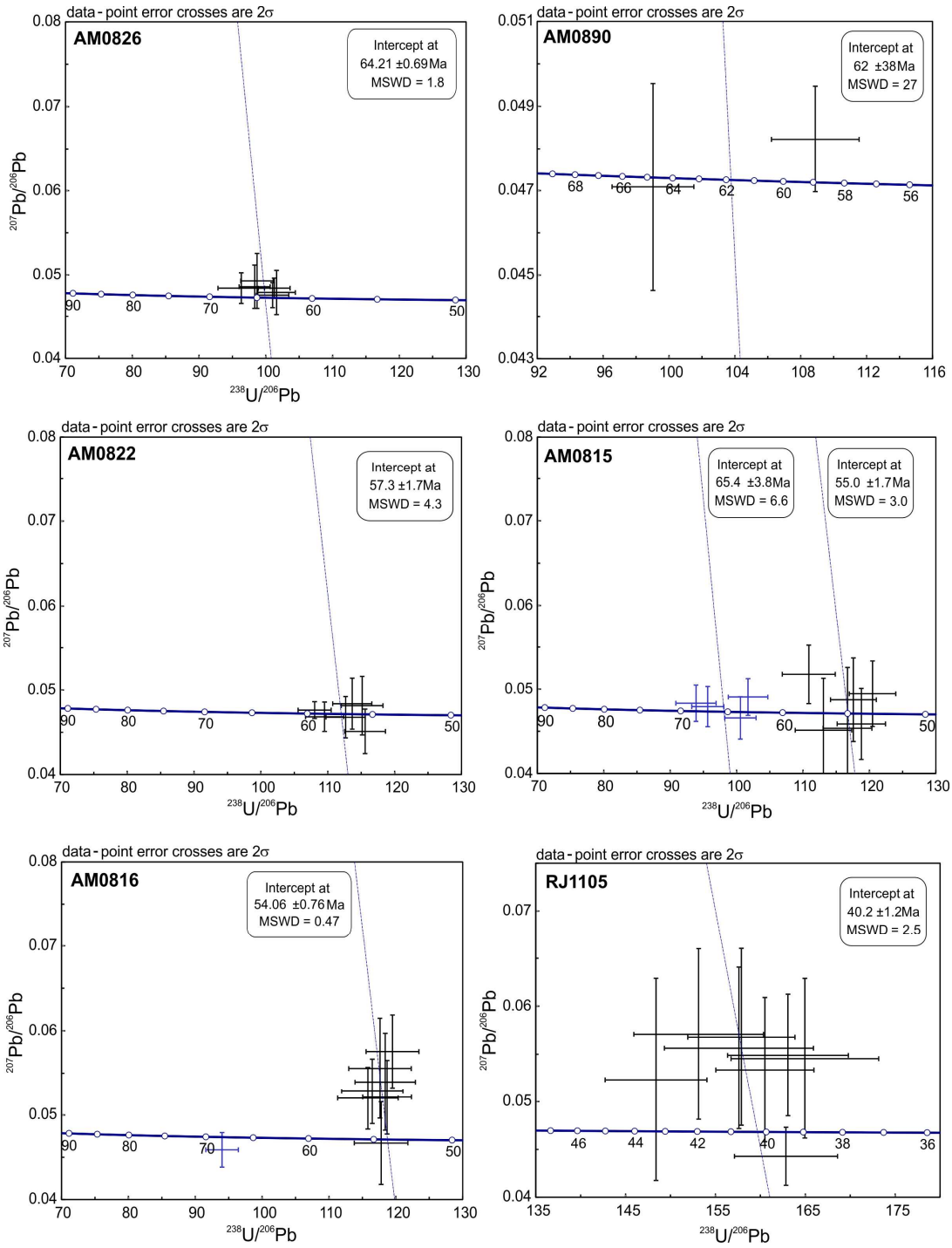
data - point error crosses are 2σ
AM0826
Intercept at
64.21 ±0.69Ma
MSWD = 1.8
data - point error crosses are 2σ
AM0890
Intercept at
62 ±38Ma
MSWD = 27
data - point error crosses are 2σ
AM0822
Intercept at
57.3 ±1.7Ma
MSWD = 4.3
data - point error crosses are 2σ
AM0815
Intercept at
65.4 ±3.8Ma
MSWD = 6.6
Intercept at
55.0 ±1.7Ma
MSWD = 3.0
data - point error crosses are 2σ
AM0816
Intercept at
54.06 ±0.76Ma
MSWD = 0.47
data - point error crosses are 2σ
RJ1105
Intercept at
40.2 ±1.2Ma
MSWD = 2.5
207Pb/206Pb
238U/206Pb

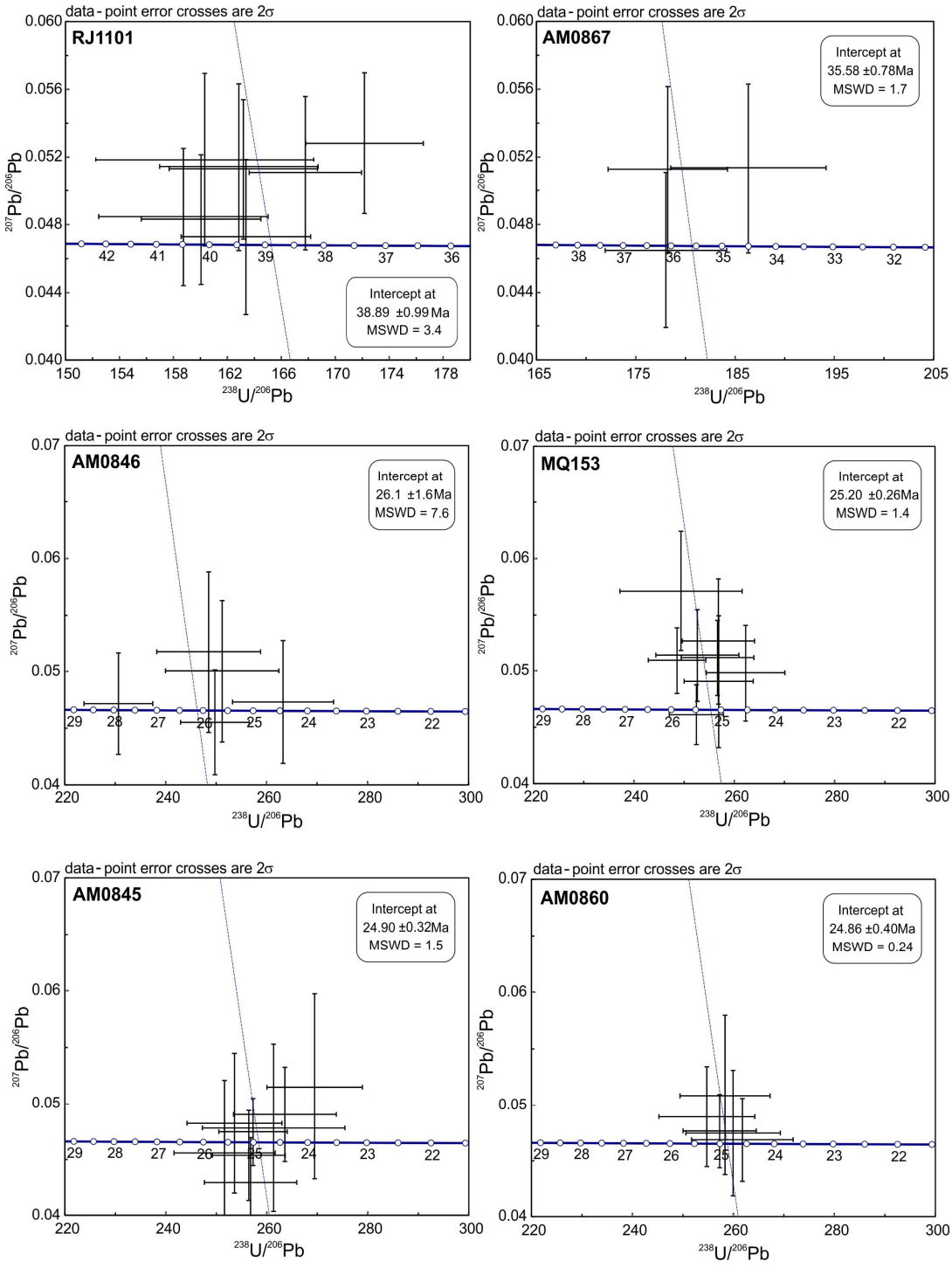
data - point error crosses are 2σ
RJ1101
Intercept at
38.89 ±0.99 Ma
MSWD = 3.4
AM0867
Intercept at
35.58 ±0.78Ma
MSWD = 1.7
AM0846
Intercept at
26.1 ±1.6Ma
MSWD = 7.6
MQ153
Intercept at
25.20 ±0.26Ma
MSWD = 1.4
AM0845
Intercept at
24.90 ±0.32Ma
MSWD = 1.5
AM0860
Intercept at
24.86 ±0.40Ma
MSWD = 0.24
207Pb/206Pb
238U/206Pb

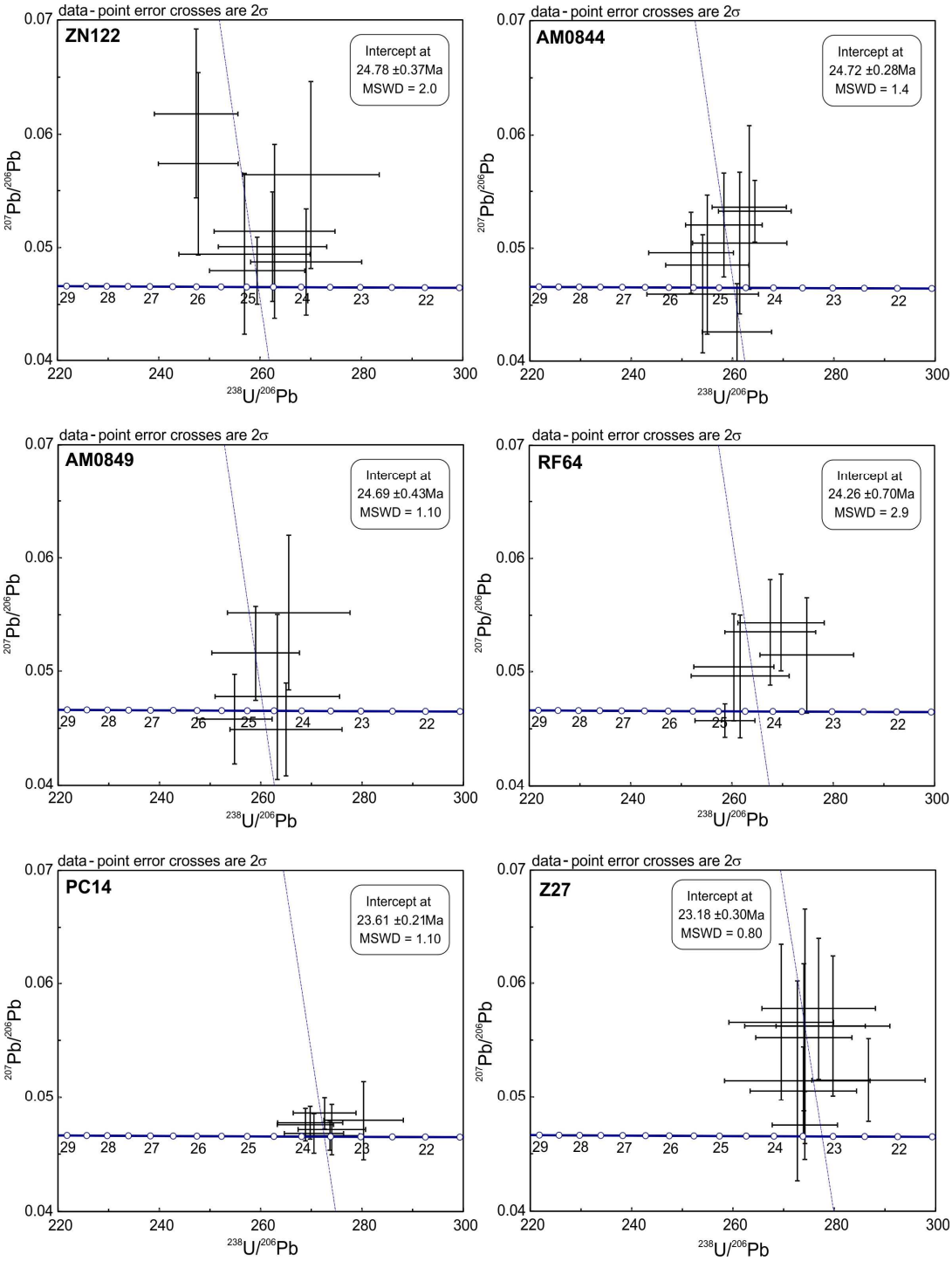
data-point error crosses are 2σ
ZN122
Intercept at
24.78 ±0.37Ma
MSWD = 2.0
AM0844
Intercept at
24.72 ±0.28Ma
MSWD = 1.4
AM0849
Intercept at
24.69 ±0.43Ma
MSWD = 1.10
RF64
Intercept at
24.26 ±0.70Ma
MSWD = 2.9
PC14
Intercept at
23.61 ±0.21Ma
MSWD = 1.10
Z27
Intercept at
23.18 ±0.30Ma
MSWD = 0.80
207Pb/206Pb
238U/206Pb

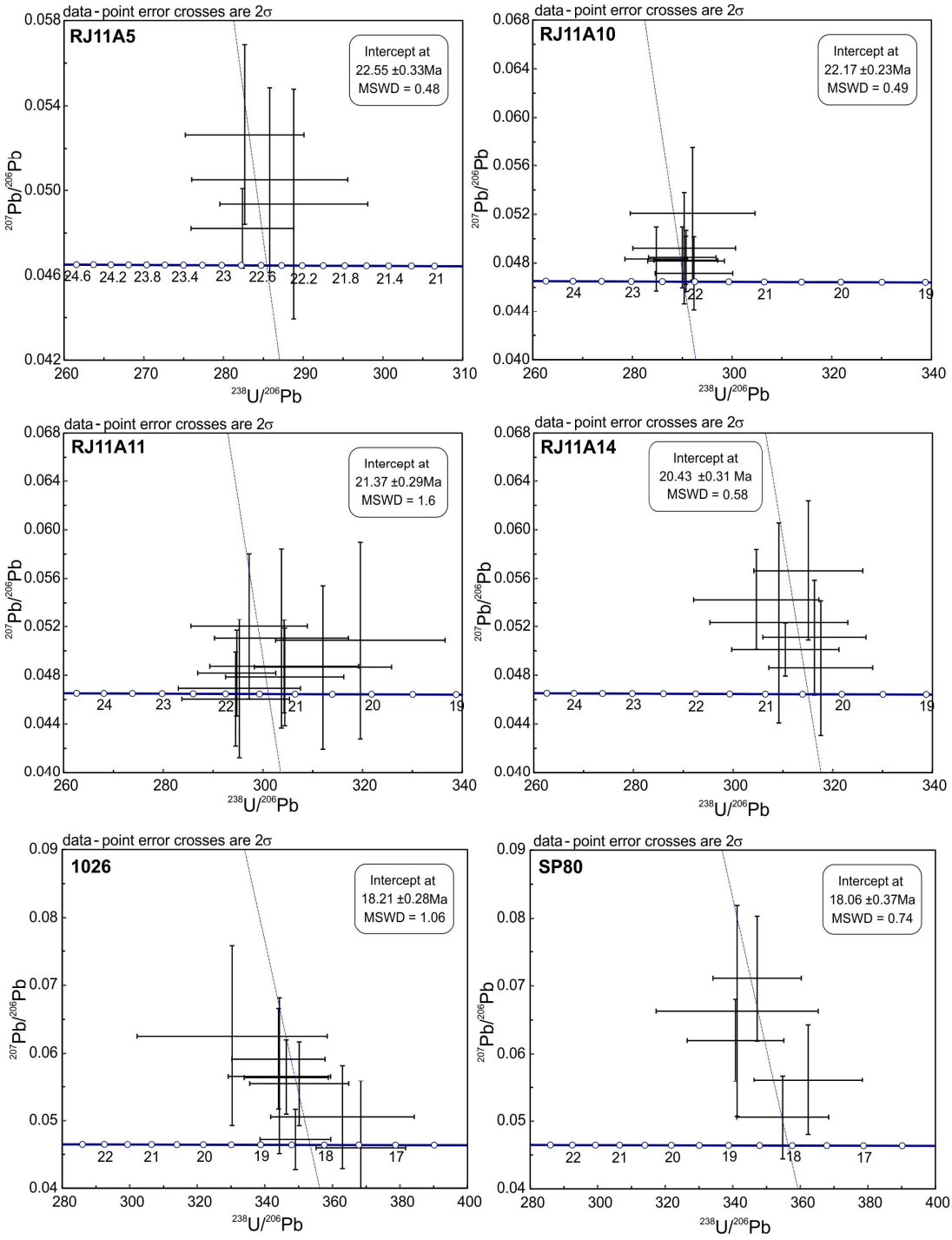
data - point error crosses are 2σ
RJ11A5
Intercept at
22.55 ±0.33Ma
MSWD = 0.48
24.6 24.2 23.8 23.4 23 22.6 22.2 21.8 21.4 21
$^{207}Pb/^{206}Pb$
$^{238}U/^{206}Pb$
data - point error crosses are 2σ
RJ11A10
Intercept at
22.17 ±0.23Ma
MSWD = 0.49
24 23 22 21 20 19
$^{207}Pb/^{206}Pb$
$^{238}U/^{206}Pb$
data - point error crosses are 2σ
RJ11A11
Intercept at
21.37 ±0.29Ma
MSWD = 1.6
24 23 22 21 20 19
$^{207}Pb/^{206}Pb$
$^{238}U/^{206}Pb$
data - point error crosses are 2σ
RJ11A14
Intercept at
20.43 ±0.31 Ma
MSWD = 0.58
24 23 22 21 20 19
$^{207}Pb/^{206}Pb$
$^{238}U/^{206}Pb$
data - point error crosses are 2σ
1026
Intercept at
18.21 ±0.28Ma
MSWD = 1.06
22 21 20 19 18 17
$^{207}Pb/^{206}Pb$
$^{238}U/^{206}Pb$
data - point error crosses are 2σ
SP80
Intercept at
18.06 ±0.37Ma
MSWD = 0.74
22 21 20 19 18 17
$^{207}Pb/^{206}Pb$
$^{238}U/^{206}Pb$

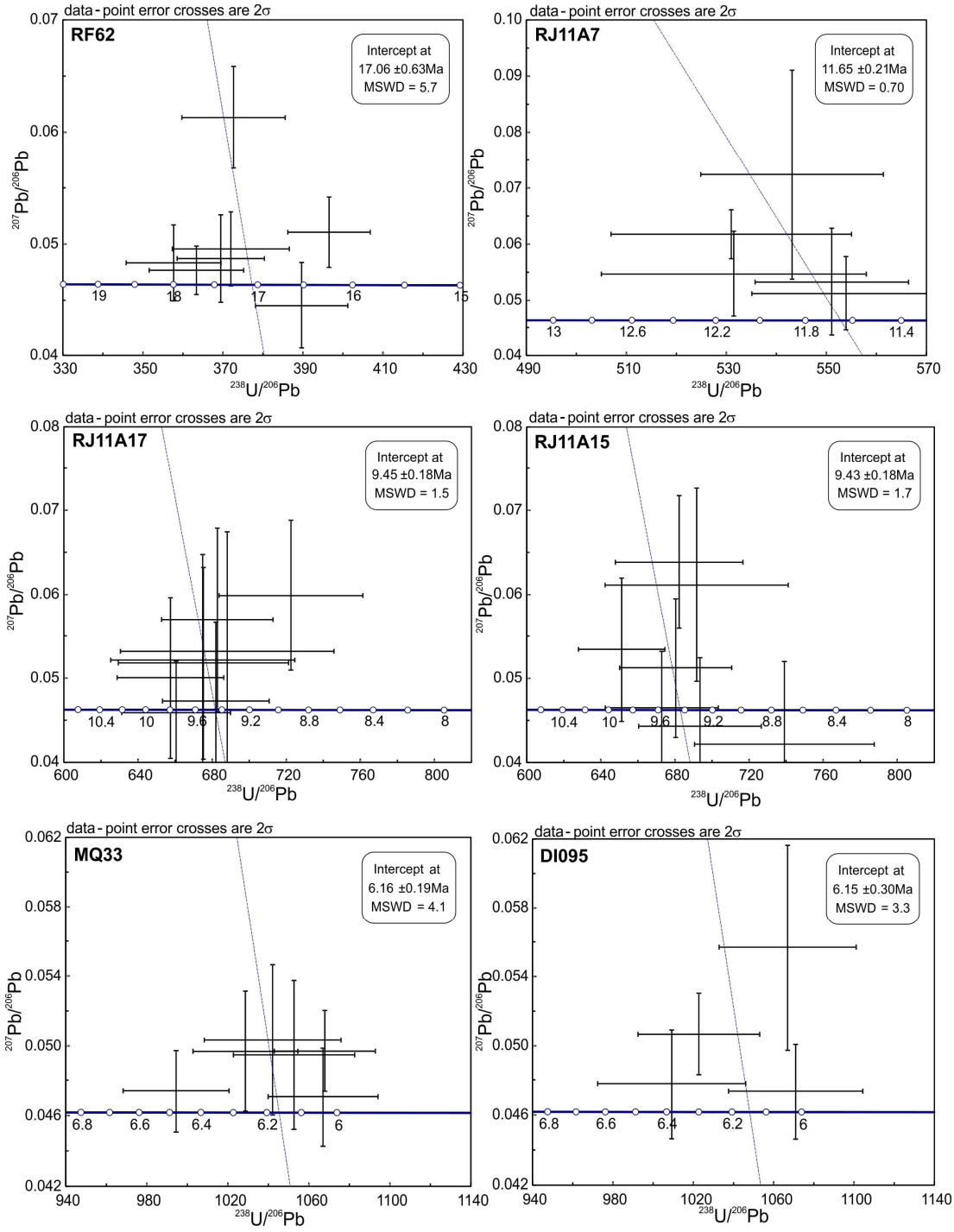
data-point error crosses are 2σ
RF62
Intercept at
17.06 ±0.63Ma
MSWD = 5.7
$^{207}Pb/^{206}Pb$
$^{238}U/^{206}Pb$
data-point error crosses are 2σ
RJ11A7
Intercept at
11.65 ±0.21Ma
MSWD = 0.70
$^{207}Pb/^{206}Pb$
$^{238}U/^{206}Pb$
data-point error crosses are 2σ
RJ11A17
Intercept at
9.45 ±0.18Ma
MSWD = 1.5
$^{207}Pb/^{206}Pb$
$^{238}U/^{206}Pb$
data-point error crosses are 2σ
RJ11A15
Intercept at
9.43 ±0.18Ma
MSWD = 1.7
$^{207}Pb/^{206}Pb$
$^{238}U/^{206}Pb$
data-point error crosses are 2σ
MQ33
Intercept at
6.16 ±0.19Ma
MSWD = 4.1
$^{207}Pb/^{206}Pb$
$^{238}U/^{206}Pb$
data-point error crosses are 2σ
DI095
Intercept at
6.15 ±0.30Ma
MSWD = 3.3
$^{207}Pb/^{206}Pb$
$^{238}U/^{206}Pb$

Appendix 1.12 Major element data for the Late Cretaceous to Miocene magmatic rocks and samples of the Permian and Triassic basement.

Geological Unit	Sample	SiO_2 (wt%)	TiO_2 (wt%)	Al_2O_3 (wt%)	Fe_2O_3 (wt%)	MnO (wt%)	MgO (wt%)	CaO (wt%)	Na_2O (wt%)	K_2O (wt%)	P_2O_5 (wt%)	LOI (wt%)	Total
Permian - Triassic basement	RJ11A18	67.41	0.58	14.79	3.84	0.08	1.52	2.86	3.45	3.09	0.17	1.86	99.65
	MQ39	72.98	0.31	13.78	1.67	0.05	0.25	0.52	3.40	5.65	0.04	0.97	99.61
	RJ11A20	73.89	0.24	13.71	1.34	0.03	0.18	0.42	3.45	5.45	0.02	1.12	99.84
	AM0862	73.00	0.32	14.20	1.59	0.05	0.22	0.14	3.44	5.33	0.03	1.19	99.51
	AM0856	73.62	0.25	13.79	1.65	0.11	0.32	1.00	4.10	3.86	0.06	0.80	99.55
	RJ1104	76.33	0.14	12.92	1.12	0.04	0.24	0.66	3.75	3.96	0.02	0.53	99.70
Cogotí Supergroup	AM0812	60.49	0.72	16.54	6.45	0.13	2.74	5.70	3.45	2.17	0.15	0.93	99.46
	AM0823	64.69	0.55	16.76	1.76	0.04	1.95	4.47	7.90	0.50	0.14	0.72	99.48
	AM0824	59.56	0.81	17.29	6.53	0.15	2.35	5.17	4.34	2.35	0.18	1.18	99.92
	AM0806	68.26	0.46	15.09	3.34	0.07	0.87	2.25	3.83	4.72	0.08	0.72	99.69
	RJ1103	61.45	0.74	16.96	5.92	0.11	2.04	4.67	4.54	2.41	0.18	0.78	99.80
	AM0826	66.54	0.55	15.58	3.99	0.03	1.28	2.72	4.19	4.14	0.10	0.60	99.73
	AM0819	59.39	1.03	16.08	7.60	0.14	2.99	5.59	3.54	2.60	0.23	0.44	99.64
	AM0822	66.36	0.42	16.78	3.94	0.16	1.05	3.33	5.20	2.19	0.19	0.34	99.94
	AMO814	56.58	0.79	17.68	7.85	0.16	3.21	7.02	3.24	1.66	0.15	1.31	99.66
	AM0815	66.70	0.43	15.70	3.90	0.08	1.62	3.72	3.90	2.59	0.11	0.99	99.72
	AM0816	66.53	0.39	15.73	3.66	0.07	1.49	3.69	3.90	2.60	0.10	1.01	99.17
	RJ1101	71.00	0.24	15.09	2.52	0.06	0.97	2.97	3.78	2.59	0.09	0.45	99.77
	RJ1109	55.33	1.22	15.43	10.39	0.19	3.68	5.94	4.32	1.32	0.38	1.54	99.75
Rio Frio Basalts	RF17	52.00	1.97	16.11	11.71	0.09	0.64	6.54	4.12	2.66	1.30	2.81	99.96
Los Elquinos Formation	AM0890	53.76	1.09	17.90	8.27	0.14	3.63	6.63	2.93	1.86	0.43	3.03	99.66
	RJ1111	54.16	0.90	16.96	7.70	0.16	5.08	6.52	3.49	2.06	0.13	2.54	99.71
Tierras Blancas Caldera	RJ1105	57.16	0.59	17.86	6.50	0.17	3.93	6.48	3.85	1.11	0.16	2.12	99.92
	RJ1106	54.01	0.68	19.33	7.79	0.21	4.11	8.02	3.39	0.55	0.14	1.45	99.69
	RJ1107	49.73	1.00	19.87	9.64	0.16	4.07	8.44	3.95	0.25	0.11	2.31	99.53
Bocatoma Unit	AM0867	54.94	0.70	17.92	5.83	0.13	2.35	6.54	3.63	1.66	0.21	6.02	99.92
	AM0870	55.90	0.68	17.44	5.60	0.13	2.25	5.90	3.50	2.85	0.21	5.08	99.54
Tilito Formation	AM0846	71.36	0.32	14.59	2.36	0.09	0.50	1.32	4.10	3.59	0.09	1.35	99.67
(Lower Doña Ana Group)	AM0847	74.68	0.23	13.38	1.50	0.08	0.17	0.91	3.85	3.79	0.06	0.85	99.51
	ZN122	60.69	0.69	15.67	6.43	0.13	3.09	5.86	2.41	1.98	0.24	2.67	99.84
	AM0844	73.85	0.23	13.42	1.53	0.06	0.20	0.74	4.45	3.83	0.06	1.13	99.51
	PC14	70.06	0.13	12.79	1.95	0.20	0.31	4.48	0.18	4.35	0.05	5.64	100.14
	Z27	66.91	0.73	15.81	4.64	0.03	0.24	2.99	3.62	3.90	0.16	0.91	99.94
Las Maquinas Basalts	MQ8	49.26	1.51	17.71	10.72	0.17	5.44	10.07	2.81	1.05	0.28	0.46	99.48
	MQ145	49.48	1.56	17.50	10.99	0.18	5.49	10.08	2.89	1.08	0.28	0.40	99.92

Geological Unit	Sample	SiO_2 (wt%)	TiO_2 (wt%)	Al_2O_3 (wt%)	Fe_2O_3 (wt%)	MnO (wt%)	MgO (wt%)	CaO (wt%)	Na_2O (wt%)	K_2O (wt%)	P_2O_5 (wt%)	LOI (wt%)	Total
Miocene Intrusives	RJ11A10	70.60	0.23	14.81	2.62	0.06	0.43	1.87	3.78	4.11	0.10	0.76	99.37
	RJ11A11	68.53	0.49	14.73	3.73	0.07	0.95	2.08	2.86	5.29	0.16	0.65	99.54
	RJ11A14	64.64	0.61	16.06	4.67	0.08	2.07	3.95	3.33	3.74	0.22	0.57	99.95
Escabroso Formation	1026	61.41	0.79	16.51	5.94	0.09	2.26	5.22	3.74	2.97	0.18	0.58	99.69
(Upper Doña Ana Group)	SP80	60.25	0.83	16.50	6.32	0.11	2.60	5.85	3.42	2.79	0.18	1.05	99.89
	AM0887	61.67	0.80	16.15	5.64	0.11	2.66	4.99	3.63	2.48	0.16	1.37	99.66
	AMO886	55.86	0.96	17.34	6.90	0.11	3.61	6.49	3.10	2.17	0.20	3.06	99.80
	MQ158	52.34	1.05	18.24	9.51	0.15	4.10	8.60	2.78	1.18	0.20	1.38	99.52
	AMO871	54.76	0.98	17.99	8.61	0.15	3.90	7.33	3.07	1.74	0.21	0.71	99.45
	AMO872	64.18	0.67	15.64	5.45	0.10	1.91	3.89	3.16	3.46	0.17	1.11	99.75
Cerro de las Tórtolas	RF62	59.47	0.88	17.69	6.07	0.06	1.27	5.49	3.76	2.94	0.22	1.76	99.62
Formation	RF65	58.17	0.87	17.18	6.45	0.10	2.77	6.41	3.50	2.59	0.22	1.31	99.57
Upper Cerro de las Tórtolas	MQ28	61.20	0.87	17.48	5.19	0.08	2.06	4.98	4.30	2.50	0.26	0.47	99.39
Formation	MQ30	61.66	0.90	17.14	4.88	0.06	2.32	4.89	4.27	2.72	0.25	0.86	99.96
Tertiary Intrusives	RJ11A7	62.61	0.62	16.67	4.33	0.07	2.32	4.60	5.09	2.38	0.22	0.79	99.71
	RJ11A17	61.96	0.58	16.58	3.81	0.07	1.41	4.61	4.65	1.96	0.24	3.76	99.64
	RJ11A15	63.00	0.63	16.95	4.10	0.07	1.60	4.46	5.06	2.13	0.26	1.33	99.58
Vacas Heladas Ignimbrites	MQ33	71.06	0.24	15.62	1.54	0.04	0.31	1.87	4.59	3.61	0.06	0.56	99.50
	DI095*	70.84	0.17	15.67	1.46	0.00	0.46	2.48	5.04	3.84	0.03	-	99.99
	MQ32	71.59	0.24	15.16	1.78	0.04	0.36	1.82	4.15	3.43	0.06	1.11	99.75
	AM0889	69.82	0.24	16.19	1.64	0.04	0.46	2.21	4.33	3.53	0.06	0.86	99.39

Values for sample DI095 are from Litvak et al. (2007).

Appendix 1.13 Trace and rare earth element data for the Late Cretaceous to Miocene magmatic rocks and samples of the Permian and Triassic basement determined by XRF and ICP-MS.

Geological Unit	Sample	Cr (ppm)	Sc (ppm)	V (ppm)	Ni (ppm)	Cu (ppm)	Zn (ppm)	Rb (ppm)	Sr (ppm)	Ba (ppm)	Y (ppm)	Nb (ppm)	Zr (ppm)	Hf (ppm)	Pb (ppm)	Th (ppm)	U (ppm)	La (ppm)	Ce (ppm)	Pr (ppm)	Nd (ppm)	Sm (ppm)	Eu (ppm)	Gd (ppm)	Tb (ppm)	Dy (ppm)	Ho (ppm)	Er (ppm)	Tm (ppm)	Yb (ppm)	Lu (ppm)
Permian –	RJ11A18	14.3	11.6	72.3	7.0	2.0	60.3	145.4	238.1	550.1	24.9	13.7	170.1	2.4	9.1	14.2	2.8	31.5	63.5	7.0	24.8	4.5	1.0	4.1	0.6	3.7	0.7	2.1	0.3	2.1	0.3
Triassic	MQ39	n.d.	8.5	5.2	1.9	2.0	46.1	253.0	106.9	1356.8	43.8	19.3	297.7		*27.9*	*24.8*	*5.5*	*60.4*	*120.0*		*48.8*										
basement	RJ11A20	n.d.	8.3	5.8	1.1	2.3	37.6	207.1	62.0	947.0	40.9	20.1	229.2	5.2	35.3	22.5	4.0	63.5	132.4	15.7	53.6	9.3	1.5	7.7	1.1	6.3	1.2	3.6	0.6	3.6	0.5
	AM0862	n.d.	10.6	2.7	1.4	1.8	61.6	209.6	94.7	1376.4	45.8	19.9	317.5					*74.4*	*147.1*		*59.8*										
	AM0856	n.d.	4.0	6.4	n.d.	4.1	28.8	113.2	128.4	721.3	22.1	20.4	156.8		*14.6*	*9.8*	*2.5*	26.5	52.9	5.9	20.4	3.7	0.7	3.2	0.5	2.9	0.6	1.7	0.3	1.9	0.3
	RJ1104	2.9	4.8	8.4	1.5	1.3	17.6	135.4	85.3	601.0	22.8	8.6	72.0	0.9	31.9	13.5	2.0	22.4	47.6	5.3	18.1	3.5	0.4	3.0	0.4	2.5	0.5	1.3	0.2	1.3	0.2
Cogotí Supergroup	AM0812	n.d.	23.3	142.1	3.7	27.5	51.2	56.2	322.9	376.7	26.4	3.6	193.8		*9.5*	*3.3*	*0.7*	10.9	25.1	3.5	15.9	4.0	1.0	4.0	0.6	4.0	0.8	2.5	0.4	2.4	0.4
	AM0823	n.d.	12.6	54.3	n.d.	7.0	16.5	13.2	248.1	295.5	28.5	6.2	324.9		*5.5*	*8.0*	*0.9*	*9.4*	*31.8*		*17.4*										
	AM0824	n.d.	22.1	118.4	9.8	57.3	78.7	75.0	335.8	495.1	29.3	6.7	223.5		*13.0*	*7.2*	*2.2*	17.9	39.9	5.3	22.2	5.0	1.3	4.8	0.8	4.6	0.9	2.8	0.4	2.8	0.4
	AM0806	n.d.	9.4	42.5	3.0	58.5	42.5	202.9	150.2	506.7	30.1	6.7	246.1		*15.9*	*22.6*	*5.6*	18.3	41.8	5.4	21.7	4.8	0.8	4.5	0.7	4.5	0.9	2.8	0.5	2.9	0.4
	RJ1103	15.5	21.1	100.6	10.2	50.0	44.3	80.6	315.1	445.7	29.8	6.1	233.2	0.6	11.6	8.1	2.0	19.0	43.4	5.5	22.8	5.0	1.2	4.8	0.8	4.6	0.9	2.8	0.4	2.7	0.4
	AM0826	n.d.	14.6	65.4	4.6	51.3	18.5	135.4	203.7	479.7	32.1	6.3	238.4		*8.6*	*18.9*	*3.7*	15.5	38.8	5.3	22.3	5.0	0.8	4.6	0.7	4.5	0.9	2.8	0.4	2.9	0.4
	AM0819	10.4	23.6	140.1	14.8	12.2	45.3	75.1	295.6	580.0	32.6	8.3	296.5		*11.2*	*7.0*	*2.2*	18.6	43.1	5.9	24.6	5.6	1.2	5.4	0.9	5.1	1.0	2.9	0.4	2.7	0.4
	AM0822	n.d.	4.4	25.2	0.1	4.9	90.7	56.9	335.4	489.7	20.0	6.5	169.3		*41.3*	*3.2*	*1.2*	17.4	36.9	4.7	18.6	3.7	1.1	3.4	0.5	2.9	0.6	1.8	0.3	1.8	0.3
	AMO814	22.8	32.7	195.2	14.6	50.9	107.4	37.2	429.6	368.3	30.0	6.1	163.7		*15.5*	*4.4*	*1.3*	*13.1*	*33.5*		*19.3*										
	AM0815	n.d.	9.8	61.3	4.5	14.4	53.3	73.3	298.5	490.5	14.9	4.3	120.5		*17.1*	*5.3*	*1.5*	32.2	64.4	7.3	25.3	4.0	0.8	3.4	0.4	2.4	0.5	1.4	0.2	1.4	0.2
	AM0816	n.d.	9.0	59.1	4.6	17.2	49.8	72.5	302.9	481.4	13.1	3.9	117.5		*16.3*	*5.0*	*1.5*	*8.4*	*22.9*		*9.7*										
	RJ1101	3.9	5.9	33.0	2.5	127.9	27.3	67.0	263.5	282.6	12.5	4.1	68.7	0.4	11.1	7.7	2.3	9.6	22.3	2.6	9.4	1.8	0.5	1.6	0.2	1.3	0.3	0.8	0.1	0.8	0.1
	RJ1109	51.2	42.7	139.3	26.4	88.0	93.5	34.2	282.1	295.7	48.8	4.9	160.5		*6.4*	*3.4*	*1.0*	*12.5*	*38.7*		*25.1*										

Geological Unit	Sample	Cr (ppm)	Sc (ppm)	V (ppm)	Ni (ppm)	Cu (ppm)	Zn (ppm)	Rb (ppm)	Sr (ppm)	Ba (ppm)	Y (ppm)	Nb (ppm)	Zr (ppm)	Hf (ppm)	Pb (ppm)	Th (ppm)	U (ppm)	La (ppm)	Ce (ppm)	Pr (ppm)	Nd (ppm)	Sm (ppm)	Eu (ppm)	Gd (ppm)	Tb (ppm)	Dy (ppm)	Ho (ppm)	Er (ppm)	Tm (ppm)	Yb (ppm)	Lu (ppm)
Rio Frio Basalts	RF17	1.9	15.4	38.0	9.1	7.7	197.8	49.5	590.8	732.2	50.9	51.4	343.7		*5.6*	*5.4*	*1.4*	*53.7*	*122.0*		*72.4*										
Los Elquinos Formation	AM0890	n.d.	23.3	181.8	7.6	20.2	66.7	47.8	581.7	438.9	27.8	7.0	151.8		*7.8*	*1.8*	*0.5*	17.9	40.5	5.5	23.8	5.3	1.5	5.0	0.8	4.5	0.9	2.6	0.4	2.5	0.4
	RJ1111	68.9	36.7	242.5	30.6	31.5	81.2	53.1	505.7	453.3	24.3	3.2	134.9	3.4	8.5	4.5	1.3	10.2	26.5	3.5	15.6	3.9	1.0	3.9	0.6	3.9	0.8	2.3	0.4	2.2	0.3
Tierras Blancas Caldera	RJ1105	51.2	24.3	145.1	36.8	116.2	213.9	42.1	440.7	261.2	13.6	2.6	63.8	0.7	14.4	1.3	0.3	7.2	17.7	2.3	10.1	2.3	0.8	2.2	0.3	2.1	0.4	1.2	0.2	1.2	0.2
	RJ1106	14.3	24.9	179.1	16.3	116.9	133.4	12.7	570.8	250.6	15.3	2.3	59.1	0.9	10.5	0.9	0.1	6.0	15.9	2.2	10.1	2.5	0.9	2.5	0.4	2.5	0.5	1.4	0.2	1.2	0.2
	RJ1107	18.9	38.1	278.0	11.5	115.9	85.0	4.6	557.3	202.9	20.8	2.2	59.5	1.8	5.7	1.2	0.4	6.8	18.2	2.5	11.8	3.2	1.1	3.3	0.5	3.5	0.7	2.1	0.3	2.0	0.3
Bocatoma Unit	AM0867	n.d.	12.5	110.6	5.7	18.8	60.8	53.7	580.2	503.6	17.4	10.1	132.0		*7.2*	*3.4*	*0.1*	21.0	43.0	5.4	21.5	4.1	1.2	3.7	0.5	3.0	0.6	1.7	0.3	1.7	0.3
	AM0870	n.d.	13.6	121.2	3.2	20.9	54.8	73.6	509.9	594.9	18.0	10.5	139.8		*7.7*	*4.7*	*0.9*	*25.1*	*49.2*		*22.2*										
Tilito Formation	AM0846	n.d.	5.9	24.9	n.d.	6.2	47.3	109.7	166.9	622.4	20.7	18.7	155.8		*25.8*	*8.4*	*2.7*	*25.3*	*51.1*		*16.4*										
(Lower Doña Ana Group)	AM0847	n.d.	3.9	8.2	n.d.	3.4	30.2	112.3	103.1	642.2	21.9	20.4	150.9		*13.6*	*9.9*	*2.6*	25.3	51.0	5.7	19.8	3.6	0.7	3.3	0.5	3.1	0.6	1.9	0.3	2.0	0.3
	ZN122	45.5	21.4	130.6	14.4	33.0	71.4	81.0	688.5	686.6	19.1	7.9	145.4	2.5	17.6	7.9	2.7	21.9	44.9	5.2	20.5	4.1	1.1	3.7	0.5	3.1	0.6	1.8	0.3	1.7	0.3
	AM0844	n.d.	3.1	8.2	n.d.	4.0	27.3	114.0	114.0	695.7	21.2	20.2	154.6		*13.7*	*9.3*	*2.1*	25.7	50.8	5.8	19.9	3.6	0.7	3.2	0.5	3.0	0.6	1.8	0.3	2.1	0.3
	Z27	6.2	13.6	65.0	5.2	13.3	34.9	127.7	260.9	646.3	25.7	12.8	259.1	2.9	16.8	8.6	1.5	28.0	58.0	6.9	26.0	5.0	1.2	4.4	0.6	3.6	0.7	1.9	0.3	1.8	0.3
Las Maquinas Basalts	MQ8	58.9	36.7	279.2	26.8	74.9	81.1	19.9	526.5	264.1	22.3	13.8	103.5	2.9	4.6	1.5	0.5	14.3	32.0	4.1	18.0	4.2	1.4	4.2	0.6	3.8	0.7	2.1	0.3	1.9	0.3
	MQ145	55.3	35.2	274.2	26.0	78.4	79.0	16.5	525.3	262.3	22.7	14.1	105.0		*2.8*	*1.3*	*0.3*	*12.9*	*33.5*		*18.8*										
Miocene Intrusives	RJ11A10	0.7	3.7	10.5	1.9	3.0	42.7	173.2	267.8	517.9	25.6	19.7	149.8	0.4	28.3	14.9	1.9	35.1	67.9	7.5	26.0	4.8	1.0	4.2	0.6	3.7	0.7	2.1	0.3	2.1	0.3
	RJ11A11	4.2	9.6	40.7	4.5	9.4	56.9	320.1	195.1	533.3	37.4	19.8	273.0	0.4	30.5	34.4	7.7	44.1	92.9	10.7	39.1	7.5	1.1	6.5	1.0	5.5	1.0	2.9	0.4	2.6	0.4
	RJ11A14	15.9	8.8	67.6	6.8	18.1	92.7	127.8	563.8	790.0	16.2	14.4	159.0	0.6	21.1	19.1	2.9	34.3	67.1	7.5	27.7	4.9	1.4	4.0	0.5	2.7	0.5	1.4	0.2	1.3	0.2
Escabroso Formation	1026	10.7	14.5	118.4	10.1	25.0	52.2	118.1	410.7	561.9	24.2	9.6	194.4	4.9	16.6	12.7	3.6	25.5	54.8	6.7	25.9	5.1	1.1	4.6	0.7	3.9	0.8	2.3	0.4	2.2	0.3
(Upper Doña Ana Group)	SP80	14.5	16.0	120.1	11.3	43.3	62.4	103.6	434.3	549.0	21.5	9.4	183.7	4.8	18.0	12.5	3.4	23.0	49.3	5.8	22.7	4.6	1.1	4.1	0.6	3.6	0.7	2.1	0.3	2.1	0.3
	AM0887	n.d.	13.8	113.8	10.9	40.1	56.7	231.0	362.9	501.2	26.8	10.4	241.5		*17.1*	*21.8*	*6.1*	26.9	58.5	7.2	27.5	5.4	1.1	4.9	0.7	4.3	0.8	2.5	0.4	2.5	0.4
	AMO886	38.8	24.4	188.5	24.9	53.6	76.7	72.8	441.2	437.3	23.5	8.7	181.9		*12.7*	*11.2*	*3.0*	*20.2*	*49.7*		*24.9*										

Geological Unit	Sample	Cr (ppm)	Sc (ppm)	V (ppm)	Ni (ppm)	Cu (ppm)	Zn (ppm)	Rb (ppm)	Sr (ppm)	Ba (ppm)	Y (ppm)	Nb (ppm)	Zr (ppm)	Hf (ppm)	Pb (ppm)	Th (ppm)	U (ppm)	La (ppm)	Ce (ppm)	Pr (ppm)	Nd (ppm)	Sm (ppm)	Eu (ppm)	Gd (ppm)	Tb (ppm)	Dy (ppm)	Ho (ppm)	Er (ppm)	Tm (ppm)	Yb (ppm)	Lu (ppm)
	MQ158	12.1	28.4	208.3	12.5	22.2	75.0	22.7	501.5	408.9	21.6	6.2	135.7	2.9	12.4	3.6	1.0	18.4	40.4	5.0	20.6	4.4	1.3	4.0	0.6	3.5	0.7	1.9	0.3	1.7	0.3
	AMO871	22.5	22.9	176.5	14.9	26.1	75.0	58.3	423.2	440.2	22.5	6.2	175.0		*10.8*	*5.0*	*1.3*	*21.6*	*47.2*		*24.8*										
	AMO872	4.5	12.8	78.9	6.3	32.5	123.0	132.4	322.6	620.1	29.6	9.9	283.9		*21.5*	*16.3*	*2.0*	*31.7*	*72.9*		*33.3*										
Cerro de las Tórtolas	RF62	23.2	20.4	147.2	17.2	35.4	74.4	127.4	503.8	495.2	18.8	10.1	138.6	3.9	12.0	15.9	3.6	24.2	49.9	5.9	22.7	4.4	1.2	3.9	0.6	3.1	0.6	1.7	0.3	1.6	0.2
Formation	RF65	20.9	16.1	138.3	17.5	64.4	58.3	108.4	515.9	446.6	18.2	9.6	132.5	3.5	15.3	14.6	4.7	22.9	47.8	5.6	21.9	4.3	1.2	3.8	0.5	3.1	0.6	1.7	0.3	1.6	0.2
Upper Cerro de las Tórtolas Formation	MQ28	17.4	10.0	108.3	10.3	31.2	66.4	82.3	691.5	733.2	11.5	10.3	173.0	4.4	18.5	7.2	2.2	27.7	56.1	6.5	24.9	4.4	1.3	3.5	0.4	2.2	0.4	1.1	0.2	1.0	0.1
	MQ30	27.9	8.7	105.7	13.0	35.3	74.6	63.2	780.5	812.7	8.6	7.7	185.9	4.5	16.7	4.5	1.2	26.1	55.1	6.6	25.8	4.5	1.3	3.3	0.4	1.8	0.3	0.8	0.1	0.6	0.1
Tertiary Intrusives	RJ11A7	97.3	12.6	119.2	22.9	22.8	70.2	36.0	979.0	754.8	10.5	8.3	131.9	1.9	11.7	1.9	0.6	20.3	42.6	5.2	20.8	3.8	1.1	2.9	0.3	1.7	0.3	0.8	0.1	0.7	0.1
	RJ11A17	11.3	7.1	77.4	6.0	2.2	172.3	35.3	814.2	640.4	9.7	8.8	142.4		*17.8*	*1.3*	*0.3*	*19.8*	*43.6*		*21.4*										
	RJ11A15	8.6	6.0	65.5	5.8	6.7	76.8	35.2	859.7	716.2	10.2	8.9	154.3	1.4	16.0	1.8	0.5	22.7	48.1	5.9	23.4	4.2	1.3	3.2	0.4	1.8	0.3	0.8	0.1	0.6	0.1
Vacas Heladas Ignimbrites	MQ33	1.3	2.7	18.8	1.9	15.9	51.6	122.2	534.7	770.1	9.2	10.4	125.8	0.9	32.1	7.2	3.6	23.2	47.4	5.4	19.6	3.2	0.8	2.3	0.3	1.3	0.2	0.7	0.1	0.6	0.1
	MQ32	0.3	2.3	21.0	1.1	29.9	71.2	112.2	527.0	737.7	8.7	9.8	125.4		*42.3*	*6.3*	*3.2*	*17.5*	*41.8*		*14.5*										
	AM0889	n.d.	3.1	18.2	n.d.	24.3	39.7	117.7	609.1	743.0	7.2	8.6	117.2		*26.2*	*5.9*	*3.1*	*15.5*	*39.6*		*13.4*										

Concentrations of U, Th, Hf and Pb and the REE elements were determined by ICP-MS, apart from where values are shown in italics and underlined. These values were determined by XRF analysis. Refer to Appendix 1.2.6 for an evaluation of the data produced by the two analytical methods.

Appendix 1.14 Geothermobarometry

1.14.1 The results of electron microprobe analysis of selected amphibole grains and amphibole-plagioclase geothermobarometry for intrusive sample RJ1103.

Sample	**RJ1103**				
Grain	RJ1103-1c	RJ1103-1r	RJ1103-1rx2	RJ1103-1rx3	RJ1103-2r
Spot	core	rim	rim	rim	rim
SiO2 (wt.%)	46.26	47.15	47.26	47.36	47.39
TiO2	1.32	1.30	1.27	1.27	1.15
Al2O3	5.78	5.44	5.60	5.47	5.41
Cr2O3	0.00	0.01	0.00	0.00	0.00
Fe2O3	8.12	7.21	8.00	7.96	7.70
FeO	9.41	9.14	8.43	9.01	9.29
MnO	0.57	0.58	0.59	0.59	0.57
MgO	12.58	13.17	13.33	12.97	12.88
CaO	11.03	11.09	11.02	10.99	11.01
Na2O	1.26	1.26	1.24	1.18	1.15
K2O	0.60	0.54	0.57	0.52	0.53
F	0.23	0.22	0.26	0.23	0.22
H2O*	1.90	1.92	1.91	1.92	1.92
Total	**99.1**	**99.0**	**99.5**	**99.5**	**99.2**
Structural formulae					
Si	6.890	6.986	6.959	6.986	7.011
Al iv	1.015	0.950	0.972	0.952	0.943
Al vi	0.000	0.000	0.000	0.000	0.000
Ti	0.148	0.145	0.141	0.141	0.128
Cr	0.000	0.001	0.000	0.000	0.000
Fe3+	0.910	0.804	0.887	0.884	0.857
Fe2+	1.173	1.133	1.038	1.112	1.150
Mn	0.072	0.073	0.074	0.074	0.071
Mg	2.793	2.909	2.927	2.851	2.840
Ca	1.760	1.760	1.739	1.737	1.746
Na	0.365	0.362	0.355	0.339	0.330
K	0.114	0.103	0.107	0.099	0.100
(Ca+Na) (B)	2.000	2.000	2.000	2.000	2.000
Na (B)	0.240	0.240	0.261	0.263	0.254
(Na+K) (A)	0.239	0.224	0.201	0.175	0.176
Mg/(Mg+Fe2)	0.704	0.720	0.738	0.719	0.712
Fe3/(Fe3+Alvi)	1.000	1.000	1.000	1.000	1.000
Sum of S2	13.000	13.000	13.000	13.000	13.000
Amphibole composition	Mg-Hbl	Mg-Hbl	Mg-Hbl	Mg-Hbl	Mg-Hbl
Pressure (kbars) calculated using the calibrations of:					
Hammarstrom & Zen (1986)	1.18	0.86	0.97	0.87	0.82
Hollister et al. (1987)	0.96	0.60	0.72	0.61	0.56
Johnson & Rutherford (1989)	0.83	0.56	0.65	0.57	0.53
Schmidt (1992)	1.82	1.51	1.62	1.52	1.48
Anderson & Smith (1995) for T=680℃	**1.79**	**1.48**	**1.59**	**1.49**	**1.45**
Temperatures (℃) calculated using the calibrations of:					
Otten (1984) (Ti in hornblende)	723	720	714	714	700
Holland and Blundy (1994) (calibtration 1)	778	760	760	754	748
Holland and Blundy (1994) (calibration 2)	**650**	**678**	**686**	**686**	**690**
Depth calculates from P=rgh	**6.7**	**5.6**	**6.0**	**5.6**	**5.5**

1.14.1 Continued

Sample					
Grain	RJ1103-3c	RJ1103-3r	RJ1103-4	RJ1103-4rg2	RJ1103-4x2
Spot	core	rim	intermediate	rim	intermediate
SiO2 (wt.%)	48.84	47.55	48.56	47.56	46.62
TiO2	1.07	1.27	1.08	1.07	1.29
Al2O3	4.98	5.58	5.01	4.93	5.77
Cr2O3	0.00	0.00	0.00	0.00	0.01
Fe2O3	6.78	7.19	8.41	8.38	7.18
FeO	8.42	9.11	8.63	8.68	9.95
MnO	0.57	0.57	0.61	0.61	0.60
MgO	14.06	13.43	13.45	13.04	12.67
CaO	11.34	11.34	11.09	10.88	11.20
Na2O	0.99	1.23	1.13	1.13	1.29
K2O	0.46	0.52	0.47	0.47	0.58
F	0.21	0.24	0.25	0.22	0.24
H2O*	1.95	1.93	1.94	1.92	1.90
Total	**99.7**	**100.0**	**100.6**	**98.9**	**99.3**
Structural formulae					
Si	7.125	6.975	7.062	7.049	6.925
Al iv	0.857	0.966	0.858	0.861	1.010
Al vi	0.000	0.000	0.000	0.000	0.000
Ti	0.117	0.140	0.118	0.119	0.144
Cr	0.000	0.000	0.000	0.000	0.001
Fe3+	0.745	0.793	0.920	0.934	0.803
Fe2+	1.027	1.118	1.049	1.076	1.236
Mn	0.071	0.071	0.076	0.077	0.076
Mg	3.058	2.937	2.916	2.882	2.806
Ca	1.773	1.782	1.728	1.728	1.783
Na	0.281	0.349	0.319	0.324	0.373
K	0.086	0.098	0.087	0.089	0.110
(Ca+Na) (B)	2.000	2.000	2.000	2.000	2.000
Na (B)	0.227	0.218	0.272	0.272	0.217
(Na+K) (A)	0.140	0.229	0.133	0.141	0.265
Mg/(Mg+Fe2)	0.749	0.724	0.735	0.728	0.694
Fe3/(Fe3+Alvi)	1.000	1.000	1.000	1.000	1.000
Sum of S2	13.000	13.000	13.000	13.000	13.000
Amphibole composition	Mg-Hbl	Mg-Hbl	Mg-Hbl	Mg-Hbl	Mg-Hbl
Pressure (kbars) calculated using the calibrations of:					
Hammarstrom & Zen (1986)	0.39	0.94	0.40	0.41	1.16
Hollister et al. (1987)	0.07	0.69	0.08	0.10	0.94
Johnson & Rutherford (1989)	0.16	0.62	0.17	0.18	0.81
Schmidt (1992)	1.07	1.59	1.08	1.09	1.80
Anderson & Smith (1995) for T=680℃	**1.04**	**1.55**	**1.05**	**1.06**	**1.77**
Temperatures (℃) calculated using the calibrations of:					
Otten (1984) (Ti in hornblende)	686	713	687	688	719
Holland and Blundy (1994) (calibtration 1)	722	764	745	749	772
Holland and Blundy (1994) (calibration 2)	**682**	**672**	**670**	**663**	**673**
Depth calculates from P=rgh	**3.9**	**5.9**	**4.0**	**4.0**	**6.7**

1.14.1 Continued

Sample					
Grain	RJ1103-5g2	RJ1103-5g3r	RJ1103-5r	RJ1103-5rx2	RJ1103-6c
Spot	intermediate	rim	rim	rim	core
SiO2 (wt.%)	47.66	47.16	47.96	47.37	47.19
TiO2	1.15	1.33	1.08	1.16	1.35
Al2O3	5.05	5.76	5.17	5.35	5.85
Cr2O3	0.00	0.00	0.00	0.01	0.01
Fe2O3	8.64	7.11	8.91	7.16	8.13
FeO	8.13	9.08	8.08	8.77	9.78
MnO	0.57	0.56	0.64	0.56	0.58
MgO	13.43	13.26	13.11	13.34	12.56
CaO	10.99	11.23	10.69	11.15	10.96
Na2O	1.12	1.23	1.13	1.08	1.40
K2O	0.46	0.53	0.45	0.50	0.57
F	0.25	0.29	0.25	0.22	0.21
H2O*	1.92	1.89	1.92	1.92	1.95
Total	**99.4**	**99.4**	**99.4**	**98.6**	**100.5**
Structural formulae					
Si	7.019	6.957	7.052	7.027	6.922
Al iv	0.876	1.001	0.896	0.935	1.012
Al vi	0.000	0.000	0.000	0.000	0.000
Ti	0.127	0.147	0.120	0.129	0.149
Cr	0.000	0.000	0.000	0.001	0.001
Fe3+	0.958	0.789	0.985	0.799	0.898
Fe2+	1.001	1.120	0.993	1.088	1.200
Mn	0.071	0.070	0.080	0.070	0.072
Mg	2.947	2.915	2.873	2.951	2.746
Ca	1.734	1.775	1.683	1.772	1.722
Na	0.320	0.351	0.322	0.312	0.397
K	0.087	0.100	0.085	0.095	0.106
(Ca+Na) (B)	2.000	2.000	2.000	2.000	2.000
Na (B)	0.266	0.225	0.317	0.228	0.278
(Na+K) (A)	0.140	0.226	0.090	0.179	0.225
Mg/(Mg+Fe2)	0.747	0.722	0.743	0.731	0.696
Fe3/(Fe3+Alvi)	1.000	1.000	1.000	1.000	1.000
Sum of S2	13.000	13.000	13.000	13.000	13.000
Amphibole composition	Mg-Hbl	Mg-Hbl	Mg-Hbl	Mg-Hbl	Mg-Hbl
Pressure (kbars) calculated using the calibrations of:					
Hammarstrom & Zen (1986)	0.49	1.11	0.59	0.78	1.17
Hollister et al. (1987)	0.18	0.89	0.29	0.51	0.95
Johnson & Rutherford (1989)	0.25	0.77	0.33	0.49	0.82
Schmidt (1992)	1.16	1.75	1.26	1.44	1.81
Anderson & Smith (1995) for T=680℃	**1.13**	**1.72**	**1.23**	**1.41**	**1.77**
Temperatures (℃) calculated using the calibrations of:					
Otten (1984) (Ti in hornblende)	698	722	689	701	725
Holland and Blundy (1994) (calibtration 1)	758	762	731	746	765
Holland and Blundy (1994) (calibration 2)	**643**	**690**	**697**	**684**	**700**
Depth calculates from P=rgh	**4.3**	**6.5**	**4.6**	**5.3**	**6.7**

1.14.1 Continued

Sample				
Grain	RJ1103-6r	RJ1103-7	RJ1103-8c	RJ1103-8r
Spot	rim	intermediate	core	rim
SiO2 (wt.%)	47.56	48.02	47.88	48.13
TiO2	1.26	1.01	1.27	1.12
Al2O3	5.58	5.01	5.55	5.02
Cr2O3	0.00	0.00	0.00	0.00
Fe2O3	7.41	7.06	7.49	6.37
FeO	9.71	9.38	9.00	8.98
MnO	0.61	0.52	0.60	0.58
MgO	12.90	13.39	13.49	13.69
CaO	11.16	11.30	11.29	11.32
Na2O	1.24	1.13	1.27	1.05
K2O	0.55	0.45	0.55	0.47
F	0.22	0.25	0.28	0.24
H2O*	1.94	1.92	1.92	1.92
Total	**100.2**	**99.4**	**100.6**	**98.9**
Structural formulae				
Si	6.984	7.074	6.980	7.102
Al iv	0.966	0.869	0.953	0.873
Al vi	0.000	0.000	0.000	0.000
Ti	0.139	0.112	0.139	0.124
Cr	0.001	0.001	0.000	0.000
Fe3+	0.819	0.783	0.822	0.708
Fe2+	1.193	1.156	1.098	1.108
Mn	0.076	0.064	0.074	0.073
Mg	2.823	2.941	2.933	3.011
Ca	1.756	1.784	1.763	1.789
Na	0.353	0.322	0.358	0.300
K	0.103	0.085	0.102	0.089
(Ca+Na) (B)	2.000	2.000	2.000	2.000
Na (B)	0.244	0.216	0.237	0.211
(Na+K) (A)	0.212	0.191	0.224	0.178
Mg/(Mg+Fe2)	0.703	0.718	0.728	0.731
Fe3/(Fe3+Alvi)	1.000	1.000	1.000	1.000
Sum of S2	13.000	13.000	13.000	13.000
Amphibole composition	Mg-Hbl	Mg-Hbl	Mg-Hbl	Mg-Hbl
Pressure (kbars) calculated using the calibrations of:				
Hammarstrom & Zen (1986)	0.94	0.45	0.87	0.47
Hollister et al. (1987)	0.69	0.14	0.62	0.17
Johnson & Rutherford (1989)	0.62	0.22	0.57	0.23
Schmidt (1992)	1.59	1.13	1.53	1.15
Anderson & Smith (1995) for T=680℃	**1.55**	**1.10**	**1.50**	**1.12**
Temperatures (℃) calculated using the calibrations of:				
Otten (1984) (Ti in hornblende)	713	680	712	694
Holland and Blundy (1994) (calibtration 1)	756	749	761	735
Holland and Blundy (1994) (calibration 2)	**689**	**663**	**675**	**679**
Depth calculates from P=rgh	**5.9**	**4.1**	**5.6**	**4.2**

1.14.2 The results of electron microprobe analysis of selected plagioclase feldspar grains from sample RJ1103.

Sample		**RJ1103**										**Average**
Grain		RJ1103-2plag	RJ1103-2plag	RJ1103-2plag2	RJ1103-3plag	RJ1103-3plag2	RJ1103-4plag	RJ1103-5plag	RJ1103-6plag	RJ1103-8plag1	RJ1103-8plag2	
Oxides	Na_2O (wt.%)	8.93	7.06	8.39	8.00	8.50	8.06	8.87	9.04	8.56	8.41	**8.38**
	SiO_2	62.00	57.13	61.01	60.17	60.74	61.14	61.91	62.77	61.31	61.41	**60.96**
	CaO	4.61	8.04	6.03	6.28	5.21	6.09	4.62	4.52	5.47	5.49	**5.64**
	Al_2O_3	23.27	26.04	24.87	24.55	23.72	24.62	23.18	23.28	23.99	23.87	**24.14**
	K_2O	0.47	0.20	0.15	0.55	0.51	0.58	0.57	0.63	0.42	0.56	**0.46**
	SrO	0.06	0.12	0.10	0.07	0.07	0.09	0.06	0.06	0.05	0.06	**0.07**
	TiO_2	0.00	0.03	0.01	0.01	0.02	0.01	0.02	0.01	0.01	0.02	**0.01**
	FeO	0.16	0.41	0.24	0.21	0.21	0.18	0.21	0.22	0.21	0.21	**0.23**
	MnO	0.00	0.01	-0.01	-0.01	0.00	-0.01	0.00	0.01	0.00	0.00	**0.00**
	NiO	0.00	0.00	0.00	0.01	0.00	-0.01	0.00	0.00	0.00	-0.01	**0.00**
	MgO	0.00	0.02	0.01	0.00	0.00	0.01	0.01	0.01	0.01	0.00	**0.01**
	BaO	0.00	0.03	0.03	0.06	0.02	0.05	-0.01	0.01	-0.02	0.02	**0.02**
	Total	**99.5**	**99.1**	**100.8**	**99.9**	**99.0**	**100.8**	**99.4**	**100.6**	**100.0**	**100.0**	**99.92**
Composition	XAn	0.22	0.38	0.28	0.29	0.25	0.28	0.22	0.21	0.26	0.26	**0.26**
	XAb	0.76	0.61	0.71	0.68	0.73	0.68	0.75	0.76	0.72	0.71	**0.71**
	XOr	0.03	0.01	0.01	0.03	0.03	0.03	0.03	0.03	0.02	0.03	**0.03**

1.14.3 The results of electron microprobe analysis of selected amphibole grains and amphibole geothermobarometry for sample RJ1106.

Sample	**RJ1106**					
Grain	RJ1106-1c	RJ1106-1r	RJ1106-3r	RJ1106-4r	RJ1106-4x2	RJ1106-5r
Spot	core	rim	rim	rim	rim	rim
SiO2 (wt.%)	44.48	44.77	46.06	47.34	49.55	46.02
TiO2	2.19	2.43	2.29	2.06	1.60	2.26
Al2O3	8.01	7.96	7.51	6.56	5.09	7.50
Cr2O3	0.00	0.01	0.00	0.00	0.00	0.00
Fe2O3	9.00	7.75	7.54	7.99	8.00	7.55
FeO	5.77	6.96	7.52	7.33	6.83	7.58
MnO	0.33	0.36	0.36	0.38	0.36	0.36
MgO	14.11	13.58	13.97	14.01	14.87	13.77
CaO	10.69	10.60	10.90	10.78	11.07	10.77
Na2O	2.29	2.17	2.19	1.80	1.23	2.13
K2O	0.25	0.27	0.28	0.25	0.24	0.30
F	0.31	0.17	0.22	0.16	0.18	0.25
H2O*	1.75	1.81	1.82	1.85	1.86	1.80
Total	**99.2**	**98.8**	**100.7**	**100.5**	**100.9**	**100.3**
Structural formula on the basis of 13 cations (Leake et al., 1997)						
Si	6.535	6.599	6.673	6.839	7.082	6.691
AlIV	1.388	1.383	1.282	1.117	0.857	1.285
Ti	0.077	0.018	0.044	0.043	0.060	0.024
Tsite	8.000	8.000	8.000	8.000	8.000	8.000
AlVI	0.000	0.000	0.000	0.000	0.000	0.000
Ti	0.164	0.252	0.205	0.181	0.112	0.223
Cr	0.000	0.001	0.000	0.000	0.000	0.000
Fe3+	0.995	0.860	0.822	0.869	0.860	0.826
Mg	3.090	2.984	3.017	3.018	3.168	2.984
Fe2+	0.709	0.858	0.911	0.886	0.816	0.922
Mn	0.041	0.045	0.045	0.046	0.044	0.045
Csite	5.000	5.000	5.000	5.000	5.000	5.000
Fe2+	0.000	0.000	0.000	0.000	0.000	0.000
Ca	1.683	1.674	1.693	1.669	1.695	1.678
Na	0.317	0.326	0.307	0.331	0.305	0.322
Bsite	2.000	2.000	2.000	2.000	2.000	2.000
Na	0.334	0.294	0.307	0.172	0.035	0.280
K	0.047	0.050	0.051	0.047	0.043	0.055
Asite	0.381	0.344	0.358	0.219	0.078	0.335
(Ca+Na)B	2.000	2.000	2.000	2.000	2.000	2.000
NaB	0.317	0.326	0.307	0.331	0.305	0.322
(Na+K)A	0.381	0.344	0.358	0.219	0.078	0.335
Mg/Mg+Fe2+	0.813	0.777	0.768	0.773	0.795	0.764
Amphibole composition	**Mg-Hbl**	**Mg-Hbl**	**Mg-Hbl**	**Mg-Hbl**	**Mg-Hbl**	**Mg-Hbl**
Pressure (kbars) calculated using the calibrations of:						
Ridolfi et al. (2010)	**1.41**	**1.40**	**1.21**	**0.96**	**0.66**	**1.22**
uncertanty (Max error)	0.16	0.15	0.13	0.11	0.07	0.13
Temperatures (℃) calculated using the calibrations of:						
Ridolfi et al. (2010)	**882**	**854**	**848**	**810**	**769**	**837**
Depth calculates from P=rgh	**5.3**	**5.3**	**4.6**	**3.6**	**2.5**	**4.6**

1.14.3 Continued

Sample					
Grain	RJ1106-5rx2	RJ1106-6	RJ1106-6r	RJ1106-7	RJ1106-7r
Spot	rim	intermediate	rim	intermediate	rim
SiO2 (wt.%)	45.78	45.87	47.12	44.45	46.17
TiO2	2.18	2.06	1.74	2.38	2.00
Al2O3	7.50	6.88	5.41	7.73	6.84
Cr2O3	0.00	0.00	0.01	0.00	0.00
Fe2O3	8.83	7.78	8.42	8.07	7.98
FeO	6.15	7.06	6.59	7.14	6.65
MnO	0.36	0.35	0.36	0.35	0.36
MgO	14.30	13.95	14.74	13.65	14.27
CaO	10.73	10.70	10.97	10.79	10.78
Na2O	2.22	2.02	1.79	2.22	2.02
K2O	0.26	0.26	0.23	0.29	0.24
F	0.26	0.18	0.16	0.24	0.21
H2O*	1.79	1.80	1.83	1.77	1.80
Total	**100.4**	**98.9**	**99.4**	**99.1**	**99.3**
Structural formula on the basis of 13 cations (Leake et al., 1997)					
Si	6.636	6.747	6.887	6.564	6.753
AlIV	1.281	1.194	0.932	1.345	1.179
Ti	0.083	0.059	0.181	0.091	0.068
Tsite	8.000	8.000	8.000	8.000	8.000
AlVI	0.000	0.000	0.000	0.000	0.000
Ti	0.155	0.169	0.010	0.173	0.153
Cr	0.000	0.000	0.001	0.000	0.000
Fe3+	0.964	0.861	0.927	0.896	0.879
Mg	3.091	3.059	3.212	3.005	3.111
Fe2+	0.746	0.868	0.805	0.882	0.813
Mn	0.044	0.044	0.045	0.044	0.044
Csite	5.000	5.000	5.000	5.000	5.000
Fe2+	0.000	0.000	0.000	0.000	0.000
Ca	1.667	1.686	1.717	1.707	1.689
Na	0.333	0.314	0.283	0.293	0.311
Bsite	2.000	2.000	2.000	2.000	2.000
Na	0.292	0.261	0.223	0.341	0.262
K	0.048	0.049	0.043	0.054	0.044
Asite	0.340	0.310	0.267	0.395	0.306
(Ca+Na)B	2.000	2.000	2.000	2.000	2.000
NaB	0.333	0.314	0.283	0.293	0.311
(Na+K)A	0.340	0.310	0.267	0.395	0.306
Mg/Mg+Fe2+	0.806	0.779	0.800	0.773	0.793
Amphibole composition	**Mg-Hbl**	**Mg-Hbl**	**Mg-Hbl**	**Mg-Hbl**	**Mg-Hbl**
Pressure (kbars) calculated using the calibrations of:					
Ridolfi et al. (2010)	**1.21**	**1.07**	**0.73**	**1.33**	**1.05**
uncertanty (Max error)	0.13	0.12	0.08	0.15	0.12
Temperatures (℃) calculated using the calibrations of:					
Ridolfi et al. (2010)	**863**	**836**	**842**	**880**	**839**
Depth calculates from P=rgh	**4.6**	**4.0**	**2.8**	**5.0**	**4.0**

1.14.3 Continued

Sample					
Grain	RJ1106-8	RJ1106-8r	RJ1106-9x2	RJ1106-9	RJ1106-10
Spot	intermediate	rim	rim	intermediate	rim
SiO2 (wt.%)	45.40	45.35	46.51	46.66	46.40
TiO2	2.19	2.29	2.13	2.14	2.10
Al2O3	7.39	7.34	6.82	6.97	7.18
Cr2O3	0.00	0.00	0.01	0.01	0.00
Fe2O3	8.40	8.52	8.88	8.06	8.60
FeO	6.61	6.50	6.48	6.31	6.74
MnO	0.38	0.35	0.37	0.36	0.36
MgO	13.87	13.69	14.32	14.68	14.29
CaO	10.61	10.79	10.78	10.80	10.91
Na2O	2.12	1.62	2.06	2.17	2.12
K2O	0.27	0.28	0.24	0.25	0.27
F	0.18	0.14	0.19	0.27	0.21
H2O*	1.81	1.82	1.83	1.80	1.83
Total	**99.2**	**98.7**	**100.6**	**100.5**	**101.0**
Structural formula on the basis of 13 cations (Leake et al., 1997)					
Si	6.661	6.678	6.724	6.740	6.690
AlIV	1.279	1.274	1.161	1.186	1.219
Ti	0.060	0.048	0.114	0.075	0.090
Tsite	8.000	8.000	8.000	8.000	8.000
AlVI	0.000	0.000	0.000	0.000	0.000
Ti	0.181	0.205	0.117	0.157	0.137
Cr	0.000	0.000	0.001	0.001	0.001
Fe3+	0.927	0.944	0.967	0.876	0.933
Mg	3.033	3.006	3.087	3.161	3.072
Fe2+	0.811	0.801	0.783	0.762	0.813
Mn	0.047	0.043	0.046	0.044	0.044
Csite	5.000	5.000	5.000	5.000	5.000
Fe2+	0.000	0.000	0.000	0.000	0.000
Ca	1.667	1.702	1.669	1.671	1.685
Na	0.333	0.298	0.331	0.329	0.315
Bsite	2.000	2.000	2.000	2.000	2.000
Na	0.271	0.165	0.247	0.279	0.277
K	0.050	0.052	0.044	0.045	0.049
Asite	0.321	0.217	0.291	0.324	0.326
(Ca+Na)B	2.000	2.000	2.000	2.000	2.000
NaB	0.333	0.298	0.331	0.329	0.315
(Na+K)A	0.321	0.217	0.291	0.324	0.326
Mg/Mg+Fe2+	0.789	0.790	0.798	0.806	0.791
Amphibole composition	**Mg-Hbl**	**Mg-Hbl**	**Mg-Hbl**	**Mg-Hbl**	**Mg-Hbl**
Pressure (kbars) calculated using the calibrations of:					
Ridolfi et al. (2010)	**1.21**	**1.20**	**1.02**	**1.06**	**1.11**
uncertanty (Max error)	0.13	0.13	0.11	0.12	0.12
Temperatures (℃) calculated using the calibrations of:					
Ridolfi et al. (2010)	**851**	**842**	**852**	**845**	**854**
Depth calculates from P=rgh	**4.6**	**4.5**	**3.9**	**4.0**	**4.2**

1.14.4 The results of electron microprobe analysis of selected amphibole grains and amphibole geothermobarometry for sample AM0867/68.

Sample	**AM0868**				
Grain	AM0868-1g1c	AM0868-4r	AM0868-5r	AM0868-6r	AM0868-8c
Spot	core	rim	rim	rim	core
SiO2 (wt.%)	44.64	46.42	45.20	45.11	45.73
TiO2	1.59	1.50	1.31	1.44	1.50
Al2O3	9.20	8.14	8.29	9.03	8.65
Cr2O3	0.01	0.01	0.01	0.00	0.00
Fe2O3	8.17	7.70	7.73	7.15	8.75
FeO	6.73	6.93	8.62	8.62	6.20
MnO	0.50	0.52	0.70	0.59	0.54
MgO	13.63	14.04	12.70	12.69	13.90
CaO	11.58	11.54	11.60	11.49	11.44
Na2O	1.45	1.33	1.31	1.36	1.36
K2O	0.71	0.64	0.65	0.80	0.64
F	0.18	0.21	0.16	0.15	0.18
H2O*	1.82	1.83	1.82	1.83	1.84
Total	**100.2**	**100.8**	**100.1**	**100.3**	**100.7**
Structural formula on the basis of 13 cations (Leake et al., 1997)					
Si	6.506	6.698	6.639	6.601	6.606
AlIV	1.494	1.302	1.361	1.399	1.394
Ti	0.000	0.000	0.000	0.000	0.000
Tsite	8.000	8.000	8.000	8.000	8.000
AlVI	0.086	0.082	0.073	0.158	0.079
Ti	0.175	0.163	0.144	0.158	0.162
Cr	0.001	0.001	0.002	0.000	0.000
Fe3+	0.896	0.836	0.855	0.787	0.951
Mg	2.961	3.019	2.780	2.768	2.993
Fe2+	0.820	0.836	1.059	1.055	0.749
Mn	0.062	0.063	0.087	0.073	0.066
Csite	5.000	5.000	5.000	5.000	5.000
Fe2+	0.000	0.000	0.000	0.000	0.000
Ca	1.809	1.784	1.825	1.801	1.770
Na	0.191	0.216	0.175	0.199	0.230
Bsite	2.000	2.000	2.000	2.000	2.000
Na	0.220	0.156	0.197	0.188	0.151
K	0.133	0.118	0.122	0.149	0.118
Asite	0.353	0.274	0.318	0.336	0.268
(Ca+Na)B	2.000	2.000	2.000	2.000	2.000
NaB	0.191	0.216	0.175	0.199	0.230
(Na+K)A	0.353	0.274	0.318	0.336	0.268
Mg/Mg+Fe2+	0.783	0.783	0.724	0.724	0.800
Amphibole composition	**Mg-Hbl**	**Mg-Hbl**	**Mg-Hbl**	**Mg-Hbl**	**Mg-Hbl**
Pressure (kbars) calculated using the calibrations of:					
Ridolfi et al. (2010)	**1.86**	**1.41**	**1.51**	**1.80**	**1.60**
uncertanty (Max error)	0.20	0.15	0.17	0.20	0.18
Temperatures (℃) calculated using the calibrations of:					
Ridolfi et al. (2010)	**874**	**838**	**841**	**855**	**851**
Depth calculates from P=rgh	**7.0**	**5.3**	**5.7**	**6.8**	**6.0**

1.14.4 Continued

Sample					
Grain	AM0868-8r	AM0868-9c	AM0868-9r	AM0868-10	AM0868-2r
Spot	rim	core	rim	intermediate	rim
SiO2 (wt.%)	47.24	45.10	46.23	46.43	43.43
TiO2	1.31	1.48	1.31	1.41	1.55
Al2O3	7.65	9.16	8.35	8.11	9.92
Cr2O3	0.01	0.01	0.00	0.00	0.01
Fe2O3	8.62	8.39	8.12	7.84	8.55
FeO	5.39	7.91	7.41	6.58	8.01
MnO	0.55	0.58	0.57	0.53	0.54
MgO	14.70	12.78	13.49	14.14	12.39
CaO	11.36	11.38	11.50	11.45	11.43
Na2O	1.27	1.40	1.31	1.40	1.52
K2O	0.50	0.79	0.65	0.58	0.90
F	0.18	0.18	0.18	0.20	0.17
H2O*	1.85	1.83	1.84	1.83	1.81
Total	**100.6**	**101.0**	**101.0**	**100.5**	**100.2**
Structural formula on the basis of 13 cations (Leake et al., 1997)					
Si	6.777	6.553	6.681	6.708	6.390
AlIV	1.223	1.447	1.319	1.292	1.610
Ti	0.000	0.000	0.000	0.000	0.000
Tsite	8.000	8.000	8.000	8.000	8.000
AlVI	0.071	0.121	0.103	0.089	0.111
Ti	0.142	0.162	0.142	0.153	0.172
Cr	0.001	0.001	0.000	0.000	0.001
Fe3+	0.931	0.917	0.883	0.853	0.946
Mg	3.143	2.767	2.906	3.045	2.717
Fe2+	0.646	0.961	0.896	0.795	0.985
Mn	0.067	0.071	0.069	0.065	0.067
Csite	5.000	5.000	5.000	5.000	5.000
Fe2+	0.000	0.000	0.000	0.000	0.000
Ca	1.746	1.771	1.781	1.773	1.802
Na	0.254	0.229	0.219	0.227	0.198
Bsite	2.000	2.000	2.000	2.000	2.000
Na	0.101	0.167	0.148	0.164	0.237
K	0.091	0.146	0.119	0.108	0.169
Asite	0.191	0.313	0.267	0.271	0.406
(Ca+Na)B	2.000	2.000	2.000	2.000	2.000
NaB	0.254	0.229	0.219	0.227	0.198
(Na+K)A	0.191	0.313	0.267	0.271	0.406
Mg/Mg+Fe2+	0.829	0.742	0.764	0.793	0.734
Amphibole composition	**Mg-Hbl**	**Mg-Hbl**	**Mg-Hbl**	**Mg-Hbl**	**Tsch-Prg**
Pressure (kbars) calculated using the calibrations of:					
Ridolfi et al. (2010)	**1.23**	**1.83**	**1.49**	**1.40**	**2.28**
uncertanty (Max error)	0.14	0.20	0.16	0.15	0.25
Temperatures (℃) calculated using the calibrations of:					
Ridolfi et al. (2010)	**821**	**857**	**836**	**836**	**888**
Depth calculates from P=rgh	**4.7**	**6.9**	**5.6**	**5.3**	**8.6**

1.14.4 Continued

Sample					
Grain	AM0868-2rx2	AM0868-7	AM0868-3c	AM0868-3r	AM0868-3rx2
Spot	rim	intermediate	core	rim	rim
SiO2 (wt.%)	43.25	44.23	42.90	42.65	42.62
TiO2	1.57	1.47	1.33	1.45	1.30
Al2O3	9.62	9.36	10.27	10.34	10.52
Cr2O3	0.01	0.00	0.01	0.00	0.00
Fe2O3	9.39	7.97	6.49	6.25	7.12
FeO	7.00	8.45	12.03	12.12	11.76
MnO	0.57	0.57	0.60	0.62	0.63
MgO	12.71	12.53	10.66	10.51	10.46
CaO	11.35	11.53	11.79	11.73	11.72
Na2O	1.47	1.40	1.43	1.37	1.34
K2O	0.88	0.91	1.23	1.28	1.31
F	0.17	0.18	0.09	0.11	0.15
H2O*	1.80	1.81	1.83	1.81	1.80
Total	**99.8**	**100.4**	**100.7**	**100.2**	**100.7**
Structural formula on the basis of 13 cations (Leake et al., 1997)					
Si	6.380	6.490	6.384	6.376	6.345
AlIV	1.620	1.510	1.616	1.624	1.655
Ti	0.000	0.000	0.000	0.000	0.000
Tsite	8.000	8.000	8.000	8.000	8.000
AlVI	0.052	0.109	0.186	0.198	0.191
Ti	0.175	0.162	0.149	0.163	0.146
Cr	0.001	0.000	0.001	0.000	0.000
Fe3+	1.043	0.880	0.727	0.703	0.798
Mg	2.794	2.740	2.365	2.341	2.321
Fe2+	0.864	1.037	1.497	1.516	1.464
Mn	0.071	0.071	0.076	0.079	0.080
Csite	5.000	5.000	5.000	5.000	5.000
Fe2+	0.000	0.000	0.000	0.000	0.000
Ca	1.794	1.813	1.880	1.878	1.869
Na	0.206	0.187	0.120	0.122	0.131
Bsite	2.000	2.000	2.000	2.000	2.000
Na	0.215	0.212	0.292	0.276	0.257
K	0.165	0.170	0.233	0.243	0.248
Asite	0.381	0.383	0.525	0.519	0.505
(Ca+Na)B	2.000	2.000	2.000	2.000	2.000
NaB	0.206	0.187	0.120	0.122	0.131
(Na+K)A	0.381	0.383	0.525	0.519	0.505
Mg/Mg+Fe2+	0.764	0.725	0.612	0.607	0.613
Amphibole composition	**Tsch-Prg**	**Tsch-Prg**	**Mg-Hst**	**Mg-Hst**	**Mg-Hst**
Pressure (kbars) calculated using the calibrations of:					
Ridolfi et al. (2010)	**2.13**	**1.97**	**2.56**	**2.64**	**2.73**
uncertanty (Max error)	0.23	0.22	0.28	0.66	0.68
Temperatures (℃) calculated using the calibrations of:					
Ridolfi et al. (2010)	**886**	**871**	**890**	**892**	**894**
Depth calculates from P=rgh	**8.0**	**7.4**	**9.7**	**10.0**	**10.3**

1.14.5 The results of electron microprobe analysis of selected amphibole grains and amphibole geothermobarometry for sample AM0870

Sample	**AM0870**			
Grain	AM0870-01x2	AM0870-06	AM0870-07	AM0870-11x2
Spot	rim	core	rim	intermediate
SiO2 (wt.%)	44.67	44.48	45.55	44.52
TiO2	1.47	1.38	1.41	1.39
Al2O3	9.18	9.54	8.46	9.09
Cr2O3	0.01	0.01	0.00	0.01
Fe2O3	7.71	8.61	8.46	7.77
FeO	7.85	8.64	7.74	8.06
MnO	0.59	0.64	0.60	0.57
MgO	12.80	11.95	12.95	12.75
CaO	11.34	11.30	11.32	11.37
Na2O	1.40	1.31	1.28	1.48
K2O	0.82	0.90	0.77	0.82
F	0.20	0.15	0.17	0.21
H2O*	1.80	1.83	1.83	1.80
Total	**99.8**	**100.7**	**100.5**	**99.8**
Structural formula on the basis of 13 cations (Leake et al., 1997)				
Si	6.558	6.509	6.636	6.549
AlIV	1.442	1.491	1.364	1.451
Ti	0.000	0.000	0.000	0.000
Tsite	8.000	8.000	8.000	8.000
AlVI	0.146	0.155	0.089	0.124
Ti	0.162	0.152	0.155	0.154
Cr	0.001	0.001	0.000	0.002
Fe3+	0.852	0.948	0.927	0.860
Mg	2.802	2.607	2.813	2.797
Fe2+	0.963	1.058	0.943	0.992
Mn	0.073	0.079	0.074	0.071
Csite	5.000	5.000	5.000	5.000
Fe2+	0.000	0.000	0.000	0.000
Ca	1.784	1.773	1.767	1.791
Na	0.216	0.227	0.233	0.209
Bsite	2.000	2.000	2.000	2.000
Na	0.182	0.143	0.129	0.213
K	0.153	0.168	0.142	0.154
Asite	0.335	0.310	0.272	0.367
(Ca+Na)B	2.000	2.000	2.000	2.000
NaB	0.216	0.227	0.233	0.209
(Na+K)A	0.335	0.310	0.272	0.367
Mg/Mg+Fe2+	0.744	0.711	0.749	0.738
Amphibole composition	**Mg-Hbl**	**Mg-Hbl**	**Mg-Hbl**	**Mg-Hbl**
Pressure (kbars) calculated using the calibrations of:				
Ridolfi et al. (2010)	**1.89**	**2.05**	**1.55**	**1.85**
uncertanty (Max error)	0.21	0.23	0.17	0.20
Temperatures (℃) calculated using the calibrations of:				
Ridolfi et al. (2010)	**862**	**860**	**839**	**862**
Depth calculates from P=rgh	**7.1**	**7.7**	**5.9**	**7.0**

1.14.5 Continued

Sample				
Grain	AM0870-13	AM0870-17x1	AM0870-03x2	AM0870-03x3
Spot	rim	core	core	rim
SiO2 (wt.%)	45.25	45.93	43.83	44.18
TiO2	1.47	1.29	1.65	1.65
Al2O3	8.91	8.58	9.96	9.31
Cr2O3	0.00	0.01	0.00	0.02
Fe2O3	8.16	7.80	8.03	7.90
FeO	7.91	7.86	7.91	7.37
MnO	0.64	0.63	0.56	0.51
MgO	12.74	13.16	12.61	13.07
CaO	11.24	11.57	11.43	11.44
Na2O	1.41	1.21	1.53	1.41
K2O	0.76	0.72	0.89	0.80
F	0.24	0.22	0.21	0.23
H2O*	1.79	1.82	1.80	1.79
Total	**100.5**	**100.8**	**100.4**	**99.7**
Structural formula on the basis of 13 cations (Leake et al., 1997)				
Si	6.600	6.664	6.422	6.495
AlIV	1.400	1.336	1.578	1.505
Ti	0.000	0.000	0.000	0.000
Tsite	8.000	8.000	8.000	8.000
AlVI	0.131	0.131	0.142	0.107
Ti	0.161	0.141	0.182	0.183
Cr	0.000	0.001	0.000	0.002
Fe3+	0.895	0.851	0.886	0.874
Mg	2.769	2.846	2.753	2.864
Fe2+	0.964	0.954	0.969	0.906
Mn	0.079	0.077	0.069	0.064
Csite	5.000	5.000	5.000	5.000
Fe2+	0.000	0.000	0.000	0.000
Ca	1.756	1.799	1.794	1.802
Na	0.244	0.201	0.206	0.198
Bsite	2.000	2.000	2.000	2.000
Na	0.153	0.139	0.228	0.204
K	0.142	0.134	0.166	0.150
Asite	0.296	0.272	0.393	0.354
(Ca+Na)B	2.000	2.000	2.000	2.000
NaB	0.244	0.201	0.206	0.198
(Na+K)A	0.296	0.272	0.393	0.354
Mg/Mg+Fe2+	0.742	0.749	0.740	0.760
Amphibole composition	**Mg-Hbl**	**Mg-Hbl**	**Tsch-Prg**	**Tsch-Prg**
Pressure (kbars) calculated using the calibrations of:				
Ridolfi et al. (2010)	**1.74**	**1.58**	**2.28**	**1.95**
uncertanty (Max error)	0.19	0.17	0.25	0.21
Temperatures (℃) calculated using the calibrations of:				
Ridolfi et al. (2010)	**849**	**841**	**887**	**874**
Depth calculates from P=rgh	**6.6**	**6.0**	**8.6**	**7.4**

1.14.5 Continued

Sample				
Grain	AM0870-11	AM0870-11x3	AM0870-12x1	AM0870-12x2
Spot	intermediate	intermediate	core	core
SiO2 (wt.%)	42.77	43.14	43.93	43.82
TiO2	1.61	1.82	1.65	1.57
Al2O3	10.33	9.96	9.77	9.95
Cr2O3	0.01	0.00	0.00	0.00
Fe2O3	7.68	7.00	7.56	8.91
FeO	9.06	9.25	8.72	7.23
MnO	0.54	0.51	0.54	0.55
MgO	11.72	12.01	12.33	12.67
CaO	11.36	11.44	11.34	11.30
Na2O	1.53	1.54	1.57	1.55
K2O	1.04	0.94	0.99	0.79
F	0.21	0.14	0.19	0.24
H2O*	1.77	1.81	1.81	1.79
Total	**99.6**	**99.6**	**100.4**	**100.4**
Structural formula on the basis of 13 cations (Leake et al., 1997)				
Si	6.358	6.403	6.454	6.412
AlIV	1.642	1.597	1.546	1.588
Ti	0.000	0.000	0.000	0.000
Tsite	8.000	8.000	8.000	8.000
AlVI	0.168	0.145	0.145	0.129
Ti	0.180	0.203	0.182	0.173
Cr	0.001	0.000	0.000	0.000
Fe3+	0.859	0.782	0.836	0.981
Mg	2.598	2.658	2.700	2.764
Fe2+	1.127	1.148	1.071	0.885
Mn	0.069	0.064	0.067	0.069
Csite	5.000	5.000	5.000	5.000
Fe2+	0.000	0.000	0.000	0.000
Ca	1.809	1.819	1.785	1.772
Na	0.191	0.181	0.215	0.228
Bsite	2.000	2.000	2.000	2.000
Na	0.249	0.264	0.232	0.212
K	0.197	0.179	0.185	0.148
Asite	0.446	0.443	0.417	0.360
(Ca+Na)B	2.000	2.000	2.000	2.000
NaB	0.191	0.181	0.215	0.228
(Na+K)A	0.446	0.443	0.417	0.360
Mg/Mg+Fe2+	0.698	0.698	0.716	0.757
Amphibole composition	**Tsch-Prg**	**Tsch-Prg**	**Tsch-Prg**	**Tsch-Prg**
Pressure (kbars) calculated using the calibrations of:				
Ridolfi et al. (2010)	**2.59**	**2.35**	**2.19**	**2.27**
uncertanty (Max error)	0.29	0.26	0.24	0.25
Temperatures (℃) calculated using the calibrations of:				
Ridolfi et al. (2010)	**897**	**891**	**880**	**884**
Depth calculates from P=rgh	**9.8**	**8.9**	**8.3**	**8.6**

1.14.6 The results of electron microprobe analysis of selected amphibole grains and amphibole geothermobarometry for sample ZN122.

Sample	**ZN122**					
Grain	ZN122-1c	ZN122-1r	ZN122-2c	ZN122-2r	ZN122-2r-repeat	ZN122-3c
Spot	core	rim	core	rim	rim	core
SiO2 (wt.%)	45.90	47.18	41.04	41.28	40.71	46.98
TiO2	1.93	1.64	2.45	2.49	2.45	1.74
Al2O3	8.12	6.95	12.52	12.95	13.05	7.15
Cr2O3	0.00	0.00	0.00	0.01	0.01	0.00
Fe2O3	6.29	7.59	8.44	8.97	8.79	7.40
FeO	7.94	6.38	3.76	3.87	3.86	7.08
MnO	0.25	0.25	0.14	0.14	0.14	0.29
MgO	14.17	15.18	14.44	14.38	14.21	14.66
CaO	11.47	11.59	11.44	11.47	11.47	11.48
Na2O	1.59	1.43	2.12	2.27	2.20	1.44
K2O	0.95	0.70	0.87	0.85	0.87	0.76
F	0.48	0.54	0.21	0.22	0.22	0.43
H2O*	1.71	1.69	1.80	1.82	1.80	1.74
Total	**100.8**	**101.1**	**99.2**	**100.7**	**99.8**	**101.2**
Structural formula on the basis of 13 cations (Leake et al., 1997)						
Si	6.657	6.777	6.009	5.966	5.940	6.763
AlIV	1.343	1.177	1.991	2.034	2.060	1.213
Ti	0.000	0.046	0.000	0.000	0.000	0.024
Tsite	8.000	8.000	8.000	8.000	8.000	8.000
AlVI	0.045	0.000	0.170	0.172	0.185	0.000
Ti	0.210	0.131	0.270	0.270	0.269	0.165
Cr	0.000	0.000	0.000	0.001	0.001	0.000
Fe3+	0.687	0.821	0.930	0.975	0.966	0.802
Mg	3.064	3.251	3.151	3.097	3.092	3.145
Fe2+	0.963	0.766	0.461	0.467	0.471	0.852
Mn	0.031	0.031	0.018	0.017	0.017	0.036
Csite	5.000	5.000	5.000	5.000	5.000	5.000
Fe2+	0.000	0.000	0.000	0.000	0.000	0.000
Ca	1.783	1.784	1.794	1.775	1.794	1.770
Na	0.217	0.216	0.206	0.225	0.206	0.230
Bsite	2.000	2.000	2.000	2.000	2.000	2.000
Na	0.231	0.182	0.395	0.412	0.415	0.172
K	0.176	0.128	0.162	0.157	0.162	0.139
Asite	0.407	0.310	0.557	0.570	0.577	0.311
(Ca+Na)B	2.000	2.000	2.000	2.000	2.000	2.000
NaB	0.217	0.216	0.206	0.225	0.206	0.230
(Na+K)A	0.407	0.310	0.557	0.570	0.577	0.311
Mg/Mg+Fe2+	0.761	0.809	0.872	0.869	0.868	0.787
Amphibole composition	**Mg-Hbl**	**Mg-Hbl**	**Mg-Hst**	**Mg-Hst**	**Mg-Hst**	**Mg-Hbl**
Pressure (kbars) calculated using the calibrations of:						
Ridolfi et al. (2010)	**1.41**	**1.04**	**4.29**	**4.58**	**4.85**	**1.10**
uncertanty (Max error)	0.16	0.11	0.47	0.50	0.53	0.12
Temperatures (℃) calculated using the calibrations of:						
Ridolfi et al. (2010)	**850**	**837**	**987**	**992**	**999**	**830**
Depth calculates from P=rgh	**5.3**	**3.9**	**16.2**	**17.3**	**18.3**	**4.1**

1.14.6 Continued

Sample						
Grain	ZN122-3r	ZN122-4c	ZN122-4r	ZN122-5	ZN122-5x2	ZN122-6
Spot	rim	core	rim			
SiO2 (wt.%)	45.70	46.37	44.33	44.66	45.12	44.86
TiO2	1.93	1.74	1.86	1.97	1.97	1.85
Al2O3	8.01	7.14	7.67	8.13	8.12	7.66
Cr2O3	0.00	0.00	0.00	0.00	0.00	0.00
Fe2O3	6.46	7.10	9.23	7.61	7.13	7.67
FeO	7.95	6.75	5.55	6.72	7.08	6.96
MnO	0.27	0.25	0.24	0.24	0.24	0.29
MgO	14.05	14.98	14.57	14.03	14.28	14.02
CaO	11.46	11.69	11.34	11.18	11.41	11.27
Na2O	1.55	1.41	1.54	1.54	1.61	1.48
K2O	0.91	0.77	0.86	0.90	0.88	0.87
F	0.34	0.51	0.47	0.48	0.48	0.39
H2O*	1.76	1.69	1.67	1.67	1.69	1.71
Total	**100.4**	**100.4**	**99.3**	**99.1**	**100.0**	**99.0**
Structural formula on the basis of 13 cations (Leake et al., 1997)						
Si	6.655	6.727	6.528	6.584	6.595	6.625
AlIV	1.345	1.220	1.332	1.413	1.398	1.333
Ti	0.000	0.053	0.140	0.004	0.007	0.041
Tsite	8.000	8.000	8.000	8.000	8.000	8.000
AlVI	0.030	0.000	0.000	0.000	0.000	0.000
Ti	0.211	0.136	0.066	0.215	0.210	0.164
Cr	0.000	0.000	0.000	0.000	0.000	0.000
Fe3+	0.708	0.775	1.023	0.844	0.784	0.853
Mg	3.050	3.239	3.197	3.083	3.111	3.088
Fe2+	0.968	0.819	0.684	0.828	0.865	0.860
Mn	0.033	0.031	0.030	0.030	0.030	0.036
Csite	5.000	5.000	5.000	5.000	5.000	5.000
Fe2+	0.000	0.000	0.000	0.000	0.000	0.000
Ca	1.789	1.817	1.789	1.765	1.787	1.783
Na	0.211	0.183	0.211	0.235	0.213	0.217
Bsite	2.000	2.000	2.000	2.000	2.000	2.000
Na	0.227	0.213	0.228	0.205	0.243	0.206
K	0.170	0.143	0.161	0.169	0.164	0.164
Asite	0.396	0.356	0.389	0.374	0.407	0.370
(Ca+Na)B	2.000	2.000	2.000	2.000	2.000	2.000
NaB	0.211	0.183	0.211	0.235	0.213	0.217
(Na+K)A	0.396	0.356	0.389	0.374	0.407	0.370
Mg/Mg+Fe2+	0.759	0.798	0.824	0.788	0.782	0.782
Amphibole composition	**Mg-Hbl**	**Mg-Hbl**	**Mg-Hbl**	**Mg-Hbl**	**Mg-Hbl**	**Mg-Hbl**
Pressure (kbars) calculated using the calibrations of:						
Ridolfi et al. (2010)	**1.39**	**1.11**	**1.30**	**1.46**	**1.43**	**1.31**
uncertanty (Max error)	0.15	0.12	0.14	0.16	0.16	0.14
Temperatures (℃) calculated using the calibrations of:						
Ridolfi et al. (2010)	**849**	**851**	**902**	**858**	**861**	**860**
Depth calculates from P=rgh	**5.2**	**4.2**	**4.9**	**5.5**	**5.4**	**4.9**

1.14.6 Continued

Sample					
Grain	ZN122-7r	ZN122-8c	ZN122-8r	ZN122-9	ZN122-10
Spot	rim	core	rim		
SiO2 (wt.%)	44.85	44.80	44.26	44.18	41.34
TiO2	1.87	1.99	1.95	1.95	3.07
Al2O3	7.76	8.78	8.45	8.14	10.79
Cr2O3	0.00	0.00	0.00	0.01	0.00
Fe2O3	7.54	7.67	8.42	6.68	7.92
FeO	7.03	7.01	7.01	7.72	8.79
MnO	0.28	0.23	0.27	0.26	0.27
MgO	14.08	13.96	13.78	13.73	12.17
CaO	11.34	11.35	11.30	11.36	11.42
Na2O	1.51	1.63	1.66	1.56	1.97
K2O	0.86	0.90	0.97	0.95	0.95
F	0.44	0.38	0.38	0.36	0.44
H2O*	1.69	1.74	1.72	1.71	1.68
Total	**99.3**	**100.4**	**100.2**	**98.6**	**100.8**
Structural formula on the basis of 13 cations (Leake et al., 1997)					
Si	6.612	6.523	6.490	6.570	6.103
AlIV	1.349	1.477	1.460	1.426	1.878
Ti	0.039	0.000	0.051	0.004	0.019
Tsite	8.000	8.000	8.000	8.000	8.000
AlVI	0.000	0.030	0.000	0.000	0.000
Ti	0.168	0.218	0.164	0.214	0.321
Cr	0.000	0.000	0.001	0.001	0.000
Fe3+	0.836	0.841	0.929	0.748	0.880
Mg	3.094	3.030	3.012	3.045	2.679
Fe2+	0.866	0.853	0.860	0.960	1.086
Mn	0.035	0.028	0.034	0.032	0.034
Csite	5.000	5.000	5.000	5.000	5.000
Fe2+	0.000	0.000	0.000	0.000	0.000
Ca	1.791	1.770	1.775	1.810	1.807
Na	0.209	0.230	0.225	0.190	0.193
Bsite	2.000	2.000	2.000	2.000	2.000
Na	0.224	0.231	0.246	0.259	0.370
K	0.162	0.167	0.181	0.180	0.178
Asite	0.386	0.399	0.426	0.439	0.548
(Ca+Na)B	2.000	2.000	2.000	2.000	2.000
NaB	0.209	0.230	0.225	0.190	0.193
(Na+K)A	0.386	0.399	0.426	0.439	0.548
Mg/Mg+Fe2+	0.781	0.780	0.778	0.760	0.712
Amphibole composition	**Mg-Hbl**	**Mg-Hbl**	**Tsch-Prg**	**Mg-Hbl**	**Mg-Hst**
Pressure (kbars) calculated using the calibrations of:					
Ridolfi et al. (2010)	**1.34**	**1.68**	**1.57**	**1.49**	**2.86**
uncertanty (Max error)	0.15	0.18	0.17	0.16	0.31
Temperatures (℃) calculated using the calibrations of:					
Ridolfi et al. (2010)	**863**	**870**	**884**	**865**	**947**
Depth calculates from P=rgh	**5.0**	**6.3**	**5.9**	**5.6**	**10.8**

1.14.7 The results of electron microprobe analysis of selected amphibole grains and amphibole geothermobarometry for sample MQ28.

Sample	**MQ28**					
Grain	MQ28-1r	MQ28-1x2	MQ28-2r	MQ28-3	MQ28-3r	MQ28-4r
Spot	rim	core	rim	intermediate	rim	rim
SiO2 (wt.%)	41.90	41.35	41.62	40.84	42.58	42.18
TiO2	3.24	2.30	3.28	2.68	3.27	2.88
Al2O3	9.99	12.64	10.47	12.09	9.81	11.48
Cr2O3	0.00	0.03	0.01	0.01	0.00	0.01
Fe2O3	7.55	6.10	5.98	6.62	5.73	6.12
FeO	6.25	4.37	7.17	5.59	6.81	4.70
MnO	0.23	0.10	0.24	0.15	0.21	0.09
MgO	14.09	15.21	13.65	14.18	14.51	15.09
CaO	11.11	12.02	11.18	11.63	11.38	11.49
Na2O	2.49	2.31	2.40	2.46	2.46	2.42
K2O	0.73	0.81	0.76	0.63	0.72	0.59
F	1.15	0.21	0.38	0.36	1.06	0.35
H2O*	1.37	1.81	1.71	1.72	1.42	1.75
Total	**100.1**	**99.3**	**98.8**	**99.0**	**100.0**	**99.2**
Structural formula on the basis of 13 cations (Leake et al., 1997)						
Si	6.175	6.039	6.185	6.031	6.260	6.161
AlIV	1.735	1.961	1.815	1.969	1.700	1.839
Ti	0.090	0.000	0.000	0.000	0.040	0.000
Tsite	8.000	8.000	8.000	8.000	8.000	8.000
AlVI	0.000	0.214	0.019	0.135	0.000	0.138
Ti	0.269	0.252	0.367	0.297	0.322	0.317
Cr	0.000	0.004	0.002	0.001	0.000	0.001
Fe3+	0.837	0.671	0.668	0.735	0.634	0.673
Mg	3.095	3.312	3.024	3.121	3.181	3.286
Fe2+	0.770	0.534	0.891	0.690	0.837	0.574
Mn	0.029	0.013	0.030	0.019	0.027	0.011
Csite	5.000	5.000	5.000	5.000	5.000	5.000
Fe2+	0.000	0.000	0.000	0.000	0.000	0.000
Ca	1.755	1.881	1.780	1.839	1.793	1.798
Na	0.245	0.119	0.220	0.161	0.207	0.202
Bsite	2.000	2.000	2.000	2.000	2.000	2.000
Na	0.467	0.535	0.470	0.544	0.495	0.485
K	0.138	0.151	0.143	0.119	0.135	0.110
Asite	0.604	0.686	0.613	0.663	0.630	0.595
(Ca+Na)B	2.000	2.000	2.000	2.000	2.000	2.000
NaB	0.245	0.119	0.220	0.161	0.207	0.202
(Na+K)A	0.604	0.686	0.613	0.663	0.630	0.595
Mg/Mg+Fe2+	0.801	0.861	0.773	0.819	0.792	0.851
Amphibole composition	**Mg-Hst**	**Mg-Hst**	**Mg-Hst**	**Mg-Hst**	**Mg-Hst**	**Mg-Hst**
Pressure (kbars) calculated using the calibrations of:						
Ridolfi et al. (2010)	**2.33**	**4.39**	**2.69**	**3.96**	**2.21**	**3.30**
uncertanty (Max error)	0.26	0.48	0.30	0.44	0.24	0.36
Temperatures (℃) calculated using the calibrations of:						
Ridolfi et al. (2010)	**968**	**1003**	**948**	**989**	**949**	**970**
Depth calculates from P=rgh	**8.8**	**16.6**	**10.1**	**15.0**	**8.4**	**12.4**

1.14.7 Continued

Sample					
Grain	MQ28-5c	MQ28-5r	MQ28-6c	MQ28-6r	MQ28-7g1c
Spot	core	rim	core	rim	core
SiO2 (wt.%)	41.23	42.95	42.51	41.98	41.62
TiO2	3.09	3.32	2.72	2.79	2.76
Al2O3	11.64	10.05	11.63	11.46	11.93
Cr2O3	0.00	0.00	0.24	0.23	0.07
Fe2O3	6.60	5.26	6.39	7.26	6.55
FeO	5.41	7.85	4.17	3.37	4.64
MnO	0.20	0.22	0.10	0.10	0.11
MgO	14.33	13.83	15.22	15.41	14.78
CaO	11.29	11.19	11.40	11.34	11.47
Na2O	2.58	2.44	2.41	2.42	2.43
K2O	0.67	0.73	0.64	0.62	0.65
F	0.30	0.42	0.17	0.52	0.20
H2O*	1.76	1.72	1.84	1.67	1.81
Total	**99.1**	**100.0**	**99.5**	**99.2**	**99.0**
Structural formula on the basis of 13 cations (Leake et al., 1997)					
Si	6.071	6.301	6.172	6.124	6.097
AlIV	1.929	1.699	1.828	1.876	1.903
Ti	0.000	0.000	0.000	0.000	0.000
Tsite	8.000	8.000	8.000	8.000	8.000
AlVI	0.090	0.039	0.163	0.096	0.156
Ti	0.342	0.366	0.297	0.306	0.304
Cr	0.000	0.000	0.027	0.026	0.008
Fe3+	0.731	0.581	0.699	0.797	0.722
Mg	3.146	3.024	3.295	3.352	3.228
Fe2+	0.667	0.963	0.506	0.411	0.569
Mn	0.024	0.027	0.013	0.012	0.014
Csite	5.000	5.000	5.000	5.000	5.000
Fe2+	0.000	0.000	0.000	0.000	0.000
Ca	1.781	1.759	1.774	1.773	1.799
Na	0.219	0.241	0.226	0.227	0.201
Bsite	2.000	2.000	2.000	2.000	2.000
Na	0.517	0.452	0.453	0.457	0.488
K	0.126	0.137	0.119	0.115	0.122
Asite	0.643	0.589	0.572	0.572	0.610
(Ca+Na)B	2.000	2.000	2.000	2.000	2.000
NaB	0.219	0.241	0.226	0.227	0.201
(Na+K)A	0.643	0.589	0.572	0.572	0.610
Mg/Mg+Fe2+	0.825	0.758	0.867	0.891	0.850
Amphibole composition	**Mg-Hst**	**Mg-Hst**	**Mg-Hst**	**Mg-Hst**	**Mg-Hst**
Pressure (kbars) calculated using the calibrations of:					
Ridolfi et al. (2010)	**3.50**	**2.34**	**3.36**	**3.27**	**3.71**
uncertanty (Max error)	0.39	0.26	0.37	0.36	0.41
Temperatures (℃) calculated using the calibrations of:					
Ridolfi et al. (2010)	**978**	**928**	**967**	**972**	**980**
Depth calculates from P=rgh	**13.2**	**8.8**	**12.7**	**12.3**	**14.0**

1.14.7 Continued

Sample					
Grain	MQ28-7g1r	MQ28-7g2r	MQ28-9c	MQ28-9i	MQ28-9r
Spot	rim	rim	core	intermediate	rim
SiO2 (wt.%)	41.67	41.52	42.06	42.98	41.73
TiO2	2.78	3.06	2.65	2.73	2.97
Al2O3	11.61	11.02	12.00	11.51	11.92
Cr2O3	0.00	0.01	0.16	0.04	0.07
Fe2O3	7.01	7.36	7.24	6.26	7.53
FeO	5.25	5.03	3.71	4.33	4.29
MnO	0.12	0.15	0.10	0.09	0.10
MgO	14.20	14.37	14.96	15.50	14.83
CaO	11.25	11.16	11.59	11.51	11.42
Na2O	2.38	2.38	2.39	2.49	2.42
K2O	0.61	0.65	0.02	0.62	0.67
F	0.63	0.92	0.15	0.19	0.81
H2O*	1.61	1.47	1.84	1.85	1.55
Total	**99.1**	**99.1**	**98.9**	**100.1**	**100.3**
Structural formula on the basis of 13 cations (Leake et al., 1997)					
Si	6.129	6.127	6.126	6.199	6.061
AlIV	1.871	1.873	1.874	1.801	1.939
Ti	0.000	0.000	0.000	0.000	0.000
Tsite	8.000	8.000	8.000	8.000	8.000
AlVI	0.141	0.043	0.185	0.155	0.101
Ti	0.307	0.340	0.290	0.296	0.324
Cr	0.000	0.001	0.019	0.004	0.008
Fe3+	0.776	0.817	0.793	0.679	0.823
Mg	3.115	3.160	3.249	3.332	3.211
Fe2+	0.646	0.620	0.452	0.522	0.521
Mn	0.015	0.018	0.012	0.011	0.012
Csite	5.000	5.000	5.000	5.000	5.000
Fe2+	0.000	0.000	0.000	0.000	0.000
Ca	1.773	1.764	1.809	1.779	1.777
Na	0.227	0.236	0.191	0.221	0.223
Bsite	2.000	2.000	2.000	2.000	2.000
Na	0.451	0.446	0.484	0.476	0.458
K	0.114	0.122	0.004	0.114	0.124
Asite	0.566	0.568	0.488	0.590	0.582
(Ca+Na)B	2.000	2.000	2.000	2.000	2.000
NaB	0.227	0.236	0.191	0.221	0.223
(Na+K)A	0.566	0.568	0.488	0.590	0.582
Mg/Mg+Fe2+	0.828	0.836	0.878	0.865	0.860
Amphibole composition	**Mg-Hst**	**Mg-Hst**	**Tsch-Prg**	**Mg-Hst**	**Mg-Hst**
Pressure (kbars) calculated using the calibrations of:					
Ridolfi et al. (2010)	**3.47**	**3.02**	**3.71**	**3.20**	**3.61**
uncertanty (Max error)	0.38	0.33	0.41	0.35	0.40
Temperatures (℃) calculated using the calibrations of:					
Ridolfi et al. (2010)	**965**	**960**	**974**	**964**	**979**
Depth calculates from P=rgh	**13.1**	**11.4**	**14.0**	**12.1**	**13.6**

1.14.7 Continued

Sample					
Grain	MQ28-10c	MQ28-10i	MQ28-10r	MQ28-11c	MQ28-11r
Spot	core	intermediate	rim	core	rim
SiO2 (wt.%)	40.85	40.31	41.38	41.76	41.33
TiO2	2.18	2.51	3.72	2.80	3.13
Al2O3	13.28	13.00	10.69	11.50	11.49
Cr2O3	0.32	0.01	0.00	0.01	0.00
Fe2O3	5.86	6.02	5.01	7.05	5.95
FeO	3.26	5.58	7.55	5.15	6.20
MnO	0.10	0.17	0.21	0.18	0.19
MgO	15.90	14.24	13.96	14.50	14.23
CaO	12.29	11.80	11.29	11.39	11.48
Na2O	2.48	2.60	2.77	2.50	2.57
K2O	0.76	0.74	0.70	0.61	0.64
F	0.09	0.31	0.95	0.26	0.36
H2O*	1.88	1.75	1.46	1.79	1.73
Total	**99.2**	**99.1**	**99.7**	**99.5**	**99.3**
Structural formula on the basis of 13 cations (Leake et al., 1997)					
Si	5.947	5.948	6.123	6.113	6.087
AlIV	2.053	2.052	1.864	1.887	1.913
Ti	0.000	0.000	0.013	0.000	0.000
Tsite	8.000	8.000	8.000	8.000	8.000
AlVI	0.225	0.209	0.000	0.097	0.082
Ti	0.239	0.279	0.401	0.308	0.347
Cr	0.036	0.001	0.000	0.001	0.000
Fe3+	0.642	0.669	0.558	0.777	0.659
Mg	3.450	3.133	3.080	3.164	3.124
Fe2+	0.397	0.689	0.934	0.631	0.764
Mn	0.012	0.021	0.026	0.023	0.024
Csite	5.000	5.000	5.000	5.000	5.000
Fe2+	0.000	0.000	0.000	0.000	0.000
Ca	1.917	1.866	1.789	1.787	1.812
Na	0.083	0.134	0.211	0.213	0.188
Bsite	2.000	2.000	2.000	2.000	2.000
Na	0.616	0.611	0.583	0.496	0.545
K	0.140	0.139	0.131	0.114	0.120
Asite	0.756	0.750	0.714	0.609	0.665
(Ca+Na)B	2.000	2.000	2.000	2.000	2.000
NaB	0.083	0.134	0.211	0.213	0.188
(Na+K)A	0.756	0.750	0.714	0.609	0.665
Mg/Mg+Fe2+	0.897	0.820	0.767	0.834	0.804
Amphibole composition	**Mg-Hst**	**Mg-Hst**	**Mg-Hst**	**Mg-Hst**	**Mg-Hst**
Pressure (kbars) calculated using the calibrations of:					
Ridolfi et al. (2010)	**5.08**	**4.96**	**2.80**	**3.33**	**3.39**
uncertanty (Max error)	0.56	0.55	0.31	0.37	0.37
Temperatures (℃) calculated using the calibrations of:					
Ridolfi et al. (2010)	**1030**	**1015**	**970**	**969**	**977**
Depth calculates from P=rgh	**19.2**	**18.7**	**10.6**	**12.6**	**12.8**

1.14.8 The results of electron microprobe analysis of selected amphibole grains and amphibole geothermobarometry for sample RJ11A7.

Sample	**RJ11A7**					
Grain	RJ11A7-1r	RJ11A7-2r	RJ11A7-4r	RJ11A7-7r	RJ11A7-8r	RJ11A7-9r
Spot	rim	rim	rim	rim	rim	rim
SiO2 (wt.%)	42.15	41.86	43.24	43.92	43.83	43.36
TiO2	2.02	1.87	1.90	1.57	1.80	1.84
Al2O3	11.83	12.59	12.09	11.84	11.67	11.67
Cr2O3	0.01	0.00	0.02	0.15	0.06	0.07
Fe2O3	6.69	7.93	8.42	7.15	7.49	7.18
FeO	4.45	4.38	1.95	0.96	2.95	2.87
MnO	0.12	0.15	0.11	0.10	0.12	0.10
MgO	15.09	14.07	16.06	17.00	15.99	16.33
CaO	11.19	10.65	10.92	10.97	11.05	11.55
Na2O	2.98	2.89	2.92	2.84	2.93	2.75
K2O	0.63	0.72	0.71	0.78	0.68	0.69
F	0.56	0.17	0.25	0.09	0.18	0.18
H2O*	1.65	1.82	1.83	1.90	1.87	1.86
Total	**99.4**	**99.1**	**100.4**	**99.3**	**100.6**	**100.5**
Structural formula on the basis of 13 cations (Leake et al., 1997)						
Si	6.159	6.125	6.182	6.290	6.260	6.208
AlIV	1.841	1.875	1.818	1.710	1.740	1.792
Ti	0.000	0.000	0.000	0.000	0.000	0.000
Tsite	8.000	8.000	8.000	8.000	8.000	8.000
AlVI	0.196	0.297	0.218	0.288	0.225	0.178
Ti	0.222	0.206	0.205	0.169	0.193	0.198
Cr	0.001	0.001	0.002	0.016	0.007	0.008
Fe3+	0.735	0.873	0.906	0.770	0.805	0.774
Mg	3.286	3.070	3.423	3.630	3.405	3.486
Fe2+	0.544	0.536	0.233	0.114	0.352	0.344
Mn	0.015	0.018	0.013	0.012	0.014	0.012
Csite	5.000	5.000	5.000	5.000	5.000	5.000
Fe2+	0.000	0.000	0.000	0.000	0.000	0.000
Ca	1.751	1.670	1.672	1.683	1.692	1.773
Na	0.249	0.330	0.328	0.317	0.308	0.227
Bsite	2.000	2.000	2.000	2.000	2.000	2.000
Na	0.597	0.489	0.482	0.472	0.502	0.536
K	0.117	0.134	0.129	0.142	0.124	0.127
Asite	0.713	0.624	0.611	0.614	0.626	0.663
(Ca+Na)B	2.000	2.000	2.000	2.000	2.000	2.000
NaB	0.249	0.330	0.328	0.317	0.308	0.227
(Na+K)A	0.713	0.624	0.611	0.614	0.626	0.663
Mg/Mg+Fe2+	0.858	0.851	0.936	0.969	0.906	0.910
Amphibole composition	**Mg-Hst**	**Mg-Hst**	**Mg-Hst**	**Mg-Hst**	**Mg-Hst**	**Mg-Hst**
Pressure (kbars) calculated using the calibrations of:						
Ridolfi et al. (2010)	**3.59**	**4.36**	**3.59**	**3.40**	**3.24**	**3.26**
uncertanty (Max error)	0.40	0.48	0.39	0.37	0.36	0.36
Temperatures (℃) calculated using the calibrations of:						
Ridolfi et al. (2010)	**972**	**968**	**964**	**959**	**952**	**966**
Depth calculates from P=rgh	**13.6**	**16.5**	**13.6**	**12.8**	**12.2**	**12.3**

1.14.9 The results of electron microprobe analysis of selected amphibole grains and amphibole geothermobarometry for sample RJ11A15.

Sample	**RJ11A15**				
Grain	RJ11A15-1c	RJ11A15-1g2	RJ11A15-1r	RJ11A15-1rx2	RJ11A15-2r
Spot	core		rim	rim	rim
SiO2 (wt.%)	46.21	46.52	45.52	47.44	46.71
TiO2	0.99	1.24	1.13	1.09	1.17
Al2O3	8.38	8.26	8.85	7.86	8.05
Cr2O3	0.00	0.00	0.00	0.00	0.00
Fe2O3	7.81	7.71	7.96	7.38	7.87
FeO	8.49	8.35	8.89	8.19	8.41
MnO	0.49	0.47	0.46	0.49	0.47
MgO	12.97	13.12	12.59	13.46	13.21
CaO	11.22	11.21	11.26	11.19	11.32
Na2O	1.77	1.67	1.75	1.63	1.65
K2O	0.49	0.50	0.66	0.49	0.47
F	0.18	0.19	0.17	0.19	0.21
H2O*	1.83	1.84	1.83	1.85	1.83
Total	**100.8**	**101.1**	**101.1**	**101.3**	**101.4**
Structural formula on the basis of 13 cations (Leake et al., 1997)					
Si	6.708	6.725	6.620	6.820	6.737
AlIV	1.292	1.275	1.380	1.180	1.263
Ti	0.000	0.000	0.000	0.000	0.000
Tsite	8.000	8.000	8.000	8.000	8.000
AlVI	0.142	0.132	0.137	0.153	0.106
Ti	0.108	0.135	0.124	0.118	0.127
Cr	0.000	0.000	0.000	0.000	0.000
Fe3+	0.853	0.839	0.871	0.799	0.854
Mg	2.806	2.827	2.730	2.886	2.841
Fe2+	1.031	1.009	1.081	0.985	1.014
Mn	0.060	0.057	0.056	0.060	0.057
Csite	5.000	5.000	5.000	5.000	5.000
Fe2+	0.000	0.000	0.000	0.000	0.000
Ca	1.745	1.737	1.754	1.724	1.749
Na	0.255	0.263	0.246	0.276	0.251
Bsite	2.000	2.000	2.000	2.000	2.000
Na	0.244	0.205	0.248	0.179	0.212
K	0.092	0.092	0.123	0.090	0.087
Asite	0.336	0.297	0.370	0.269	0.298
(Ca+Na)B	2.000	2.000	2.000	2.000	2.000
NaB	0.255	0.263	0.246	0.276	0.251
(Na+K)A	0.336	0.297	0.370	0.269	0.298
Mg/Mg+Fe2+	0.731	0.737	0.716	0.746	0.737
Amphibole composition	**Mg-Hbl**	**Mg-Hbl**	**Mg-Hbl**	**Mg-Hbl**	**Mg-Hbl**
Pressure (kbars) calculated using the calibrations of:					
Ridolfi et al. (2010)	**1.51**	**1.45**	**1.70**	**1.31**	**1.38**
uncertanty (Max error)	0.17	0.16	0.19	0.14	0.15
Temperatures (℃) calculated using the calibrations of:					
Ridolfi et al. (2010)	**830**	**826**	**844**	**811**	**823**
Depth calculates from P=rgh	**5.7**	**5.5**	**6.4**	**4.9**	**5.2**

1.14.9 Continued

Sample					
Grain	RJ11A15-2rx2	RJ11A15-3c	RJ11A15-4c	RJ11A15-4m	RJ11A15-4r
Spot	rim	core	core		rim
SiO2 (wt.%)	46.30	42.76	44.58	44.83	44.81
TiO2	1.04	2.20	1.36	1.37	1.18
Al2O3	8.17	12.43	10.09	9.92	9.17
Cr2O3	0.01	0.02	0.30	0.02	0.02
Fe2O3	8.15	6.43	5.76	6.73	7.56
FeO	8.27	6.04	10.36	10.08	10.30
MnO	0.43	0.10	0.43	0.42	0.46
MgO	13.09	14.24	11.96	12.09	11.87
CaO	11.30	11.51	11.43	11.41	11.41
Na2O	1.59	2.63	1.93	1.92	1.84
K2O	0.54	0.62	0.70	0.73	0.67
F	0.16	0.11	0.20	0.21	0.18
H2O*	1.84	1.88	1.82	1.82	1.82
Total	**100.9**	**101.0**	**100.9**	**101.5**	**101.3**
Structural formula on the basis of 13 cations (Leake et al., 1997)					
Si	6.714	6.158	6.518	6.517	6.552
AlIV	1.286	1.842	1.482	1.483	1.448
Ti	0.000	0.000	0.000	0.000	0.000
Tsite	8.000	8.000	8.000	8.000	8.000
AlVI	0.111	0.267	0.257	0.216	0.133
Ti	0.113	0.238	0.149	0.150	0.130
Cr	0.001	0.002	0.035	0.002	0.002
Fe3+	0.890	0.697	0.633	0.736	0.832
Mg	2.829	3.056	2.606	2.621	2.587
Fe2+	1.003	0.727	1.267	1.225	1.259
Mn	0.053	0.013	0.053	0.052	0.057
Csite	5.000	5.000	5.000	5.000	5.000
Fe2+	0.000	0.000	0.000	0.000	0.000
Ca	1.755	1.777	1.790	1.778	1.788
Na	0.245	0.223	0.210	0.222	0.212
Bsite	2.000	2.000	2.000	2.000	2.000
Na	0.203	0.511	0.337	0.318	0.309
K	0.100	0.114	0.131	0.135	0.125
Asite	0.303	0.624	0.469	0.454	0.434
(Ca+Na)B	2.000	2.000	2.000	2.000	2.000
NaB	0.245	0.223	0.210	0.222	0.212
(Na+K)A	0.303	0.624	0.469	0.454	0.434
Mg/Mg+Fe2+	0.738	0.808	0.673	0.682	0.673
Amphibole composition	**Mg-Hbl**	**Mg-Hst**	**Mg-Hbl**	**Mg-Hbl**	**Mg-Hbl**
Pressure (kbars) calculated using the calibrations of:					
Ridolfi et al. (2010)	**1.43**	**3.99**	**2.34**	**2.21**	**1.86**
uncertanty (Max error)	0.16	0.44	0.59	0.24	0.20
Temperatures (℃) calculated using the calibrations of:					
Ridolfi et al. (2010)	**826**	**967**	**876**	**871**	**855**
Depth calculates from P=rgh	**5.4**	**15.1**	**8.8**	**8.4**	**7.0**

1.14.9 Continued

Sample					
Grain	RJ11A15-5rx1	RJ11A15-5rx2	RJ11A15-7r	RJ11A15-8c	RJ11A15-8rx1
Spot	rim	rim	rim	core	rim
SiO2 (wt.%)	46.05	47.23	44.68	45.37	45.69
TiO2	1.04	0.96	1.08	1.30	1.13
Al2O3	8.66	7.51	9.20	9.01	8.65
Cr2O3	0.00	0.00	0.01	0.01	0.00
Fe2O3	7.53	8.01	6.96	7.46	6.97
FeO	9.29	8.24	10.86	9.47	9.84
MnO	0.43	0.41	0.44	0.45	0.43
MgO	12.61	13.35	11.62	12.41	12.44
CaO	11.36	11.24	11.42	11.26	11.44
Na2O	1.70	1.58	1.81	1.89	1.75
K2O	0.56	0.39	0.68	0.63	0.52
F	0.18	0.21	0.19	0.20	0.19
H2O*	1.84	1.83	1.81	1.82	1.82
Total	**101.2**	**101.0**	**100.8**	**101.3**	**100.9**
Structural formula on the basis of 13 cations (Leake et al., 1997)					
Si	6.679	6.824	6.574	6.598	6.666
AlIV	1.321	1.176	1.426	1.402	1.334
Ti	0.000	0.000	0.000	0.000	0.000
Tsite	8.000	8.000	8.000	8.000	8.000
AlVI	0.159	0.103	0.170	0.143	0.153
Ti	0.114	0.105	0.119	0.142	0.124
Cr	0.000	0.000	0.001	0.001	0.000
Fe3+	0.821	0.870	0.771	0.817	0.765
Mg	2.725	2.876	2.548	2.691	2.705
Fe2+	1.127	0.996	1.336	1.152	1.200
Mn	0.053	0.050	0.054	0.056	0.053
Csite	5.000	5.000	5.000	5.000	5.000
Fe2+	0.000	0.000	0.000	0.000	0.000
Ca	1.766	1.740	1.800	1.755	1.788
Na	0.234	0.260	0.200	0.245	0.212
Bsite	2.000	2.000	2.000	2.000	2.000
Na	0.245	0.183	0.317	0.288	0.282
K	0.103	0.071	0.128	0.116	0.097
Asite	0.348	0.254	0.446	0.404	0.379
(Ca+Na)B	2.000	2.000	2.000	2.000	2.000
NaB	0.234	0.260	0.200	0.245	0.212
(Na+K)A	0.348	0.254	0.446	0.404	0.379
Mg/Mg+Fe2+	0.707	0.743	0.656	0.700	0.693
Amphibole composition	**Mg-Hbl**	**Mg-Hbl**	**Mg-Hbl**	**Mg-Hbl**	**Mg-Hbl**
Pressure (kbars) calculated using the calibrations of:					
Ridolfi et al. (2010)	**1.61**	**1.21**	**1.91**	**1.77**	**1.63**
uncertanty (Max error)	0.18	0.13	0.21	0.19	0.18
Temperatures (℃) calculated using the calibrations of:					
Ridolfi et al. (2010)	**835**	**805**	**853**	**850**	**839**
Depth calculates from P=rgh	**6.1**	**4.6**	**7.2**	**6.7**	**6.2**

1.14.9 Continued

Sample			
Grain	RJ11A15-8rx2	RJ11A15-9c	RJ11A15-9r
Spot	rim	core	rim
SiO_2 (wt.%)	46.43	45.23	46.71
TiO_2	1.04	1.19	1.02
Al_2O_3	8.13	9.19	8.22
Cr_2O_3	0.01	0.00	0.00
Fe_2O_3	7.01	7.83	7.36
FeO	9.51	9.26	8.41
MnO	0.45	0.46	0.45
MgO	12.88	12.42	13.14
CaO	11.49	11.35	11.15
Na_2O	1.71	1.91	1.70
K_2O	0.50	0.55	0.50
F	0.18	0.18	0.18
H2O*	1.84	1.83	1.84
Total	**101.2**	**101.4**	**100.7**
Structural formula on the basis of 13 cations (Leake et al., 1997)			
Si	6.736	6.570	6.769
AlIV	1.264	1.430	1.231
Ti	0.000	0.000	0.000
Tsite	8.000	8.000	8.000
AlVI	0.126	0.143	0.173
Ti	0.113	0.130	0.111
Cr	0.001	0.000	0.000
Fe^{3+}	0.765	0.856	0.802
Mg	2.786	2.690	2.839
Fe^{2+}	1.153	1.125	1.019
Mn	0.055	0.056	0.056
Csite	5.000	5.000	5.000
Fe^{2+}	0.000	0.000	0.000
Ca	1.786	1.766	1.732
Na	0.214	0.234	0.268
Bsite	2.000	2.000	2.000
Na	0.267	0.303	0.209
K	0.092	0.102	0.092
Asite	0.359	0.405	0.302
(Ca+Na)B	2.000	2.000	2.000
NaB	0.214	0.234	0.268
(Na+K)A	0.359	0.405	0.302
$Mg/Mg+Fe^{2+}$	0.707	0.705	0.736
Amphibole composition	**Mg-Hbl**	**Mg-Hbl**	**Mg-Hbl**
Pressure (kbars) calculated using the calibrations of:			
Ridolfi et al. (2010)	**1.42**	**1.85**	**1.45**
uncertanty (Max error)	0.16	0.20	0.16
Temperatures (℃) calculated using the calibrations of:			
Ridolfi et al. (2010)	**826**	**855**	**821**
Depth calculates from P=rgh	**5.4**	**7.0**	**5.5**

Appendix 1.15 Ar-Ar dating

As a result of the lack of zircon present in two key samples (basatic andesite, RJ1111 and andesite, AM0887) plagioclase separates from these samples were sent to the Open University for $^{40}Ar/^{39}Ar$ dating, due to the lack of a similar facility at the University of Edinburgh.

1.15.1 Sample Preparation

Mineral separation procedures were essentially the same as those used to separate zircon (Appendix 1.1.3), but in this instance the LST float was collected (plagioclase has a specific gravity of 2.55 to 2.76). Plagioclase grains were individually picked under a binocular microscope (~0.2 grams) and sent to the Ar-Ar Research Laboratory at the Open University, Milton Keynes. The plagioclase separates were cleaned ultrasonically in alternate acetone and de-ionised water, dried using the hotplate, and packaged in aluminium foil packets of ca. 10mm x 10mm in size prior to irradiation.

1.15.2 Irradiation

Samples were irradiated at the McMaster Nuclear Reactor (McMaster University, Canada) for 100 hours. Cadmium shielding was used and the samples were held in position 8E. Neutron flux was monitored using biotite mineral standard GA1550 which has an age of 98.8 ± 0.5 Ma (Renne et al., 1998). Standards were packed for irradiation either side of the unknown samples and analysed using the single grain fusion method using the same laser and mass spectrometer as was used for the unknowns. The resulting J values are listed in Table A1.8. Results were corrected ^{37}Ar decay, and neutron-induced interference reactions. The following correction factors were used: $(^{39}Ar/^{37}Ar)_{Ca}$ = 0.00065±0.00000325, $(^{36}Ar/^{37}Ar)_{Ca}$ = 0.000265±0.000001325, and $(^{40}Ar/^{39}Ar)_{K}$ = 0.0085±0.0000425; based on analyses of Ca and K salts.

Sample	J Value	Error (%)
RJ111	0.005195	0.5
AM0887	0.005195	0.5

Table A1.8. J values and associated errors used to correct for each sample.

1.15.3 Analysis

The irradiated mineral separates were loaded into an ultra-high vacuum system and mounted on a New Wave Research UP-213 stage. A 1059nm CSI fibre laser was focussed into the sample chamber and was used to step heat the samples. Extracted gases were cleaned for 5 minutes using two SAES AP-10 getters running at 450 °C and room temperature, after passing through a liquid nitrogen trap. Following this the cleaned gases were let into the mass spectrometer for measurement. The gas clean-up and inlet system is fully automated and the mass spectrometer used was an MAP 215-50 which was operated by Labiew software. System blanks were measured before and after every two sample analyses. The mass discrimination value for atmospheric $^{40}Ar/^{36}Ar$ was measured at 283. Isotopes of ^{40}Ar, ^{39}Ar, ^{38}Ar, ^{37}Ar, and ^{36}Ar were measured fifteen times per scan, and for ten scans. The final measurements are extrapolations back to the inlet time.

1.15.4 Data Reduction

The system blanks measured before and after every two sample analyses and were extracted from the raw sample data. All data corrections were carried out using an Excel macro and ages were calculated using Isoplot 3 (Ludwig, 2008). All ages are reported at the 2σ level and include a 0.5% error on the J value. Plateau criteria of at least 50% of the ^{39}Ar release in at least 3 consecutive steps were used.

1.15.5 Results

The $^{40}Ar/^{39}Ar$ data is presented in Table A1.9.

	^{40}Ar	+/-	^{39}Ar	+/-	^{38}Ar	+/-	^{37}Ar	+/-	^{36}Ar	+/-	^{40}Ar*/^{39}Ar	+/-	Age	+/-	+/-(no	J
RJ1111																
Step 1	0.202197	0.002593	0.002921	0.000186	0.000075	0.000061	0.012776	0.000398	0.000583	0.000055	10.256299	5.715332	93.650547	50.857510	**50.855463**	
Step 2	0.363540	0.003214	0.000644	0.000080	0.000289	0.000061	0.001453	0.000398	0.001076	0.000055	70.855786	27.378293	565.433547	187.571490	**187.555788**	
Step 3	3.790920	0.008723	0.036596	0.000562	0.002916	0.000123	0.053976	0.000398	0.010742	0.000142	16.851030	1.199586	151.396834	10.363226	**10.337758**	
Step 4	6.143687	0.016951	0.038683	0.000675	0.004051	0.000174	0.135080	0.000398	0.017610	0.000192	24.294937	1.584826	214.432531	13.227389	**13.188703**	
Step 5	3.702720	0.011382	0.070646	0.000572	0.002773	0.000153	0.280554	0.000398	0.010452	0.000132	8.693825	0.580199	79.693678	5.217331	**5.202750**	
Step 6	4.251393	0.014123	0.082471	0.000932	0.003407	0.000194	0.474240	0.000399	0.011501	0.000192	10.342754	0.716826	94.419666	6.392224	**6.375654**	
Step 7	4.872369	0.017686	0.173481	0.000994	0.004960	0.000184	0.654968	0.000399	0.011603	0.000142	8.322389	0.266838	76.359873	2.426181	**2.397207**	
Step 8	6.540297	0.010984	0.351708	0.002223	0.007086	0.000225	1.827702	0.000399	0.014032	0.000231	6.806414	0.201441	62.689034	1.849308	**1.823469**	
Step 9	3.383844	0.008451	0.305333	0.001986	0.004930	0.000102	1.619887	0.000399	0.004407	0.000074	6.817415	0.088673	62.788611	0.859896	**0.802635**	
Step 10	4.063579	0.009520	0.384903	0.002389	0.006217	0.000215	1.811424	0.000399	0.005216	0.000093	6.552785	0.085914	60.391695	0.833397	**0.778695**	
Step 11	2.853896	0.007721	0.321683	0.002027	0.004480	0.000143	1.054165	0.000399	0.002567	0.000065	6.513799	0.076055	60.038305	0.750031	**0.689473**	
Step 12	2.701018	0.008061	0.286210	0.001387	0.003775	0.000133	1.108531	0.000400	0.002582	0.000132	6.770884	0.143170	62.367381	1.331970	**1.296224**	
Step 13	1.884800	0.005200	0.203287	0.001624	0.003029	0.000194	0.766817	0.000408	0.001745	0.000048	6.734552	0.091364	62.038416	0.881735	**0.827333**	
AM0887																
Step 1	-0.004010	0.003117	-0.000809	0.001060	-0.000030	0.000050	-0.004088	0.005798	-0.000022	0.000032	-3.171279	-12.994383	-29.969346	123.825790	**123.825698**	
Step 2	0.452740	0.003343	0.018938	0.001179	0.000533	0.000087	0.074129	0.005800	0.001337	0.000056	3.044213	0.909857	28.307657	8.395759	**8.394584**	
Step 3	0.712082	0.004481	0.061664	0.001197	0.001228	0.000146	0.202764	0.005804	0.001923	0.000093	2.332896	0.455730	21.732889	4.221424	**4.220042**	
Step 4	0.812110	0.005176	0.182142	0.001338	0.002689	0.000146	0.744755	0.005806	0.001719	0.000047	1.669324	0.082556	15.577760	0.770991	**0.767081**	
Step 5	0.887835	0.004225	0.229655	0.001956	0.003333	0.000227	0.936827	0.005810	0.001368	0.000056	2.105203	0.076390	19.623228	0.714891	**0.708200**	
Step 6	0.721884	0.004728	0.238377	0.001887	0.003261	0.000247	1.022325	0.005811	0.000646	0.000056	2.227838	0.074221	20.759794	0.695351	**0.687650**	
Step 7	0.347801	0.003328	0.136495	0.001547	0.001759	0.000126	0.736400	0.005818	0.000152	0.000047	2.220051	0.107972	20.687648	1.005664	**1.000391**	
Step 8	1.317129	0.003380	0.548208	0.005398	0.007156	0.000146	3.344619	0.005819	0.000680	0.000047	2.035885	0.033045	18.980481	0.320670	**0.306459**	
Step 9	2.245784	0.004019	0.936902	0.003919	0.012378	0.000196	5.946798	0.005822	0.000981	0.000056	2.087699	0.020290	19.460944	0.211556	**0.188120**	
Step 10	1.758958	0.004407	0.792868	0.003889	0.010774	0.000328	5.142362	0.005824	0.000364	0.000103	2.082836	0.040219	19.415857	0.385199	**0.372901**	
Step 11	1.144476	0.004792	0.517416	0.003533	0.006808	0.000298	3.448277	0.005827	0.000233	0.000056	2.078911	0.036238	19.379466	0.349549	**0.336000**	
Step 12	1.203383	0.004268	0.537643	0.003317	0.007105	0.000298	3.423898	0.005828	0.000379	0.000047	2.029768	0.029967	18.923752	0.293432	**0.277926**	

Table A1.9. ^{40}Ar/^{39}Ar age data.

1.15.5.1 Sample RJ1111

Sample RJ111 produced a plateau age of 61.2 ±1.0 Ma, containing 73% of the released gas (Fig. A1.4a). The inverse isochron correlation plot (Fig. A1.4b) produced an age within error of the plateau age, at 58.1 ±2.0 Ma. The best age estimate for sample RJ1111 is 61.2 ±1.0 Ma.

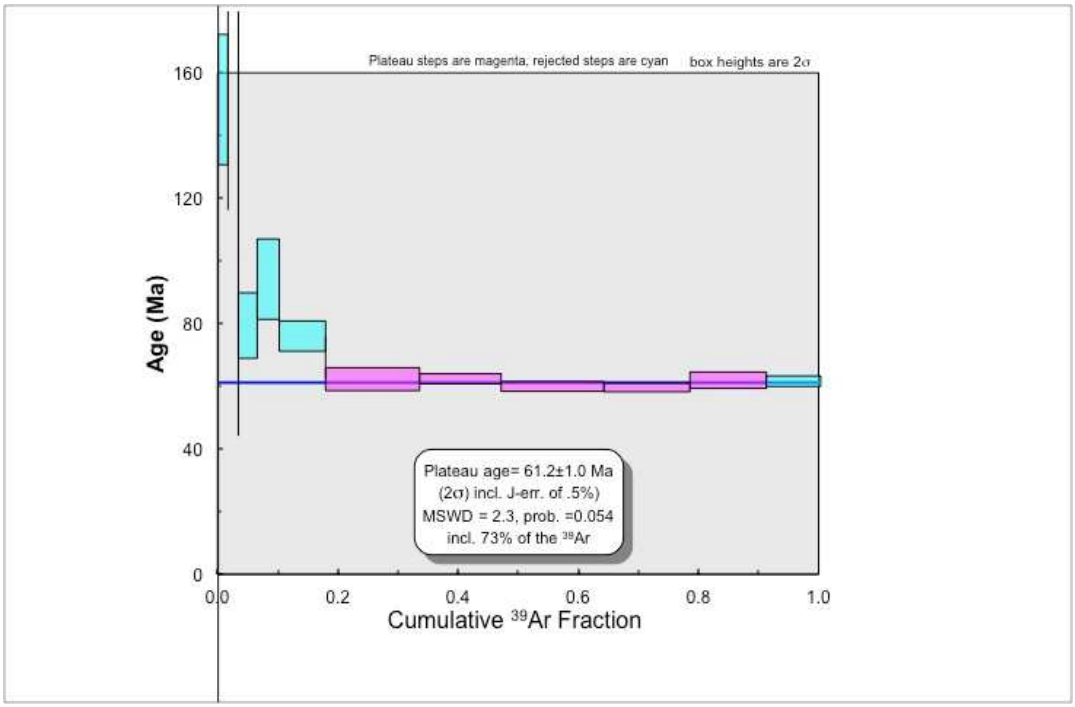

Figure A1.4a. Sample RJ1111 step-heating release spectrum.

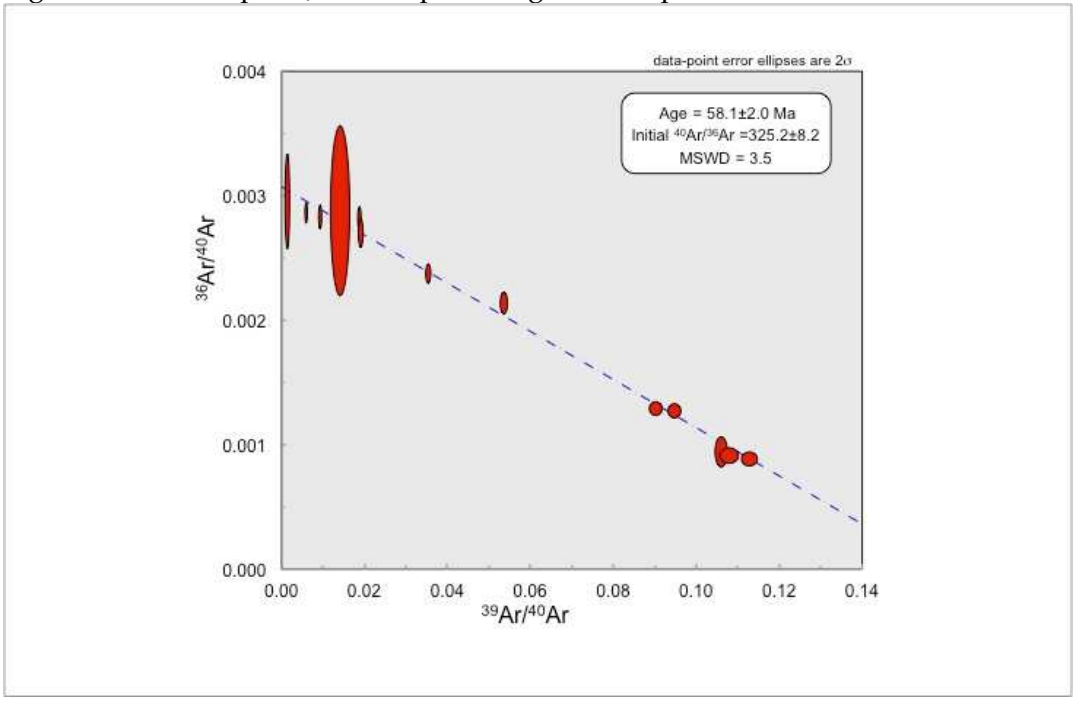

Figure A1.4b. Sample RJ1111 inverse isochron correlation plot.

1.15.5.2 Sample AM0887

Sample AM0887 produced a plateau age of 19.34 ±0.30 Ma, containing 73% of the released gas (Fig. A1.5a). The inverse isochron correlation plot (Fig. A1.5b) produced an age within error of the plateau age, at 19.35 ±0.60 Ma. The best age estimate for sample AM00887 is 19.34 ±0.30 Ma.

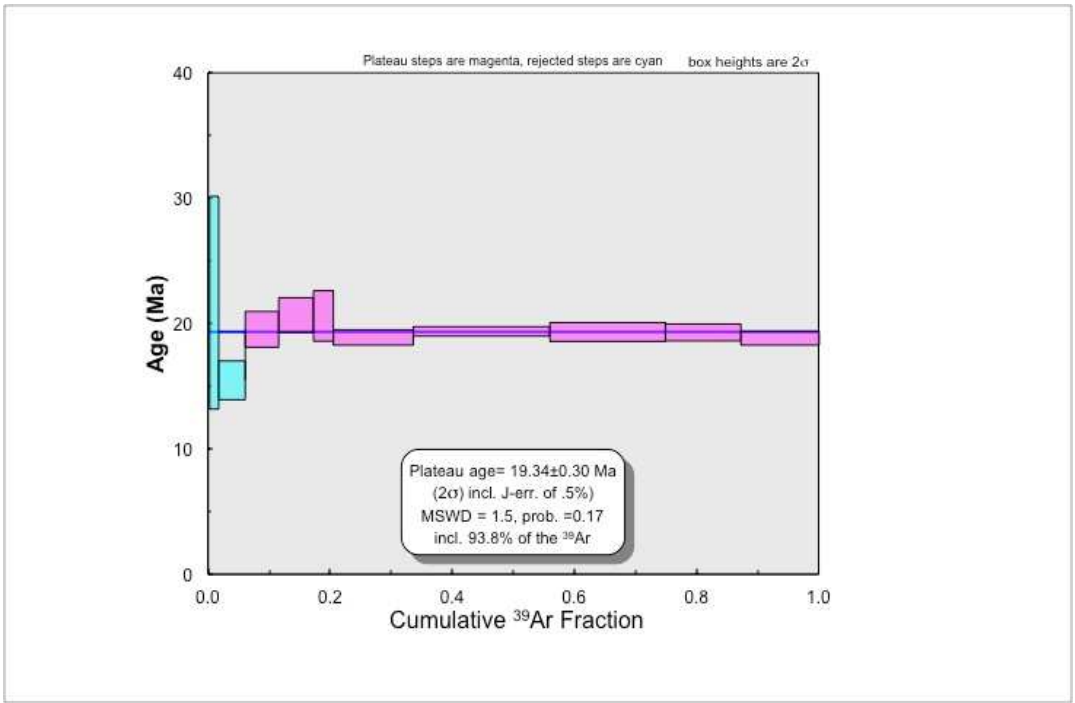

Figure A1.5a. Sample AM0887 step-heating release spectrum.

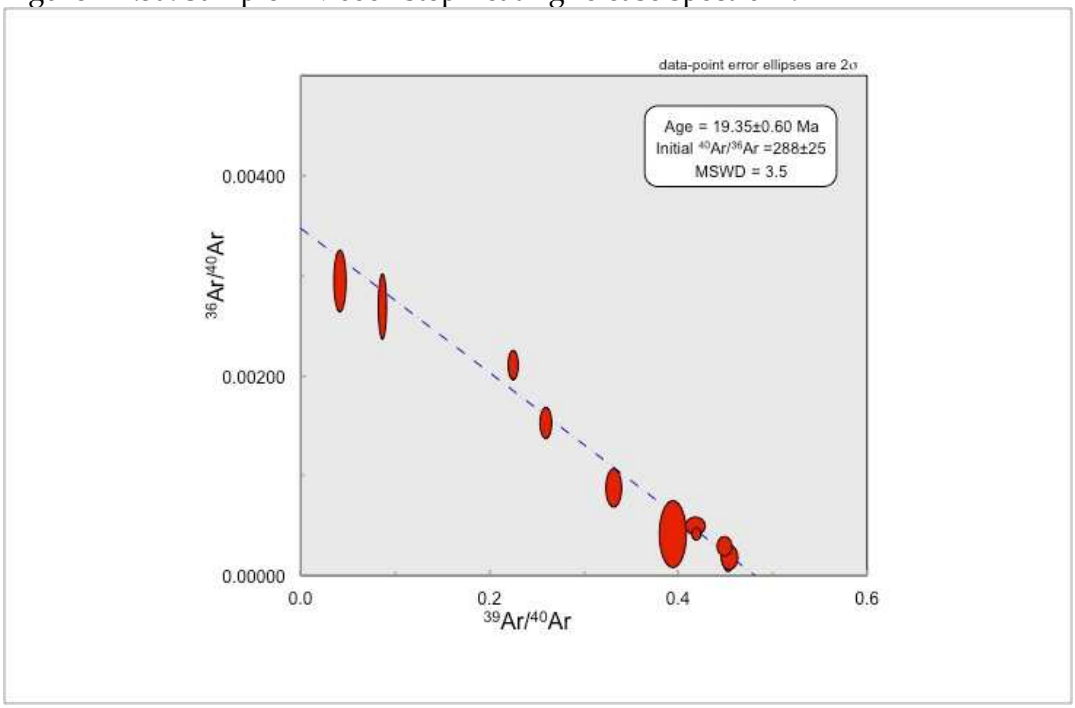

Figure A1.5b.Sample AM0887 inverse isochron correlation plot.

Appendix 1.16 References

Cardó, R., and Díaz, I.N., 1999, Hoja Geológica 3169-I, Rodeo, provincias de San Juan: Buenos Aires, Instituto de Geología y Recursos Minerales, Servicio Geológico Minero Argentino.

Claoué-Long, J.C., Compston, W., Roberts, J., and Fanning, C.M., 1995, Two Carboniferous ages: A comparison of SHRIMP zircon dating with conventional zircon ages and 40Ar/39Ar analysis, *in* Berggren, W.A., Kent, D.V., Aubrey, M.-P., and Hardenbol, J., eds., Geochronology, Time Scales and Global Stratigraphic Correlation, Volume 4: SEPM Spec Publ, p. 3-21.

Compston, W., Williams, I.S., and Meyer, C., 1984, U-Pb geochronology of zircons from lunar breccia 73217 using a high mass-resolution ion microprobe: Journal of Geophysical Research Supplement, v. 89, p. B525 - B534.

Davis, D.W., Krogh, T.E., and Williams, I.S., 2003, Historical development of zircon geochronology: Reviews in Mineralogy and Geochemistry, v. 53, p. 145-181.

Fitton, J.G., and Godard, M., 2004, Origin and evolution of magmas on the Ontong Java Plateau: Geological Society, London, Special Publications, v. 229, p. 151-178.

Fitton, J.G., Saunders, A.D., Larsen, L.M., Hardarson, B.S., and Norry, M.J., 1998, Volcanic rocks from the southeast Greenland margin at 63°N : Composition, petrogenesis, and mantle sources: Proceedings of the Ocean Drilling Programme, v. Scientific Results 152, p. 331 - 350.

Govindaraju, K., 1994, 1994 compilation of working values and sample description for 383 geostandards: Geostandards Newsletter, v. 18, p. 1-158.

Ireland, T.R., and Williams, I.S., 2003, Considerations in zircon geochronology by SIMS: Reviews in Mineralogy and Geochemistry, v. 53, p. 215-241.

Jackson, S.E., Pearson, N.J., Griffin, W.L., and Belousova, E.A., 2004, The application of laser ablation-inductively coupled plasma-mass spectrometry to in situ U-Pb zircon geochronology: Chemical Geology, v. 211, p. 47-69.

Jochum, K.P., and Nohl, U., 2008, Reference materials in geochemistry and environmental research and the GeoReM database: Chemical Geology, v. 253, p. 50-53.

Litvak, V.D., Poma, S., and Kay, S.M., 2007, Paleogene and Neogene magmatism in the Valle del Cura region: New perspective on the evolution of the Pampean flat slab, San Juan province, Argentina: Journal of South American Earth Sciences, v. 24, p. 117 - 137.

Ludwig, K.R., 2008, User's Manual for Isoplot 3.7 - A Geochronological Toolkit for Microsoft Excel: Berkeley Geochronology Center Special Publication, v. 4.

Olive, V., Ellam, R.M., and Wilson, L., 2001, A Protocol for the Determination of the Rare Earth Elements at Picomole Level in Rocks by ICP-MS: Results on Geological Reference Materials USGS PCC-1 and DTS-1: Geostandards Newsletter, v. 25, p. 219-228.

Renne, P.R., Swisher, C.C., Deino, A.L., Karner, D.B., Owens, T.L., and DePaolo, D.J., 1998, Intercalibration of standards, absolute ages and uncertainties in<

sup> 40</sup> Ar/< sup> 39</sup> Ar dating: Chemical Geology, v. 145, p. 117-152.

Reynolds, R.C., 1963, Matrix corrections in trace element analysis by X-ray flourescence: estimation of the mass absorption coefficient by Compton scattering: American Mineralogist, v. 48, p. 1133 - 1143.

Schärer, U., 1984, The effect of initial ^{230}Th disequilibrium on young U-Pb ages: the Makalu case, Himalaya: Earth and Planetary Science Letters, v. 67, p. 191 - 204.

Schuhmacher, M., de Chambost, E., McKeegan, K.D., Harrison, T.M., and Migeon, H.N., 1993, In situ U/Pb dating of zircon with Cameca ims 1270, *in* Benninghoven, A., Nihei, Y., Shimizu, R., and Werner, H.W., eds., Secondary Ion Mass Spectrometry SIMIS IX: Chichester, John Wiley, p. 919 - 922.

Whitehouse, M.J., Claesson, S., Sunde, T., and Vestin, J., 1997, Ion microprobe U-Pb zircon geochronology and correlation of Archaen gneisses from the Lewisian Complex of Gruinard Bay, northwest Scotland.: Geochimica et Cosmochimica Acta, v. 61, p. 4429 - 4438.

Wiedenbeck, M., Allé, P., Corfu, F., Griffin, W.L., Meier, M., Oberli, F., Von Quadt, A., Roddick, J.C., and Spiegel, W., 1995, Three natural zircon standards for U-Th-Pb, Lu-Hf, trace element and REE analyses: Geostandards Newsletter, v. 19, p. 1 - 23.

Williams, I.S., and Claesson, S., 1987, Isotopic evidence for the Precambrian provenance and Caledonian metamorphism of high-grade paragneisses from the Seve Nappes, Scandinavian Caledonides II. Ion microprobe zircon U-Th-Pb.: Contributions to Mineralogy and Petrology, v. 97, p. 205 - 217.

Appendix 2

Refer to Appendix 1.1 for mineral separation methods and sample preparation procedures.

Appendix 2.1 Zircon Imaging

Prior to isotopic analysis individual zircon grains were imaged and characterised using a Philips XL30CP Scanning Electron Microscope (SEM) at the University of Edinburgh in order to determine the presence or absence of multiple growth phases, xenocrystic cores, inclusions, and cracks. Imaging was carried out in both secondary electron (SE) and backscatter electron (BSE) modes, and suitable, representative zircons and specific locations for analysis were identified. Cathodoluminescence (CL) imaging was not carried out prior to analysis in order to limit the burning of the epoxy and the creation of topography on the surface of the grain mounts. A summary of zircon morphologies and characteristics is presented in Appendix 2.2. Subsequent to analysis all analysed zircons were imaged on a SEM in both CL and secondary electron SE modes to check the exact position of analysis, and to ensure the absence of cracks and inclusions at the bottom of the analysis pits. Data obtained from any problematic analysis locations (e.g., over cracks) were rejected. In order to retrieve a coupled record of U-Pb, O and Hf isotope ratios great care was taken to target the same growth zones with each type of analysis (Figure A2.1).

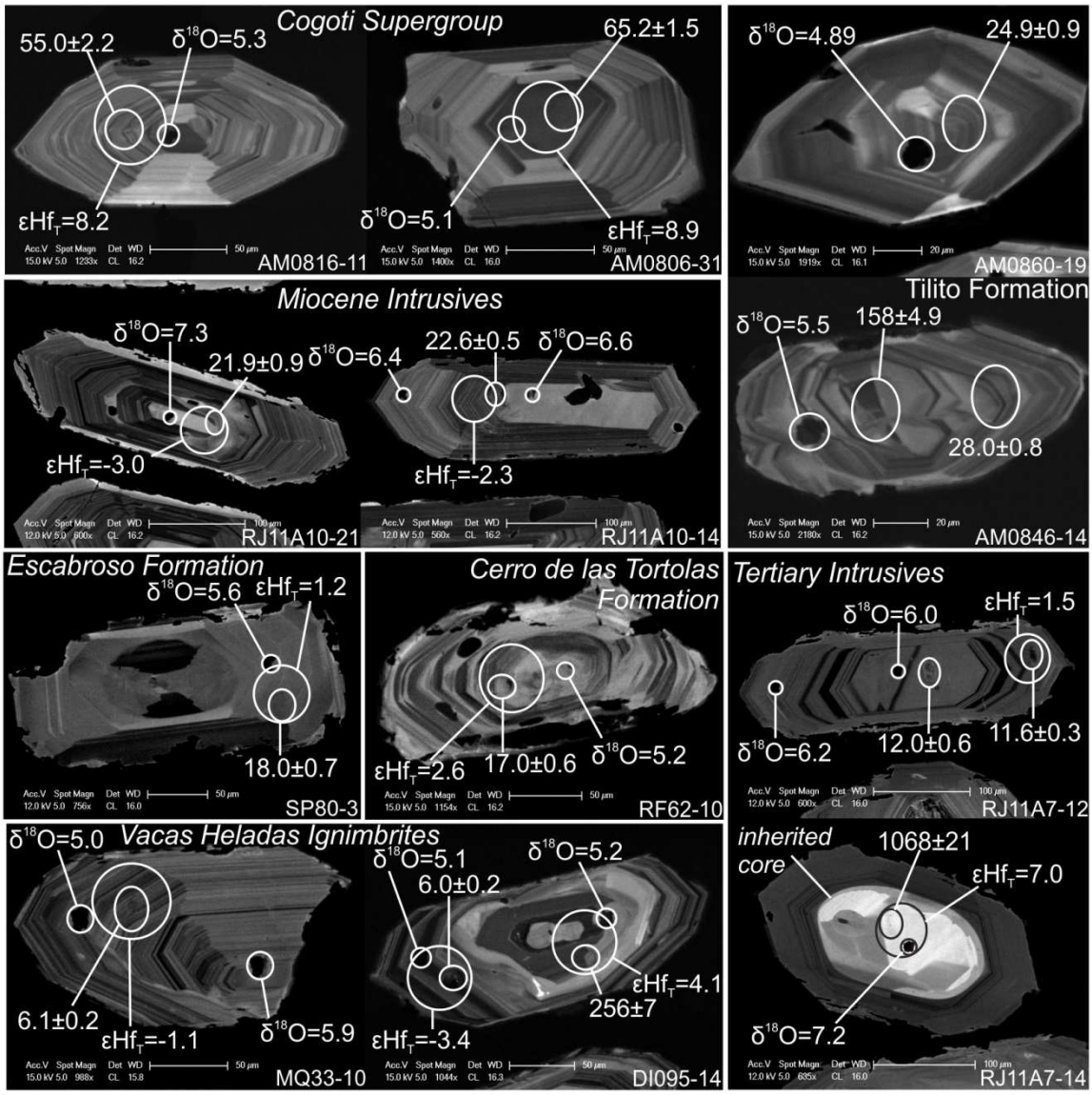

Figure A2.1 Cathdoluminescence (CL) images of representative zircon grains from select samples highlighting the presence of internal growth zoning, inherited cores and the locations of *in-situ* isotopic analysis. The relative areas analysed by the different techniques are also indicated. The U-Pb ages are presented as the $^{206}Pb/^{238}U$ ages for the individual zircon grains and the errors are quoted at the 2σ level.

Appendix 2.2 Zircon morphologies and characteristics

Geological Group/Formation/Unit	Sample	Zircon Length Range (µm)		Aspect ratio (w:l)	Crystal shape	Apparent xenocrystic cores
		min	max			
Cogotí Supergroup	AM0812	200	400	1:1.5 - 1:3	euhedral	
	AM0823	120	320	1:2 - 1:3	sub - euhedral	
	RJ1103	150	350	1:2 - 1:4	euhedral	
	AM0806	150	450	1:2 - 1:3	euhedral	
	AM0824	100	300	1:1.5 - 1:3	euhedral	
	AM0826	150	350	1:1.5 - 1:3	euhedral	
	AM0822	60	380	1:1.5 - 1:3	sub - euhedral	
	AM0815	100	300	1:2 - 1:3.5	euhedral	
	AM0816	100	600	1:1.5 - 1:3	euhedral	
	RJ1101	200	550	1:1.5 - 1:3	euhedral	
Los Elquinos Formation	AM0890	50	60	1:1.5	subhedral	
Botacoma Unit	AM0867	100	210	1:2	sub - euhedral	yes
Tierras Blancas Caldera	RJ1105	150	300	1:1.5 - 1:2.5	subhedral	
Tilito Formation (Lower Doña Ana Group)	MQ153	150	350	1:2 - 1:2.5	sub - euhedral	
	AM0845	100	210	1:2 - 1:3	euhedral	yes
	AM0846	60	200	1:1.5 - 1:3	sub - euhedral	yes
	AM0860	60	210	1:1.5 - 1:3	sub - euhedral	
	RF64	100	350	1:1.5 - 1:3	sub - euhedral	yes
	ZN122	80	200	1:1.5 - 1:3	sub - euhedral	
	AM0844	80	210	1:2 - 1:3	euhedral	yes
	AM0849	100	300	1:1.5 - 1:3.5	sub - euhedral	
	PC14	100	300	1:2 - 1:3	euhedral	
	Z27	150	500	1:1.5 - 1:3	euhedral	
Las Trancas Formation	RJ11A5	100	350	1:3 - 1:4	sub - euhedral	yes
Miocene Intrusives	RJ11A10	200	550	1:3 - 1:4	euhedral	
	RJ11A11	250	550	1:2 - 1:4	euhedral	
	RJ11A14	150	420	1:2 - 1:3.5	euhedral	yes
Escabroso Formation (Upper Doña Ana Group)	SP80	120	450	1:1.5 - 1:3	sub - euhedral	
	1026	100	450	1:2 - 1:2.5	sub - euhedral	
Cerro de las Tórtolas Formation	RF62	100	230	1:1.5 - 1:2	subhedral	
Tertiary Intrusives	RJ11A7	150	600	1:2 - 1:3	euhedral	yes
	RJ11A15	200	520	1:2 - 1:3	euhedral	yes
	RJ11A17	250	550	1:2 - 1:3	euhedral	yes
Vacas Heladas Ignimbrites	DI095	100	350	1:2 - 1:3	euhedral	yes
	MQ33	150	350	1:2 - 1:3	euhedral	yes

Appendix 2.3 Oxygen isotope analysis

Oxygen isotope analysis was carried out on the Cameca ims 1270 secondary ion mass spectrometer (SIMS) at the Edinburgh Ion Microprobe Facility (EIMF), University of Edinburgh, between 1st – 5th August 2011 and 23rd – 27th January 2012. For SIMS analysis a gold coat was applied to the sample mounts in order to produce a uniform conducting surface and to prevent charging of the sample during sputtering. Subsequent to oxygen isotope analysis U-Pb dating was carried out on selected zircon grains, also using the Cameca ims 1270 ion microprobe. A full methodology and the results of U-Pb dating are presented in Appendix 1.1, 1.10 and 1.11 and discussed in Chapter 2.

2.3.1 Analytical conditions

Secondary O^- ions were produced by bombarding the surface of the target with a ~5nA primary $^{133}Cs^+$ beam, with a diameter of <20 μm. The secondary O^- ions were accelerated at 10kV and $^{16}O^-$ and $^{18}O^-$ were measured simultaneously on dual Faraday cups (L'2 and H'2) with typical count rates of ~$2x10^9$ and ~$4x10^6$ respectively. A normal incidence electron flood gun was used to neutralise charging of the sample during the analysis. Each analysis involved a pre-sputtering time of 40 seconds, this was followed by automatic secondary beam alignment, entrance slit centring, and then 20 cycles of oxygen isotope analysis, each cycle lasting 5 seconds.

2.3.2 Data collection

A total of 518 oxygen isotope analyses were made on unknown zircons by SIMS from 46 samples, over 10 analytical sessions (a session is defined as a period where no changes in analytical conditions, such as changes to the primary beam and/or the

electron gun, have occurred). Typically 11 representative zircon grains were analysed per sample, with multiple (core and rim) analyses on selected grains.

2.3.3 Drift correction

All of the analytical sessions show evidence for instrumental drift over the course of the session, as shown by the systematic change in measured $^{18}O/^{16}O$ of the standard (refer to Appendix 2.5). In the most extreme case this resulted in a -1.6‰ difference in the $\delta^{18}O$ obtained for the standard between the start and the end of the session. For each analytical session a regression was calculated for the $^{18}O/^{16}O$ measured for the standard as a function of analytical order. A linear drift correction, related to analytical order, was then applied to all of the data collected in the analytical session depending on the resulting linear correlation coefficients (refer to Appendix 2.5).

2.3.4 Data correction

In order to correct for instrumental mass fractionation (IMF (‰) ($[(^{18}O/^{16}O)_{SIMS} - (^{18}O/^{16}O)_{actual}] / (^{18O}/^{16}O)_{actual}$) x 1000)) and instrumental drift, all data were normalised to an internal laboratory standard ('Laura' $\delta^{18}O_{VSMOW}$ = 5.3‰, analysed at SUERC) which was analysed in blocks of 5, after every set of 10 to 15 unknown zircon analyses, throughout all analytical sessions. The unknown zircon analyses were normalised to the daily average $^{18}O/^{16}O$ value obtained for 'Laura'.

The internal precision of individual analyses based on the standard error of the mean ranged from 0.04‰ to 0.40‰ (1σ). The external precision, based on the reproducibility of the zircon standard (after drift correction), ranged between 0.22‰ (n=35) and 0.53‰ (n=15) (at the 2σ level) over the 10 analytical sessions (Appendix 2.5). Errors on the individual unknowns are quoted as the external precision for the analytical session at the 2σ level.

2.3.5 Correction for HfO_2 concentrations

Variations in HfO_2 concentrations in zircon have been shown to cause variations in instrumental mass fractionation (Peck et al., 2001). Subsequent to SIMS analysis all zircons were analysed for HfO_2 concentrations using the Cameca SX100 electron microprobe (EPMA) at the University of Edinburgh. The analyses were made next to the SIMS oxygen pits using a beam size of 2μm with an accelerating voltage of 17kV and a beam current of 100nA. Various zircon standards were also analysed as part of both the SIMS and EPMA analytical sessions. The HfO_2 concentrations of the unknown zircons range from 0.82 to 2.34 wt.%, with an average of 1.32 wt.% and a standard deviation of 0.22 wt.% (n=514) (Appendix 2.8). An average HfO_2 concentration of 1.31 ±0.07 wt.% (n=32) (2σ) was obtained for zircon standard 'Laura' (Appendix 2.9). It has been suggested that the correction for IMF caused by variations in HfO_2 will be minor if a standard of the same composition is used (Valley, 2003); this renders correction for IMF unnecessary in this case.

Appendix 2.4 Lu-Hf isotope analysis

Lu-Hf isotopic compositions of zircons were measured *in-situ* using a Finnigan Neptune multi-collector inductively-coupled plasma mass spectrometer (MC-ICP-MS) combined with a New Wave Research UP193HE laser ablation system at the Bristol Isotope Group (BIG), University of Bristol. The analyses were carried out in two analytical sessions between the 17th – 19th October 2011 and the 2nd – 4th April 2012, following the methods outlined in Hawkesworth and Kemp (2006).

The zircon grains selected for Hf isotope analysis were those with existing oxygen isotope data and (in most cases) U-Pb data, in order to allow the correlation of the different data sets. The Hf isotope analysis targeted the same spot as the U-Pb SIMS analysis, or at least the same growth zone, as determined by cathodoluminescence imaging (Fig. A2.1). Care was taken to avoid any cracks and inclusions. Where possible, multiple analyses (core and rim) were carried out on single zircon grains in order to obtain information on inheritance and growth history.

2.4.1 Analytical conditions

Laser ablation was performed in an atmosphere composed of helium mixed with argon and nitrogen, using a spot size of between 40μm and 50μm, and a laser frequency of 4 Hz. The energy density of the laser beam was 6 J/cm^2, resulting in an ablation rate of between 0.5 and 0.9μm/s. Each analysis typically lasted 140 seconds and comprised of two gas blank measurements (40 seconds each) and an ablation period of 60 seconds. At a spot size of 40μm, typical total Hf beam intensities varied between 10 and 20 V for zircon standards Plesovice and Mud Tank and between 7 and 12 V for Temora-2. At a spot size of 50μm, typical total Hf beam intensities varied between 17 and 25 V for Plesovice and Mud Tank (Appendix 2.7). Internal precision routinely varied between 50 - 100 ppm (2σ) for Plesovice and Mud Tank

and between 60 - 160 ppm (2σ) for Temora-2, reflecting the lower signal intensity (Appendix 2.7). The internal precision on the unknowns reflects a similar range, between 48 and 194 ppm (2σ), with an average value of 89 ppm (2σ) (Appendix 2.6). The accuracy and long term reproducibility of the analyses were assessed by analysing three zircon standards: Plesovice ($^{176}Hf/^{177}Hf$ = 0.282488±0.000023, *n*=106 at 40μm and $^{176}Hf/^{177}Hf$ = 0.282496±0.000009, *n*=21 at 50μm), Mud Tank ($^{176}Hf/^{177}Hf$ = 0.282522±0.000019, *n*=86 at 40μm and $^{176}Hf/^{177}Hf$ = 0.282527±0.000007, *n*=18 at 50μm) and Temora-2 ($^{176}Hf/^{177}Hf$ = 0.282697±0.000036, *n*=24 at 40μm) (all errors at 2σ level) throughout the analytical sessions (Appendix 2.7). Therefore the external precision on εHf values, based on the reproducibility of the zircon standards, ranges from 0.2 to 1.3 (at the 2σ level).

2.4.2 Data corrections

Corrections for mass bias and interferences were made following the procedure implemented by the Bristol Isotope Group (BIG) (e.g., Hawkesworth and Kemp, 2006). To correct for the isobaric interference of ^{176}Yb, the interference-free ^{171}Yb was measured and corrected for mass bias effects using an exponential law and a $^{173}Yb/^{171}Yb$ ratio of 1.130172 (Segal et al., 2003; Kemp et al., 2009). The mass bias corrected ^{171}Yb was monitored during the analysis and the magnitude of the ^{176}Yb interference on ^{176}Hf was calculated using a $^{176}Yb/^{171}Yb$ ratio of 0.897145 (Segal et al., 2003). To correct for the isobaric interference of ^{176}Lu, the interference-free ^{175}Lu was measured and corrected for mass bias effects, assuming similar behaviour to Yb (βLu = βYb) (e.g., Woodhead et al., 2004) and using an exponential law. The mass bias corrected ^{175}Lu was monitored during the analysis and the magnitude of the ^{176}Lu interference on ^{176}Hf was calculated using a $^{176}Lu/^{175}Lu$ ratio of 0.02655 (Vervoort et al., 2004). Finally, the corrected $^{176}Hf/^{177}Hf$ values were normalised to JMC-475 ($^{176}Hf/^{177}Hf_{solution}$ = 0.283137 for data collected in 2011 and $^{176}Hf/^{177}Hf_{solution}$ = 0.283135 for data collected in 2012).

2.4.3 Data reduction

In some cases the laser ablated right through the zircon grain and into the epoxy. Here the Lu-Hf isotope values were calculated from <60 seconds of ablation. In two zircon grains (RJ11A15-22 and RJ11A17-10r) the laser appears to have ablated material from older cores and younger rims leading to anomalous Hf isotope results. These two analyses have been omitted from the dataset (Appendix 2.6).

2.4.4 Calculation of initial εHf values

Initial εHf values were determined using individual zircon $^{206}Pb/^{238}U$ ages obtained from SIMS analysis. In the few instances where a $^{206}Pb/^{238}U$ age was not available or the U-Pb analysis was rejected due to high common Pb or analytical problems, the Concordia age for the sample was used. The epsilon values are reported relative to CHUR (chondritic uniform reservoir) values, calculated from present day values of $^{176}Lu/^{177}Hf = 0.0336$ and $^{176}Hf/^{177}Hf = 0.282785$ (Bouvier et al., 2008). Hf model ages for zircons were calculated using the initial $^{176}Hf/^{177}Hf$ ratio (derived from the U-Pb age), a $^{176}Hf/^{177}Hf$ ratio of 0.283158 for present day new crust (NC) (Dhuime et al., 2011), and assuming a $^{176}Lu/^{177}Hf$ ratio of 0.015 (intermediate) for the source magma from which the zircon crystallized (Griffin et al., 2000). A ^{176}Lu decay constant of 1.867×10^{-11} y^{-1} (Söderlund et al., 2004) is used throughout. All data is presented in Appendix 2.6.

Appendix 2.5 Zircon oxygen isotope data determined by SIMS

Analytical Session 1 (01.08.11)

Analytical order	Sample-grain(c/r)	$^{18}O/^{16}O$ measured	1σ	% Std Err (1σ)	$\delta^{18}O_{(VSMOW)}$	Drift correction factor	$\delta^{18}O_{(VSMOW)}$ (drift corrected)	Analytical uncertainty (±)
1	**Laura**	0.0020088	0.0000003	0.013	**5.33**	0.0020090	**5.20**	
2	**Laura**	0.0020095	0.0000005	0.024	**5.64**	0.0020090	**5.51**	
3	**Laura**	0.0020094	0.0000005	0.025	**5.62**	0.0020090	**5.50**	
4	**Laura**	0.0020092	0.0000004	0.018	**5.52**	0.0020090	**5.41**	
5	**Laura**	0.0020093	0.0000005	0.023	**5.56**	0.0020090	**5.44**	
6	**Laura**	0.0020087	0.0000005	0.023	**5.26**	0.0020090	**5.15**	
7	**Laura**	0.0020086	0.0000004	0.020	**5.22**	0.0020090	**5.12**	
8	**Laura**	0.0020095	0.0000006	0.028	**5.64**	0.0020090	**5.55**	
9	**Laura**	0.0020081	0.0000005	0.025	**4.98**	0.0020090	**4.89**	
10	**Laura**	0.0020089	0.0000003	0.017	**5.35**	0.0020089	**5.27**	
22	**Laura**	0.0020089	0.0000006	0.032	**5.36**	0.0020088	**5.33**	
23	**Laura**	0.0020089	0.0000004	0.019	**5.36**	0.0020088	**5.34**	
24	**Laura**	0.0020087	0.0000006	0.028	**5.29**	0.0020088	**5.27**	
25	**Laura**	0.0020084	0.0000004	0.019	**5.13**	0.0020088	**5.11**	
26	**Laura**	0.0020079	0.0000004	0.020	**4.86**	0.0020088	**4.85**	
40	**Laura**	0.0020095	0.0000004	0.019	**5.65**	0.0020087	**5.71**	
41	**Laura**	0.0020083	0.0000003	0.016	**5.06**	0.0020086	**5.12**	
42	**Laura**	0.0020091	0.0000005	0.023	**5.49**	0.0020086	**5.56**	
43	**Laura**	0.0020090	0.0000004	0.020	**5.42**	0.0020086	**5.50**	
44	**Laura**	0.0020090	0.0000004	0.019	**5.39**	0.0020086	**5.47**	
60	**Laura**	0.0020085	0.0000002	0.012	**5.17**	0.0020085	**5.32**	
61	**Laura**	0.0020080	0.0000003	0.013	**4.91**	0.0020084	**5.07**	
62	**Laura**	0.0020086	0.0000004	0.018	**5.19**	0.0020084	**5.36**	
63	**Laura**	0.0020085	0.0000005	0.026	**5.16**	0.0020084	**5.33**	
64	**Laura**	0.0020081	0.0000004	0.018	**4.94**	0.0020084	**5.12**	
Average		0.0020088			**5.30**		**5.30**	
1σ		0.0000005			**0.24**		**0.21**	
2σ		0.0000010			**0.48**		**0.42**	
SEM		0.0000002			**0.10**		**0.08**	
n		25			**25**		**25**	
Unknowns								
11	**91500**	0.0020188	0.0000004	0.019	**10.34**	0.0020089	**10.26**	0.42
12	**RJ0824-23**	0.0020094	0.0000004	0.018	**5.63**	0.0020089	**5.55**	0.42
13	**RJ0824-22**	0.0020090	0.0000003	0.016	**5.43**	0.0020089	**5.35**	0.42
14	**RJ0824-21**	0.0020099	0.0000003	0.016	**5.89**	0.0020089	**5.82**	0.42
15	**RJ0824-20**	0.0020101	0.0000004	0.019	**5.96**	0.0020089	**5.90**	0.42
16	**RJ0824-19**	0.0020088	0.0000004	0.019	**5.29**	0.0020089	**5.23**	0.42
17	**RJ0824-18**	0.0020089	0.0000004	0.019	**5.34**	0.0020089	**5.29**	0.42
18	**RJ0824-17**	0.0020084	0.0000004	0.019	**5.12**	0.0020089	**5.07**	0.42
19	**RJ0824-16**	0.0020094	0.0000004	0.018	**5.61**	0.0020089	**5.56**	0.42
20	**RJ0824-15**	0.0020094	0.0000002	0.012	**5.62**	0.0020088	**5.59**	0.42
21	**RJ0824-14**	0.0020100	0.0000005	0.023	**5.90**	0.0020088	**5.87**	0.42
27	**RJ0806-1c**	0.0020088	0.0000003	0.015	**5.33**	0.0020088	**5.32**	0.42

28	**RJ0806-14**	0.0020094	0.0000003	0.013	**5.60**	0.0020088	**5.60**	0.42
29	**RJ0806-15**	0.0020091	0.0000004	0.022	**5.45**	0.0020088	**5.45**	0.42
30	**RJ0806-1r**	0.0020090	0.0000004	0.022	**5.42**	0.0020087	**5.43**	0.42
31	**RJ0806-8**	0.0020099	0.0000003	0.017	**5.88**	0.0020087	**5.90**	0.42
32	**RJ0806-9**	0.0020095	0.0000004	0.018	**5.68**	0.0020087	**5.71**	0.42
33	**RJ0806-10c**	0.0020092	0.0000004	0.018	**5.53**	0.0020087	**5.55**	0.42
34	**RJ0806-10r**	0.0020089	0.0000003	0.017	**5.38**	0.0020087	**5.41**	0.42
35	**RJ0806-11**	0.0020096	0.0000005	0.024	**5.71**	0.0020087	**5.74**	0.42
36	**RJ0806-12**	0.0020087	0.0000002	0.012	**5.28**	0.0020087	**5.32**	0.42
37	**RJ0806-13**	0.0020097	0.0000004	0.022	**5.76**	0.0020087	**5.80**	0.42
38	**RJ0806-16**	0.0020092	0.0000003	0.015	**5.51**	0.0020087	**5.56**	0.42
39	**RJ0806-18**	0.0020101	0.0000005	0.027	**5.99**	0.0020087	**6.04**	0.42
59	**RJ0812-10**	0.0020097	0.0000002	0.012	**5.79**	0.0020085	**5.94**	0.42

Analytical Session 2 (02.08.11a)

Analytical order	**Sample-grain(c/r)**	**$^{18}O/^{16}O$ measured**	**1σ**	**% Std Err (1σ)**	**$\delta^{18}O_{(VSMOW)}$**	**Drift correction factor**	**$\delta^{18}O_{(VSMOW)}$ (drift corrected)**	**Analytical uncertainty (±)**
1	**Laura**	0.0020080	0.0000002	0.010	**5.96**	0.0020075	**5.57**	
2	**Laura**	0.0020074	0.0000002	0.011	**5.65**	0.0020075	**5.27**	
3	**Laura**	0.0020081	0.0000003	0.012	**6.00**	0.0020075	**5.64**	
4	**Laura**	0.0020070	0.0000003	0.015	**5.45**	0.0020074	**5.10**	
5	**Laura**	0.0020071	0.0000002	0.008	**5.50**	0.0020074	**5.17**	
6	**Laura**	0.0020082	0.0000003	0.013	**6.03**	0.0020074	**5.72**	
7	**Laura**	0.0020072	0.0000002	0.011	**5.54**	0.0020073	**5.24**	
8	**Laura**	0.0020070	0.0000003	0.013	**5.43**	0.0020073	**5.15**	
9	**Laura**	0.0020071	0.0000002	0.011	**5.47**	0.0020073	**5.20**	
10	**Laura**	0.0020073	0.0000003	0.015	**5.57**	0.0020072	**5.32**	
21	**Laura**	0.0020063	0.0000003	0.016	**5.08**	0.0020069	**5.01**	
22	**Laura**	0.0020065	0.0000002	0.010	**5.17**	0.0020068	**5.11**	
23	**Laura**	0.0020064	0.0000003	0.014	**5.14**	0.0020068	**5.10**	
24	**Laura**	0.0020070	0.0000005	0.025	**5.42**	0.0020068	**5.39**	
25	**Laura**	0.0020069	0.0000002	0.009	**5.36**	0.0020067	**5.35**	
36	**Laura**	0.0020061	0.0000003	0.017	**4.98**	0.0020064	**5.14**	
37	**Laura**	0.0020061	0.0000005	0.023	**5.00**	0.0020064	**5.18**	
38	**Laura**	0.0020067	0.0000005	0.023	**5.29**	0.0020063	**5.49**	
39	**Laura**	0.0020062	0.0000003	0.016	**5.06**	0.0020063	**5.27**	
40	**Laura**	0.0020063	0.0000002	0.011	**5.07**	0.0020063	**5.30**	
54	**Laura**	0.0020061	0.0000003	0.014	**4.96**	0.0020058	**5.42**	
55	**Laura**	0.0020055	0.0000003	0.017	**4.67**	0.0020058	**5.14**	
56	**Laura**	0.0020061	0.0000004	0.017	**4.97**	0.0020058	**5.46**	
57	**Laura**	0.0020058	0.0000004	0.020	**4.82**	0.0020057	**5.32**	
58	**Laura**	0.0020060	0.0000006	0.028	**4.92**	0.0020057	**5.44**	
Average		0.0020067			**5.30**		**5.30**	
1σ		0.0000007			**0.37**		**0.18**	
2σ		0.0000015			**0.73**		**0.36**	
SEM		0.0000003			**0.15**		**0.07**	
n		25			**25**		**25**	
Unknowns								
11	**RJ0812-11**	0.0020072	0.0000003	0.013	**5.56**	0.0020072	**5.32**	0.36

12	**RJ0812-15**	0.0020072	0.0000003	0.014	**5.52**	0.0020072	**5.30**	0.36
13	**RJ0812-15**	0.0020078	0.0000003	0.015	**5.82**	0.0020071	**5.62**	0.36
14	**RJ0812-16**	0.0020072	0.0000003	0.015	**5.55**	0.0020071	**5.36**	0.36
15	**RJ0812-19**	0.0020082	0.0000002	0.012	**6.02**	0.0020071	**5.85**	0.36
16	**RJ0812-21**	0.0020084	0.0000003	0.016	**6.12**	0.0020070	**5.97**	0.36
17	**RJ0812-22**	0.0020077	0.0000003	0.016	**5.79**	0.0020070	**5.65**	0.36
18	**RJ0812-23**	0.0020074	0.0000003	0.013	**5.65**	0.0020070	**5.53**	0.36
19	**RJ0812-26**	0.0020070	0.0000002	0.012	**5.45**	0.0020069	**5.34**	0.36
20	**RJ0812-27**	0.0020071	0.0000001	0.007	**5.50**	0.0020069	**5.41**	0.36
26	**RJ0855-2c**	0.0020084	0.0000003	0.014	**6.12**	0.0020067	**6.12**	0.36
27	**RJ0855-2r**	0.0020075	0.0000002	0.010	**5.71**	0.0020067	**5.73**	0.36
28	**RJ0855-3**	0.0020084	0.0000004	0.019	**6.12**	0.0020067	**6.16**	0.36
29	**RJ0855-4c**	0.0020075	0.0000003	0.013	**5.68**	0.0020066	**5.74**	0.36
30	**RJ0855-4r**	0.0020063	0.0000003	0.015	**5.09**	0.0020066	**5.16**	0.36
31	**RJ0855-9c**	0.0020068	0.0000003	0.016	**5.35**	0.0020066	**5.43**	0.36
32	**RJ0855-10**	0.0020067	0.0000004	0.022	**5.27**	0.0020065	**5.37**	0.36
33	**RJ0855-11**	0.0020065	0.0000003	0.017	**5.18**	0.0020065	**5.30**	0.36
34	**RJ0844-2c**	0.0020062	0.0000004	0.018	**5.03**	0.0020065	**5.17**	0.36
35	**RJ0844-2r**	0.0020057	0.0000002	0.012	**4.78**	0.0020064	**4.93**	0.36
41	**RJ0844-3**	0.0020050	0.0000002	0.012	**4.46**	0.0020062	**4.70**	0.36
42	**RJ0844-5**	0.0020060	0.0000004	0.020	**4.95**	0.0020062	**5.21**	0.36
43	**RJ0844-7**	0.0020051	0.0000003	0.017	**4.48**	0.0020062	**4.76**	0.36
44	**RJ0826-27**	0.0020068	0.0000004	0.021	**5.33**	0.0020061	**5.62**	0.36
45	**RJ0826-25**	0.0020064	0.0000002	0.012	**5.14**	0.0020061	**5.45**	0.36
46	**RJ0826-23**	0.0020059	0.0000005	0.022	**4.88**	0.0020061	**5.21**	0.36
47	**RJ0826-19**	0.0020065	0.0000004	0.021	**5.19**	0.0020060	**5.53**	0.36
48	**RJ0826-17c**	0.0020061	0.0000006	0.030	**5.00**	0.0020060	**5.36**	0.36
49	**RJ0826-17r**	0.0020065	0.0000004	0.019	**5.17**	0.0020060	**5.55**	0.36
50	**RJ0826-14c**	0.0020060	0.0000004	0.022	**4.94**	0.0020060	**5.33**	0.36
51	**RJ0826-14r**	0.0020056	0.0000005	0.025	**4.73**	0.0020059	**5.13**	0.36
52	**RJ0826-5**	0.0020060	0.0000004	0.019	**4.94**	0.0020059	**5.36**	0.36
53	**RJ0826-1**	0.0020052	0.0000005	0.024	**4.53**	0.0020059	**4.97**	0.36

Analytical Session 3 (02.08.11b)

Analytical order	Sample-grain(c/r)	$^{18}O/^{16}O$ measured	1σ	% Std Err (1σ)	$\delta^{18}O_{(VSMOW)}$	Drift correction factor	$\delta^{18}O_{(VSMOW)}$ (drift corrected)	Analytical uncertainty (±)
1	**Laura**	0.0020071	0.0000004	0.021	**5.26**	0.0020071	**5.28**	
2	**Laura**	0.0020072	0.0000004	0.021	**5.35**	0.0020071	**5.37**	
3	**Laura**	0.0020073	0.0000003	0.014	**5.40**	0.0020071	**5.42**	
4	**Laura**	0.0020071	0.0000002	0.011	**5.26**	0.0020071	**5.28**	
5	**Laura**	0.0020070	0.0000006	0.028	**5.25**	0.0020071	**5.27**	
16	**Laura**	0.0020078	0.0000004	0.022	**5.64**	0.0020071	**5.65**	
17	**Laura**	0.0020068	0.0000004	0.018	**5.13**	0.0020071	**5.13**	
18	**Laura**	0.0020066	0.0000003	0.014	**5.04**	0.0020071	**5.05**	
19	**Laura**	0.0020070	0.0000004	0.020	**5.23**	0.0020071	**5.23**	
20	**Laura**	0.0020070	0.0000003	0.015	**5.24**	0.0020071	**5.24**	
36	**Laura**	0.0020068	0.0000003	0.017	**5.15**	0.0020072	**5.13**	
37	**Laura**	0.0020069	0.0000003	0.014	**5.19**	0.0020072	**5.17**	
38	**Laura**	0.0020075	0.0000003	0.017	**5.48**	0.0020072	**5.46**	
39	**Laura**	0.0020077	0.0000004	0.019	**5.60**	0.0020072	**5.58**	

40	**Laura**	0.0020071	0.0000004	0.020	**5.28**	0.0020072	**5.26**	
Average		0.0020071			**5.30**		**5.30**	
1σ		0.0000003			**0.17**		**0.17**	
2σ		0.0000007			**0.33**		**0.33**	
SEM		0.0000002			**0.09**		**0.09**	
n		15			**15**		**15**	
Unknowns								
6	**RJ0853-8**	0.0020072	0.0000004	0.020	**5.35**	0.0020071	**5.37**	0.33
7	**RJ0853-9**	0.0020067	0.0000004	0.020	**5.07**	0.0020071	**5.09**	0.33
8	**RJ0853-10**	0.0020070	0.0000004	0.019	**5.21**	0.0020071	**5.22**	0.33
9	**RJ0853-15right**	0.0020061	0.0000004	0.018	**4.79**	0.0020071	**4.80**	0.33
10	**RJ0853-15left**	0.0020069	0.0000002	0.011	**5.17**	0.0020071	**5.18**	0.33
11	**RJ0853-19**	0.0020068	0.0000003	0.016	**5.13**	0.0020071	**5.14**	0.33
12	**RJ0853-20c**	0.0020073	0.0000004	0.020	**5.38**	0.0020071	**5.39**	0.33
13	**RJ0853-20r**	0.0020067	0.0000003	0.015	**5.10**	0.0020071	**5.11**	0.33
14	**RJ0853-22**	0.0020068	0.0000004	0.018	**5.13**	0.0020071	**5.14**	0.33
15	**RJ0853-23**	0.0020061	0.0000004	0.022	**4.77**	0.0020071	**4.77**	0.33
21	**RJ0823-11**	0.0020074	0.0000004	0.019	**5.41**	0.0020071	**5.40**	0.33
22	**RJ0823-12**	0.0020070	0.0000003	0.015	**5.25**	0.0020071	**5.24**	0.33
23	**RJ0823-13**	0.0020085	0.0000003	0.013	**5.96**	0.0020071	**5.95**	0.33
24	**RJ0823-19**	0.0020075	0.0000003	0.016	**5.47**	0.0020072	**5.46**	0.33
25	**RJ0823-20**	0.0020088	0.0000005	0.027	**6.14**	0.0020072	**6.13**	0.33
26	**RJ0815-1**	0.0020065	0.0000003	0.016	**4.97**	0.0020072	**4.96**	0.33
27	**RJ0815-9**	0.0020067	0.0000003	0.013	**5.10**	0.0020072	**5.09**	0.33
28	**RJ0815-10**	0.0020077	0.0000003	0.013	**5.58**	0.0020072	**5.57**	0.33
29	**RJ0815-12**	0.0020070	0.0000005	0.025	**5.25**	0.0020072	**5.24**	0.33
30	**RJ0815-14**	0.0020084	0.0000003	0.016	**5.95**	0.0020072	**5.94**	0.33
31	**RJ0816-1**	0.0020074	0.0000004	0.021	**5.42**	0.0020072	**5.41**	0.33
32	**RJ0816-5**	0.0020081	0.0000003	0.015	**5.80**	0.0020072	**5.78**	0.33
33	**RJ0816-9**	0.0020079	0.0000004	0.020	**5.70**	0.0020072	**5.69**	0.33
34	**RJ0816-10**	0.0020079	0.0000005	0.027	**5.67**	0.0020072	**5.66**	0.33
35	**RJ0816-11**	0.0020071	0.0000004	0.020	**5.29**	0.0020072	**5.27**	0.33

Analytical Session 4 (03.08.11)

Analytical order	Sample-grain(c/r)	$^{18}O/^{16}O$ measured	1σ	% Std Err (1σ)	$\delta^{18}O_{(VSMOW)}$	Drift correction factor	$\delta^{18}O_{(VSMOW)}$ (drift corrected)	Analytical uncertainty (±)
1	**Laura**	0.0020088	0.0000003	0.014	**5.54**	0.0020093	**5.07**	
2	**Laura**	0.0020087	0.0000002	0.011	**5.51**	0.0020092	**5.05**	
3	**Laura**	0.0020086	0.0000003	0.014	**5.45**	0.0020092	**4.99**	
4	**Laura**	0.0020092	0.0000003	0.017	**5.75**	0.0020092	**5.31**	
5	**Laura**	0.0020089	0.0000002	0.012	**5.58**	0.0020092	**5.15**	
6	**Laura**	0.0020086	0.0000003	0.015	**5.44**	0.0020091	**5.02**	
7	**Laura**	0.0020089	0.0000002	0.012	**5.61**	0.0020091	**5.20**	
8	**Laura**	0.0020088	0.0000002	0.011	**5.56**	0.0020091	**5.16**	
9	**Laura**	0.0020090	0.0000002	0.010	**5.67**	0.0020091	**5.29**	
10	**Laura**	0.0020091	0.0000004	0.020	**5.69**	0.0020091	**5.31**	
21	**Laura**	0.0020084	0.0000002	0.011	**5.34**	0.0020088	**5.09**	
22	**Laura**	0.0020092	0.0000002	0.012	**5.74**	0.0020088	**5.50**	
23	**Laura**	0.0020090	0.0000002	0.012	**5.64**	0.0020088	**5.41**	

24	**Laura**	0.0020082	0.0000003	0.015	**5.25**	0.0020087	**5.02**	
25	**Laura**	0.0020087	0.0000003	0.013	**5.48**	0.0020087	**5.27**	
36	**Laura**	0.0020090	0.0000004	0.019	**5.63**	0.0020085	**5.54**	
37	**Laura**	0.0020087	0.0000004	0.021	**5.49**	0.0020085	**5.41**	
38	**Laura**	0.0020091	0.0000003	0.015	**5.68**	0.0020084	**5.61**	
39	**Laura**	0.0020093	0.0000004	0.018	**5.81**	0.0020084	**5.75**	
40	**Laura**	0.0020094	0.0000003	0.014	**5.83**	0.0020084	**5.79**	
41	**Laura**	0.0020092	0.0000004	0.021	**5.73**	0.0020084	**5.69**	
42	**Laura**	0.0020090	0.0000003	0.016	**5.65**	0.0020084	**5.62**	
43	**Laura**	0.0020086	0.0000003	0.013	**5.47**	0.0020083	**5.45**	
44	**Laura**	0.0020082	0.0000002	0.012	**5.26**	0.0020083	**5.25**	
45	**Laura**	0.0020080	0.0000002	0.012	**5.14**	0.0020083	**5.15**	
59	**Laura**	0.0020086	0.0000002	0.010	**5.43**	0.0020080	**5.59**	
60	**Laura**	0.0020084	0.0000002	0.012	**5.35**	0.0020080	**5.52**	
61	**Laura**	0.0020085	0.0000003	0.016	**5.41**	0.0020079	**5.60**	
62	**Laura**	0.0020078	0.0000004	0.018	**5.04**	0.0020079	**5.23**	
63	**Laura**	0.0020079	0.0000002	0.008	**5.11**	0.0020079	**5.31**	
79	**Laura**	0.0020075	0.0000005	0.023	**4.90**	0.0020075	**5.27**	
80	**Laura**	0.0020077	0.0000003	0.016	**5.02**	0.0020075	**5.41**	
81	**Laura**	0.0020069	0.0000002	0.011	**4.59**	0.0020075	**4.99**	
82	**Laura**	0.0020073	0.0000004	0.019	**4.77**	0.0020075	**5.19**	
83	**Laura**	0.0020070	0.0000002	0.009	**4.64**	0.0020075	**5.06**	
96	**Laura**	0.0020068	0.0000005	0.027	**4.56**	0.0020072	**5.12**	
97	**Laura**	0.0020074	0.0000003	0.017	**4.85**	0.0020072	**5.43**	
98	**Laura**	0.0020074	0.0000005	0.026	**4.84**	0.0020071	**5.43**	
99	**Laura**	0.0020069	0.0000005	0.027	**4.58**	0.0020071	**5.18**	
100	**Laura**	0.0020057	0.0000004	0.022	**3.98**	0.0020071	**4.59**	
Average		0.0020083			**5.30**		**5.30**	
1σ		0.0000009			**0.43**		**0.25**	
2σ		0.0000017			**0.86**		**0.50**	
SEM		0.0000003			**0.14**		**0.08**	
n		40			**40**		**40**	
Unknowns								
11	**RJ0806-31**	0.0020087	0.0000003	0.014	**5.49**	0.0020090	**5.13**	0.50
12	**RJ0806-34**	0.0020090	0.0000002	0.010	**5.66**	0.0020090	**5.31**	0.50
13	**RJ0806-37**	0.0020086	0.0000008	0.040	**5.46**	0.0020090	**5.12**	0.50
14	**RJ0807-23**	0.0020062	0.0000003	0.014	**4.23**	0.0020090	**3.89**	0.50
15	**RJ0807-26**	0.0020051	0.0000004	0.018	**3.70**	0.0020089	**3.38**	0.50
16	**RJ0807-28**	0.0020066	0.0000002	0.012	**4.45**	0.0020089	**4.14**	0.50
17	**RJ0807-35c**	0.0020096	0.0000002	0.012	**5.97**	0.0020089	**5.67**	0.50
18	**RJ0807-35r**	0.0020065	0.0000002	0.009	**4.40**	0.0020089	**4.11**	0.50
19	**RJ0812-38**	0.0020087	0.0000003	0.013	**5.51**	0.0020089	**5.23**	0.50
20	**RJ0812-40**	0.0020096	0.0000003	0.015	**5.95**	0.0020088	**5.68**	0.50
26	**RJ0845-16c**	0.0020143	0.0000002	0.012	**8.28**	0.0020087	**8.08**	0.50
27	**RJ0845-17**	0.0020085	0.0000004	0.019	**5.41**	0.0020087	**5.22**	0.50
28	**RJ0845-20**	0.0020094	0.0000003	0.013	**5.85**	0.0020087	**5.67**	0.50
29	**RJ0845-21**	0.0020094	0.0000003	0.015	**5.84**	0.0020086	**5.67**	0.50
30	**RJ0845-22**	0.0020084	0.0000006	0.028	**5.32**	0.0020086	**5.17**	0.50
31	**RJ0845-23**	0.0020091	0.0000003	0.015	**5.72**	0.0020086	**5.57**	0.50
32	**RJ0845-25**	0.0020086	0.0000005	0.023	**5.44**	0.0020086	**5.30**	0.50

33	**RJ0845-26**	0.0020123	0.0000004	0.021	**7.30**	0.0020086	**7.18**	0.50
34	**RJ0845-33**	0.0020092	0.0000003	0.016	**5.77**	0.0020085	**5.65**	0.50
35	**RJ0845-34**	0.0020085	0.0000005	0.023	**5.39**	0.0020085	**5.28**	0.50
46	**RJ0823-21**	0.0020091	0.0000003	0.013	**5.71**	0.0020083	**5.72**	0.50
47	**RJ0823-23**	0.0020088	0.0000003	0.013	**5.55**	0.0020082	**5.58**	0.50
48	**RJ0823-25**	0.0020079	0.0000002	0.011	**5.11**	0.0020082	**5.15**	0.50
49	**RJ0823-32**	0.0020089	0.0000004	0.018	**5.62**	0.0020082	**5.67**	0.50
50	**RJ0823-35**	0.0020090	0.0000005	0.024	**5.67**	0.0020082	**5.73**	0.50
51	**RJ0823-38**	0.0020097	0.0000003	0.016	**5.98**	0.0020082	**6.05**	0.50
52	**RJ0853-32**	0.0020084	0.0000003	0.016	**5.35**	0.0020081	**5.43**	0.50
53	**RJ0853-35**	0.0020080	0.0000003	0.016	**5.14**	0.0020081	**5.23**	0.50
54	**RJ0853-38**	0.0020081	0.0000004	0.018	**5.20**	0.0020081	**5.30**	0.50
55	**RJ0826-32**	0.0020084	0.0000005	0.022	**5.37**	0.0020081	**5.48**	0.50
56	**RJ0826-34**	0.0020085	0.0000003	0.017	**5.40**	0.0020080	**5.53**	0.50
57	**RJ0826-35**	0.0020088	0.0000002	0.011	**5.52**	0.0020080	**5.66**	0.50
58	**RJ0826-38**	0.0020082	0.0000003	0.015	**5.24**	0.0020080	**5.39**	0.50
64	**RJ0815-21**	0.0020082	0.0000003	0.016	**5.27**	0.0020079	**5.48**	0.50
65	**RJ0815-24**	0.0020094	0.0000003	0.016	**5.85**	0.0020079	**6.08**	0.50
66	**RJ0815-25**	0.0020087	0.0000003	0.016	**5.52**	0.0020078	**5.75**	0.50
67	**RJ0815-19**	0.0020087	0.0000004	0.021	**5.52**	0.0020078	**5.77**	0.50
68	**RJ0815-34**	0.0020088	0.0000002	0.010	**5.53**	0.0020078	**5.79**	0.50
69	**RJ0816-17**	0.0020091	0.0000003	0.016	**5.71**	0.0020078	**5.98**	0.50
70	**RJ0816-24**	0.0020087	0.0000004	0.021	**5.52**	0.0020077	**5.80**	0.50
71	**RJ0816-28**	0.0020092	0.0000004	0.022	**5.73**	0.0020077	**6.03**	0.50
72	**RJ0816-32**	0.0020091	0.0000002	0.012	**5.70**	0.0020077	**6.00**	0.50
73	**RJ0816-38**	0.0020086	0.0000003	0.014	**5.44**	0.0020077	**5.75**	0.50
74	**RJ0844-14**	0.0020081	0.0000002	0.010	**5.18**	0.0020077	**5.51**	0.50
75	**RJ0844-20**	0.0020073	0.0000001	0.007	**4.79**	0.0020076	**5.13**	0.50
76	**RJ0844-23**	0.0020078	0.0000004	0.018	**5.04**	0.0020076	**5.38**	0.50
77	**RJ0844-26**	0.0020078	0.0000002	0.009	**5.05**	0.0020076	**5.41**	0.50
78	**RJ0844-34**	0.0020077	0.0000004	0.017	**5.00**	0.0020076	**5.37**	0.50
84	**RJ0824-48**	0.0020085	0.0000004	0.022	**5.41**	0.0020074	**5.84**	0.50
85	**RJ0824-47**	0.0020074	0.0000005	0.027	**4.84**	0.0020074	**5.28**	0.50
86	**RJ0824-44**	0.0020077	0.0000004	0.018	**4.99**	0.0020074	**5.45**	0.50
87	**RJ0855-14**	0.0020083	0.0000004	0.022	**5.32**	0.0020074	**5.78**	0.50
88	**RJ0855-20**	0.0020096	0.0000003	0.017	**5.94**	0.0020073	**6.41**	0.50
89	**RJ0855-23r**	0.0020079	0.0000004	0.019	**5.12**	0.0020073	**5.61**	0.50
90	**RJ0855-23l**	0.0020084	0.0000003	0.016	**5.33**	0.0020073	**5.83**	0.50
91	**RJ0855-30c**	0.0020084	0.0000002	0.010	**5.36**	0.0020073	**5.87**	0.50
92	**RJ0855-30r**	0.0020081	0.0000004	0.020	**5.18**	0.0020073	**5.70**	0.50
93	**RJ0855-31**	0.0020082	0.0000003	0.015	**5.25**	0.0020072	**5.78**	0.50
94	**RJ0845-14**	0.0020072	0.0000006	0.028	**4.75**	0.0020072	**5.30**	0.50
95	**RJ0845-18**	0.0020073	0.0000005	0.023	**4.79**	0.0020072	**5.34**	0.50

Analytical Session 5 (04.08.11)

Analytical order	Sample-grain(c/r)	$^{18}O/^{16}O$ measured	1σ	% Std Err (1σ)	$\delta^{18}O_{(VSMOW)}$	Drift correction factor	$\delta^{18}O_{(VSMOW)}$ (drift corrected)	Analytical uncertainty (±)
1	**Laura**	0.0020100	0.0000004	0.019	**5.65**	0.0020095	**5.54**	
2	**Laura**	0.0020093	0.0000004	0.018	**5.32**	0.0020095	**5.20**	
3	**Laura**	0.0020095	0.0000003	0.017	**5.42**	0.0020095	**5.30**	

4	**Laura**	0.0020095	0.0000004	0.018	**5.42**	0.0020095	**5.30**	
5	**Laura**	0.0020095	0.0000003	0.014	**5.43**	0.0020095	**5.32**	
6	**Laura**	0.0020100	0.0000004	0.020	**5.69**	0.0020095	**5.58**	
7	**Laura**	0.0020099	0.0000002	0.010	**5.60**	0.0020095	**5.50**	
8	**Laura**	0.0020098	0.0000002	0.008	**5.58**	0.0020095	**5.47**	
9	**Laura**	0.0020102	0.0000002	0.009	**5.74**	0.0020095	**5.64**	
10	**Laura**	0.0020094	0.0000003	0.017	**5.35**	0.0020095	**5.24**	
21	**Laura**	0.0020099	0.0000003	0.014	**5.59**	0.0020094	**5.51**	
22	**Laura**	0.0020099	0.0000003	0.014	**5.63**	0.0020094	**5.55**	
23	**Laura**	0.0020096	0.0000002	0.012	**5.47**	0.0020094	**5.40**	
24	**Laura**	0.0020096	0.0000003	0.017	**5.47**	0.0020094	**5.40**	
25	**Laura**	0.0020100	0.0000003	0.016	**5.64**	0.0020094	**5.57**	
35	**Laura**	0.0020080	0.0000003	0.016	**4.66**	0.0020094	**4.61**	
36	**Laura**	0.0020089	0.0000004	0.022	**5.13**	0.0020094	**5.08**	
37	**Laura**	0.0020089	0.0000005	0.025	**5.14**	0.0020094	**5.09**	
38	**Laura**	0.0020087	0.0000004	0.020	**5.02**	0.0020094	**4.97**	
39	**Laura**	0.0020082	0.0000006	0.028	**4.77**	0.0020094	**4.72**	
55	**Laura**	0.0020089	0.0000003	0.017	**5.09**	0.0020093	**5.08**	
56	**Laura**	0.0020090	0.0000003	0.013	**5.17**	0.0020093	**5.16**	
57	**Laura**	0.0020094	0.0000003	0.015	**5.34**	0.0020093	**5.33**	
58	**Laura**	0.0020092	0.0000004	0.018	**5.27**	0.0020093	**5.27**	
59	**Laura**	0.0020086	0.0000003	0.016	**4.94**	0.0020093	**4.93**	
76	**Laura**	0.0020091	0.0000003	0.013	**5.23**	0.0020092	**5.26**	
77	**Laura**	0.0020093	0.0000002	0.012	**5.29**	0.0020092	**5.32**	
78	**Laura**	0.0020093	0.0000003	0.013	**5.31**	0.0020092	**5.35**	
79	**Laura**	0.0020092	0.0000003	0.013	**5.25**	0.0020092	**5.29**	
80	**Laura**	0.0020092	0.0000004	0.018	**5.24**	0.0020092	**5.28**	
96	**Laura**	0.0020094	0.0000002	0.010	**5.35**	0.0020091	**5.41**	
97	**Laura**	0.0020089	0.0000003	0.013	**5.09**	0.0020091	**5.16**	
98	**Laura**	0.0020092	0.0000002	0.011	**5.27**	0.0020091	**5.34**	
99	**Laura**	0.0020092	0.0000002	0.010	**5.29**	0.0020091	**5.36**	
100	**Laura**	0.0020093	0.0000003	0.013	**5.32**	0.0020091	**5.40**	
116	**Laura**	0.0020091	0.0000004	0.022	**5.19**	0.0020091	**5.30**	
117	**Laura**	0.0020097	0.0000002	0.009	**5.52**	0.0020091	**5.63**	
118	**Laura**	0.0020092	0.0000002	0.012	**5.25**	0.0020091	**5.36**	
119	**Laura**	0.0020090	0.0000003	0.013	**5.16**	0.0020091	**5.27**	
120	**Laura**	0.0020091	0.0000002	0.008	**5.21**	0.0020090	**5.33**	
131	**Laura**	0.0020093	0.0000004	0.019	**5.32**	0.0020090	**5.45**	
132	**Laura**	0.0020085	0.0000003	0.014	**4.92**	0.0020090	**5.06**	
133	**Laura**	0.0020087	0.0000003	0.017	**5.01**	0.0020090	**5.15**	
134	**Laura**	0.0020091	0.0000003	0.014	**5.23**	0.0020090	**5.37**	
135	**Laura**	0.0020097	0.0000002	0.011	**5.52**	0.0020090	**5.66**	
Average		0.0020093			**5.30**		**5.30**	
1σ		0.0000005			**0.24**		**0.22**	
2σ		0.0000010			**0.48**		**0.44**	
SEM		0.0000001			**0.07**		**0.07**	
n		45			**45**		**45**	
Unknowns								
11	**RJ0890-4**	0.0020087	0.0000002	0.009	**5.00**	0.0020095	**4.90**	0.44
12	**RJ0890-1**	0.0020107	0.0000003	0.015	**6.01**	0.0020095	**5.91**	0.44

13	**RJ0819-2**	0.0020094	0.0000003	0.016	**5.34**	0.0020095	**5.25**	0.44
14	**RJ0862-6**	0.0020114	0.0000002	0.011	**6.35**	0.0020095	**6.25**	0.44
15	**RJ0862-10**	0.0020106	0.0000003	0.015	**5.94**	0.0020095	**5.85**	0.44
16	**RJ0862-13**	0.0020100	0.0000003	0.017	**5.65**	0.0020095	**5.56**	0.44
17	**RJ0862-20**	0.0020129	0.0000004	0.017	**7.13**	0.0020095	**7.04**	0.44
18	**RJ0862-24**	0.0020105	0.0000002	0.010	**5.91**	0.0020094	**5.82**	0.44
19	**RJ0862-1**	0.0020090	0.0000004	0.020	**5.17**	0.0020094	**5.09**	0.44
20	**RJ0862-32**	0.0020099	0.0000004	0.019	**5.61**	0.0020094	**5.53**	0.44
26	**RJ0862-9**	0.0020099	0.0000004	0.020	**5.63**	0.0020094	**5.56**	0.44
27	**RJ0862-22**	0.0020099	0.0000005	0.023	**5.63**	0.0020094	**5.57**	0.44
28	**RJ0862-35**	0.0020100	0.0000003	0.017	**5.66**	0.0020094	**5.59**	0.44
29	**RJ0867-2**	0.0020105	0.0000006	0.028	**5.89**	0.0020094	**5.82**	0.44
30	**RJ0867-5**	0.0020098	0.0000006	0.029	**5.55**	0.0020094	**5.49**	0.44
31	**RJ0867-8**	0.0020102	0.0000003	0.013	**5.77**	0.0020094	**5.71**	0.44
32	**RJ0867-9**	0.0020116	0.0000003	0.016	**6.47**	0.0020094	**6.41**	0.44
33	**RJ0867-11**	0.0020109	0.0000005	0.023	**6.09**	0.0020094	**6.03**	0.44
34	**RJ0867-13**	0.0020107	0.0000003	0.017	**6.02**	0.0020094	**5.96**	0.44
40	**RJ0877-8**	0.0020079	0.0000006	0.031	**4.62**	0.0020094	**4.58**	0.44
41	**RJ0877-11**	0.0020073	0.0000004	0.018	**4.31**	0.0020094	**4.27**	0.44
42	**RJ0877-17**	0.0020082	0.0000004	0.019	**4.75**	0.0020094	**4.71**	0.44
43	**RJ0877-18**	0.0020082	0.0000002	0.012	**4.78**	0.0020093	**4.74**	0.44
44	**RJ0877-20**	0.0020083	0.0000004	0.018	**4.83**	0.0020093	**4.79**	0.44
45	**RJ0877-23**	0.0020078	0.0000004	0.020	**4.55**	0.0020093	**4.52**	0.44
46	**RJ0877-24**	0.0020078	0.0000004	0.022	**4.54**	0.0020093	**4.51**	0.44
47	**RJ0877-28**	0.0020082	0.0000003	0.015	**4.78**	0.0020093	**4.75**	0.44
48	**RJ0877-31c**	0.0020092	0.0000004	0.020	**5.26**	0.0020093	**5.23**	0.44
49	**RJ0877-31r**	0.0020088	0.0000004	0.018	**5.05**	0.0020093	**5.02**	0.44
50	**RJ0877-35**	0.0020095	0.0000004	0.020	**5.42**	0.0020093	**5.39**	0.44
51	**RJ0877-38**	0.0020088	0.0000004	0.021	**5.08**	0.0020093	**5.06**	0.44
52	**RJ0857-9**	0.0020097	0.0000005	0.023	**5.53**	0.0020093	**5.51**	0.44
53	**RJ0857-12**	0.0020102	0.0000003	0.013	**5.74**	0.0020093	**5.72**	0.44
54	**RJ0857-16**	0.0020099	0.0000004	0.018	**5.59**	0.0020093	**5.58**	0.44
60	**RJ0857-17**	0.0020099	0.0000005	0.023	**5.62**	0.0020093	**5.62**	0.44
61	**RJ0857-18**	0.0020101	0.0000003	0.015	**5.72**	0.0020093	**5.72**	0.44
62	**RJ0857-21**	0.0020101	0.0000003	0.014	**5.71**	0.0020093	**5.71**	0.44
63	**RJ0857-22**	0.0020087	0.0000002	0.010	**5.03**	0.0020093	**5.03**	0.44
64	**RJ0857-25**	0.0020101	0.0000002	0.011	**5.70**	0.0020093	**5.71**	0.44
65	**RJ0857-30**	0.0020104	0.0000003	0.017	**5.84**	0.0020093	**5.84**	0.44
66	**RJ0857-33**	0.0020099	0.0000005	0.023	**5.64**	0.0020093	**5.64**	0.44
67	**RJ0846-8**	0.0020090	0.0000002	0.010	**5.14**	0.0020093	**5.15**	0.44
68	**RJ0846-12**	0.0020079	0.0000001	0.007	**4.60**	0.0020093	**4.61**	0.44
69	**RJ0846-14r**	0.0020095	0.0000002	0.012	**5.43**	0.0020092	**5.45**	0.44
70	**RJ0846-15**	0.0020087	0.0000002	0.012	**4.99**	0.0020092	**5.01**	0.44
71	**RJ0846-17**	0.0020094	0.0000002	0.012	**5.36**	0.0020092	**5.37**	0.44
72	**RJ0846-18**	0.0020094	0.0000003	0.014	**5.34**	0.0020092	**5.36**	0.44
73	**RJ0846-21**	0.0020092	0.0000002	0.012	**5.25**	0.0020092	**5.27**	0.44
74	**RJ0846-22**	0.0020089	0.0000002	0.010	**5.10**	0.0020092	**5.13**	0.44
75	**RJ0846-28**	0.0020088	0.0000003	0.015	**5.07**	0.0020092	**5.09**	0.44
81	**RJ0849-4**	0.0020104	0.0000002	0.012	**5.84**	0.0020092	**5.88**	0.44
82	**RJ0849-7**	0.0020084	0.0000003	0.017	**4.85**	0.0020092	**4.89**	0.44
83	**RJ0849-10**	0.0020084	0.0000002	0.012	**4.87**	0.0020092	**4.91**	0.44

84	**RJ0849-14**	0.0020086	0.0000003	0.016	**4.94**	0.0020092	**4.99**	0.44
85	**RJ0849-16**	0.0020085	0.0000003	0.015	**4.90**	0.0020092	**4.94**	0.44
86	**RJ0849-17**	0.0020078	0.0000003	0.017	**4.58**	0.0020092	**4.63**	0.44
87	**RJ0849-18**	0.0020088	0.0000003	0.015	**5.06**	0.0020092	**5.11**	0.44
88	**RJ0849-25**	0.0020093	0.0000003	0.016	**5.30**	0.0020092	**5.35**	0.44
89	**RJ0849-27**	0.0020084	0.0000003	0.014	**4.87**	0.0020092	**4.92**	0.44
90	**RJ0849-21**	0.0020080	0.0000003	0.015	**4.64**	0.0020092	**4.70**	0.44
91	**RJ0860-2**	0.0020081	0.0000004	0.020	**4.71**	0.0020092	**4.77**	0.44
92	**RJ0860-3**	0.0020081	0.0000002	0.012	**4.73**	0.0020092	**4.79**	0.44
93	**RJ0860-11**	0.0020082	0.0000003	0.013	**4.78**	0.0020092	**4.84**	0.44
94	**RJ0860-13**	0.0020079	0.0000004	0.022	**4.63**	0.0020091	**4.69**	0.44
95	**RJ0860-19**	0.0020083	0.0000004	0.019	**4.83**	0.0020091	**4.89**	0.44
101	**RJ0860-14**	0.0020086	0.0000002	0.012	**4.98**	0.0020091	**5.06**	0.44
102	**RJ0860-20**	0.0020080	0.0000002	0.011	**4.65**	0.0020091	**4.73**	0.44
103	**RJ0860-22**	0.0020084	0.0000002	0.009	**4.86**	0.0020091	**4.94**	0.44
104	**RJ0860-25**	0.0020081	0.0000002	0.009	**4.70**	0.0020091	**4.78**	0.44
105	**RJ0860-31**	0.0020082	0.0000003	0.015	**4.77**	0.0020091	**4.86**	0.44
106	**RJ0822-7**	0.0020092	0.0000003	0.016	**5.26**	0.0020091	**5.35**	0.44
107	**RJ0822-10**	0.0020094	0.0000002	0.008	**5.37**	0.0020091	**5.46**	0.44
108	**RJ0822-11**	0.0020095	0.0000003	0.014	**5.42**	0.0020091	**5.51**	0.44
109	**RJ0822-14**	0.0020095	0.0000002	0.009	**5.41**	0.0020091	**5.50**	0.44
110	**RJ0822-15c**	0.0020090	0.0000003	0.012	**5.15**	0.0020091	**5.25**	0.44
111	**RJ0822-15r**	0.0020084	0.0000002	0.010	**4.88**	0.0020091	**4.98**	0.44
112	**RJ0822-16**	0.0020098	0.0000003	0.013	**5.55**	0.0020091	**5.65**	0.44
113	**RJ0822-19**	0.0020092	0.0000002	0.012	**5.28**	0.0020091	**5.38**	0.44
114	**RJ0822-21**	0.0020090	0.0000002	0.008	**5.15**	0.0020091	**5.25**	0.44
115	**RJ0822-12**	0.0020091	0.0000003	0.013	**5.20**	0.0020091	**5.31**	0.44
121	**RJ0892-5**	0.0020110	0.0000002	0.009	**6.17**	0.0020090	**6.29**	0.44
122	**RJ0892-10**	0.0020107	0.0000002	0.011	**6.02**	0.0020090	**6.13**	0.44
123	**RJ0892-14**	0.0020101	0.0000002	0.010	**5.69**	0.0020090	**5.81**	0.44
124	**RJ0892-15**	0.0020106	0.0000003	0.013	**5.95**	0.0020090	**6.07**	0.44
125	**RJ0892-17**	0.0020110	0.0000003	0.013	**6.18**	0.0020090	**6.31**	0.44
126	**RJ0892-19**	0.0020113	0.0000002	0.011	**6.30**	0.0020090	**6.43**	0.44
127	**RJ0892-21**	0.0020107	0.0000004	0.018	**6.00**	0.0020090	**6.12**	0.44
128	**RJ0892-22**	0.0020103	0.0000004	0.019	**5.82**	0.0020090	**5.95**	0.44
129	**RJ0892-27**	0.0020111	0.0000004	0.019	**6.20**	0.0020090	**6.33**	0.44
130	**RJ0892-33**	0.0020106	0.0000004	0.020	**5.94**	0.0020090	**6.07**	0.44

Analytical Session 6 (23.01.12)

Analytical order	**Sample-grain(c/r)**	**$^{18}O/^{16}O$ measured**	**1σ**	**% Std Err (1σ)**	**$\delta^{18}O_{(VSMOW)}$**	**Drift correction factor**	**$\delta^{18}O_{(VSMOW)}$ (drift corrected)**	**Analytical uncertainty (±)**
1	**Laura**	0.0020120	0.0000002	0.008	**5.41**	0.0020119	**5.37**	
2	**Laura**	0.0020120	0.0000002	0.012	**5.43**	0.0020119	**5.39**	
3	**Laura**	0.0020123	0.0000002	0.011	**5.56**	0.0020118	**5.53**	
4	**Laura**	0.0020118	0.0000001	0.006	**5.30**	0.0020118	**5.27**	
5	**Laura**	0.0020116	0.0000002	0.011	**5.23**	0.0020118	**5.20**	
6	**Laura**	0.0020117	0.0000002	0.011	**5.28**	0.0020118	**5.25**	
7	**Laura**	0.0020121	0.0000002	0.009	**5.48**	0.0020118	**5.45**	
8	**Laura**	0.0020115	0.0000002	0.011	**5.14**	0.0020118	**5.11**	
9	**Laura**	0.0020112	0.0000002	0.011	**4.99**	0.0020118	**4.96**	

10	**Laura**	0.0020121	0.0000002	0.010	**5.44**	0.0020118	**5.41**	
21	**Laura**	0.0020120	0.0000002	0.009	**5.41**	0.0020118	**5.39**	
22	**Laura**	0.0020114	0.0000002	0.011	**5.10**	0.0020118	**5.09**	
23	**Laura**	0.0020117	0.0000002	0.012	**5.24**	0.0020118	**5.22**	
24	**Laura**	0.0020118	0.0000002	0.011	**5.31**	0.0020118	**5.29**	
25	**Laura**	0.0020120	0.0000002	0.009	**5.39**	0.0020118	**5.37**	
36	**Laura**	0.0020120	0.0000002	0.011	**5.41**	0.0020118	**5.41**	
37	**Laura**	0.0020122	0.0000002	0.009	**5.52**	0.0020118	**5.51**	
38	**Laura**	0.0020114	0.0000002	0.011	**5.10**	0.0020118	**5.10**	
39	**Laura**	0.0020118	0.0000002	0.009	**5.31**	0.0020118	**5.30**	
40	**Laura**	0.0020115	0.0000002	0.008	**5.17**	0.0020118	**5.16**	
56	**Laura**	0.0020121	0.0000002	0.009	**5.45**	0.0020118	**5.46**	
57	**Laura**	0.0020119	0.0000003	0.013	**5.34**	0.0020118	**5.35**	
58	**Laura**	0.0020120	0.0000003	0.015	**5.39**	0.0020118	**5.41**	
59	**Laura**	0.0020118	0.0000002	0.009	**5.32**	0.0020118	**5.34**	
60	**Laura**	0.0020118	0.0000002	0.010	**5.30**	0.0020118	**5.31**	
76	**Laura**	0.0020114	0.0000002	0.009	**5.09**	0.0020117	**5.11**	
77	**Laura**	0.0020120	0.0000001	0.007	**5.39**	0.0020117	**5.42**	
78	**Laura**	0.0020116	0.0000002	0.008	**5.19**	0.0020117	**5.22**	
79	**Laura**	0.0020119	0.0000002	0.010	**5.35**	0.0020117	**5.37**	
80	**Laura**	0.0020117	0.0000002	0.011	**5.27**	0.0020117	**5.30**	
96	**Laura**	0.0020121	0.0000001	0.005	**5.46**	0.0020117	**5.51**	
97	**Laura**	0.0020120	0.0000002	0.009	**5.43**	0.0020117	**5.48**	
98	**Laura**	0.0020115	0.0000002	0.010	**5.15**	0.0020117	**5.19**	
99	**Laura**	0.0020113	0.0000002	0.011	**5.07**	0.0020117	**5.12**	
100	**Laura**	0.0020114	0.0000002	0.011	**5.09**	0.0020117	**5.13**	
Average		0.0020118			**5.30**		**5.30**	
1σ		0.0000003			**0.15**		**0.14**	
2σ		0.0000006			**0.29**		**0.29**	
SEM		0.0000001			**0.05**		**0.05**	
n		35			**35**		**35**	
Unknowns								
11	**RJ1101-26**	0.0020124	0.0000002	0.012	**5.61**	0.0020118	**5.58**	0.29
12	**RJ1101-25**	0.0020120	0.0000001	0.006	**5.42**	0.0020118	**5.39**	0.29
13	**RJ1101-20**	0.0020122	0.0000003	0.013	**5.53**	0.0020118	**5.50**	0.29
14	**RJ1101-19**	0.0020127	0.0000002	0.009	**5.76**	0.0020118	**5.74**	0.29
15	**RJ1101-18r**	0.0020130	0.0000002	0.010	**5.89**	0.0020118	**5.87**	0.29
16	**RJ1101-18c**	0.0020120	0.0000001	0.007	**5.39**	0.0020118	**5.36**	0.29
17	**RJ1101-15**	0.0020123	0.0000002	0.009	**5.54**	0.0020118	**5.51**	0.29
18	**RJ1101-11**	0.0020122	0.0000002	0.011	**5.53**	0.0020118	**5.51**	0.29
19	**RJ1101-10**	0.0020123	0.0000002	0.011	**5.55**	0.0020118	**5.53**	0.29
20	**RJ1101-4**	0.0020121	0.0000002	0.012	**5.45**	0.0020118	**5.43**	0.29
26	**RJ1103-12**	0.0020128	0.0000002	0.009	**5.79**	0.0020118	**5.78**	0.29
27	**RJ1103-15**	0.0020121	0.0000002	0.008	**5.48**	0.0020118	**5.47**	0.29
28	**RJ1103-16**	0.0020128	0.0000002	0.012	**5.82**	0.0020118	**5.80**	0.29
29	**RJ1103-17c**	0.0020117	0.0000003	0.015	**5.26**	0.0020118	**5.25**	0.29
30	**RJ1103-17r**	0.0020124	0.0000002	0.010	**5.60**	0.0020118	**5.59**	0.29
31	**RJ1103-19c**	0.0020126	0.0000002	0.010	**5.73**	0.0020118	**5.72**	0.29
32	**RJ1103-19r**	0.0020122	0.0000003	0.014	**5.48**	0.0020118	**5.47**	0.29
33	**RJ1103-20**	0.0020124	0.0000003	0.014	**5.59**	0.0020118	**5.58**	0.29

34	**RJ1103-22**	0.0020128	0.0000003	0.012	**5.82**	0.0020118	**5.81**	0.29
35	**RJ1103-26**	0.0020128	0.0000003	0.013	**5.82**	0.0020118	**5.81**	0.29
41	**RJ1103-14**	0.0020131	0.0000003	0.014	**5.98**	0.0020118	**5.98**	0.29
42	**RJ1103-30**	0.0020120	0.0000002	0.011	**5.40**	0.0020118	**5.40**	0.29
43	**RJ1104-1**	0.0020126	0.0000003	0.014	**5.70**	0.0020118	**5.70**	0.29
44	**RJ1104-3**	0.0020132	0.0000002	0.012	**5.98**	0.0020118	**5.98**	0.29
45	**RJ1104-5c**	0.0020139	0.0000002	0.011	**6.37**	0.0020118	**6.37**	0.29
46	**RJ1104-5r**	0.0020130	0.0000002	0.010	**5.89**	0.0020118	**5.90**	0.29
47	**RJ1104-8**	0.0020132	0.0000002	0.012	**6.00**	0.0020118	**6.01**	0.29
48	**RJ1104-14**	0.0020133	0.0000002	0.011	**6.08**	0.0020118	**6.08**	0.29
49	**RJ1104-18**	0.0020134	0.0000003	0.014	**6.13**	0.0020118	**6.13**	0.29
50	**RJ1104-20c**	0.0020132	0.0000003	0.016	**6.00**	0.0020118	**6.01**	0.29
51	**RJ1104-20r**	0.0020127	0.0000002	0.008	**5.78**	0.0020118	**5.78**	0.29
52	**RJ1104-23**	0.0020133	0.0000001	0.007	**6.06**	0.0020118	**6.07**	0.29
53	**RJ1104-30c**	0.0020131	0.0000002	0.009	**5.95**	0.0020118	**5.95**	0.29
54	**RJ1104-30r**	0.0020131	0.0000003	0.013	**5.98**	0.0020118	**5.99**	0.29
55	**RJ1104-17**	0.0020133	0.0000003	0.014	**6.08**	0.0020118	**6.09**	0.29
61	**RJ1105-1**	0.0020126	0.0000002	0.008	**5.72**	0.0020118	**5.73**	0.29
62	**RJ1105-2**	0.0020125	0.0000002	0.009	**5.66**	0.0020118	**5.67**	0.29
63	**RJ1105-3**	0.0020121	0.0000002	0.009	**5.44**	0.0020117	**5.45**	0.29
64	**RJ1105-4**	0.0020117	0.0000002	0.012	**5.27**	0.0020117	**5.29**	0.29
65	**RJ1105-5**	0.0020118	0.0000002	0.009	**5.29**	0.0020117	**5.30**	0.29
66	**RJ1105-6**	0.0020122	0.0000003	0.015	**5.48**	0.0020117	**5.50**	0.29
67	**RJ1105-9**	0.0020125	0.0000001	0.006	**5.65**	0.0020117	**5.67**	0.29
68	**RJ11A5-2**	0.0020180	0.0000003	0.014	**8.43**	0.0020117	**8.45**	0.29
69	**RJ11A5-3**	0.0020146	0.0000002	0.008	**6.70**	0.0020117	**6.72**	0.29
70	**RJ11A5-5**	0.0020137	0.0000002	0.009	**6.26**	0.0020117	**6.28**	0.29
71	**RJ11A5-6**	0.0020207	0.0000002	0.011	**9.76**	0.0020117	**9.78**	0.29
72	**RJ11A5-7**	0.0020140	0.0000002	0.012	**6.41**	0.0020117	**6.43**	0.29
73	**RJ11A5-8**	0.0020150	0.0000002	0.009	**6.90**	0.0020117	**6.92**	0.29
74	**RJ11A7-12c**	0.0020132	0.0000002	0.011	**6.02**	0.0020117	**6.04**	0.29
75	**RJ11A7-12r**	0.0020135	0.0000002	0.009	**6.14**	0.0020117	**6.17**	0.29
81	**RJ11A7-7**	0.0020128	0.0000002	0.009	**5.83**	0.0020117	**5.86**	0.29
82	**RJ11A7-10c**	0.0020126	0.0000002	0.010	**5.69**	0.0020117	**5.72**	0.29
83	**RJ11A7-10r**	0.0020129	0.0000002	0.012	**5.84**	0.0020117	**5.88**	0.29
84	**RJ11A7-13**	0.0020132	0.0000002	0.008	**6.02**	0.0020117	**6.05**	0.29
85	**RJ11A7-14**	0.0020155	0.0000002	0.010	**7.16**	0.0020117	**7.20**	0.29
86	**RJ11A7-15a**	0.0020126	0.0000002	0.008	**5.72**	0.0020117	**5.76**	0.29
87	**RJ11A7-15b**	0.0020126	0.0000002	0.011	**5.68**	0.0020117	**5.72**	0.29
88	**RJ11A7-21**	0.0020122	0.0000003	0.013	**5.53**	0.0020117	**5.57**	0.29
89	**RJ11A7-22**	0.0020142	0.0000002	0.009	**6.52**	0.0020117	**6.56**	0.29
90	**RJ11A7-28c**	0.0020146	0.0000002	0.009	**6.72**	0.0020117	**6.76**	0.29
91	**RJ11A7-31c**	0.0020121	0.0000002	0.010	**5.47**	0.0020117	**5.51**	0.29
92	**RJ11A7-31r**	0.0020124	0.0000002	0.008	**5.61**	0.0020117	**5.65**	0.29
93	**RJ11A10-2**	0.0020152	0.0000002	0.008	**7.01**	0.0020117	**7.05**	0.29
94	**RJ11A10-13c**	0.0020156	0.0000002	0.009	**7.21**	0.0020117	**7.25**	0.29
95	**RJ11A10-13r**	0.0020147	0.0000002	0.012	**6.76**	0.0020117	**6.80**	0.29
101	**RJ11A10-28**	0.0020151	0.0000002	0.010	**6.98**	0.0020117	**7.02**	0.29
102	**RJ11A10-26**	0.0020144	0.0000003	0.014	**6.60**	0.0020117	**6.65**	0.29
103	**RJ11A10-22**	0.0020148	0.0000001	0.007	**6.81**	0.0020117	**6.86**	0.29
104	**RJ11A10-21**	0.0020157	0.0000002	0.008	**7.25**	0.0020117	**7.30**	0.29

105	**RJ11A10-17**	0.0020146	0.0000003	0.015	**6.70**	0.0020117	**6.75**	0.29
106	**RJ11A10-14c**	0.0020144	0.0000002	0.011	**6.59**	0.0020117	**6.64**	0.29
107	**RJ11A10-14r**	0.0020138	0.0000003	0.014	**6.32**	0.0020117	**6.37**	0.29
108	**RJ11A10-11**	0.0020134	0.0000002	0.009	**6.12**	0.0020117	**6.17**	0.29
109	**RJ11A10-9c**	0.0020149	0.0000003	0.015	**6.87**	0.0020117	**6.93**	0.29
110	**RJ11A10-9r**	0.0020143	0.0000003	0.013	**6.56**	0.0020117	**6.61**	0.29
111	**RJ11A11-23**	0.0020146	0.0000002	0.011	**6.72**	0.0020117	**6.78**	0.29
112	**RJ11A11-22a**	0.0020147	0.0000002	0.008	**6.78**	0.0020117	**6.83**	0.29
113	**RJ11A11-22b**	0.0020150	0.0000002	0.010	**6.92**	0.0020117	**6.97**	0.29
114	**RJ11A11-15**	0.0020150	0.0000003	0.013	**6.89**	0.0020117	**6.95**	0.29
115	**RJ11A11-14**	0.0020139	0.0000002	0.010	**6.36**	0.0020117	**6.42**	0.29

Analytical Session 7 (24.01.12)

Analytical order	Sample-grain(c/r)	$^{18}O/^{16}O$ measured	1σ	% Std Err (1σ)	$\delta^{18}O_{(VSMOW)}$	Drift correction factor	$\delta^{18}O_{(VSMOW)}$ (drift corrected)	Analytical uncertainty (±)
1	**Laura**	0.0020140	0.0000002	0.008	**5.39**	0.0020143	**5.17**	
2	**Laura**	0.0020144	0.0000001	0.006	**5.58**	0.0020143	**5.36**	
3	**Laura**	0.0020141	0.0000002	0.009	**5.44**	0.0020143	**5.23**	
4	**Laura**	0.0020150	0.0000002	0.010	**5.85**	0.0020143	**5.65**	
5	**Laura**	0.0020140	0.0000001	0.006	**5.36**	0.0020143	**5.16**	
6	**Laura**	0.0020140	0.0000002	0.010	**5.37**	0.0020142	**5.17**	
7	**Laura**	0.0020145	0.0000003	0.012	**5.62**	0.0020142	**5.43**	
8	**Laura**	0.0020142	0.0000002	0.008	**5.46**	0.0020142	**5.28**	
9	**Laura**	0.0020141	0.0000001	0.007	**5.42**	0.0020142	**5.24**	
10	**Laura**	0.0020145	0.0000002	0.009	**5.64**	0.0020142	**5.46**	
21	**Laura**	0.0020143	0.0000001	0.007	**5.54**	0.0020141	**5.41**	
22	**Laura**	0.0020136	0.0000001	0.004	**5.19**	0.0020141	**5.07**	
23	**Laura**	0.0020144	0.0000002	0.010	**5.55**	0.0020141	**5.44**	
24	**Laura**	0.0020141	0.0000002	0.008	**5.43**	0.0020141	**5.32**	
25	**Laura**	0.0020144	0.0000001	0.007	**5.59**	0.0020141	**5.49**	
41	**Laura**	0.0020137	0.0000001	0.007	**5.22**	0.0020139	**5.20**	
42	**Laura**	0.0020139	0.0000001	0.006	**5.33**	0.0020139	**5.31**	
43	**Laura**	0.0020137	0.0000001	0.007	**5.23**	0.0020139	**5.21**	
44	**Laura**	0.0020135	0.0000002	0.009	**5.13**	0.0020139	**5.11**	
45	**Laura**	0.0020137	0.0000002	0.012	**5.25**	0.0020139	**5.24**	
61	**Laura**	0.0020141	0.0000002	0.009	**5.43**	0.0020137	**5.50**	
62	**Laura**	0.0020134	0.0000002	0.008	**5.07**	0.0020137	**5.15**	
63	**Laura**	0.0020136	0.0000002	0.010	**5.18**	0.0020137	**5.26**	
64	**Laura**	0.0020133	0.0000002	0.008	**5.02**	0.0020137	**5.10**	
65	**Laura**	0.0020137	0.0000002	0.009	**5.21**	0.0020137	**5.30**	
81	**Laura**	0.0020138	0.0000002	0.011	**5.28**	0.0020135	**5.45**	
82	**Laura**	0.0020134	0.0000001	0.006	**5.05**	0.0020135	**5.22**	
83	**Laura**	0.0020133	0.0000002	0.009	**5.02**	0.0020135	**5.19**	
84	**Laura**	0.0020137	0.0000001	0.007	**5.24**	0.0020135	**5.42**	
85	**Laura**	0.0020133	0.0000002	0.009	**5.02**	0.0020135	**5.21**	
101	**Laura**	0.0020136	0.0000002	0.010	**5.16**	0.0020133	**5.42**	
102	**Laura**	0.0020137	0.0000003	0.014	**5.22**	0.0020133	**5.49**	
103	**Laura**	0.0020131	0.0000002	0.012	**4.95**	0.0020133	**5.22**	
104	**Laura**	0.0020134	0.0000002	0.010	**5.09**	0.0020133	**5.37**	
105	**Laura**	0.0020132	0.0000002	0.010	**4.97**	0.0020133	**5.26**	

Average		0.0020139			**5.30**		**5.30**	
1σ		0.0000004			**0.22**		**0.14**	
2σ		0.0000009			**0.44**		**0.27**	
SEM		0.0000001			**0.07**		**0.05**	
n		35			**35**		**35**	
Unknowns								
11	**RJ11A11-12**	0.0020184	0.0000001	0.007	**7.56**	0.0020142	**7.39**	0.27
12	**RJ11A11-11**	0.0020179	0.0000001	0.007	**7.32**	0.0020142	**7.15**	0.27
13	**RJ11A11-9**	0.0020179	0.0000002	0.009	**7.32**	0.0020142	**7.16**	0.27
14	**RJ11A11-13**	0.0020181	0.0000001	0.005	**7.42**	0.0020142	**7.26**	0.27
15	**RJ11A11-28**	0.0020171	0.0000002	0.010	**6.93**	0.0020142	**6.77**	0.27
16	**PC14-8**	0.0020170	0.0000002	0.009	**6.89**	0.0020141	**6.74**	0.27
17	**PC14-7r**	0.0020166	0.0000002	0.008	**6.68**	0.0020141	**6.53**	0.27
18	**PC14-6c**	0.0020168	0.0000001	0.006	**6.79**	0.0020141	**6.65**	0.27
19	**PC14-6r**	0.0020164	0.0000001	0.006	**6.57**	0.0020141	**6.44**	0.27
20	**PC14-5**	0.0020166	0.0000002	0.008	**6.69**	0.0020141	**6.56**	0.27
26	**PC14-4**	0.0020167	0.0000001	0.007	**6.70**	0.0020140	**6.60**	0.27
27	**PC14-3**	0.0020157	0.0000001	0.007	**6.24**	0.0020140	**6.15**	0.27
28	**PC14-1**	0.0020163	0.0000002	0.009	**6.54**	0.0020140	**6.45**	0.27
29	**SP80-1a**	0.0020148	0.0000002	0.010	**5.79**	0.0020140	**5.71**	0.27
30	**SP80-1b**	0.0020144	0.0000002	0.010	**5.59**	0.0020140	**5.51**	0.27
31	**SP80-2**	0.0020145	0.0000002	0.009	**5.60**	0.0020140	**5.53**	0.27
32	**SP80-3**	0.0020145	0.0000001	0.006	**5.62**	0.0020140	**5.55**	0.27
33	**SP80-4**	0.0020145	0.0000002	0.008	**5.60**	0.0020140	**5.54**	0.27
34	**SP80-5**	0.0020148	0.0000001	0.007	**5.79**	0.0020140	**5.73**	0.27
35	**SP80-10**	0.0020145	0.0000002	0.010	**5.61**	0.0020140	**5.56**	0.27
36	**SP80-8**	0.0020151	0.0000002	0.010	**5.93**	0.0020140	**5.88**	0.27
37	**RJ11A14-25**	0.0020174	0.0000002	0.008	**7.09**	0.0020139	**7.05**	0.27
38	**RJ11A14-23**	0.0020180	0.0000002	0.010	**7.36**	0.0020139	**7.32**	0.27
39	**RJ11A14-20**	0.0020176	0.0000002	0.010	**7.20**	0.0020139	**7.16**	0.27
40	**RJ11A14-18c**	0.0020177	0.0000002	0.009	**7.24**	0.0020139	**7.21**	0.27
46	**RJ11A14-18r**	0.0020169	0.0000001	0.007	**6.85**	0.0020139	**6.84**	0.27
47	**RJ11A14-17c**	0.0020170	0.0000002	0.010	**6.88**	0.0020138	**6.89**	0.27
48	**RJ11A14-17r**	0.0020173	0.0000002	0.008	**7.03**	0.0020138	**7.03**	0.27
49	**RJ11A14-16**	0.0020180	0.0000002	0.009	**7.38**	0.0020138	**7.39**	0.27
50	**RJ11A14-15**	0.0020168	0.0000002	0.011	**6.79**	0.0020138	**6.81**	0.27
51	**RJ11A14-14**	0.0020170	0.0000001	0.007	**6.88**	0.0020138	**6.90**	0.27
52	**RJ11A14-10**	0.0020179	0.0000002	0.012	**7.34**	0.0020138	**7.36**	0.27
53	**RJ11A14-7**	0.0020179	0.0000002	0.008	**7.31**	0.0020138	**7.34**	0.27
54	**MQ153-1**	0.0020135	0.0000002	0.009	**5.14**	0.0020138	**5.17**	0.27
55	**MQ153-2**	0.0020142	0.0000002	0.009	**5.46**	0.0020138	**5.50**	0.27
56	**MQ153-3c**	0.0020145	0.0000002	0.008	**5.60**	0.0020138	**5.65**	0.27
57	**MQ153-4c**	0.0020161	0.0000001	0.007	**6.42**	0.0020138	**6.47**	0.27
58	**MQ153-4r**	0.0020148	0.0000002	0.011	**5.75**	0.0020137	**5.80**	0.27
59	**MQ153-5**	0.0020151	0.0000002	0.011	**5.93**	0.0020137	**5.99**	0.27
60	**MQ153-6**	0.0020153	0.0000002	0.007	**6.00**	0.0020137	**6.07**	0.27
66	**MQ153-8**	0.0020136	0.0000002	0.010	**5.17**	0.0020137	**5.26**	0.27
67	**MQ153-9**	0.0020141	0.0000002	0.011	**5.45**	0.0020137	**5.55**	0.27
68	**MQ153-12**	0.0020142	0.0000002	0.008	**5.49**	0.0020136	**5.59**	0.27
69	**MQ153-16**	0.0020142	0.0000002	0.009	**5.49**	0.0020136	**5.60**	0.27

70	**1026-19c**	0.0020142	0.0000002	0.009	**5.46**	0.0020136	**5.57**	0.27
71	**1026-19r**	0.0020138	0.0000002	0.009	**5.27**	0.0020136	**5.39**	0.27
72	**1026-18**	0.0020139	0.0000002	0.008	**5.35**	0.0020136	**5.47**	0.27
73	**1026-16a**	0.0020141	0.0000002	0.010	**5.40**	0.0020136	**5.53**	0.27
74	**1026-16b**	0.0020141	0.0000002	0.008	**5.42**	0.0020136	**5.55**	0.27
75	**1026-14**	0.0020144	0.0000002	0.012	**5.56**	0.0020136	**5.70**	0.27
76	**1026-11**	0.0020141	0.0000002	0.010	**5.43**	0.0020136	**5.57**	0.27
77	**1026-10**	0.0020142	0.0000002	0.008	**5.49**	0.0020136	**5.64**	0.27
78	**1026-9**	0.0020138	0.0000002	0.009	**5.28**	0.0020135	**5.43**	0.27
79	**1026-5**	0.0020144	0.0000002	0.008	**5.58**	0.0020135	**5.74**	0.27
80	**1026-4**	0.0020142	0.0000002	0.010	**5.47**	0.0020135	**5.63**	0.27
86	**RJ11A15-24c**	0.0020175	0.0000001	0.007	**7.13**	0.0020135	**7.32**	0.27
87	**RJ11A15-24r**	0.0020156	0.0000002	0.009	**6.17**	0.0020135	**6.37**	0.27
88	**RJ11A15-22**	0.0020149	0.0000002	0.009	**5.85**	0.0020135	**6.05**	0.27
89	**RJ11A15-19**	0.0020159	0.0000002	0.010	**6.33**	0.0020134	**6.54**	0.27
90	**RJ11A15-16**	0.0020132	0.0000001	0.007	**4.99**	0.0020134	**5.20**	0.27
91	**RJ11A15-15c**	0.0020153	0.0000002	0.010	**6.04**	0.0020134	**6.25**	0.27
92	**RJ11A15-15r**	0.0020152	0.0000002	0.009	**6.00**	0.0020134	**6.21**	0.27
93	**RJ11A15-14c**	0.0020155	0.0000002	0.009	**6.11**	0.0020134	**6.33**	0.27
94	**RJ11A15-14r**	0.0020158	0.0000002	0.010	**6.30**	0.0020134	**6.52**	0.27
95	**RJ11A15-11**	0.0020151	0.0000001	0.007	**5.94**	0.0020134	**6.17**	0.27
96	**RJ11A15-10**	0.0020171	0.0000001	0.007	**6.90**	0.0020134	**7.14**	0.27
97	**RJ11A15-7**	0.0020153	0.0000002	0.010	**6.01**	0.0020134	**6.25**	0.27
98	**RJ11A15-5a**	0.0020154	0.0000003	0.013	**6.06**	0.0020134	**6.30**	0.27
99	**RJ11A15-5b**	0.0020159	0.0000002	0.010	**6.33**	0.0020133	**6.58**	0.27
100	**RJ11A17-16**	0.0020169	0.0000002	0.010	**6.83**	0.0020133	**7.09**	0.27

Analytical Session 8 (25.01.12)

Analytical order	Sample-grain(c/r)	$^{18}O/^{16}O$ measured	1σ	% Std Err (1σ)	$\delta^{18}O_{(VSMOW)}$	Drift correction factor	$\delta^{18}O_{(VSMOW)}$ (drift corrected)	Analytical uncertainty (±)
11	**Laura**	0.0020110	0.0000002	0.008	**5.63**	0.0020109	**5.38**	
12	**Laura**	0.0020108	0.0000002	0.009	**5.54**	0.0020108	**5.30**	
13	**Laura**	0.0020111	0.0000002	0.008	**5.66**	0.0020108	**5.43**	
14	**Laura**	0.0020107	0.0000001	0.007	**5.45**	0.0020108	**5.22**	
15	**Laura**	0.0020112	0.0000002	0.007	**5.71**	0.0020108	**5.49**	
26	**Laura**	0.0020106	0.0000002	0.008	**5.42**	0.0020106	**5.28**	
27	**Laura**	0.0020110	0.0000002	0.009	**5.60**	0.0020106	**5.47**	
28	**Laura**	0.0020107	0.0000002	0.010	**5.46**	0.0020106	**5.34**	
29	**Laura**	0.0020104	0.0000002	0.010	**5.31**	0.0020106	**5.20**	
30	**Laura**	0.0020108	0.0000001	0.006	**5.50**	0.0020106	**5.39**	
46	**Laura**	0.0020104	0.0000002	0.009	**5.34**	0.0020103	**5.35**	
47	**Laura**	0.0020102	0.0000001	0.006	**5.21**	0.0020103	**5.23**	
48	**Laura**	0.0020097	0.0000002	0.008	**4.95**	0.0020103	**4.98**	
49	**Laura**	0.0020100	0.0000002	0.009	**5.14**	0.0020103	**5.18**	
50	**Laura**	0.0020101	0.0000002	0.009	**5.17**	0.0020103	**5.21**	
66	**Laura**	0.0020096	0.0000001	0.007	**4.90**	0.0020100	**5.07**	
67	**Laura**	0.0020096	0.0000002	0.011	**4.90**	0.0020100	**5.08**	
68	**Laura**	0.0020096	0.0000002	0.009	**4.92**	0.0020100	**5.11**	
69	**Laura**	0.0020100	0.0000002	0.008	**5.11**	0.0020100	**5.30**	
70	**Laura**	0.0020099	0.0000002	0.009	**5.08**	0.0020100	**5.28**	

86	**Laura**	0.0020101	0.0000002	0.010	**5.16**	0.0020097	**5.48**	
87	**Laura**	0.0020097	0.0000002	0.008	**4.99**	0.0020097	**5.32**	
88	**Laura**	0.0020104	0.0000002	0.008	**5.31**	0.0020097	**5.65**	
89	**Laura**	0.0020097	0.0000001	0.007	**4.99**	0.0020097	**5.33**	
90	**Laura**	0.0020099	0.0000002	0.008	**5.07**	0.0020097	**5.42**	
Average		0.0020103			**5.26**		**5.30**	
1σ		0.0000005			**0.26**		**0.15**	
2σ		0.0000010			**0.52**		**0.30**	
SEM		0.0000002			**0.10**		**0.06**	
n		25			**25**		**25**	
Unknowns								
16	**RJ11A17-3**	0.0020135	0.0000002	0.011	**6.88**	0.0020108	**6.67**	0.30
17	**RJ11A17-7**	0.0020174	0.0000001	0.007	**8.84**	0.0020108	**8.63**	0.30
18	**RJ11A17-9c**	0.0020163	0.0000002	0.009	**8.26**	0.0020108	**8.06**	0.30
19	**RJ11A17-9r**	0.0020146	0.0000002	0.008	**7.40**	0.0020107	**7.21**	0.30
20	**RJ11A17-11**	0.0020131	0.0000002	0.010	**6.69**	0.0020107	**6.50**	0.30
21	**RJ11A17-12**	0.0020124	0.0000002	0.010	**6.31**	0.0020107	**6.13**	0.30
22	**RJ11A17-8**	0.0020127	0.0000002	0.008	**6.46**	0.0020107	**6.29**	0.30
23	**RJ11A17-14**	0.0020140	0.0000002	0.011	**7.11**	0.0020107	**6.95**	0.30
24	**RJ11A17-17c**	0.0020122	0.0000001	0.007	**6.20**	0.0020107	**6.05**	0.30
25	**RJ11A17-17r**	0.0020117	0.0000002	0.010	**5.97**	0.0020106	**5.83**	0.30
31	**RJ11A18-4**	0.0020123	0.0000002	0.010	**6.25**	0.0020106	**6.15**	0.30
32	**RJ11A18-7**	0.0020119	0.0000001	0.007	**6.06**	0.0020105	**5.97**	0.30
33	**RJ11A18-9c**	0.0020120	0.0000003	0.012	**6.12**	0.0020105	**6.04**	0.30
34	**RJ11A18-9r**	0.0020118	0.0000001	0.007	**6.00**	0.0020105	**5.93**	0.30
35	**RJ11A18-10**	0.0020117	0.0000002	0.008	**5.97**	0.0020105	**5.90**	0.30
36	**RJ11A18-11**	0.0020121	0.0000002	0.011	**6.15**	0.0020105	**6.09**	0.30
37	**RJ11A18-13c**	0.0020120	0.0000002	0.008	**6.11**	0.0020105	**6.06**	0.30
38	**RJ11A18-13r**	0.0020121	0.0000002	0.009	**6.19**	0.0020104	**6.14**	0.30
39	**RJ11A18-14a**	0.0020118	0.0000002	0.009	**6.04**	0.0020104	**6.01**	0.30
40	**RJ11A18-14b**	0.0020116	0.0000002	0.011	**5.91**	0.0020104	**5.88**	0.30
41	**RJ11A18-19**	0.0020123	0.0000001	0.007	**6.28**	0.0020104	**6.26**	0.30
42	**RJ11A18-26**	0.0020122	0.0000002	0.008	**6.24**	0.0020104	**6.23**	0.30
43	**RJ11A18-29**	0.0020123	0.0000002	0.010	**6.28**	0.0020104	**6.27**	0.30
44	**Z27-4**	0.0020098	0.0000001	0.007	**5.04**	0.0020104	**5.05**	0.30
45	**Z27-7**	0.0020104	0.0000002	0.008	**5.31**	0.0020103	**5.32**	0.30
51	**Z27-11**	0.0020105	0.0000001	0.007	**5.36**	0.0020102	**5.42**	0.30
52	**Z27-13c**	0.0020096	0.0000002	0.011	**4.93**	0.0020102	**4.99**	0.30
53	**Z27-13r**	0.0020093	0.0000002	0.011	**4.79**	0.0020102	**4.86**	0.30
54	**Z27-14**	0.0020088	0.0000002	0.011	**4.53**	0.0020102	**4.61**	0.30
55	**Z27-15**	0.0020091	0.0000002	0.008	**4.69**	0.0020102	**4.77**	0.30
56	**Z27-17**	0.0020097	0.0000002	0.011	**4.96**	0.0020102	**5.05**	0.30
57	**Z27-18**	0.0020092	0.0000003	0.013	**4.74**	0.0020102	**4.84**	0.30
58	**Z27-22**	0.0020087	0.0000002	0.008	**4.48**	0.0020101	**4.59**	0.30
59	**Z27-16**	0.0020095	0.0000001	0.007	**4.85**	0.0020101	**4.96**	0.30
60	**MQ33-4c**	0.0020105	0.0000002	0.008	**5.36**	0.0020101	**5.49**	0.30
61	**MQ33-4r**	0.0020099	0.0000002	0.008	**5.07**	0.0020101	**5.20**	0.30
62	**MQ33-7**	0.0020100	0.0000002	0.011	**5.15**	0.0020101	**5.28**	0.30
63	**MQ33-8**	0.0020099	0.0000002	0.011	**5.07**	0.0020101	**5.21**	0.30
64	**MQ33-9**	0.0020112	0.0000002	0.011	**5.70**	0.0020101	**5.86**	0.30

65	**MQ33-10r**	0.0020095	0.0000002	0.009	**4.85**	0.0020100	**5.01**	0.30
71	**MQ33-10c**	0.0020112	0.0000003	0.015	**5.72**	0.0020099	**5.93**	0.30
72	**MQ33-11c**	0.0020105	0.0000003	0.015	**5.37**	0.0020099	**5.59**	0.30
73	**MQ33-11r**	0.0020107	0.0000002	0.009	**5.47**	0.0020099	**5.69**	0.30
74	**MQ33-11ad.**	0.0020101	0.0000001	0.007	**5.16**	0.0020099	**5.39**	0.30
75	**MQ33-12**	0.0020099	0.0000003	0.013	**5.07**	0.0020099	**5.30**	0.30
76	**MQ33-14c**	0.0020092	0.0000003	0.013	**4.71**	0.0020099	**4.96**	0.30
77	**MQ33-15**	0.0020105	0.0000002	0.010	**5.36**	0.0020099	**5.61**	0.30
78	**MQ33-17**	0.0020137	0.0000002	0.008	**6.99**	0.0020098	**7.25**	0.30
79	**MQ33-19**	0.0020109	0.0000002	0.011	**5.55**	0.0020098	**5.82**	0.30
80	**RJ11A17-1**	0.0020112	0.0000002	0.012	**5.70**	0.0020098	**5.98**	0.30
81	**RJ11A17-6**	0.0020117	0.0000003	0.014	**5.98**	0.0020098	**6.27**	0.30
82	**RJ11A17-10r**	0.0020120	0.0000002	0.010	**6.14**	0.0020098	**6.43**	0.30
83	**RJ11A17-10c**	0.0020125	0.0000002	0.009	**6.37**	0.0020098	**6.66**	0.30
84	**RJ11A17-13**	0.0020114	0.0000002	0.007	**5.83**	0.0020097	**6.14**	0.30
85	**RJ11A17-18**	0.0020103	0.0000002	0.008	**5.27**	0.0020097	**5.59**	0.30

Analytical Session 9 (26.01.12)

Analytical order	**Sample-grain(c/r)**	**$^{18}O/^{16}O$ measured**	**1σ**	**% Std Err (1σ)**	**$\delta^{18}O_{(VSMOW)}$**	**Drift correction factor**	**$\delta^{18}O_{(VSMOW)}$ (drift corrected)**	**Analytical uncertainty (±)**
1	**Laura**	0.0020141	0.0000001	0.006	**5.75**	0.0020139	**5.41**	
2	**Laura**	0.0020143	0.0000001	0.006	**5.84**	0.0020139	**5.51**	
3	**Laura**	0.0020139	0.0000002	0.007	**5.67**	0.0020139	**5.34**	
4	**Laura**	0.0020139	0.0000002	0.009	**5.65**	0.0020138	**5.33**	
5	**Laura**	0.0020137	0.0000001	0.005	**5.55**	0.0020138	**5.24**	
6	**Laura**	0.0020141	0.0000002	0.008	**5.74**	0.0020138	**5.43**	
7	**Laura**	0.0020142	0.0000002	0.007	**5.81**	0.0020138	**5.51**	
8	**Laura**	0.0020143	0.0000001	0.006	**5.82**	0.0020138	**5.53**	
9	**Laura**	0.0020140	0.0000001	0.006	**5.70**	0.0020138	**5.41**	
10	**Laura**	0.0020137	0.0000002	0.008	**5.57**	0.0020138	**5.29**	
21	**Laura**	0.0020131	0.0000001	0.007	**5.23**	0.0020136	**5.01**	
22	**Laura**	0.0020138	0.0000002	0.008	**5.61**	0.0020136	**5.40**	
23	**Laura**	0.0020134	0.0000002	0.007	**5.39**	0.0020136	**5.19**	
24	**Laura**	0.0020137	0.0000001	0.006	**5.54**	0.0020136	**5.34**	
25	**Laura**	0.0020132	0.0000001	0.007	**5.31**	0.0020136	**5.12**	
41	**Laura**	0.0020135	0.0000001	0.007	**5.42**	0.0020134	**5.33**	
42	**Laura**	0.0020133	0.0000002	0.008	**5.35**	0.0020134	**5.26**	
43	**Laura**	0.0020129	0.0000002	0.009	**5.12**	0.0020134	**5.04**	
44	**Laura**	0.0020131	0.0000002	0.008	**5.23**	0.0020134	**5.16**	
45	**Laura**	0.0020132	0.0000001	0.007	**5.32**	0.0020133	**5.25**	
61	**Laura**	0.0020131	0.0000002	0.008	**5.25**	0.0020131	**5.28**	
62	**Laura**	0.0020128	0.0000001	0.007	**5.10**	0.0020131	**5.14**	
63	**Laura**	0.0020124	0.0000002	0.008	**4.91**	0.0020131	**4.95**	
64	**Laura**	0.0020127	0.0000001	0.006	**5.05**	0.0020131	**5.10**	
65	**Laura**	0.0020130	0.0000002	0.009	**5.21**	0.0020131	**5.26**	
81	**Laura**	0.0020132	0.0000001	0.006	**5.28**	0.0020129	**5.43**	
82	**Laura**	0.0020128	0.0000002	0.009	**5.10**	0.0020129	**5.26**	
83	**Laura**	0.0020131	0.0000002	0.010	**5.26**	0.0020129	**5.42**	
84	**Laura**	0.0020129	0.0000002	0.008	**5.16**	0.0020129	**5.33**	
85	**Laura**	0.0020129	0.0000001	0.004	**5.15**	0.0020129	**5.32**	

101	**Laura**	0.0020127	0.0000002	0.008	**5.05**	0.0020127	**5.32**	
102	**Laura**	0.0020125	0.0000002	0.009	**4.96**	0.0020126	**5.24**	
103	**Laura**	0.0020128	0.0000001	0.007	**5.09**	0.0020126	**5.38**	
104	**Laura**	0.0020125	0.0000002	0.008	**4.94**	0.0020126	**5.23**	
105	**Laura**	0.0020121	0.0000001	0.007	**4.77**	0.0020126	**5.07**	
121	**Laura**	0.0020129	0.0000002	0.009	**5.13**	0.0020124	**5.53**	
122	**Laura**	0.0020128	0.0000002	0.009	**5.08**	0.0020124	**5.49**	
123	**Laura**	0.0020126	0.0000001	0.006	**5.00**	0.0020124	**5.41**	
124	**Laura**	0.0020127	0.0000002	0.008	**5.04**	0.0020124	**5.45**	
125	**Laura**	0.0020123	0.0000002	0.011	**4.83**	0.0020124	**5.26**	
Average		0.0020132			**5.30**		**5.30**	
1σ		0.0000006			**0.30**		**0.15**	
2σ		0.0000012			**0.59**		**0.29**	
SEM		0.0000002			**0.09**		**0.05**	
n		40			**40**		**40**	
Unknowns								
11	**RF64-18**	0.0020126	0.0000001	0.004	**4.99**	0.0020138	**4.71**	0.29
12	**RF64-17**	0.0020132	0.0000002	0.009	**5.28**	0.0020137	**5.01**	0.29
13	**RF64-13**	0.0020129	0.0000002	0.010	**5.13**	0.0020137	**4.86**	0.29
14	**RF64-10**	0.0020129	0.0000001	0.007	**5.15**	0.0020137	**4.90**	0.29
15	**RF64-5**	0.0020129	0.0000001	0.006	**5.17**	0.0020137	**4.92**	0.29
16	**RF64-26**	0.0020166	0.0000002	0.008	**7.00**	0.0020137	**6.75**	0.29
17	**RF64-24**	0.0020132	0.0000001	0.006	**5.31**	0.0020137	**5.07**	0.29
18	**RF64-23**	0.0020126	0.0000001	0.007	**4.99**	0.0020137	**4.75**	0.29
19	**RF64-21**	0.0020132	0.0000001	0.007	**5.31**	0.0020137	**5.09**	0.29
20	**RF64-19**	0.0020122	0.0000002	0.009	**4.79**	0.0020136	**4.57**	0.29
26	**RJ11A20-10**	0.0020153	0.0000002	0.009	**6.34**	0.0020136	**6.16**	0.29
27	**RJ11A20-12**	0.0020159	0.0000002	0.008	**6.64**	0.0020136	**6.46**	0.29
28	**RJ11A20-14c**	0.0020158	0.0000002	0.009	**6.60**	0.0020135	**6.42**	0.29
29	**RJ11A20-14r**	0.0020156	0.0000001	0.006	**6.48**	0.0020135	**6.32**	0.29
30	**RJ11A20-15**	0.0020163	0.0000002	0.010	**6.84**	0.0020135	**6.68**	0.29
31	**RJ11A20-17**	0.0020157	0.0000001	0.006	**6.56**	0.0020135	**6.41**	0.29
32	**RJ11A20-18a**	0.0020161	0.0000002	0.012	**6.72**	0.0020135	**6.58**	0.29
33	**RJ11A20-18b**	0.0020157	0.0000002	0.008	**6.57**	0.0020135	**6.43**	0.29
34	**RJ11A20-20**	0.0020139	0.0000001	0.007	**5.67**	0.0020135	**5.53**	0.29
35	**RJ11A20-24**	0.0020156	0.0000002	0.008	**6.51**	0.0020135	**6.38**	0.29
36	**RJ11A20-35**	0.0020143	0.0000001	0.006	**5.87**	0.0020135	**5.75**	0.29
37	**RJ11A20-19**	0.0020172	0.0000002	0.008	**7.28**	0.0020134	**7.16**	0.29
38	**PC14-22**	0.0020151	0.0000002	0.008	**6.24**	0.0020134	**6.13**	0.29
39	**PC14-23**	0.0020151	0.0000002	0.008	**6.23**	0.0020134	**6.13**	0.29
40	**PC14-26**	0.0020154	0.0000001	0.005	**6.40**	0.0020134	**6.30**	0.29
46	**PC14-27**	0.0020151	0.0000002	0.010	**6.24**	0.0020133	**6.18**	0.29
47	**PC14-30**	0.0020150	0.0000002	0.009	**6.20**	0.0020133	**6.14**	0.29
48	**PC14-20c**	0.0020151	0.0000002	0.008	**6.26**	0.0020133	**6.21**	0.29
49	**MQ39-13**	0.0020125	0.0000002	0.011	**4.97**	0.0020133	**4.92**	0.29
50	**MQ39-21**	0.0020119	0.0000002	0.010	**4.63**	0.0020133	**4.59**	0.29
51	**MQ39-22**	0.0020129	0.0000001	0.007	**5.16**	0.0020133	**5.12**	0.29
52	**MQ39-23c**	0.0020147	0.0000002	0.008	**6.07**	0.0020133	**6.04**	0.29
53	**MQ39-23r**	0.0020149	0.0000001	0.007	**6.14**	0.0020132	**6.12**	0.29
54	**MQ39-24**	0.0020125	0.0000002	0.009	**4.95**	0.0020132	**4.93**	0.29

55	**MQ39-28**	0.0020121	0.0000002	0.007	**4.76**	0.0020132	**4.75**	0.29
56	**MQ39-30**	0.0020121	0.0000002	0.009	**4.74**	0.0020132	**4.73**	0.29
57	**MQ39-31**	0.0020159	0.0000002	0.009	**6.67**	0.0020132	**6.67**	0.29
58	**MQ39-26**	0.0020124	0.0000002	0.008	**4.90**	0.0020132	**4.91**	0.29
59	**SP80-14**	0.0020122	0.0000002	0.011	**4.82**	0.0020132	**4.84**	0.29
60	**MQ153-20**	0.0020123	0.0000002	0.008	**4.86**	0.0020132	**4.89**	0.29
66	**RF62-6**	0.0020126	0.0000002	0.011	**5.00**	0.0020131	**5.06**	0.29
67	**RF62-8**	0.0020128	0.0000002	0.010	**5.11**	0.0020131	**5.18**	0.29
68	**RF62-9**	0.0020122	0.0000002	0.008	**4.79**	0.0020131	**4.86**	0.29
69	**RF62-10**	0.0020129	0.0000002	0.009	**5.16**	0.0020130	**5.24**	0.29
70	**RF62-11**	0.0020128	0.0000002	0.008	**5.08**	0.0020130	**5.17**	0.29
71	**RF62-12**	0.0020132	0.0000001	0.006	**5.28**	0.0020130	**5.37**	0.29
72	**RF62-14**	0.0020129	0.0000002	0.010	**5.13**	0.0020130	**5.22**	0.29
73	**RF62-15**	0.0020129	0.0000001	0.007	**5.16**	0.0020130	**5.26**	0.29
74	**RF62-18**	0.0020124	0.0000002	0.010	**4.91**	0.0020130	**5.02**	0.29
75	**RF62-21**	0.0020120	0.0000001	0.007	**4.71**	0.0020130	**4.83**	0.29
76	**RF62-22**	0.0020126	0.0000002	0.009	**4.98**	0.0020130	**5.10**	0.29
77	**ZN122-15**	0.0020137	0.0000001	0.007	**5.53**	0.0020129	**5.65**	0.29
78	**ZN122-17**	0.0020135	0.0000002	0.008	**5.43**	0.0020129	**5.57**	0.29
79	**ZN122-18c**	0.0020138	0.0000002	0.010	**5.60**	0.0020129	**5.74**	0.29
80	**ZN122-18r**	0.0020137	0.0000002	0.009	**5.54**	0.0020129	**5.69**	0.29
86	**ZN122-19**	0.0020129	0.0000001	0.007	**5.15**	0.0020128	**5.34**	0.29
87	**ZN122-22**	0.0020130	0.0000002	0.012	**5.18**	0.0020128	**5.37**	0.29
88	**ZN122-25**	0.0020127	0.0000002	0.012	**5.05**	0.0020128	**5.25**	0.29
89	**DI095-8c**	0.0020134	0.0000001	0.007	**5.41**	0.0020128	**5.61**	0.29
90	**DI095-8r**	0.0020122	0.0000002	0.010	**4.81**	0.0020128	**5.01**	0.29
91	**DI095-12**	0.0020134	0.0000002	0.011	**5.40**	0.0020128	**5.62**	0.29
92	**DI095-14i**	0.0020126	0.0000002	0.009	**5.01**	0.0020128	**5.23**	0.29
93	**DI095-14r**	0.0020124	0.0000003	0.013	**4.89**	0.0020128	**5.11**	0.29
94	**DI095-15c**	0.0020134	0.0000001	0.007	**5.38**	0.0020127	**5.61**	0.29
95	**DI095-15r**	0.0020132	0.0000002	0.011	**5.31**	0.0020127	**5.55**	0.29
96	**DI095-16c**	0.0020134	0.0000003	0.016	**5.41**	0.0020127	**5.65**	0.29
97	**DI095-17**	0.0020131	0.0000002	0.012	**5.24**	0.0020127	**5.49**	0.29
98	**DI095-20**	0.0020132	0.0000003	0.013	**5.29**	0.0020127	**5.54**	0.29
99	**DI095-21**	0.0020133	0.0000002	0.010	**5.33**	0.0020127	**5.59**	0.29
100	**DI095-18**	0.0020134	0.0000003	0.013	**5.38**	0.0020127	**5.64**	0.29
106	**DI095-13**	0.0020129	0.0000002	0.008	**5.16**	0.0020126	**5.47**	0.29
107	**DI095-24**	0.0020142	0.0000002	0.011	**5.78**	0.0020126	**6.09**	0.29
108	**Z27-35**	0.0020121	0.0000001	0.007	**4.75**	0.0020126	**5.07**	0.29
109	**Z27-34**	0.0020123	0.0000002	0.011	**4.87**	0.0020126	**5.19**	0.29
110	**Z27-33**	0.0020122	0.0000001	0.007	**4.78**	0.0020125	**5.11**	0.29
111	**Z27-32**	0.0020129	0.0000002	0.008	**5.13**	0.0020125	**5.47**	0.29
112	**MQ28-1**	0.0020150	0.0000002	0.010	**6.19**	0.0020125	**6.53**	0.29
113	**MQ28-3**	0.0020129	0.0000002	0.011	**5.14**	0.0020125	**5.49**	0.29
114	**RF65-2**	0.0020125	0.0000001	0.007	**4.93**	0.0020125	**5.28**	0.29
115	**RJ1101-42**	0.0020125	0.0000002	0.010	**4.95**	0.0020125	**5.31**	0.29
116	**RJ1101-33**	0.0020126	0.0000002	0.008	**5.01**	0.0020125	**5.38**	0.29
117	**RJ1101-34c**	0.0020130	0.0000002	0.011	**5.22**	0.0020125	**5.59**	0.29
118	**RJ1101-34r**	0.0020129	0.0000001	0.006	**5.17**	0.0020124	**5.54**	0.29
119	**RJ1104-36**	0.0020146	0.0000002	0.011	**5.99**	0.0020124	**6.38**	0.29
120	**RJ1104-33**	0.0020141	0.0000001	0.007	**5.75**	0.0020124	**6.15**	0.29

Analytical Session 10 (27.01.12)

Analytical order	Sample-grain(c/r)	$^{18}O/^{16}O$ measured	1σ	% Std Err (1σ)	$\delta^{18}O_{(VSMOW)}$	Drift correction factor	$\delta^{18}O_{(VSMOW)}$ (drift corrected)	Analytical uncertainty (±)
1	**Laura**	0.0020139	0.0000002	0.008	**5.30**	0.0020138	**5.33**	
2	**Laura**	0.0020138	0.0000001	0.006	**5.24**	0.0020138	**5.26**	
3	**Laura**	0.0020137	0.0000001	0.007	**5.19**	0.0020138	**5.22**	
4	**Laura**	0.0020142	0.0000001	0.006	**5.48**	0.0020138	**5.50**	
5	**Laura**	0.0020138	0.0000001	0.006	**5.25**	0.0020138	**5.27**	
6	**Laura**	0.0020137	0.0000002	0.009	**5.23**	0.0020138	**5.25**	
7	**Laura**	0.0020136	0.0000002	0.008	**5.18**	0.0020139	**5.20**	
8	**Laura**	0.0020135	0.0000002	0.010	**5.12**	0.0020139	**5.14**	
9	**Laura**	0.0020136	0.0000001	0.006	**5.17**	0.0020139	**5.19**	
10	**Laura**	0.0020141	0.0000002	0.008	**5.42**	0.0020139	**5.44**	
11	**Laura**	0.0020138	0.0000001	0.007	**5.25**	0.0020139	**5.26**	
12	**Laura**	0.0020136	0.0000002	0.012	**5.16**	0.0020139	**5.17**	
13	**Laura**	0.0020138	0.0000001	0.005	**5.24**	0.0020139	**5.25**	
14	**Laura**	0.0020144	0.0000002	0.008	**5.53**	0.0020139	**5.54**	
15	**Laura**	0.0020138	0.0000001	0.006	**5.28**	0.0020139	**5.29**	
16	**Laura**	0.0020140	0.0000002	0.008	**5.33**	0.0020139	**5.35**	
17	**Laura**	0.0020140	0.0000002	0.008	**5.36**	0.0020139	**5.37**	
18	**Laura**	0.0020138	0.0000002	0.009	**5.25**	0.0020139	**5.26**	
19	**Laura**	0.0020139	0.0000002	0.008	**5.30**	0.0020139	**5.31**	
20	**Laura**	0.0020138	0.0000001	0.007	**5.26**	0.0020139	**5.27**	
31	**Laura**	0.0020137	0.0000002	0.008	**5.23**	0.0020139	**5.23**	
32	**Laura**	0.0020139	0.0000001	0.005	**5.33**	0.0020139	**5.33**	
33	**Laura**	0.0020142	0.0000002	0.008	**5.48**	0.0020139	**5.48**	
34	**Laura**	0.0020141	0.0000002	0.008	**5.41**	0.0020139	**5.41**	
35	**Laura**	0.0020136	0.0000001	0.007	**5.15**	0.0020139	**5.15**	
46	**Laura**	0.0020142	0.0000001	0.007	**5.45**	0.0020139	**5.44**	
47	**Laura**	0.0020143	0.0000002	0.008	**5.49**	0.0020139	**5.48**	
48	**Laura**	0.0020140	0.0000002	0.008	**5.34**	0.0020139	**5.33**	
49	**Laura**	0.0020138	0.0000002	0.012	**5.26**	0.0020139	**5.25**	
50	**Laura**	0.0020140	0.0000001	0.007	**5.33**	0.0020139	**5.32**	
61	**Laura**	0.0020138	0.0000001	0.006	**5.26**	0.0020139	**5.24**	
62	**Laura**	0.0020141	0.0000002	0.008	**5.41**	0.0020139	**5.39**	
63	**Laura**	0.0020138	0.0000001	0.006	**5.23**	0.0020139	**5.21**	
64	**Laura**	0.0020135	0.0000001	0.006	**5.12**	0.0020139	**5.10**	
65	**Laura**	0.0020139	0.0000001	0.007	**5.31**	0.0020139	**5.29**	
Average		0.0020139			**5.30**		**5.30**	
1σ		0.0000002			**0.11**		**0.11**	
2σ		0.0000004			**0.22**		**0.22**	
SEM		0.0000001			**0.04**		**0.04**	
n		35			**35**		**35**	
Unknowns								
21	**RJ1103-33**	0.0020147	0.0000002	0.008	**5.71**	0.0020139	**5.72**	0.22
22	**RJ1103-40**	0.0020147	0.0000001	0.005	**5.71**	0.0020139	**5.72**	0.22
23	**RJ1105-11**	0.0020139	0.0000002	0.008	**5.32**	0.0020139	**5.32**	0.22
24	**RJ1105-15**	0.0020143	0.0000001	0.006	**5.51**	0.0020139	**5.51**	0.22

25	**RJ1105-17**	0.0020142	0.0000001	0.007	**5.47**	0.0020139	**5.48**	0.22
26	**RJ11A5-18**	0.0020206	0.0000002	0.008	**8.65**	0.0020139	**8.65**	0.22
27	**RJ11A5-17**	0.0020186	0.0000001	0.007	**7.66**	0.0020139	**7.66**	0.22
28	**RJ11A5-16**	0.0020165	0.0000002	0.008	**6.61**	0.0020139	**6.62**	0.22
29	**RJ11A5-19**	0.0020202	0.0000002	0.008	**8.43**	0.0020139	**8.43**	0.22
30	**RJ11A5-26**	0.0020165	0.0000002	0.008	**6.62**	0.0020139	**6.62**	0.22
36	**RJ11A10-34**	0.0020183	0.0000001	0.007	**7.48**	0.0020139	**7.48**	0.22
37	**RJ11A10-36**	0.0020179	0.0000002	0.010	**7.32**	0.0020139	**7.32**	0.22
38	**RJ11A7-34**	0.0020156	0.0000002	0.009	**6.17**	0.0020139	**6.17**	0.22
39	**RJ11A7-41**	0.0020152	0.0000001	0.007	**5.96**	0.0020139	**5.96**	0.22
40	**RJ11A11-40**	0.0020191	0.0000002	0.008	**7.92**	0.0020139	**7.92**	0.22
41	**RJ11A11-36c**	0.0020180	0.0000002	0.008	**7.36**	0.0020139	**7.35**	0.22
42	**RJ11A11-36r**	0.0020179	0.0000002	0.007	**7.31**	0.0020139	**7.30**	0.22
43	**RJ11A11-35**	0.0020186	0.0000001	0.005	**7.67**	0.0020139	**7.66**	0.22
44	**RJ11A17-22**	0.0020178	0.0000002	0.008	**7.24**	0.0020139	**7.23**	0.22
45	**RJ11A17-27**	0.0020159	0.0000002	0.009	**6.29**	0.0020139	**6.28**	0.22
51	**RJ11A15-27**	0.0020162	0.0000002	0.008	**6.45**	0.0020139	**6.43**	0.22
52	**RJ11A15-29**	0.0020161	0.0000002	0.007	**6.41**	0.0020139	**6.40**	0.22
53	**1026-36**	0.0020144	0.0000001	0.007	**5.58**	0.0020139	**5.56**	0.22
54	**1026-35**	0.0020147	0.0000002	0.009	**5.71**	0.0020139	**5.69**	0.22
55	**1026-33**	0.0020145	0.0000002	0.010	**5.61**	0.0020139	**5.60**	0.22
56	**RJ11A18-32**	0.0020162	0.0000002	0.008	**6.47**	0.0020139	**6.46**	0.22
57	**RJ11A18-35**	0.0020160	0.0000002	0.009	**6.37**	0.0020139	**6.36**	0.22
58	**RJ11A18-38**	0.0020153	0.0000002	0.009	**6.01**	0.0020139	**5.99**	0.22
59	**RF64-3**	0.0020134	0.0000002	0.008	**5.06**	0.0020139	**5.04**	0.22
60	**MQ39-25**	0.0020137	0.0000001	0.005	**5.19**	0.0020139	**5.17**	0.22

Appendix 2.6 Zircon Lu-Hf isotope data determined by LA-MC-ICP-MS

Sample	Number of ratios (NB/59)	Spot size	U-Pb Age (Ma)	±1σ	$^{176}Hf/^{177}Hf$ (JMC 475 corr)	±2σ	$^{176}Lu/^{177}Hf$	±2σ	$^{176}Yb/^{177}Hf$	$^{176}Hf/^{177}Hf_T$	±2σ	Internal precision (ppm) (2σ)	εHf_T	±2σ	T(NC) (Ma)	Notes
Pluton Tocota (Colangüil Batholith)																
RJ11A18-04	**59**	40µ	278.7	2.7	0.282699	0.000028	0.001002	0.000020	0.037414	**0.282694**	**0.000028**	100	**3.0**	1.0	**900**	
RJ11A18-09r	**59**	40µ	282.0	3.1	0.282675	0.000025	0.000502	0.000009	0.018836	**0.282672**	**0.000025**	87	**2.3**	0.9	**947**	
RJ11A18-11c	**59**	40µ	270.8	2.9	0.282689	0.000027	0.000885	0.000044	0.033809	**0.282685**	**0.000027**	97	**2.5**	1.0	**926**	
RJ11A18-13r	**59**	40µ	282.6	2.9	0.282682	0.000023	0.000435	0.000003	0.016567	**0.282679**	**0.000023**	83	**2.6**	0.8	**930**	
RJ11A18-14	**59**	40µ	278.1	3.7	0.282691	0.000026	0.000649	0.000033	0.024023	**0.282688**	**0.000026**	91	**2.7**	0.9	**914**	
RJ11A18-19	**59**	40µ	283.5	2.9	0.282672	0.000026	0.000526	0.000011	0.020392	**0.282669**	**0.000026**	94	**2.2**	0.9	**953**	
RJ11A18-29	**59**	40µ	278.8	3.2	0.282657	0.000026	0.000873	0.000058	0.034819	**0.282652**	**0.000026**	90	**1.5**	0.9	**996**	
Choiyoi Group																
AM0862-10	**59**	40µ	274.7	3.8	0.282597	0.000025	0.001752	0.000026	0.063532	**0.282588**	**0.000025**	88	**-0.8**	0.9	**1145**	
AM0862-13	**59**	40µ	263.9	3.8	0.282585	0.000030	0.001634	0.000042	0.059034	**0.282577**	**0.000030**	106	**-1.5**	1.1	**1179**	
AM0862-20c	**59**	40µ	271.4	4.0	0.282560	0.000027	0.000929	0.000067	0.034157	**0.282556**	**0.000027**	94	**-2.1**	0.9	**1223**	
AM0862-24	**59**	40µ	266.8	3.6	0.282624	0.000031	0.001305	0.000042	0.047392	**0.282618**	**0.000031**	108	**0.0**	1.1	**1083**	
AM0862-32	**59**	40µ	270.6	4.2	0.282596	0.000026	0.001265	0.000016	0.045462	**0.282590**	**0.000026**	92	**-0.9**	0.9	**1144**	
RJ11A20-12	**59**	40µ	268.1	2.9	0.282629	0.000026	0.001194	0.000015	0.046024	**0.282623**	**0.000026**	91	**0.2**	0.9	**1071**	
RJ11A20-14	**59**	40µ	268.3	3.0	0.282577	0.000027	0.001246	0.000068	0.043375	**0.282571**	**0.000027**	96	**-1.6**	1.0	**1190**	
RJ11A20-15	**59**	40µ	277.5	3.0	0.282578	0.000027	0.000723	0.000009	0.027187	**0.282574**	**0.000027**	96	**-1.3**	1.0	**1175**	
RJ11A20-17	**59**	40µ	*269.6*	*7.0*	0.282660	0.000034	0.002143	0.000044	0.082836	**0.282650**	**0.000034**	121	**1.2**	1.2	**1007**	
RJ11A20-18	**29**	40µ	270.7	3.0	0.282595	0.000040	0.001919	0.000275	0.081770	**0.282585**	**0.000040**	141	**-1.1**	1.4	**1156**	Drilled through
RJ11A20-20	**59**	40µ	265.5	3.0	0.282637	0.000028	0.001221	0.000050	0.048306	**0.282631**	**0.000028**	98	**0.5**	1.0	**1053**	
MQ39-13	**47**	40µ	270.9	3.8	0.282590	0.000033	0.001013	0.000090	0.039079	**0.282585**	**0.000033**	117	**-1.0**	1.2	**1155**	Drilled through
MQ39-21	**59**	40µ	269.3	3.7	0.282639	0.000023	0.000997	0.000018	0.038343	**0.282634**	**0.000023**	81	**0.6**	0.8	**1044**	
MQ39-22	**59**	40µ	271.6	3.1	0.282652	0.000030	0.001507	0.000026	0.059210	**0.282644**	**0.000030**	106	**1.1**	1.1	**1019**	
MQ39-23	**59**	40µ	273.6	3.2	0.282556	0.000028	0.001043	0.000019	0.040569	**0.282550**	**0.000028**	101	**-2.2**	1.0	**1234**	

Sample	Number of ratios (NB/59)	Spot size	U-Pb Age (Ma)	±1σ	$^{176}Hf/^{177}Hf$ (JMC 475 corr)	±2σ	$^{176}Lu/^{177}Hf$	±2σ	$^{176}Yb/^{177}Hf$	$^{176}Hf/^{177}Hf_T$	±2σ	Internal precision (ppm) (2σ)	εHf_T	±2σ	T(NC) (Ma)	Notes
MQ39-24	**49**	40µ	273.5	2.9	0.282699	0.000055	0.002008	0.000137	0.081051	**0.282689**	**0.000055**	194	**2.7**	1.9	**914**	Drilled into inclusion
MQ39-28	**59**	40µ	264.3	2.8	0.282609	0.000033	0.001263	0.000021	0.048595	**0.282602**	**0.000033**	117	**-0.6**	1.2	**1120**	
MQ39-30	**59**	40µ	271.1	3.9	0.282594	0.000032	0.001386	0.000020	0.054318	**0.282587**	**0.000032**	111	**-1.0**	1.1	**1150**	
MQ39-31	**36**	40µ	273.1	3.8	0.282586	0.000033	0.001061	0.000051	0.041408	**0.282580**	**0.000033**	118	**-1.2**	1.2	**1164**	Drilled through
Plastos Blancos Group																
AM0853-08	**59**	40µ	*261.0*	*6.0*	0.282717	0.000028	0.002996	0.000048	0.110833	**0.282703**	**0.000028**	99	**2.9**	1.0	**891**	
AM0853-15	**59**	40µ	265.1	2.9	0.282698	0.000048	0.003084	0.000158	0.121433	**0.282683**	**0.000048**	169	**2.3**	1.7	**933**	
AM0853-19	**59**	40µ	262.1	2.8	0.282761	0.000039	0.004460	0.000087	0.160902	**0.282739**	**0.000039**	138	**4.2**	1.4	**806**	
AM0853-20	**59**	40µ	266.8	2.8	0.282698	0.000029	0.002630	0.000049	0.094500	**0.282685**	**0.000029**	102	**2.4**	1.0	**927**	
AM0853-22	**59**	40µ	264.0	2.9	0.282687	0.000034	0.002704	0.000116	0.096471	**0.282674**	**0.000034**	121	**1.9**	1.2	**955**	
AM0853-23	**59**	40µ	*261.0*	*6.0*	0.282670	0.000034	0.003325	0.000050	0.118481	**0.282654**	**0.000034**	121	**1.2**	1.2	**1004**	
AM0853-38	**59**	40µ	263.2	2.9	0.282677	0.000039	0.003216	0.000099	0.118277	**0.282662**	**0.000039**	139	**1.5**	1.4	**984**	
AM0855-23	**50**	50µ	*248.6*	*5.5*	0.282619	0.000018	0.001324	0.000036	0.043899	**0.282613**	**0.000018**	64	**-0.6**	0.6	**1105**	Drilled through
AM0855-30	**59**	50µ	248.9	3.1	0.282627	0.000022	0.001768	0.000170	0.062769	**0.282619**	**0.000022**	78	**-0.3**	0.8	**1091**	
AM0855-31	**28**	50µ	*248.6*	*5.5*	0.282619	0.000023	0.001391	0.000021	0.052324	**0.282612**	**0.000023**	83	**-0.6**	0.8	**1107**	Drilled through
El León Unit (Ingaguás Supergroup)																
RJ1104-1	**59**	50µ	217.3	2.1	0.282695	0.000019	0.001268	0.000052	0.047735	**0.282690**	**0.000019**	67	**1.5**	0.7	**948**	
RJ1104-3	**59**	50µ	222.8	2.2	0.282698	0.000017	0.001092	0.000027	0.040097	**0.282693**	**0.000017**	61	**1.7**	0.6	**937**	
RJ1104-8	**55**	40µ	218.2	3.1	0.282672	0.000030	0.001333	0.000051	0.048434	**0.282667**	**0.000030**	106	**0.7**	1.1	**1002**	Drilled through
RJ1104-14	**59**	50µ	217.2	2.4	0.282706	0.000017	0.001267	0.000088	0.047582	**0.282701**	**0.000017**	61	**1.9**	0.6	**922**	
RJ1104-18	**59**	50µ	223.2	2.2	0.282697	0.000017	0.001249	0.000055	0.047618	**0.282691**	**0.000017**	60	**1.7**	0.6	**941**	
RJ1104-20r	**59**	50µ	224.9	2.1	0.282684	0.000016	0.000921	0.000007	0.033993	**0.282680**	**0.000016**	58	**1.3**	0.6	**967**	
RJ1104-23	**59**	50µ	230.0	2.5	0.282706	0.000018	0.001405	0.000077	0.054293	**0.282700**	**0.000018**	62	**2.1**	0.6	**917**	
RJ1104-36	**59**	40µ	222.1	3.0	0.282725	0.000030	0.001843	0.000085	0.065261	**0.282717**	**0.000030**	104	**2.5**	1.0	**882**	
Cogotí Supergroup																
AM0806-08	**59**	40µ	65.7	0.8	0.282995	0.000020	0.000559	0.000019	0.019314	**0.282994**	**0.000020**	69	**8.8**	0.7	**342**	

Sample	Number of ratios (NB/59)	Spot size	U-Pb Age (Ma)	±1σ	$^{176}Hf/^{177}Hf$ (JMC 475 corr)	±2σ	$^{176}Lu/^{177}Hf$	±2σ	$^{176}Yb/^{177}Hf$	$^{176}Hf/^{177}Hf_T$	±2σ	Internal precision (ppm) (2σ)	εHf_T	±2σ	T(NC) (Ma)	Notes
AM0806-11	**59**	40µ	65.9	0.9	0.282979	0.000024	0.000697	0.000057	0.022602	**0.282978**	**0.000024**	86	**8.3**	0.9	**379**	
AM0806-12	**59**	40µ	65.4	0.8	0.283011	0.000019	0.000998	0.000035	0.033314	**0.283010**	**0.000019**	66	**9.4**	0.7	**304**	
AM0806-13	**59**	40µ	70.2	0.8	0.282980	0.000021	0.000518	0.000017	0.017580	**0.282979**	**0.000021**	73	**8.4**	0.7	**373**	
AM0806-18	**59**	40µ	63.7	0.9	0.283015	0.000018	0.000757	0.000031	0.025363	**0.283015**	**0.000018**	65	**9.5**	0.7	**295**	
AM0806-31	**59**	40µ	65.2	0.8	0.282996	0.000023	0.001210	0.000043	0.043071	**0.282995**	**0.000023**	81	**8.9**	0.8	**339**	
AM0806-34	**59**	40µ	62.7	0.9	0.283007	0.000023	0.000747	0.000013	0.026595	**0.283006**	**0.000023**	80	**9.2**	0.8	**314**	
AM0806-37	**59**	40µ	63.3	0.9	0.282990	0.000022	0.000630	0.000003	0.022341	**0.282989**	**0.000022**	78	**8.6**	0.8	**354**	
AM0812-14	**59**	40µ	73.7	1.4	0.282997	0.000024	0.001873	0.000056	0.062174	**0.282994**	**0.000024**	84	**9.0**	0.8	**336**	
AM0812-16	**59**	40µ	72.2	2.1	0.283007	0.000020	0.000952	0.000026	0.030393	**0.283005**	**0.000020**	71	**9.4**	0.7	**311**	
AM0812-19	**59**	40µ	76.2	1.6	0.283000	0.000030	0.001355	0.000015	0.046688	**0.282998**	**0.000030**	105	**9.2**	1.1	**324**	
AM0812-21	**59**	40µ	71.1	5.1	0.283001	0.000020	0.001286	0.000114	0.046457	**0.282999**	**0.000020**	71	**9.2**	0.7	**325**	
AM0812-22	**59**	40µ	71.7	1.0	0.283000	0.000020	0.000913	0.000023	0.030380	**0.282999**	**0.000020**	70	**9.2**	0.7	**325**	
AM0812-23	**59**	40µ	72.5	1.0	0.282998	0.000027	0.002051	0.000035	0.072458	**0.282995**	**0.000027**	97	**9.0**	1.0	**335**	
AM0812-26	**59**	40µ	73.4	1.6	0.282996	0.000023	0.000653	0.000047	0.021456	**0.282995**	**0.000023**	81	**9.0**	0.8	**335**	
AM0812-38	**59**	40µ	73.6	1.1	0.282987	0.000027	0.001308	0.000062	0.045786	**0.282985**	**0.000027**	96	**8.7**	1.0	**356**	
AM0812-40	**53**	40µ	71.9	1.0	0.283020	0.000026	0.001794	0.000246	0.067182	**0.283017**	**0.000026**	93	**9.8**	0.9	**283**	Drilled through
AM0815-01	**59**	40µ	67.3	0.8	0.283012	0.000020	0.001096	0.000020	0.034445	**0.283010**	**0.000020**	72	**9.5**	0.7	**302**	
AM0815-09	**59**	40µ	68.6	1.1	0.283001	0.000016	0.001316	0.000064	0.041897	**0.282999**	**0.000016**	56	**9.1**	0.6	**327**	
AM0815-10	**59**	40µ	57.9	1.0	0.283015	0.000026	0.001550	0.000034	0.049390	**0.283013**	**0.000026**	92	**9.4**	0.9	**301**	
AM0815-12	**59**	40µ	64.1	0.8	0.283008	0.000024	0.001281	0.000022	0.044554	**0.283007**	**0.000024**	85	**9.3**	0.8	**312**	
AM0815-14	**59**	40µ	63.3	0.9	0.282995	0.000015	0.000598	0.000015	0.019942	**0.282994**	**0.000015**	54	**8.8**	0.5	**343**	
AM0815-19	**59**	40µ	53.4	0.8	0.283025	0.000022	0.001257	0.000093	0.038921	**0.283024**	**0.000022**	78	**9.6**	0.8	**280**	
AM0815-21	**59**	40µ	54.7	0.8	0.283029	0.000021	0.000974	0.000030	0.030189	**0.283028**	**0.000021**	75	**9.8**	0.8	**269**	
AM0815-24	**59**	40µ	55.3	0.9	0.283009	0.000021	0.000730	0.000015	0.022352	**0.283008**	**0.000021**	75	**9.1**	0.8	**316**	
AM0815-25	**59**	40µ	54.3	0.8	0.283004	0.000022	0.000977	0.000024	0.029743	**0.283003**	**0.000022**	79	**8.9**	0.8	**328**	
AM0815-34	**59**	40µ	*55.0*	*1.7*	0.283015	0.000016	0.000899	0.000023	0.027537	**0.283014**	**0.000016**	56	**9.3**	0.6	**301**	
AM0816-01	**59**	40µ	54.0	1.0	0.283019	0.000020	0.000845	0.000037	0.028894	**0.283019**	**0.000020**	70	**9.5**	0.7	**292**	
AM0816-05	**56**	40µ	*54.1*	*0.6*	0.283001	0.000019	0.001029	0.000019	0.033800	**0.283000**	**0.000019**	67	**8.8**	0.7	**335**	Drilled through
AM0816-09	**53**	40µ	53.3	0.9	0.283015	0.000024	0.000909	0.000016	0.028909	**0.283014**	**0.000024**	84	**9.3**	0.8	**302**	Drilled through

Sample	Number of ratios (NB/59)	Spot size	U-Pb Age (Ma)	±1σ	$^{176}Hf/^{177}Hf$ (JMC 475 corr)	±2σ	$^{176}Lu/^{177}Hf$	±2σ	$^{176}Yb/^{177}Hf$	$^{176}Hf/^{177}Hf_T$	±2σ	Internal precision (ppm) (2σ)	εHf_T	±2σ	T(NC) (Ma)	Notes
AM0816-10	**59**	40µ	54.3	1.1	0.283021	0.000022	0.000987	0.000041	0.029624	**0.283020**	**0.000022**	79	**9.5**	0.8	**288**	
AM0816-11	**59**	40µ	55.0	1.1	0.282984	0.000021	0.000807	0.000016	0.023629	**0.282983**	**0.000021**	76	**8.2**	0.8	**375**	
AM0816-17	**59**	40µ	55.1	1.0	0.283003	0.000022	0.001173	0.000017	0.038225	**0.283002**	**0.000022**	77	**8.9**	0.8	**330**	
AM0816-28	**59**	40µ	54.8	0.9	0.283025	0.000020	0.001025	0.000031	0.033353	**0.283024**	**0.000020**	70	**9.7**	0.7	**278**	
AM0816-32	**59**	40µ	54.0	0.8	0.283036	0.000022	0.000795	0.000028	0.025896	**0.283035**	**0.000022**	78	**10.0**	0.8	**254**	
AM0816-38	**59**	40µ	68.6	0.9	0.283007	0.000021	0.001628	0.000079	0.052526	**0.283005**	**0.000021**	74	**9.3**	0.7	**315**	
AM0819-05	**59**	40µ	70.2	1.2	0.282982	0.000020	0.001329	0.000059	0.047778	**0.282980**	**0.000020**	71	**8.5**	0.7	**371**	
AM0822-10	**40**	40µ	56.0	0.8	0.282998	0.000035	0.002707	0.000124	0.087339	**0.282995**	**0.000035**	123	**8.7**	1.2	**345**	Drilled through
AM0822-12	**59**	40µ	55.9	0.7	0.283015	0.000042	0.005082	0.000197	0.173706	**0.283010**	**0.000042**	148	**9.2**	1.5	**310**	
AM0822-14	**59**	40µ	58.3	0.8	0.283051	0.000044	0.007901	0.000224	0.281863	**0.283042**	**0.000044**	155	**10.4**	1.5	**234**	
AM0822-15c	**39**	40µ	59.2	0.7	0.282985	0.000046	0.004547	0.000189	0.123705	**0.282979**	**0.000046**	161	**8.2**	1.6	**380**	Drilled through
AM0822-16	**59**	40µ	57.3	0.7	0.282974	0.000034	0.003398	0.000043	0.109717	**0.282971**	**0.000034**	120	**7.8**	1.2	**402**	
AM0822-19	**59**	40µ	56.7	0.7	0.282987	0.000036	0.004180	0.000051	0.134991	**0.282982**	**0.000036**	126	**8.2**	1.3	**374**	
AM0823-11	**59**	40µ	70.4	0.8	0.282997	0.000021	0.000742	0.000003	0.024252	**0.282996**	**0.000021**	75	**9.0**	0.7	**334**	
AM0823-12	**59**	40µ	70.9	1.0	0.282981	0.000026	0.001609	0.000072	0.055023	**0.282979**	**0.000026**	90	**8.4**	0.9	**372**	
AM0824-15	**59**	40µ	64.6	1.0	0.282987	0.000022	0.000532	0.000011	0.017557	**0.282987**	**0.000022**	77	**8.6**	0.8	**359**	
AM0824-16	**59**	40µ	63.8	1.0	0.282994	0.000024	0.000954	0.000019	0.032839	**0.282993**	**0.000024**	86	**8.8**	0.9	**345**	
AM0824-18	**59**	40µ	64.5	0.9	0.282978	0.000022	0.001171	0.000071	0.040344	**0.282977**	**0.000022**	77	**8.2**	0.8	**383**	
AM0824-20	**59**	40µ	65.4	0.9	0.282988	0.000022	0.000921	0.000019	0.032338	**0.282987**	**0.000022**	78	**8.6**	0.8	**359**	
AM0824-21	**59**	40µ	66.1	0.8	0.282988	0.000023	0.000535	0.000008	0.017313	**0.282988**	**0.000023**	83	**8.6**	0.8	**356**	
AM0824-22	**59**	40µ	64.9	0.8	0.282973	0.000028	0.001750	0.000049	0.059668	**0.282971**	**0.000028**	100	**8.0**	1.0	**395**	
AM0824-23	**59**	40µ	64.8	0.9	0.282964	0.000020	0.000907	0.000021	0.032038	**0.282963**	**0.000020**	70	**7.7**	0.7	**414**	
AM0824-47	**59**	40µ	64.9	0.8	0.282963	0.000027	0.000901	0.000007	0.032983	**0.282962**	**0.000027**	97	**7.7**	1.0	**416**	
AM0826-01	**59**	40µ	65.1	0.8	0.282999	0.000018	0.000720	0.000009	0.022692	**0.282998**	**0.000018**	64	**9.0**	0.6	**333**	
AM0826-14	**59**	40µ	*64.2*	*0.7*	0.282980	0.000021	0.000530	0.000015	0.016227	**0.282980**	**0.000021**	74	**8.3**	0.7	**376**	
AM0826-17	**59**	40µ	*64.2*	*0.7*	0.282997	0.000020	0.001217	0.000063	0.038448	**0.282995**	**0.000020**	71	**8.9**	0.7	**339**	
AM0826-19	**59**	40µ	63.4	0.9	0.282998	0.000022	0.000628	0.000010	0.019694	**0.282998**	**0.000022**	78	**8.9**	0.8	**335**	
AM0826-25	**59**	40µ	63.6	0.7	0.282986	0.000022	0.000764	0.000087	0.023704	**0.282985**	**0.000022**	77	**8.5**	0.8	**363**	

Sample	Number of ratios (NB/59)	Spot size	U-Pb Age (Ma)	±1σ	$^{176}Hf/^{177}Hf$ (JMC 475 corr)	±2σ	$^{176}Lu/^{177}Hf$	±2σ	$^{176}Yb/^{177}Hf$	$^{176}Hf/^{177}Hf_T$	±2σ	Internal precision (ppm) (2σ)	εHf_T	±2σ	T(NC) (Ma)	Notes
AM0826-27	**59**	40µ	63.8	0.8	0.282975	0.000022	0.000846	0.000003	0.026409	**0.282974**	**0.000022**	78	**8.1**	0.8	**388**	
AM0826-32	**59**	40µ	66.2	1.2	0.282982	0.000020	0.000703	0.000087	0.024593	**0.282982**	**0.000020**	70	**8.4**	0.7	**370**	
AM0826-35	**59**	40µ	65.4	0.8	0.283000	0.000021	0.000833	0.000019	0.027874	**0.282999**	**0.000021**	74	**9.0**	0.7	**330**	
RJ1101-04	**59**	40µ	37.2	0.5	0.283026	0.000017	0.000616	0.000023	0.018508	**0.283026**	**0.000017**	60	**9.3**	0.6	**286**	
RJ1101-10	**59**	50µ	39.3	0.7	0.283039	0.000021	0.001070	0.000068	0.034494	**0.283038**	**0.000021**	74	**9.8**	0.7	**256**	
RJ1101-11	**59**	50µ	39.9	1.0	0.283036	0.000020	0.000723	0.000037	0.024307	**0.283035**	**0.000020**	69	**9.7**	0.7	**262**	
RJ1101-15	**59**	50µ	40.2	0.6	0.283045	0.000018	0.001016	0.000011	0.032484	**0.283044**	**0.000018**	65	**10.1**	0.6	**241**	
RJ1101-18c	**59**	50µ	39.4	0.6	0.283067	0.000022	0.001106	0.000014	0.039011	**0.283066**	**0.000022**	77	**10.8**	0.8	**190**	
RJ1101-18r	**59**	50µ	*38.9*	*1.0*	0.283048	0.000017	0.000473	0.000017	0.014728	**0.283047**	**0.000017**	60	**10.1**	0.6	**235**	
RJ1101-25	**59**	50µ	39.3	0.7	0.283060	0.000022	0.001362	0.000030	0.040779	**0.283059**	**0.000022**	77	**10.6**	0.8	**207**	
RJ1101-26	**59**	50µ	38.2	0.5	0.283041	0.000017	0.001530	0.000037	0.050683	**0.283040**	**0.000017**	60	**9.9**	0.6	**252**	
RJ1101-34r	**55**	40µ	40.5	0.8	0.283040	0.000024	0.001181	0.000159	0.035879	**0.283039**	**0.000024**	84	**9.9**	0.8	**254**	Drilled through
RJ1103-14	**59**	50µ	64.4	1.1	0.283002	0.000021	0.001796	0.000075	0.067123	**0.283000**	**0.000021**	74	**9.0**	0.7	**329**	
RJ1103-17	**59**	50µ	64.3	0.9	0.283015	0.000015	0.000605	0.000004	0.021500	**0.283014**	**0.000015**	53	**9.5**	0.5	**295**	
RJ1103-19r	**59**	50µ	66.2	0.7	0.282996	0.000021	0.001283	0.000028	0.046974	**0.282994**	**0.000021**	73	**8.9**	0.7	**341**	
RJ1103-22	**59**	50µ	64.6	0.7	0.282991	0.000018	0.000740	0.000012	0.026418	**0.282990**	**0.000018**	63	**8.7**	0.6	**352**	
RJ1103-26	**59**	40µ	64.0	0.7	0.282993	0.000023	0.000614	0.000002	0.021713	**0.282992**	**0.000023**	80	**8.7**	0.8	**347**	
RJ1103-40	**59**	40µ	64.0	0.8	0.282991	0.000020	0.000678	0.000004	0.023714	**0.282990**	**0.000020**	72	**8.7**	0.7	**352**	
Los Elquinos Formation																
AM0890-01	**59**	40µ	65.1	0.8	0.282990	0.000021	0.001049	0.000029	0.035801	**0.282989**	**0.000021**	75	**8.7**	0.8	**354**	
AM0890-04	**37**	40µ	58.7	0.7	0.283013	0.000023	0.000803	0.000024	0.025007	**0.283012**	**0.000023**	82	**9.3**	0.8	**303**	Drilled through
Terras Blancas Caldera																
RJ1105-1	**59**	50µ	39.1	0.8	0.283016	0.000019	0.001929	0.000104	0.068692	**0.283015**	**0.000019**	66	**9.0**	0.7	**310**	
RJ1105-2	**59**	50µ	40.4	1.1	0.283021	0.000015	0.000788	0.000023	0.026753	**0.283020**	**0.000015**	53	**9.2**	0.5	**297**	
RJ1105-3	**59**	50µ	40.3	0.8	0.283004	0.000021	0.001593	0.000053	0.052022	**0.283003**	**0.000021**	74	**8.6**	0.7	**337**	
RJ1105-4	**59**	40µ	43.1	0.8	0.283026	0.000024	0.000601	0.000007	0.020370	**0.283025**	**0.000024**	85	**9.5**	0.8	**283**	
RJ1105-5	**59**	50µ	39.8	0.7	0.283004	0.000021	0.001718	0.000038	0.054628	**0.283003**	**0.000021**	76	**8.6**	0.8	**337**	

Sample	Number of ratios (NB/59)	Spot size	U-Pb Age (Ma)	±1σ	$^{176}Hf/^{177}Hf$ (JMC 475 corr)	±2σ	$^{176}Lu/^{177}Hf$	±2σ	$^{176}Yb/^{177}Hf$	$^{176}Hf/^{177}Hf_T$	±2σ	Internal precision (ppm) (2σ)	εHf_T	±2σ	T(NC) (Ma)	Notes
RJ1105-6	**59**	40µ	41.5	1.0	0.283021	0.000026	0.001074	0.000030	0.033079	**0.283021**	**0.000026**	93	**9.3**	0.9	**295**	
RJ1105-11	**59**	40µ	39.6	0.7	0.283035	0.000028	0.002293	0.000136	0.073630	**0.283033**	**0.000028**	99	**9.7**	1.0	**266**	
RJ1105-17	**42**	40µ	38.7	1.0	0.283045	0.000025	0.001364	0.000079	0.044647	**0.283044**	**0.000025**	87	**10.0**	0.9	**242**	
Bocatoma Unit																
AM0867-05	**49**	40µ	36.3	0.6	0.282817	0.000018	0.000979	0.000066	0.031436	**0.282816**	**0.000018**	63	**1.9**	0.6	**775**	Drilled through
AM0867-08	**59**	40µ	36.1	0.6	0.282847	0.000021	0.000908	0.000006	0.027322	**0.282846**	**0.000021**	74	**3.0**	0.7	**704**	
AM0867-09	**59**	40µ	171.8	4.1	0.282688	0.000021	0.000637	0.000036	0.022232	**0.282686**	**0.000021**	73	**0.3**	0.7	**986**	Inherited core
AM0867-11	**59**	40µ	34.5	0.7	0.282848	0.000027	0.001498	0.000067	0.044718	**0.282847**	**0.000027**	95	**3.0**	0.9	**704**	
AM0867-13	**55**	40µ	*35.6*	*0.8*	0.282834	0.000023	0.000994	0.000025	0.029863	**0.282833**	**0.000023**	80	**2.5**	0.8	**736**	Drilled through
Tilito Formation (Lower Doña Ana Group)																
AM0844-01	**53**	40µ	24.3	0.3	0.282836	0.000026	0.002959	0.000040	0.092634	**0.282834**	**0.000026**	91	**2.3**	0.9	**740**	Drilled through
AM0844-02	**59**	40µ	24.5	0.7	0.282843	0.000027	0.002350	0.000049	0.073893	**0.282842**	**0.000027**	96	**2.6**	1.0	**722**	
AM0844-03	**59**	40µ	241.0	2.7	0.282771	0.000024	0.002473	0.000015	0.086468	**0.282760**	**0.000024**	84	**4.5**	0.8	**771**	Inherited core
AM0844-05	**59**	40µ	24.9	0.4	0.282851	0.000025	0.002201	0.000054	0.068713	**0.282850**	**0.000025**	88	**2.9**	0.9	**703**	
AM0844-07	**59**	40µ	25.5	0.6	0.282855	0.000039	0.004608	0.000290	0.149376	**0.282853**	**0.000039**	138	**3.0**	1.4	**697**	
AM0844-20	**59**	40µ	24.8	0.3	0.282873	0.000025	0.003107	0.000079	0.105875	**0.282872**	**0.000025**	89	**3.6**	0.9	**652**	
AM0844-26	**59**	40µ	*24.7*	*0.3*	0.282862	0.000028	0.002207	0.000042	0.074883	**0.282861**	**0.000028**	99	**3.2**	1.0	**678**	
AM0844-34	**59**	50µ	24.3	0.3	0.282849	0.000029	0.002333	0.000049	0.078305	**0.282848**	**0.000029**	103	**2.8**	1.0	**709**	
AM0845-14	**59**	40µ	25.4	0.5	0.282906	0.000028	0.002296	0.000063	0.085046	**0.282905**	**0.000028**	97	**4.8**	1.0	**575**	
AM0845-16c	**59**	40µ	278.5	2.9	0.282588	0.000018	0.001288	0.000030	0.047451	**0.282581**	**0.000018**	63	**-1.0**	0.6	**1160**	Inherited core
AM0845-17	**59**	40µ	24.5	0.9	0.282874	0.000025	0.002195	0.000072	0.078695	**0.282873**	**0.000025**	87	**3.6**	0.9	**157407**	
AM0845-21	**59**	40µ	24.7	0.7	0.282906	0.000031	0.002218	0.000156	0.078290	**0.282905**	**0.000031**	109	**4.8**	1.1	**575**	
AM0845-23	**59**	40µ	25.2	0.4	0.282876	0.000035	0.002580	0.000086	0.090633	**0.282875**	**0.000035**	123	**3.7**	1.2	**646**	
AM0845-25	**39**	40µ	25.1	0.3	0.282853	0.000038	0.002414	0.000088	0.088451	**0.282852**	**0.000038**	133	**2.9**	1.3	**699**	Drilled through
AM0845-26	**48**	40µ	276.7	2.9	0.282607	0.000028	0.000757	0.000031	0.028090	**0.282603**	**0.000028**	98	**-0.3**	1.0	**1110**	Inherited core / drilled through grain
AM0845-34	**44**	40µ	23.8	0.4	0.282859	0.000025	0.002333	0.000081	0.082525	**0.282858**	**0.000025**	90	**3.1**	0.9	**685**	Drilled through
AM0846-08	**26**	40µ	25.9	0.4	0.282857	0.000027	0.001387	0.000068	0.041593	**0.282856**	**0.000027**	94	**3.1**	0.9	**687**	Drilled through

Sample	Number of ratios (NB/59)	Spot size	U-Pb Age (Ma)	±1σ	$^{176}Hf/^{177}Hf$ (JMC 475 corr)	±2σ	$^{176}Lu/^{177}Hf$	±2σ	$^{176}Yb/^{177}Hf$	$^{176}Hf/^{177}Hf_T$	±2σ	Internal precision (ppm) (2σ)	εHf_T	±2σ	T(NC) (Ma)	Notes
AM0846-14c	**49**	40µ	158.0	2.4	0.282769	0.000017	0.000780	0.000015	0.024439	**0.282767**	**0.000017**	62	**2.9**	0.6	**810**	Inherited core / drilled through grain
AM0846-14r	**59**	40µ	28.0	0.4	0.282815	0.000020	0.001068	0.000065	0.030869	**0.282815**	**0.000020**	72	**1.7**	0.7	**783**	
AM0846-17	**59**	40µ	*26.1*	*1.6*	0.282891	0.000030	0.002774	0.000097	0.091261	**0.282889**	**0.000030**	107	**4.3**	1.1	**611**	
AM0846-18c	**59**	40µ	*26.1*	*1.6*	0.282862	0.000018	0.001192	0.000064	0.033658	**0.282862**	**0.000018**	64	**3.3**	0.6	**675**	
AM0846-20	**59**	40µ	25.9	0.5	0.282776	0.000023	0.001233	0.000101	0.037174	**0.282775**	**0.000023**	82	**0.2**	0.8	**875**	
AM0846-22	**59**	40µ	24.6	0.5	0.282854	0.000025	0.002568	0.000143	0.086471	**0.282853**	**0.000025**	90	**2.9**	0.9	**697**	
AM0849-10	**36**	40µ	24.8	0.4	0.282885	0.000035	0.002468	0.000058	0.084535	**0.282884**	**0.000035**	125	**4.1**	1.3	**624**	Drilled through
AM0849-16	**59**	40µ	24.4	0.5	0.282851	0.000026	0.002635	0.000069	0.087153	**0.282850**	**0.000026**	92	**2.8**	0.9	**703**	
AM0849-17	**59**	40µ	25.4	0.4	0.282896	0.000025	0.002833	0.000172	0.097285	**0.282895**	**0.000025**	90	**4.4**	0.9	**599**	
AM0849-18	**59**	40µ	24.5	0.6	0.282861	0.000026	0.002421	0.000052	0.080046	**0.282860**	**0.000026**	94	**3.2**	0.9	**680**	
AM0849-25	**59**	40µ	24.1	0.5	0.282879	0.000027	0.001826	0.000118	0.060925	**0.282878**	**0.000027**	97	**3.8**	1.0	**638**	
AM0849-27	**42**	40µ	*24.7*	*0.4*	0.282887	0.000038	0.002469	0.000142	0.090556	**0.282885**	**0.000038**	134	**4.1**	1.3	**621**	Drilled through
AM0860-03	**59**	40µ	24.7	0.5	0.282850	0.000027	0.002111	0.000053	0.068706	**0.282849**	**0.000027**	97	**2.8**	1.0	**705**	
AM0860-11	**59**	40µ	25.3	0.5	0.282891	0.000026	0.002588	0.000090	0.085021	**0.282889**	**0.000026**	91	**4.3**	0.9	**611**	
AM0860-13	**59**	40µ	*24.9*	*0.4*	0.282890	0.000026	0.003217	0.000045	0.108325	**0.282889**	**0.000026**	93	**4.2**	0.9	**613**	
AM0860-14	**35**	40µ	24.9	0.4	0.282843	0.000036	0.002654	0.000157	0.086523	**0.282842**	**0.000036**	128	**2.6**	1.3	**723**	Drilled through
AM0860-22	**25**	40µ	25.1	0.4	0.282877	0.000035	0.003134	0.000058	0.103981	**0.282876**	**0.000035**	122	**3.8**	1.2	**644**	Drilled through
PC14-03	**59**	40µ	23.4	0.2	0.282727	0.000034	0.002473	0.000106	0.092189	**0.282726**	**0.000034**	119	**-1.6**	1.2	**991**	
PC14-04	**59**	40µ	23.5	0.3	0.282705	0.000022	0.001605	0.000018	0.062098	**0.282705**	**0.000022**	78	**-2.3**	0.8	**1040**	
PC14-06	**59**	40µ	23.8	0.2	0.282758	0.000032	0.003298	0.000067	0.122148	**0.282756**	**0.000032**	112	**-0.5**	1.1	**920**	
PC14-07	**59**	40µ	23.6	0.3	0.282737	0.000027	0.002656	0.000028	0.103110	**0.282736**	**0.000027**	94	**-1.2**	0.9	**967**	
PC14-08	**59**	40µ	23.0	0.3	0.282687	0.000023	0.001383	0.000075	0.052399	**0.282686**	**0.000023**	83	**-3.0**	0.8	**1083**	
PC14-23	**59**	40µ	23.4	0.3	0.282688	0.000028	0.002498	0.000025	0.097975	**0.282687**	**0.000028**	100	**-3.0**	1.0	**1082**	
PC14-27	**56**	40µ	23.7	0.3	0.282708	0.000030	0.001922	0.000029	0.074926	**0.282707**	**0.000030**	107	**-2.2**	1.1	**1034**	Drilled through
RF64-13	**59**	40µ	24.6	0.4	0.282885	0.000028	0.001692	0.000077	0.065217	**0.282884**	**0.000028**	101	**4.1**	1.0	**624**	
RF64-17	**59**	40µ	23.3	0.4	0.282885	0.000039	0.002395	0.000022	0.094578	**0.282884**	**0.000039**	137	**4.0**	1.4	**624**	
RF64-18	**59**	40µ	23.9	0.4	0.282886	0.000037	0.001392	0.000010	0.050909	**0.282885**	**0.000037**	130	**4.1**	1.3	**622**	
RF64-23	**59**	40µ	24.5	0.3	0.282900	0.000051	0.008718	0.000739	0.320215	**0.282896**	**0.000051**	180	**4.5**	1.8	**597**	

Sample	Number of ratios (NB/59)	Spot size	U-Pb Age (Ma)	±1σ	$^{176}Hf/^{177}Hf$ (JMC 475 corr)	±2σ	$^{176}Lu/^{177}Hf$	±2σ	$^{176}Yb/^{177}Hf$	$^{176}Hf/^{177}Hf_T$	±2σ	Internal precision (ppm) (2σ)	εHf_T	±2σ	T(NC) (Ma)	Notes
RF64-24	**59**	40µ	23.7	0.4	0.282873	0.000025	0.001309	0.000059	0.048500	**0.282873**	**0.000025**	89	**3.6**	0.9	**651**	
RF64-25	**57**	40µ	388.1	5.3	0.282448	0.000032	0.001056	0.000319	0.038298	**0.282440**	**0.000032**	112	**-3.6**	1.1	**1411**	Inherited core / drilled through grain
Z27-07	**59**	40µ	23.5	0.3	0.282804	0.000034	0.001155	0.000066	0.042219	**0.282803**	**0.000034**	121	**1.2**	1.2	**813**	
Z27-11r	**59**	40µ	23.6	0.5	0.282817	0.000027	0.000750	0.000005	0.027443	**0.282817**	**0.000027**	97	**1.7**	1.0	**780**	
Z27-13c	**59**	40µ	23.4	0.4	0.282843	0.000035	0.001584	0.000087	0.061210	**0.282842**	**0.000035**	125	**2.5**	1.3	**722**	
Z27-13r	**59**	40µ	23.2	0.5	0.282848	0.000024	0.000934	0.000080	0.033258	**0.282848**	**0.000024**	84	**2.7**	0.8	**709**	
Z27-14	**59**	40µ	23.5	0.6	0.282792	0.000026	0.000729	0.000018	0.027011	**0.282791**	**0.000026**	93	**0.7**	0.9	**840**	
Z27-15	**59**	40µ	23.0	0.5	0.282891	0.000028	0.001692	0.000105	0.066276	**0.282890**	**0.000028**	100	**4.2**	1.0	**612**	
Z27-17	**59**	40µ	22.4	0.4	0.282830	0.000023	0.000905	0.000046	0.033159	**0.282830**	**0.000023**	80	**2.1**	0.8	**751**	
Z27-18	**59**	40µ	22.8	0.5	0.282836	0.000030	0.001058	0.000042	0.040447	**0.282835**	**0.000030**	108	**2.3**	1.1	**738**	
ZN122-15	**57**	40µ	25.0	0.6	0.282808	0.000029	0.000543	0.000039	0.019953	**0.282808**	**0.000029**	103	**1.4**	1.0	**800**	Drilled through
ZN122-17	**59**	40µ	24.4	0.6	0.282801	0.000027	0.000653	0.000009	0.024321	**0.282801**	**0.000027**	94	**1.1**	0.9	**817**	
ZN122-18c	**59**	40µ	24.8	0.5	0.282833	0.000031	0.000738	0.000012	0.027984	**0.282833**	**0.000031**	111	**2.2**	1.1	**743**	
ZN122-19r	**59**	40µ	25.6	0.4	0.282838	0.000029	0.000443	0.000007	0.016529	**0.282838**	**0.000029**	102	**2.4**	1.0	**732**	
ZN122-25	**59**	40µ	25.7	0.4	0.282822	0.000026	0.001048	0.000070	0.038741	**0.282821**	**0.000026**	92	**1.8**	0.9	**769**	
MQ153-03	**59**	40µ	25.6	0.3	0.282801	0.000028	0.001047	0.000049	0.038749	**0.282801**	**0.000028**	101	**1.1**	1.0	**817**	
MQ153-04c	**59**	40µ	25.4	0.4	0.282849	0.000027	0.001129	0.000015	0.042071	**0.282848**	**0.000027**	96	**2.8**	1.0	**707**	
MQ153-05	**59**	40µ	25.5	0.6	0.282798	0.000029	0.000765	0.000016	0.028758	**0.282798**	**0.000029**	102	**1.0**	1.0	**824**	
MQ153-06	**59**	40µ	24.5	0.4	0.282816	0.000023	0.000727	0.000004	0.026595	**0.282815**	**0.000023**	82	**1.6**	0.8	**784**	
MQ153-09	**59**	40µ	24.9	0.3	0.282853	0.000025	0.000999	0.000057	0.035714	**0.282852**	**0.000025**	88	**2.9**	0.9	**698**	
MQ153-12	**59**	40µ	25.8	0.3	0.282819	0.000025	0.000854	0.000013	0.030867	**0.282819**	**0.000025**	87	**1.8**	0.9	**774**	

Las Trancas Formation

RJ11A5-3	**59**	50µ	22.8	0.3	0.282809	0.000026	0.002146	0.000067	0.081946	**0.282808**	**0.000026**	90	**1.3**	0.9	**802**	
RJ11A5-6	**59**	50µ	257.5	2.9	0.282575	0.000019	0.000711	0.000016	0.028953	**0.282572**	**0.000019**	68	**-1.8**	0.7	**1194**	Inherited core
RJ11A5-7	**59**	50µ	22.7	0.3	0.282887	0.000022	0.001646	0.000041	0.058705	**0.282886**	**0.000022**	79	**4.1**	0.8	**620**	
RJ11A5-8	**59**	40µ	22.3	0.4	0.282737	0.000027	0.001631	0.000044	0.059380	**0.282736**	**0.000027**	96	**-1.2**	1.0	**969**	
RJ11A5-18b	**19**	40µ	273.1	3.6	0.282596	0.000037	0.000753	0.000029	0.027170	**0.282592**	**0.000037**	130	**-0.7**	1.3	**1137**	Inherited core / drilled through grain

Sample	Number of ratios (NB/59)	Spot size	U-Pb Age (Ma)	±1σ	$^{176}Hf/^{177}Hf$ (JMC 475 corr)	±2σ	$^{176}Lu/^{177}Hf$	±2σ	$^{176}Yb/^{177}Hf$	$^{176}Hf/^{177}Hf_T$	±2σ	Internal precision (ppm) (2σ)	εHf_T	±2σ	T(NC) (Ma)	Notes
RJ11A5-26	**20**	40µ	22.5	0.4	0.282830	0.000037	0.001799	0.000122	0.066043	**0.282830**	**0.000037**	130	**2.1**	1.3	**752**	Drilled through
Miocene Intrusives																
RJ11A10-2	**59**	50µ	22.1	0.4	0.282704	0.000019	0.001250	0.000088	0.045989	**0.282704**	**0.000019**	69	**-2.4**	0.7	**1043**	
RJ11A10-9r	**59**	50µ	22.2	0.3	0.282692	0.000023	0.001452	0.000012	0.054312	**0.282691**	**0.000023**	82	**-2.8**	0.8	**1071**	
RJ11A10-11	**59**	50µ	22.1	0.2	0.282683	0.000014	0.001530	0.000039	0.056516	**0.282682**	**0.000014**	51	**-3.1**	0.5	**1093**	
RJ11A10-13r	**59**	50µ	22.1	0.3	0.282682	0.000018	0.001130	0.000017	0.041524	**0.282682**	**0.000018**	63	**-3.2**	0.6	**1093**	
RJ11A10-14c	**59**	50µ	22.6	0.2	0.282706	0.000017	0.001900	0.000036	0.069528	**0.282705**	**0.000017**	61	**-2.3**	0.6	**1040**	
RJ11A10-17	**59**	50µ	22.1	0.3	0.282728	0.000024	0.002672	0.000465	0.100494	**0.282726**	**0.000024**	84	**-1.6**	0.8	**990**	
RJ11A10-21	**59**	50µ	21.9	0.5	0.282687	0.000020	0.000810	0.000029	0.029781	**0.282687**	**0.000020**	70	**-3.0**	0.7	**1082**	
RJ11A11-9	**59**	50µ	21.8	0.3	0.282720	0.000023	0.001007	0.000057	0.036991	**0.282719**	**0.000023**	81	**-1.8**	0.8	**1007**	
RJ11A11-35	**59**	40µ	21.6	0.4	0.282704	0.000027	0.000694	0.000025	0.026772	**0.282704**	**0.000027**	95	**-2.4**	1.0	**1043**	
RJ11A11-36	**59**	40µ	21.9	0.4	0.282704	0.000023	0.000958	0.000054	0.035252	**0.282704**	**0.000023**	81	**-2.4**	0.8	**1043**	
RJ11A14-07	**49**	40µ	20.3	0.3	0.282748	0.000026	0.000731	0.000024	0.026531	**0.282748**	**0.000026**	91	**-0.9**	0.9	**943**	Drilled through
RJ11A14-15	**59**	40µ	138.1	2.6	0.282579	0.000046	0.000580	0.000018	0.020809	**0.282578**	**0.000046**	164	**-4.3**	1.6	**1257**	Inherited core
RJ11A14-16	**59**	50µ	20.7	0.5	0.282686	0.000021	0.000387	0.000001	0.014001	**0.282686**	**0.000021**	76	**-3.1**	0.8	**1086**	
RJ11A14-17	**59**	50µ	20.7	0.4	0.282745	0.000020	0.000463	0.000018	0.017483	**0.282745**	**0.000020**	72	**-1.0**	0.7	**949**	
RJ11A14-18	**59**	50µ	21.0	0.4	0.282710	0.000018	0.000715	0.000008	0.028569	**0.282710**	**0.000018**	62	**-2.2**	0.6	**1030**	
RJ11A14-20	**59**	40µ	20.3	0.3	0.282697	0.000024	0.000565	0.000012	0.021583	**0.282697**	**0.000024**	84	**-2.7**	0.8	**1060**	
RJ11A14-23	**59**	40µ	20.2	0.4	0.282681	0.000026	0.000677	0.000043	0.025476	**0.282681**	**0.000026**	93	**-3.2**	0.9	**1097**	
Escabroso Formation (Upper Doña Ana Formation)																
1026-04	**59**	40µ	18.5	0.3	0.282780	0.000026	0.000680	0.000030	0.025406	**0.282779**	**0.000026**	93	**0.2**	0.9	**871**	
1026-09	**59**	40µ	18.5	0.4	0.282790	0.000019	0.000480	0.000013	0.017153	**0.282790**	**0.000019**	66	**0.6**	0.7	**847**	
1026-11	**59**	40µ	18.2	0.4	0.282809	0.000023	0.000556	0.000011	0.020202	**0.282809**	**0.000023**	80	**1.2**	0.8	**803**	
1026-14	**59**	40µ	18.5	0.4	0.282759	0.000024	0.000513	0.000003	0.018733	**0.282758**	**0.000024**	84	**-0.5**	0.8	**919**	
1026-16b	**59**	40µ	18.4	0.3	0.282820	0.000018	0.000851	0.000029	0.032379	**0.282819**	**0.000018**	64	**1.6**	0.6	**778**	
1026-18	**59**	40µ	17.7	0.5	0.282806	0.000022	0.000405	0.000003	0.014795	**0.282806**	**0.000022**	77	**1.1**	0.8	**811**	

Sample	Number of ratios (NB/59)	Spot size	U-Pb Age (Ma)	±1σ	$^{176}Hf/^{177}Hf$ (JMC 475 corr)	±2σ	$^{176}Lu/^{177}Hf$	±2σ	$^{176}Yb/^{177}Hf$	$^{176}Hf/^{177}Hf_T$	±2σ	Internal precision (ppm) (2σ)	εHf_T	±2σ	T(NC) (Ma)	Notes
1026-19	**59**	40µ	19.1	0.8	0.282840	0.000027	0.000748	0.000010	0.027327	**0.282840**	**0.000027**	94	**2.4**	0.9	**730**	
1026-33	**59**	40µ	17.5	0.3	0.282814	0.000022	0.000651	0.000056	0.024701	**0.282814**	**0.000022**	78	**1.4**	0.8	**791**	
SP80-1a	**59**	40µ	18.1	0.3	0.282788	0.000027	0.000661	0.000020	0.024403	**0.282788**	**0.000027**	94	**0.5**	0.9	**852**	
SP80-1b	**59**	40µ	*18.1*	*0.4*	0.282798	0.000023	0.000458	0.000007	0.016981	**0.282797**	**0.000023**	83	**0.8**	0.8	**829**	
SP80-2	**59**	40µ	18.4	0.6	0.282823	0.000025	0.000459	0.000004	0.017296	**0.282823**	**0.000025**	87	**1.7**	0.9	**770**	
SP80-3r	**59**	40µ	18.0	0.3	0.282807	0.000021	0.000493	0.000004	0.018428	**0.282807**	**0.000021**	75	**1.2**	0.8	**807**	
SP80-4	**59**	40µ	17.6	0.4	0.282785	0.000024	0.000443	0.000004	0.016053	**0.282785**	**0.000024**	85	**0.4**	0.9	**859**	
SP80-5	**59**	40µ	*18.1*	*0.4*	0.282816	0.000026	0.000599	0.000023	0.021834	**0.282815**	**0.000026**	93	**1.5**	0.9	**788**	
Cerro de las Tórtolas Formation																
RF62-8	**54**	40µ	17.4	0.3	0.282839	0.000026	0.000597	0.000009	0.021505	**0.282838**	**0.000026**	90	**2.3**	0.9	**735**	Drilled through
RF62-9	**46**	40µ	17.7	0.3	0.282846	0.000027	0.000928	0.000017	0.033947	**0.282846**	**0.000027**	97	**2.5**	1.0	**717**	Drilled through
RF62-10	**59**	40µ	17.0	0.3	0.282849	0.000024	0.000795	0.000045	0.028257	**0.282849**	**0.000024**	86	**2.6**	0.9	**711**	
RF62-11r	**59**	40µ	17.3	0.3	0.282828	0.000025	0.000457	0.000007	0.016444	**0.282828**	**0.000025**	87	**1.9**	0.9	**758**	
RF62-12	**59**	40µ	*17.1*	*0.6*	0.282832	0.000024	0.000854	0.000013	0.031674	**0.282831**	**0.000024**	85	**2.0**	0.9	**751**	
RF62-22	**54**	40µ	16.2	0.2	0.282825	0.000028	0.000854	0.000022	0.030906	**0.282824**	**0.000028**	98	**1.7**	1.0	**768**	Drilled through
Tertiary Intrusives																
RJ11A7-10r	**59**	50µ	11.5	0.2	0.282807	0.000019	0.001029	0.000006	0.038745	**0.282806**	**0.000019**	66	**1.0**	0.7	**812**	
RJ11A7-12r	**54**	50µ	11.6	0.2	0.282821	0.000016	0.001144	0.000060	0.036018	**0.282821**	**0.000016**	57	**1.5**	0.6	**779**	Drilled through
RJ11A7-13	**59**	50µ	*11.7*	*0.2*	0.282804	0.000019	0.000822	0.000045	0.026338	**0.282804**	**0.000019**	67	**0.9**	0.7	**819**	
RJ11A7-14	**59**	50µ	1068.1	10.5	0.282315	0.000018	0.000538	0.000027	0.021165	**0.282304**	**0.000018**	62	**7.0**	0.6	**1281**	Inherited core
RJ11A7-15a	**59**	50µ	11.9	0.3	0.282810	0.000017	0.001410	0.000110	0.048331	**0.282810**	**0.000017**	59	**1.1**	0.6	**804**	
RJ11A7-15b	**59**	50µ	*11.7*	*0.2*	0.282813	0.000014	0.001184	0.000148	0.037912	**0.282813**	**0.000014**	48	**1.2**	0.5	**157450**	
RJ11A7-21	**59**	50µ	11.6	0.2	0.282792	0.000023	0.000924	0.000047	0.032510	**0.282792**	**0.000023**	80	**0.5**	0.8	**846**	
RJ11A7-28	**59**	40µ	1249.4	10.9	0.282243	0.000022	0.001660	0.000038	0.063491	**0.282204**	**0.000022**	79	**7.5**	0.8	**1391**	Inherited core
RJ11A15-07	**59**	40µ	1225.7	11.7	0.282262	0.000025	0.000802	0.000026	0.031758	**0.282243**	**0.000025**	87	**8.4**	0.9	**1318**	Inherited core
RJ11A15-11	**59**	50µ	9.3	0.2	0.282669	0.000018	0.000841	0.000021	0.030477	**0.282669**	**0.000018**	64	**-3.9**	0.6	**1131**	
RJ11A15-14r	**59**	50µ	9.2	0.3	0.282677	0.000018	0.000785	0.000052	0.027787	**0.282677**	**0.000018**	64	**-3.6**	0.6	**1112**	

Sample	Number of ratios (NB/59)	Spot size	U-Pb Age (Ma)	±1σ	$^{176}Hf/^{177}Hf$ (JMC 475 corr)	±2σ	$^{176}Lu/^{177}Hf$	±2σ	$^{176}Yb/^{177}Hf$	$^{176}Hf/^{177}Hf_T$	±2σ	Internal precision (ppm) (2σ)	εHf_T	±2σ	T(NC) (Ma)	Notes
RJ11A15-15	**59**	50µ	*9.4*	*0.2*	0.282680	0.000018	0.000972	0.000053	0.034509	**0.282679**	**0.000018**	65	**-3.5**	0.7	**1107**	
RJ11A15-16	**59**	50µ	249.0	2.6	0.282735	0.000019	0.001005	0.000010	0.032448	**0.282730**	**0.000019**	68	**3.6**	0.7	**835**	Inherited core
RJ11A15-19	**59**	50µ	9.8	0.2	0.282676	0.000018	0.001243	0.000038	0.044863	**0.282676**	**0.000018**	63	**-3.6**	0.6	**1115**	
RJ11A15-22	**59**	40µ	1039.6	14.5	0.282260	0.000023	0.000710	0.000056	0.026680	**0.282247**	**0.000023**	82	**4.3**	0.8	**1432**	Drilled into core - omitted
RJ11A15-27	**52**	40µ	9.3	0.2	0.282673	0.000026	0.000787	0.000027	0.027209	**0.282673**	**0.000026**	91	**-3.8**	0.9	**1122**	Drilled through
RJ11A15-29	**59**	40µ	9.4	0.2	0.282704	0.000021	0.000875	0.000018	0.030139	**0.282704**	**0.000021**	75	**-2.7**	0.8	**1051**	
RJ11A17-07	**59**	50µ	239.7	3.0	0.282549	0.000017	0.000488	0.000007	0.022748	**0.282546**	**0.000017**	58	**-3.1**	0.6	**1264**	Inherited core
RJ11A17-10r	**59**	50µ	8.4	0.4	0.282419	0.000029	0.000147	0.000012	0.006339	**0.282419**	**0.000029**	104	**-12.7**	1.0	**1703**	Drilled into core - omitted
RJ11A17-22	**35**	40µ	1066.0	13.7	0.282368	0.000028	0.001384	0.000046	0.048970	**0.282340**	**0.000028**	101	**8.2**	1.0	**1200**	Inherited core / drilled through grain
RJ11A17-26	**34**	40µ	8.8	0.2	0.282670	0.000028	0.000745	0.000063	0.026316	**0.282670**	**0.000028**	99	**-3.9**	1.0	**1130**	Drilled through
Vacas Heladas Ignimbrites																
MQ33-07	**59**	40µ	6.3	0.1	0.282753	0.000019	0.000698	0.000033	0.023168	**0.282753**	**0.000019**	68	**-1.0**	0.7	**940**	
MQ33-10r	**59**	40µ	6.1	0.1	0.282751	0.000022	0.001130	0.000019	0.042405	**0.282751**	**0.000022**	78	**-1.1**	0.8	**944**	
MQ33-11c	**59**	40µ	6.2	0.1	0.282733	0.000025	0.000858	0.000029	0.028729	**0.282733**	**0.000025**	90	**-1.7**	0.9	**985**	
MQ33-11r	**59**	40µ	6.0	0.1	0.282743	0.000018	0.001117	0.000025	0.043756	**0.282743**	**0.000018**	64	**-1.3**	0.6	**962**	
MQ33-12	**59**	40µ	9.8	0.2	0.282785	0.000023	0.000912	0.000056	0.030510	**0.282785**	**0.000023**	80	**0.2**	0.8	**863**	Inherited core
MQ33-14	**59**	40µ	15.1	0.2	0.282809	0.000023	0.000664	0.000022	0.022231	**0.282809**	**0.000023**	80	**1.2**	0.8	**804**	Inherited core
MQ33-15	**59**	40µ	6.0	0.1	0.282741	0.000026	0.001159	0.000023	0.045506	**0.282741**	**0.000026**	91	**-1.4**	0.9	**967**	
MQ33-17	**59**	40µ	255.7	2.7	0.282660	0.000026	0.000902	0.000030	0.032555	**0.282655**	**0.000026**	94	**1.1**	0.9	**1003**	Inherited core
DI095-12	**51**	40µ	*6.2*	*0.3*	0.282739	0.000027	0.000553	0.000032	0.017289	**0.282739**	**0.000027**	96	**-1.5**	1.0	**972**	Drilled through
DI095-14i	**44**	40µ	256.3	3.4	0.282752	0.000035	0.002500	0.000169	0.109697	**0.282740**	**0.000035**	122	**4.1**	1.2	**808**	Inherited core / drilled through grain
DI095-14r	**59**	40µ	6.0	0.1	0.282685	0.000024	0.000454	0.000029	0.017339	**0.282685**	**0.000024**	87	**-3.4**	0.9	**1096**	
DI095-15c	**59**	40µ	*6.2*	*0.3*	0.282808	0.000031	0.001056	0.000010	0.039750	**0.282808**	**0.000031**	109	**1.0**	1.1	**812**	
DI095-15r	**59**	40µ	6.0	0.1	0.282745	0.000022	0.001409	0.000026	0.056393	**0.282745**	**0.000022**	77	**-1.3**	0.8	**958**	
DI095-16	**59**	40µ	270.7	3.0	0.282684	0.000030	0.001387	0.000084	0.055358	**0.282677**	**0.000030**	108	**2.2**	1.1	**943**	Inherited core
DI095-17	**59**	40µ	6.3	0.1	0.282748	0.000022	0.000887	0.000005	0.034904	**0.282748**	**0.000022**	76	**-1.2**	0.8	**951**	
DI095-20	**22**	40µ	6.4	0.1	0.282710	0.000034	0.001102	0.000091	0.039331	**0.282709**	**0.000034**	119	**-2.5**	1.2	**1040**	Drilled through
DI095-21r	**46**	40µ	*6.2*	*0.3*	0.282775	0.000031	0.000751	0.000069	0.027869	**0.282775**	**0.000031**	109	**-0.2**	1.1	**889**	Drilled through

U-Pb ages which are shown in italics and underlined represent the sample average U-Pb age (as determined by Concordia diagrams or Tera-Wasserburg plots) used to calculate εHf_T values for individual zircon analyses.

Appendix 2.7 Lu-Hf isotope data for zircon standards determined by LA-MC-ICP-MS

Date	Analysis order	Number of ratios (NB/59)	Spot size	$^{176}Hf/^{177}Hf$	±	$^{178}Hf/^{177}Hf$	±	$^{176}Lu/^{177}Hf$	±	$^{176}Yb/^{177}Hf$	±	Yb/Hf	Total Hf (V)	$^{176}Hf/^{177}Hf$ (JMC 475 corr)	±2σ	Internal precision (ppm) (2σ)	Notes
Plesovice																	
17.10.2011	Ples1-1	59	40	0.282464	0.000008	1.46720	0.00002	0.000139	0.000001	0.00780	0.00006	0.011	17.9	**0.282487**	0.000015	53	
17.10.2011	Ples1-2	59	40	0.282450	0.000008	1.46720	0.00003	0.000140	0.000001	0.00779	0.00004	0.011	17.7	**0.282473**	0.000017	59	
17.10.2011	Ples1-3	59	40	0.282460	0.000009	1.46715	0.00002	0.000140	0.000001	0.00782	0.00004	0.011	17.5	**0.282483**	0.000018	64	
17.10.2011	Ples2-1	59	40	0.282455	0.000009	1.46721	0.00003	0.000143	0.000001	0.00823	0.00006	0.012	15.7	**0.282478**	0.000017	61	
17.10.2011	Ples2-2	59	40	0.282458	0.000010	1.46721	0.00002	0.000140	0.000001	0.00806	0.00004	0.011	15.4	**0.282481**	0.000019	68	
17.10.2011	Ples2-3	59	40	0.282455	0.000008	1.46721	0.00002	0.000139	0.000001	0.00799	0.00004	0.011	15.1	**0.282478**	0.000017	60	
17.10.2011	Ples3-1	59	40	0.282448	0.000008	1.46719	0.00002	0.000140	0.000001	0.00720	0.00004	0.010	16.8	**0.282471**	0.000017	60	
17.10.2011	Ples3-2	59	40	0.282451	0.000009	1.46720	0.00003	0.000135	0.000000	0.00705	0.00004	0.010	16.0	**0.282474**	0.000017	61	
17.10.2011	Ples3-3	59	40	0.282473	0.000009	1.46719	0.00003	0.000136	0.000000	0.00702	0.00003	0.010	15.4	**0.282496**	0.000019	66	
17.10.2011	Ples4-1	59	40	0.282455	0.000007	1.46719	0.00002	0.000146	0.000001	0.00745	0.00005	0.011	16.7	**0.282478**	0.000015	53	
17.10.2011	Ples4-2	59	40	0.282457	0.000008	1.46718	0.00002	0.000144	0.000001	0.00734	0.00004	0.010	16.4	**0.282480**	0.000017	59	
17.10.2011	Ples4-3	59	40	0.282478	0.000008	1.46723	0.00003	0.000139	0.000001	0.00721	0.00004	0.010	15.9	**0.282502**	0.000017	60	
17.10.2011	Ples5-1	59	40	0.282455	0.000007	1.46719	0.00002	0.000146	0.000001	0.00745	0.00005	0.011	16.7	**0.282478**	0.000015	53	
17.10.2011	Ples5-2	59	40	0.282457	0.000008	1.46718	0.00002	0.000144	0.000001	0.00734	0.00004	0.010	16.4	**0.282480**	0.000017	59	
17.10.2011	Ples5-3	59	40	0.282478	0.000008	1.46723	0.00003	0.000139	0.000001	0.00721	0.00004	0.010	15.9	**0.282502**	0.000017	60	
17.10.2011	Ples6-1	59	40	0.282466	0.000008	1.46721	0.00003	0.000135	0.000001	0.00721	0.00007	0.010	16.7	**0.282489**	0.000015	54	
17.10.2011	Ples6-2	59	40	0.282455	0.000008	1.46718	0.00003	0.000138	0.000001	0.00705	0.00004	0.010	16.2	**0.282478**	0.000017	60	
17.10.2011	Ples6-3	59	40	0.282469	0.000007	1.46719	0.00003	0.000133	0.000000	0.00687	0.00004	0.010	16.0	**0.282493**	0.000015	52	
18.10.2011	Ples2-1	59	40	0.282454	0.000008	1.46720	0.00003	0.000135	0.000001	0.00772	0.00007	0.011	16.5	**0.282477**	0.000017	59	
18.10.2011	Ples2-2	59	40	0.282449	0.000010	1.46717	0.00004	0.000135	0.000000	0.00760	0.00006	0.011	16.4	**0.282473**	0.000021	73	
18.10.2011	Ples2-3	59	40	0.28247	0.000010	1.46718	0.00003	0.00013	0.00000	0.00752	0.00005	0.011	16.6	**0.282490**	0.000020	72	
18.10.2011	Ples3-1	59	40	0.28246	0.000010	1.46719	0.00003	0.00014	0.00000	0.00728	0.00005	0.010	15.3	**0.282485**	0.000020	69	
18.10.2011	Ples3-2	59	40	0.28247	0.000008	1.46718	0.00003	0.00013	0.00000	0.00714	0.00005	0.010	15.3	**0.282496**	0.000015	54	
18.10.2011	Ples3-3	59	40	0.28245	0.000010	1.46720	0.00002	0.00014	0.00000	0.00720	0.00004	0.010	14.9	**0.282474**	0.000020	70	
18.10.2011	Ples4-1	59	40	0.28247	0.000010	1.46715	0.00003	0.00013	0.00000	0.00733	0.00004	0.010	14.0	**0.282491**	0.000020	72	
18.10.2011	Ples4-2	59	40	0.28245	0.000008	1.46720	0.00003	0.00013	0.00000	0.00730	0.00003	0.010	14.0	**0.282474**	0.000017	60	
18.10.2011	Ples4-3	59	40	0.28248	0.000010	1.46719	0.00002	0.00013	0.00000	0.00723	0.00003	0.010	14.4	**0.282500**	0.000019	69	
18.10.2011	Ples5-1	59	40	0.28246	0.000007	1.46718	0.00002	0.00013	0.00000	0.00729	0.00001	0.010	23.4	**0.282478**	0.000014	49	
18.10.2011	Ples5-2	59	40	0.28247	0.000006	1.46718	0.00002	0.00013	0.00000	0.00717	0.00002	0.010	24.9	**0.282490**	0.000012	44	
18.10.2011	Ples5-3	59	40	0.28248	0.000005	1.46717	0.00002	0.00013	0.00000	0.00722	0.00003	0.010	25.9	**0.282499**	0.000010	37	
18.10.2011	Ples6-1	59	40	0.28246	0.000008	1.46719	0.00002	0.00014	0.00000	0.00776	0.00004	0.011	15.3	**0.282486**	0.000016	58	

Date	Analysis order	Number of ratios (NB/59)	Spot size	$^{176}Hf/^{177}Hf$	±	$^{178}Hf/^{177}Hf$	±	$^{176}Lu/^{177}Hf$	±	$^{176}Yb/^{177}Hf$	±	Yb/Hf	Total Hf (V)	$^{176}Hf/^{177}Hf$ (JMC 475 corr)	±2σ	Internal precision (ppm) (2σ)	Notes
18.10.2011	Ples6-2	59	40	0.28247	0.000009	1.46719	0.00003	0.00014	0.00000	0.00769	0.00004	0.011	15.3	**0.282494**	0.000019	66	
18.10.2011	Ples6-3	59	40	0.28246	0.000010	1.46718	0.00003	0.00014	0.00000	0.00756	0.00003	0.011	15.0	**0.282486**	0.000021	73	
18.10.2011	Ples7-1	59	40	0.28248	0.000008	1.46716	0.00003	0.00013	0.00000	0.00713	0.00003	0.010	13.9	**0.282507**	0.000016	57	
18.10.2011	Ples7-2	59	40	0.28247	0.000008	1.46721	0.00002	0.00014	0.00000	0.00728	0.00005	0.010	15.0	**0.282492**	0.000015	54	
18.10.2011	Ples7-3	59	40	0.28246	0.000010	1.46723	0.00003	0.00013	0.00000	0.00720	0.00005	0.010	15.3	**0.282485**	0.000021	74	
18.10.2011	Ples8-1	59	40	0.28245	0.000010	1.46720	0.00003	0.00013	0.00000	0.00744	0.00004	0.010	14.3	**0.282469**	0.000020	70	
18.10.2011	Ples8-2	59	40	0.28244	0.000010	1.46718	0.00004	0.00013	0.00000	0.00726	0.00003	0.010	14.5	**0.282463**	0.000020	70	
18.10.2011	Ples8-3	59	40	0.28246	0.000009	1.46719	0.00003	0.00013	0.00000	0.00726	0.00003	0.010	14.0	**0.282480**	0.000018	63	
18.10.2011	Ples9-1	59	40	0.28247	0.000010	1.46719	0.00004	0.00013	0.00000	0.00720	0.00003	0.010	14.0	**0.282491**	0.000020	72	
18.10.2011	Ples9-2	59	40	0.28247	0.000009	1.46718	0.00003	0.00014	0.00000	0.00737	0.00004	0.010	15.5	**0.282490**	0.000018	63	
18.10.2011	Ples9-3	59	40	0.28245	0.000008	1.46721	0.00002	0.00014	0.00000	0.00742	0.00003	0.010	15.4	**0.282477**	0.000016	57	
19.10.2011	Ples3-1	59	40	0.28246	0.000009	1.46721	0.00003	0.00014	0.00000	0.00767	0.00007	0.011	15.1	**0.282482**	0.000018	64	
19.10.2011	Ples3-2	59	40	0.28246	0.000008	1.46718	0.00003	0.00014	0.00000	0.00759	0.00007	0.011	15.2	**0.282482**	0.000016	57	
19.10.2011	Ples3-3	59	40	0.28245	0.000009	1.46717	0.00004	0.00014	0.00000	0.00757	0.00006	0.011	15.2	**0.282475**	0.000019	66	
19.10.2011	Ples4-1	59	40	0.28248	0.000009	1.46717	0.00003	0.00014	0.00000	0.00759	0.00007	0.011	15.8	**0.282506**	0.000017	62	
19.10.2011	Ples4-2	59	40	0.28245	0.000009	1.46719	0.00004	0.00013	0.00000	0.00758	0.00006	0.011	15.5	**0.282473**	0.000017	61	
19.10.2011	Ples4-3	59	40	0.28245	0.000010	1.46719	0.00005	0.00013	0.00000	0.00748	0.00005	0.011	14.9	**0.282474**	0.000021	74	
19.10.2011	Ples5-1	59	40	0.28247	0.000011	1.46716	0.00004	0.00013	0.00000	0.00764	0.00006	0.011	15.8	**0.282495**	0.000022	79	
19.10.2011	Ples5-2	59	40	0.28244	0.000009	1.46720	0.00003	0.00014	0.00000	0.00801	0.00006	0.011	16.2	**0.282463**	0.000017	61	
19.10.2011	Ples5-3	59	40	0.28247	0.000010	1.46720	0.00003	0.00014	0.00000	0.00767	0.00004	0.011	15.2	**0.282496**	0.000019	68	
19.10.2011	Ples6-1	59	40	0.28247	0.000008	1.46720	0.00003	0.00014	0.00000	0.00730	0.00007	0.010	15.3	**0.282496**	0.000016	58	
19.10.2011	Ples6-2	59	40	0.28247	0.000009	1.46718	0.00004	0.00014	0.00000	0.00723	0.00007	0.010	15.5	**0.282488**	0.000019	66	
19.10.2011	Ples6-3	59	40	0.28248	0.000009	1.46720	0.00004	0.00013	0.00000	0.00712	0.00006	0.010	15.4	**0.282503**	0.000018	64	
19.10.2011	Ples7-1	59	40	0.28247	0.000008	1.46722	0.00003	0.00009	0.00000	0.00524	0.00011	0.007	14.3	**0.282490**	0.000017	59	
19.10.2011	Ples7-2	59	40	0.28245	0.000009	1.46718	0.00002	0.00011	0.00000	0.00574	0.00007	0.008	14.3	**0.282476**	0.000018	63	
19.10.2011	Ples7-3	59	40	0.28248	0.000008	1.46719	0.00002	0.00014	0.00000	0.00765	0.00004	0.011	14.7	**0.282508**	0.000017	58	
19.10.2011	Ples8-01	59	40	0.28246	0.000008	1.46717	0.00003	0.00014	0.00000	0.00716	0.00005	0.010	14.6	**0.282479**	0.000017	60	
19.10.2011	Ples8-02	59	40	0.28246	0.000009	1.46717	0.00003	0.00014	0.00000	0.00712	0.00004	0.010	14.6	**0.282487**	0.000018	65	
19.10.2011	Ples8-03	59	40	0.28247	0.000010	1.46720	0.00003	0.00014	0.00000	0.00728	0.00005	0.010	14.6	**0.282490**	0.000021	74	
19.10.2011	Ples10-01	59	40	0.28248	0.000009	1.46720	0.00003	0.00014	0.00000	0.00743	0.00008	0.011	16.7	**0.282499**	0.000019	66	
19.10.2011	Ples10-02	59	40	0.28246	0.000009	1.46721	0.00003	0.00014	0.00000	0.00740	0.00008	0.010	16.4	**0.282484**	0.000018	63	
19.10.2011	Ples10-03	59	40	0.28246	0.000009	1.46718	0.00003	0.00009	0.00000	0.00514	0.00005	0.007	15.4	**0.282482**	0.000018	62	
02.04.2012	Ples1-1	59	50	0.28247	0.000011	1.46720	0.00003	0.00010	0.00000	0.00589	0.00001	0.008	14.0	**0.282491**	0.000022	79	
02.04.2012	Ples1-2	59	50	0.28247	0.000011	1.46721	0.00002	0.00013	0.00000	0.00781	0.00002	0.011	13.6	**0.282491**	0.000022	78	
02.04.2012	Ples1-3	58	50	0.28247	0.000010	1.46721	0.00002	0.00013	0.00000	0.00748	0.00004	0.011	13.8	**0.282492**	0.000019	68	Started late

Date	Analysis order	Number of ratios (NB/59)	Spot size	$^{176}Hf/^{177}Hf$	±	$^{178}Hf/^{177}Hf$	±	$^{176}Lu/^{177}Hf$	±	$^{176}Yb/^{177}Hf$	±	Yb/Hf	Total Hf (V)	$^{176}Hf/^{177}Hf$ (JMC 475 corr)	±2σ	Internal precision (ppm) (2σ)	Notes
02.04.2012	Ples2-1	59	40	0.28246	0.000013	1.46725	0.00003	0.00010	0.00000	0.00592	0.00004	0.008	9.9	**0.282482**	0.000026	91	
02.04.2012	Ples2-2	59	40	0.28247	0.000012	1.46722	0.00003	0.00011	0.00000	0.00636	0.00004	0.009	9.9	**0.282494**	0.000023	82	
02.04.2012	Ples2-3	59	40	0.28248	0.000011	1.46728	0.00003	0.00011	0.00000	0.00638	0.00002	0.009	10.4	**0.282501**	0.000023	80	
02.04.2012	Ples3-1	59	50	0.28248	0.000009	1.46726	0.00003	0.00014	0.00000	0.00816	0.00002	0.011	19.3	**0.282503**	0.000019	66	
02.04.2012	Ples3-2	59	50	0.28248	0.000008	1.46722	0.00002	0.00014	0.00000	0.00808	0.00002	0.011	19.6	**0.282508**	0.000017	59	
02.04.2012	Ples3-3	59	50	0.28246	0.000009	1.46724	0.00002	0.00015	0.00000	0.00829	0.00002	0.012	19.6	**0.282482**	0.000018	65	
02.04.2012	Ples4-1	59	50	0.28247	0.000008	1.46721	0.00002	0.00014	0.00000	0.00773	0.00002	0.011	18.5	**0.282499**	0.000016	56	
02.04.2012	Ples4-2	59	50	0.28246	0.000009	1.46722	0.00002	0.00014	0.00000	0.00751	0.00002	0.011	18.8	**0.282488**	0.000019	67	
02.04.2012	Ples4-3	59	50	0.28247	0.000009	1.46723	0.00002	0.00014	0.00000	0.00758	0.00002	0.011	19.6	**0.282496**	0.000019	66	
02.04.2012	Ples5-1	59	50	0.28247	0.000008	1.46723	0.00002	0.00014	0.00000	0.00795	0.00003	0.011	20.5	**0.282492**	0.000016	58	
02.04.2012	Ples5-2	59	50	0.28248	0.000009	1.46723	0.00002	0.00015	0.00000	0.00804	0.00002	0.011	20.3	**0.282502**	0.000017	61	
02.04.2012	Ples5-3	59	50	0.28247	0.000009	1.46724	0.00003	0.00014	0.00000	0.00790	0.00002	0.011	20.6	**0.282495**	0.000018	64	
02.04.2012	Ples6-1	59	50	0.28246	0.000007	1.46723	0.00003	0.00014	0.00000	0.00798	0.00001	0.011	23.0	**0.282488**	0.000015	53	
02.04.2012	Ples6-2	59	50	0.28247	0.000008	1.46723	0.00002	0.00014	0.00000	0.00805	0.00001	0.011	22.8	**0.282499**	0.000017	59	
02.04.2012	Ples6-3	59	50	0.28247	0.000007	1.46722	0.00002	0.00014	0.00000	0.00796	0.00001	0.011	22.9	**0.282491**	0.000014	50	
02.04.2012	Ples7-1	59	50	0.28247	0.000008	1.46724	0.00002	0.00014	0.00000	0.00821	0.00001	0.012	24.6	**0.282495**	0.000016	56	
02.04.2012	Ples7-2	59	50	0.28249	0.000008	1.46724	0.00002	0.00014	0.00000	0.00813	0.00002	0.011	24.2	**0.282516**	0.000015	55	
02.04.2012	Ples7-3	59	50	0.28247	0.000007	1.46724	0.00002	0.00014	0.00000	0.00797	0.00002	0.011	24.2	**0.282497**	0.000015	52	
03.04.2012	Ples2-1	59	50	0.28245	0.000007	1.46723	0.00002	0.00014	0.00000	0.00799	0.00002	0.011	22.5	**0.282478**	0.000013	47	
03.04.2012	Ples2-2	59	50	0.28248	0.000007	1.46725	0.00003	0.00014	0.00000	0.00808	0.00002	0.011	22.6	**0.282501**	0.000014	51	
03.04.2012	Ples2-3	59	50	0.28248	0.000009	1.46725	0.00002	0.00014	0.00000	0.00790	0.00002	0.011	22.9	**0.282505**	0.000018	65	
03.04.2012	Ples3-1	59	40	0.28246	0.000011	1.46723	0.00003	0.00013	0.00000	0.00775	0.00007	0.011	11.1	**0.282483**	0.000021	76	
03.04.2012	Ples3-2	59	40	0.28246	0.000010	1.46725	0.00003	0.00013	0.00000	0.00772	0.00004	0.011	11.9	**0.282483**	0.000021	73	
03.04.2012	Ples3-3	58	40	0.28245	0.000013	1.46724	0.00003	0.00013	0.00000	0.00759	0.00006	0.011	12.0	**0.282477**	0.000026	91	
03.04.2012	Ples4-1	59	40	0.28247	0.000013	1.46726	0.00003	0.00013	0.00000	0.00788	0.00003	0.011	12.8	**0.282493**	0.000026	92	
03.04.2012	Ples4-2	59	40	0.28246	0.000014	1.46723	0.00004	0.00012	0.00000	0.00708	0.00005	0.010	12.4	**0.282480**	0.000029	102	
03.04.2012	Ples4-3	59	40	0.28247	0.000012	1.46721	0.00003	0.00012	0.00000	0.00688	0.00005	0.010	12.0	**0.282498**	0.000023	82	
03.04.2012	Ples5-1	59	40	0.28246	0.000012	1.46724	0.00004	0.00013	0.00000	0.00789	0.00004	0.011	12.8	**0.282483**	0.000023	82	
03.04.2012	Ples5-2	59	40	0.28246	0.000011	1.46725	0.00003	0.00011	0.00000	0.00617	0.00004	0.009	12.7	**0.282481**	0.000022	79	
03.04.2012	Ples5-3	59	40	0.28247	0.000011	1.46724	0.00003	0.00013	0.00000	0.00754	0.00005	0.011	12.8	**0.282492**	0.000023	80	
03.04.2012	Ples6-1	59	40	0.28248	0.000010	1.46727	0.00003	0.00013	0.00000	0.00750	0.00004	0.011	13.4	**0.282507**	0.000021	73	
03.04.2012	Ples6-2	59	40	0.28248	0.000011	1.46725	0.00003	0.00012	0.00000	0.00704	0.00004	0.010	12.8	**0.282502**	0.000023	81	
03.04.2012	Ples6-3	59	40	0.28245	0.000011	1.46723	0.00003	0.00012	0.00000	0.00678	0.00003	0.010	12.6	**0.282478**	0.000022	79	
03.04.2012	Ples7-1	59	40	0.28248	0.000009	1.46723	0.00003	0.00013	0.00000	0.00726	0.00004	0.010	12.4	**0.282500**	0.000018	65	
03.04.2012	Ples7-2	59	40	0.28245	0.000011	1.46724	0.00003	0.00011	0.00000	0.00644	0.00004	0.009	12.3	**0.282477**	0.000022	78	

Date	Analysis order	Number of ratios (NB/59)	Spot size	$^{176}Hf/^{177}Hf$	±	$^{178}Hf/^{177}Hf$	±	$^{176}Lu/^{177}Hf$	±	$^{176}Yb/^{177}Hf$	±	Yb/Hf	Total Hf (V)	$^{176}Hf/^{177}Hf$ (JMC 475 corr)	±2σ	Internal precision (ppm) (2σ)	Notes
03.04.2012	Ples7-3	59	40	0.28248	0.000010	1.46726	0.00003	0.00013	0.00000	0.00747	0.00003	0.011	12.6	**0.282505**	0.000021	73	
03.04.2012	Ples8-1	59	40	0.28247	0.000012	1.46724	0.00003	0.00011	0.00000	0.00606	0.00006	0.009	13.5	**0.282498**	0.000023	83	
03.04.2012	Ples8-2	59	40	0.28247	0.000010	1.46725	0.00003	0.00014	0.00000	0.00778	0.00004	0.011	13.0	**0.282495**	0.000020	72	
03.04.2012	Ples8-3	59	40	0.28247	0.000011	1.46723	0.00003	0.00009	0.00000	0.00516	0.00002	0.007	12.8	**0.282495**	0.000022	77	
04.04.2012	Ples1-1	59	40	0.28245	0.000013	1.46722	0.00004	0.00011	0.00000	0.00662	0.00004	0.009	12.7	**0.282473**	0.000025	89	
04.04.2012	Ples1-2	59	40	0.28246	0.000015	1.46724	0.00004	0.00010	0.00000	0.00571	0.00003	0.008	13.1	**0.282480**	0.000029	104	
04.04.2012	Ples1-3	59	40	0.28246	0.000015	1.46725	0.00004	0.00011	0.00000	0.00628	0.00009	0.009	12.9	**0.282484**	0.000030	107	
04.04.2012	Ples2-1	59	40	0.28246	0.000013	1.46722	0.00004	0.00011	0.00000	0.00667	0.00008	0.009	11.0	**0.282482**	0.000025	90	
04.04.2012	Ples3-1	59	40	0.28248	0.000014	1.46726	0.00005	0.00010	0.00000	0.00615	0.00006	0.009	15.2	**0.282508**	0.000028	99	
04.04.2012	Ples3-2	59	40	0.28248	0.000014	1.46728	0.00004	0.00012	0.00000	0.00708	0.00003	0.010	14.1	**0.282502**	0.000028	100	
04.04.2012	Ples3-3	59	40	0.28247	0.000013	1.46727	0.00003	0.00012	0.00000	0.00678	0.00001	0.010	13.9	**0.282500**	0.000026	92	
04.04.2012	Ples4-1	59	40	0.28248	0.000013	1.46726	0.00003	0.00012	0.00000	0.00743	0.00007	0.010	13.2	**0.282501**	0.000025	89	
04.04.2012	Ples4-2	59	40	0.28246	0.000013	1.46726	0.00004	0.00015	0.00000	0.00833	0.00002	0.012	12.1	**0.282483**	0.000026	93	
04.04.2012	Ples4-3	59	40	0.28248	0.000012	1.46724	0.00003	0.00015	0.00000	0.00831	0.00002	0.012	12.5	**0.282506**	0.000024	86	
04.04.2012	Ples5-1	59	40	0.28246	0.000012	1.46726	0.00003	0.00013	0.00000	0.00754	0.00006	0.011	15.0	**0.282481**	0.000023	83	
04.04.2012	Ples5-2	59	40	0.28245	0.000009	1.46720	0.00003	0.00014	0.00000	0.00791	0.00002	0.011	14.9	**0.282477**	0.000017	61	
04.04.2012	Ples5-3	59	40	0.28246	0.000013	1.46729	0.00003	0.00008	0.00000	0.00470	0.00002	0.007	14.9	**0.282490**	0.000026	91	
04.04.2012	PlesDown6-1	59	40	0.28248	0.000011	1.46728	0.00003	0.00015	0.00000	0.00822	0.00001	0.012	14.2	**0.282503**	0.000022	77	
04.04.2012	PlesDown6-2	59	40	0.28250	0.000010	1.46727	0.00003	0.00015	0.00000	0.00810	0.00002	0.011	14.4	**0.282522**	0.000020	70	
04.04.2012	PlesDown6-3	59	40	0.28245	0.000011	1.46725	0.00003	0.00014	0.00000	0.00793	0.00002	0.011	14.1	**0.282473**	0.000023	80	
04.04.2012	Ples7-1	59	40	0.28246	0.000012	1.46723	0.00003	0.00010	0.00000	0.00588	0.00008	0.008	13.0	**0.282486**	0.000023	83	
04.04.2012	Ples7-2	59	40	0.28248	0.000011	1.46724	0.00003	0.00011	0.00000	0.00643	0.00001	0.009	13.4	**0.282509**	0.000022	76	
04.04.2012	Ples7-3	59	40	0.28246	0.000010	1.46726	0.00003	0.00011	0.00000	0.00641	0.00001	0.009	13.9	**0.282483**	0.000020	70	
04.04.2012	Ples8-1	59	40	0.28248	0.000011	1.46727	0.00003	0.00010	0.00000	0.00570	0.00002	0.008	14.3	**0.282503**	0.000023	81	
04.04.2012	Ples8-2	59	40	0.28246	0.000010	1.46726	0.00003	0.00012	0.00000	0.00741	0.00004	0.010	14.6	**0.282482**	0.000020	70	
04.04.2012	Ples8-3	59	40	0.28247	0.000011	1.46728	0.00003	0.00011	0.00000	0.00649	0.00006	0.009	14.2	**0.282498**	0.000021	74	

Average	**for 40µm**	**0.282488**
	2σ	**0.000023**
	n	**106**
Average	**for 50µm**	**0.282496**
	2σ	**0.000009**
	n	**21**

Mud Tank

17.10.2011	Mud-4-1	59	40	0.282489	0.000008	1.46720	0.00002	0.000016	0.000000	0.00065	0.00001	0.001	18.3	**0.282512**	0.000016	57	
17.10.2011	Mud-4-2	59	40	0.282481	0.000008	1.46720	0.00002	0.000017	0.000000	0.00068	0.00001	0.001	18.1	**0.282504**	0.000016	58	

Date	Analysis order	Number of ratios (NB/59)	Spot size	$^{176}Hf/^{177}Hf$	±	$^{178}Hf/^{177}Hf$	±	$^{176}Lu/^{177}Hf$	±	$^{176}Yb/^{177}Hf$	±	Yb/Hf	Total Hf (V)	$^{176}Hf/^{177}Hf$ (JMC 475 corr)	±2σ	Internal precision (ppm) (2σ)	Notes
17.10.2011	Mud-4-3	59	40	0.282494	0.000008	1.46721	0.00002	0.000018	0.000000	0.00072	0.00001	0.001	17.8	**0.282517**	0.000016	56	
17.10.2011	Mud-5-1	59	40	0.282493	0.000007	1.46719	0.00002	0.000016	0.000000	0.00068	0.00000	0.001	17.4	**0.282516**	0.000015	53	
17.10.2011	Mud-5-2	59	40	0.282482	0.000008	1.46719	0.00002	0.000018	0.000000	0.00073	0.00001	0.001	17.1	**0.282505**	0.000016	58	
17.10.2011	Mud-5-3	59	40	0.282502	0.000008	1.46715	0.00002	0.000019	0.000000	0.00076	0.00001	0.001	16.7	**0.282525**	0.000016	57	
17.10.2011	Mud-6-1	59	40	0.282497	0.000009	1.46721	0.00002	0.000018	0.000000	0.00075	0.00001	0.001	17.1	**0.282520**	0.000018	62	
17.10.2011	Mud-6-2	59	40	0.282500	0.000008	1.46721	0.00002	0.000019	0.000000	0.00079	0.00001	0.001	16.1	**0.282523**	0.000016	56	
17.10.2011	Mud-6-3	59	40	0.282492	0.000007	1.46720	0.00002	0.000016	0.000000	0.00066	0.00001	0.001	17.1	**0.282515**	0.000014	48	
17.10.2011	Mud-7-1	59	40	0.282489	0.000008	1.46720	0.00002	0.000017	0.000000	0.00071	0.00001	0.001	15.6	**0.282512**	0.000017	60	
17.10.2011	Mud-7-2	45	40	0.282495	0.000010	1.46718	0.00003	0.000017	0.000000	0.00071	0.00001	0.001	12.7	**0.282518**	0.000019	68	Drilled through
17.10.2011	Mud-7-3	59	40	0.282495	0.000009	1.46721	0.00002	0.000019	0.000000	0.00077	0.00001	0.001	14.5	**0.282518**	0.000018	63	
18.10.2011	Mud1-01	59	40	0.282507	0.000009	1.46718	0.00002	0.000016	0.000000	0.00070	0.00001	0.001	15.1	**0.282530**	0.000018	64	
18.10.2011	Mud1-02	59	40	0.282496	0.000007	1.46715	0.00002	0.000016	0.000000	0.00070	0.00001	0.001	14.9	**0.282519**	0.000015	52	
18.10.2011	Mud1-03	59	40	0.282493	0.000009	1.46718	0.00002	0.000016	0.000000	0.00069	0.00001	0.001	15.3	**0.282516**	0.000018	63	
18.10.2011	Mud2-01	59	40	0.282492	0.000008	1.46717	0.00003	0.000018	0.000000	0.00080	0.00001	0.001	14.9	**0.282515**	0.000016	57	
18.10.2011	Mud2-02	59	40	0.282488	0.000008	1.46721	0.00003	0.000017	0.000000	0.00075	0.00001	0.001	15.1	**0.282511**	0.000016	57	
18.10.2011	Mud2-03	59	40	0.282487	0.000009	1.46719	0.00003	0.000016	0.000000	0.00071	0.00001	0.001	15.1	**0.282510**	0.000018	65	
18.10.2011	Mud3-01	59	40	0.282511	0.000008	1.46720	0.00003	0.000016	0.000000	0.00072	0.00001	0.001	15.1	**0.282534**	0.000016	58	
18.10.2011	Mud3-02	59	40	0.282496	0.000008	1.46720	0.00002	0.000018	0.000000	0.00078	0.00001	0.001	14.7	**0.282519**	0.000016	57	
18.10.2011	Mud3-03	59	40	0.282503	0.000008	1.46717	0.00002	0.000016	0.000000	0.00069	0.00001	0.001	14.9	**0.282526**	0.000017	60	
18.10.2011	Mud5-01	59	40	0.282488	0.000008	1.46718	0.00003	0.000017	0.000000	0.00077	0.00001	0.001	16.0	**0.282511**	0.000015	54	
18.10.2011	Mud5-02	59	40	0.282496	0.000009	1.46719	0.00002	0.000016	0.000000	0.00069	0.00001	0.001	16.3	**0.282519**	0.000017	61	
18.10.2011	Mud5-03	59	40	0.282509	0.000009	1.46720	0.00002	0.000016	0.000000	0.00072	0.00001	0.001	14.7	**0.282532**	0.000018	65	
18.10.2011	Mud6-01	59	40	0.282510	0.000008	1.46715	0.00003	0.000015	0.000000	0.00068	0.00000	0.001	15.0	**0.282533**	0.000016	56	
18.10.2011	Mud6-02	59	40	0.282500	0.000007	1.46718	0.00003	0.000016	0.000000	0.00070	0.00001	0.001	15.2	**0.282523**	0.000014	50	
18.10.2011	Mud6-03	59	40	0.282482	0.000009	1.46719	0.00003	0.000020	0.000000	0.00089	0.00001	0.001	14.2	**0.282505**	0.000017	61	
18.10.2011	Mud7-01	59	40	0.282487	0.000009	1.46718	0.00003	0.000018	0.000000	0.00081	0.00001	0.001	15.2	**0.282510**	0.000018	62	
18.10.2011	Mud7-02	59	40	0.282500	0.000010	1.46719	0.00002	0.000016	0.000000	0.00071	0.00001	0.001	14.9	**0.282523**	0.000020	72	
18.10.2011	Mud7-03	59	40	0.282498	0.000009	1.46719	0.00002	0.000019	0.000000	0.00086	0.00001	0.001	15.0	**0.282521**	0.000017	61	
18.10.2011	Mud8-01	59	40	0.282491	0.000008	1.46719	0.00002	0.000016	0.000000	0.00075	0.00001	0.001	16.3	**0.282514**	0.000016	57	
18.10.2011	Mud8-02	59	40	0.282486	0.000007	1.46720	0.00002	0.000016	0.000000	0.00071	0.00001	0.001	16.1	**0.282509**	0.000014	50	
18.10.2011	Mud8-03	59	40	0.282499	0.000008	1.46720	0.00002	0.000017	0.000000	0.00078	0.00001	0.001	15.9	**0.282523**	0.000016	56	
19.10.2011	Mud2-01	59	40	0.282505	0.000007	1.46719	0.00002	0.000016	0.000000	0.00077	0.00001	0.001	15.1	**0.282528**	0.000014	51	
19.10.2011	Mud2-02	59	40	0.282509	0.000010	1.46723	0.00002	0.000020	0.000000	0.00092	0.00001	0.001	13.5	**0.282532**	0.000021	73	
19.10.2011	Mud2-03	59	40	0.282495	0.000009	1.46718	0.00004	0.000016	0.000000	0.00076	0.00001	0.001	13.5	**0.282518**	0.000019	67	
19.10.2011	Mud3-01	59	40	0.282493	0.000009	1.46718	0.00002	0.000019	0.000000	0.00090	0.00001	0.001	14.3	**0.282516**	0.000018	63	

Date	Analysis order	Number of ratios (NB/59)	Spot size	$^{176}Hf/^{177}Hf$	±	$^{178}Hf/^{177}Hf$	±	$^{176}Lu/^{177}Hf$	±	$^{176}Yb/^{177}Hf$	±	Yb/Hf	Total Hf (V)	$^{176}Hf/^{177}Hf$ (JMC 475 corr)	±2σ	Internal precision (ppm) (2σ)	Notes
19.10.2011	Mud3-02	59	40	0.282484	0.000009	1.46718	0.00003	0.000020	0.000000	0.00091	0.00001	0.001	14.0	**0.282507**	0.000018	63	
19.10.2011	Mud3-03	59	40	0.282494	0.000008	1.46719	0.00002	0.000015	0.000000	0.00067	0.00001	0.001	15.4	**0.282517**	0.000016	56	
19.10.2011	Mud4-01	59	40	0.282492	0.000009	1.46719	0.00002	0.000016	0.000000	0.00068	0.00001	0.001	15.7	**0.282515**	0.000017	61	
19.10.2011	Mud4-02	59	40	0.282494	0.000007	1.46718	0.00002	0.000017	0.000000	0.00072	0.00001	0.001	16.0	**0.282517**	0.000014	49	
19.10.2011	Mud4-03	59	40	0.282513	0.000007	1.46718	0.00002	0.000016	0.000000	0.00069	0.00001	0.001	16.3	**0.282536**	0.000014	48	
02.04.2012	Mud1-01	59	40	0.282520	0.000015	1.46727	0.00004	0.000016	0.000000	0.00075	0.00001	0.001	8.2	**0.282545**	0.000029	104	
02.04.2012	Mud1-02	59	40	0.282499	0.000011	1.46723	0.00004	0.000016	0.000000	0.00074	0.00001	0.001	8.6	**0.282524**	0.000022	77	
02.04.2012	Mud1-03	59	40	0.282507	0.000014	1.46726	0.00003	0.000015	0.000000	0.00070	0.00001	0.001	8.9	**0.282532**	0.000028	100	
02.04.2012	Mud2-01	59	50	0.282501	0.000009	1.46725	0.00003	0.000015	0.000000	0.00074	0.00001	0.001	17.2	**0.282526**	0.000018	63	
02.04.2012	Mud2-02	59	50	0.282509	0.000009	1.46725	0.00003	0.000015	0.000000	0.00074	0.00000	0.001	17.3	**0.282534**	0.000017	60	
02.04.2012	Mud2-03	59	50	0.282494	0.000009	1.46724	0.00003	0.000015	0.000000	0.00074	0.00000	0.001	17.9	**0.282519**	0.000018	62	
02.04.2012	Mud3-01	59	50	0.282502	0.000010	1.46722	0.00003	0.000015	0.000000	0.00074	0.00000	0.001	19.4	**0.282527**	0.000020	70	
02.04.2012	Mud3-02	59	50	0.282494	0.000007	1.46724	0.00003	0.000015	0.000000	0.00076	0.00000	0.001	19.2	**0.282519**	0.000014	49	
02.04.2012	Mud3-03	59	50	0.282500	0.000009	1.46721	0.00003	0.000016	0.000000	0.00079	0.00000	0.001	19.4	**0.282525**	0.000018	65	
02.04.2012	Mud4-01	59	50	0.282519	0.000008	1.46724	0.00002	0.000016	0.000000	0.00080	0.00001	0.001	18.6	**0.282544**	0.000016	57	
02.04.2012	Mud4-02	59	50	0.282503	0.000009	1.46723	0.00003	0.000015	0.000000	0.00076	0.00000	0.001	19.5	**0.282528**	0.000018	65	
02.04.2012	Mud4-03	59	50	0.282497	0.000009	1.46722	0.00002	0.000016	0.000000	0.00078	0.00000	0.001	19.4	**0.282523**	0.000018	64	
02.04.2012	Mud5-01	59	50	0.282501	0.000008	1.46726	0.00002	0.000015	0.000000	0.00077	0.00000	0.001	21.5	**0.282526**	0.000016	57	
02.04.2012	Mud5-02	59	50	0.282499	0.000007	1.46726	0.00002	0.000015	0.000000	0.00076	0.00000	0.001	21.7	**0.282524**	0.000014	49	
02.04.2012	Mud5-03	59	50	0.282505	0.000009	1.46724	0.00002	0.000015	0.000000	0.00076	0.00000	0.001	21.3	**0.282530**	0.000018	63	
03.04.2012	Mud1-01	59	40	0.282499	0.000014	1.46728	0.00003	0.000016	0.000000	0.00079	0.00001	0.001	11.1	**0.282524**	0.000027	96	
03.04.2012	Mud1-02	59	40	0.282514	0.000013	1.46727	0.00003	0.000015	0.000000	0.00072	0.00001	0.001	11.8	**0.282539**	0.000026	94	
03.04.2012	Mud2-01	59	50	0.282499	0.000011	1.46723	0.00004	0.000016	0.000000	0.00079	0.00000	0.001	20.4	**0.282524**	0.000022	78	
03.04.2012	Mud2-02	59	50	0.282511	0.000012	1.46725	0.00004	0.000018	0.000000	0.00087	0.00000	0.001	19.7	**0.282536**	0.000025	88	
03.04.2012	Mud2-03	59	50	0.282485	0.000009	1.46724	0.00003	0.000019	0.000000	0.00095	0.00000	0.001	19.4	**0.282510**	0.000019	67	
03.04.2012	Mud3-01	59	50	0.282500	0.000009	1.46723	0.00003	0.000016	0.000000	0.00080	0.00000	0.001	20.5	**0.282525**	0.000019	67	
03.04.2012	Mud3-02	53	50	0.282508	0.000009	1.46726	0.00003	0.000016	0.000000	0.00078	0.00000	0.001	21.1	**0.282533**	0.000019	67	
03.04.2012	Mud3-03	59	50	0.282503	0.000009	1.46727	0.00003	0.000016	0.000000	0.00078	0.00000	0.001	21.9	**0.282528**	0.000018	63	
03.04.2012	Mud4-01	59	40	0.282497	0.000010	1.46724	0.00003	0.000015	0.000000	0.00077	0.00001	0.001	14.8	**0.282522**	0.000020	71	
03.04.2012	Mud4-02	59	40	0.282502	0.000010	1.46726	0.00002	0.000016	0.000000	0.00078	0.00001	0.001	14.5	**0.282527**	0.000020	69	
03.04.2012	Mud4-03	59	40	0.282504	0.000010	1.46727	0.00003	0.000016	0.000000	0.00078	0.00001	0.001	14.6	**0.282529**	0.000019	69	
03.04.2012	Mud5-01	59	40	0.282501	0.000009	1.46725	0.00003	0.000016	0.000000	0.00078	0.00001	0.001	14.5	**0.282526**	0.000018	63	
03.04.2012	Mud5-02	59	40	0.282481	0.000009	1.46726	0.00003	0.000018	0.000000	0.00088	0.00001	0.001	13.8	**0.282506**	0.000018	63	
03.04.2012	Mud5-03	59	40	0.282506	0.000010	1.46726	0.00003	0.000019	0.000000	0.00091	0.00001	0.001	13.5	**0.282531**	0.000019	68	
03.04.2012	Mud6-01	59	40	0.282489	0.000010	1.46728	0.00003	0.000019	0.000000	0.00092	0.00001	0.001	13.2	**0.282514**	0.000020	71	

Date	Analysis order	Number of ratios (NB/59)	Spot size	$^{176}Hf/^{177}Hf$	±	$^{178}Hf/^{177}Hf$	±	$^{176}Lu/^{177}Hf$	±	$^{176}Yb/^{177}Hf$	±	Yb/Hf	Total Hf (V)	$^{176}Hf/^{177}Hf$ (JMC 475 corr)	±2σ	Internal precision (ppm) (2σ)	Notes
03.04.2012	Mud6-02	59	40	0.282510	0.000008	1.46726	0.00002	0.000017	0.000000	0.00082	0.00001	0.001	13.2	**0.282535**	0.000017	60	
03.04.2012	Mud6-03	59	40	0.282499	0.000010	1.46725	0.00002	0.000017	0.000000	0.00083	0.00001	0.001	13.1	**0.282524**	0.000021	73	
03.04.2012	Mud7-01	59	40	0.282505	0.000011	1.46725	0.00003	0.000017	0.000000	0.00080	0.00001	0.001	12.9	**0.282530**	0.000022	80	
03.04.2012	Mud7-02	59	40	0.282507	0.000009	1.46726	0.00002	0.000016	0.000000	0.00079	0.00001	0.001	13.5	**0.282532**	0.000018	65	
03.04.2012	Mud7-03	59	40	0.282483	0.000011	1.46726	0.00003	0.000016	0.000000	0.00078	0.00000	0.001	13.1	**0.282508**	0.000021	76	
03.04.2012	Mud8-01	59	40	0.282512	0.000012	1.46727	0.00003	0.000016	0.000000	0.00080	0.00001	0.001	13.2	**0.282537**	0.000024	86	
03.04.2012	Mud8-02	59	40	0.282500	0.000012	1.46724	0.00003	0.000019	0.000000	0.00091	0.00001	0.001	13.1	**0.282525**	0.000023	81	
03.04.2012	Mud8-03	59	40	0.282508	0.000009	1.46726	0.00003	0.000019	0.000000	0.00092	0.00001	0.001	13.0	**0.282533**	0.000019	66	
03.04.2012	Mud9-01	59	40	0.282508	0.000009	1.46725	0.00003	0.000018	0.000000	0.00087	0.00001	0.001	13.6	**0.282533**	0.000018	63	
03.04.2012	Mud9-02	59	40	0.282505	0.000009	1.46727	0.00002	0.000017	0.000000	0.00083	0.00001	0.001	13.5	**0.282530**	0.000019	66	
03.04.2012	Mud9-03	59	40	0.282501	0.000011	1.46723	0.00003	0.000016	0.000000	0.00078	0.00000	0.001	13.4	**0.282526**	0.000021	75	
03.04.2012	Mud-a	59	40	0.282488	0.000012	1.46727	0.00004	0.000015	0.000000	0.00075	0.00001	0.001	12.1	**0.282513**	0.000024	84	
04.04.2012	Mud1-01	59	40	0.282513	0.000012	1.46726	0.00004	0.000018	0.000000	0.00089	0.00001	0.001	14.3	**0.282539**	0.000023	82	
04.04.2012	Mud2-1	59	40	0.282494	0.000011	1.46727	0.00003	0.000016	0.000000	0.00076	0.00001	0.001	13.2	**0.282519**	0.000022	79	
04.04.2012	Mud3-01	59	40	0.282495	0.000013	1.46726	0.00003	0.000016	0.000000	0.00079	0.00001	0.001	14.6	**0.282520**	0.000025	90	
04.04.2012	Mud3-02	59	40	0.282504	0.000010	1.46725	0.00003	0.000016	0.000000	0.00079	0.00001	0.001	14.1	**0.282529**	0.000019	68	
04.04.2012	Mud3-03	59	40	0.282488	0.000012	1.46730	0.00003	0.000016	0.000000	0.00080	0.00001	0.001	14.1	**0.282513**	0.000024	85	
04.04.2012	Mud4-01	59	40	0.282498	0.000010	1.46727	0.00003	0.000016	0.000000	0.00079	0.00001	0.001	14.2	**0.282523**	0.000021	74	
04.04.2012	Mud4-02	59	40	0.282495	0.000010	1.46727	0.00003	0.000017	0.000000	0.00082	0.00000	0.001	13.9	**0.282520**	0.000020	71	
04.04.2012	Mud4-03	59	40	0.282512	0.000011	1.46727	0.00003	0.000016	0.000000	0.00078	0.00001	0.001	13.7	**0.282537**	0.000022	77	
04.04.2012	Mud5-01	59	40	0.282487	0.000011	1.46725	0.00003	0.000016	0.000000	0.00078	0.00001	0.001	15.5	**0.282512**	0.000023	81	
04.04.2012	Mud5-02	59	40	0.282499	0.000009	1.46727	0.00002	0.000017	0.000000	0.00081	0.00001	0.001	13.5	**0.282524**	0.000019	67	
04.04.2012	Mud5-03	59	40	0.282515	0.000010	1.46726	0.00003	0.000018	0.000000	0.00084	0.00001	0.001	13.3	**0.282540**	0.000021	74	
04.04.2012	Mud6-01	59	40	0.282488	0.000011	1.46729	0.00004	0.000016	0.000000	0.00079	0.00001	0.001	14.4	**0.282513**	0.000022	79	
04.04.2012	Mud6-02	59	40	0.282487	0.000009	1.46730	0.00003	0.000017	0.000000	0.00085	0.00001	0.001	14.3	**0.282512**	0.000018	65	
04.04.2012	Mud6-03	59	40	0.282490	0.000011	1.46723	0.00003	0.000016	0.000000	0.00079	0.00001	0.001	14.9	**0.282515**	0.000022	80	
04.04.2012	Mud7-01	59	40	0.282498	0.000010	1.46730	0.00003	0.000017	0.000000	0.00083	0.00001	0.001	14.8	**0.282523**	0.000020	71	
04.04.2012	Mud7-02	59	40	0.282501	0.000011	1.46726	0.00003	0.000018	0.000000	0.00086	0.00001	0.001	14.5	**0.282526**	0.000021	76	
04.04.2012	Mud7-03	59	40	0.282481	0.000011	1.46724	0.00003	0.000018	0.000000	0.00087	0.00001	0.001	14.4	**0.282506**	0.000022	77	
04.04.2012	Mud8-01	59	40	0.282513	0.000012	1.46726	0.00003	0.000018	0.000000	0.00087	0.00001	0.001	13.9	**0.282538**	0.000024	84	
04.04.2012	Mud8-02	59	40	0.282501	0.000011	1.46725	0.00003	0.000017	0.000000	0.00081	0.00000	0.001	14.1	**0.282526**	0.000021	75	
04.04.2012	Mud8-03	59	40	0.282497	0.000009	1.46726	0.00003	0.000019	0.000000	0.00092	0.00001	0.001	14.6	**0.282522**	0.000018	64	
												Average	**for 40µm**	**0.282522**			
													2σ	**0.000019**			
													n	**86**			

Date	Analysis order	Number of ratios (NB/59)	Spot size	$^{176}Hf/^{177}Hf$	±	$^{178}Hf/^{177}Hf$	±	$^{176}Lu/^{177}Hf$	±	$^{176}Yb/^{177}Hf$	±	Yb/Hf	Total Hf (V)	$^{176}Hf/^{177}Hf$ (JMC 475 corr)	±2σ	Internal precision (ppm) (2σ)	Notes
												Average	**for 50µm**	**0.282527**			
													2σ	**0.000007**			
													n	**18**			
Temora-2																	
17.10.2011	Tem1-1	46	40	0.282677	0.000013	1.46712	0.00004	0.000774	0.000013	0.02669	0.00025	0.038	9.4	**0.282700**	0.000026	92	Drilled through
17.10.2011	Tem1-2	32	40	0.282648	0.000015	1.46712	0.00005	0.000570	0.000004	0.02088	0.00024	0.030	8.2	**0.282671**	0.000031	109	Drilled through
17.10.2011	Tem1-3	59	40	0.282655	0.000010	1.46721	0.00002	0.000568	0.000006	0.02030	0.00008	0.029	12.3	**0.282678**	0.000020	71	
17.10.2011	Tem2-1	47	40	0.282657	0.000011	1.46714	0.00003	0.000480	0.000004	0.01557	0.00009	0.022	9.9	**0.282680**	0.000023	81	Drilled through
17.10.2011	Tem2-2	59	40	0.282679	0.000011	1.46718	0.00002	0.000515	0.000004	0.01643	0.00015	0.023	11.7	**0.282702**	0.000022	78	
17.10.2011	Tem2-3	59	40	0.282704	0.000009	1.46719	0.00002	0.000693	0.000011	0.02153	0.00042	0.030	12.0	**0.282727**	0.000019	66	
18.10.2011	Tem1-1	59	40	0.282665	0.000015	1.46718	0.00003	0.001515	0.000103	0.05562	0.00359	0.078	9.2	**0.282688**	0.000030	107	
18.10.2011	Tem1-2	42	40	0.282679	0.000015	1.46719	0.00003	0.000805	0.000013	0.02941	0.00054	0.041	8.7	**0.282702**	0.000031	109	Drilled through
18.10.2011	Tem1-3	59	40	0.282673	0.000013	1.46718	0.00002	0.001334	0.000013	0.04365	0.00040	0.061	11.7	**0.282697**	0.000026	90	
18.10.2011	Tem2-1	59	40	0.282663	0.000011	1.46722	0.00002	0.000583	0.000010	0.02042	0.00026	0.029	11.1	**0.282686**	0.000022	79	
18.10.2011	Tem2-2	59	40	0.282664	0.000011	1.46722	0.00003	0.001047	0.000015	0.03467	0.00033	0.049	11.5	**0.282687**	0.000023	80	
19.10.2011	Tem1-1	57	40	0.282677	0.000015	1.46720	0.00003	0.001385	0.000006	0.04965	0.00045	0.070	9.0	**0.282700**	0.000030	107	Drilled through
19.10.2011	Tem1-2	59	40	0.282668	0.000013	1.46718	0.00003	0.000897	0.000004	0.03147	0.00031	0.044	9.6	**0.282691**	0.000025	90	
03.04.2012	Tem1-1	59	40	0.282653	0.000013	1.46723	0.00003	0.001497	0.000009	0.05363	0.00066	0.075	9.4	**0.282678**	0.000026	92	
03.04.2012	Tem1-2	43	40	0.282719	0.000023	1.46733	0.00005	0.002085	0.000027	0.06618	0.00057	0.093	7.1	**0.282744**	0.000046	163	Drilled through
03.04.2012	Tem1-3	22	40	0.282671	0.000018	1.46730	0.00004	0.001078	0.000006	0.04276	0.00009	0.060	4.7	**0.282696**	0.000035	125	Drilled through
03.04.2012	Tem1-4	46	40	0.282705	0.000019	1.46732	0.00005	0.001683	0.000008	0.06021	0.00044	0.085	8.2	**0.282731**	0.000037	131	Drilled through
03.04.2012	Tem3-1	39	40	0.282664	0.000016	1.46725	0.00004	0.001090	0.000002	0.04140	0.00032	0.058	7.2	**0.282689**	0.000031	110	Drilled through
03.04.2012	Tem3-2	23	40	0.282670	0.000020	1.46727	0.00006	0.000961	0.000006	0.03754	0.00046	0.053	4.0	**0.282695**	0.000041	144	Drilled through
03.04.2012	Tem3-3	45	40	0.282665	0.000014	1.46725	0.00004	0.001596	0.000015	0.05703	0.00060	0.080	8.1	**0.282690**	0.000027	97	Drilled through
03.04.2012	Tem-a	51	40	0.282682	0.000013	1.46720	0.00004	0.000904	0.000020	0.03477	0.00078	0.049	8.9	**0.282707**	0.000026	92	Drilled through
03.04.2012	Tem-b	59	40	0.282655	0.000016	1.46724	0.00003	0.001667	0.000004	0.06861	0.00029	0.096	7.9	**0.282680**	0.000033	116	
04.04.2012	Tem1-2	59	40	0.282662	0.000012	1.46725	0.00003	0.000435	0.000005	0.01660	0.00017	0.023	9.1	**0.282687**	0.000025	88	
04.04.2012	Tem1-3	57	40	0.282698	0.000015	1.46728	0.00004	0.000869	0.000007	0.03101	0.00024	0.043	8.8	**0.282723**	0.000031	109	Drilled through
												Average	**for 40µm**	**0.282697**			
													2σ	**0.000036**			
													n	**24**			

Appendix 2.8 Major and trace element compositions of zircons determined by EPMA

Sample- zircon grain	ZrO_2	SiO_2	HfO_2	P_2O_5	Y_2O_3	Yb_2O_3	TiO_2	Lu_2O_3	ThO_2	UO_2	Total
1026-10	66.0	32.9	1.29	0.02	0.06	0.02	0.02	0.01	0.01	-	**100.3**
1026-11	65.8	32.7	1.23	0.04	0.18	0.04	0.01	0.01	0.04	-	**100.0**
1026-14	65.9	32.9	1.26	0.04	0.07	0.04	0.00	0.00	0.00	-	**100.2**
1026-16a	66.1	33.0	1.21	0.04	0.10	0.03	0.01	0.02	0.02	-	**100.5**
1026-16b	65.6	32.8	1.29	0.04	0.17	0.04	0.01	0.00	0.01	-	**99.9**
1026-18	65.9	32.8	1.28	0.03	0.08	0.01	0.00	0.01	0.02	-	**100.1**
1026-19c	66.2	32.8	1.16	0.01	0.10	0.03	0.01	0.00	0.00	-	**100.3**
1026-19r	65.9	32.6	1.22	0.01	0.04	0.02	0.01	0.00	0.00	-	**99.8**
1026-4	65.6	32.8	1.32	0.03	0.18	0.04	0.00	0.00	0.02	-	**100.0**
1026-5	65.6	32.9	1.27	0.04	0.16	0.04	0.02	0.00	0.02	-	**100.0**
1026-9	66.0	32.7	1.23	0.03	0.09	0.03	0.00	0.00	0.00	-	**100.1**
AM0806-10c	65.0	32.6	1.50	0.06	0.22	0.07	-	0.01	0.06	-	**99.5**
AM0806-10r	64.8	32.5	1.53	0.08	0.24	0.07	-	0.01	0.13	-	**99.3**
AM0806-11	65.4	32.7	1.28	0.04	0.11	0.03	-	0.01	0.01	-	**99.6**
AM0806-12	65.4	32.6	1.39	0.03	0.17	0.04	-	0.00	0.03	-	**99.6**
AM0806-13	65.2	32.6	1.35	0.04	0.21	0.04	-	0.00	0.02	-	**99.5**
AM0806-15	65.5	32.8	1.44	0.04	0.10	0.02	-	0.01	0.00	-	**99.8**
AM0806-16	65.4	32.5	1.41	0.04	0.09	0.02	-	0.01	0.02	-	**99.5**
AM0806-18	65.4	32.6	1.35	0.05	0.10	0.04	-	0.02	0.01	-	**99.5**
AM0806-1c2	65.7	32.4	1.55	0.11	0.14	0.06	0.00	0.00	0.03	0.06	**100.1**
AM0806-1r2	66.1	32.6	1.50	0.04	0.12	0.03	0.01	0.00	0.03	0.07	**100.5**
AM0806-31	65.5	32.7	1.27	0.04	0.23	0.06	-	0.01	0.05	-	**99.9**
AM0806-34	65.8	32.7	1.37	0.04	0.09	0.03	-	0.01	0.00	-	**100.0**
AM0806-37	65.6	32.7	1.44	0.04	0.11	0.04	-	0.00	0.02	-	**100.0**
AM0806-8	65.2	32.6	1.41	0.05	0.12	0.03	-	0.01	0.01	-	**99.4**
AM0806-9	65.4	32.7	1.40	0.03	0.07	0.02	-	0.01	0.00	-	**99.7**
AM0812-10	65.7	32.7	1.20	0.08	0.16	0.04	-	0.01	0.02	-	**100.0**
AM0812-11	65.5	32.8	1.20	0.07	0.30	0.07	-	0.01	0.01	-	**100.0**
AM0812-14	65.5	32.6	1.27	0.06	0.11	0.06	-	0.00	0.00	-	**99.6**
AM0812-15	65.4	32.6	1.18	0.07	0.30	0.07	-	0.00	0.02	-	**99.6**
AM0812-16	65.5	32.6	1.29	0.05	0.10	0.02	-	0.02	0.01	-	**99.6**
AM0812-19	65.4	32.7	1.26	0.06	0.24	0.07	-	0.01	0.01	-	**99.8**
AM0812-21	65.2	32.6	1.16	0.07	0.30	0.08	-	0.01	0.02	-	**99.4**
AM0812-22	65.2	32.7	1.35	0.07	0.14	0.06	-	0.00	0.00	-	**99.5**
AM0812-23	65.2	32.6	1.24	0.07	0.26	0.08	-	0.02	0.02	-	**99.5**
AM0812-26	65.1	32.4	1.15	0.13	0.56	0.12	-	0.03	0.03	-	**99.5**
AM0812-27	65.2	32.7	1.32	0.09	0.10	0.03	-	0.01	0.00	-	**99.5**
AM0812-38	65.4	32.6	1.23	0.04	0.14	0.04	-	0.00	0.01	-	**99.5**
AM0812-40	65.0	32.6	1.16	0.11	0.46	0.09	-	0.01	0.03	-	**99.4**
AM0815-1	65.1	32.6	1.42	0.06	0.14	0.06	-	0.00	0.01	-	**99.4**
AM0815-9	66.0	32.8	1.25	0.07	0.13	0.06	-	0.00	0.03	-	**100.4**
AM0815-10	65.5	32.5	1.15	0.14	0.13	0.04	-	0.01	0.01	-	**99.5**
AM0815-12	65.2	32.5	1.26	0.05	0.25	0.05	-	0.01	0.03	-	**99.4**
AM0815-14	65.7	32.9	1.53	0.04	0.08	0.01	-	0.00	0.01	-	**100.2**
AM0815-19	65.7	32.7	1.14	0.08	0.11	0.04	-	0.02	0.01	-	**99.8**
AM0815-24	66.0	32.8	1.11	0.05	0.12	0.04	-	0.01	0.01	-	**100.1**
AM0815-25	65.7	32.8	1.36	0.04	0.12	0.03	-	0.02	0.00	-	**100.1**
AM0815-34	65.5	32.6	1.37	0.05	0.13	0.04	-	0.02	0.01	-	**99.7**
AM0816-1c	65.7	32.7	1.37	0.03	0.14	0.05	-	0.00	0.00	-	**100.0**
AM0816-1r	65.6	32.7	1.39	0.05	0.17	0.04	-	0.00	0.01	-	**99.9**
AM0816-5	65.5	32.5	1.26	0.07	0.20	0.04	-	0.00	0.02	-	**99.6**
AM0816-9	65.9	32.7	1.25	0.03	0.06	0.02	-	0.01	0.01	-	**99.9**
AM0816-10	65.9	32.6	1.21	0.04	0.12	0.03	-	0.01	0.00	-	**99.8**
AM0816-11	65.6	32.8	1.28	0.04	0.10	0.05	-	0.00	0.01	-	**99.9**

Sample- zircon grain	ZrO_2	SiO_2	HfO_2	P_2O_5	Y_2O_3	Yb_2O_3	TiO_2	Lu_2O_3	ThO_2	UO_2	Total
AM0816-17	65.5	32.7	1.37	0.04	0.12	0.03	-	0.00	0.01	-	**99.8**
AM0816-24	65.4	32.7	1.49	0.04	0.09	0.04	-	0.01	0.01	-	**99.7**
AM0816-28	65.6	32.7	1.32	0.06	0.13	0.06	-	0.01	0.01	-	**99.8**
AM0816-32	65.4	32.5	1.25	0.09	0.21	0.09	-	0.01	0.01	-	**99.6**
AM0816-38	65.8	32.8	1.23	0.07	0.14	0.06	-	0.02	0.00	-	**100.1**
AM0819-2	65.4	32.5	1.39	0.06	0.13	0.05	-	0.01	0.00	-	**99.5**
AM0822-7	65.1	32.4	0.97	0.26	0.55	0.23	-	0.07	0.06	-	**99.6**
AM0822-10	65.6	32.6	0.93	0.12	0.37	0.12	-	0.03	0.02	-	**99.7**
AM0822-11	64.5	32.3	1.08	0.18	0.70	0.20	-	0.05	0.07	-	**99.1**
AM0822-12	65.5	32.6	1.14	0.03	0.14	0.05	-	0.01	0.02	-	**99.5**
AM0822-14	65.3	32.5	1.13	0.12	0.26	0.10	-	0.02	0.02	-	**99.4**
AM0822-15c2	66.1	32.5	0.82	0.79	0.22	0.19	0.01	0.04	0.02	-	**100.8**
AM0822-15r2	63.5	31.7	0.93	0.27	1.01	0.26	0.01	0.05	1.11	-	**99.2**
AM0822-16	65.1	32.6	0.99	0.11	0.45	0.14	-	0.03	0.03	-	**99.4**
AM0823-11	65.5	32.7	1.33	0.06	0.11	0.03	-	0.00	0.02	-	**99.8**
AM0823-12	65.6	32.8	1.48	0.04	0.06	0.04	-	0.01	0.01	-	**100.0**
AM0823-13	65.0	32.5	1.45	0.11	0.27	0.08	-	0.00	0.08	-	**99.5**
AM0823-19	65.3	32.6	1.46	0.04	0.08	0.02	-	0.02	0.00	-	**99.6**
AM0823-20	65.4	32.6	1.52	0.02	0.04	0.02	-	0.00	0.01	-	**99.6**
AM0823-21	65.2	32.6	1.29	0.09	0.45	0.12	-	0.02	0.06	-	**99.8**
AM0823-23	65.7	32.6	1.37	0.08	0.18	0.05	-	0.00	0.03	-	**100.0**
AM0823-25	65.9	32.9	1.46	0.05	0.11	0.04	-	0.02	0.02	-	**100.5**
AM0823-32	65.5	32.8	1.39	0.04	0.15	0.03	-	0.01	0.01	-	**99.9**
AM0823-35	65.4	32.8	1.46	0.05	0.23	0.06	-	0.03	0.00	-	**100.0**
AM0823-38	64.8	32.5	1.87	0.06	0.25	0.07	-	0.02	0.12	-	**99.6**
AM0824-14	65.8	32.6	1.20	0.06	0.10	0.03	-	0.00	0.02	-	**99.8**
AM0824-15	65.7	32.7	1.32	0.04	0.08	0.02	-	0.00	0.01	-	**99.8**
AM0824-16	65.8	32.7	1.22	0.05	0.09	0.03	-	0.01	0.00	-	**99.9**
AM0824-17	65.6	32.6	1.46	0.04	0.11	0.04	-	0.01	0.01	-	**99.9**
AM0824-18	65.8	32.7	1.29	0.04	0.11	0.03	-	0.00	0.01	-	**100.0**
AM0824-19	65.8	32.8	1.38	0.03	0.07	0.01	-	0.01	0.00	-	**100.1**
AM0824-20	65.6	32.6	1.24	0.05	0.10	0.04	-	0.01	0.00	-	**99.7**
AM0824-21	65.8	32.7	1.33	0.03	0.05	0.02	-	0.01	0.00	-	**99.9**
AM0824-22	65.7	32.7	1.26	0.04	0.08	0.02	-	0.01	0.00	-	**99.8**
AM0824-23	65.7	32.7	1.33	0.02	0.07	0.02	-	0.01	0.02	-	**99.9**
AM0824-44	65.6	32.6	1.30	0.04	0.10	0.04	-	0.00	0.02	-	**99.8**
AM0824-47	65.9	32.7	1.25	0.04	0.08	0.03	-	0.01	0.00	-	**100.1**
AM0824-48	65.7	32.7	1.22	0.05	0.18	0.05	-	0.00	0.01	-	**99.9**
AM0826-1	65.2	32.7	2.19	0.01	0.04	0.02	-	0.01	0.01	-	**100.2**
AM0826-5	65.0	32.4	1.26	0.12	0.53	0.13	-	0.01	0.10	-	**99.5**
AM0826-14c	65.4	32.6	1.41	0.05	0.28	0.07	-	0.00	0.05	-	**99.8**
AM0826-14r	65.7	32.9	1.60	0.02	0.07	0.04	-	0.00	0.02	-	**100.3**
AM0826-17c	65.1	32.6	1.24	0.08	0.44	0.10	-	0.01	0.11	-	**99.7**
AM0826-17r	65.6	32.8	1.50	0.06	0.20	0.06	-	0.02	0.07	-	**100.3**
AM0826-19	65.6	32.8	1.34	0.04	0.18	0.05	-	0.01	0.01	-	**100.0**
AM0826-23	65.3	32.6	1.38	0.05	0.26	0.07	-	0.01	0.05	-	**99.8**
AM0826-25	65.4	32.7	1.31	0.05	0.25	0.08	-	0.00	0.06	-	**99.9**
AM0826-27	65.5	32.7	1.39	0.04	0.11	0.04	-	0.00	0.02	-	**99.8**
AM0826-32	65.5	32.6	1.36	0.04	0.21	0.06	-	0.01	0.03	-	**99.8**
AM0826-34	65.1	32.6	1.44	0.10	0.29	0.06	-	0.02	0.10	-	**99.7**
AM0826-35	65.6	32.7	1.28	0.05	0.23	0.04	-	0.01	0.04	-	**99.9**
AM0826-38	65.5	32.7	1.40	0.03	0.09	0.04	-	0.00	0.01	-	**99.8**
AM0844-1	65.6	32.6	1.04	0.16	0.39	0.11	-	0.03	0.02	-	**100.0**
AM0844-2c	65.1	32.5	1.03	0.25	0.61	0.15	-	0.03	0.06	-	**99.6**
AM0844-2r	65.5	32.7	1.47	0.18	0.24	0.08	-	0.02	0.02	-	**100.2**
AM0844-3	65.8	32.6	1.12	0.10	0.26	0.06	-	0.02	0.04	-	**100.1**
AM0844-5	65.1	32.4	0.98	0.21	0.50	0.13	-	0.01	0.05	-	**99.4**
AM0844-7	65.7	32.6	1.36	0.06	0.10	0.03	-	0.00	0.00	-	**99.9**

Sample- zircon grain	ZrO_2	SiO_2	HfO_2	P_2O_5	Y_2O_3	Yb_2O_3	TiO_2	Lu_2O_3	ThO_2	UO_2	Total
AM0844-14	65.2	32.4	1.09	0.17	0.35	0.12	-	0.03	0.02	-	**99.4**
AM0844-20	64.9	32.4	1.49	0.32	0.42	0.14	-	0.03	0.03	-	**99.7**
AM0844-23	65.1	32.5	1.02	0.20	0.46	0.13	-	0.01	0.03	-	**99.5**
AM0844-26	65.8	32.6	1.01	0.22	0.27	0.10	-	0.02	0.03	-	**100.0**
AM0844-34	65.5	32.6	1.16	0.12	0.27	0.09	-	0.02	0.00	-	**99.8**
AM0845-14	64.8	32.4	1.46	0.17	0.30	0.09	-	0.02	0.03	-	**99.3**
AM0845-16	65.3	32.5	1.18	0.10	0.25	0.05	-	0.01	0.12	-	**99.5**
AM0845-17	65.7	32.7	1.18	0.12	0.21	0.06	-	0.01	0.03	-	**100.0**
AM0845-18	65.7	32.6	1.15	0.13	0.14	0.04	-	0.00	0.01	-	**99.7**
AM0845-20	65.5	32.5	1.02	0.10	0.30	0.08	-	0.02	0.05	-	**99.6**
AM0845-21	65.4	32.6	1.03	0.07	0.24	0.07	-	0.03	0.01	-	**99.5**
AM0845-22	64.7	32.4	1.48	0.27	0.37	0.12	-	0.03	0.04	-	**99.4**
AM0845-23	65.7	32.7	1.03	0.15	0.34	0.10	-	0.01	0.01	-	**100.0**
AM0845-25	65.3	32.5	1.22	0.13	0.26	0.08	-	0.01	0.05	-	**99.6**
AM0845-26	65.8	32.8	1.47	0.05	0.09	0.03	-	0.00	0.03	-	**100.3**
AM0845-33	65.4	32.5	1.00	0.19	0.41	0.10	-	0.02	0.04	-	**99.6**
AM0845-34	65.5	32.5	1.00	0.14	0.28	0.09	-	0.01	0.04	-	**99.6**
AM0846-8	65.8	32.7	1.29	0.10	0.17	0.06	-	0.01	0.02	-	**100.2**
AM0846-12	65.6	32.6	0.96	0.05	0.37	0.08	-	0.00	0.04	-	**99.7**
AM0846-14c	65.7	32.6	1.24	0.03	0.07	0.02	-	0.01	0.01	-	**99.7**
AM0846-14r	65.5	32.5	1.13	0.04	0.08	0.05	-	0.00	0.01	-	**99.3**
AM0846-15	65.7	32.7	1.08	0.10	0.20	0.05	-	0.02	0.02	-	**99.9**
AM0846-17	65.8	32.6	1.08	0.11	0.14	0.05	-	0.01	0.01	-	**99.8**
AM0846-18	65.6	32.7	1.41	0.02	0.07	0.02	-	0.01	0.00	-	**99.8**
AM0846-20c	65.8	32.6	1.29	0.02	0.09	0.03	-	0.01	0.02	-	**99.8**
AM0846-20r	65.9	32.5	1.22	0.03	0.06	0.02	-	0.01	0.01	-	**99.8**
AM0846-21	65.8	32.5	1.04	0.09	0.28	0.07	-	0.01	0.03	-	**99.9**
AM0846-22	66.1	32.8	1.09	0.11	0.13	0.04	-	0.00	0.01	-	**100.2**
AM0846-28r	65.4	32.4	1.33	0.07	0.19	0.06	-	0.01	0.12	-	**99.5**
AM0849-4c	65.4	32.3	1.36	0.25	0.29	0.10	-	0.02	0.03	-	**99.7**
AM0849-7	65.9	32.6	0.97	0.09	0.27	0.09	-	0.00	0.02	-	**100.0**
AM0849-10	65.7	32.5	1.06	0.18	0.21	0.07	-	0.00	0.00	-	**99.7**
AM0849-14	65.6	32.5	1.02	0.12	0.28	0.07	-	0.02	0.01	-	**99.7**
AM0849-16	65.4	32.5	1.05	0.14	0.30	0.10	-	0.02	0.03	-	**99.6**
AM0849-17	64.6	32.4	1.52	0.24	0.44	0.14	-	0.02	0.04	-	**99.3**
AM0849-18	65.3	32.5	1.02	0.12	0.24	0.09	-	0.01	0.01	-	**99.3**
AM0849-25	65.1	32.4	1.17	0.12	0.35	0.10	-	0.02	0.04	-	**99.3**
AM0849-27	65.6	32.5	0.99	0.11	0.22	0.08	-	0.03	0.02	-	**99.6**
AM0853-8	64.8	32.6	1.04	0.14	0.60	0.15	0.00	0.02	0.02	-	**99.4**
AM0853-9	65.1	32.4	1.15	0.14	0.24	0.07	0.00	0.02	0.02	-	**99.2**
AM0853-10	66.1	32.6	0.88	0.18	0.48	0.11	0.01	0.01	0.02	0.06	**100.4**
AM0853-22	65.7	32.5	0.90	0.12	0.55	0.11	0.00	0.01	0.04	0.05	**100.0**
AM0853-38	65.1	32.5	0.87	0.22	0.53	0.11	0.00	0.03	0.05	-	**99.4**
AM0860-2	65.7	32.5	1.16	0.10	0.30	0.10	-	0.02	0.02	-	**99.9**
AM0860-3	65.8	32.6	1.09	0.15	0.17	0.05	-	0.00	0.00	-	**99.9**
AM0860-11	65.2	32.3	1.05	0.25	0.31	0.09	-	0.02	0.01	-	**99.2**
AM0860-13c	65.5	32.4	1.06	0.18	0.19	0.07	-	0.01	0.00	-	**99.4**
AM0860-14	65.7	32.5	0.92	0.13	0.24	0.07	-	0.01	0.02	-	**99.5**
AM0860-19c	65.1	32.4	1.01	0.19	0.49	0.12	-	0.03	0.05	-	**99.4**
AM0860-20	65.9	32.6	1.06	0.13	0.14	0.04	-	0.00	0.01	-	**99.9**
AM0860-22	65.8	32.5	0.99	0.18	0.23	0.07	-	0.01	0.02	-	**99.8**
AM0860-25	65.3	32.4	1.04	0.17	0.42	0.11	-	0.02	0.03	-	**99.5**
AM0860-31	65.7	32.6	1.18	0.20	0.40	0.11	-	0.02	0.12	-	**100.3**
AM0862-1	65.7	32.4	1.12	0.10	0.17	0.05	0.01	0.02	0.01	0.02	**99.6**
AM0862-6	66.1	32.9	0.94	0.08	0.31	0.05	0.01	0.02	0.03	0.02	**100.5**
AM0862-9	65.4	32.4	1.06	0.11	0.24	0.06	0.00	0.01	0.01	-	**99.3**
AM0862-10	65.4	32.5	1.13	0.10	0.17	0.05	0.00	0.02	0.00	-	**99.3**
AM0862-13	65.6	32.6	1.08	0.10	0.16	0.04	0.02	0.00	0.00	-	**99.6**

Sample- zircon grain	ZrO_2	SiO_2	HfO_2	P_2O_5	Y_2O_3	Yb_2O_3	TiO_2	Lu_2O_3	ThO_2	UO_2	Total
AM0862-20c	65.4	32.6	1.25	0.02	0.10	0.02	0.01	0.01	0.01	-	**99.5**
AM0862-22	65.3	32.5	1.07	0.09	0.16	0.04	0.00	0.00	0.01	-	**99.1**
AM0862-24	65.6	32.7	1.14	0.08	0.14	0.04	0.01	0.01	0.02	-	**99.7**
AM0862-32	65.2	32.5	1.05	0.07	0.28	0.06	0.02	0.01	0.02	-	**99.2**
AM0862-35	65.5	32.5	1.00	0.14	0.28	0.08	0.00	0.02	0.01	-	**99.5**
AM0867-2	65.8	32.7	1.25	0.03	0.14	0.05	-	0.02	0.02	-	**100.0**
AM0867-5	65.7	32.6	1.26	0.02	0.10	0.04	-	0.00	0.03	-	**99.7**
AM0867-8c	65.9	32.8	1.35	0.02	0.04	0.03	-	0.00	0.01	-	**100.1**
AM0867-9c	65.7	32.6	1.16	0.06	0.09	0.01	-	0.01	0.02	-	**99.7**
AM0867-11	66.3	32.6	1.11	0.05	0.08	0.05	-	0.01	0.01	-	**100.2**
AM0867-13	65.5	32.6	1.25	0.03	0.07	0.03	-	0.01	0.01	-	**99.6**
AM0890-1c	65.9	32.8	1.33	0.03	0.16	0.06	-	0.02	0.02	-	**100.4**
AM0890-4	64.9	32.5	2.00	0.00	0.05	0.04	-	0.00	0.01	-	**99.4**
DI095-08c	65.4	32.7	1.40	0.02	0.14	0.05	0.01	0.01	0.04	-	**99.8**
DI095-08r	65.2	32.7	1.73	0.02	0.17	0.05	0.01	0.00	0.03	-	**99.9**
DI095-12	65.8	33.0	1.58	0.00	0.02	0.01	0.00	0.00	0.00	-	**100.4**
DI095-13	65.8	32.8	1.68	0.00	0.02	0.01	0.00	0.01	0.02	-	**100.3**
DI095-14c	66.0	32.6	1.43	0.00	0.06	0.01	0.00	0.00	0.01	-	**100.1**
DI095-14r	64.8	32.5	1.62	0.05	0.31	0.09	0.01	0.02	0.05	-	**99.5**
DI095-15c	66.0	32.8	1.05	0.05	0.20	0.05	0.00	0.01	0.01	-	**100.2**
DI095-15r	65.5	33.0	1.65	0.03	0.25	0.06	0.00	0.01	0.03	-	**100.5**
DI095-16	65.4	32.7	1.16	0.05	0.37	0.08	0.00	0.02	0.02	-	**99.8**
DI095-17	64.9	32.4	1.65	0.02	0.17	0.05	0.01	0.01	0.05	-	**99.2**
DI095-18	65.8	32.6	1.56	0.00	0.03	0.01	0.01	0.00	0.01	-	**100.0**
DI095-20	65.7	32.9	1.61	0.00	0.05	0.04	0.01	0.01	0.03	-	**100.3**
DI095-21c	65.8	32.8	1.59	0.01	0.04	0.03	0.00	0.00	0.01	-	**100.2**
DI095-21r	65.7	32.5	1.17	0.01	0.07	0.02	0.00	0.01	0.00	-	**99.5**
DI095-24	65.9	32.8	1.46	0.01	0.08	0.01	0.01	0.01	0.00	-	**100.3**
MQ153-1c	65.4	32.7	1.10	0.08	0.45	0.13	0.01	0.03	0.10	-	**100.0**
MQ153-1r	65.9	32.8	1.37	0.01	0.06	0.02	0.01	0.00	0.01	-	**100.1**
MQ153-2	65.9	32.5	1.21	0.04	0.10	0.02	0.00	0.00	0.01	-	**99.7**
MQ153-3	65.9	32.8	1.22	0.08	0.17	0.07	0.01	0.03	0.00	-	**100.2**
MQ153-4c	65.9	32.6	1.28	0.03	0.08	0.04	0.01	0.00	0.02	-	**100.0**
MQ153-4r	65.6	32.8	1.46	0.05	0.13	0.03	0.01	0.00	0.02	-	**100.0**
MQ153-5	66.0	32.8	1.26	0.04	0.08	0.02	0.00	0.00	0.00	-	**100.2**
MQ153-6	66.1	32.7	1.24	0.03	0.06	0.02	0.00	0.01	0.01	-	**100.1**
MQ153-8	65.7	32.8	1.35	0.06	0.16	0.05	0.00	0.01	0.03	-	**100.2**
MQ153-9	66.0	32.8	1.25	0.04	0.08	0.02	0.01	0.00	0.03	-	**100.2**
MQ153-12	65.8	32.7	1.29	0.10	0.22	0.06	0.00	0.01	0.10	-	**100.2**
MQ153-16	65.8	32.7	1.22	0.07	0.17	0.05	0.01	0.01	0.05	-	**100.1**
MQ153-20	66.1	32.8	1.23	0.02	0.09	0.03	0.00	0.01	0.00	-	**100.3**
MQ28-1	65.7	32.8	1.19	0.08	0.22	0.07	0.00	0.03	0.00	-	**100.0**
MQ28-3	65.7	32.8	1.26	0.03	0.10	0.02	0.00	0.01	0.07	-	**100.0**
MQ33-4a	65.6	32.9	1.63	0.00	0.15	0.03	0.00	0.01	0.03	-	**100.4**
MQ33-4b	65.7	32.8	1.52	0.02	0.08	0.04	0.01	0.00	0.02	-	**100.2**
MQ33-7	65.5	32.6	1.67	0.00	0.08	0.02	0.02	0.01	0.04	-	**99.9**
MQ33-8	65.7	32.7	1.55	0.01	0.08	0.02	0.00	0.00	0.05	-	**100.2**
MQ33-9	65.4	32.5	1.59	0.03	0.11	0.03	0.00	0.01	0.04	-	**99.7**
MQ33-9c	65.8	32.6	1.31	0.08	0.14	0.03	0.01	0.00	0.05	-	**100.1**
MQ33-10c	65.3	32.6	1.39	0.02	0.15	0.03	0.00	0.00	0.06	-	**99.5**
MQ33-10r	65.5	32.9	1.81	0.03	0.20	0.06	0.00	0.01	0.02	-	**100.5**
MQ33-11c	65.6	32.9	1.63	0.02	0.09	0.03	0.00	0.00	0.03	-	**100.3**
MQ33-11r	65.3	32.7	1.84	0.01	0.12	0.04	0.01	0.01	0.03	-	**100.1**
MQ33-12	65.8	32.7	1.46	0.00	0.05	0.02	0.01	0.00	0.02	-	**100.1**
MQ33-14	65.9	32.7	1.35	0.02	0.08	0.01	0.01	0.00	0.03	-	**100.1**
MQ33-15	65.5	32.8	1.68	0.04	0.22	0.05	0.00	0.01	0.05	-	**100.3**
MQ33-15c	66.0	32.8	1.49	0.01	0.05	0.01	0.01	0.00	0.01	-	**100.4**
MQ33-17	65.8	32.8	1.49	0.00	0.05	0.02	0.00	0.00	0.04	-	**100.2**

Sample- zircon grain	ZrO_2	SiO_2	HfO_2	P_2O_5	Y_2O_3	Yb_2O_3	TiO_2	Lu_2O_3	ThO_2	UO_2	Total
MQ33-19	65.3	32.8	1.92	0.00	0.09	0.04	0.01	0.00	0.03	-	**100.3**
MQ39-13	66.4	32.8	1.01	0.03	0.09	0.02	0.00	0.00	0.00	-	**100.3**
MQ39-21	66.0	32.7	1.04	0.09	0.18	0.05	0.00	0.02	0.02	-	**100.1**
MQ39-22	65.6	32.7	1.15	0.06	0.28	0.07	0.00	0.01	0.03	-	**99.9**
MQ39-23	66.1	32.8	1.07	0.04	0.18	0.05	0.01	0.01	0.01	-	**100.2**
MQ39-24	66.0	32.8	1.01	0.08	0.33	0.08	0.00	0.02	0.03	-	**100.3**
MQ39-25	65.7	32.6	1.03	0.10	0.39	0.09	0.00	0.01	0.03	-	**99.9**
MQ39-26	66.4	32.9	1.01	0.07	0.10	0.03	0.00	0.01	0.00	-	**100.5**
MQ39-28	66.2	32.9	1.12	0.08	0.13	0.03	0.01	0.00	0.02	-	**100.5**
MQ39-30	65.9	32.7	1.01	0.08	0.28	0.08	0.02	0.00	0.01	-	**100.0**
MQ39-31	65.9	32.8	1.21	0.07	0.18	0.06	0.01	0.01	0.02	-	**100.2**
PC14-1a	65.1	32.7	1.58	0.13	0.28	0.08	0.01	0.03	0.04	-	**100.0**
PC14-1b	64.3	32.7	1.73	0.08	0.62	0.15	0.00	0.02	0.12	-	**99.7**
PC14-4	64.6	32.5	1.65	0.19	0.42	0.10	0.00	0.00	0.05	-	**99.6**
PC14-5	64.5	32.5	1.57	0.25	0.48	0.13	0.00	0.01	0.15	-	**99.6**
PC14-6c	65.6	32.7	1.09	0.20	0.25	0.09	0.00	0.02	0.03	-	**100.0**
PC14-6r	64.0	32.4	1.61	0.31	0.61	0.17	0.01	0.02	0.22	-	**99.4**
PC14-7	65.0	32.6	1.56	0.24	0.49	0.15	0.00	0.02	0.09	-	**100.2**
PC14-8	65.4	32.8	1.56	0.06	0.14	0.06	0.00	0.00	0.01	-	**100.0**
PC14-20c	64.1	32.2	1.51	0.61	0.80	0.21	0.00	0.04	0.12	-	**99.6**
PC14-22	64.6	32.4	1.54	0.24	0.49	0.13	0.00	0.02	0.18	-	**99.6**
PC14-23	64.3	32.2	1.61	0.28	0.52	0.14	0.01	0.03	0.17	-	**99.3**
PC14-26	64.4	32.4	1.52	0.28	0.58	0.18	0.01	0.04	0.11	-	**99.6**
PC14-27	64.7	32.5	1.55	0.20	0.41	0.12	0.01	0.01	0.17	-	**99.6**
PC14-30	64.9	32.4	1.47	0.44	0.49	0.16	0.01	0.04	0.03	-	**100.0**
RF62-06	65.7	32.5	1.42	0.01	0.05	0.03	0.01	0.00	0.01	-	**99.8**
RF62-08	66.0	33.0	1.47	0.01	0.07	0.03	0.00	0.01	0.04	-	**100.6**
RF62-09	65.7	32.8	1.48	0.04	0.12	0.05	0.00	0.02	0.06	-	**100.2**
RF62-10	66.1	32.8	1.56	0.02	0.06	0.03	0.00	0.01	0.03	-	**100.6**
RF62-11	66.0	32.7	1.42	0.03	0.07	0.01	0.00	0.00	0.01	-	**100.2**
RF62-12	65.9	32.8	1.27	0.04	0.10	0.02	0.00	0.01	0.03	-	**100.2**
RF62-15	66.0	32.8	1.30	0.06	0.13	0.03	0.02	0.00	0.05	-	**100.4**
RF62-21	65.8	32.9	1.50	0.05	0.13	0.04	0.00	0.02	0.07	-	**100.5**
RF62-22	65.9	33.0	1.28	0.08	0.09	0.02	0.01	0.01	0.01	-	**100.3**
RF64-03	64.6	32.4	1.21	0.13	0.39	0.13	0.00	0.02	0.44	-	**99.4**
RF64-05	65.9	32.7	1.26	0.03	0.10	0.03	0.00	0.02	0.04	-	**100.1**
RF64-10	66.0	32.9	1.18	0.07	0.13	0.03	0.01	0.02	0.00	-	**100.3**
RF64-13	64.7	32.5	1.03	0.22	0.90	0.20	0.01	0.05	0.09	-	**99.7**
RF64-17	65.4	32.5	1.06	0.13	0.48	0.12	0.00	0.00	0.03	-	**99.8**
RF64-18	66.0	32.9	1.23	0.08	0.17	0.05	0.01	0.01	0.01	-	**100.4**
RF64-19	65.1	32.6	1.08	0.20	0.58	0.17	0.02	0.03	0.14	-	**100.0**
RF64-21	66.0	32.8	1.28	0.06	0.16	0.06	0.01	0.01	0.01	-	**100.4**
RF64-23	64.1	32.3	0.95	0.35	0.85	0.31	0.01	0.06	0.34	-	**99.2**
RF64-24	66.2	32.6	1.20	0.06	0.12	0.04	0.00	0.02	0.00	-	**100.3**
RF64-26c	66.2	32.8	1.24	0.01	0.07	0.00	0.00	0.00	0.01	-	**100.4**
RF64-26r	65.5	32.7	1.48	0.07	0.16	0.07	0.00	0.01	0.00	-	**100.0**
RF65-2	65.9	32.8	1.21	0.06	0.27	0.07	0.01	0.01	0.11	-	**100.4**
RJ1101-04	65.6	32.8	1.56	0.03	0.06	0.02	0.00	0.00	0.00	-	**100.1**
RJ1101-10	65.9	32.7	1.45	0.00	0.02	0.01	0.00	0.01	0.00	-	**100.1**
RJ1101-11	65.0	32.8	2.08	0.01	0.02	0.02	0.01	0.00	0.00	-	**99.9**
RJ1101-15	65.6	32.8	1.36	0.01	0.11	0.06	0.00	0.01	0.02	-	**100.0**
RJ1101-18c	65.5	32.9	1.35	0.04	0.15	0.04	0.00	0.01	0.01	-	**100.0**
RJ1101-18r	64.4	32.6	2.34	0.05	0.21	0.08	0.00	0.02	0.05	-	**99.7**
RJ1101-19	65.6	32.8	1.56	0.02	0.05	0.00	0.01	0.01	0.00	-	**100.0**
RJ1101-20	65.7	32.6	1.33	0.04	0.10	0.03	0.01	0.01	0.01	-	**99.9**
RJ1101-25	65.4	32.5	1.40	0.04	0.09	0.04	0.01	0.01	0.02	-	**99.5**
RJ1101-25c	65.7	32.6	1.24	0.03	0.10	0.04	0.00	0.02	0.00	-	**99.7**
RJ1101-26	65.5	32.6	1.41	0.04	0.15	0.05	0.01	0.00	0.00	-	**99.7**

Sample- zircon grain	ZrO_2	SiO_2	HfO_2	P_2O_5	Y_2O_3	Yb_2O_3	TiO_2	Lu_2O_3	ThO_2	UO_2	Total
RJ1101-33	66.1	32.8	1.33	0.02	0.06	0.02	0.01	0.01	0.00	-	**100.4**
RJ1101-34c	66.0	32.8	1.41	0.04	0.13	0.03	0.01	0.01	0.01	-	**100.4**
RJ1101-34r	66.0	32.7	1.32	0.03	0.07	0.02	0.01	0.00	0.01	-	**100.1**
RJ1101-42	65.6	32.7	1.38	0.09	0.16	0.04	0.00	0.01	0.03	-	**100.0**
RJ1103-12	65.8	33.0	1.31	0.03	0.09	0.02	0.00	0.00	0.01	-	**100.3**
RJ1103-14	65.5	32.9	1.38	0.04	0.18	0.06	0.01	0.00	0.01	-	**100.1**
RJ1103-15	65.8	32.9	1.46	0.02	0.06	0.03	0.00	0.01	0.01	-	**100.3**
RJ1103-16a	66.0	32.8	1.16	0.05	0.12	0.04	0.01	0.01	0.01	-	**100.1**
RJ1103-16b	65.9	32.9	1.20	0.05	0.10	0.03	0.00	0.01	0.01	-	**100.2**
RJ1103-17c	64.8	32.8	1.38	0.15	0.65	0.14	0.00	0.04	0.11	-	**100.1**
RJ1103-17r	65.6	32.9	1.40	0.04	0.09	0.03	0.01	0.01	0.02	-	**100.1**
RJ1103-19c	65.6	32.8	1.07	0.05	0.33	0.07	0.01	0.00	0.04	-	**100.0**
RJ1103-19c2	65.3	32.6	1.08	0.08	0.43	0.10	0.01	0.02	0.03	-	**99.7**
RJ1103-19r	65.7	32.8	1.57	0.02	0.08	0.03	0.00	0.00	0.00	-	**100.2**
RJ1103-20	65.6	32.8	1.44	0.03	0.07	0.01	0.01	0.01	0.02	-	**100.0**
RJ1103-22	66.0	32.8	1.43	0.03	0.07	0.01	0.00	0.00	0.01	-	**100.4**
RJ1103-22c	65.8	32.9	1.34	0.04	0.10	0.03	0.04	0.01	0.01	-	**100.3**
RJ1103-26	65.9	33.0	1.37	0.03	0.10	0.02	0.00	0.00	0.01	-	**100.4**
RJ1103-30	65.8	32.8	1.37	0.05	0.11	0.03	0.01	0.01	0.02	-	**100.2**
RJ1103-33	66.1	32.8	1.30	0.05	0.11	0.04	0.00	0.02	0.00	-	**100.5**
RJ1103-40	65.9	32.7	1.31	0.04	0.09	0.02	0.00	0.01	0.02	-	**100.0**
RJ1104-01	66.0	32.8	1.12	0.04	0.19	0.05	0.00	0.01	0.04	-	**100.2**
RJ1104-01r	64.9	32.6	1.48	0.10	0.34	0.12	0.00	0.02	0.10	-	**99.6**
RJ1104-03	65.6	32.8	1.30	0.04	0.16	0.04	0.00	0.01	0.01	-	**99.9**
RJ1104-05c	65.5	32.8	1.34	0.04	0.15	0.05	0.00	0.01	0.02	-	**99.9**
RJ1104-05r	65.5	32.8	1.42	0.08	0.21	0.09	0.00	0.01	0.06	-	**100.1**
RJ1104-08	65.7	32.6	1.29	0.03	0.10	0.03	0.00	0.02	0.02	-	**99.8**
RJ1104-14	65.6	32.8	1.45	0.05	0.09	0.03	0.00	0.00	0.02	-	**100.0**
RJ1104-17	65.6	32.8	1.47	0.04	0.07	0.02	0.00	0.00	0.01	-	**100.0**
RJ1104-18	65.7	32.6	1.08	0.07	0.21	0.06	0.01	0.00	0.02	-	**99.8**
RJ1104-20c	65.5	32.8	1.59	0.02	0.07	0.02	0.00	0.00	0.02	-	**100.0**
RJ1104-20r	64.4	32.5	1.76	0.19	0.45	0.13	0.01	0.04	0.09	-	**99.6**
RJ1104-23	65.3	32.5	1.39	0.20	0.24	0.08	0.01	0.02	0.05	-	**99.8**
RJ1104-30c	65.6	32.7	1.15	0.05	0.29	0.07	0.00	0.01	0.03	-	**99.9**
RJ1104-30r	64.8	32.5	1.54	0.13	0.34	0.09	0.00	0.01	0.18	-	**99.6**
RJ1104-33	66.1	32.8	1.28	0.05	0.11	0.03	0.00	0.00	0.01	-	**100.3**
RJ1104-36	66.2	32.8	1.09	0.05	0.13	0.04	0.00	0.01	0.02	-	**100.4**
RJ1105-01a	65.6	32.6	1.14	0.06	0.28	0.08	0.00	0.00	0.00	-	**99.8**
RJ1105-01b	65.9	32.7	1.18	0.04	0.09	0.04	0.00	0.00	0.00	-	**100.0**
RJ1105-02	65.7	32.9	1.13	0.09	0.19	0.05	0.00	0.01	0.01	-	**100.0**
RJ1105-03a	65.9	32.8	1.11	0.05	0.10	0.03	0.01	0.01	0.00	-	**100.0**
RJ1105-03b	65.6	32.8	1.12	0.04	0.17	0.05	0.01	0.01	0.01	-	**99.8**
RJ1105-04	65.9	32.7	1.25	0.03	0.08	0.03	0.01	0.02	0.00	-	**100.1**
RJ1105-05	65.7	32.5	1.06	0.06	0.15	0.05	0.00	0.01	0.01	-	**99.6**
RJ1105-06	65.9	32.7	1.10	0.04	0.12	0.03	0.01	0.00	0.02	-	**99.9**
RJ1105-09	65.5	32.5	1.09	0.07	0.19	0.06	0.00	0.02	0.00	-	**99.5**
RJ1105-11	65.9	32.7	1.09	0.08	0.21	0.07	0.02	0.01	0.00	-	**100.1**
RJ1105-15	66.1	32.7	1.11	0.04	0.09	0.03	0.00	0.01	0.00	-	**100.0**
RJ1105-17	65.7	32.6	1.17	0.17	0.25	0.09	0.00	0.02	0.00	-	**100.0**
RJ11A10-2	65.7	32.8	1.16	0.06	0.20	0.08	0.01	0.01	0.00	-	**100.0**
RJ11A10-9c	65.4	32.7	1.36	0.09	0.29	0.05	0.00	0.00	0.03	-	**99.9**
RJ11A10-9r	65.1	32.5	1.58	0.12	0.22	0.07	0.00	0.00	0.03	-	**99.7**
RJ11A10-11	64.8	32.6	1.64	0.15	0.31	0.10	0.00	0.01	0.02	-	**99.6**
RJ11A10-13c	63.5	31.9	1.30	0.48	0.89	0.23	0.01	0.04	0.26	-	**98.6**
RJ11A10-13r	65.3	32.5	1.40	0.09	0.17	0.08	0.00	0.01	0.00	-	**99.6**
RJ11A10-14c	65.0	32.2	1.55	0.15	0.17	0.05	0.00	0.02	0.01	-	**99.2**
RJ11A10-14r	65.2	32.3	1.35	0.09	0.17	0.07	0.00	0.00	0.01	-	**99.2**
RJ11A10-17	65.5	32.6	1.52	0.07	0.14	0.05	0.00	0.01	0.02	-	**99.9**

Sample- zircon grain	ZrO_2	SiO_2	HfO_2	P_2O_5	Y_2O_3	Yb_2O_3	TiO_2	Lu_2O_3	ThO_2	UO_2	Total
RJ11A10-17c	65.2	32.5	1.14	0.16	0.37	0.11	0.00	0.03	0.05	-	**99.6**
RJ11A10-17r	65.4	32.8	1.34	0.12	0.24	0.09	0.01	0.01	0.02	-	**100.1**
RJ11A10-21	65.6	32.4	1.21	0.13	0.15	0.05	0.00	0.01	0.00	-	**99.5**
RJ11A10-22	65.0	32.5	1.51	0.10	0.23	0.07	0.00	0.02	0.04	-	**99.5**
RJ11A10-26	65.1	32.4	1.40	0.10	0.26	0.08	0.01	0.02	0.00	-	**99.4**
RJ11A10-28	64.8	32.4	1.86	0.08	0.18	0.06	0.01	0.01	0.01	-	**99.4**
RJ11A10-34	65.5	32.6	1.04	0.11	0.35	0.10	0.01	0.01	0.04	-	**99.7**
RJ11A10-36	65.4	32.7	1.73	0.08	0.13	0.06	0.01	0.00	0.03	-	**100.1**
RJ11A10-36r	65.3	32.5	1.36	0.12	0.20	0.08	0.02	0.01	0.04	-	**99.6**
RJ11A11-9c	65.5	32.5	1.15	0.04	0.21	0.05	0.02	0.00	0.01	-	**99.6**
RJ11A11-9r	65.6	32.5	1.19	0.03	0.08	0.01	0.00	0.00	0.01	-	**99.5**
RJ11A11-11	65.7	32.8	1.25	0.04	0.08	0.02	0.02	0.01	0.00	-	**100.0**
RJ11A11-12	65.9	32.4	1.13	0.06	0.11	0.04	0.01	0.00	0.00	-	**99.6**
RJ11A11-13a	65.6	32.6	1.20	0.04	0.17	0.05	0.01	0.01	0.03	-	**99.8**
RJ11A11-13b	65.8	32.7	1.18	0.04	0.09	0.02	0.00	0.00	0.00	-	**99.8**
RJ11A11-14	65.6	32.8	1.21	0.05	0.11	0.02	0.01	0.02	0.00	-	**99.9**
RJ11A11-15	65.8	32.8	1.22	0.04	0.09	0.02	0.01	0.00	0.00	-	**100.0**
RJ11A11-22a	65.7	32.8	1.19	0.04	0.18	0.04	0.01	0.00	0.01	-	**100.0**
RJ11A11-22b	65.5	32.7	1.18	0.04	0.17	0.04	0.01	0.00	0.02	-	**99.7**
RJ11A11-23	66.1	32.8	1.25	0.04	0.09	0.02	0.01	0.01	0.01	-	**100.3**
RJ11A11-28	65.7	32.8	1.28	0.03	0.11	0.03	0.00	0.00	0.02	-	**99.9**
RJ11A11-35	65.9	32.9	1.24	0.06	0.18	0.04	0.01	0.00	0.03	-	**100.3**
RJ11A11-36c	66.0	32.9	1.17	0.03	0.20	0.05	0.02	0.00	0.04	-	**100.5**
RJ11A11-36r	65.9	32.7	1.23	0.06	0.12	0.04	0.01	0.01	0.02	-	**100.1**
RJ11A11-40	66.0	32.6	1.28	0.12	0.19	0.05	0.00	0.01	0.00	-	**100.2**
RJ11A14-7	65.8	32.8	1.28	0.04	0.08	0.03	0.00	0.00	0.00	-	**100.1**
RJ11A14-10	65.5	32.7	1.17	0.07	0.08	0.03	0.01	0.01	0.01	-	**99.5**
RJ11A14-14	65.9	33.0	1.45	0.01	0.05	0.01	0.00	0.01	0.00	-	**100.4**
RJ11A14-15	65.5	32.8	1.44	0.04	0.09	0.03	0.00	0.01	0.01	-	**99.9**
RJ11A14-15c1	65.4	32.7	1.53	0.09	0.18	0.07	0.00	0.01	0.00	-	**100.0**
RJ11A14-15c2	65.3	32.9	1.75	0.04	0.14	0.04	0.00	0.02	0.02	-	**100.2**
RJ11A14-16	65.8	32.8	1.31	0.02	0.06	0.02	0.00	0.01	0.00	-	**99.9**
RJ11A14-17c	65.1	32.9	1.78	0.01	0.15	0.05	0.01	0.01	0.05	-	**100.0**
RJ11A14-17r	66.1	33.0	1.33	0.01	0.04	0.00	0.00	0.02	0.01	-	**100.5**
RJ11A14-18	65.6	32.9	1.34	0.03	0.16	0.05	0.01	0.00	0.01	-	**100.1**
RJ11A14-20	65.5	32.7	1.23	0.03	0.19	0.04	0.01	0.00	0.02	-	**99.7**
RJ11A14-23	65.9	32.9	1.17	0.04	0.18	0.04	0.01	0.01	0.01	-	**100.3**
RJ11A14-25	65.8	32.9	1.22	0.04	0.16	0.04	0.01	0.00	0.02	-	**100.2**
RJ11A15-5	65.7	32.7	1.44	0.01	0.13	0.04	0.01	0.02	0.01	-	**100.0**
RJ11A15-7	65.9	32.8	1.15	0.07	0.14	0.04	0.01	0.01	0.00	-	**100.1**
RJ11A15-7r	65.8	33.0	1.48	0.00	0.05	0.01	0.00	0.01	0.02	-	**100.3**
RJ11A15-10	65.6	32.6	1.07	0.05	0.30	0.07	0.00	0.02	0.02	-	**99.8**
RJ11A15-11	65.6	32.7	1.46	0.02	0.07	0.03	0.00	0.00	0.01	-	**99.9**
RJ11A15-14c	65.9	32.9	1.46	0.01	0.06	0.03	0.00	0.01	0.02	-	**100.3**
RJ11A15-14r	65.8	32.8	1.37	0.00	0.06	0.02	0.01	0.01	0.01	-	**100.0**
RJ11A15-15c	66.0	32.7	1.45	0.00	0.04	0.01	0.01	0.01	0.00	-	**100.2**
RJ11A15-15r	65.1	32.6	1.43	0.02	0.22	0.07	0.00	0.01	0.02	-	**99.5**
RJ11A15-16	65.5	32.7	1.72	0.02	0.08	0.02	0.00	0.00	0.02	-	**100.0**
RJ11A15-19a	65.5	32.8	1.46	0.02	0.19	0.06	0.00	0.00	0.00	-	**100.0**
RJ11A15-19b	65.7	32.6	1.40	0.03	0.09	0.02	0.01	0.02	0.01	-	**99.9**
RJ11A15-22c	65.7	32.7	1.42	0.04	0.08	0.03	0.00	0.00	0.01	-	**100.0**
RJ11A15-22r	65.5	32.6	1.35	0.02	0.09	0.02	0.00	0.00	0.00	-	**99.5**
RJ11A15-24c	64.6	32.5	2.23	0.09	0.13	0.07	0.01	0.01	0.00	-	**99.6**
RJ11A15-24r	65.8	32.6	1.35	0.01	0.06	0.02	0.01	0.01	0.00	-	**99.9**
RJ11A15-27	66.1	33.1	1.37	0.01	0.13	0.05	0.00	0.03	0.02	-	**100.7**
RJ11A15-29	65.9	32.7	1.37	0.02	0.14	0.04	0.01	0.01	0.00	-	**100.1**
RJ11A17-1	65.9	32.8	1.40	0.01	0.11	0.01	0.01	0.01	0.01	-	**100.2**
RJ11A17-3	66.0	32.7	1.30	0.03	0.12	0.03	0.00	0.01	0.01	-	**100.2**

Sample- zircon grain	ZrO_2	SiO_2	HfO_2	P_2O_5	Y_2O_3	Yb_2O_3	TiO_2	Lu_2O_3	ThO_2	UO_2	Total
RJ11A17-6	65.5	32.7	1.41	0.02	0.13	0.06	0.01	0.01	0.00	-	**99.9**
RJ11A17-7	65.4	32.7	1.88	0.10	0.17	0.02	0.00	0.02	0.02	-	**100.3**
RJ11A17-8	65.7	32.8	1.40	0.02	0.14	0.05	0.00	0.01	0.02	-	**100.2**
RJ11A17-8r	65.6	32.7	1.41	0.00	0.06	0.00	0.01	0.00	0.00	-	**99.8**
RJ11A17-9c	65.1	32.6	1.73	0.24	0.24	0.08	0.00	0.01	0.02	-	**100.1**
RJ11A17-9r	66.1	32.9	1.30	0.05	0.09	0.03	0.00	0.00	0.01	-	**100.5**
RJ11A17-10c	66.1	32.9	1.27	0.01	0.06	0.02	0.01	0.01	0.00	-	**100.4**
RJ11A17-10r	65.8	32.8	1.52	0.00	0.04	0.02	0.01	0.01	0.00	-	**100.2**
RJ11A17-10r2	65.9	33.0	1.43	0.00	0.03	0.01	0.00	0.00	0.00	-	**100.3**
RJ11A17-11	65.8	32.8	1.44	0.02	0.07	0.02	0.00	0.01	0.01	-	**100.2**
RJ11A17-12	65.6	32.8	1.39	0.02	0.14	0.05	0.00	0.01	0.01	-	**100.0**
RJ11A17-13	65.7	32.9	1.48	0.01	0.15	0.06	0.01	0.02	0.00	-	**100.4**
RJ11A17-13c	65.8	32.8	1.29	0.10	0.13	0.05	0.00	0.02	0.01	-	**100.2**
RJ11A17-14	66.2	32.9	1.03	0.02	0.04	0.01	0.01	0.00	0.01	-	**100.2**
RJ11A17-16	65.2	32.8	1.70	0.06	0.24	0.07	0.00	0.01	0.05	-	**100.2**
RJ11A17-16r	65.6	32.7	1.38	0.00	0.05	0.01	0.01	0.00	0.01	-	**99.7**
RJ11A17-17c	65.7	32.7	1.45	0.05	0.12	0.05	0.01	0.00	0.00	-	**100.2**
RJ11A17-17r	65.9	32.9	1.42	0.02	0.08	0.02	0.00	0.01	0.00	-	**100.4**
RJ11A17-18	66.0	32.8	1.42	0.03	0.08	0.04	0.00	0.01	0.02	-	**100.4**
RJ11A17-22	65.6	32.7	1.86	0.07	0.08	0.04	0.01	0.00	0.01	-	**100.3**
RJ11A17-26	65.7	32.6	1.44	0.02	0.11	0.03	0.01	0.00	0.02	-	**99.9**
RJ11A18-4	65.8	32.6	1.11	0.04	0.21	0.05	0.01	0.01	0.00	-	**99.7**
RJ11A18-7	65.8	32.6	1.18	0.04	0.15	0.04	0.01	0.01	0.01	-	**99.8**
RJ11A18-9	66.0	32.7	1.16	0.03	0.07	0.02	0.01	0.00	0.00	-	**100.0**
RJ11A18-9r	65.7	32.8	1.42	0.02	0.06	0.02	0.01	0.00	0.01	-	**100.0**
RJ11A18-9r	65.8	32.9	1.44	0.00	0.05	0.01	0.00	0.00	0.01	-	**100.1**
RJ11A18-10	66.0	32.9	1.07	0.04	0.21	0.04	0.00	0.01	0.01	-	**100.3**
RJ11A18-11	66.0	32.7	1.10	0.03	0.18	0.06	0.01	0.01	0.01	-	**100.2**
RJ11A18-13c	66.0	32.8	1.11	0.04	0.17	0.04	0.00	0.00	0.00	-	**100.1**
RJ11A18-13r	66.0	32.7	1.22	0.03	0.09	0.02	0.01	0.00	0.00	-	**100.0**
RJ11A18-14	66.0	32.8	1.28	0.05	0.06	0.02	0.00	0.01	0.00	-	**100.1**
RJ11A18-19	66.1	32.7	1.16	0.05	0.09	0.02	0.01	0.01	0.00	-	**100.1**
RJ11A18-26	66.0	32.8	1.21	0.03	0.05	0.01	0.00	0.01	0.02	-	**100.2**
RJ11A18-29	66.0	32.9	1.21	0.04	0.16	0.04	0.00	0.02	0.00	-	**100.3**
RJ11A20-10(x2)	66.2	32.8	1.14	0.05	0.16	0.03	0.01	0.01	0.02	-	**100.3**
RJ11A20-12	65.9	32.8	1.14	0.07	0.27	0.06	0.00	0.01	0.02	-	**100.2**
RJ11A20-14c	66.0	32.6	1.29	0.04	0.11	0.02	0.01	0.00	0.01	-	**100.1**
RJ11A20-14r	65.9	32.9	1.38	0.04	0.15	0.04	0.01	0.01	0.06	-	**100.5**
RJ11A20-15	66.1	32.9	1.23	0.05	0.10	0.03	0.00	0.01	0.01	-	**100.5**
RJ11A20-17	65.9	32.6	1.08	0.04	0.17	0.05	0.00	0.01	0.01	-	**99.9**
RJ11A20-18	65.7	33.0	1.14	0.06	0.35	0.08	0.02	0.01	0.03	-	**100.4**
RJ11A20-19	65.8	32.9	1.44	0.03	0.10	0.04	0.01	0.01	0.05	-	**100.4**
RJ11A20-20	66.1	32.9	1.17	0.05	0.11	0.04	0.01	0.01	0.01	-	**100.4**
RJ11A20-24	66.2	33.0	1.26	0.13	0.15	0.06	0.01	0.00	0.00	-	**100.8**
RJ11A20-35c	66.1	32.7	1.06	0.11	0.22	0.05	0.00	0.00	0.01	-	**100.2**
RJ11A20-35r	66.1	32.7	1.08	0.08	0.20	0.05	0.01	0.01	0.01	-	**100.2**
RJ11A5-02	65.9	33.0	1.17	0.06	0.20	0.05	0.00	0.01	0.02	-	**100.4**
RJ11A5-03	65.8	32.8	1.30	0.10	0.13	0.05	0.01	0.00	0.00	-	**100.2**
RJ11A5-05	65.8	32.8	0.84	0.08	0.39	0.13	0.00	0.03	0.07	-	**100.1**
RJ11A5-06	66.0	32.8	1.28	0.18	0.16	0.04	0.00	0.00	0.01	-	**100.5**
RJ11A5-07	66.0	32.7	0.98	0.02	0.14	0.05	0.00	0.00	0.08	-	**99.9**
RJ11A5-08	66.0	33.0	0.94	0.03	0.21	0.07	0.00	0.00	0.02	-	**100.2**
RJ11A5-16	65.7	32.5	1.24	0.07	0.24	0.07	0.00	0.01	0.04	-	**99.9**
RJ11A5-17	65.4	32.7	1.67	0.11	0.09	0.05	0.00	0.01	0.00	-	**100.1**
RJ11A5-18a	65.2	32.6	1.53	0.17	0.29	0.05	0.00	0.02	0.04	-	**99.9**
RJ11A5-18b	65.4	32.7	1.81	0.08	0.09	0.05	0.00	0.01	0.00	-	**100.1**
RJ11A5-19	64.9	32.4	1.82	0.38	0.12	0.07	0.00	0.01	0.00	-	**99.7**
RJ11A5-26	65.1	32.5	1.38	0.35	0.46	0.12	0.02	0.03	0.04	-	**99.9**

Sample- zircon grain	ZrO_2	SiO_2	HfO_2	P_2O_5	Y_2O_3	Yb_2O_3	TiO_2	Lu_2O_3	ThO_2	UO_2	Total
RJ11A7-07	65.2	32.6	1.51	0.06	0.17	0.05	0.01	0.01	0.00	-	**99.6**
RJ11A7-10r	65.5	32.9	2.00	0.00	0.00	0.01	0.00	0.00	0.00	-	**100.3**
RJ11A7-12c	65.4	32.8	1.62	0.00	0.05	0.03	0.00	0.02	0.00	-	**99.9**
RJ11A7-12r	65.5	32.9	1.74	0.01	0.03	0.00	0.00	0.00	0.01	-	**100.2**
RJ11A7-13	66.0	32.8	1.07	0.00	0.04	0.01	0.00	0.01	0.01	-	**99.9**
RJ11A7-14c	65.9	32.8	1.18	0.03	0.06	0.01	0.00	0.00	0.00	-	**100.0**
RJ11A7-14r	65.2	32.6	1.84	0.00	0.04	0.02	0.01	0.01	0.00	-	**99.7**
RJ11A7-15a	65.4	32.7	1.72	0.01	0.05	0.01	0.00	0.00	0.02	-	**99.9**
RJ11A7-15b	65.5	32.7	1.76	0.01	0.04	0.03	0.00	0.01	0.00	-	**100.0**
RJ11A7-21	65.7	32.8	1.43	0.02	0.09	0.04	0.00	0.00	0.03	-	**100.0**
RJ11A7-22c	65.6	32.9	1.38	0.02	0.04	0.02	0.00	0.00	0.00	-	**100.0**
RJ11A7-22r	65.1	32.6	1.87	0.01	0.04	0.03	0.00	0.01	0.00	-	**99.7**
RJ11A7-28c	64.9	32.6	1.74	0.11	0.36	0.12	0.00	0.00	0.04	-	**99.8**
RJ11A7-28r	65.0	32.6	1.85	0.01	0.06	0.00	0.00	0.03	0.02	-	**99.6**
RJ11A7-31c	64.4	32.5	1.94	0.35	0.47	0.10	0.00	0.01	0.03	-	**99.8**
RJ11A7-31r	65.4	32.7	1.70	0.00	0.03	0.01	0.00	0.01	0.01	-	**99.9**
RJ11A7-34	66.0	33.0	1.70	0.00	0.02	0.00	0.00	0.00	0.00	-	**100.8**
RJ11A7-41	65.7	32.8	1.71	0.00	0.04	0.01	0.00	0.00	0.02	-	**100.3**
RJ11A7-41c	65.5	32.8	1.64	0.00	0.05	0.08	0.01	0.00	0.00	-	**100.0**
SP80-1a	66.0	32.7	1.18	0.05	0.10	0.05	0.00	0.01	0.01	-	**100.0**
SP80-1b	65.8	32.8	1.32	0.02	0.07	0.01	0.01	0.01	0.02	-	**100.2**
SP80-2a	65.9	32.8	1.31	0.05	0.17	0.02	0.01	0.02	0.02	-	**100.3**
SP80-2b	66.0	32.7	1.34	0.04	0.05	0.03	0.01	0.01	0.02	-	**100.2**
SP80-3c	66.0	32.8	1.23	0.04	0.08	0.02	0.01	0.00	0.02	-	**100.1**
SP80-3r	66.1	32.8	1.29	0.04	0.08	0.02	0.00	0.02	0.00	-	**100.3**
SP80-4	65.9	32.8	1.37	0.05	0.08	0.02	0.00	0.01	0.01	-	**100.2**
SP80-5	66.2	32.8	1.38	0.04	0.06	0.02	0.00	0.01	0.01	-	**100.5**
SP80-8	66.0	32.9	1.31	0.03	0.07	0.02	0.00	0.01	0.00	-	**100.3**
SP80-10	66.0	33.0	1.30	0.02	0.03	0.01	0.01	0.00	0.02	-	**100.4**
SP80-14	66.1	32.9	1.29	0.04	0.08	0.03	0.01	0.01	0.00	-	**100.6**
Z27-4	65.8	32.9	1.32	0.05	0.10	0.04	0.01	0.02	0.00	-	**100.2**
Z27-7	66.1	32.8	1.28	0.02	0.04	0.03	0.00	0.02	0.01	-	**100.2**
Z27-11	66.0	32.6	1.14	0.08	0.14	0.06	0.00	0.00	0.01	-	**100.1**
Z27-11c	65.8	32.7	1.17	0.07	0.20	0.05	0.00	0.01	0.03	-	**100.1**
Z27-13c	65.9	32.9	1.17	0.06	0.24	0.07	0.01	0.01	0.03	-	**100.3**
Z27-13r	66.0	32.8	1.13	0.06	0.14	0.05	0.00	0.01	0.02	-	**100.2**
Z27-14	66.2	32.9	1.16	0.05	0.11	0.04	0.00	0.00	0.01	-	**100.4**
Z27-15	65.7	32.8	1.29	0.07	0.28	0.06	0.01	0.02	0.03	-	**100.3**
Z27-16	66.1	32.9	1.23	0.04	0.13	0.03	0.00	0.01	0.00	-	**100.4**
Z27-17	65.9	32.5	1.10	0.05	0.23	0.06	0.01	0.02	0.01	-	**99.9**
Z27-18	65.8	32.5	1.13	0.05	0.22	0.06	0.00	0.01	0.02	-	**99.9**
Z27-22	66.2	33.0	1.29	0.03	0.07	0.00	0.01	0.01	0.01	-	**100.6**
Z27-32	65.8	32.6	1.06	0.13	0.41	0.13	0.00	0.02	0.04	-	**100.2**
Z27-33	66.2	32.8	1.16	0.07	0.14	0.04	0.00	0.01	0.01	-	**100.3**
Z27-34	65.9	32.6	1.14	0.04	0.21	0.06	0.00	0.00	0.02	-	**100.0**
Z27-35	66.1	33.0	1.10	0.06	0.11	0.03	0.01	0.02	0.00	-	**100.4**
ZN122-15	66.1	32.8	1.28	0.03	0.07	0.02	0.00	0.00	0.02	-	**100.2**
ZN122-16	66.0	32.4	1.22	0.04	0.08	0.01	0.01	0.00	0.03	-	**99.7**
ZN122-17	66.3	32.9	1.18	0.05	0.09	0.01	0.01	0.01	0.02	-	**100.6**
ZN122-18c	66.0	32.9	1.24	0.03	0.18	0.04	0.00	0.01	0.02	-	**100.4**
ZN122-18r	65.8	32.9	1.35	0.02	0.05	0.02	0.00	0.01	0.01	-	**100.1**
ZN122-19	66.0	32.7	1.33	0.05	0.06	0.03	0.01	0.01	0.01	-	**100.1**
ZN122-22	66.0	32.8	1.23	0.04	0.10	0.03	0.00	0.00	0.01	-	**100.1**
ZN122-25	66.2	32.8	1.20	0.06	0.08	0.03	0.00	0.00	0.01	-	**100.3**
		MIN	0.82								
		MAX	2.34								
		Average	1.32								
		1σ	0.22								

Sample- zircon grain	ZrO_2	SiO_2	HfO_2	P_2O_5	Y_2O_3	Yb_2O_3	TiO_2	Lu_2O_3	ThO_2	UO_2	Total
		2σ	0.45								

Appendix 2.9 Major and trace element composition of zircon standard 'Laura' determined by EPMA

Laura	ZrO_2	SiO_2	HfO_2	P_2O_5	Y_2O_3	Yb_2O_3	TiO_2	Lu_2O_3	ThO_2	Total
	65.83	32.94	1.33	0.00	0.010	0.003	0.000	0.000	0.020	**100.1**
	65.66	32.69	1.30	0.00	0.009	0.000	0.002	0.000	0.000	**99.7**
	65.68	32.76	1.29	0.00	0.004	0.000	0.003	0.000	0.013	**99.8**
	65.93	32.96	1.29	0.00	0.005	0.000	0.000	0.000	0.008	**100.2**
	65.57	32.67	1.29	0.00	0.008	0.003	0.000	0.000	0.007	**99.5**
	65.87	32.86	1.29	0.00	0.010	0.006	0.008	0.002	0.000	**100.0**
	65.58	32.79	1.32	0.00	0.003	0.003	0.001	0.000	0.003	**99.7**
	65.94	32.86	1.31	0.00	0.005	0.000	0.000	0.002	0.007	**100.1**
	65.78	32.80	1.34	0.00	0.000	0.005	0.011	0.000	0.000	**99.9**
	66.15	32.90	1.31	0.00	0.000	0.000	0.003	0.000	0.008	**100.4**
	65.80	32.88	1.33	0.00	0.004	0.000	0.000	0.000	0.000	**100.0**
	65.87	32.77	1.33	0.00	0.007	0.000	0.009	0.000	0.009	**100.0**
	65.84	32.61	1.33	0.00	0.000	0.000	0.014	0.013	0.000	**99.8**
	66.02	32.91	1.31	0.00	0.000	0.000	0.011	0.011	0.015	**100.3**
	65.90	32.65	1.34	0.00	0.005	0.000	0.003	0.000	0.016	**99.9**
	66.28	33.01	1.27	0.00	0.012	0.006	0.005	0.006	0.000	**100.6**
	65.90	32.89	1.34	0.00	0.007	0.002	0.000	0.000	0.009	**100.1**
	66.32	33.08	1.28	0.00	0.007	0.000	0.008	0.000	0.007	**100.7**
	66.10	32.79	1.28	0.00	0.010	0.008	0.000	0.000	0.008	**100.2**
	65.94	32.95	1.31	0.00	0.007	0.000	0.010	0.000	0.000	**100.2**
	66.10	32.90	1.26	0.00	0.007	0.000	0.020	0.005	0.005	**100.3**
	66.08	32.81	1.29	0.00	0.012	0.000	0.007	0.000	0.000	**100.2**
	66.23	33.03	1.28	0.00	0.011	0.006	0.000	0.000	0.000	**100.6**
	65.87	32.79	1.32	0.00	0.005	0.003	-	0.000	0.001	**100.0**
	65.94	32.87	1.33	0.00	0.000	0.011	-	0.001	0.003	**100.2**
	65.84	32.74	1.27	0.00	0.011	0.000	-	0.001	0.010	**99.9**
	66.37	32.89	1.39	0.00	0.009	0.000	-	0.000	0.001	**100.7**
	65.99	32.74	1.39	0.00	0.004	0.003	-	0.000	0.024	**100.2**
	66.00	32.83	1.38	0.00	0.004	0.009	-	0.000	0.011	**100.2**
	66.00	32.89	1.33	0.00	0.005	0.013	-	0.013	0.000	**100.3**
	65.89	32.75	1.30	0.00	0.009	0.000	-	0.000	0.000	**99.9**
	65.84	32.84	1.30	0.00	0.010	0.004	-	0.000	0.009	**100.0**
Average	65.94	32.84	1.31	0.00	0.006	0.003	0.005	0.002	0.006	**100.1**
2σ	0.39	0.22	0.07	0.00	0.007	0.007	0.011	0.008	0.013	**0.6**

Appendix 2.10 Compiled zircon isotope data for all analysed zircon grains and cores

Formation	Sample	Grain/spot	$\delta^{18}O_{(VSMOW)}$ (‰)	±2σ	$^{176}Hf/^{177}Hf$	±2σ	$^{176}Lu/^{177}Hf$	±2σ	$^{206}Pb/^{238}U$ age (Ma)	±2σ	$\varepsilon Hf_{(T)}$	±2σ	T(NC) (Ma)
Pluton Tocota	RJ11A18	4	6.15	0.30	0.282699	0.000028	0.001002	0.000020	278.7	5.5	3.0	1.0	
(Colangüil Batholith)		7	5.97	0.30									
		9c	6.04	0.30									
		9r	5.93	0.30	0.282675	0.000025	0.000502	0.000009	282.0	6.1	2.3	0.9	
		10	5.90	0.30									
		11	6.09	0.30	0.282689	0.000027	0.000885	0.000044	270.8	5.7	2.5	1.0	
		13c	6.06	0.30									
		13r	6.14	0.30	0.282682	0.000023	0.000435	0.000003	282.6	5.8	2.6	0.8	
		14a	6.01	0.30	0.282691	0.000026	0.000649	0.000033	278.1	7.5	2.7	0.9	
		14b	5.88	0.30									
		19	6.26	0.30	0.282672	0.000026	0.000526	0.000011	283.5	5.9	2.2	0.9	
		26	6.23	0.30									
		29	6.27	0.30	0.282657	0.000026	0.000873	0.000058	278.8	6.3	1.5	0.9	
		32	6.46	0.22									
		35	6.36	0.22									
		38	5.99	0.22									
Choiyoi Group	RJ11A20	10	6.16	0.29									
		12	6.46	0.29	0.282629	0.000026	0.001194	0.000015	268.1	5.7	0.2	0.9	
		14c	6.42	0.29	0.282577	0.000027	0.001246	0.000068	268.3	6.0	-1.6	1.0	
		14r	6.32	0.29									
		15	6.68	0.29	0.282578	0.000027	0.000723	0.000009	277.5	6.1	-1.3	1.0	
		17	6.41	0.29	0.282660	0.000034	0.002143	0.000044	269.6*	7.0*	1.2	1.2	
		18a	6.58	0.29	0.282595	0.000040	0.001919	0.000275	270.7	5.9	-1.1	1.4	
		18b	6.43	0.29									
		19	7.16	0.29									
		20	5.53	0.29	0.282637	0.000028	0.001221	0.000050	265.5	6.0	0.5	1.0	
		24	6.38	0.29									
		35c	5.75	0.29									
		35r							266.2	6.3			
Choiyoi Group	MQ39	13	4.92	0.29	0.282590	0.000033	0.001013	0.000090	270.9	7.6	-1.0	1.2	
		21	4.59	0.29	0.282639	0.000023	0.000997	0.000018	269.3	7.3	0.6	0.8	

Formation	Sample	Grain/spot	$\delta^{18}O_{(VSMOW)}$ (‰)	±2σ	$^{176}Hf/^{177}Hf$	±2σ	$^{176}Lu/^{177}Hf$	±2σ	$^{206}Pb/^{238}U$ age (Ma)	±2σ	$\varepsilon Hf_{(T)}$	±2σ	T(NC) (Ma)
		22	5.12	0.29	0.282652	0.000030	0.001507	0.000026	271.6	6.2	1.1	1.1	
		23c	6.04	0.29	0.282556	0.000028	0.001043	0.000019	273.6	6.5	-2.2	1.0	
		23r	6.12	0.29									
		24	4.93	0.29	0.282699	0.000055	0.002008	0.000137	273.5	5.8	2.7	1.9	
		25	5.17	0.22									
		26	4.91	0.29									
		28	4.75	0.29	0.282609	0.000033	0.001263	0.000021	264.3	5.7	-0.6	1.2	
		30	4.73	0.29	0.282594	0.000032	0.001386	0.000020	271.1	7.7	-1.0	1.1	
		31	6.67	0.29	0.282586	0.000033	0.001061	0.000051	273.1	7.7	-1.2	1.2	
Choiyoi Group	AM0862	1	5.09	0.44									
		6	6.25	0.44									
		9	5.56	0.44									
		10	5.85	0.44	0.282597	0.000025	0.001752	0.000026	274.7	7.5	-0.8	0.9	
		13	5.56	0.44	0.282585	0.000030	0.001634	0.000042	263.9	7.7	-1.5	1.1	
		20	7.04	0.44									
		20c			0.282560	0.000027	0.000929	0.000067	271.4	8.0	-2.1	0.9	
		20r							270.3	7.3			
		22	5.57	0.44									
		24	5.82	0.44	0.282624	0.000031	0.001305	0.000042	266.8	7.3	0.0	1.1	
		32	5.53	0.44	0.282596	0.000026	0.001265	0.000016	270.6	8.4	-0.9	0.9	
		35	5.59	0.44									
Formation Plastos Blancos (Ingaguás Supergroup)	AM0853	8	5.37	0.33	0.282717	0.000028	0.002996	0.000048	261.0*	6.0*	2.9	1.0	
		9	5.09	0.33									
		10	5.22	0.33									
		15r	4.80	0.33					263.4	5.5			
		15l	5.18	0.33	0.282698	0.000048	0.003084	0.000158	265.1	5.8	2.3	1.7	
		19	5.14	0.33	0.282761	0.000039	0.004460	0.000087	262.1	5.6	4.2	1.4	
		20c	5.39	0.33									
		20r	5.11	0.33	0.282698	0.000029	0.002630	0.000049	266.8	5.6	2.4	1.0	
		22	5.14	0.33	0.282687	0.000034	0.002704	0.000116	264.0	5.8	1.9	1.2	
		23	4.77	0.33	0.282670	0.000034	0.003325	0.000050	261.0*	6.0*	1.2	1.2	
		38			0.282677	0.000039	0.003216	0.000099	263.2	5.8	1.5	1.4	
Formation Plastos Blancos (Ingaguás Supergroup)	AM0855	2c	6.12	0.36					250.0	5.8			
		2r	5.73	0.36									

Formation	Sample	Grain/spot	$\delta^{18}O_{(VSMOW)}$ (‰)	±2σ	$^{176}Hf/^{177}Hf$	±2σ	$^{176}Lu/^{177}Hf$	±2σ	$^{206}Pb/^{238}U$ age (Ma)	±2σ	$\varepsilon Hf_{(T)}$	±2σ	T(NC) (Ma)
		3	6.16	0.36					252.0	5.8			
		4c	5.74	0.36									
		4r	5.16	0.36									
		9c	5.43	0.36					248.5	6.0			
		10	5.37	0.36									
		11	5.30	0.36					248.7	6.3			
		14	5.78	0.50									
		20	6.41	0.50									
		23r	5.61	0.50					247.0	5.6			
		23l	5.83	0.50	0.282619	0.000018	0.001324	0.000036	248.6*	5.5*	-0.6	0.6	
		30c	5.87	0.50					248.0	5.9			
		30r	5.70	0.50	0.282627	0.000022	0.001768	0.000170	248.9	6.2	-0.3	0.8	
		31	5.78	0.50	0.282619	0.000023	0.001391	0.000021	248.6*	5.5*	-0.6	0.8	
El León Unit	RJ1104	1	5.70	0.29	0.282695	0.000019	0.001268	0.000052	217.3	4.2	1.5	0.7	
(Ingaguás Supergroup)		3	5.98	0.29	0.282698	0.000017	0.001092	0.000027	222.8	4.3	1.7	0.6	
		5c	6.37	0.29									
		5r	5.90	0.29									
		8	6.01	0.29	0.282672	0.000030	0.001333	0.000051	218.2	6.2	0.7	1.1	
		14	6.08	0.29	0.282706	0.000017	0.001267	0.000088	217.2	4.9	1.9	0.6	
		17	6.09	0.29									
		18	6.13	0.29	0.282697	0.000017	0.001249	0.000055	223.2	4.5	1.7	0.6	
		20c	6.01	0.29									
		20r	5.78	0.29	0.282684	0.000016	0.000921	0.000007	224.9	4.2	1.3	0.6	
		23	6.07	0.29	0.282706	0.000018	0.001405	0.000077	230.0	5.0	2.1	0.6	
		30c	5.95	0.29									
		30r	5.99	0.29									
		33	6.15	0.29									
		36	6.38	0.29	0.282725	0.000030	0.001843	0.000085	222.1	6.1	2.5	1.0	
Cogotí Supergroup	AM0812	10	5.94	0.42					72.2	1.9			
		11	5.32	0.36					74.5	2.5			
		14	5.30	0.36	0.282997	0.000024	0.001873	0.000056	73.7	2.7	9.0	0.8	336
		15	5.62	0.36									
		16	5.36	0.36	0.283007	0.000020	0.000952	0.000026	72.2	4.2	9.4	0.7	311
		19	5.85	0.36	0.283000	0.000030	0.001355	0.000015	76.2	3.1	9.2	1.1	324

Formation	Sample	Grain/spot	$\delta^{18}O_{(VSMOW)}$ (‰)	±2σ	$^{176}Hf/^{177}Hf$	±2σ	$^{176}Lu/^{177}Hf$	±2σ	$^{206}Pb/^{238}U$ age (Ma)	±2σ	$\varepsilon Hf_{(T)}$	±2σ	T(NC) (Ma)
		21	5.97	0.36	0.283001	0.000020	0.001286	0.000114	71.1	10.1	9.2	0.7	325
		22	5.65	0.36	0.283000	0.000020	0.000913	0.000023	71.7	1.9	9.2	0.7	325
		23	5.53	0.36	0.282998	0.000027	0.002051	0.000035	72.5	2.0	9.0	1.0	335
		26	5.34	0.36	0.282996	0.000023	0.000653	0.000047	73.4	3.2	9.0	0.8	335
		27	5.41	0.36									
		38	5.23	0.50	0.282987	0.000027	0.001308	0.000062	73.6	2.2	8.7	1.0	356
		40	5.68	0.50	0.283020	0.000026	0.001794	0.000246	71.9	2.0	9.8	0.9	283
Cogotí Supergroup	AM0823	11	5.40	0.33	0.282997	0.000021	0.000742	0.000003	70.4	1.6	9.0	0.7	334
		12	5.24	0.33	0.282981	0.000026	0.001609	0.000072	70.9	2.0	8.4	0.9	372
		13	5.95	0.33									
		19	5.46	0.33					68.3	1.8			
		20	6.13	0.33									
		21	5.72	0.50									
		23	5.58	0.50					71.3	2.5			
		25	5.15	0.50									
		32	5.67	0.50					70.4	2.7			
		35	5.73	0.50					69.9	1.7			
		38	6.05	0.50					69.8	1.5			
Cogotí Supergroup	AM0824	14	5.87	0.42									
		15	5.59	0.42	0.282987	0.000022	0.000532	0.000011	64.6	2.0	8.6	0.8	359
		16	5.56	0.42	0.282994	0.000024	0.000954	0.000019	63.8	2.0	8.8	0.9	345
		17	5.07	0.42									
		18	5.29	0.42	0.282978	0.000022	0.001171	0.000071	64.5	1.8	8.2	0.8	383
		19	5.23	0.42									
		20	5.90	0.42	0.282988	0.000022	0.000921	0.000019	65.4	1.7	8.6	0.8	359
		21	5.82	0.42	0.282988	0.000023	0.000535	0.000008	66.1	1.7	8.6	0.8	356
		22	5.35	0.42	0.282973	0.000028	0.001750	0.000049	64.9	1.5	8.0	1.0	395
		23	5.55	0.42	0.282964	0.000020	0.000907	0.000021	64.8	1.8	7.7	0.7	414
		44	5.45	0.50									
		47	5.28	0.50	0.282963	0.000027	0.000901	0.000007	64.9	1.7	7.7	1.0	416
		48	5.84	0.50									
Cogotí Supergroup	AM0806	1c	5.32	0.42									
		1r	5.43	0.42									
		14	5.60	0.42									

Formation	Sample	Grain/spot	$\delta^{18}O_{(VSMOW)}$ (‰)	±2σ	$^{176}Hf/^{177}Hf$	±2σ	$^{176}Lu/^{177}Hf$	±2σ	$^{206}Pb/^{238}U$ age (Ma)	±2σ	$\varepsilon Hf_{(T)}$	±2σ	T(NC) (Ma)
		15	5.45	0.42									
		8	5.90	0.42	0.282995	0.000020	0.000559	0.000019	65.7	1.6	8.8	0.7	342
		9	5.71	0.42									
		10c	5.55	0.42									
		10r	5.41	0.42									
		11	5.74	0.42	0.282979	0.000024	0.000697	0.000057	65.9	1.8	8.3	0.9	379
		12	5.32	0.42	0.283011	0.000019	0.000998	0.000035	65.4	1.7	9.4	0.7	304
		13	5.80	0.42	0.282980	0.000021	0.000518	0.000017	70.2	1.7	8.4	0.7	373
		16	5.56	0.42									
		18	6.04	0.42	0.283015	0.000018	0.000757	0.000031	63.7	1.7	9.5	0.7	295
		31	5.13	0.50	0.282996	0.000023	0.001210	0.000043	65.2	1.5	8.9	0.8	339
		34	5.31	0.50	0.283007	0.000023	0.000747	0.000013	62.7	1.9	9.2	0.8	314
		37	5.12	0.50	0.282990	0.000022	0.000630	0.000003	63.3	1.8	8.6	0.8	354
Cogotí Supergroup	RJ1103	12	5.78	0.29									
		14	5.98	0.29	0.283002	0.000021	0.001796	0.000075	64.4	2.1	9.0	0.7	329
		15	5.47	0.29									
		16	5.80	0.29					64.0	1.8			
		17c	5.25	0.29					70.4	1.4			
		17r	5.59	0.29	0.283015	0.000015	0.000605	0.000004	64.3	1.8	9.5	0.5	295
		19c	5.72	0.29									
		19r	5.47	0.29	0.282996	0.000021	0.001283	0.000028	66.2	1.5	8.9	0.7	341
		20	5.58	0.29									
		22	5.81	0.29	0.282991	0.000018	0.000740	0.000012	64.6	1.4	8.7	0.6	352
		26	5.81	0.29	0.282993	0.000023	0.000614	0.000002	64.0	1.3	8.7	0.8	347
		30	5.40	0.29					63.8	1.7			
		33	5.72	0.22									
		40	5.72	0.22	0.282991	0.000020	0.000678	0.000004	64.0	1.6	8.7	0.7	352
Cogotí Supergroup	AM0826	1	4.97	0.36	0.282999	0.000018	0.000720	0.000009	65.1	1.6	9.0	0.6	333
		5	5.36	0.36									
		14c	5.33	0.36									
		14r	5.13	0.36	0.282980	0.000021	0.000530	0.000015	64.2*	0.7*	8.3	0.7	376
		17c	5.36	0.36	0.282997	0.000020	0.001217	0.000063	64.2*	0.7*	8.9	0.7	339
		17r	5.55	0.36									
		19	5.53	0.36	0.282998	0.000022	0.000628	0.000010	63.4	1.8	8.9	0.8	335

Formation	Sample	Grain/spot	$\delta^{18}O_{(VSMOW)}$ (‰)	±2σ	$^{176}Hf/^{177}Hf$	±2σ	$^{176}Lu/^{177}Hf$	±2σ	$^{206}Pb/^{238}U$ age (Ma)	±2σ	$\varepsilon Hf_{(T)}$	±2σ	T(NC) (Ma)
		23	5.21	0.36									
		25	5.45	0.36	0.282986	0.000022	0.000764	0.000087	63.6	1.5	8.5	0.8	363
		27	5.62	0.36	0.282975	0.000022	0.000846	0.000003	63.8	1.5	8.1	0.8	388
		32	5.48	0.50	0.282982	0.000020	0.000703	0.000087	66.2	2.4	8.4	0.7	370
		34	5.53	0.50									
		35	5.66	0.50	0.283000	0.000021	0.000833	0.000019	65.4	1.5	9.0	0.7	330
		38	5.39	0.50									
Los Elquinos Formation	AM0890	1	5.91	0.44	0.282990	0.000021	0.001049	0.000029	65.1	1.6	8.7	0.8	354
		4	4.90	0.44	0.283013	0.000023	0.000803	0.000024	58.7	1.4	9.3	0.8	303
Cogotí Supergroup	AM0822	7	5.35	0.44									
		10	5.46	0.44	0.282998	0.000035	0.002707	0.000124	56.0	1.5	8.7	1.2	345
		11	5.51	0.44									
		12	5.31	0.44	0.283015	0.000042	0.005082	0.000197	55.9	1.5	9.2	1.5	310
		14	5.50	0.44	0.283051	0.000044	0.007901	0.000224	58.3	1.5	10.4	1.5	234
		15	5.25	0.44	0.282985	0.000046	0.004547	0.000189	59.2	1.4	8.2	1.6	380
		16	5.65	0.44	0.282974	0.000034	0.003398	0.000043	57.3	1.5	7.8	1.2	402
		19	5.38	0.44	0.282987	0.000036	0.004180	0.000051	56.7	1.5	8.2	1.3	374
		21	5.25	0.44									
Cogotí Supergroup	AM0815	*1*	*4.96*	*0.33*	*0.283012*	*0.000020*	*0.001096*	*0.000020*	*67.3*	*1.7*	*9.5*	*0.7*	*302*
		9	*5.09*	*0.33*	*0.283001*	*0.000016*	*0.001316*	*0.000064*	*68.6*	*2.2*	*9.1*	*0.6*	*327*
		10	5.57	0.33	0.283015	0.000026	0.001550	0.000034	57.9	2.1	9.4	0.9	301
		12	*5.24*	*0.33*	*0.283008*	*0.000024*	*0.001281*	*0.000022*	*64.1*	*1.5*	*9.3*	*0.8*	*312*
		14	*5.94*	*0.33*	*0.282995*	*0.000015*	*0.000598*	*0.000015*	*63.3*	*1.9*	*8.8*	*0.5*	*343*
		19	5.77	0.50	0.283025	0.000022	0.001257	0.000093	53.4	1.5	9.6	0.8	280
		21	5.48	0.50	0.283029	0.000021	0.000974	0.000030	54.7	1.6	9.8	0.8	269
		24a	6.08	0.50	0.283009	0.000021	0.000730	0.000015	55.3	1.7	9.1	0.8	316
		24b							57.1	2.1			
		25	5.75	0.50	0.283004	0.000022	0.000977	0.000024	54.3	1.7	8.9	0.8	328
		34	5.79	0.50	0.283015	0.000016	0.000899	0.000023	55.0*	1.7*	9.3	0.6	301
Cogotí Supergroup	AM0816	1c			0.283019	0.000020	0.000845	0.000037	54.0	2.1	9.5	0.7	292
		1r	5.41	0.33					55.4	2.2			
		5	5.78	0.33	0.283001	0.000019	0.001029	0.000019	54.1*	0.8*	8.8	0.7	335
		9	5.69	0.33	0.283015	0.000024	0.000909	0.000016	53.3	1.8	9.3	0.8	302
		10	5.66	0.33	0.283021	0.000022	0.000987	0.000041	54.3	2.2	9.5	0.8	288

Formation	Sample	Grain/spot	$\delta^{18}O_{(VSMOW)}$ (‰)	±2σ	$^{176}Hf/^{177}Hf$	±2σ	$^{176}Lu/^{177}Hf$	±2σ	$^{206}Pb/^{238}U$ age (Ma)	±2σ	$\varepsilon Hf_{(T)}$	±2σ	T(NC) (Ma)
		11	5.27	0.33	0.282984	0.000021	0.000807	0.000016	55.0	2.2	8.2	0.8	375
		17	5.98	0.50	0.283003	0.000022	0.001173	0.000017	55.1	2.0	8.9	0.8	330
		28	6.03	0.50	0.283025	0.000020	0.001025	0.000031	54.8	1.9	9.7	0.7	278
		32	6.00	0.50	0.283036	0.000022	0.000795	0.000028	54.0	1.7	10.0	0.8	254
		38	*5.75*	*0.50*	*0.283007*	*0.000021*	*0.001628*	*0.000079*	*68.6*	*1.8*	*9.3*	*0.7*	*315*
Tierras Blancas Caldera	RJ1105	1	5.73	0.29	0.283016	0.000019	0.001929	0.000104	39.1	1.6	9.0	0.7	310
		2	5.67	0.29	0.283021	0.000015	0.000788	0.000023	40.4	2.1	9.2	0.5	297
		3	5.45	0.29	0.283004	0.000021	0.001593	0.000053	40.3	1.5	8.6	0.7	337
		4	5.29	0.29	0.283026	0.000024	0.000601	0.000007	43.1	1.6	9.5	0.8	283
		5	5.30	0.29	0.283004	0.000021	0.001718	0.000038	39.8	1.4	8.6	0.8	337
		6	5.50	0.29	0.283021	0.000026	0.001074	0.000030	41.5	2.0	9.3	0.9	295
		9	5.67	0.29									
		11	5.32	0.22	0.283035	0.000028	0.002293	0.000136	39.6	1.4	9.7	1.0	266
		15	5.51	0.22									
		17	5.48	0.22	0.283045	0.000025	0.001364	0.000079	38.7	1.9	10.0	0.9	242
Cogotí Supergroup	RJ1101	4	5.43	0.29	0.283026	0.000017	0.000616	0.000023	37.2	0.9	9.3	0.6	286
		10	5.53	0.29	0.283039	0.000021	0.001070	0.000068	39.3	1.4	9.8	0.7	256
		11	5.51	0.29	0.283036	0.000020	0.000723	0.000037	39.9	2.0	9.7	0.7	262
		15	5.51	0.29	0.283045	0.000018	0.001016	0.000011	40.2	1.1	10.1	0.6	241
		18c	5.36	0.29	0.283067	0.000022	0.001106	0.000014	39.4	1.2	10.8	0.8	190
		18r	5.87	0.29	0.283048	0.000017	0.000473	0.000017	38.9*	1.0*	10.1	0.6	235
		19	5.74	0.29									
		20	5.50	0.29									
		25	5.39	0.29	0.283060	0.000022	0.001362	0.000030	39.3	1.3	10.6	0.8	207
		26	5.58	0.29	0.283041	0.000017	0.001530	0.000037	38.2	0.9	9.9	0.6	252
		33	5.38	0.29									
		34c	5.59	0.29									
		34r	5.54	0.29	0.283040	0.000024	0.001181	0.000159	40.5	1.6	9.9	0.8	254
		42	5.31	0.29									
Botacoma Unit	AM0867	5	5.49	0.44	0.282817	0.000018	0.000979	0.000066	36.3	1.2	1.9	0.6	
		8	5.71	0.44	0.282847	0.000021	0.000908	0.000006	36.1	1.2	3.0	0.7	
		9	*6.41*	*0.44*	*0.282688*	*0.000021*	*0.000637*	*0.000036*	*171.8*	*8.2*	*0.3*	*0.7*	
		11	6.03	0.44	0.282848	0.000027	0.001498	0.000067	34.5	1.4	3.0	0.9	
		13	5.96	0.44	0.282834	0.000023	0.000994	0.000025	35.6*	0.8*	2.5	0.8	

Formation	Sample	Grain/spot	$\delta^{18}O_{(VSMOW)}$ (‰)	±2σ	$^{176}Hf/^{177}Hf$	±2σ	$^{176}Lu/^{177}Hf$	±2σ	$^{206}Pb/^{238}U$ age (Ma)	±2σ	$\varepsilon Hf_{(T)}$	±2σ	T(NC) (Ma)
Tilito Formation	AM0846	8	5.15	0.44	0.282857	0.000027	0.001387	0.000068	25.9	0.7	3.1	0.9	
(Lower Doña Ana Group)		*14c*			*0.282769*	*0.000017*	*0.000780*	*0.000015*	*158.0*	*4.9*	*2.9*	*0.6*	
		14r	5.45	0.44	0.282815	0.000020	0.001068	0.000065	28.0	0.8	1.7	0.7	
		17	5.37	0.44	0.282891	0.000030	0.002774	0.000097	26.1*	1.6*	4.3	1.1	
		18c	5.36	0.44	0.282862	0.000018	0.001192	0.000064	26.1*	1.6*	3.3	0.6	
		18r							25.6	1.1			
		20	5.27	0.44	0.282776	0.000023	0.001233	0.000101	25.9	1.1	0.2	0.8	
		22	5.13	0.44	0.282854	0.000025	0.002568	0.000143	24.6	0.9	2.9	0.9	
Tilito Formation)	MQ153	1	5.17	0.27					25.0	0.7			
(Lower Doña Ana Group		2	5.50	0.27									
		3	5.65	0.27	0.282801	0.000028	0.001047	0.000049	25.6	0.5	1.1	1.0	
		4c	6.47	0.27	0.282849	0.000027	0.001129	0.000015	25.4	0.8	2.8	1.0	
		4r	5.80	0.27					25.0	0.7			
		5	5.99	0.27	0.282798	0.000029	0.000765	0.000016	25.5	1.2	1.0	1.0	
		6	6.07	0.27	0.282816	0.000023	0.000727	0.000004	24.5	0.7	1.6	0.8	
		8	5.26	0.27									
		9	5.55	0.27	0.282853	0.000025	0.000999	0.000057	24.9	0.7	2.9	0.9	
		12	5.59	0.27	0.282819	0.000025	0.000854	0.000013	25.8	0.6	1.8	0.9	
		16	5.60	0.27									
		20	4.89	0.29									
Tilito Formation	AM0845	14a	5.30	0.50					25.2	0.9			
(Lower Doña Ana Group)		14b			0.282906	0.000028	0.002296	0.000063	25.4	0.9	4.8	1.0	
		16c	*8.08*	*0.50*	*0.282588*	*0.000018*	*0.001288*	*0.000030*	*278.5*	*5.9*	*-1.0*	*0.6*	
		17c			0.282874	0.000025	0.002195	0.000072	24.5	0.9	3.6	0.9	
		17r	5.22	0.50					25.7	1.0			
		21	5.67	0.50	0.282906	0.000031	0.002218	0.000156	24.7	1.3	4.8	1.1	
		23	5.57	0.50	0.282876	0.000035	0.002580	0.000086	25.2	0.7	3.7	1.2	
		25	5.30	0.50	0.282853	0.000038	0.002414	0.000088	25.1	0.7	2.9	1.3	
		26	*7.18*	*0.50*	*0.282607*	*0.000028*	*0.000757*	*0.000031*	*276.7*	*5.8*	*-0.3*	*1.0*	
		34	5.28	0.50	0.282859	0.000025	0.002333	0.000081	23.8	0.8	3.1	0.9	
Tilito Formation	AM0860	2	4.77	0.44									
(Lower Doña Ana Group)		3	4.79	0.44	0.282850	0.000027	0.002111	0.000053	24.7	0.9	2.8	1.0	
		11	4.84	0.44	0.282891	0.000026	0.002588	0.000090	25.3	0.9	4.3	0.9	
		13	4.69	0.44	0.282890	0.000026	0.003217	0.000045	24.9*	0.4*	4.2	0.9	

Formation	Sample	Grain/spot	$\delta^{18}O_{(VSMOW)}$ (‰)	±2σ	$^{176}Hf/^{177}Hf$	±2σ	$^{176}Lu/^{177}Hf$	±2σ	$^{206}Pb/^{238}U$ age (Ma)	±2σ	$\varepsilon Hf_{(T)}$	±2σ	T(NC) (Ma)
		14	5.06	0.44	0.282843	0.000036	0.002654	0.000157	24.9	0.9	2.6	1.3	
		19	4.89	0.44					24.9	0.9			
		20	4.73	0.44									
		22	4.94	0.44	0.282877	0.000035	0.003134	0.000058	25.1	0.7	3.8	1.2	
		25	4.78	0.44									
		31	4.86	0.44									
Tilito Formation	ZN122	15	5.65	0.29	0.282808	0.000029	0.000543	0.000039	25.0	1.3	1.4	1.0	
(Lower Doña Ana Group)		16							23.6	1.2			
		17	5.57	0.29	0.282801	0.000027	0.000653	0.000009	24.4	1.1	1.1	0.9	
		18c	5.74	0.29	0.282833	0.000031	0.000738	0.000012	24.8	0.9	2.2	1.1	
		18r	5.69	0.29					23.9	1.0			
		19c							24.5	1.0			
		19r	5.34	0.29	0.282838	0.000029	0.000443	0.000007	25.6	0.9	2.4	1.0	
		22	5.37	0.29									
		25	5.25	0.29	0.282822	0.000026	0.001048	0.000070	25.7	0.8	1.8	0.9	
Tilito Formation	AM0844	1			0.282836	0.000026	0.002959	0.000040	24.3	0.7	2.3	0.9	
(Lower Doña Ana Group)		2c	5.17	0.36	0.282843	0.000027	0.002350	0.000049	24.5	1.4	2.6	1.0	
		2r	4.93	0.36									
		3	*4.70*	*0.36*	*0.282771*	*0.000024*	*0.002473*	*0.000015*	*241.0*	*5.3*	*4.5*	*0.8*	
		4							25.3	0.8			
		5	5.21	0.36	0.282851	0.000025	0.002201	0.000054	24.9	0.7	2.9	0.9	
		6							24.6	0.9			
		7c	4.76	0.36	0.282855	0.000039	0.004608	0.000290	25.5	1.1	3.0	1.4	
		7r							25.6	0.9			
		20	5.13	0.50	0.282873	0.000025	0.003107	0.000079	24.8	0.6	3.6	0.9	
		26	5.41	0.50	0.282862	0.000028	0.002207	0.000042	24.7*	0.3*	3.2	1.0	
		34	5.37	0.50	0.282849	0.000029	0.002333	0.000049	24.3	0.7	2.8	1.0	
Tilito Formation	AM0849	4	5.88	0.44									
(Lower Doña Ana Group)		7	4.89	0.44									
		10	4.91	0.44	0.282885	0.000035	0.002468	0.000058	24.8	0.8	4.1	1.3	
		14	4.99	0.44									
		16	4.94	0.44	0.282851	0.000026	0.002635	0.000069	24.4	1.0	2.8	0.9	
		17	4.63	0.44	0.282896	0.000025	0.002833	0.000172	25.4	0.7	4.4	0.9	
		18	5.11	0.44	0.282861	0.000026	0.002421	0.000052	24.5	1.1	3.2	0.9	

Formation	Sample	Grain/spot	$\delta^{18}O_{(VSMOW)}$ (‰)	±2σ	$^{176}Hf/^{177}Hf$	±2σ	$^{176}Lu/^{177}Hf$	±2σ	$^{206}Pb/^{238}U$ age (Ma)	±2σ	$\varepsilon Hf_{(T)}$	±2σ	T(NC) (Ma)
		21	4.70	0.44									
		25	5.35	0.44	0.282879	0.000027	0.001826	0.000118	24.1	1.1	3.8	1.0	
		27	4.92	0.44	0.282887	0.000038	0.002469	0.000142	24.7*	0.4*	4.1	1.3	
Tilito Formation	RF64	3	5.04	0.22									
(Lower Doña Ana Group)		5	4.92	0.29									
		10	4.90	0.29					24.6	0.9			
		13	4.86	0.29	0.282885	0.000028	0.001692	0.000077	24.6	0.7	4.1	1.0	
		17	5.01	0.29	0.282885	0.000039	0.002395	0.000022	23.3	0.8	4.0	1.4	
		18	4.71	0.29	0.282886	0.000037	0.001392	0.000010	23.9	0.8	4.1	1.3	
		19	4.57	0.29									
		21	5.09	0.29									
		23	4.75	0.29	0.282900	0.000051	0.008718	0.000739	24.5	0.6	4.5	1.8	
		24	5.07	0.29	0.282873	0.000025	0.001309	0.000059	23.7	0.7	3.6	0.9	
		26	*6.75*	*0.29*	*0.282448*	*0.000032*	*0.001056*	*0.000319*	*388.1*	*10.5*	*-3.6*	*1.1*	
Tilito Formation	PC14	1	6.45	0.27									
(Lower Doña Ana Group)		3	6.15	0.27	0.282727	0.000034	0.002473	0.000106	23.4	0.5	-1.6	1.2	
		4	6.60	0.27	0.282705	0.000022	0.001605	0.000018	23.5	0.6	-2.3	0.8	
		5	6.56	0.27									
		6c	6.65	0.27									
		6r	6.44	0.27	0.282758	0.000032	0.003298	0.000067	23.8	0.5	-0.5	1.1	
		7	6.53	0.27	0.282737	0.000027	0.002656	0.000028	23.6	0.5	-1.2	0.9	
		8	6.74	0.27	0.282687	0.000023	0.001383	0.000075	23.0	0.6	-3.0	0.8	
		20	6.21	0.29									
		22	6.13	0.29									
		23	6.13	0.29	0.282688	0.000028	0.002498	0.000025	23.4	0.5	-3.0	1.0	
		26	6.30	0.29									
		27	6.18	0.29	0.282708	0.000030	0.001922	0.000029	23.7	0.6	-2.2	1.1	
		30	6.14	0.29									
Tilito Formation	Z27	4	5.05	0.30									
(Lower Doña Ana Group)		7	5.32	0.30	0.282804	0.000034	0.001155	0.000066	23.5	0.6	1.2	1.2	
		11	5.42	0.30	0.282817	0.000027	0.000750	0.000005	23.6	0.9	1.7	1.0	
		13c	4.99	0.30	0.282843	0.000035	0.001584	0.000087	23.4	0.9	2.5	1.3	
		13r	4.86	0.30	0.282848	0.000024	0.000934	0.000080	23.2	1.0	2.7	0.8	
		14	4.61	0.30	0.282792	0.000026	0.000729	0.000018	23.5	1.2	0.7	0.9	

Formation	Sample	Grain/spot	$\delta^{18}O_{(VSMOW)}$ (‰)	±2σ	$^{176}Hf/^{177}Hf$	±2σ	$^{176}Lu/^{177}Hf$	±2σ	$^{206}Pb/^{238}U$ age (Ma)	±2σ	$\varepsilon Hf_{(T)}$	±2σ	T(NC) (Ma)
		15	4.77	0.30	0.282891	0.000028	0.001692	0.000105	23.0	0.9	4.2	1.0	
		16	4.96	0.30									
		17	5.05	0.30	0.282830	0.000023	0.000905	0.000046	22.4	0.9	2.1	0.8	
		18	4.84	0.30	0.282836	0.000030	0.001058	0.000042	22.8	0.9	2.3	1.1	
		22	4.59	0.30									
		32	5.47	0.29									
		33	5.11	0.29					23.3	0.8			
		34	5.19	0.29									
		35	5.07	0.29									
Las Trancas Formation	RJ11A5	3	6.72	0.29	0.282809	0.000026	0.002146	0.000067	22.8	0.5	1.3	0.9	
		6	*9.78*	*0.29*	*0.282575*	*0.000019*	*0.000711*	*0.000016*	*257.5*	*5.9*	*-1.8*	*0.7*	
		7	6.43	0.29	0.282887	0.000022	0.001646	0.000041	22.7	0.6	4.1	0.8	
		8	6.92	0.29	0.282737	0.000027	0.001631	0.000044	22.3	0.7	-1.2	1.0	
		18	*8.65*	*0.22*	*0.282596*	*0.000037*	*0.000753*	*0.000029*	*273.1*	*7.2*	*-0.7*	*1.3*	
		26	6.62	0.22	0.282830	0.000037	0.001799	0.000122	22.5	0.8	2.1	1.3	
Miocene Intrusives	RJ11A10	2	7.05	0.29	0.282704	0.000019	0.001250	0.000088	22.1	0.8	-2.4	0.7	
		9c	6.93	0.29									
		9r	6.61	0.29	0.282692	0.000023	0.001452	0.000012	22.2	0.5	-2.8	0.8	
		11	6.17	0.29	0.282683	0.000014	0.001530	0.000039	22.1	0.5	-3.1	0.5	
		13c	7.25	0.29									
		13r	6.80	0.29	0.282682	0.000018	0.001130	0.000017	22.1	0.6	-3.2	0.6	
		14c	6.64	0.29	0.282706	0.000017	0.001900	0.000036	22.6	0.5	-2.3	0.6	
		14r	6.37	0.29									
		17	6.75	0.29	0.282728	0.000024	0.002672	0.000465	22.1	0.6	-1.6	0.8	
		21	7.30	0.29	0.282687	0.000020	0.000810	0.000029	21.9	0.9	-3.0	0.7	
		22	6.86	0.29									
		26	6.65	0.29									
		28	7.02	0.29									
		34	7.48	0.22									
		36	7.32	0.22									
Miocene Intrusives	RJ11A11	9	7.16	0.27	0.282720	0.000023	0.001007	0.000057	21.8	0.6	-1.8	0.8	
		11	7.15	0.27					20.1	1.1			
		12	7.39	0.27					20.6	0.9			
		13	7.26	0.27									

Formation	Sample	Grain/spot	$\delta^{18}O_{(VSMOW)}$ (‰)	±2σ	$^{176}Hf/^{177}Hf$	±2σ	$^{176}Lu/^{177}Hf$	±2σ	$^{206}Pb/^{238}U$ age (Ma)	±2σ	$\varepsilon Hf_{(T)}$	±2σ	T(NC) (Ma)
		14	6.42	0.29									
		15	6.95	0.29					21.8	0.9			
		22a	6.83	0.29					21.2	0.8			
		22b	6.97	0.29					21.1	0.9			
		23	6.78	0.29					21.1	1.0			
		28	6.77	0.27									
		35	7.66	0.22	0.282704	0.000027	0.000694	0.000025	21.6	0.8	-2.4	1.0	
		36c	7.35	0.22	0.282704	0.000023	0.000958	0.000054	21.9	0.8	-2.4	0.8	
		36r	7.30	0.22									
		40	7.92	0.22									
Miocene Intrusives	RJ11A14	7	7.34	0.27	0.282748	0.000026	0.000731	0.000024	20.3	0.7	-0.9	0.9	
		15	*6.81*	*0.27*	*0.282579*	*0.000046*	*0.000580*	*0.000018*	*138.1*	*5.2*	*-4.3*	*1.6*	
		16	7.39	0.27	0.282686	0.000021	0.000387	0.000001	20.7	0.9	-3.1	0.8	
		17c	6.89	0.27	0.282745	0.000020	0.000463	0.000018	20.7	0.7	-1.0	0.7	
		17r	7.03	0.27									
		18c	7.21	0.27	0.282710	0.000018	0.000715	0.000008	21.0	0.9	-2.2	0.6	
		18r	6.84	0.27									
		20	7.16	0.27	0.282697	0.000024	0.000565	0.000012	20.3	0.7	-2.7	0.8	
		23	7.32	0.27	0.282681	0.000026	0.000677	0.000043	20.2	0.7	-3.2	0.9	
Escabroso Formation	1026	4	5.63	0.27	0.282780	0.000026	0.000680	0.000030	18.5	0.6	0.2	0.9	
(Upper Doña Ana Group)		5	5.74	0.27									
		9	5.43	0.27	0.282790	0.000019	0.000480	0.000013	18.5	0.8	0.6	0.7	
		10	5.64	0.27									
		11	5.57	0.27	0.282809	0.000023	0.000556	0.000011	18.2	0.8	1.2	0.8	
		14	5.70	0.27	0.282759	0.000024	0.000513	0.000003	18.5	0.7	-0.5	0.8	
		16a	5.53	0.27	0.282820	0.000018	0.000851	0.000029	18.4	0.7	1.6	0.6	
		16b	5.55	0.27									
		18	5.47	0.27	0.282806	0.000022	0.000405	0.000003	17.7	1.0	1.1	0.8	
		19c	5.57	0.27	0.282840	0.000027	0.000748	0.000010	19.1	1.6	2.4	0.9	
		19r	5.39	0.27									
		33	5.60	0.22	0.282814	0.000022	0.000651	0.000056	17.5	0.6	1.4	0.8	
		35	5.69	0.22									
		36	5.56	0.22									
Escabroso Formation	SP80	1a	5.71	0.27	0.282788	0.000027	0.000661	0.000020	18.1	0.7	0.5	0.9	

Formation	Sample	Grain/spot	$\delta^{18}O_{(VSMOW)}$ (‰)	±2σ	$^{176}Hf/^{177}Hf$	±2σ	$^{176}Lu/^{177}Hf$	±2σ	$^{206}Pb/^{238}U$ age (Ma)	±2σ	$\varepsilon Hf_{(T)}$	±2σ	T(NC) (Ma)
(Upper Doña Ana Group)		1b	5.51	0.27	0.282798	0.000023	0.000458	0.000007	18.1*	0.4*	0.8	0.8	
		2	5.53	0.27	0.282823	0.000025	0.000459	0.000004	18.4	1.3	1.7	0.9	
		3	5.55	0.27	0.282807	0.000021	0.000493	0.000004	18.0	0.7	1.2	0.8	
		4	5.54	0.27	0.282785	0.000024	0.000443	0.000004	17.6	0.8	0.4	0.9	
		5	5.73	0.27	0.282816	0.000026	0.000599	0.000023	18.1*	0.4*	1.5	0.9	
		8	5.88	0.27									
		10	5.56	0.27					18.6	0.8			
		14	4.84	0.29									
Cerro de las	RF62	6	5.06	0.29									
Tórtolas Formation		8	5.18	0.29	0.282839	0.000026	0.000597	0.000009	17.4	0.5	2.3	0.9	
		9	4.86	0.29	0.282846	0.000027	0.000928	0.000017	17.7	0.6	2.5	1.0	
		10	5.24	0.29	0.282849	0.000024	0.000795	0.000045	17.0	0.6	2.6	0.9	
		11a							16.6	0.5			
		11b	5.17	0.29	0.282828	0.000025	0.000457	0.000007	17.3	0.7	1.9	0.9	
		12	5.37	0.29	0.282832	0.000024	0.000854	0.000013	17.1*	0.6*	2.0	0.9	
		14	5.22	0.29									
		15	5.26	0.29									
		21	4.83	0.29					18.0	0.6			
		22	5.10	0.29	0.282825	0.000028	0.000854	0.000022	16.2	0.4	1.7	1.0	
Tertiary Intrusives	RJ11A7	10c	5.72	0.29									
		10r	5.88	0.29	0.282807	0.000019	0.001029	0.000006	11.5	0.4	1.0	0.7	
		12c	6.04	0.29					12.0	0.6			
		12r	6.17	0.29	0.282821	0.000016	0.001144	0.000060	11.6	0.3	1.5	0.6	
		13	6.05	0.29	0.282804	0.000019	0.000822	0.000045	11.7*	0.2*	0.9	0.7	
		14	*7.20*	*0.29*	*0.282315*	*0.000018*	*0.000538*	*0.000027*	*1068.1*	*20.9*	*7.0*	*0.6*	*1281*
		15a	5.76	0.29	0.282810	0.000017	0.001410	0.000110	11.9	0.5	1.1	0.6	
		15b	5.72	0.29	0.282813	0.000014	0.001184	0.000148	11.7*	0.2*	1.2	0.5	
		21	5.57	0.29	0.282792	0.000023	0.000924	0.000047	11.6	0.4	0.5	0.8	
		28c	*6.76*	*0.29*	*0.282243*	*0.000022*	*0.001660*	*0.000038*	*1249.4*	*21.9*	*7.5*	*0.8*	*1391*
Tertiary Intrusives	RJ11A17	1	5.98	0.30					9.5	0.7			
		3	6.67	0.30					9.8	0.4			
		6	6.27	0.30					9.5	0.4			
		7	*8.63*	*0.30*	*0.282549*	*0.000017*	*0.000488*	*0.000007*	*239.7*	*5.9*	*-3.1*	*0.6*	
		8	6.29	0.30					9.3	0.4			

Formation	Sample	Grain/spot	$\delta^{18}O_{(VSMOW)}$ (‰)	±2σ	$^{176}Hf/^{177}Hf$	±2σ	$^{176}Lu/^{177}Hf$	±2σ	$^{206}Pb/^{238}U$ age (Ma)	±2σ	$\varepsilon Hf_{(T)}$	±2σ	T(NC) (Ma)
		10c	6.66	0.30									
		10r	6.43	0.30					8.4'	0.7'			
		11c	6.50	0.30					9.8	0.4			
		13c							*264.0*	*7.2*			
		13r	6.14	0.30					9.5	0.6			
		14	6.95	0.30					9.5	0.8			
		15							9.3	0.8			
		22	*7.23*	*0.22*	*0.282368*	*0.000028*	*0.001384*	*0.000046*	*1066.0*	*27.5*	*8.2*	*1.0*	*1200*
		26	6.28	0.22	0.282670	0.000028	0.000745	0.000063	8.8	0.5	-3.9	1.0	
Tertiary Intrusives	RJ11A15	*7*	*6.25*	*0.27*	*0.282262*	*0.000025*	*0.000802*	*0.000026*	*1225.7*	*23.4*	*8.4*	*0.9*	*1318*
		11	6.17	0.27	0.282669	0.000018	0.000841	0.000021	9.3	0.5	-3.9	0.6	
		14c	6.33	0.27					8.7	0.6			
		14r	6.52	0.27	0.282677	0.000018	0.000785	0.000052	9.2	0.7	-3.6	0.6	
		15c	6.25	0.27	0.282680	0.000018	0.000972	0.000053	9.4*	0.2*	-3.5	0.7	
		15r	6.21	0.27									
		16	*5.20*	*0.27*	*0.282735*	*0.000019*	*0.001005*	*0.000010*	*249.0*	*5.2*	*3.6*	*0.7*	
		19	6.54	0.27	0.282676	0.000018	0.001243	0.000038	9.8	0.4	-3.6	0.6	
		22c	*6.05*	*0.27*					*1039.6*	*29.0*			
		22r							9.6	0.4			
		27	6.43	0.22	0.282673	0.000026	0.000787	0.000027	9.3	0.4	-3.8	0.9	
		29	6.40	0.22	0.282704	0.000021	0.000875	0.000018	9.4	0.4	-2.7	0.8	
Vacas Heladas	MQ33	4c	5.49	0.30					6.5	0.2			
Ignimbrites		4r	5.20	0.30									
		7	5.28	0.30	0.282753	0.000019	0.000698	0.000033	6.3	0.2	-1.0	0.7	
		9	*5.86*	*0.30*					*204.1*	*4.5*			
		10r	5.01	0.30	0.282751	0.000022	0.001130	0.000019	6.1	0.2	-1.1	0.8	
		10c	5.93	0.30									
		11c	5.59	0.30	0.282733	0.000025	0.000858	0.000029	6.2	0.2	-1.7	0.9	
		11r	5.69	0.30	0.282743	0.000018	0.001117	0.000025	6.0	0.1	-1.3	0.6	
		11ad.	5.39	0.30									
		12	*5.30*	*0.30*	*0.282785*	*0.000023*	*0.000912*	*0.000056*	*9.8*	*0.3*	*0.2*	*0.8*	
		14	*4.96*	*0.30*	*0.282809*	*0.000023*	*0.000664*	*0.000022*	*15.1*	*0.4*	*1.2*	*0.8*	
		15	5.61	0.30	0.282741	0.000026	0.001159	0.000023	6.0	0.2	-1.4	0.9	
		17	*7.25*	*0.30*	*0.282660*	*0.000026*	*0.000902*	*0.000030*	*255.7*	*5.4*	*1.1*	*0.9*	

Formation	Sample	Grain/spot	$\delta^{18}O_{(VSMOW)}$ (‰)	±2σ	$^{176}Hf/^{177}Hf$	±2σ	$^{176}Lu/^{177}Hf$	±2σ	$^{206}Pb/^{238}U$ age (Ma)	±2σ	$\varepsilon Hf_{(T)}$	±2σ	T(NC) (Ma)
Vacas Heladas	DI095	12	5.62	0.29	0.282739	0.000027	0.000553	0.000032	6.2*	0.3*	-1.5	1.0	
Ignimbrites		*14i*	*5.23*	*0.29*	*0.282752*	*0.000035*	*0.002500*	*0.000169*	*256.3*	*6.8*	*4.1*	*1.2*	
		14r	5.11	0.29	0.282685	0.000024	0.000454	0.000029	6.0	0.2	-3.4	0.9	
		15c	5.61	0.29	0.282808	0.000031	0.001056	0.000010	6.2*	0.3*	1.0	1.1	
		15r	5.55	0.29	0.282745	0.000022	0.001409	0.000026	6.0	0.2	-1.3	0.8	
		16	*5.65*	*0.29*	*0.282684*	*0.000030*	*0.001387*	*0.000084*	*270.7*	*6.0*	*2.2*	*1.1*	
		17	5.49	0.29	0.282748	0.000022	0.000887	0.000005	6.3	0.2	-1.2	0.8	
		20	5.54	0.29	0.282710	0.000034	0.001102	0.000091	6.4	0.2	-2.5	1.2	
		21	5.59	0.29	0.282775	0.000031	0.000751	0.000069	6.2*	0.3*	-0.2	1.1	

* ages indicate the sample average U-Pb age (as determined by Concordia diagrams or Tera-Wasserburg plots) used to calculate εHf_T values for individual zircon analyses.

Appendix 2.11 References

Bouvier, A., Vervoort, J.D., and Patchett, P.J., 2008, The Lu-Hf and Sm-Nd isotopic composition of CHUR: Constraints from unequilibrated chondrites and implications for the bulk composition of terrestrial planets: Earth and Planetary Science Letters, v. 273, p. 48-57.

Dhuime, B., Hawkesworth, C., and Cawood, P., 2011, When Continents Formed: Science, v. 331, p. 154-155.

Griffin, W.L., Pearson, N.J., Belousova, E., Jackson, S.E., van Achterbergh, E., O'Reilly, S.Y., and Shee, S.R., 2000, The Hf isotope composition of cratonic mantle: LAM-MC-ICPMS analysis of zircon megacrysts in kimberlites: Geochimica et Cosmochimica Acta, v. 64, p. 133-147.

Hawkesworth, C.J., and Kemp, A.I.S., 2006, Using hafnium and oxygen isotopes in zircons to unravel the record of crustal evolution: Chemical Geology, v. 226, p. 144 - 162.

Kemp, A.I.S., Foster, G.L., Schersten, A., Whitehouse, M.J., Darling, J., and Storey, C., 2009, Concurrent Pb-Hf isotope analysis of zircon by laser ablation multi-collector ICP-MS, with implications for the crustal evolution of Greenland and the Himalayas: Chemical Geology, v. 261, p. 244-260.

Peck, W.H., Valley, J.W., Wilde, S.A., and Graham, C.M., 2001, Oxygen isotope ratios and rare earth elements in 3.3 to 4.4 Ga zircons: Ion microprobe evidence for high $\delta^{18}O$ continental crust and oceans in the Early Archean: Geochimica et Cosmochimica Acta, v. 65, p. 4215 - 4229.

Segal, I., Halicz, L., and Platzner, I.T., 2003, Accurate isotope ratio measurements of ytterbium by multiple collection inductively coupled plasma mass spectrometry applying erbium and hafnium in an improved double external normalization procedure: Journal of Analytical Atomic Spectrometry, v. 18, p. 1217-1223.

Söderlund, U., Patchett, P.J., Vervoort, J.D., and Isachsen, C.E., 2004, The 176Lu decay constant determined by Lu-Hf and U-Pb isotope systematics of Precambrian mafic intrusions: Earth and Planetary Science Letters, v. 219, p. 311-324.

Valley, J.W., 2003, Oxygen isotopes in zircon, *in* Hanchar, J.M., and Hoskin, P.W.O., eds., Zircons, Volume 53: Chantilly, Virginia, Reviews in Mineralogy and Geochemistry, Mineralogical Society of America, p. 343 - 386.

Vervoort, J.D., Patchett, P.J., Söderlund, U., and Baker, M., 2004, Isotopic composition of Yb and the determination of Lu concentrations and Lu/Hf ratios by isotope dilution using MC-ICPMS: Geochem. Geophys. Geosyst., v. 5, p. Q11002.

Woodhead, J., Hergt, J., Shelley, M., Eggins, S., and Kemp, R., 2004, Zircon Hf-isotope analysis with an excimer laser, depth profiling, ablation of complex geometries, and concomitant age estimation: Chemical Geology, v. 209, p. 121-135.

Appendix 3

Appendix 3.1 Sample preparation

3.1.1 Mineral separation

In order to separate mineral phases hosting melt inclusions, for *in-situ* analysis, ~5 kg of each rock sample was broken down into ~6 cm square blocks and crushed using a tungsten carbide jaw crusher. The rock chips resulting from crushing were then sieved into < 2mm, < 1mm and < 0.5 mm size fractions. Any large rock chips were reintroduced to the jaw crusher. In order to avoid the possibility of cross contamination all machinery, sieves and glassware were thoroughly cleaned with water and acetone before and after each sample. Mineral phases hosting melt inclusions (pyroxene and zircon) were then separated from the sieved size fractions using a number of traditional mineral separation techniques.

3.1.1.1 Density separation using a Gemini table

A Gemini shaking table at the University of Glasgow was used to separate out minerals of different density from the crushed samples. Each sample was introduced to the Gemini table in turn. As water flowed over the ribbed surface of the table and the table shook, the high density minerals were trapped in the ribs and carried down to the far end of the table, while the low density minerals were washed off early. The minerals were then collected in different containers depending where they were washed off the table. The exact set up (i.e., water flow rate and positioning of the collection buckets) of the table varied depending on the quantity of the sample being separated. Once collected the different density separations were dried in a drying cupboard. Pyroxene and zircon occurred in the high density (heavy) mineral fraction.

3.1.1.2 Magnetic separation

A strong hand magnet was then passed over each of the heavy mineral fractions in order to remove any magnetic minerals such as magnetite and any iron fillings that may have been picked up off the equipment. A S.G. Frantz magnetic separator was then used to separate the minerals according to their magnetic susceptibility. Augite is magnetic at 0.4 amperes, enstatite is magnetic at 1.2 amperes and zircon is nonmagnetic at 1.2 amperes. The Frantz was set up with a slope of 20° and a tilt of 20°. Each sample was then run though the Frantz in turn and the voltage was increased in a stepwise fashion to separate augite, enstatite and zircon.

3.1.1.3 Heavy liquid separation

Lithium heteropolytungstate (LST), a heavy liquid with a normal operating density of 2.85g/cc, was then used to separate out minerals of different densities from the magnetic and nonmagnetic fractions. The LST was held in a separating funnel and each sample fraction was poured into the LST in turn. The sample was stirred into the LST so that all the grains were 'wetted' and then left to stand until all the mineral grains had either sunk to the bottom (the sink) or risen to the surface (the float). The sink was then drained off onto a filter paper and the pure LST collected. The mineral grains in the sink were then washed with distilled water and the washings containing LST collected separately. The float was then drained through a different filter paper and the pure LST collected. The float was also washed with distilled water and the washings containing LST collected. Both the sink and the float were then dried in a drying cupboard at ~40 °C. The pure LST was reused in further separations, while the washings containing LST were filtered under vacuum and heated, in order to remove the water and restore the correct density. The densities of the minerals of interest (augite, enststite and zircon) are greater than 2.85g/cc, so all appear in the sink.

3.1.2 Mounting, grinding and polishing

After mineral separation individual zircon and pyroxene grains were hand-picked under a binocular microscope. Picked pyroxene grains were mounted onto a glass slide using a temporary adhesive (Crystalbond) and ground on silicon carbide paper (grade P2500) to reveal the presence of melt inclusions. The melt inclusions were studied under a petrographic microscope to check for the presence of daughter minerals and vapour bubbles and to ensure the absence of any cracks (evidence the melt inclusion has not behaved as a closed system). Where the melt inclusions appeared glassy or contained only a minor vapour or shrinkage bubble the pyroxene grains were ground to expose the melt inclusions at the surface. The mineral grains were then removed from the Crystalbond using a soldering iron, cleaned in acetone and remounted (when completely dry) in epoxy resin. The epoxy grain mounts were then lightly ground and polished with 0.3μm Al_2O_3 paste to obtain a surface suitable for analysis.

Prior to melt inclusion analysis, the zircon grains were mounted in epoxy resin for *in-situ* U-Pb dating, oxygen and hafnium isotope analysis (Chapter 3 and Appendix 2). Subsequently, zircon grains containing melt inclusions from select samples were removed from the epoxy grain mounts using a scalpel. These zircon grains were then individually mounted in epoxy resin in 3.5mm (diameter) x 5mm aluminium or brass tubes, similar to the method proposed by Thomas and Bodnar (2002). These individual grain mounts were then ground and polished with 0.3μm Al_2O_3 paste to expose the melt inclusions at the surface. After the final stage of polishing the tubes were inserted into brass or stainless steel holders suitable for SIMS analysis.

3.1.3 Melt inclusion re-homogenisation

Where the pyroxene hosted melt inclusions appeared devitrified (and contained a vapour bubble and mineral phases) the pyroxene grains were ground until the melt inclusions could be viewed clearly and were then removed from the Crystalbond

using a soldering iron and cleaned in acetone. These melt inclusions were then re-homogenised using a Linkam TS1400XY heating stage.

Pyroxene grains were placed on a sapphire plate and inserted into the ceramic furnace. The X-Y position of the sapphire plate was then adjusted to allow the melt inclusions to be viewed using a Leitz Metallux petrographic microscope combined with a QICAM Fast 1394 camera during heating. Argon gas was circulated through the stage during heating at a constant flow rate of approximately 0.1 litre/minute, to prevent oxidation (Esposito et al., 2012). The Ar gas was cleaned prior to circulation using a Zr getter heated to ~750 °C. A graphite ring was also placed around the pyroxene grain to convert any additional free O_2 present in the heating chamber into CO_2 and CO (Oskarsson and Hansteen, 1992). The oxidation state inside the chamber was also monitored using a NiNiO buffer. A stepped heating profile was used (Table A3.1) and the melt inclusions were monitored and photographed using a QICAM Fast 1394 camera during heating (Fig. A3.1). On the disappearance of the vapour bubble and/or daughter minerals the pyroxene grain was removed from the furnace and the melt inclusion quenched. The quench rate for the Linkam TS1400XY stage has been determined to be ~240 °C/s from 1400 to 800 °C (Esposito et al., 2012). The heating stage was routinely calibrated using the melting temperature of Au (1064.2 °C); the difference between the known melting temperature and the measured temperature was always <5 °C.

Heating Profile 1		
Temperature ℃	**Heating rate ^{0}C/min**	**Samples**
25 – 900	100	1026 AM0887 (1-5)
900 – 1000	50	
1000 - 1200	25	
1200 - 1300	10	
1300 - 1360	5	
Heating Profile 2		
Temperature ℃	**Heating rate ^{0}C/min**	**Samples**
25 – 1000	100	1026 AM0887 ZN122 RJ1111 RF62
1000 - 1100	50	
1100 - 1150	25	
1150 - 1200	10	
1200 - 1225	5	
1225 - 1250	2	
1250 - 1300	1	

Table A3.1. Heating profiles.

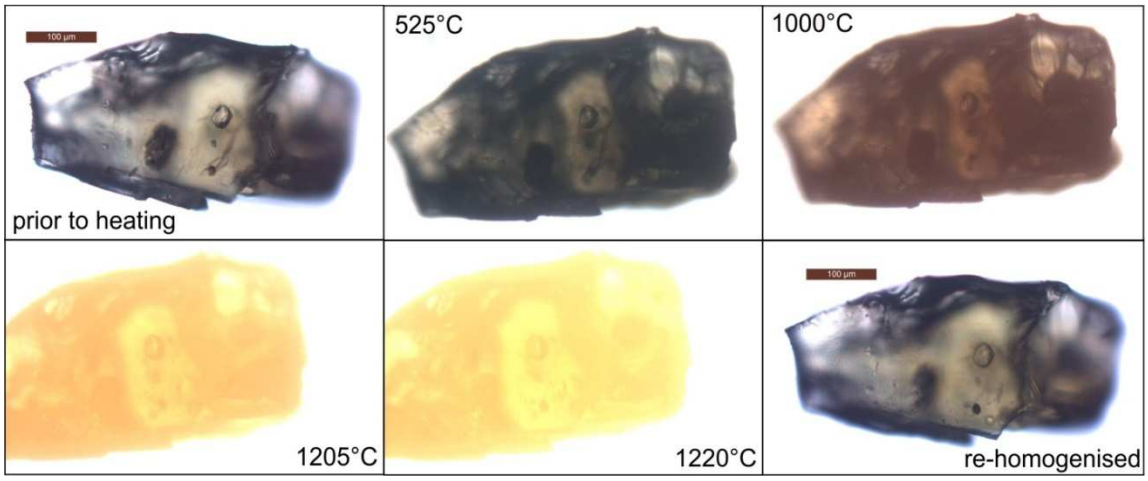

Figure A3.1. Photomicrographs taken at various temperatures during the re-homogenisation of an augite-hosted melt inclusion from sample AM0887. Prior to heating the melt inclusion contains two unidentified daughter minerals and a vapour bubble. After quenching at 1220 °C, the melt inclusion contains a homogeneous glass at ambient conditions.

The pyroxene grains hosting re-homogenised melt inclusions were then mounted individually in epoxy resin in 3.5mm (diameter) x 5mm aluminium or brass tubes, in the same way as the zircon grains containing melt inclusions. These individual grain mounts were then ground and polished with 0.3µm Al_2O_3 paste to expose the re-homogenised melt inclusions at the surface. After the final stage of polishing the tubes were inserted into brass or stainless steel holders suitable for SIMS analysis.

Appendix 3.2 Boron isotope analysis

Boron isotope analyses were performed on a Cameca ims 1270 secondary ion mass spectrometer (SIMS) at the Edinburgh Ion Microprobe Facility (EIMF), University of Edinburgh between the 4th and 10th March 2013. Prior to SIMS analysis the samples were ultrasonically cleaned in petroleum spirit and deionised water. A gold coat was applied in order to produce a uniform conducting surface and to prevent the sample from charging during analysis.

3.2.1 Analytical conditions

Positive secondary ions of $^{10}B^+$ and $^{11}B^+$ were produced by a 5nA, $^{16}O^{2-}$ primary beam with a net impact energy of 22keV, focused to a ~25μm spot size. The secondary ions were analysed using a mass resolution (ΔM) of ~2400 (sufficient to resolve mass interferences of $^{9}Be^{1}H^+$ (ΔM = 1400) and $^{10}B^{1}H^+$ (ΔM = 900)) using an energy window 100 eV, a 400 μm contrast aperture and a field aperture suitable for the beam diameter. The beam was manually centred by adjusting lens 4, X/Y deflectors before each analysis. Prior to each analysis the samples were pre-sputtered for 30 seconds to remove surface contamination. B isotope ratios were measured for 60 cycles, with each cycle consisting of 8 seconds of counting on $^{10}B^+$, 3 seconds counting on $^{11}B^+$ and 1 second counting on $^{28}Si^{2+}$. Ion counts were measured using a single electron multiplier in magnetic peak switching mode. Counts were dead time corrected using a value of 51 nS.

The boron isotope ratios of the melt inclusions and host phenocrysts were determined relative to the reference material GSD-1G (10.1 $‰_{NIST951}$ ±1.0 (2σ) (Jochum et al., 2011)), which was analysed throughout the analytical session. The $\delta^{11}B$ of each melt inclusion was calculated using the following equation:

$\delta^{11}B_{(sample)} = ((\delta^{11}B_{(GSD\text{-}1G\ accepted\ value)} + 1000) \times (^{11}B/^{10}B_{(sample\ measured)} / {}^{11}B/^{10}B_{(GSD\text{-}1G\ measured)})) - 1000$

Where $^{11}B/^{10}B_{(GSD\text{-}1G\ measured)}$ is the average $^{11}B/^{10}B$ ratio of GSD-1G measured during the same analytical session (a session is defined as a period where no changes in analytical conditions were made, including sample exchange). The unknown analyses were split into 20 analytical sessions. Analyses of 3-5 unknowns were bracketed by 2-3 analyses of standard GSD-1G (Appendix 3.5).

3.2.2 Data correction

During SIMS analysis the count rate of isotopes varies during the sputtering process. A correction was made for the varying count rates with time using the linear interpolation approach of Coakley et al. (2005).

3.2.3 Data processing

A total of 16 boron isotope analyses of melt inclusions were ruled out due to low or variable boron count rates, or analytical issues (e.g., duo spike). Individual analysis cycles which produced $^{11}B/^{10}B$ which were greater than 4σ away from the average $^{11}B/^{10}B$ (spikes) were rejected and an average was taken of the count rates before and after. This data processing was applied to 20 analyses out of 189 in total (refer to Appendix 3.5).

A total of 70 successful boron isotope analyses were made on melt inclusions (55 hosted in pyroxene and 15 hosted in zircon), from 8 samples. The internal precision of individual standard analyses, based on the standard error of the mean, ranged from 0.55 – 0.68 ‰ (1σ). The internal precision of the unknowns is dependent on boron content (i.e., count rate) and ranged from 0.29 – 1.33 ‰ (1σ) for melt inclusion analyses, and 2.84 – 6.27 ‰ (1σ) for mineral analyses (Appendix 3.5). The external

precision of the analyses is estimated from the external reproducibility of the standard GSD-1G, and is typically 0.23‰ (n=13) (quoted as the standard error of the mean at the 1σ level). Twelve analyses were also carried out on host phenocryst phases (Appendix 3.5 and summarised in Table A3.2).

The analytical uncertainties quoted on the individual unknowns are propagated uncertainties, which take into account both the uncertainty on the individual analysis (internal precision) and the reproducibility of the standard in the analytical session (external precision). The analytical uncertainty on the individual unknowns are quoted at the 2σ level and calculated using the following equation:

$$Analytical\ Uncertainty = \sqrt{\left(\frac{SEM_{(GSD-1G\ measurements)}}{\overline{x}^{11}B/^{10}B_{(GSD-1G\ measurements)}}\right)^2 + \left(\frac{SEM_{(sample\ measurement)}}{^{11}B/^{10}B_{(sample\ measurement)}}\right)^2}$$

Where SEM represents the standard error of the mean, GSD-1G measurements represents the $^{11}B/^{10}B$ ratio of GSD-1G measured during the same analytical session.

Sample-phenocryst	Host mineral phase	B (ppm)	$\delta^{11}B$ (‰)	Analytical uncertainty (± ‰)
RJ1111-4	augite	1.5	-16.4	9.1
RJ1111-6	augite	*1.4*	-8.7	7.5
RJ1111-MB1glassy	augite	*0.9*	-6.2	8.2
ZN122-8	augite	2.8	-	-
ZN122-10	augite	0.7	-13.1	12.6
Z27-A13	zircon	0.4	-	-
AM0887-6	augite	2.9	-14.3	7.0
AM0887-8	enstatite	0.5	-	-
AM0887-15	augite	*1.5*	-0.9	6.8
AM0887-MB5 glassy	augite	*0.7*	-6.4	9.2
1026-UA4	zircon	1.2	-	-
1026-A3	zircon	0.5	-	-
1026-A5	zircon	*0.7*	-31.7	11.2
1026-A7	zircon	0.6	-	-
1026-A9	zircon	0.8	-	-
1026-4	augite	2.0	-	-
1026-6	augite	*2.0*	-11.8	5.8
1026-8	augite	2.1	-	-
1026-B2	augite	*0.8*	-9.8	9.1
1026-B11	augite	*1.0*	-6.4	8.3
1026-MB2	augite	1.5	-	-
RF62-7	augite	2.4	-	-
RF65-1	augite	2.5	-	-
RF65-MB3	augite	*1.4*	-14.2	6.7

Table A3.2. Boron concentrations and isotope ratios of host mineral phases. Boron concentrations calculated from the average counts obtained from the boron isotope analysis are displayed in italics and underlined. The analytical uncertainties on the $\delta^{11}B$ values are propagated uncertainties quoted at the 2σ level. NB, the large uncertainties on the $\delta^{11}B$ values are a reflection of the low concentrations of the boron in the host phenocryst phases. Full results are presented in Appendix 3.5 and 3.7.

Appendix 3.3 Trace and rare earth element analysis

A total of 72 (58 hosted in pyroxene and 14 hosted in zircon) melt inclusions and 15 host mineral phases were analysed for selected trace (TE) and rare earth elements (REE) on the Cameca ims 4f secondary ion mass spectrometer (SIMS) at the Edinburgh Ion Microprobe Facility (EIMF), University of Edinburgh, between the 11th and 15th March 2013. Where possible the melt inclusions which had previously been analysed for boron isotopic composition were analysed. Where this was not possible (usually due to the size of the melt inclusions) analyses were made of melt inclusions from the same phenocryst as those analysed for boron isotope composition.

3.3.1 Analytical conditions

Analyses were made using a primary beam of $^{16}O^-$ ions with an operating potential of 10kV and a beam current of 5nA. The primary beam was focused to a spot size of ~20μm at the sample surface. Positive secondary ions were extracted at 4500 V and using energy offset of 75 eV ±20 eV. Due to the size of the melt inclusions the TE and REE analysis was generally made down the pits generated by the boron isotope analysis (specified when not the case, Appendix 3.6) (Fig. A3.2). Counting times for each acquisition cycle were 2 seconds for ^{30}Si, 3 seconds for ^{47}Ti, ^{88}Sr, ^{89}Y, ^{90}Zr, ^{138}Ba, ^{140}Ce, ^{154}Gd, ^{156}Gd and 5 seconds for ^{11}B, ^{93}Nb, ^{139}La, ^{141}Pr, ^{143}Nd, ^{149}Sm, ^{151}Eu, ^{157}Gd, ^{159}Tb, ^{161}Dy, ^{165}Ho, ^{167}Er, ^{169}Tm, ^{171}Yb, ^{175}Lu, ^{232}Th and ^{282}U and analyses were made over 10 cycles. Peak positions were verified before each analysis and mass 130.5 was measured to check for background counts, which were found to be insignificant. The relative ion yields measured for the reference material GSD-1G (Jochum et al., 2011) was used to calibrate the melt inclusion data and showed no systematic drift through the course of the analyses. Corrections were made for oxide interferences of light REE (LREE) on the heavy REE (HREE) and of BaO on Eu. The magnitude of

the corrections were based on the CeO/Ce measured for the REE-bearing glass standard under the same analytical conditions and the BaO/Ba measured on a number of melt inclusion glasses and then applied to the data.

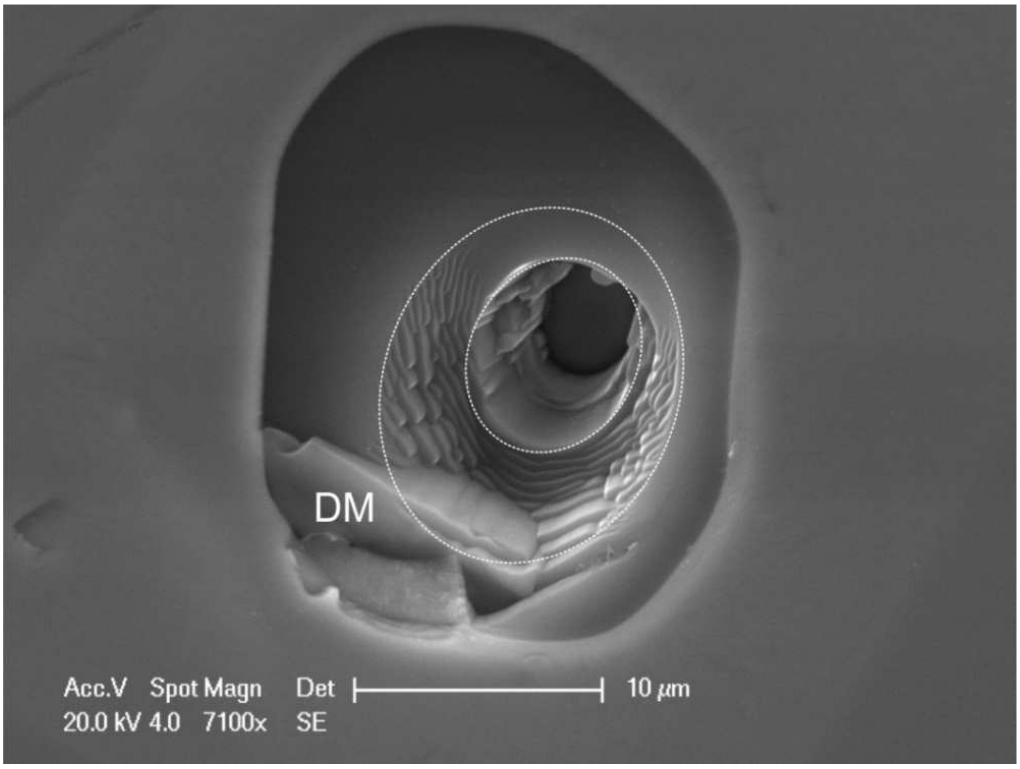

Figure A3.2. Secondary electron image showing the pits created by the two stages of SIMS analysis conducted on a zircon-hosted, melt inclusion (1026-A6-MI1). The largest oval represents the pit generated by the boron isotope analysis and the smaller oval the pit generated by the trace and rare earth element analysis. The daughter mineral (DM) has been identified as magnetite.

Individual analysis cycles were checked by monitoring certain TE (specifically Y and Ti for pyroxene hosted melt inclusions and Zr, Th and U for zircon hosted melt inclusions) to ensure the beam was not sputtering through the melt inclusion glass into the host mineral phase. Where the analysis was found to be sputtering into the host mineral (the case for 6 melt inclusions) only the first 4 to 7 analysis cycles were used (refer to Appendix 3.6).

The absolute elements concentrations were calculated using the in house, JCION5 software and by normalising the intensities to ^{30}Si. The Si concentrations for individual melt inclusions were determined by electron microprobe (EPMA) (Appendix 3.8). Due to the small size of some melt inclusions EPMA analysis was not possible for all melt inclusions, so for the purpose of normalising to ^{30}Si, the average Si concentrations for the re-homogenised / unre-homogenised melt inclusions from the particular sample were used.

Based on repeated measurement of the reference material GSD-1G, precision (% P) is always <3 % relative (1σ) for all elements apart from Th, where precision was 5.7 % relative (1σ) (Table A3.3). For the elements discussed in Chapter 4 (B, Nb and Zr) a precision of <2.6 % relative (1σ) was obtained (Table A3.3). Analysis of a number of secondary standards (NIST SRM 610 and BCR-2G) indicates that accuracy is <7.3 % relative (1σ) for the elements discussed in Chapter 4 (B, Nb and Zr), apart from for B concentrations in BCR-2G where accuracy is <25.6 % relative (1σ) (Table A3.4). This is likely to reflect to low concentration of B present in BCR-2G (6 ppm).

	GSD-1G Average	1σ	%P
B (ppm)	**53.97**	**0.24**	**0.45**
Ti	6379.08	62.27	0.98
Sr	59.81	0.61	1.02
Y	37.72	0.20	0.52
Zr	**39.18**	**0.31**	**0.80**
Nb	**40.46**	**1.03**	**2.55**
Ba	53.26	1.34	2.51
La	34.05	0.60	1.77
Ce	34.42	0.47	1.37
Pr	37.41	0.45	1.20
Nd	39.99	0.24	0.61
Sm	39.16	1.15	2.94
Eu	35.96	0.45	1.27
Gd	49.81	1.34	2.70
Tb	41.27	0.52	1.26
Dy	44.06	0.63	1.44
Ho	44.12	0.29	0.65
Er	35.39	0.75	2.11
Tm	44.35	0.86	1.95
Yb	47.77	0.47	0.99
Lu	49.14	0.74	1.51
Th	29.58	1.68	5.68
U	28.40	0.80	2.82
n	*4*		

Table A3.3. Precision estimates for trace and rare earth element concentrations (ppm) based on repeat analysis of reference material GSD-1G by SIMS at the Edinburgh Ion Microprobe Facility (EIMF), University of Edinburgh. 1σ is the standard deviation of the repeat analyses and % P is the percentage precision at the 1σ level.

	NIST SRM 610			Published	Accuracy	BCR-2G			Published	Accuracy
	Average	1σ	%P	values	% difference	Average	1σ	%P	values	% difference
B (ppm)	**325**	**4.6**	**1.3**	**350**	**7.2**	**4.5**	**0.23**	**4.7**	**6.0**	**25.55**
Ti	517	7.2	1.7	452	14.5	13660.6	70.93	0.6	14100.0	3.12
Sr	598	6.3	1.2	516	16.1	323.5	2.85	1.0	342.0	5.41
Y	501	4.1	0.9	462	8.5	33.3	0.27	0.9	35.0	4.85
Zr	**469**	**6.6**	**1.5**	**448**	**4.6**	**180.2**	**2.12**	**1.3**	**184.0**	**2.04**
Nb	**492**	**13.9**	**2.9**	**465**	**5.9**	**11.8**	**0.26**	**2.3**	**12.5**	**5.33**
Ba	529	9.2	2.2	452	17.1	627.5	7.86	1.6	683.0	8.13
La	521	7.9	1.7	440	18.3	24.0	0.23	1.1	24.7	2.69
Ce	534	8.3	1.9	453	17.8	50.7	0.87	2.1	53.3	4.94
Pr	514	7.0	1.6	448	14.7	6.4	0.08	1.4	6.7	4.52
Nd	505	6.3	1.4	430	17.5	27.1	1.09	4.5	28.9	6.10
Sm	553	7.1	1.6	453	22.0	6.5	0.27	5.0	6.6	1.53
Eu	542	6.2	1.3	447	21.3	2.0	0.13	7.2	2.0	0.95
Gd	463	12.1	2.6	449	3.2	7.5	0.40	5.5	6.7	12.14
Tb	504	6.5	1.5	437	15.4	1.1	0.05	5.0	1.0	9.38
Dy	492	4.6	1.1	437	12.6	6.7	0.14	2.4	6.4	4.45
Ho	498	5.3	1.2	449	10.8	1.3	0.05	4.6	1.3	4.13
Er	481	5.2	1.2	455	5.7	3.7	0.16	5.1	3.7	1.05
Tm	462	5.7	1.4	435	6.1	0.5	0.06	12.8	0.5	0.62
Yb	473	8.6	1.9	450	5.2	2.4	0.23	10.1	3.4	29.19
Lu	449	9.0	2.1	439	2.3	0.5	0.04	7.5	0.5	2.11
Th	619	13.0	2.9	457	35.4	5.6	0.28	7.1	5.9	5.76
U	653	11.9	2.6	462	41.5	1.8	0.12	9.4	1.7	5.14
n	*4*					*5*				

Table A3.4. Accuracy and precision estimates for trace and rare earth element concentrations (ppm) based on repeat analysis of reference materials NIST SRM 610 and BCR-2G by SIMS at the Edinburgh Ion Microprobe Facility (EIMF), University of Edinburgh. 1σ is the standard deviation of the repeat analyses and % P is the percentage precision at the 1σ level. The trace and rare earth element concentrations have been normalised to GSD-1G and these values have been compared to the published values in order to assess accuracy. Accuracy is expressed as a percentage difference between the measured and published values. The published values are those of Jochum and Nohl (2008).

Boron concentrations for melt inclusions without corresponding TE analyses were calculated from the average boron count rate from the boron isotope analysis (assuming a constant 5nA beam current) and normalised to the reference material GSD-1G (B = 50 ±20 ppm (Jochum and Nohl, 2008; Jochum et al., 2011)). On average there is an 18 ppm difference between the boron concentrations calculated using this method and the concentrations measured during the TE analysis (Figure A3.3).

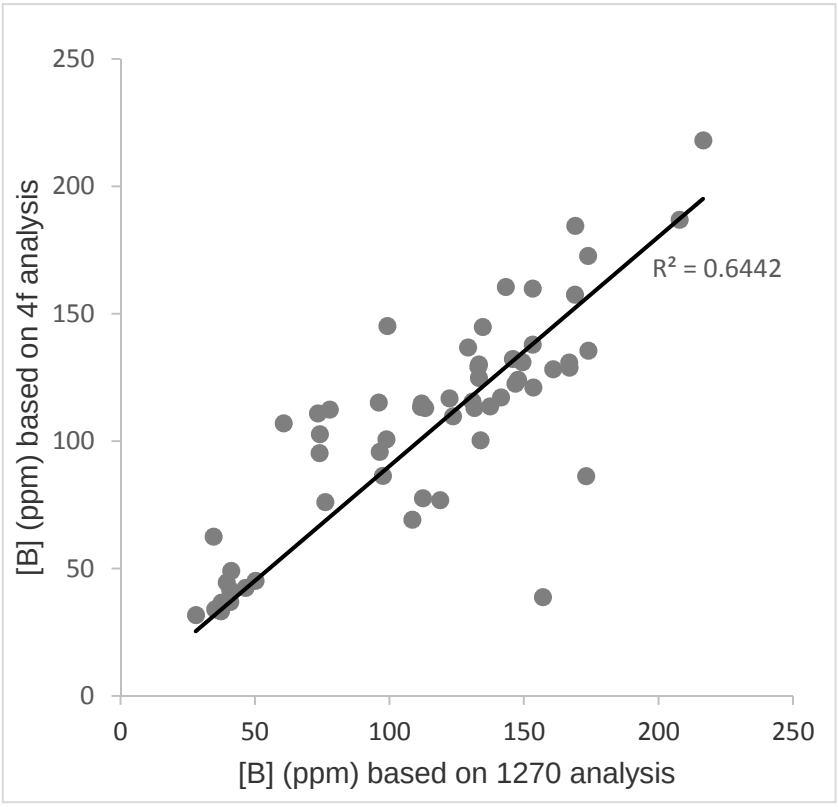

Figure A3.3. Boron concentrations calculated from the average boron count rate from the boron isotope analysis on the Cameca ims 1270 SIMS plotted against the corresponding boron concentration measured in the TE analysis on the Cameca ims 4f SIMS for melt inclusions which were analysed using both methods.

Appendix 3.4 Major element analysis

Subsequent to SIMS analysis the major element compositions of the melt inclusions and host mineral phases were determined using the Cameca SX100 electron microprobe (EPMA) at the School of GeoSciences, University of Edinburgh. Prior to analysis the gold coat (used for SIMS analysis) was removed, the samples were cleaned in DI water and petroleum spirit, and coated in carbon. All analyses were made using an accelerating voltage of 15 kV and a 5μm beam. The beam diameter was measured by taking a secondary electron image of the contamination spot deposited on the standards following the method of Hayward (2012). For analysis of melt inclusion glasses, Na, Mg, Al, Si, K, Ca and Fe were analysed with a beam current of 2nA, and P, Ti and Mn with a beam current of 80nA. For mineral analysis, Na, Mg, Al, Si, Ca and Fe were analysed using a beam current of 4nA, and K, Ti, Mn, Cr and Ni using a beam current of 100nA. Na and K were measured first to minimize the effect of volatisation. Peak counting times were 20s on majors, 30s on traces in clinopyroxene and 60s on traces in glasses, and 3s on the background.

For instrument calibration the standards used were jadeite for Na, spinel for Mg and Al, orthoclase for K, wollastonite for Si and Ca, synthetic fayalite for Fe, Durango apatite for P, rutile for Ti, and pure metals for Mn, Cr and Ni. Analyses of glass standards Lapari (rhyolitic), BCR-2G (basaltic), GSD-1G (basaltic) and a mineral standard, Block 8 - cpx (clinopyroxene), were routinely made throughout the analytical session. Accuracy and precision estimates based on the repeat analysis of these standards are presented in Tables A3.5 and A3.6. Data reduction was carried out in Cameca's PeakSight software and totals which were outside the range of 97 – 101% were discarded. The results of major element analysis of melt inclusion glasses are presented in Appendix 3.8, the results of major element analysis of the host mineral phases are presented in Appendix 1.8.

	Lipari			Published	Accuracy	BCR-2G			Published	Accuracy	GSD-1G			Published	Accuracy
	Average	1σ	%P	values	% difference	Average	1σ	%P	values	% difference	Average	1σ	%P	values	% difference
SiO_2 (wt.%)	74.13	0.67	0.9	74.03	0.1	54.69	0.48	0.9	54.4	0.5	53.10	0.39	0.7	53.2	0.2
Na_2O	4.09	0.11	2.6	4.060	0.7	3.27	0.11	3.4	3.23	1.1	3.70	0.08	2.2	3.6	2.9
MgO	0.04	0.02	43.0	0.00	-	3.61	0.06	1.6	3.56	1.4	3.65	0.07	1.8	3.6	1.3
Al_2O_3	13.04	0.18	1.4	12.72	2.5	13.58	0.18	1.3	13.40	1.4	13.49	0.16	1.2	13.4	0.7
K_2O	5.07	0.16	3.1	5.18	2.1	1.77	0.07	4.0	1.74	1.8	3.12	0.05	1.8	3	3.9
CaO	0.75	0.04	5.7	0.720	4.1	7.18	0.12	1.6	7.06	1.7	7.24	0.13	1.7	7.2	0.5
FeO	1.56	0.13	8.4	1.73	9.7	12.44	0.27	2.1	12.40	0.3	13.08	0.31	2.4	13.3	1.6
P_2O_5	0.005	0.005	100.2	0.00	-	0.34	0.01	3.8	0.37	8.6	0.22	0.01	3.4	0.25	13.9
TiO_2	0.08	0.004	5.1	0.08	4.5	2.27	0.01	0.5	2.27	0.2	1.28	0.01	0.7	1.24	3.5
MnO	0.07	0.01	9.5	0.08	14.5	0.20	0.01	3.6	0.19	5.3	0.03	0.01	21.8	0.02	34.4
Total	98.83	0.71		98.60		99.36	0.63				98.90	0.69			
n	*28*					*35*					*14*				

Table A3.5. Accuracy and precision estimates for major and minor element concentrations (wt.%) based on repeat analysis of glass standards, Lapari (rhyolitic), BCR-2G (basaltic) and GSD-1G (basaltic), by electron microprobe at the University of Edinburgh. 1σ is the standard deviation of the repeat analyses and %P is the percentage precision. Accuracy is expressed as a percentage difference between the measured and published values. The published values for BCR-2G and GSD-1G are from the compilation of Jochum and Nohl (2008), the values for Lipari are those of R.S.J Sparks (pers. comm.) and were determined by XRF analysis.

	Block 8 - cpx			Published	Accuracy
	Average	1σ	%P	values	% difference
SiO_2 (wt.%)	50.92	0.28	0.5	50.72	0.4
Na_2O	0.76	0.04	5.6	0.73	3.5
MgO	8.31	0.08	0.9	8.02	3.6
K_2O	n.d.	-	-	-	-
CaO	23.27	0.17	0.7	22.8	2.0
FeO	16.42	0.19	1.1	16.75	2.0
P_2O_5	-	-	-	-	-
TiO_2	n.d.	-	-	-	-
MnO	0.514	0.013	2.5	0.53	3.1
NiO	n.d.	-	-	-	-
Total	100.2	0.4			
n	*34*				

Table A3.6. Accuracy and precision estimates for major and minor element concentrations (wt.%) based on repeat analysis of internal standard, Block 8 – cpx (clinopyroxene), by electron microprobe at the University of Edinburgh. 1σ is the standard deviation of the repeat analyses and %P is the percentage precision. Accuracy is expressed as a percentage difference between the measured and the accepted values.

Appendix 3.5 Boron isotopic compositions of pyroxene- and zircon- hosted melt inclusions and host mineral phases, determined by SIMS analysis, and presented in analytical order with associated standard (GSD-1G) analyses

Standard or Sample-phenocryst-melt inclusion/host	Analysis number	Analytical session	Mean $^{11}B/^{10}B$ time interpolated	standard error mean ‰ (i.e. internal precision)	^{10}B counts	error	Average $^{11}B/Si^{2+}$	error	Average Si^{2+} counts (5nA)	Average ^{10}B counts (5nA)	[B] ppm	$\delta^{11}B$	Analytical uncertainty (±) (2σ)	Notes
GSD-1G RH block	43	-	3.947	0.57	11091	10	1.36	0.0013	25171	13624	-	**7.9**	-	
GSD-1G RH block	44	-	3.951	0.57	10941	8	1.35	0.0009	25034	13510	-	**9.0**	-	
GSD-1G RH block	45	-	3.950	0.57	10935	9	1.36	0.0013	24759	13539	-	**8.8**	-	
GSD-1G	46	1	3.954	0.58	10399	44	1.35	0.0012	23919	12808	-	**9.8**	-	
GSD-1G	47	1	3.951	0.57	10793	10	1.32	0.0012	25238	13253	-	**8.9**	-	
1026-B1-MI1	48	1	3.924	2.90	424	10	0.05	0.0012	12577	520	2.0	**2.0**	5.9	low counts - overlap on host?
1026-B2-MI1	49	1	3.931	0.39	24020	79	1.43	0.0030	52041	29296	112.0	**3.8**	1.2	
1026-B2-MI1 augite	50	1	3.878	4.53	175	1	0.03	0.0002	19507	213	0.8	**-9.8**	9.1	
1026-B3-MI1	51	1	3.931	1.17	2608	71	0.29	0.0073	28002	3194	12.2	**3.9**	2.5	low counts - overlap on host?
GSD-1G	52	1	3.961	0.58	10437	9	1.32	0.0012	24459	12783	-	**11.6**	-	
GSD-1G	53	1	3.957	0.57	11032	6	1.32	0.0018	25982	13473	-	**10.6**	-	spike removed
1026-B17-MI1	54	1	3.936	0.32	34629	55	1.76	0.0010	61068	41716	160.9	**5.2**	1.1	
1026-B14-MI1	55	1	3.935	0.31	37682	79	1.96	0.0016	31529	45106	174.0	**4.9**	1.1	
1026-B11 aguite	56	1	3.891	4.14	209	2	0.03	0.0003	10800	250	1.0	**-6.4**	8.3	
1026-B11-MI1	57	1	3.930	0.33	33414	57	1.82	0.0010	57245	39737	153.3	**3.7**	1.1	
GSD-1G	58	1	3.953	0.58	10638	9	1.38	0.0013	24133	12638	-	**9.6**	-	slight beam drop and spike in analysis
1026-6 augite	59	1	3.870	2.84	444	10	0.06	0.0013	24611	522	2.0	**-11.8**	5.8	
1026-6-MI1	60	1	3.938	0.57	11144	958	1.30	0.0179	17014	20009	-	**5.6**	1.5	duo spike
GSD-1G RH block	61	-	3.950	0.57	10841	11	1.33	0.0013	24190	13849	-	**10.7**	-	
GSD-1G RH block	62	-	3.954	0.58	10590	7	1.32	0.0012	23625	13974	-	**11.9**	-	

Standard or Sample-phenocryst-melt inclusion/host	Analysis number	Analytical session	Mean $^{11}B/^{10}B$ time interpolated	standard error mean ‰ (i.e. internal precision)	^{10}B counts	error	Average $^{11}B/Si^{2+}$	error	Average Si^{2+} counts (5nA)	Average ^{10}B counts (5nA)	[B] ppm	$\delta^{11}B$	Analytical uncertainty (±) (2σ)	Notes
GSD-1G RH block	63	-	3.951	0.58	10670	13	1.36	0.0013	23333	13881	-	**11.0**	-	
1026-9-MI1	64	2	3.877	1.28	2208	105	0.41	0.0188	8064	2880	11.2	**-8.0**	2.7	low counts - overlap on host?
1026-8-MI1	65	2	3.930	0.32	34293	126	1.86	0.0026	27818	44693	173.1	**5.6**	1.1	
1026-8-MI2	66	2	3.929	0.35	28861	99	1.73	0.0024	49376	37656	145.9	**5.5**	1.2	
1026-6-MI1 repeat	67	2	3.933	0.40	22250	9	1.27	0.0011	53073	29013	112.4	**6.5**	1.2	
GSD-1G larger grain	68	2	3.943	0.60	9966	11	1.60	0.0016	18325	12978	-	**9.1**	-	
GSD-1G larger grain	69	2	3.947	0.60	9835	8	1.55	0.0014	18484	12834	-	**10.0**	-	spike removed
RJ1111-15-MI1	70	2	3.914	0.50	14155	20	1.48	0.0012	27731	18524	74.1	**1.7**	1.4	
RJ1111-12-MI1	71	2	3.922	0.37	25418	48	1.82	0.0028	40207	33480	133.8	**3.7**	1.2	spike removed
RJ1111-11-MI1	72	2	3.897	3.08	378	3	0.05	0.0005	19656	498	2.0	**-2.7**	6.2	low counts - overlap on host?
RJ1111-6-MI1	73	2	3.914	0.36	27920	88	2.05	0.0043	39150	36960	147.8	**1.5**	1.2	
RJ1111-6 augite	74	2	3.874	3.72	261	4	0.05	0.0006	15886	346	1.4	**-8.7**	7.5	
GSD-1G larger grain	75	2	3.940	0.61	9551	12	1.55	0.0016	17892	12575	-	**8.2**	-	
GSD-1G larger grain	76	2	3.947	0.63	8871	8	1.61	0.0017	16050	11640	-	**9.9**	-	
RJ1111-1-MI1	77	3	3.932	0.50	14115	6	1.35	0.0019	15649	18481	66.2	**6.8**	1.1	variable counts - edge of the grain
RJ1111-2-MI1	78	3	3.912	0.96	3899	8	0.48	0.0005	23740	5097	18.3	**1.5**	2.0	
RJ1111-4-MI1	79	3	3.909	0.39	23754	66	1.95	0.0025	35203	31152	111.7	**0.7**	0.9	
RJ1111-4-MI2	80	3	3.914	0.46	16632	75	1.64	0.0021	29468	21713	77.8	**2.0**	1.0	
RJ1111-4 augite	81	3	3.842	4.55	175	2	0.03	0.0004	14942	229	0.8	**-16.4**	9.1	
GSD-1G	82	3	3.946	0.58	10710	15	1.36	0.0011	23091	13949	-	**10.4**	-	
RJ1111-4-MI3	83	3	3.912	0.43	19621	22	1.73	0.0013	33153	25481	96.3	**1.4**	0.9	
GSD-1G	84	3	3.946	0.61	9609	16	1.63	0.0030	8921	12504	-	**10.2**	-	spike removed
AM0887-6-MI1	85	3	3.920	0.37	26265	54	1.81	0.0015	42610	33942	130.9	**3.7**	0.8	
AM0887-6-MI2	86	3	3.920	0.38	24481	49	1.87	0.0015	38582	31712	122.3	**3.5**	0.9	spike removed

Standard or Sample-phenocryst-melt inclusion/host	Analysis number	Analytical session	Mean $^{11}B/^{10}B$ time interpolated	standard error mean ‰ (i.e. internal precision)	^{10}B counts	error	Average $^{11}B/Si^{2+}$	error	Average Si^{2+} counts (5nA)	Average ^{10}B counts (5nA)	[B] ppm	$\delta^{11}B$	Analytical uncertainty (±) (2σ)	Notes
AM0887-6 augite	87	3	3.850	3.48	306	21	0.05	0.0036	16277	396	1.5	**-14.3**	7.0	
AM0887-12-MI1	88	3	3.934	0.40	21753	36	1.41	0.0020	45477	28119	108.4	**7.2**	0.9	
AM0887-10-MI1	89	3	3.929	0.33	33489	46	1.84	0.0017	53846	43242	166.8	**5.8**	0.8	
GSD-1G	90	3	3.944	0.59	10360	10	1.38	0.0015	22290	13426	-	**9.7**	-	
GSD-1G	91	4	3.950	0.55	11681	13	1.36	0.0015	25351	15331	-	**9.3**	-	
RF62-MB2-MI1	92	4	3.926	0.31	36973	30	1.72	0.0065	63437	48208	157.1	**3.2**	0.8	
RJ1111-MB2-MI1	93	4	3.917	0.34	31388	81	1.91	0.0017	48435	40900	133.3	**0.8**	0.8	
RJ1111-MB1-MI1	94	4	3.917	0.34	31724	48	1.99	0.0017	46729	41343	134.7	**0.9**	0.8	
RJ1111-MB1glassy-MI1	95	4	3.893	3.63	274	7	0.03	0.0009	24271	357	1.2	**-5.4**	7.3	low counts - overlap on host?
RJ1111-MB1glassy augite	96	4	3.890	4.09	215	2	0.03	0.0003	19737	280	0.9	**-6.2**	8.2	
GSD-1G	97	4	3.952	0.55	11843	19	1.35	0.0013	26004	15449	-	**9.8**	-	
GSD-1G	98	4	3.957	0.55	11674	18	1.32	0.0014	13333	15255	-	**10.9**	-	
ZN122-MB6-MI1	99	4	3.880	3.12	369	3	0.04	0.0003	23325	483	1.6	**-8.7**	6.3	low counts - overlap on host?
AM0887-MB2-MI1	100	4	3.924	0.41	21462	31	1.34	0.0012	46700	28242	93.8	**2.7**	0.9	
AM0887-MB6-MI1	101	4	3.921	0.46	16824	30	1.31	0.0017	37642	22080	73.4	**1.7**	1.0	
AM0887-MB5glassy-MI1	102	4	3.883	1.70	1236	25	0.13	0.0022	26853	1619	5.4	**-7.8**	3.4	low counts - overlap on host?
AM0887-MB5glassy augite	103	4	3.889	4.61	169	2	0.02	0.0003	19950	222	0.7	**-6.4**	9.2	
GSD-1G	104	4	3.954	0.56	11158	16	1.35	0.0012	24555	14679	-	**10.3**	-	
GSD-1G	105	4	3.955	0.56	11238	14	1.32	0.0013	25163	14809	-	**10.5**	-	
1026-MB2-MI1	106	4	3.932	0.38	25118	142	1.84	0.0061	40103	33107	109.8	**4.6**	0.9	
RF65-MB3-MI1	107	4	3.923	0.49	14745	108	1.41	0.0060	15519	19409	64.4	**2.4**	1.1	
RF65-MB3 augite	108	4	3.858	3.36	319	2	0.05	0.0003	20509	419	1.4	**-14.2**	6.7	
AM0887-MB11-MI1	109	4	3.920	0.53	12584	40	1.10	0.0020	33730	16515	54.8	**1.5**	1.2	
GSD-1G	110	4	3.951	0.55	11633	18	1.36	0.0013	25882	15338	-	**9.5**	-	

Standard or Sample-phenocryst-melt inclusion/host	Analysis number	Analytical session	Mean $^{11}B/^{10}B$ time interpolated	standard error mean ‰ (i.e. internal precision)	^{10}B counts	error	Average $^{11}B/Si^{2+}$	error	Average Si^{2+} counts (5nA)	Average ^{10}B counts (5nA)	[B] ppm	$\delta^{11}B$	Analytical uncertainty (±) (2σ)	Notes
GSD-1G	111	4	3.951	0.55	11602	16	1.32	0.0011	26379	15456	-	**9.5**	-	
NIST 610	112	4	3.882	0.27	50332	111	3.66	0.0034	19980	67159	220.8	**-8.2**	0.7	
NIST 610	113	4	3.882	0.27	50049	115	3.65	0.0034	40616	66462	218.5	**-8.2**	0.7	
GSD-1G	114	4	3.947	0.56	11502	15	1.38	0.0013	25145	15276	-	**8.4**	-	spike removed
GSD-1G	115	4	3.953	0.55	11633	22	1.33	0.0011	26323	15459	-	**10.1**	-	
GSD-1G	116	4	3.955	0.56	11418	9	1.30	0.0013	26526	15282	-	**10.6**	-	
GSD-1G	117	4	3.954	0.56	11143	6	1.30	0.0013	25749	14940	-	**10.4**	-	
GSD-1G	118	4	3.959	0.56	11330	9	1.31	0.0012	26447	14607	-	**11.5**	-	
GSD-1G	119	4	3.956	0.55	11853	11	1.31	0.0011	27644	15310	-	**10.7**	-	
GSD-1G	120	5	3.945	0.58	10538	11	1.48	0.0014	10814	13648	-	**10.8**	-	spike removed
AM0887-15 augite	121	5	3.899	3.39	315	8	0.05	0.0013	16872	408	1.5	**-0.9**	6.8	
AM0887-15-MI1	122	5	3.932	0.39	23164	24	1.68	0.0012	39630	30053	113.3	**7.5**	1.1	
AM0887-15-MI2	123	5	3.927	0.42	20205	16	1.41	0.0016	41457	26209	98.8	**6.1**	1.1	
GSD-1G	124	5	3.941	0.61	9698	12	1.44	0.0011	19407	12943	-	**9.9**	-	
GSD-1G	125	5	3.940	0.60	10003	10	1.41	0.0012	20201	13190	-	**9.6**	-	
GSD-1G	126	6	3.948	0.58	10489	15	1.46	0.0018	20418	13835	-	**10.5**	-	
AM0887-8-MI1	127	6	3.926	0.38	24233	49	1.84	0.0030	36711	31945	118.9	**4.9**	1.1	
AM0887-16-MI1	128	6	3.940	0.42	19878	109	1.47	0.0068	37809	26220	97.6	**8.6**	1.2	
AM0887-17-MI1	129	6	3.928	0.65	8306	13	0.68	0.0008	18211	10954	40.8	**5.5**	1.5	
GSD-1G	130	6	3.944	0.60	9892	30	1.45	0.0018	20912	13041	-	**9.7**	-	spike removed
GSD-1G	131	7	3.953	0.58	10495	9	1.35	0.0012	23807	13808	-	**10.9**	-	
ZN122-8-MI1	132	7	3.914	0.79	5767	13	0.44	0.0006	40098	7592	28.1	**0.9**	1.7	
ZN122-1-MI1	133	7	3.913	0.68	7695	11	0.59	0.0007	39395	10182	37.6	**0.6**	1.6	
ZN122-5-MI1	134	7	3.910	0.65	8320	18	0.58	0.0007	40217	11032	40.8	**-0.2**	1.5	spike removed

Standard or Sample-phenocryst-melt inclusion/host	Analysis number	Analytical session	Mean $^{11}B/^{10}B$ time interpolated	standard error mean ‰ (i.e. internal precision)	^{10}B counts	error	Average $^{11}B/Si^{2+}$	error	Average Si^{2+} counts (5nA)	Average ^{10}B counts (5nA)	[B] ppm	$\delta^{11}B$	Analytical uncertainty (±) (2σ)	Notes
GSD-1G	135	7	3.949	0.60	9765	7	1.46	0.0017	19611	13004	-	**9.9**	-	
GSD-1G	136	7	3.946	0.58	10493	9	1.31	0.0011	23582	13936	-	**9.1**	-	
GSD-1G	137	7	3.952	0.60	10018	10	1.37	0.0013	21795	13344	-	**10.5**	-	
GSD-1G	138	8	3.952	0.57	10848	11	1.33	0.0011	12091	14419	-	**10.1**	-	
ZN122-10-MI1	139	8	3.904	0.67	7853	18	0.54	0.0007	42193	10549	37.2	**-1.9**	1.8	
RF65-1-MI1	140	8	3.937	0.31	35990	16	2.39	0.0031	44845	47959	169.1	**6.4**	1.3	
ZN122-10 augite	141	8	3.861	6.27	93	3	0.01	0.0005	20377	124	0.4	**-13.1**	12.6	
GSD-1G	142	8	3.955	0.58	10472	20	1.30	0.0018	24086	14033	-	**11.1**	-	
GSD-1G	143	8	3.948	0.58	10525	11	1.32	0.0021	11692	14087	-	**9.1**	-	spike removed
GSD-1G	144	9	3.949	0.57	11011	18	1.34	0.0010	24609	14748	-	**9.4**	-	
GSD-1G	145	9	3.956	0.57	10895	23	1.30	0.0010	25138	14556	-	**11.1**	-	
AM0887-MB5-MI1	146	9	3.933	0.34	30974	73	1.69	0.0009	55037	41647	141.4	**5.2**	1.2	
AM0887-MB17-MI1	147	9	3.931	0.34	30106	65	1.57	0.0010	28021	40471	137.4	**4.7**	1.2	
AM0887-MB13-MI1	148	9	3.933	0.36	26921	47	1.50	0.0012	25915	36400	123.6	**5.2**	1.3	spike removed
AM0887-MB12-MI1	149	9	3.928	0.33	31938	67	1.72	0.0011	26843	43251	146.9	**3.9**	1.2	
GSD-1G	150	9	3.951	0.57	10985	14	1.34	0.0013	11911	14871	-	**9.8**	-	
RF62-MB3-MI1	151	9	3.929	1.33	2015	66	0.24	0.0074	12293	2729	9.3	**4.1**	2.8	
RJ1111-MB3-MI1	152	9	3.826	0.53	12865	2109	-	-	-	-	112.9	**-22.2**	-	duo spike
GSD-1G	154	10	3.959	0.60	10014	23	1.35	0.0012	9983	14099	-	**11.2**	-	beam tuning
GSD-1G	155	10	3.959	0.61	9502	78	1.35	0.0012	8366	13775	-	**11.2**	-	beam tuning
GSD-1G	156	10	3.951	0.60	9885	5	1.40	0.0012	9968	13716	-	**9.0**	-	
GSD-1G	157	10	3.953	0.60	9779	7	1.37	0.0014	9932	13793	-	**9.6**	-	
RJ1111-MB4-MI1	158	10	3.923	0.37	25927	28	1.88	0.0012	19318	36331	133.2	**1.9**	1.3	
RJ1111-MB5-MI1	159	10	3.921	0.35	29005	37	1.85	0.0015	21732	40758	149.5	**1.5**	1.2	

Standard or Sample-phenocryst-melt inclusion/host	Analysis number	Analytical session	Mean $^{11}B/^{10}B$ time interpolated	standard error mean ‰ (i.e. internal precision)	^{10}B counts	error	Average $^{11}B/Si^{2+}$	error	Average Si^{2+} counts (5nA)	Average ^{10}B counts (5nA)	[B] ppm	$\delta^{11}B$	Analytical uncertainty (±) (2σ)	Notes
GSD-1G	160	10	3.962	0.61	9639	6	1.30	0.0013	10421	13564	-	**11.9**	-	
GSD-1G	161	10	3.958	0.61	9618	7	1.31	0.0014	10413	13459	-	**11.0**	-	
1026-MB11-MI1	162	10	3.936	0.33	32858	19	2.13	0.0019	21714	45783	169.0	**5.2**	1.2	
RJ1111-MB11glassy-MI1	163	10	3.927	1.49	1612	11	0.19	0.0012	11751	2246	8.3	**3.0**	3.1	low counts - overlap on host?
GSD-1G	164	10	3.954	0.60	9779	8	1.38	0.0013	10019	13621	-	**9.8**	-	
GSD-1G larger repolished	165	11	3.958	0.58	10570	8	1.39	0.0026	10770	14690	-	**11.3**	-	spike removed
1026-A3-MI1	166	11	3.917	0.36	27343	462	2.02	0.0389	19133	37824	128.9	**0.7**	1.5	dropping counts - overlap on host?
1026-A6-MI1	167	11	3.934	0.42	20275	29	1.54	0.0032	18621	28182	96.1	**5.1**	1.6	
1026-A2-MI1	168	11	3.927	0.36	28262	24	1.92	0.0019	20793	39029	133.0	**3.3**	1.5	
GSD-1G larger repolished	169	11	3.954	0.58	10534	7	1.38	0.0013	10931	14610	-	**10.1**	-	
GSD-1G larger repolished	170	11	3.949	0.58	10623	7	1.41	0.0014	10694	14707	-	**8.9**	-	
GSD-1G smaller repolished	171	12	3.950	0.64	8613	6	1.33	0.0013	9240	11895	-	**10.5**	-	
1026-A9-MI1	172	12	3.936	0.35	28658	19	1.73	0.0022	23622	39378	166.9	**6.8**	0.8	
1026-A5-MI1	173	12	3.935	0.40	22592	22	1.56	0.0020	20681	31039	131.6	**6.6**	0.9	spike removed
1026-A5 zircon	174	12	3.786	5.61	124	18	0.05	0.0067	3576	170	0.7	**-31.7**	11.2	primarily surface contamination
1026-A10-MI1	175	12	3.936	0.45	17255	20	1.51	0.0016	16480	23520	99.7	**6.6**	1.0	
GSD-1G smaller repolished	176	12	3.948	0.64	8640	8	1.32	0.0017	9455	11797	-	**9.9**	-	
GSD-1G smaller repolished	177	12	3.948	0.64	8603	7	1.32	0.0013	9444	11694	-	**9.9**	-	
GSD-1G larger repolished	178	13	3.942	0.64	8697	7	1.38	0.0016	9087	11911	-	**9.0**	-	spike removed
RF62-2-MI1	179	13	3.940	0.39	22970	55	1.88	0.0018	17686	31204	129.2	**8.4**	1.5	
RF62-4-MI1	180	13	3.924	0.45	17629	71	1.95	0.0033	13007	23954	99.2	**4.4**	1.5	
RF62-3-MI1	181	13	3.934	0.52	13134	27	1.44	0.0014	13197	17904	74.1	**6.8**	1.6	
GSD-1G larger repolished	182	13	3.950	0.63	8846	12	1.34	0.0014	9537	12058	-	**11.1**	-	
GSD-1G larger repolished	183	13	3.947	0.63	9005	7	1.35	0.0012	9656	12262	-	**10.2**	-	spike removed

Standard or Sample-phenocryst-melt inclusion/host	Analysis number	Analytical session	Mean $^{11}B/^{10}B$ time interpolated	standard error mean ‰ (i.e. internal precision)	^{10}B counts	error	Average $^{11}B/Si^{2+}$	error	Average Si^{2+} counts (5nA)	Average ^{10}B counts (5nA)	[B] ppm	$\delta^{11}B$	Analytical uncertainty (±) (2σ)	Notes
GSA	184	13	4.006	0.97	3729	4	0.59	0.0007	9413	5054	20.9	**25.3**	2.3	
GSD-1G RH block	185	-	3.958	0.65	8387	6	1.27	0.0022	8874	12362	-	**12.8**	-	
GSD-1G RH block	186	-	3.953	0.62	9140	6	1.31	0.0010	10116	12516	-	**11.4**	-	
GSD-1G RH block	187	-	3.955	0.62	9163	5	1.28	0.0014	10461	12425	-	**12.1**	-	
GSD-1G larger repolished	188	14	3.948	0.60	9867	7	1.41	0.0014	10216	13341	-	**10.2**	-	
GSD-1G larger repolished	189	14	3.951	0.60	9769	9	1.33	0.0014	10800	13211	-	**11.0**	-	
1026-UA-1-MI1	190	14	3.904	0.34	31393	377	2.17	0.0287	20923	42252	162.5	**-0.9**	1.3	overlap on edge - potential contamination
GSD-1G larger repolished	191	14	3.944	0.62	9255	10	1.49	0.0012	9115	12439	-	**9.1**	-	
1026-UA-4-MI1	192	14	3.927	0.56	11180	18	1.41	0.0021	11561	15095	60.7	**4.9**	1.6	spike removed
GSD-1G smaller repolished	193	15	3.952	0.63	8972	32	1.37	0.0017	9664	12052	-	**9.6**	-	
1026-A7-MI1	194	15	3.937	0.34	30443	84	2.18	0.0029	20348	40878	173.9	**5.9**	1.2	
1027-A7-MI2	195	15	3.940	0.36	27943	134	2.11	0.0045	20232	36078	153.4	**6.7**	1.2	spike removed
GSD-1G smaller repolished	196	15	3.956	0.63	8851	17	1.32	0.0016	10211	11459	-	**10.6**	-	
GSD-1G larger repolished	197	16	3.961	0.62	9305	7	1.29	0.0014	11014	12044	-	**9.0**	-	
Z27-A8-MI1	198	16	3.895	0.61	9647	160	0.95	0.0171	15296	12474	53.5	**-7.7**	1.6	dropping counts - overlap with zircon
Z27-A6-MI1	199	16	3.914	0.84	4999	22	0.57	0.0014	13223	6474	27.8	**-2.9**	2.0	
Z27-A13-MI1	200	16	3.916	0.71	7116	6	0.63	0.0008	17029	9205	39.5	**-2.5**	1.8	
Z27-A9-MI1	201	16	3.909	0.69	7401	23	0.68	0.0031	16375	9591	41.1	**-4.2**	1.7	
GSD-1G larger repolished	202	16	3.967	0.64	8619	12	1.25	0.0020	10498	11168	-	**10.6**	-	spike removed
GSD-1G larger repolished	203	16	3.967	0.63	9083	9	1.26	0.0014	11036	11755	-	**10.7**	-	
NIST 610	204	16	3.897	0.30	40368	45	3.45	0.0030	17559	52262	224.2	**-7.3**	1.2	
GSD-1G larger repolished	205	-	3.962	0.66	8093	8	1.26	0.0012	8729	11840	-	**10.1**	-	
GSD-1G larger repolished	206	-	3.957	0.64	8682	6	1.27	0.0013	9539	12451	-	**8.9**	-	
GSD-1G larger repolished	207	-	3.967	0.66	8162	12	1.25	0.0013	9150	11523	-	**11.4**	-	

Standard or Sample-phenocryst-melt inclusion/host	Analysis number	Analytical session	Mean $^{11}B/^{10}B$ time interpolated	standard error mean ‰ (i.e. internal precision)	^{10}B counts	error	Average $^{11}B/Si^{2+}$	error	Average Si^{2+} counts (5nA)	Average ^{10}B counts (5nA)	[B] ppm	$\delta^{11}B$	Analytical uncertainty (±) (2σ)	Notes
GSD-1G smaller repolished	208	17	3.948	0.68	7651	22	1.42	0.0015	7294	11048	-	**9.6**	-	
MQ153-A1-MI1	209	17	3.906	0.78	5930	24	0.53	0.0024	15041	8670	37.4	**-1.2**	1.6	
MQ153-UA3-MI1	210	17	3.833	3.35	336	35	0.18	0.0176	2456	499	2.1	**-20.0**	6.7	low counts - overlap on host?
MQ153-UA2-MI1	211	17	3.890	0.77	6057	12	0.69	0.0013	11511	8940	38.5	**-5.4**	1.6	
GSD-1G smaller repolished	212	17	3.952	0.67	7990	6	1.36	0.0014	7649	12088	-	**10.5**	-	
GSD-1G smaller repolished	213	17	3.951	0.68	7758	18	1.33	0.0015	7679	11683	-	**10.2**	-	
GSD-1G new	214	18	3.955	0.60	9806	9	1.29	0.0014	11908	12378	-	**9.5**	-	
GSD-1G new	215	18	3.961	0.61	9587	10	1.30	0.0014	11511	12129	-	**11.0**	-	spike removed
RF62-7-MI1	216	18	3.921	0.29	41046	54	2.96	0.0060	21510	51830	207.8	**0.8**	0.9	
RF62-7-MI2	217	18	3.923	0.29	42981	66	3.04	0.0021	22075	54034	216.6	**1.3**	0.9	
RF62-5-MI1	218	18	3.932	0.48	15713	69	1.68	0.0018	15816	18979	76.1	**3.6**	1.2	
RF62-9-MI1	219	18	3.936	0.81	5375	30	1.13	0.0023	5217	8636	34.6	**4.7**	1.8	
GSD-1G new	220	18	3.956	0.61	9571	8	1.29	0.0011	10926	12908	-	**9.9**	-	
RF62-8-MI1	221	18	3.920	0.37	26596	31	2.12	0.0015	18448	35591	143.2	**0.6**	1.0	spike removed
RF62-8-MI2	222	18	3.923	0.35	28722	30	2.10	0.0013	20234	38090	153.3	**1.3**	1.0	
GSD-1G new	223	18	3.957	0.63	9052	11	1.28	0.0011	10626	11946	-	**10.0**	-	
GSD-1G smaller repolished	224	19	3.957	0.59	10332	18	1.31	0.0013	11932	13550	-	**10.9**	-	
Z27-UA2-MI1	225	19	3.914	0.59	10254	13	0.62	0.0010	24571	13406	50.2	**-0.2**	1.9	
Z27-A12-MI1	226	19	3.894	0.62	9399	86	0.81	0.0076	17084	12443	46.6	**-5.3**	1.9	
GSD-1G smaller repolished	227	19	3.951	0.60	10026	17	1.33	0.0017	11322	13169	-	**9.4**	-	
GSD-1G new	228	20	3.947	0.63	9052	7	1.28	0.0011	10648	11875	-	**8.5**	-	
ZN122-6-MI1	229	20	3.913	0.75	6355	14	0.46	0.0005	20601	8322	35.2	**-0.4**	3.6	
RF62-10-MI1	230	20	3.927	0.37	26255	338	2.22	0.0038	17764	34252	144.8	**3.3**	3.3	
RF62-12-MI1	231	20	3.898	1.48	1631	6	0.23	0.0011	11004	2101	8.9	**-4.2**	4.4	low counts - overlap on host?

Standard or Sample-phenocryst-melt inclusion/host	Analysis number	Analytical session	Mean $^{11}B/^{10}B$ time interpolated	standard error mean ‰ (i.e. internal precision)	^{10}B counts	error	Average $^{11}B/Si^{2+}$	error	Average Si^{2+} counts (5nA)	Average ^{10}B counts (5nA)	[B] ppm	$\delta^{11}B$	Analytical uncertainty (±) (2σ)	Notes
GSD-1G new	232	20	3.960	0.62	9191	9	1.27	0.0018	11122	11778	-	**11.7**	-	

Appendix 3.6 Trace and rare earth element concentrations of pyroxene- and zircon hosted melt inclusions determined by SIMS analysis

Sample-phenocryst-melt inclusion	Host Mineral	Melt inclusion condition	Analysis location	Trace and rare earth elements (ppm)																						# of cycles
				B	Ti	Sr	Y	Zr	Nb	Ba	La	Ce	Pr	Nd	Sm	Eu	Gd	Tb	Dy	Ho	Er	Tm	Yb	Lu	Th	U	
RJ1111-1-MI1	Augite	Re	δ11B pit	80.7	5118.4	102.1	28.9	160.7	5.2	290.1	10.96	26.81	3.68	17.86	4.70	0.37	4.60	0.83	5.11	1.07	3.35	0.48	3.16	0.56	8.15	2.53	10
RJ1111-4-MI1	Augite	Re	δ11B pit	113.4	2199.9	37.0	13.6	210.7	7.1	208.6	17.65	36.99	4.31	15.98	2.95	0.18	2.62	0.45	2.39	0.54	1.48	0.26	1.61	0.25	14.09	4.23	10
RJ1111-4-MI2	Augite	Re	δ11B pit	112.4	2656.6	65.6	9.3	132.3	6.2	326.0	9.30	20.63	2.40	9.31	2.07	0.23	0.93	0.23	2.12	0.42	1.07	0.14	1.27	0.19	13.17	5.01	10
RJ1111-4-MI3	Augite	Re	δ11B pit	95.8	3649.7	77.4	29.1	228.2	5.5	355.4	16.25	39.93	5.08	21.26	5.45	0.28	4.55	0.74	5.44	1.19	3.58	0.45	3.76	0.57	12.91	3.69	10
RJ1111-6-MI1	Augite	Re	δ11B pit	124.1	1841.2	33.4	21.1	262.7	6.0	223.4	16.09	36.28	4.64	18.66	4.34	0.32	2.90	0.58	3.11	0.85	2.02	0.32	2.44	0.35	13.43	3.70	10
RJ1111-12-MI1	Augite	Re	δ11B pit	100.3	3766.4	67.1	32.2	231.3	5.7	365.5	15.58	38.42	5.04	22.84	5.63	0.48	4.75	0.92	5.76	1.21	3.42	0.60	3.79	0.55	11.92	3.79	10
RJ1111-12-MI2	Augite	Re	new spot	76.7	3208.7	63.4	36.3	164.2	4.2	305.9	12.20	32.01	4.81	21.12	6.04	0.77	5.84	1.08	6.18	1.38	3.87	0.53	3.82	0.52	9.14	2.78	10
RJ1111-15-MI1	Augite	Re	δ11B pit	95.3	2726.7	51.2	18.1	234.3	5.0	257.5	11.59	25.82	3.29	13.52	3.11	0.39	2.08	0.42	3.03	0.71	1.87	0.28	2.23	0.38	11.12	3.65	10
RJ1111-MB1-MI1	Augite	Gl	repolished	144.8	2239.7	106.8	23.0	283.1	7.9	566.3	18.55	43.23	5.44	22.55	4.40	2.16	4.85	0.66	4.18	0.82	2.23	0.30	1.63	0.36	15.66	5.02	10
RJ1111-MB2-MI1	Augite	Gl	repolished	130.1	2697.2	154.7	18.3	291.5	8.2	544.7	19.67	42.29	4.77	18.51	3.51	2.12	4.69	0.64	3.85	0.68	1.71	0.25	0.65	0.34	13.13	4.30	10
RJ1111-MB3-MI1	Augite	Gl	δ11B pit	137.4	2178.1	129.3	18.6	269.6	8.0	514.0	17.53	39.97	4.67	18.94	3.59	1.64	4.41	0.57	3.53	0.79	1.68	0.26	1.59	0.32	14.63	4.53	10
RJ1111-MB4-MI1	Augite	Gl	δ11B pit	124.7	2278.8	128.1	29.7	230.4	6.6	479.8	18.59	41.85	5.54	22.04	5.66	1.49	4.69	0.91	5.69	1.13	3.15	0.41	3.04	0.52	15.29	5.19	10
RJ1111-MB5-MI1	Augite	Gl	δ11B pit	130.9	2382.9	131.2	19.0	263.1	7.1	459.9	20.60	46.22	5.15	20.46	3.54	1.42	3.54	0.61	3.02	0.75	2.20	0.31	1.51	0.37	13.26	3.87	10
MQ153-A1-MI1	Zircon	Gl	new spot	33.2	227.7	79.5	42.3	2734.7	21.1	241.5	21.86	39.89	3.43	10.58	2.05	0.81	2.79	0.53	4.28	1.41	5.36	0.99	8.08	1.40	57.43	45.00	10
ZN122-1-MI1	Augite	Re	δ11B pit	36.6	3227.9	100.4	73.3	197.2	11.4	602.7	63.01	149.63	18.49	79.12	17.70	1.32	13.50	2.74	14.30	2.72	7.75	1.10	8.29	0.85	24.03	7.23	10
ZN122-5-MI1	Augite	Re	δ11B pit	36.8	1154.6	76.3	39.1	99.2	7.1	537.8	35.01	88.84	10.26	39.78	8.91	0.31	5.33	1.25	7.79	1.46	4.53	0.52	4.09	0.50	16.93	3.92	10
ZN122-6-MI1	Augite	Re	δ11B pit	34.0	1165.4	68.9	47.4	108.8	9.9	710.2	25.45	61.67	7.86	35.67	9.75	0.02	6.74	1.57	9.38	1.96	4.66	0.74	5.04	0.56	17.71	5.57	10
ZN122-8-MI1	Augite	Re	δ11B pit	31.7	924.5	140.4	54.4	165.0	10.8	655.7	72.83	164.26	20.49	90.43	18.43	1.34	15.59	2.10	10.88	2.08	5.04	0.67	3.44	0.58	18.44	5.94	10
ZN122-10-MI1	Augite	Re	δ11B pit	33.4	2194.0	96.9	30.2	121.2	8.4	749.3	29.11	61.55	7.11	30.62	6.76	0.00	6.01	1.04	5.99	1.31	3.02	0.56	3.49	0.46	20.61	5.94	10
Z27-UA2-MI1	Zircon	Gl	δ11B pit	45.2	1287.8	71.6	78.7	2336.1	7.9	708.9	24.59	39.91	4.84	16.90	3.86	1.21	3.79	0.96	8.25	2.44	9.91	1.64	11.03	1.81	37.56	15.38	10
Z27-A6-MI2	Zircon	Gl	new spot	48.0	960.7	36.8	249.5	16631.6	15.9	514.2	23.65	40.85	4.68	16.14	4.53	2.24	9.55	2.58	26.22	8.05	33.88	6.44	51.04	10.31	83.51	31.95	10
Z27-A9-MI1	Zircon	Gl	δ11B pit	49.0	1295.9	45.1	59.0	39682.3	33.6	521.4	23.86	37.83	4.95	19.57	3.59	1.07	3.53	0.60	6.49	2.26	8.93	1.74	15.64	3.64	22.11	11.37	7
Z27-A12-MI1	Zircon	Gl	δ11B pit	42.4	1102.7	42.6	48.3	317.4	14.3	616.8	27.73	43.85	5.42	17.38	3.74	1.83	4.85	0.88	5.98	1.53	5.66	0.87	6.34	0.94	33.65	13.16	10
Z27-A13-MI1	Zircon	Gl	δ11B pit	44.5	1123.8	74.7	159.6	877.0	16.6	712.0	49.88	100.28	14.58	57.08	12.63	3.16	12.98	3.27	23.90	5.54	18.10	2.68	17.41	2.53	29.76	7.84	10
AM0887-6-MI1	Augite	Re	δ11B pit	115.5	1779.7	63.1	19.6	309.0	12.6	502.0	21.89	47.62	5.31	19.56	3.65	0.39	2.78	0.53	3.27	0.74	2.48	0.32	2.59	0.41	44.60	13.03	10
AM0887-6-MI2	Augite	Re	δ11B pit	116.7	2059.4	65.2	17.3	303.7	13.2	490.1	20.31	43.01	4.92	18.06	3.60	0.37	2.52	0.52	2.65	0.70	1.84	0.28	2.50	0.32	42.25	12.10	10
AM0887-8-MI1	Enstatite	Re	δ11B pit	76.8	1427.9	69.6	17.4	238.9	11.2	350.9	21.44	47.50	5.25	17.84	3.58	0.97	2.93	0.53	3.36	0.71	1.79	0.27	1.38	0.32	28.61	8.35	10
AM0887-10-MI1	Augite	Re	δ11B pit	130.8	1896.7	51.8	24.3	241.6	13.4	214.6	27.26	66.37	7.31	25.99	4.94	0.50	4.37	0.56	4.05	0.89	2.53	0.39	3.21	0.41	53.50	14.77	10

Sample-phenocryst-melt inclusion	Host Mineral	Melt inclusion condition	Analysis location	Trace and rare earth elements (ppm)																								# of cycles
				B	Ti	Sr	Y	Zr	Nb	Ba	La	Ce	Pr	Nd	Sm	Eu	Gd	Tb	Dy	Ho	Er	Tm	Yb	Lu	Th	U	
AM0887-10-MI2	Augite	Re	new spot	116.2	1916.2	59.0	25.2	300.5	14.2	220.5	30.40	68.53	7.79	28.24	5.02	0.58	3.76	0.62	4.17	0.94	2.59	0.42	3.13	0.41	45.43	13.39	10
AM0887-12-MI1	Enstatite	Re	δ11B pit	69.1	3413.5	52.0	18.8	255.3	10.4	318.0	19.56	44.54	5.24	22.00	4.74	0.71	4.42	0.59	3.83	0.72	1.96	0.26	1.95	0.24	24.47	6.98	10
AM0887-15-MI1	Augite	Re	δ11B pit	112.9	1875.0	50.2	24.6	333.7	12.0	409.5	27.92	62.78	7.08	25.40	4.99	0.06	4.10	0.71	3.74	0.98	3.19	0.42	3.37	0.48	51.77	14.73	10
AM0887-15-MI2	Augite	Re	δ11B pit	100.7	2465.9	68.7	61.6	306.2	13.2	355.8	66.73	162.04	20.78	88.48	18.47	1.52	15.43	2.29	12.20	2.06	5.76	0.69	3.74	0.61	42.82	11.81	10
AM0887-16-MI1	Enstatite	Re	δ11B pit	86.4	2287.9	65.2	9.5	325.2	14.4	241.5	13.27	28.80	3.19	11.83	2.13	0.45	2.08	0.24	2.01	0.38	1.09	0.15	1.02	0.17	33.88	9.92	10
AM0887-17-MI1	Augite	Re	δ11B pit	41.5	3968.2	179.1	17.7	152.7	10.7	533.7	24.68	47.92	5.25	20.22	3.82	0.33	2.75	0.52	3.29	0.61	2.26	0.26	2.70	0.35	22.51	6.16	10
AM0887-MB5-MI1	Augite	Gl	δ11B pit	117.1	1446.9	92.3	14.8	353.7	14.1	596.2	28.65	60.02	6.17	21.74	3.55	1.13	2.25	0.48	2.80	0.60	1.65	0.23	1.28	0.29	46.56	13.04	10
AM0887-MB6-MI1	Augite	Gl	repolished	110.8	2069.6	115.5	15.9	328.4	16.0	606.7	23.60	53.49	5.97	20.43	3.26	1.57	3.75	0.57	2.69	0.61	1.72	0.20	1.12	0.28	46.98	13.67	10
AM0887-MB12-MI1	Augite	Gl	δ11B pit	122.5	1548.8	83.6	17.4	329.5	11.7	555.1	29.55	60.68	6.30	22.13	4.33	1.20	3.67	0.49	2.52	0.75	2.05	0.22	2.04	0.37	42.22	12.31	10
AM0887-MB13-MI1	Augite	Gl	δ11B pit	109.8	2262.9	70.3	12.5	332.9	14.3	493.3	15.47	34.37	3.72	13.16	2.36	1.21	2.51	0.40	2.04	0.47	1.26	0.19	0.91	0.27	38.37	12.01	10
AM0887-MB17-MI1	Augite	Gl	δ11B pit	113.6	1426.8	40.5	20.1	163.2	9.4	84.0	26.93	55.89	5.75	21.61	4.17	0.27	3.13	0.51	3.53	0.68	2.28	0.31	2.27	0.38	48.21	13.76	10
1026-UA-4-MI1	Zircon	Gl	δ11B pit	107.0	526.2	92.3	40.6	50872.4	14.7	628.3	24.35	52.58	5.73	18.64	3.03	1.02	1.98	0.59	4.20	1.36	4.55	0.97	9.20	1.81	21.64	13.01	4
1026-A2-MI1	Zircon	Gl	δ11B pit	129.1	3571.1	76.9	58.4	381.7	29.4	498.4	68.92	180.11	23.17	84.55	16.49	1.88	9.78	2.03	11.29	1.72	4.45	0.74	4.28	0.40	11.21	6.29	5
1026-A3-MI1	Zircon	Gl	δ11B pit	127.9	251.7	33.4	1.3	69.7	0.6	288.7	4.81	6.11	0.51	1.68	0.19	0.23	0.25	0.04	0.38	0.07	0.17	0.04	0.34	0.03	1.19	0.43	10
1026-A5-MI1	Zircon	Gl	δ11B pit	113.0	705.2	84.9	31.6	83.2	10.7	609.4	22.69	48.80	5.13	18.63	3.75	1.65	3.89	0.76	5.61	1.09	3.24	0.52	2.55	0.66	31.12	10.52	10
1026-A6-MI1	Zircon	Gl	δ11B pit	115.1	1268.0	103.1	13.7	3838.6	11.8	886.6	18.79	39.21	4.74	16.05	3.08	1.16	1.86	0.34	2.87	0.55	1.62	0.23	1.71	0.29	13.66	8.06	4
1026-A7-MI1	Zircon	Gl	δ11B pit	172.7	661.1	79.9	15.8	121.3	9.2	525.6	24.70	53.14	5.89	23.09	3.86	1.70	3.88	0.55	3.11	0.64	1.52	0.10	0.91	0.18	25.35	6.55	10
1026-A7-MI2	Zircon	Gl	δ11B pit	121.0	660.3	166.6	9.0	1133.4	6.7	1088.4	11.90	18.37	1.71	6.54	0.86	2.03	1.15	0.18	1.65	0.49	0.75	0.09	1.13	0.20	19.16	9.29	10
1026-A9-MI1	Zircon	Gl	δ11B pit	128.8	745.2	81.6	16.7	72.1	8.4	472.9	15.24	24.76	2.05	6.48	1.00	0.63	1.10	0.23	1.78	0.53	1.66	0.31	2.10	0.36	25.99	11.08	10
1026-1-MI1	Augite	Re	δ11B pit	107.8	905.9	37.5	14.4	128.3	8.4	410.0	15.52	35.50	3.95	14.08	2.71	0.00	1.64	0.38	2.80	0.55	1.77	0.26	2.06	0.21	26.41	6.93	10
1026-2-MI1	Augite	Re	δ11B pit	111.1	1104.7	40.0	19.1	278.8	11.3	422.8	18.91	42.73	4.83	18.70	3.63	0.10	2.36	0.47	3.29	0.80	2.25	0.32	2.39	0.41	25.98	7.73	10
1036-3-MI1	Augite	Re	offset on pit	111.3	1010.4	41.9	26.7	221.6	10.0	424.8	23.50	51.53	6.09	21.87	4.21	0.60	4.47	0.74	5.50	1.07	2.76	0.38	2.42	0.43	27.00	7.47	10
1036-3-MI2	Augite	Re	new spot	82.6	1408.3	55.6	58.6	185.9	7.6	440.9	22.03	57.75	8.38	40.20	11.36	0.75	9.00	1.73	10.49	2.29	5.96	0.94	5.47	0.70	21.81	5.56	10
1026-4-MI1	Augite	Re	δ11B pit	135.4	760.3	24.8	19.6	161.4	10.3	302.6	18.05	41.19	4.66	19.23	4.00	0.27	3.14	0.49	3.75	0.65	2.07	0.26	2.01	0.31	28.60	9.75	10
1026-6-MI1	Augite	Re	δ11B pit	77.6	1635.3	85.1	43.1	244.6	10.5	547.6	37.78	96.58	12.41	53.94	11.31	0.68	8.29	1.66	8.71	1.86	5.13	0.74	5.38	0.65	27.10	7.21	10
1026-8-MI1	Augite	Re	new spot	86.2	2726.2	79.5	38.2	170.0	8.3	680.6	23.97	58.14	7.19	30.03	7.37	0.00	6.02	1.18	6.20	1.58	3.98	0.62	3.94	0.47	22.10	5.61	10
1026-8-MI2	Augite	Re	δ11B pit	132.2	1038.3	32.1	13.2	232.1	12.8	383.0	17.22	36.97	4.12	14.52	2.67	0.00	1.17	0.36	1.81	0.54	1.45	0.24	1.87	0.22	30.60	8.35	10
1026-B2-MI1	Augite	Gl	δ11B pit	114.7	845.3	71.4	15.9	222.9	8.3	597.7	23.99	50.76	5.63	21.18	4.56	1.40	3.61	0.42	3.00	0.69	2.31	0.24	1.63	0.36	26.77	6.99	5
1026-B8-MI1	Augite	Gl	new spot	121.7	1091.6	64.5	17.3	216.4	11.2	574.3	18.45	40.98	4.69	17.32	3.53	1.78	3.12	0.53	3.04	0.69	1.64	0.21	1.04	0.30	26.22	7.24	10
1026-B11-MI1	Augite	Gl	offset on pit	137.9	1102.8	52.1	26.5	219.0	9.2	356.1	28.80	66.16	7.46	27.21	4.75	1.19	4.56	0.66	4.17	0.94	2.54	0.39	2.16	0.41	32.09	8.50	10
1026-B14-MI1	Enstatite	Gl	offset on pit	135.5	1092.3	60.1	13.5	166.0	9.9	509.4	24.27	51.50	5.47	20.51	4.02	2.25	4.10	0.55	2.89	0.56	1.44	0.13	0.44	0.18	30.22	7.87	10
1026-B17-MI1	Augite	Gl	δ11B pit	128.1	1320.7	58.8	18.3	223.5	10.7	668.8	19.40	42.96	5.05	18.74	3.67	1.62	2.87	0.36	2.99	0.79	1.64	0.27	2.08	0.35	29.32	8.25	10

Sample-phenocryst-melt inclusion	Host Mineral	Melt inclusion condition	Analysis location	Trace and rare earth elements (ppm)																								# of cycles
				B	Ti	Sr	Y	Zr	Nb	Ba	La	Ce	Pr	Nd	Sm	Eu	Gd	Tb	Dy	Ho	Er	Tm	Yb	Lu	Th	U	
1026-MB2-MI2	Augite	Gl	repolished	158.2	707.4	47.2	35.8	179.7	13.1	385.0	35.66	85.92	10.15	37.02	7.07	1.20	6.21	1.01	6.45	1.25	3.81	0.47	2.99	0.52	35.94	9.66	10
1026-MB11-MI1	Enstatite	Gl	δ11B pit	157.4	1989.1	80.4	18.5	191.7	13.0	483.5	30.98	63.27	7.08	25.52	4.45	1.56	4.57	0.64	3.85	0.76	1.82	0.19	0.44	0.23	37.45	9.54	10
RF62-2-MI1	Augite	Re	δ11B pit	136.7	1204.7	102.9	27.2	219.8	10.6	513.5	23.76	53.67	6.60	26.24	6.03	0.10	3.20	0.81	4.87	1.06	3.19	0.41	3.42	0.48	31.85	15.32	10
RF62-3-MI1	Augite	Re	δ11B pit	102.7	1360.9	109.4	35.3	192.9	9.4	412.6	22.61	55.31	7.31	30.30	7.69	0.37	5.58	1.19	6.84	1.38	3.63	0.56	4.58	0.61	32.49	10.85	10
RF62-4-MI1	Augite	Re	δ11B pit	145.2	1779.1	59.6	33.0	109.2	10.1	224.1	36.78	84.01	9.48	37.99	8.03	0.37	5.21	0.88	6.00	1.22	3.42	0.48	4.41	0.45	54.09	18.06	10
RF62-7-MI1	Augite	Re	δ11B pit	186.8	496.8	34.9	7.5	80.7	5.2	81.4	12.98	25.13	2.65	9.12	2.10	0.08	0.86	0.15	1.46	0.20	1.01	0.12	1.16	0.14	56.45	20.48	10
RF62-7-MI2	Augite	Re	δ11B pit	218.0	832.7	40.6	14.6	103.9	10.3	76.6	13.57	27.90	3.49	13.52	2.77	0.10	1.61	0.38	2.71	0.50	1.99	0.21	1.91	0.22	63.45	21.10	10
RF62-8-MI1	Augite	Re	δ11B pit	160.5	464.3	73.1	31.4	119.5	10.5	307.2	24.78	57.07	7.25	28.15	6.59	0.45	3.95	0.88	5.23	1.20	3.78	0.47	3.38	0.54	61.92	22.32	10
RF62-8-MI2	Augite	Re	δ11B pit	159.8	318.8	63.1	21.2	112.0	9.3	374.9	21.84	46.71	5.41	19.77	4.53	0.01	2.18	0.65	3.26	0.80	2.50	0.35	2.31	0.35	37.27	20.08	10
RF62-9-MI1	Augite	Re	δ11B pit	62.5	2370.2	112.3	69.4	144.1	8.4	371.5	28.72	77.98	11.13	55.78	16.18	1.18	11.44	2.25	13.68	2.86	8.03	1.09	9.10	0.91	25.99	7.53	10
RF62-MB2-MI1	Augite	Gl	repolished	38.7	836.0	31.7	36.8	49.0	1.9	94.1	6.17	23.31	3.98	21.14	6.94	1.02	6.64	1.18	7.82	1.58	3.77	0.53	3.54	0.52	8.94	4.01	10
RF65-1-MI1	Augite	Gl	δ11B pit	184.4	1139.7	72.7	17.4	132.0	8.5	221.5	31.34	64.56	7.81	32.67	6.35	0.92	4.54	0.88	4.24	0.72	1.77	0.16	0.89	0.18	39.65	14.63	5

* 'Re' represents melt inclusions which have been re-homogenised and 'Gl' represents glassy melt inclusions which may include vapour/shrinkage bubbles and/or minor daughter mineral phases. The # of cycles refers to the number of analysis cycles accepted.

Appendix 3.7 Trace and rare earth element concentrations of host mineral phases determined by SIMS analysis

Sample-	Mineral	Trace and rare earth elements (ppm)																					
Grain	Phase	B	Ti	Sr	Y	Zr	Nb	Ba	La	Ce	Pr	Nd	Sm	Eu	Gd	Tb	Dy	Ho	Er	Tm	Yb	Lu	Th	U
RJ1111-4	augite	1.5	3940	24.3	39	33	0.06	0.03	3.08	11.83	2.50	15.53	5.82	1.12	5.88	1.15	6.99	1.54	3.80	0.62	3.79	0.48	0.12	0.02
ZN122-8	augite	2.8	885	154.5	66	20	0.09	34.93	8.54	38.33	7.54	42.31	11.98	1.71	12.49	2.27	12.45	2.70	6.24	0.86	5.70	0.77	0.19	0.00
ZN122-10	augite	0.7	1345	23.8	66	31	0.05	0.06	8.96	38.26	7.74	45.28	15.34	2.01	11.19	2.25	12.88	2.55	6.59	0.87	5.62	0.85	0.11	0.00
Z27-A13	zircon	0.4	1957	2.8	1238	2941	24.34	4.14	0.26	20.41	0.14	1.49	3.67	0.96	16.86	7.03	92.00	37.64	183.34	40.73	365.17	83.81	80.45	146.15
AM0887-6	augite	2.9	2690	27.0	95	66	0.06	0.27	9.85	42.59	8.74	53.11	18.29	2.29	15.76	3.10	18.10	3.72	9.22	1.31	9.55	1.24	0.50	0.02
AM0887-8	enstatite	0.5	825	0.2	16	6	0.03	0.07	0.04	0.31	0.09	0.57	0.37	0.05	0.90	0.25	1.82	0.54	2.30	0.43	4.09	0.66	0.03	0.04
1026-UA4	zircon	1.2	1905	3.2	557	1322	9.28	3.43	0.15	13.21	0.06	0.76	1.67	0.37	7.77	3.34	43.31	15.96	79.31	17.01	145.81	32.80	68.15	114.33
1026-A3	zircon	0.5	1953	3.1	840	1996	9.89	3.69	0.17	14.61	0.12	1.61	3.78	0.67	14.44	5.79	68.84	24.33	114.08	23.82	205.90	45.35	80.85	106.63
1026-A7	zircon	0.6	2113	3.4	1414	3359	13.59	3.85	0.19	15.84	0.23	4.20	6.94	1.04	28.55	10.12	115.44	41.60	184.35	35.91	288.34	61.75	158.67	189.46
1026-A9	zircon	0.8	1974	3.1	842	2000	8.43	4.31	0.18	16.19	0.13	1.70	3.39	0.62	14.60	5.88	66.77	24.74	112.95	23.52	203.03	43.29	106.83	152.46
1026-4	augite	2.0	851	16.6	132	20	0.04	0.09	11.40	57.67	11.91	75.57	26.77	1.76	20.85	4.06	26.96	5.22	13.40	2.03	11.96	1.73	0.18	0.11
1026-8	augite	2.1	1193	17.4	97	31	0.09	0.07	10.41	48.08	9.73	57.93	18.71	1.86	15.79	3.21	21.42	3.72	9.72	1.24	10.20	1.06	2.17	0.00
1026-MB2	augite	1.5	1030	14.8	126	25	0.05	0.08	12.88	61.06	12.94	70.38	24.25	1.89	22.26	4.06	25.43	4.84	12.11	1.71	10.90	1.53	0.11	0.02
RF62-7	augite	2.4	1133	23.7	99	18	0.05	0.00	10.73	50.27	10.25	59.44	21.54	1.74	17.20	3.14	20.96	3.65	9.00	1.33	8.56	1.39	0.13	0.03
RF65-1	augite	2.5	1662	25.9	88	34	0.05	0.04	10.25	46.94	9.22	54.17	17.58	1.77	14.58	2.78	18.63	3.37	8.96	1.12	7.66	1.17	0.35	0.06

Appendix 3.8 Major element concentrations for pyroxene- and zircon- hosted melt inclusions determined by EPMA

Sample	Sample-phenocryst-melt inclusion	Host mineral	Melt inclusion condition	Major elements (wt.%) SiO_2	TiO_2	Al_2O_3	FeO	MnO	MgO	CaO	Na_2O	K_2O	P_2O_5	Total	Notes
RJ1111	RJ1111-1-MI2	Augite	re-homogenised	63.25	0.81	11.14	7.48	0.15	4.32	6.88	3.70	2.46	0.16	100.4	
	RJ1111-4-MI1	Augite	re-homogenised	61.27	0.83	10.34	7.99	0.19	4.79	7.46	3.24	2.49	0.06	98.7	
	RJ1111-4-MI2	Augite	re-homogenised	67.59	0.48	12.79	4.28	0.09	2.71	5.33	3.27	3.75	0.08	100.4	
	RJ1111-6-MI1	Augite	re-homogenised	62.80	1.02	9.86	8.44	0.20	3.69	6.21	3.16	2.76	0.04	98.2	
	RJ1111-6-MI2	Augite	re-homogenised	70.09	0.61	12.32	4.47	0.11	1.86	3.88	3.67	3.92	0.06	101.0	
	RJ1111-12-MI2	Augite	re-homogenised	62.21	0.85	10.82	7.35	0.17	3.72	6.34	3.37	2.79	0.08	97.7	
	RJ1111-12-MI3	Augite	re-homogenised	63.99	0.76	10.65	6.62	0.16	3.44	5.97	3.10	3.09	0.04	97.8	
	RJ1111-MB1-MI1	Augite	glassy (±VB ± minor DM)	73.77	0.39	14.85	0.56	0.06	0.10	1.17	4.47	4.58	0.11	100.0	
	RJ1111-MB2-MI1	Augite	glassy (±VB ± minor DM)	73.57	0.44	15.05	0.52	0.05	0.09	1.32	4.88	4.30	0.26	100.5	
MQ153	**MQ153-A1-MI1**	Zircon	glassy (±VB ± minor DM)	74.65	0.04	12.75	0.60	0.00	0.01	0.02	5.39	4.81	0.01	98.3	
	MQ153-A8-MI1	Zircon	glassy (±VB ± minor DM)	76.86	0.00	12.04	0.21	0.05	0.00	0.23	3.41	5.89	0.00	98.7	
	MQ153-UA2-MI1	Zircon	glassy (±VB ± minor DM)	75.68	0.00	12.14	0.02	0.01	0.02	0.40	3.43	5.55	0.02	97.3	
	MQ153-UA3-MI1	Zircon	glassy (±VB ± minor DM)	75.22	0.04	13.58	0.35	0.01	0.01	0.08	5.06	5.30	0.00	99.6	
	MQ153-UA4-MI1	Zircon	glassy (±VB ± minor DM)	72.40	0.03	13.13	0.26	0.01	0.01	0.47	3.41	6.08	0.00	95.8	Low total
ZN122	ZN122-5-MI1	Augite	re-homogenised	68.62	0.12	9.88	2.10	0.10	2.46	4.55	2.95	4.69	0.14	95.6	Low total
	ZN122-8-MI1	Augite	re-homogenised	69.50	0.16	10.63	3.05	0.14	2.71	5.19	2.59	3.93	0.03	97.9	
	ZN122-10-MI1	Augite	re-homogenised	63.39	0.26	8.72	4.21	0.15	3.78	4.64	2.79	4.10	0.02	92.1	Low total
Z27	**Z27-A6-MI2**	Zircon	glassy (±VB ± minor DM)	74.78	0.19	11.73	1.46	0.03	0.28	0.78	3.24	5.48	0.01	98.0	
	Z27-A12-MI1	Zircon	glassy (±VB ± minor DM)	74.70	0.16	12.44	0.46	0.00	0.00	0.47	3.77	5.46	0.02	97.5	
	Z27-A12-MI2	Zircon	glassy (±VB ± minor DM)	72.90	0.09	13.31	0.57	0.00	0.03	0.57	4.45	5.28	0.03	97.2	
	Z27-A13-MI1	Zircon	glassy (±VB ± minor DM)	75.91	0.07	13.32	0.50	0.00	0.09	0.50	4.15	5.28	0.02	99.9	
	Z27-UA1-MI1	Zircon	glassy (±VB ± minor DM)	75.25	0.08	13.83	0.37	0.00	0.04	0.57	3.80	5.50	0.04	99.5	
	Z27-UA2-MI1	Zircon	glassy (±VB ± minor DM)	78.34	0.19	14.05	0.43	0.01	0.09	0.81	3.23	4.95	0.00	102.1	High total

	Z27-UA3-MI1	Zircon	glassy (±VB ± minor DM)	76.15	0.31	14.30	0.29	0.02	0.00	0.01	3.76	5.63	0.03	100.5	
	Z27-UA4-MI1	Zircon	glassy (±VB ± minor DM)	75.14	0.04	13.36	0.25	0.02	0.10	0.31	4.01	5.46	0.02	98.7	
AM0887	AM0887-6-MI2	Augite	re-homogenised	69.49	0.39	12.44	1.18	0.07	1.60	3.07	3.36	4.83	0.04	96.5	Low total
	AM0887-10-MI1	Augite	re-homogenised	75.57	0.29	13.32	0.60	0.03	0.08	1.15	3.58	4.09	0.04	98.8	
	AM0887-10-MI2	Augite	re-homogenised	71.30	0.34	12.52	1.15	0.06	1.30	2.51	3.11	4.69	0.04	97.0	
	AM0887-15-MI3	Augite	re-homogenised	72.02	0.42	11.45	3.29	0.07	1.74	3.01	3.33	4.41	0.04	99.8	
	AM0887-16-MI1	Enstatite	re-homogenised	72.02	0.42	11.45	3.29	0.07	1.74	3.01	3.33	4.41	0.04	99.8	
	AM0887-17-MI1	Augite	re-homogenised	64.34	0.34	12.19	3.62	0.14	4.36	6.31	3.43	2.92	0.15	97.8	
	AM0887-MB2-MI1	Enstatite	glassy (±VB ± minor DM)	75.21	0.43	13.46	1.29	0.03	0.03	0.85	3.89	5.15	0.05	100.4	
	AM0887-MB5-MI1	Augite	glassy (±VB ± minor DM)	72.93	0.20	13.60	0.37	0.04	0.05	0.60	3.83	5.45	0.04	97.1	
	AM0887-MB6-MI1	Augite	glassy (±VB ± minor DM)	73.67	0.34	14.11	0.21	0.02	0.00	0.75	4.00	5.29	0.05	98.4	
	AM0887-MB9-MI1	Augite	glassy (±VB ± minor DM)	74.40	0.20	13.57	0.49	0.03	0.00	0.59	3.64	5.83	0.03	98.8	
	AM0887-MB13-MI2	Augite	glassy (±VB ± minor DM)	74.43	0.43	13.30	0.44	0.02	0.01	0.34	3.88	6.09	0.04	99.0	
1026	**1026-1-MI1**	Augite	re-homogenised	68.04	0.27	9.05	5.03	0.16	4.31	6.69	2.40	3.51	0.01	99.5	
	1026-3-MI1	Augite	re-homogenised	72.91	0.19	11.91	2.10	0.06	1.51	3.02	2.82	4.83	0.02	99.4	
	1026-4-MI1	Augite	re-homogenised	74.41	0.14	12.08	1.19	0.06	0.97	2.38	2.54	5.27	0.02	99.1	
	1026-7-MI1	Augite	re-homogenised	74.18	0.14	11.15	1.84	0.06	1.03	2.66	2.51	5.14	0.03	98.7	
	1026-8-MI1	Augite	re-homogenised	65.99	0.40	9.12	6.99	0.16	3.77	6.22	2.44	3.72	0.02	98.8	
	1026-13-MI1	Augite	re-homogenised	75.10	0.14	12.13	0.71	0.04	0.70	1.96	2.81	5.60	0.02	99.2	
	1026-13-MI2	Augite	re-homogenised	76.01	0.18	12.44	0.64	0.04	0.61	2.05	2.96	5.16	0.03	100.1	
	1026-13-MI3	Augite	re-homogenised	74.02	0.14	11.88	0.90	0.06	1.31	2.87	2.83	4.85	0.03	98.9	
	1026-B11-MI1	Augite	glassy (±VB ± minor DM)	76.70	0.15	12.26	0.36	0.03	0.01	0.67	2.87	5.62	0.01	98.7	
	1026-B11-MI2	Augite	glassy (±VB ± minor DM)	76.85	0.14	12.19	0.51	0.03	0.03	0.76	3.07	5.54	0.02	99.1	
	1026-B14-MI1	Enstatite	glassy (±VB ± minor DM)	74.50	0.17	11.74	3.39	0.09	1.34	0.64	2.88	5.21	0.03	100.0	
	1026-B17-MI1	Augite	glassy (±VB ± minor DM)	74.74	0.24	11.94	0.48	0.03	0.02	0.50	3.38	5.82	0.02	97.2	
	1026-MB2-MI2	Augite	glassy (±VB ± minor DM)	76.83	0.14	12.74	0.70	0.04	0.01	0.73	3.30	5.78	0.01	100.3	
	1026-A2-MI1	Zircon	glassy (±VB ± minor DM)	74.91	0.12	12.84	0.12	0.00	0.00	0.33	4.05	5.81	0.01	98.2	

	1026-A3-MI1	Zircon	glassy (±VB ± minor DM)	70.53	0.09	16.60	0.47	0.00	0.12	0.82	4.40	7.55	0.00	100.6	
	1026-A5-MI1	Zircon	glassy (±VB ± minor DM)	74.28	0.09	12.87	0.24	0.00	0.01	0.50	3.39	5.43	0.03	96.8	Low total
	1026-A7-MI1	Zircon	glassy (±VB ± minor DM)	75.61	0.09	13.13	0.15	0.01	0.00	0.32	3.07	5.86	0.02	98.2	
	1026-A9-MI2	Zircon	glassy (±VB ± minor DM)	75.05	0.15	13.24	0.13	0.01	0.02	0.29	3.28	5.79	0.01	98.0	
	1026-A11-MI1	Zircon	glassy (±VB ± minor DM)	66.94	0.00	19.95	0.56	0.00	0.01	1.59	6.82	5.03	0.02	100.9	
	1026-UA1-MI1	Zircon	glassy (±VB ± minor DM)	74.99	0.11	13.15	0.35	0.00	0.00	0.44	3.58	5.56	0.03	98.2	
	1026-UA3-MI1	Zircon	glassy (±VB ± minor DM)	73.71	0.04	12.38	0.32	0.00	0.02	0.63	3.61	5.87	0.02	96.6	Low total
RF62	RF62-3-MI1	Augite	re-homogenised	63.80	0.32	10.62	3.72	0.11	2.59	4.87	3.03	4.24	0.03	93.3	Low total
	RF62-5-MI1	Augite	re-homogenised	64.23	1.70	8.24	6.18	0.10	3.13	6.31	2.37	4.03	0.67	96.9	Low total
	RF62-7-MI2	Augite	re-homogenised	63.63	0.17	10.40	5.44	0.18	3.09	6.12	2.32	4.16	0.01	95.5	Low total
	RF62-8-MI2	Augite	re-homogenised	68.69	0.16	10.40	2.35	0.10	2.96	4.99	2.97	4.53	0.00	97.1	
	RF62-9-MI1	Augite	re-homogenised	64.10	0.34	10.06	5.19	0.15	4.29	7.06	3.05	3.52	0.21	98.0	
	RF62-MB2-MI1	Augite	glassy (±VB ± minor DM)	74.86	0.05	13.69	0.38	0.02	0.01	0.56	3.39	6.67	0.03	99.7	
RF65	**RF65-MB3-MI1**	Augite	glassy (±VB ± minor DM)	71.32	0.12	11.77	1.42	0.14	2.21	4.38	2.84	4.82	0.02	99.0	

Boron concentrations and boron isotopic compositions have been determined for the melt inclusions highlighted in bold.

Appendix 3.9 An evaluation of the effects of melt inclusion re-homogenisation

3.9.1 The requirement for melt inclusion re-homogenisation

Melt inclusions are small droplets (~1 - 300 μm) of silicate melt which are trapped within igneous phenocrysts as they crystallise (Sorby, 1858). They provide a useful tool with which to investigate magmatic processes as the surrounding host mineral protects the trapped melt inclusion from late stage processes occurring in the melt, such as degassing. Therefore, the composition of the melt inclusion reflects the composition of the melt at the time of crystallisation (e.g., Roedder, 1979; Roedder, 1984; Lowenstern, 1995; Sobolev, 1996; Lowenstern, 2003; Schiano, 2003). At the time of entrapment the majority of melt inclusions contain only one phase, a silicate melt, however some melt inclusions undergo post-entrapment modifications. These modifications include, the crystallisation of the host mineral phase onto the melt inclusion wall, the formation of a shrinkage bubble or a vapour bubble containing volatiles originally dissolved in the melt, and/or the partial or complete crystallisation of the melt inclusion (e.g., Sorby, 1858; Roedder, 1979; Roedder, 1984). The extent of these post-entrapment modifications relates to the pressure-temperature path of the melt inclusion prior to and during natural quenching. For example, rapidly crystallised and erupted material usually contains a higher proportion of glassy melt inclusions, while slowly cooled deposits contain more crystalline melt inclusions (e.g., Frezzotti, 2001 and references therein). Where a melt inclusion shows evidence of post-entrapment modifications, heating is required to return the melt inclusion to its original state as a homogeneous melt. This is followed by rapid quenching in order to obtain a homogeneous glass for microanalysis.

The majority of melt inclusions present in magmatic rock samples, analysed as part of this study, show evidence for post-entrapment modifications with the presence of

daughter mineral phases, vapour bubbles and devitrified glass. On this basis, melt inclusions hosted in pyroxene were re-homogenised using a Linkam TS1400XY heating stage (Appendix 3.1.3). The temperatures at which re-homogenisation was achieved are presented in Table 4.2 (Chapter 4).

3.9.2 Potential effects of the heating process

A microscope mounted heating stage is designed to allow careful observation and monitoring of the melt inclusion during heating and to enable the melt inclusion to be quenched as soon as all the mineral phases have disappeared into the melt. This is to prevent overheating and equilibration between the melt and the host mineral. Although this method was used in this study there is some evidence to suggest partial equilibration between the melt and the host mineral. Major, trace and rare earth element concentrations obtained for some re-homogenised melt inclusions are indicative of the melting and incorporation of the host mineral into the melt (Figure A3.4). It is possible that this represents the melting of the host mineral phase crystallised onto the melt inclusion wall during natural cooling, in which case the composition of the re-homogenised melt inclusion would be representative of the trapped melt composition. However, differentiating between this process and the melting of the host phenocryst is extremely difficult, as (1) the mineral crystallised onto the melt inclusion wall is optically indistinguishable from the host phenocryst, and (2) they are compositionally identical (Danyushevsky et al., 2002). On this basis the reliability of certain major, trace and rare earth element concentrations (i.e. those compatible in pyroxene) obtained for re-homogenised melt inclusions is questionable.

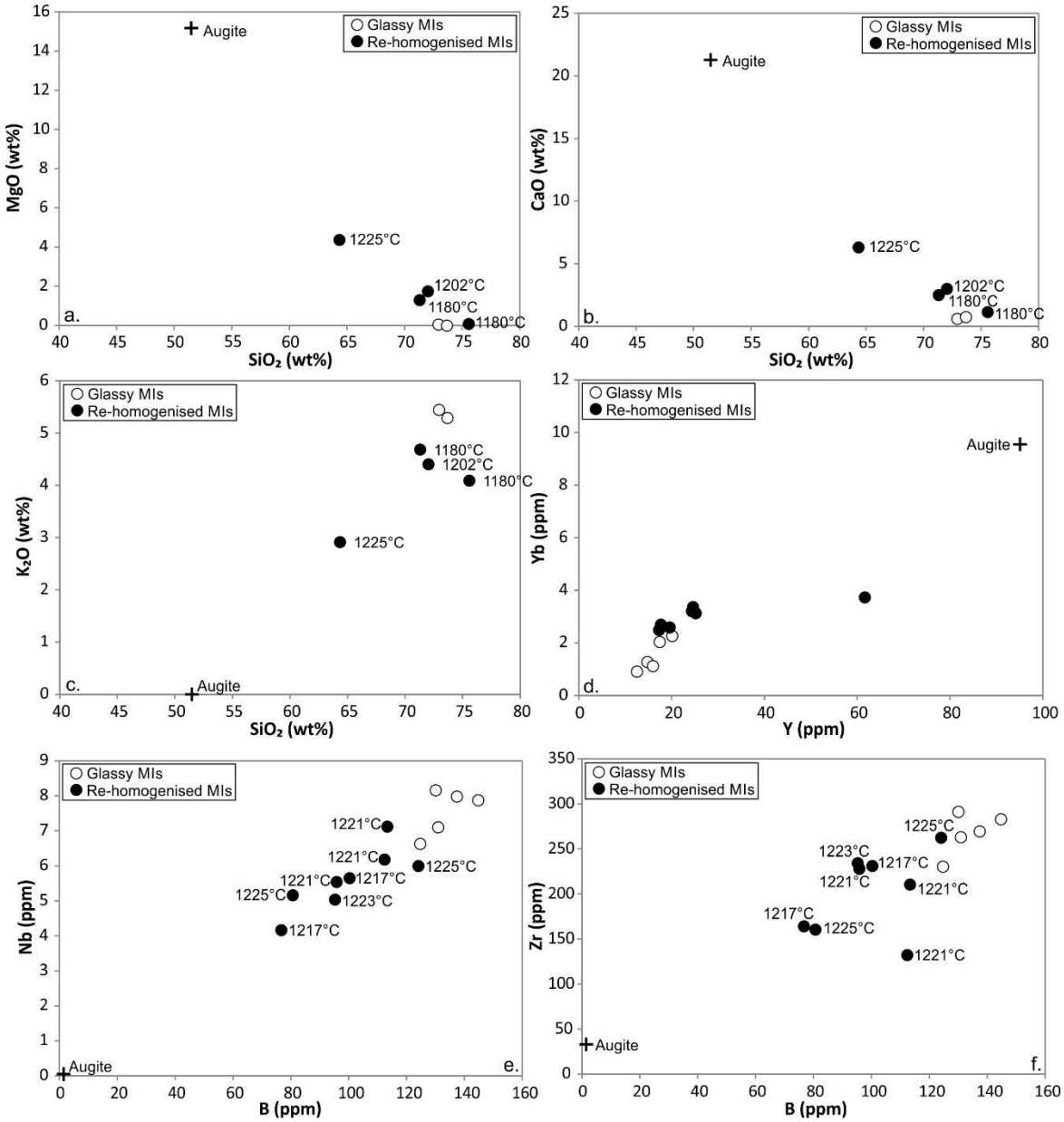

Figure A3.4. Compositions of glassy and re-homogenised melt inclusions demonstrating potential equilibration between the melt and the host mineral phase as a result of the re-homogenisation process. a and b) Increasing concentrations of MgO (wt.%) and CaO (wt.%) and decreasing concentrations of SiO_2 (wt.%) are shown to relate to increasing temperatures of re-homogenisation. This is indicative of increased equilibration between the melt inclusions and the host mineral phase (augite) at higher temperatures. The data presented is from sample AM0887 and the composition of the host aguite is also shown. c) Decreasing concentrations of K_2O (wt.%) and SiO_2 (wt.%) observed with increasing re-homogenisation temperatures. Potassium is incompatible in augite and therefore equilibration between the silicate melt and the host augite would lead to dilution of the K_2O content in the melt inclusion. Data obtained for sample AM0887. d) A plot of Y vs. Yb (ppm)

(compatible elements in augite) showing the higher concentrations obtained for re-homogenised melt inclusion compared to glassy, unheated melt inclusions from sample AM0887. This could reflect equilibration between the melt inclusion and the host mineral phase during heating. e and f) Plots of B vs. Nb and B vs. Zr (ppm) for both glassy and re-homogenised melt inclusions hosted in augite from sample RJ1111, showing that lower concentrations were obtained for the re-homogenised melt inclusions. This can be attributed to dilution due to the addition of material which doesn't contain B, Nb and Zr to the melt. As these elements are incompatible in augite, the host mineral phase is a potential source of dilution. Alternatively the melting of daughter mineral phases present in the devitrified melt inclusions also could account for the dilution. No correlation is observed between the temperature of re-homogenisation and the concentrations of B, Nb and Zr.

3.9.3 The reliability of trace element concentrations obtained for re-homogenised melt inclusions

Certain analysed elements are incompatible in pyroxene and therefore are only likely to be present in the melt inclusion. These elements include B, Sr, Zr, Nb, Ba, U and Th. Analysis of the host mineral phases confirms the low concentrations of these elements in augite and enstatite phenocrysts (Appendix 3.7). On this basis, the concentrations of these elements obtained for re-homogenised melt inclusions are considered likely to reflect the original composition of the trapped melt. In order to account for the differences between glassy and re-homogenised melt inclusions (Fig. A3.4 e and f) these elements are primarily presented as ratios (e.g., B/Nb, B/Zr, Chapter 4).

The concentrations of elements obtained for re-homogenised melt inclusions, which are compatible in pyroxene (e.g., Y and the REEs), are considered unreliable due to the potential effects of partial equilibration between the melt inclusion and the pyroxene host during heating. A number of methods were implemented to try and correct for the effects of the re-homogenisation process, but these proved unsuccessful. This was partially due to problems differentiating between the melting of pyroxene crystallised from the trapped melt onto the melt inclusion walls, and additions from the host phenocryst. As a result, only certain elements

have been included in the interpretation of the melt inclusion data presented in Chapter 4.

Appendix 3.10 References

Coakley, K.J., Simons, D.S., and Leifer, A.M., 2005, Secondary ion mass spectrometry measurements of isotopic ratios: correction for time varying count rate: International Journal of Mass Spectrometry, v. 240, p. 107-120.

Danyushevsky, L.V., McNeill, A.W., and Sobolev, A.V., 2002, Experimental and petrological studies of melt inclusions in phenocrysts from mantle-derived magmas: an overview of techniques, advantages and complications: Chemical Geology, v. 183, p. 5-24.

Esposito, R., Klebesz, R., Bartoli, O., Klyukin, Y.I., Moncada, D., Doherty, A.L., and Bodnar, R.J., 2012, Application of the Linkam TS1400XY heating stage to melt inclusion studies: Central European Journal of Geosciences, v. 4, p. 208-218.

Frezzotti, M.-L., 2001, Silicate-melt inclusions in magmatic rocks: applications to petrology: Lithos, v. 55, p. 273-299.

Hayward, C., 2012, High spatial resolution electron probe microanalysis of tephras and melt inclusions without beam-induced chemical modification: The Holocene, v. 22, p. 119-125.

Jochum, K.P., and Nohl, U., 2008, Reference materials in geochemistry and environmental research and the GeoReM database: Chemical Geology, v. 253, p. 50-53.

Jochum, K.P., Wilson, S.A., Abouchami, W., Amini, M., Chmeleff, J., Eisenhauer, A., Hegner, E., Iaccheri, L.M., Kieffer, B., and Krause, J., 2011, GSD-1G and MPI-DING Reference Glasses for In Situ and Bulk Isotopic Determination: Geostandards and Geoanalytical Research, v. 35, p. 193-226.

Lowenstern, J.B., 1995, Applications of silicate-melt inclusions to the study of magmatic volatiles, *in* Thompson, J.F.H., ed., Magmas, Fluids and Ore Deposits, Volume 23, Mineralogical Association Canada Short Course, p. 71 - 99.

Lowenstern, J.B., 2003, Melt inclusions come of age: volatiles, volcanoes, and Sorby's legacy, *in* De Vivo, B., and Bodnar, R.J., eds., Melt Inclusions in Volcanic Systems: Methods, Applications and Problems, Volume 5: Amsterdam, Elsevier, p. 1 - 22.

Oskarsson, N., and Hansteen, T.H., 1992, The use of graphite for the removal of oxygen from nitrogen purge gas in high temperature microthermometry using the Linkam TH1500 stage: European Journal of Mineralogy, v. 4, p. 865-871.

Roedder, E., 1979, Origin and significance of magmatic inclusions: Bull. Mineral., v. 102, p. 487-510.

Roedder, E., 1984, Fluid Inclusions: Reviews Mineral., v. 12, p. 644.

Schiano, P., 2003, Primitive mantle magmas recorded as silicate melt inclusions in igneous minerals: Earth-Science Reviews, v. 63, p. 121-144.

Sobolev, A.V., 1996, Melt Inclusions in Minerals as a Source of Principle Petrological Information: Petrology, v. 4, p. 209 - 220.

Sorby, H.C., 1858, On the Microscopical, Structure of Crystals, indicating the Origin of Minerals and Rocks: Quarterly Journal of the Geological Society, v. 14, p. 453-500.

Thomas, J.B., and Bodnar, R.J., 2002, A technique for mounting and polishing melt inclusions in small (< 1 mm) crystals: American Mineralogist, v. 87, p. 1505-1508.